Molecular tagging velocimetry in rarefied and confined gas flows

Dominique Fratantonio

Université Fédérale

Toulouse Midi-Pyrénées

THÈSE

En vue de l'obtention du

DOCTORAT DE L'UNIVERSITÉ DE TOULOUSE

Délivré par :

Institut National des Sciences Appliquées de Toulouse (INSA de Toulouse)

Présentée et soutenue par :
Dominique FRATANTONIO
le vendredi 18 janvier 2019

Titre :

Molecular tagging velocimetry in rarefied and confined gas flows

---

École doctorale et discipline ou spécialité :
ED MEGEP : Mécanique, Energétique, Génie civil & Procédé

Unité de recherche :
Institut Clément Ader (ICA)

Directeur/trice(s) de Thèse :

Stéphane COLIN & Marcos ROJAS-CARDENAS

Jury :
Gian Luca MORINI, Professor at Università di Bologna, Rapporteur
Salvador MONTERO, Professor Emeritus at IEM-CSIC de Madrid, Rapporteur
Annie COLIN, Professor at ESPCI de Paris, Examinateur
Irina GRAUR, Professor at Université d'Aix-Marseille, Examinateur
Aldo FREZZOTTI, Professor at Politecnico di Milano, Examinateur
Christine BARROT, Maître de conférences at IUT-GMP de Toulouse, Examinateur
Stéphane COLIN, Professeur at INSA de Toulouse, Directeur de thèse
Marcos ROJAS-CARDENAS, Maître de conférences at INSA de Toulouse, Co-directeur de thèse

A Minù, Gioacchino, Giada e Yanick.

- ♥ ♠ ♣ ♦ -

Acknowledgments

This work would have not been possible without the emotional and scientific support of many. During 3 years in Toulouse, the number of people that contributed to make me grow up in different ways is huge. If your name does not figure out in these pages, although you contributed to the occurrence of this work, forgive me. My brain has a very limited memory size and random selectivity.

Firstly, big thanks to the member of the jury, Prof. Annie Colin, Prof. Irina Graur, Prof. Salvador Montero, Prof. Gianluca Morini, and Prof. Aldo Frezzotti, for having been present at my Ph.D. defense and for having carefully read this manuscript.

Thanks to my Ph.D. and life supervisor, Stéphane Colin and Marcos Rojas-Cardenas, who have played the role of chiefs, fathers, and brothers. Chiefs, because during the development of this project, they have been able to understand when it was necessary to guide me and help me and when it was the moment to give me freedom and to give space to my personal creativity. Fathers, for being supportive and understanding in my personal (sometimes slightly dramatic) matters. Brothers, for all the laughs and the beers.

Thanks to the whole microfluidic team, for their help and friendship. Christine Barrot, Pascal Magaud, Lucien Baldas, Ahmad Batik, Batul Batik, Nicolas Laurien, Gamin, Hacene Si-Hadj Mohand, Daniel Mariuta, Thome Thome, Georges Chabouh (booob habibi mi fra), Georges Saliba, Shiqi, Jie Chien, Yan Feng, Rodrigo (yooooo man!).

Thanks to Ernane, my first office mate, who knows everything about football and the names of all possible comestible parts of animals. Our common inability to speak French and curiosity towards the unknown help us to drastically improved outselves. Cada enxadada uma miñoca, my friend.

Thanks to the whole ICA group, in particular Dong Hai, Jim, Florian, Vivien, Léonard, Fu Jiang, Iwey, Louis, Geneviève, Laure, Simon, Adama, Alexandra, Landry, Colo, Wafaa, Montassar, Amin, Ange, Yann.

Thanks to all people of the MIGRATE project for the great conference meetings and the amazing time all over Europe.

Special thanks to Prof. Stefan Stefanov and Elena Miteva for being such good hosts during my Bulgarian experience. In Sofia, I could learn a lot about DSMC, Bulgarian culture, and the art of drinking Rakija: “You need to drink in big quantities, but slowly.”

Other special thanks to M. Cedric Degouet from LaVision, for the constant assistance, for his excellent professionality and for sharing with me crucial knowledge which helped me better understanding CCD cameras and laser systems.

Thanks to the Spanish dream team, Javier, Alejandro, Samu (un giorno all'improvviso!), Lopez, Guillermo, David, for the crazy time in Toulouse and in Benicassim, and for introducing me to climbing.

Thanks to Sara Bessegato, who allowed me to experience a wide spectrum of emotions, some of which unknown to me until a couple of years ago, and who helped me knowing better myself, my qualities, and my defects.

Guillermo Lopez Quesada, known as El Diablo. Crazy man and great friend. He made me be wiser and more stupid at the same time. We grew up together. Our intellectual growth spike is represented by the Tequila Suicide, a secret knowledge that all the world envies us. I will never forget all our night (hetero) adventures in Shanghai, because I have nothing to forget. I actually do not remember a thing. I still do not know where Shanghai is. It was something like l'Isla de Muerte: you cannot find it if you do not get lost both physically and spiritually. Gracias hermano.

Thanks to dude! Varun Yeachana, who has been at my side during most of the experimental work and with who I shared very good times in Sofia and Greece (with Shiqi as well!!). I saw him growing up during these 3 years, from a shy, mind-chained dude to an unleashed crazy animal party guy who now is a free man.

Thanks to Irene Lbeas, for the nightly kebab and champagne, and to Giorgios Tatsios, the reason why now I remember by heart the most important phone number, 0534674176.

Thanks to Julien Cochet, who let me discover something that I did not know was still truly existing in our times. The first time I saw him performing magic, I was speechless. I still remember that feeling of not having a clue of what just happened in front of my eyes, that mixed excitement of surprise and hope that the impossible was indeed possible in a world full of disenchanted people overwhelmed by progress and technology. Thanks to Julien, I now have the privilege of seeing again and reproducing those same feelings in the faces of all the persons to whom I perform magic tricks. The real magic happens in the eyes of the people.

Merci à Carole Dautel, femme incroyable d'une bonté sans limite. Merci pour avoir été toujours présente et prête à m'aider en cas de besoin. Tu as été comme une mère pour moi. Merci mon amie. Je te souhaite le mieux, à toi et à tes fils.

Grazie infinite Francesco De Giorgi e Silvio Akitani. Amici miei, nonostante la mia ripetutata mancata partecipazione alla vita notturna Tolosana, mi avete sempre supportato, constantemente e incondizionatamente, in qualsiasi mia scelta di vita, giusta o sbagliata che sia, come due veri fratelli. I più grandi bomber che abbia mai

incontrato, con una grande mente perversamente geniale e con un cuore ancora più grande. Grazie ragazzi, grazie altrettanto.

Thanks to Maria Giselle Fernandez, for her love and her support in the last year of my Ph.D. The writing of this manuscript has been much sweeter with her constant presence at my side. Thanks to her, I could trace the route of the next steps of my journey. Regardless of future events, she will always have a special place in my heart. Gracias de todo, mi pupi.

Finally, thanks to my always present superheroes. My mother Minù, my father Gioacchino, and my brothers, Giada and Yanick. These four magicians ♥, ♠, ♣, ♦ and their unconditional love have never stopped surprising me.

Because of all these people, now I am better scientist and a better person.

Sincerely,

Dominique

Abstract

Molecular tagging velocimetry (MTV) is an optic experimental technique widely employed for measuring the velocity field in fluid flows. The measuring principle is based on the tracking of molecules able to emit light in response to a laser excitation. By seeding the flow with this tracer, local velocity measurements can be carried out by following the displacement of the emitting molecules. While this technique has already been successfully applied in liquid and gas flows, the application to rarefied and confined gas flows is still a challenge due to the high molecular diffusion and the low emitted light from the tracer at low pressures. The interest in applying MTV in rarefied conditions derives from the absence of local experimental data that can allow a better understanding on the mechanisms of interaction between the gas molecules and the wall surface. Theoretical and numerical analysis predicted a non-zero velocity at the wall, which has been, up to now, only indirectly measured by means of global quantities, such as the mass flow rate in microchannel flows. In this work, an experimental analysis of the intensity and lifetime of the photoluminescence of the molecular tracers employed, i.e., acetone and diacetyl, is presented. This study revealed the importance of the triplet-triplet annihilation phenomenon in determining the observed phosphorescence decay. Moreover, this analysis allowed to estimate the best working conditions for applying MTV to rarefied gas flows. Thus, MTV has been applied to gas-tracer mixtures at low pressures in a millimetric rectangular channel producing the first gas flow visualizations in the slip flow regime and the first preliminary measurements of the slip velocity at the wall.

Keywords: Molecular tagging velocimetry, rarefied gas flows, slip velocity, acetone, diacetyl, phosphorescence, molecular diffusion, DSMC, triplet-triplet annihilation.

Résumé

Le marquage moléculaire est une technique expérimentale permettant d'effectuer de manière peu intrusive de la vélocimétrie au sein des écoulements. La mesure est basée sur le suivi de molécules capable d'émettre de la lumière suite à une excitation par une source laser. La mesure locale de vitesse est alors déduite de la visualisation du déplacement des molécules traceuses. Bien que la vélocimétrie par marquage moléculaire (MTV) ait déjà été utilisée avec succès pour des écoulements liquides ou gazeux, son application à des écoulements gazeux raréfiés internes reste encore un défi en raison de la diffusion moléculaire élevée et de la faiblesse de l'émission lumineuse à basse pression. Néanmoins, pouvoir appliquer la MTV en condition de gaz raréfié est particulièrement intéressant du fait du manque de données expérimentales locales nécessaires à une meilleure compréhension des mécanismes d'interaction moléculaire entre le gaz et une surface solide. Les analyses théoriques et numériques mettent en évidence une vitesse non nulle à paroi, qui, jusqu'à maintenant, a pu être quantifiée expérimentalement uniquement de manière indirecte, par des mesures de quantités globales telles que le débit massique à travers des microcanaux. Dans ce travail, une étude expérimentale a été menée sur l'intensité et le temps de vie de la photoluminescence des traceurs moléculaires utilisés, à savoir l'acétone et le diacétyle vapeurs. Cette étude a démontré l'importance du processus d'annihilation triplet-triplet sur l'émission phosphorescente expérimentalement observée. En outre, cette analyse a permis d'estimer les conditions expérimentales optimales pour l'application de la MTV aux gaz raréfiés. Ainsi, la MTV a été appliquée à des écoulements de mélanges gaz-traceur à basses pressions dans un canal millimétrique de section rectangulaire, fournissant ainsi les premiers résultats de vélocimétrie en régime d'écoulement légèrement raréfié.

Mots clés: Vélocimétrie par marquage moléculaire, écoulements gazeux raréfiés, acétone, diacétyle, phosphorescence, DSMC, annihilation triplet-triplet.

Table of Contents

Roman letters

A	Area of the channel section	[m^2]
A_θ	Langmuir adsorption equation coefficient	[-]
$A_{n,m}$	Fourier coefficients for 2D velocity profile	[-]
a	Channel aspect ratio	[-]
a_i	Fitting coefficients	[-]
B	Coefficient	[-]
b	Channel width	[m]
A_{ads}, B_{ads}	Calibration coefficients for PSMF	[-]
C_1, C_2	Slip velocity boundary condition coefficients	[-]
C_f	Friction coefficient	[-]
C_{ICCD}	Gain conversion coefficient	[-]
c	Speed of light	[m s^{-1}]
$\bar{\boldsymbol{c}}$	Mean gas velocity	[m s^{-1}]
$\boldsymbol{c}$	Molecular velocity vector	[m s^{-1}]
$\boldsymbol{c}_r$	Relative molecular velocity	[m s^{-1}]
$\overline{c'}$	Mean thermal speed	[m s^{-1}]
c_i	Polynomial coefficient of pressure distribution	[-]
c_C	High-order slip boundary condition coefficient	[-]
c_s	Speed of sound	[m/s]
c_p	Specific heat at constant pressure	[J kg^{-1} K^{-1}]
c_V	Specific heat at constant volume	[J kg^{-1} K^{-1}]
D	Diffusion coefficient	[m^2 s^{-1}]
D_{ii}	Self-diffusion coefficient	[m^2 s^{-1}]
D_{ij}	Mutual-diffusion coefficient	[m^2 s^{-1}]
D_{eff}	Effective diffusion coefficient	[m^2 s^{-1}]
D_l	Laser beam diameter (FWHM)	[m]
D_h	Hydraulic diameter	[m]
$D_{o,1}$	Primary Nikkor objective aperture	[m]
$D_{o,2}$	Secondary Nikkor objective aperture	[m]
D_p	Diameter of gas circuit component	[m]
d	Molecular diameter	[m]
d_{cyl}	Cylinder diameter	[m]
d_f	Focal distance of the objectives	[m]

$d_{o,1}$	Distance between the two objective lenses	[m]
$d_{o,2}$	Distance between the lens and the photocathode	[m]
d_{pip}	Pipette diameter	[m]
E_{ph}	Photon energy	[J]
E_l	Average laser energy	[J]
E_{S_0}	Energy level in the ground singlet state	[J]
E_{S_0-0}	Lowest energy level in the ground singlet state	[J]
$\Delta E_{thermal}$	Thermal energy stored in roto-vibrational modes	[J]
F	Force	[N]
F_V	Volume force	[N]
F_S	Surface force	[N]
f	Lens focal length	[m]
f_1	Primary Nikkor objective focal length	[m]
f_2	Secondary Nikkor objective focal length	[m]
$f/\#$	f-number of a lens	[-]
f_l	Focal length of the focusing lens	[m]
f_w	Wall function for high-order slip boundary condition	[-]
G	IRO gain	[-]
g	Input signal to a linear system	[-]
H	Channel height	[m]
H_{MTV}	Channel height used for velocity reconstruction	[m]
h	Plank constant	[-]
I_0	Initial emission rate	[ph s^{-1}]
I_{in}	Laser energy density	[ph m^{-2}]
I_f	Fluorescence emission rate	[ph s^{-1}]
I_{ph}	Phosphorescence emission rate	[ph s^{-1}]
$\boldsymbol{J}$	Diffusive flux	[m^{-2} s^{-1}]
J_{in}	Laser irradiance	[J $m^{-2}s^{-1}$]
K_Q	Quenching rate constant	[s^{-1}]
K_c	Head losses due to sudden section contraction	[-]
K_e	Head losses due to sudden section expansion	[-]
k_B	Boltzmann constant	[m^2 kg s^{-2} K^{-1}]
k_f	Fluorescence emission rate constant	[s^{-1}]
k_{ph}	Phosphorescence emission rate constant	[s^{-1}]

$k_{ph,tot}$	Radiative and internal non-radiative processes rate constant	[s^{-1}]
k_{TTA}	Triplet-triplet annihilation rate constant	[$m^3\ s^{-1}$]
k_{ISC}	Intersystem crossing rate constant	[s^{-1}]
k_r	Radiative de-excitation rate constant	[s^{-1}]
k_{nr}	Non-radiative de-excitation rate constant	[s^{-1}]
k_{nr,T_1}	Internal non-radiative rate constant in the triplet state	[s^{-1}]
k_{vr}	Vibrational-relaxation rate constant	[s^{-1}]
k_Q	Quenching rate constant per quencher molecule density	[$m^3\ s^{-1}$]
k_λ	Mean free path coefficient	[-]
L	Channel length	[m]
L_o	Image on the focal plane of the objectives	[m]
L'_o	Image on the focal plane of the objectives	[m]
L_c	Characteristic length	[m]
L_x, L_y	Field of view dimensions	[m]
L_p	Length of gas circuit component	[m]
Δl	Displacement	[m]
ℓ	Optical length of medium	[m]
M	Molar mass	[kg mol^{-1}]
M^2	M square of the laser beam	[-]
m	Molecular mass	[kg]
m_b	Mass of the empty bottle	[kg]
m_{b,H_2O}	Mass of the bottle filled with water	[kg]
m_g	Mass of gas	[kg]
$\dot{m}$	Mass flow rate	[kg s^{-1}]
m_e	Magnification factor of the external optics	[-]
m_{ICCD}	Total magnification factor of ICCD	[-]
m_i	Magnification factor of the internal optics	[-]
N	Number of molecules	[-]
N_{S_1}	Number of singlet molecules	[-]
N_{T_1}	Number of triplet molecules	[-]
N_c	Number of counts	[-]
N_{coll}	Number of collisions	[-]
N_{ex}	Number of excited molecules	[-]
N_{e^-}	Number of electrons	[-]

N_i	Number of averaged images	[-]
N_l	Number of laser pulses per image	[-]
$N_{n,m}$	Fourier coefficients for 2D velocity profile	[-]
N_{ph}	Number of photons	[-]
N_v	Number of vibrational modes	[-]
n	Molecular density	[m^{-3}]
n_{ex}	Molecular density of excited molecules	[m^{-3}]
n_Q	Molecular density of quenching species	[m^{-3}]
n_{S_1}	Molecular density of singlet molecules	[m^{-3}]
n_{T_1}	Molecular density of triplet molecules	[m^{-3}]
$n_{T_1,y}$	Number of triplet molecules per unit length	[m^{-1}]
P	Perimeter of the channel section	[m]
p	Pressure	[Pa]
p_{in}	Inlet pressure	[Pa]
p_{out}	Outlet pressure	[Pa]
Δp	Inlet-outlet pressure difference	[Pa]
Δp_c	Head losses due to sudden section contraction	[Pa]
Δp_e	Head losses due to sudden section expansion	[Pa]
Δp_d	Distributed head losses	[Pa]
p_1, p_2, p_3, p_4	Pressure from sensor 1, 2, 3, and 4	[Pa]
p_c	Pressure at the central section along the channel length	[Pa]
p_{cr}	Critical pressure	[Pa]
$\langle p_Q \rangle$	Probability of molecular quenching	[-]
$\langle p_{vr} \rangle$	Probability of vibrational-relaxation	[-]
Q_{CCD}	Quantum efficiency of the CCD	[-]
Q_e	Quantum efficiency of IRO photocathode	[-]
q_p	Heat power	[W]
R	Radius	[m]
R_s	Specific ideal gas constant	[J kg^{-1} K^{-1}]
R_{univ}	Universal ideal gas constant	[J K^{-1} mol^{-1}]
r	Radial distance	[m]
r_w	Laser beam waist	[m]
S	Signal intensity	[-]
$\tilde{S}$	1D signal distribution	[-]

S_0	Ground singlet state	[-]
S_1	First excited singlet state	[-]
S_2	Second excited singlet state	[-]
S_f	Total fluorescence light emitted	[-]
S_{ph}	Total phosphorescence light emitted	[-]
S_{gp}	Gaussian peak intensity	[-]
S_{ICCD}	ICCD sensitivity	[-]
$S_{x,i}$	Displacement basis functions for velocity reconstruction	[m]
s_x	Displacement profile function	[m]
$s_{x,j}$	Displacement data	[m]
Δs_x	Displacement profile thickness	[m]
Δs_∞	Asymptotic displacement profile thickness	[m]
T	Temperature	[K]
T_{cr}	Critical temperature	[K]
T_1	Triplet state	[-]
t	Time	[s]
t_{CCD}	Exposure time of the CCD	[s]
Δt	Time interval	[s]
Δt_{gate}	IRO gate	[s]
u, v, w	Velocity components	[m s^{-1}]
U_i	Velocity basis functions for velocity reconstruction	[m s^{-1}]
$\boldsymbol{u}$	Gas velocity vector	[m s^{-1}]
$\bar{u}$	Mean velocity	[m s^{-1}]
u_{cp}	Centerline Poiseuille axial velocity	[m s^{-1}]
u_{slip}	Slip velocity	[m s^{-1}]
u_{DSMC}	Velocity profile computed by DSMC	[m s^{-1}]
u_{2D}	Velocity distribution on a cross-section	[m s^{-1}]
u_z	Velocity profile at position *z* along the channel width	[m s^{-1}]
$\bar{u}_{CV}$	Average of the velocity profile measured by CV	[m s^{-1}]
$\bar{u}_{MTV}$	Average of the velocity profile measured by MTV	[m s^{-1}]
$u_{slip,CV}$	Slip velocity estimated by CV	[m s^{-1}]
V	Volume	[m^3]
$\dot{V}$	Volume flow rate	[m^3 s^{-1}]
V_R	Reservoir volume	[m^3]

V_b	Bottle or balloon volume	[m^3]
V_{T1}	Tank T1 volume	[m^3]
V_{T2}	Tank T2 volume	[m^3]
V_D	Downstream volume	[m^3]
x, y, z	Spatial coordinates	[m]
y_t, y_b	Top and bottom wall position on the image	[m]
y_c	Position of the channel centerline on the image	[m]
x_d	Hydrodynamic development length	[m]

Greek letters

α	Angle	[rad]
α_1	Half-angle of the primary objective aperture	[rad]
β_{u1}	Correction factor on slip velocity	[-]
Γ_S	Spin multiplicity	[-]
γ	Ratio of the specific heats	[-]
δ	Molecular mean space	[m]
$\alpha_i, \bar{\beta}_m, \bar{\delta}_n$	Eigenvalues	[-]
ϵ	Height-to-length ratio / thermal fluctuations error	[-]
ε	Error	[-]
ε_v^k	Cumulative error on velocity reconstruction	[-]
ε_r^k	Local relative error on velocity reconstruction	[-]
$\varepsilon_{TL}, \varepsilon_{\sigma_x^2}, \varepsilon_{s_x}, \varepsilon_{2D}$	Objective functions for optimization algorithms	[-]
ζ	Second viscosity coefficient	[Pa s]
η	Coefficient of IPL collisional model	[-]
η_p	Efficiency conversion of photodetector	[-]
η_o	Fraction of collected light by external optics	[-]
η_{ICCD}	ICCD Efficiency conversion	[-]
ϑ	Laser divergence half-angle	[rad]
θ	Percentage of vapor saturation	[-]
κ_o	High-order slip boundary condition coefficient	[-]
$\mathbf{\Lambda}$	Matrix of displacement basis functions	
λ	Mean free path	[m]
λ_e	Wavelength of emitted photon	[m]
λ_{ex}	Laser wavelength	[m]

μ	Dynamic viscosity	[Pa s]
μ_{e^-}	Average value of emitted electrons	[-]
μ_N	Average number of molecules	[-]
μ_{RON}	Average read out noise	[-]
μ_r	Radial mean position of light distribution	[m]
ν, ν_{rate}	Collisional frequency	[s^{-1}]
ν_i	Vibrational frequency	[s^{-1}]
ν_e	Frequency of emitted photon	[s^{-1}]
ν_{ex}	Laser excitation frequency	[s^{-1}]
ϕ	Quantum yield	[-]
ϕ_0	Quantum yield without quenching	[-]
ϕ_f	Fluorescence quantum yield	[-]
ϕ_{ph}	Phosphorescence quantum yield	[-]
ϕ_{ISC}	Intersystem crossing quantum yield	[-]
$\tilde{\phi}$	Compressibility coefficient in pressure distribution	[-]
Π	Inlet-outlet pressure ratio	[-]
ρ	Gas density	[kg m^{-3}]
ρ_{H_2O}	Liquid water density	[kg m^{-3}]
σ	Tangential accommodation coefficient	[-]
σ_{abs}	Absorption cross-section	[m^2]
σ_{dark}	Standard deviation of CCD dark noise	[-]
σ_{e^-}	Standard deviation of shot noise	[-]
σ_{E_l}	Standard deviation of average laser energy	[J]
σ_{ICCD}	ICCD standard deviation on counts	[-]
σ_Q	Standard deviation of quantization error	[-]
σ_{shot}	Standard deviation of shot noise in counts	[-]
σ_r	Standard deviation of axisymmetric distribution	[m]
σ_T	Total collision cross section	[m^2]
σ_{V_R}	Standard deviation on reservoir volume	[m^3]
$\sigma_{V_{T1}}$	Standard deviation on tank T1 volume	[m^3]
$\sigma_{V_{T2}}$	Standard deviation on tank T2 volume	[m^3]
$\sigma_x, \sigma_y, \sigma_z$	Standard deviation in the direction *x*, *y*, and *z*	[m]
$\hat{\sigma}^2$	FWHM of Lorentzian distribution	[m]
τ	Emission lifetime	[s]

τ_0	Emission lifetime without quenching	[s]
τ_{fluid}	Characteristic time of the fluid flow	[s]
τ_f	Characteristic time of fluorescence emission	[s]
τ_{ph}	Characteristic time of phosphorescence emission	[s]
τ_{ISC}	Characteristic time of intersystem crossing	[s]
τ_{S_1}	Singlet lifetime	[s]
τ_{T_1}	Triplet lifetime	[s]
τ_{p-PIV}	Characteristic time of accelerating particle	[s]
$\bar{\tau}_w$	Mean shear stress at the wall	[Pa]
χ	Tracer molecular concentration	[-]
$\tilde{\chi}$	Momentum-flux integral	[-]
Ψ_i	Base functions for velocity distribution	[-]
Ω	Solid angle of the primary objective	[sr]
Ω_i	Coefficients for 2D velocity profile	[-]
ω	Coefficient of IPL collisional model	[-]

Non-dimensional number

Pr	Prandtl number
Kn	Knudsen number
Re	Reynolds number
Ma	Mach number

Subscripts

Ac	Acetone
Ar	Argon
Di	Diacetyl
He	Helium
eq	Equilibrium
n	Unit vector normal to the wall
s	Unit vector tangential to the wall
w	Wall
cr	Critical
min	Minimum

in	Channel inlet
out	Channel outlet
$plane, \mathrm{ns}$	Parallel plates with no-slip boundary condition
$plane, \mathrm{S1}$	Parallel plates with first-order boundary condition
$plane, \mathrm{S2}$	Parallel plates with second-order boundary condition
$rect, \mathrm{S1}$	Rectangular channel with first-order boundary condition
$rect, \mathrm{S2}$	Rectangular channel with second-order boundary condition

Acronyms

AR	Anti-reflective
BGK	Bhatnagar-Gross-Krook-Burnett
BPP	Beam product parameter
CCD	Charge-coupled device
DDS	Drug delivery systems
DOF	Depth of focus
DRIE	Deep reactive-ion etching
DSMC	Direct Simulation Monte Carlo
EDM	Electro discharge machining
FACS	Fluorescent activated cell sorting
FOV	Field of view
FP	Fabry-Periot
FWHM	Full width at half-maximum
HTV	Hydroxyl tagging velocimetry
IC	Integrated circuits
ICCD	Intensified CCD
IRO	Intensifier relay optics
LB	Lattice Boltzmann or Langmuir-Blodgett
LDA	Laser-doppler anemometry
LIF	Laser-induced fluorescence
LIGA	Lithographie Galvanoformung Abformung
LIP	Laser-induced phosphorescence
LIPA	Laser-induced photochemical anemometry
MACS	Magnetic activated cell sorting

MCP	Micro-channel plate
MEMS	Micro-electro-mechanical systems
MT	Molecular tagging
MTM	Molecular tagging manometry
MTT	Molecular tagging thermometry
MTV	Molecular tagging velocimetry
NTV	Nitric oxide tagging velocimetry
OTV	Ozone tagging velocimetry
PHANTOMM	Photoactivated non-intrusive tracing of molecular motion
PIV	Particle image velocimetry
PMV	Pattern matching velocimetry
PSMF	Pressure sensitive molecular film
PSP	Pressure sensitive paint
PTU	Programmable timing unit
RBC	Red blood cells
RELIEF	Raman excitation plus laser-induced electronic fluorescence
RTD	Resistance temperature detector
SC	Semiconductor
SNR	Signal-to-noise ratio
TCR	Temperature coefficient of resistance
TFTC	Thin-film thermocouple
TL	Total light
TMAC	Tangential accommodation coefficient
TSP	Temperature sensitive paint
TTA	Triplet-triplet annihilation
VOC	Volatile organic compounds

Chapter 1

Introduction

In this first chapter, a brief introduction on MEMS technology and on the development of microfabrication techniques is presented. A section is dedicated to microfluidic devices and their wide applications to scientific and commercial fields. At microscales, the physical behavior of microsystems is dominated by surface effects and new micro-effects appear. The concept of gas rarefaction is introduced, along with its macroscopic influences on the gas dynamics. The necessity of new experimental data for better understanding these microscale phenomena is pointed out. Finally, the objectives and contributions of this work are defined and inserted inside this context, and the organization of this document is described.

1.1 MEMS technology

During the second half of the XX century, the development of solid-state electronics kept improving the manufacturing techniques, which were able to produce electric components of submicrometric size. However, integrated circuits (IC) could not communicate with the external environment, for which integrated sensors and actuators were necessary. It is from this idea of providing “eyes” and “arms” to the IC that the concept of micro-electro-mechanical systems (MEMS) was born. MEMS are microdevices that integrate electrical components and mechanical components. However, the early micromachining techniques could only fabricate mechanical parts with dimensions around the sub-millimeter, i.e., with sizes definitely bigger than the electrical parts. In the 1980s, a new fabrication technique, named surface manufacturing, was proposed by Howe and Muller (1983), which could be used to fabricate micron-sized mechanical devices with complex geometries from polycrystalline silicon (poly-Si). As the development of new microfabrication techniques made the design of MEMS possible, the practical interest and the scientific inquiry on these systems quickly increased in the last decades. MEMS have received a lot of attention due to their appealing properties of low volume, low weight, low energy consumption, and system integration.

Their possible applications cover a very wide spectrum of fields. There are many examples of MEMS that found a commercial application and that are present in many of our daily life utilities. Great examples are the micro-accelerometers employed in the airbag systems in cars or in most nowadays smartphones. These microsensors are usually constituted of a comb-drive structure, which was first developed by Tang et al. (1992). Figure 1.1 shows a typical electrostatic comb-drive mechanism with typical dimensions on the order of 100 μm. The moving comb is sustained by a cantilever beam that allows it to move horizontally. The acceleration is measured from the variation of capacitance due to the motion of the moving fingers with respect to the static fingers. The same

microstructure and principle can be employed in micro-gyroscopes (Acar & Shkel, 2005, Pyatishev et al., 2017) and micro-actuators (Hirano et al., 1992).

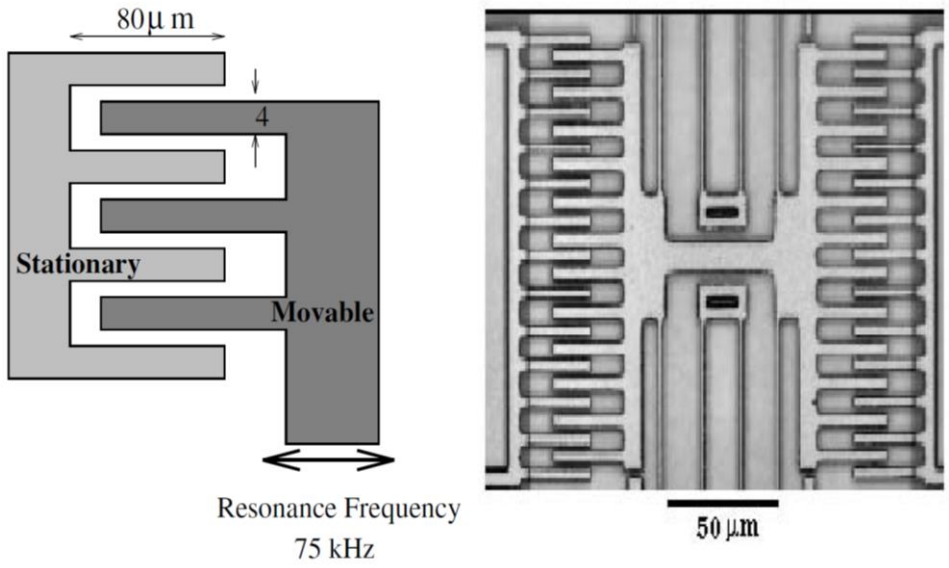

(a) (b)

Figure 1.1. (a) Diagram of the typical comb-drive structure and typical dimensions; (b) actual electrostatic comb-drive. Figure from Karniadakis *et al*. (2006).

In these electrostatic actuators, the driving force is inversely proportional to the size of the gap between the static comb and the moving comb. Since the common lithography and etching systems on usual poly-Si do not have the required precision for making submicron gaps, Hirano *et al*. (1992) applied an alternative fabrication technique named oxidation machining, proposed by Furuhata *et al*. (1991). This new technique allowed to produce sub-micron gaps between the electrodes by means of thermal oxidation of the poly-Si, without the necessity of employing the limited etching capability.

The micromanufacturing techniques have seen in the past years a development and an adaptation to the increased demanding of miniaturization along with fabrication precision. Other microfabrication techniques are bulk silicon micromachining, LIGA (Lithographie Galvanoformung Abformung) and EDM (Electro Discharge Machining). Starting from the manufacturing techniques of the semiconductor industries based on silicon or glass materials, polymer/plastic-based microdevices were afterward introduced because cheaper and easier to be machined.

The comb-drive accelerometer is also a good example of mixed domain system. The frequency response analysis of the system requires a correct calculation of the damping force on the comb oscillation, which is mainly due to the viscous forces of the air lying between the comb gaps. MEMS are multidisciplinary systems and, therefore,

scientific research from different fields need to interact in order to control and predict the behavior of these microdevices.

1.2 Microfluidic systems in MEMS

There is a group of MEMS where the sensing and the actuation are made through microfluidic systems. Microfluidic devices have an important role as they appear in a wide variety of application fields. Microchannels, microvalves, micropumps, micro-heat exchangers, micro-separators, micromixers, and micro-actuators are possible microfluidic elements that can be found in MEMS.

Figure 1.2 shows two different examples of micropumps: the first one is a peristaltic micropump and the second one is an example of the so-called Knudsen pump.

The peristaltic micropump functioning is based on gas compression produced by means of variations of the gas volume. A combination of microvalves and activated membranes can produce this effect. Jeong *et al*. (2005) fabricated a peristaltic micropump with polydimethylsiloxane (PDMS) elastomer on a glass substrate. The membrane is driven by microheaters that heat the gas from one side of the membrane. The heating of a cavity can provide a fast gas expansion able to drive the membrane in a controlled way. Since the volume of gas to be heated for activating the membranes is very small, the heating-cooling cycle can be very fast and can quickly follow an electrical trigger.

Figure 1.2b compares a dime with a 48-stage Knudsen micropump fabricated at the University of Michigan (Gupta *et al*., 2012). The single silicon wafer pump is constituted by narrow channels with a height of 0.15 μm and monolithically integrates several Pirani gauges (Chae *et al*., 2005) for the experimental analysis of the pump characteristics. In comparison with the peristaltic pump, the Knudsen pump does not require any moving part. The driving force of a Knudsen pump is based on the thermal transpiration effect: a thermal gradient imposed along the wall of the narrow channels constituting the micro-system generates a gas flow in the direction of increasing temperature. This phenomenon becomes relevant only when the gas is at specific rarefied conditions. Even though the mass flow rates generated by thermal transpiration is very small and on the orders of 10^{-13} kg/s, it has been experimentally demonstrated that a multi-stage Knudsen pump can create a pressure drop of 100 kPa.

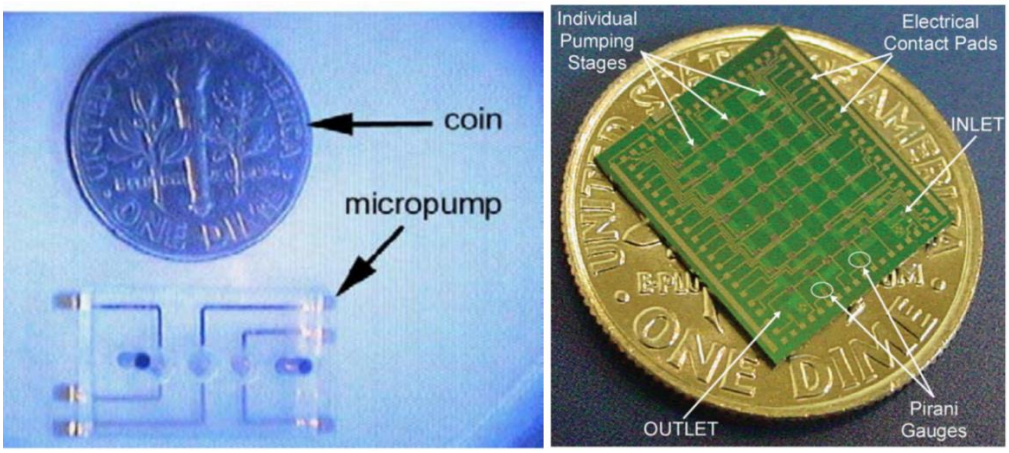

(a) (b)

Figure 1.2. (a) A peristaltic micropump (Jeong *et al*., 2005) and (b) a Knudsen micropump (Gupta *et al*., 2012).

Microfluidic devices are very important for fluid transport and cells analysis in the biomedical field. Drug delivery systems (DDS) based on MEMS can move and control a specific amount of drug with high precision. MEMS technology provides medical instruments less invasive than the conventional ones, such as micro-endoscopes and endoscope capsules for the gastrointestinal tract (Munoz *et al*., 2014), and micro-needles array for controlled drug delivery. These technological advances reduce the pain and possible tissue damage on patients. Moreover, there are some areas of the body that are quite challenging sites for drug delivery. The intravenous administration of drugs for treating some neurodegenerative diseases, such as the Alzheimer and brain tumors, is a therapy made inefficient by the physical barrier separating the brain organ from the blood circulation. MEMS technology may overcome this problem by targeting these sites through localized drug delivery systems, but many challenges remain to be solved, e.g., biocompatibility and implantation problems (Lee *et al*., 2018).

Lab-on-a-chip devices for cells analysis represent another important example of microfluidic devices application in the biomedical field. Figure 1.3 shows two examples of cells sorting strategies: the micro magnetic activated cells sorting (µMACS) and the micro fluorescent activated cells sorting (µFACS). In µMACS, cells from a sample are labeled with paramagnetic microparticles and are guided in a channel by means of two buffer streams. The channel can have a diameter of 100 µm, with cells of 5-10 µm. A permanent magnet induces the labeled cells to migrate toward the collecting outlet. In µFACS, cells are labeled with fluorescent particles. An optic sensor opens a valve when the labeled cells are detected through the main stream in the channel. Since a residual amount of non-labeled cells always pass through the collecting outlet, a series of additional µFACS is necessary to make a complete separation of the cells of interest from the rest of the group cells.

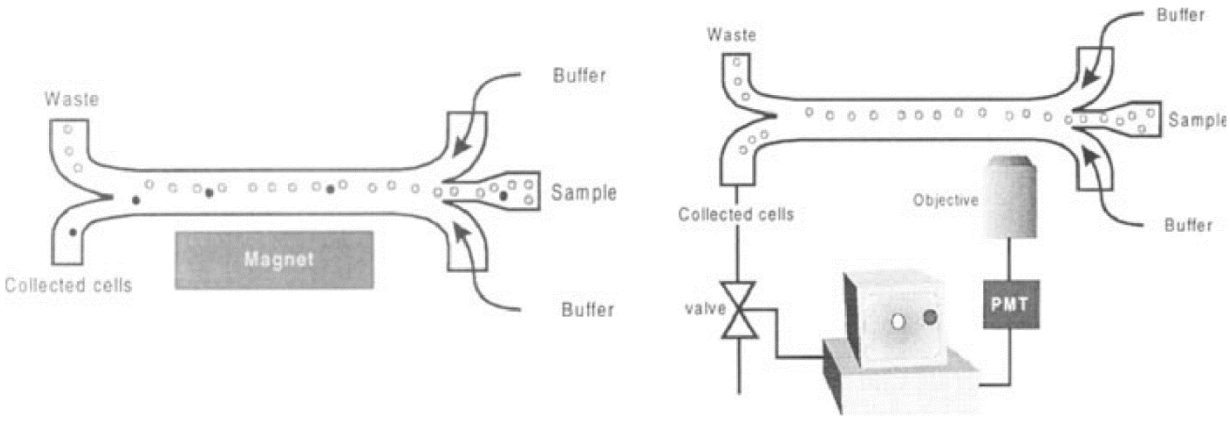

(a) (b)

Figure 1.3. Schematization of the labeling cells sorting techniques: (a) µMACS and (b) µFACS. Figures from Telleman *et al.* (1998).

Qu *et al*. (2008) applied the same principle of µMACS but without any cells labeling. In this work, a glass microfluidic chip exploits the native magnetic properties of red blood cells (RBC) for making a continuous sorting. A nickel wire with a diameter of 69 µm is introduced in a trapezoidal channel with a 149-µm top width, a 287-µm bottom width, and a depth of 73 µm. By means of an external magnetic field, the nickel wire produces a magnetic gradient that attracts RBC, which paramagnetic properties derive from the deoxyhemoglobin, and rejects white blood cells, which are diamagnetic (Figure 1.4).

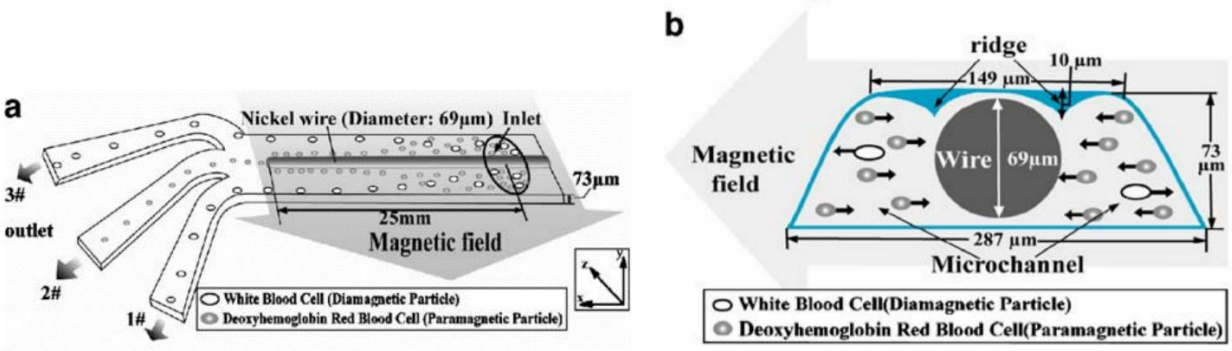

Figure 1.4. Schematic representation of the microfluidic chip for RBC sorting designed by Qu *et al*. (2008): (a) structure of the overall system; (b) section of the microchannel of the chip. Figures readapted from Qu *et al*. (2008).

In the aeronautical sector, microfluidic actuators are interesting devices for the active control of the flow separation on aerodynamic surfaces and of high-speed jet noise (Cattafesta *et al*., 2011). Synthetic pulsed microjets are an example of active microfluidic actuation that can be employed for boundary layer control (Lee *et al*., 2003). In these devices, a membrane, which can be activated electrodynamically or by means of a piezoelectric, oscillates for generating through a small channel or an orifice a zero-net mass flow with a non-zero average velocity (Figure

1.5a). In the literature, synthetic pulsed microjets have been fabricated with orifice diameters of about 150 µm (Coe *et al*., 1995). However, the real application of these microdevices for active flow control on civil transport airplanes is prevented by the strong noise induced by the membrane vibration (Jabbal *et al*., 2010) and by the considerable cost in terms of weight that the corresponding power transmission system would require (Batikh *et al*., 2017). Synthetic pulsed microjets found, instead, a real application in the informatics industry, being already commercialized as cooling devices (Synjet®) for electronic components.

Fluidic oscillators are passive actuators that can generate a sweeping jet when supplied with a pressurized fluid. The fact that compressed air is already available on an airplane makes this type of actuators interesting for aeronautical applications. The very interesting aspect of these systems is the absence of moving parts, which is a great advantage both from a fabrication and a reliability point of view. The sketch of the fluidic oscillator in Figure 1.5b is a good representation of the Coanda effect (Coanda, 1936), which is the main mechanism that generates an oscillatory jet at the device outlet. The Coanda effect takes the name from the Romanian aerodynamicist Henri Coanda and represents the tendency of a fluid flow to follow the boundaries of a wall in its vicinity. As shown in Figure 5b, this mechanism makes the central flow periodically oscillate between the two feedback paths, thus producing at the microfluidic outlet a sweeping jet with a specific oscillation frequency. Gregory *et al.* (2007) patented a microfluidic oscillator able to generate an oscillating jet with a width of 325 µm and at frequencies higher than 20 kHz. It is not guaranteed that by further reducing the size of the device the Coanda effect is still present and exploitable for producing a sweeping jet.

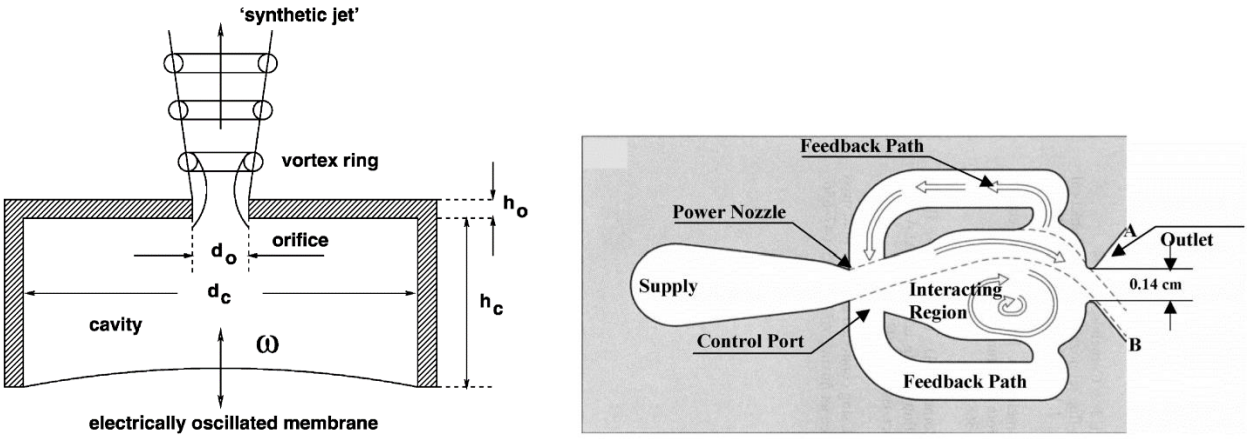

Figure 1.5. (a) Schematic of a pulsed microjet (Mallinson *et al*., 2003) and (b) of a fluidic oscillator (Raman & Raghu, 2004).

In the spatial industry, micro-propulsion on micro-spacecrafts is useful for attitude control, gravitational compensation, and orbit adjustments. In the work of Janson *et al.* (1999), a 1-cm micro-thruster for nanosatellites was fabricated by bonding three micromachined layers, as shown in Figure 1.6a. In particular, the nozzle (Figure

1.6b) has a throat diameter of 100 μm, and it was fabricated by laser-machining in a Foturan® substrate, a common photosensitive glass-ceramic employed in MEMS technology (Williams *et al*., 2010).

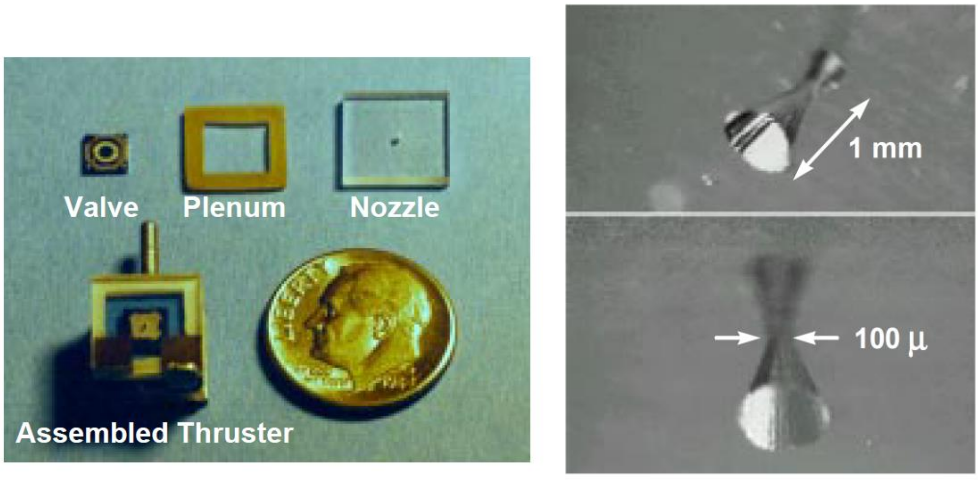

(a) (b)

Figure 1.6. (a) Single components of a micro-thruster and assembled version; (b) micro-nozzle used in the micro-thruster in (a). Figures from Janson *et al*. (1999).

Micro-gas chromatographs are another example of lab-on-a-chip that finds important applications in the aerospace and chemical industries. Chemical instrumentations with low volume and low weight for in-situ measurements in astrobiology are important, given the reduced payload requirements in space applications. Moreover, volatile organic compounds (VOCs), such as formaldehyde, are possible health hazards in working and closed environments. VOCs have high saturation vapor pressures and can be released by furniture and building materials through evaporation or sublimation at ambient temperature. Portable gas analyzers are, therefore, important for testing air quality in these environments.

1.3 Scale effects at the microscale

As the development of the microfabrication processes made microdevices design possible, the scientific research focused its resources in controlling and better understanding the physical behavior of microdevices. Micro-systems behave quite differently from their corresponding macro versions. As the device becomes smaller, the inertial forces decrease, and surface forces tend to gain importance with respect to volume forces. By considering a system with a characteristic length scale L_c, the surface forces F_s scale to the square of L_c, whereas the volume forces F_V scale to the third power of L_c, so that the surface-to-volume forces ratio

$$\frac{F_s}{F_V} \propto \frac{L_c^2}{L_c^3} = \frac{1}{L_c} \tag{1.1}$$

tends to increase as the device shrinks down.

The micromotor of Fan *et al*. (1988) is one of the very first examples of micromachines. A scanning-electronic-microscopy (SEM) of the electrostatically-driven motor is shown in Figure 1.7, where its real dimensions are put in evidence by a piece of human hair positioned in front of it. First experiments on this micromotor showed that the motion of the central rotor was prevented by the friction forces with the substrate. They noticed that the friction depends on the area of the contact surface, in contrast with the common friction law employed at macroscale for which the friction force is only proportional to the normal force exerting at the contact surface. This is an example of how surface effects dominate the mechanics in microdevices and a demonstration of how mathematical models that well represent physical processes at macroscales may not be valid at microscales.

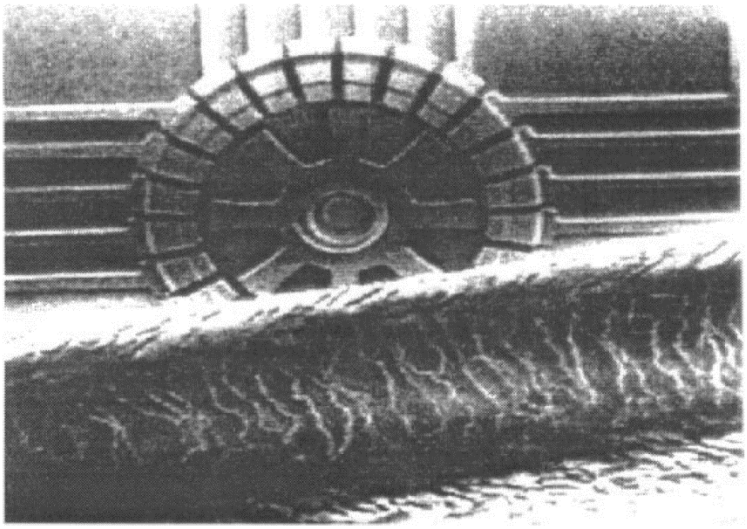

Figure 1.7. Micromotor fabricated by Fan *et al.* (1988), compared with a piece of human hair.

In microfluidic devices, the large surface-to-volume forces ratio makes the viscous effects dominate the inertial ones, resulting in flows at low Reynolds numbers. In the same manner, as the size of the fluid volume becomes smaller, the thermal inertia reduces and the heat fluxes, proportional to the surface of heat exchange, gain importance. As a consequence of the modification of the balance between surface and volume contributions, the dynamical response of the fluid system becomes faster, as demonstrated, for instance, by the thermally-driven membrane actuation of the peristaltic micropump discussed in the previous section (Figure 1.2a).

1.4 Gas microflows

In gas systems, the number and the intensity of the intermolecular interactions are small when compared to liquid systems. In gas microflows, the flow dynamics can take place on characteristic lengths that are comparable to those of the molecular dynamics. In this situation, the dynamics at microscopic level has a direct influence on the

macroscopic-thermodynamic properties of the gas flow. This micro-effect is called rarefaction, and it is a consequence of the relatively-low number of intermolecular collisions inside the control volume. The Knudsen number, $Kn = \lambda/L_c$, where λ is the mean free path of the molecules and L_c is the characteristic size of the system, identifies the degree of gas rarefaction. Most of the microfluidic devices work in the slip flow regime, with Kn in the range [10^{-3}; 10^{-1}], which is considered as characterized by slightly rarefied gas conditions. This regime can be reached either in a microfluidic device, where L_c is low, or in a bigger system at low pressure, which results in a high mean free path λ. In this rarefaction regime, the classical continuum representation of the flow is still acceptable for fluid particles that are far enough from the system's solid boundaries, i.e. at a distance larger than the well-known Knudsen layer thickness, which is considered to be on the order of λ. For those systems that involve wall-gas interactions, e.g., in micro channels or in channels at low average pressure, the number of collisions between the wall surfaces and the gas molecules gains importance with respect to intermolecular collisions, thus producing a thermodynamic non-equilibrium state of the gas in the vicinity of the wall. At a macroscopic level, this produces a velocity slip and a temperature jump at the wall (Colin, 2005), i.e., non-negligible discontinuities of the kinematic and thermodynamic parameters between fluid and surface. These rarefaction effects strongly influence the heat and mass transfers. Therefore, a correct modeling of the thermodynamic disequilibrium at the wall is crucial for an accurate prediction of the mass flow rates and heat fluxes within the microdevice. Experimental observations and analysis of the rarefaction effects are needed for the validation and the accuracy quantification of the numerous theoretical and numerical analysis already existing in the literature.

With the increasing interest of the scientific community towards the physics at microscales, the experimental techniques for analyzing such types of microsystems has been developing accordingly. In microfluidic devices, very low mass flow rates require high-precision and sensitive instrumentation. The control of the microenvironment, e.g., in terms of surface roughness, working fluid composition, or temperature and pressure distributions, is of significant importance for a correct analysis of the microflow. It is common that pressure and temperature sensors are monolithically integrated during the fabrication of the microfluidic chip, e.g., the Pirani gauges of the Knudsen pump of Figure 1.2b. Nevertheless, in order to reduce the intrusiveness of the measurements, many experimental techniques adopted for microfluidic analysis are based on optical methods and electrochemical methods (Wu & Gu, 2011).

1.5 The objective of the work

In this context, this work aims to the application of an optical velocimetry technique, the molecular tagging velocimetry (MTV), to rarefied gas flows in a channel with a rectangular section. The final goal is to provide local measurements of the slip velocity at the wall that characterizes gas flows in the slip regime.

MTV is an optical, low-intrusive technique that can provide local measurements of the velocity field in fluid flows. By exploiting the laser-induced emission of a suitable molecular tracer previously added to the main flow, the velocity field is measured by tracking the displacement of the emitting molecules.

As explained in the previous section, the rarefaction regime can be achieved either by increasing the mean free path λ, reducing the gas pressure, or by reducing the smaller dimension of the system, which corresponds, in our problem, to the height H of the channel. Since the laser beam diameter can hardly be smaller than about 30 μm for technological reasons, the height of the channel is constrained to be not smaller than about 1 mm, in order to keep a reasonable spatial resolution. Consequently, Knudsen numbers corresponding to the targeted slip flow regime can only be reached by decreasing the average pressure of the gas-tracer mixture. Further details on this constraint and the implementation of MTV are provided in Chapter 5.

Previous works have already made a lot of progress in the direction of applying MTV in rarefied conditions. Samouda *et al.* (2015) have demonstrated that MTV can provide good results in a millimetric rectangular channel for a non-rarefied gas flow at atmospheric pressure and ambient temperature. However, they noticed that a deduction of the velocity profile by assuming it was simply homothetic of the displacement profile resulted in an artificial velocity slip at the wall, which was totally unexpected for the employed Knudsen numbers. Subsequently, Frezzotti *et al.* (2015) explained that this unexpected phenomenon is a consequence of a combined effect of advection and molecular diffusion of the tracer in the background gas flow that generates a non-zero molecular displacement at the wall. Moreover, the same authors proposed a numerical method based on a simple advection-diffusion equation that was able to correctly reconstruct the velocity profile from the displacement of the tagged line. By means of the Direct Simulation Monte Carlo (DSMC) method, it was possible to numerically verify the existence of a displacement slip at the wall caused by the advection-diffusion mechanism and not linked to a velocity slip at the wall. A reconstruction method of the velocity profile from the displacement profile was developed and validated with numerical experiments. Si Hadj Mohand *et al.* (2017) successfully applied this reconstruction method on MTV data in a millimetric channel and correctly extracted the velocity profile at atmospheric and sub-atmospheric pressures down to a minimum average pressure of 42 kPa. At this pressure level in a 1-mm deep channel, the flow is still in a non-rarefied regime.

Even though a lot of progress has been done towards the final objective, the application to gas flows in rarefied conditions has been prevented up to now by certain difficulties.

Firstly, the existence of a suitable molecular tracer that could generate a durable and intense light signal in rarefied conditions and that could make the velocity measurement possible was not evident. The increasing molecular diffusion and the smaller number of tracer molecules at low pressures let the light signal quickly vanish before any tracer displacement could be measured. A research aimed to solve this scientific barrier is at the center of the

first part of this work. Data on photoluminescence found in literature could not provide enough information to reveal if a specific molecular tracer combined with our experimental facilities could be successfully employed for our specific application. For this reason, an experimental campaign aimed at the investigation of the photoluminescence properties at low pressures of the molecular tracers of interest has been carried out.

Secondly, an experimental apparatus capable of generating a desired gas flow rate at low pressures in the channel and, at the same time, adapted to the experimental requirements for applying MTV needed to be designed. The application of MTV requires a stable flow rate with stable thermodynamic conditions when the measurements of the tracer displacement is made. The experimental setup should also guarantee a leakage-free environment and a compatibility with the chemical properties of the molecular tracer employed. Moreover, it should envisage the possibility of integrating a second measurement technique applicable to the tested flow conditions, which is necessary for the verification and the validation of the velocity measurements provided by MTV.

Thus, this work provides an experimental study on photoluminescence of acetone and diacetyl vapors that demonstrates the presence of an exploitable light signal at low pressures under certain operation conditions. After removing this scientific barrier, a novel experimental setup has been designed and built. This experimental setup allows for the application of MTV to gas mixture flows at low pressures and integrates the "dynamic" constant-volume technique, which is capable of providing a measurement of the mass flow rate in the tested channel. Finally, MTV is applied to gas flows in the slip regime and the first ever flow visualizations of the molecular displacement in channel flows at pressures on the order of 1 kPa are presented. Moreover, by means of an improved version of the reconstruction method previously proposed by Frezzotti *et al*. (2015), the first MTV measurements of the slip velocity at the wall are reported.

1.6 Organization and contributions of the thesis

This document has been structured in 7 chapters.

In Chapter 2, the concepts of rarefaction and thermodynamic non-equilibrium are discussed in more details. The rarefaction regimes are defined and the available mathematical models for each of them are reviewed. Particular attention is devoted to the models and the experimental data available in the literature related to the slip flow regime. The analytical solution for a steady, viscous, locally-incompressible, and locally fully-developed gas flow in a channel with rectangular cross-section is discussed in terms of mass flow rate, velocity profile, and pressure distribution along the channel. These mathematical tools will be used for the characterization of the experimental flow conditions inside the tested channel.

Chapter 3 presents the currently available experimental techniques for analyzing rarefied gas flows. The techniques are sorted by quantity to be measured: mass flow rate, pressure, temperature, and velocity. Firstly, a review on

pressure and temperature microsensors that are integrated in the microdevices is presented. Mass flow rate measurements can be carried out by means of either commercially available microsensors or specific experimental techniques. The performances of both the flow rate measurement techniques are discussed for application in gas microflows. Finally, a section is dedicated to the presentation of the available opto-chemical techniques for pressure, temperature, and velocity field measurements. Here, the general principle of MTV is described, and the different types of implementation are discussed. The literature about this technique is reviewed even for its application to liquid flows, for the sake of completeness.

In Chapter 4, the experimental facilities employed in this work are presented. The characteristics of the laser system, of the CCD camera, and of the gas circuit elements are discussed in detail. Two experimental setups are presented. The first one is devoted to the analysis of the photoluminescence lifetime of acetone and diacetyl vapors. These experiments are carried out in a chamber test with the vapor in a quiescent state. A second experimental setup has been built for the application of MTV to gas flows at low pressures.

Chapter 5 is dedicated to the experimental analysis of the photoluminescence properties of acetone and diacetyl vapors. In the first part of this chapter, the experimental data are analyzed from a qualitative point of view in the perspective of applying MTV to gas flows at low pressures. In the second part, a quantitative analysis of the same experimental data on acetone and diacetyl photoluminescence is presented. The big amount of data gathered shed light on the most important intramolecular phenomena to be taken into account for a correct description of the laser-induced emission. A mathematical model capable of describing our experimental observations is proposed. A parameter identification algorithm based on this same model is employed for a quantitative characterization of the photoluminescence (intramolecular) and kinetic (intermolecular) properties of acetone and diacetyl vapors, that is the triplet-triplet annihilation rate and the self-diffusion coefficient as a function of pressure.

Chapter 6 presents the experimental results obtained by MTV. The reconstruction method is described and applied to numerical experiments produced by DSMC. The experimental conditions of interest for the application of MTV are defined based on the experimental results of Chapter 5. The experimental gas flow conditions that can be generated by the new experimental setup are thoroughly analyzed. The “dynamic” volume technique is applied to measure the mass flow rate and is combined to theoretical solutions to provide an estimation of the thermodynamic properties and of the average velocity of the gas flow investigated by MTV. The post-processing procedure that is systematically applied to each image provided by MTV is explained in detail. Finally, MTV is applied to gas flows in non-rarefied conditions and, afterwards, to gas flows in the slip regime. Velocity measurements carried out by means of a novel time-correlation reconstruction method are presented and discussed.

In the last chapter, the experimental and numerical results provided by this work are summarized and discussed. The goals achieved are compared to the objectives that have been initially defined, and the next steps for further improving MTV measurements in rarefied gas flows are identified.

To summarize, the contributions given by this work are:

- experimental data on photoluminescence of acetone and diacetyl vapors at low pressures and comparative discussion with experimental data found in the literature;
- the mathematical representation of photoluminescence data for the parameter identification of the triplet-triplet annihilation rate and the self-diffusion coefficient of acetone and diacetyl;
- a novel experimental setup for the simultaneous application of MTV and constant volume technique to gas flows at low pressures;
- the development of new image fitting algorithms and of a time-correlation reconstruction method;
- experimental results of flow visualization of molecular displacement in gas flows in the slip regime and experimental evidences of the theoretically predicted molecular slip at the wall;
- MTV measurements of velocity profile characterized by slip velocity at the wall.

References

Acar, C., & Shkel, A. M. (2005). Structurally decoupled micromachined gyroscopes with post-release capacitance enhancement. *Journal of Micromechanics and Microengineering*, *15*(5), 1092.

Batikh, A., Baldas, L., & Colin, S. (2017, February). Application of active flow control on aircrafts-state of the art. In *International Workshop on Aircraft System Technologies* (Vol. 2017).

Cattafesta III, L. N., & Sheplak, M. (2011). Actuators for active flow control. *Annual Review of Fluid Mechanics*, *43*, 247-272.

Chae, J., Stark, B. H., & Najafi, K. (2005). A micromachined Pirani gauge with dual heat sinks. *IEEE Transactions on Advanced Packaging*, *28*(4), 619-625.

Coanda, H. (1936). Lifting Device Coanda Effect. *US Patent*, *3261*, 162.

Coe, D. J., Allen, M. G., Smith, B. L., & Glezer, A. (1995, June). Addressable micromachined jet arrays. In *Solid-State Sensors and Actuators, 1995 and Eurosensors IX.. Transducers' 95. The 8th International Conference on* (Vol. 2, pp. 329-332). IEEE.

Colin, S. (2004, January). Rarefaction and compressibility effects on steady or transient gas flows in microchannels. In *ASME 2004 2nd International Conference on Microchannels and Minichannels* (pp. 13-24). American Society of Mechanical Engineers.

Fan, L. S., Tai, Y. C., & Muller, R. S. (1988, December). IC-processed electrostatic micro-motors. In *Electron Devices Meeting, 1988. IEDM'88. Technical Digest., International* (pp. 666-669). IEEE.

Frezzotti, A., Mohand, H. S. H., Barrot, C., & Colin, S. (2015). Role of diffusion on molecular tagging velocimetry technique for rarefied gas flow analysis. *Microfluidics and Nanofluidics*, *19*(6), 1335-1348.

Furuhata, T., Hirano, T., Gabriel, K. J., & Fujita, H. (1991, January). Sub-micron gaps without sub-micron etching. In *Micro Electro Mechanical Systems, 1991, MEMS'91, Proceedings. An Investigation of Micro Structures, Sensors, Actuators, Machines and Robots. IEEE* (pp. 57-62). IEEE.

Gregory, J. W., Sullivan, J. P., Raman, G., & Raghu, S. (2007). Characterization of the microfluidic oscillator. *AIAA journal*, *45*(3), 568-576.

Gupta, N. K., An, S., & Gianchandani, Y. B. (2012). A Si-micromachined 48-stage Knudsen pump for on-chip vacuum. *Journal of Micromechanics and Microengineering*, *22*(10), 105026.

Hirano, T., Furuhata, T., Gabriel, K. J., & Fujita, H. (1992). Design, fabrication, and operation of submicron gap comb-drive microactuators. *Journal of Microelectromechanical systems*, *1*(1), 52-59.

Howe, R. T., & Muller, R. S. (1983). Polycrystalline silicon micromechanical beams. *Journal of the Electrochemical Society*, *130*(6), 1420-1423.

Lee, H. J., Choi, N., Yoon, E. S., & Cho, I. J. (2018). MEMS devices for drug delivery. *Advanced drug delivery reviews*, *128*, 132-147.

Mallinson, S. G., Kwok, C. Y., & Reizes, J. A. (2003). Numerical simulation of micro-fabricated zero mass-flux jet actuators. *Sensors and Actuators A: Physical*, *105*(3), 229-236.

Mohand, H. S. H., Frezzotti, A., Brandner, J. J., Barrot, C., & Colin, S. (2017). Molecular tagging velocimetry by direct phosphorescence in gas microflows: correction of Taylor dispersion. *Experimental Thermal and Fluid Science*, *83*, 177-190.

Munoz, F., Alici, G., & Li, W. (2014). A review of drug delivery systems for capsule endoscopy. *Advanced drug delivery reviews*, *71*, 77-85.

Karniadakis, G., Beskok, A., & Aluru, N. (2006). *Microflows and nanoflows: fundamentals and simulation* (Vol. 29). Springer Science & Business Media.

Jabbal, M., Liddle, S. C., & Crowther, W. J. (2010). Active flow control systems architectures for civil transport aircraft. *Journal of Aircraft*, *47*(6), 1966-1981.

Janson, S. W., Helvajian, H., Hansen, W. W., & Lodmell, J. (1999, April). Microthrusters for nanosatellites. In *Second International Conference on Integrated Micro Nanotechnology for Space Applications* (pp. 1-17).

Jeong, O. C., Park, S. W., Yang, S. S., & Pak, J. J. (2005). Fabrication of a peristaltic PDMS micropump. *Sensors and Actuators A: Physical*, *123*, 453-458.

Pyatishev, E. N., Enns, Y. B., Kazakin, A. N., Kleimanov, R. V., Korshunov, A. V., & Nikitin, N. Y. (2017, May). MEMS GYRO comb-shaped drive with enlarged capacity gradient. In *Integrated Navigation Systems (ICINS), 2017 24th Saint Petersburg International Conference on* (pp. 1-3). IEEE.

Qu, B. Y., Wu, Z. Y., Fang, F., Bai, Z. M., Yang, D. Z., & Xu, S. K. (2008). A glass microfluidic chip for continuous blood cell sorting by a magnetic gradient without labeling. *Analytical and bioanalytical chemistry*, *392*(7-8), 1317.

Raman, G., & Raghu, S. (2004). Cavity resonance suppression using miniature fluidic oscillators. *AIAA journal*, *42*(12), 2608-2612.

Samouda, F., Colin, S., Barrot, C., Baldas, L., & Brandner, J. J. (2015). Micro molecular tagging velocimetry for analysis of gas flows in mini and micro systems. *Microsystem Technologies*, *21*(3), 527-537.

Sharipov, F., & Seleznev, V. (1998). Data on internal rarefied gas flows. *Journal of Physical and Chemical Reference Data*, *27*(3), 657-706.

Tang, W. C., Lim, M. G., & Howe, R. T. (1992). Electrostatic comb drive levitation and control method. *Journal of Microelectromechanical systems*, *1*(4), 170-178.

Telleman, P., Larsen, U. D., Philip, J., Blankenstein, G., & Wolff, A. (1998). Cell sorting in microfluidic systems. In *Micro Total Analysis Systems' 98* (pp. 39-44). Springer, Dordrecht.

Williams, J. D., Schmidt, C., & Serkland, D. (2010). Processing advances in transparent Foturan® MEMS. *Applied Physics A*, *99*(4), 777-782.

Wu, J., & Gu, M. (2011). Microfluidic sensing: state of the art fabrication and detection techniques. *Journal of biomedical optics*, *16*(8), 080901.

Chapter 2

Mathematical models for rarefied gas flows

In this chapter, a brief introduction on kinetic theory and the physics of rarefied gas flows is presented. The definition of thermodynamic non-equilibrium is discussed. The most important parameters for the analysis of the molecular dynamics are introduced and the mathematical models for the description of intermolecular collisions and gas-surface interactions are discussed. Four regimes of rarefaction are identified, and a brief review of the theoretical models available in the literature for each rarefaction regime is presented. Afterwards, the pressure-driven, steady, isothermal, locally fully-developed, and locally incompressible gas flow in a channel is mathematically described through simplified models, providing analytical solutions for the mass flow rate and the pressure distribution along the channel. These theoretical tools will be used for the validation and the processing of the experimental data in the follow-up of this work.

2.1 Dilute gas

In a *simple gas*, all molecules of the system belong to the same chemical species. Based on the chemical composition of the species, the molecule is characterized by a molecular mass, m, and a specific geometrical structure that depends on the disposition of the atoms. While the molecular mass is easily computable once the atomic composition is known, the quantification of the size of a molecule is more difficult to be uniquely defined. In kinetic theory, the 'size' of a molecule is quantified by its kinetic diameter d. For monatomic molecules, such as helium or hydrogen, the kinetic diameter can be easily identified with the diameter of the spherical electronic cloud surrounding the nucleus. Differently, polyatomic molecules, such as acetone and diacetyl, have a complex electronic cloud that is difficult to be associated to the diameter of a sphere. However, the main purpose of the kinetic theory is to describe the interactions that happen at the molecular level. The kinetic diameter, more than being considered as a 'size', defines the probability that one molecule could interact with another molecule. The electric field of a molecule has an extension that increases with d. Molecules with a big kinetic diameter interact with the surrounded molecules with higher probabilities than molecules with small kinetic diameter (Bird, 1994).

A second important characteristic length is the mean molecular spacing, which defines at the molecular level the space occupied by one single molecule. Let us consider a thermodynamic system of volume V composed of a certain number N of molecules. The molecular density number $n = N/V$ corresponds to the number of molecules per unit volume. The average size of the volume in which one single molecule can move without encountering, most likely, another molecule is defined by the mean molecular spacing $\delta = n^{-1/3}$. This characteristic length provides information on the probability of having an interaction between two molecules. It is evident that a gas

with a high density number n, or with a small δ, is characterized by very frequent interactions between the molecules. However, the mean molecular spacing is not the only parameter that determines the rate of intermolecular interactions in a gas. The length δ is a static characteristic of the gas and it does not say anything on the molecular speed of the molecules. In the limit case, if all molecules do not move, even though δ is very small, the molecules would never collide.

In kinetic theory, the intermolecular interaction is commonly called collision. If the molecules are simplified as hard spheres with diameter d, two molecules interact as soon as they collide, that is when the distance between their centers coincides with the sum of their molecular radii (Figure 2.1). Therefore, in the hard sphere approximation, the area

$$\sigma_T = \pi d^2, \tag{2.1}$$

around one molecule is called the total collisional cross section and quantifies the likelihood of a collisional event with other molecules. The hard sphere model is a very simplified representation of the more complex attractive-repulsive force field acting on the molecules, but it is still widely employed for its simplicity and for its ability to capture many of the macroscopic behavior of a gas system. As it will be discussed in Section 2.3, depending on the collisional model adopted, the "effective area" σ_T of the likelihood of a scattering event can assume different expressions and can depend on molecular properties other than the molecular diameter, such as the relative velocity between two colliding molecules. Even though the electrostatic interaction between two molecules has short-range and long-range components and is more complex than two colliding spheres, this event is always referred to as collision.

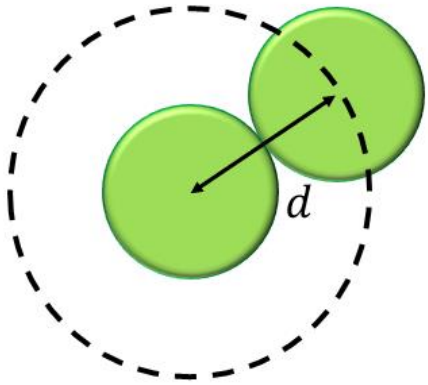

Figure 2.1. Collisional distance in a hard sphere model.

One of the most important parameters that characterize the dynamics at the molecular level is the collision frequency ν. In order to obtain an expression of this quantity as a function of the molecular properties, i.e., the

kinetic diameter and the molecular velocity, a test molecule with velocity $\boldsymbol{c}_t$ is considered. If the number of collisions in a time interval Δt is not high enough to distort the molecule trajectory, the relative velocity of molecules that belong to the velocity class $\boldsymbol{c}_i$ with respect to the test molecule is $\boldsymbol{c}_{r,i} = \boldsymbol{c}_t - \boldsymbol{c}_i$. Therefore, the relative displacement of the test molecule with respect to the molecules of the selected velocity class is $\boldsymbol{c}_{r,i}\Delta t$. The volume $\sigma_T \boldsymbol{c}_{r,i}\Delta t$ represents the space region of possible collision of the test molecule with other molecules. If the molecular density is n and the fraction of molecules of class $\boldsymbol{c}_i$ is $\Delta n_i/n$, the number of collisional events N_{coll} occurring in the time interval Δt is obtained by summing over all classes of velocity, namely over all values of $\boldsymbol{c}_{r,i}$:

$$N_{coll} = \Delta t n \sum_i \sigma_T \boldsymbol{c}_{r,i}\, \Delta n_i/n = \Delta t n \overline{\sigma_T \boldsymbol{c}_r}. \tag{2.2}$$

Since σ_T can generally depend also on the relative velocity $\boldsymbol{c}_{r,i}$, the total collisional cross-section takes part in the average operator. The mean frequency rate per molecule is, then,

$$\nu_{rate} = n\overline{\sigma_T \boldsymbol{c}_r}. \tag{2.3}$$

In the case of the hard sphere model, the frequency collision becomes $\nu_{rate} = n\pi d^2 \overline{\boldsymbol{c}_r}$. If the lifetime of a collision, which is of the order of $\sqrt{\overline{\sigma_T}}/\overline{\boldsymbol{c}_r}$, is much lower than the characteristic time between two successive collisions $\tau_{coll} \cong (n\sigma_T \overline{\boldsymbol{c}_r})^{-1}$, the probability that two colliding molecules would collide with a third partner is very low. In this case,

$$\left(\sqrt{\overline{\sigma_T}}/\overline{\boldsymbol{c}_r}\right)(n\sigma_T \overline{\boldsymbol{c}_r}) = \sigma_T^{3/2} n = \pi^{3/2}\left(\frac{d}{\delta}\right)^3 \ll 1. \tag{2.4}$$

The condition

$$\delta \gg d, \tag{2.5}$$

defines a *dilute gas*, for which the most probable events are binary collisions and ternary-collision events can be neglected. Another important characteristic length at microscale is the mean free path λ of the molecules, i.e., the mean distance traveled by a molecule between two successive collisions and is defined as:

$$\lambda = \frac{\overline{c'}}{\nu_{rate}} = \frac{\overline{c'}}{n\overline{\sigma_T \boldsymbol{c}_r}}, \tag{2.6}$$

where $\overline{c'}$ is the average thermal speed. The average thermal speed $\overline{c'} = \overline{|\boldsymbol{c} - \bar{\boldsymbol{c}}|}$ is the mean relative speed of all molecular velocities with respect to the mean macroscopic velocity of the flow $\bar{\boldsymbol{c}}$. By considering Eqs. (2.1) and (2.6), the mean free path can be rewritten as

$$\lambda = \left(\frac{\overline{c'}}{\overline{c_r}}\right)\left(\frac{\delta}{d}\right)^2 \frac{\delta}{\pi}, \tag{2.7}$$

where $\overline{c'}/\overline{c_r}$ is in the order of unity. As a consequence of Eqs. (2.5) and (2.7), in a dilute gas $\lambda \gg \delta \gg d$. Differently, in a dense gas, the mean molecular space is on the order of the kinetic diameter, and $\lambda \sim \delta \sim d$.

2.2 Fluctuations on the macroscopic properties

The mean operation can be applied on any number of samples. However, if the number of molecules on which the average is carried out is not significant, the mean value is not representative of the fluid property nor gives a valuable information. Actually, every mean value is characterized by an interval of confidence, that is a probability to be around the mean within a certain interval. The mean is subjected to statistical fluctuations which extension depends on the size of the molecular population in the chosen sample volume. Let's consider a region of fluid characterized by a molecular density n. The number of molecules that are present in a volume V is in average nV, and the probability $P(N)$ of having a certain number of molecules N in the volume V is defined by a Poisson distribution function, characterized by an expected value of $\mu_N = nV$ (Bird, 1994):

$$P(N) = e^{-nV}\frac{(nV)^N}{N!}. \tag{2.8}$$

For the central limit theorem, as N becomes very large, the Poisson distribution tends to coincide to a Gaussian distribution with a standard deviation σ_{std} equal to the square root of the mean, $\sqrt{\mu_N} = \sqrt{nV}$. This means, when N is big enough, that the number of molecules in volume V is within $nV - 2\sqrt{nV}$ and $nV + 2\sqrt{nV}$ with a probability of $\mathrm{erf}\,(2/\sqrt{2}) \cong 95\%$. It must be noticed that the interval of fluctuations $\pm A\sqrt{nV}$ becomes larger as the volume V becomes bigger, but the relative fluctuation, $\sigma_{std}/\mu_N = 1/\sqrt{nV}$, decreases. By rewriting the molecular density, n, in terms of the mean molecular spacing $\delta = n^{-1/3}$ and the control volume, V, in terms of characteristic length $L_V = V^{1/3}$, the control volume contains a big number of molecules if:

$$L_V \gg \delta. \tag{2.9}$$

A macroscopic property computed on a volume V, such as the pressure or the temperature, is characterized by a standard deviation that is inversely proportional to the square root of the number of molecules in the chosen volume, $\sqrt{nV}$. Condition (2.9) guarantees that any average property computed on the volume V is subjected to limited fluctuations, thus the macroscopic quantities are meaningfully informative on the fluid characteristic.

2.3 Intermolecular collisions

In the case of diatomic or polyatomic molecules, the field of interaction depends on the orientation of the molecules. However, the molecules are randomly oriented and the number of intermolecular interactions in a gas is so high that the molecule orientation does not play an important role in the determination of the macroscopic properties of the fluid flow. For this reason, the electrostatic force field is considered as spherically symmetric. The dependency of the force from the distance between the centers of two molecules is qualitatively depicted in Figure 2.2. At large distances, the intermolecular force tends to attract the two molecules, but as they get closer to a certain distance, the molecules start to repulse each other. The repulsion distance is determined by the kinetic diameter of the molecules.

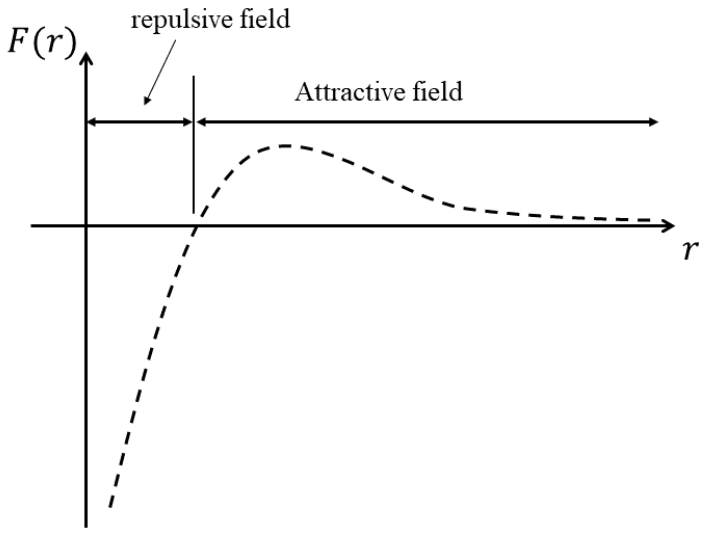

Figure 2.2. Qualitative illustration of the attractive-repulsive force between two molecules.

The analytical approach of the molecular dynamics requires a simplification of the real force field of Figure 2.2. The acceptable model for the intermolecular interactions needs to provide a correct description of the macroscopic behavior of the fluid flow, e.g., the relationship between the transport properties and the thermodynamic quantities.

A general model that embeds a group of important collisional models is the inverse power law (IPL) model. It neglects the attractive component of the force and represents only the repulsion between colliding molecules. The force F is assumed to be inversely proportional to a certain power η of the intermolecular distance r:

$$F \propto \frac{1}{r^{\eta}}. \tag{2.10}$$

Assuming the gas to be ideal and making use of the Chapman-Enskog theory, the IPL collision model provide the following general expressions for the mean free path and the dynamic viscosity:

$$\lambda = k_\lambda \frac{\mu}{\rho\sqrt{R_s T}} = k_\lambda \frac{\mu\sqrt{R_s T}}{p}, \quad \mu = \mu_0 \left(\frac{T}{T_0}\right)^\omega, \tag{2.11}$$

where p is the gas pressure, ρ is the gas density, T is the gas temperature, μ is the gas viscosity, μ_0 is the viscosity at a reference temperature T_0, $\omega = (\eta + 3)/[2(\eta - 1)]$, k_λ is the mean free path coefficient, which depends on the chosen collisional model, and $R_s = R_{univ}/M$ is the specific gas constant, which corresponds to the universal ideal gas constant R_{univ} divided by the molar mass M of the gas. The expression for the collision rate takes the form

$$\nu_{rate} = k_\nu \frac{\rho R_s T}{\mu} = k_\nu \frac{p}{\mu}, \tag{2.12}$$

in which the value of the collision rate coefficient k_ν is, like k_λ, dependent of the chosen collisional model. Because at thermodynamic equilibrium the average thermal speed is

$$\bar{c'} = \sqrt{8R_s T/\pi}, \tag{2.13}$$

Eq. (2.6) yields

$$k_\lambda = \sqrt{\frac{8}{\pi}} \frac{1}{k_\nu}. \tag{2.14}$$

The hard sphere (HS) model belongs to this category and can be recovered by setting $\eta \to \infty$, which provides a gas with a viscosity proportional to the power 0.5. However, real gases show a dependency of the viscosity from the temperature with a power in the range $0.5 < \omega \leq 1$, at least for most of the usual gases. Bird (1981) improved the HS model by introducing the variable hard sphere (VHS) model in order to represent more realistically the relationship between temperature and viscosity. In order to do so, Bird introduced a kinetic diameter inversely proportional to a certain power of the relative velocity speed c_r. Koura and Matsumoto (1991) further improved the model of Bird by introducing the variable soft sphere (VSS) model. Another collisional model that can be used for analytical studies is the Maxwell model (MM), even though it is an unrealistic model, since the collision probability does not depend on the relative speed, and ω is set to unity. The HS, VHS, VSS, and MM models all belong to the category of IPL models. The values of IPL coefficients for each of these models are listed in Table 2.1.

A more realistic collisional model is provided by the Lennard-Jones (LJ) potential. Differently from the IPL, this model takes into account the attractive component of the intermolecular interaction, even though the complexity increases. The IPL models predict a viscosity that is constant or is a power of the temperature. The attractive component of the force field influences the viscosity at very low temperatures only. The VHS and VSS models are then a simpler choice for predicting the behavior of real gases at standard temperatures.

IPL model	η	ω	k_λ	k_ν
Hard Sphere (HS)	∞	$\frac{1}{2}$	$\frac{16}{5\sqrt{2\pi}} \cong 1.277$	$\frac{5}{4}$
Variable Hard Sphere (VHS)	η	$\frac{\eta+3}{2(\eta-1)}$	$\frac{2(7-2\omega)(5-2\omega)}{15\sqrt{2\pi}}$	$\frac{30}{(7-2\omega)(5-2\omega)}$
Maxwell molecules (MM)	5	1	$\sqrt{\frac{2}{\pi}} \cong 0.7979$	2
Variable Soft Sphere (VSS)	η	$\frac{\eta+3}{2(\eta-1)}$	$\frac{4\alpha(7-2\omega)(5-2\omega)}{5(\alpha+1)(\alpha+2)\sqrt{2\pi}}$	$\frac{5(\alpha+1)(\alpha+2)}{\alpha(7-2\omega)(5-2\omega)}$

Table 2.1. Values of coefficients η, ω, k_λ and k_ν for different IPL collision models. Coefficient α is an adjusting parameter depending on the gas and introduced for the VSS models.

2.4 Gas-surface collisions

The question of which boundary condition at the wall surface best represents the macroscopic effects produced by the phenomena at a molecular level has been faced for a long time, even for the case of non-rarefied gas, and has been subject to the opinions of many great researchers of fluid dynamics, including Bernoulli, Euler, Navier, Stokes, Hagen, Helmholtz, Poisson, Poiseuille, Maxwell, Prandtl and many others (Lauga *et al.*, 2006). In the treatise *Mémoire sur les lois du mouvement des fluides* of 1813, Navier developed a mathematical description of a general velocity slip on a surface, introducing linear boundary conditions that are still nowadays employed. It was only after 1923, when Taylor demonstrated the efficacy of the no-slip boundary condition by applying it in the stability analysis of the Taylor-Couette flow, that the no-slip condition has begun to be the standard boundary condition, revealing itself to be the most appropriate one for the majority of fluid dynamics problems.

However, the fact that the no-slip boundary condition was not the appropriate one for rarefied gas flows was already clear even before the beginning of the XX century. The first evidences of velocity slip at the wall in rarefied gas flows traces back to 1875, when Kundt and Warburg carried out a series of experiments at low pressures (Kennard, 1938). In a series of lectures of 1879, Maxwell proposed a mathematical representation of the slip velocity at the wall for rarefied gases, which is still nowadays widely adopted. While investigating the stresses and the motion of gas molecules in rarefied conditions due to temperature gradients, Maxwell proposed a theoretical model for describing the interaction between the gas molecules and the wall surface. He postulated that a fraction $1-\sigma$ of the molecules impacting on the surface is perfectly reflected by the wall, while the rest of these molecules, that is the fraction σ, is diffusively reflected as a consequence of complex absorbing phenomena that depend on the nature of the gas and on the roughness and the material of the wall. In the case of $\sigma = 0$, the momentum component tangential to the wall of the incident molecule does not change after the collision with the wall surface. In this ideal case, the surface is perfectly specular and, since there is no momentum exchanged in the tangential

direction, it is as if the flow was inviscid. However, the surface is never perfectly specular and σ assumes values between 0 and 1, so that the reflection can be considered to be always partly diffusive. Figure 2.3 illustrates the two situations of perfectly specular reflection and diffuse reflection. Coefficient σ is dimensionless and is known as the *tangential momentum accommodation coefficient* (TMAC).

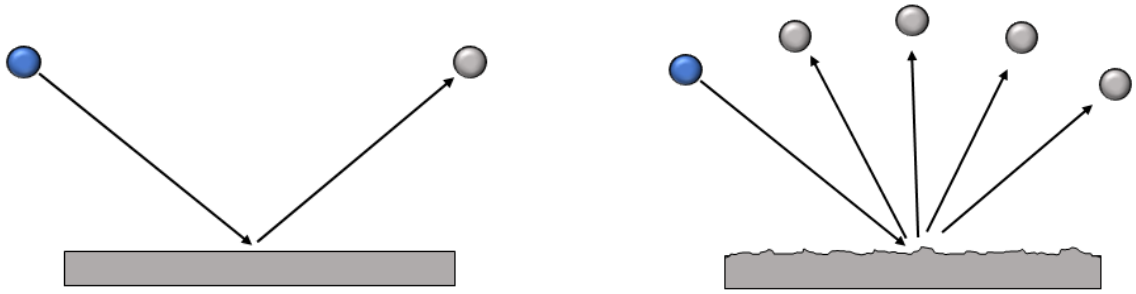

(a) (b)

Figure 2.3. Illustration of (a) specular and (b) diffusive reflection of a molecule on a solid surface.

2.5 Rarefaction regimes

Thermodynamic non-equilibrium in gas flows occurs when the intermolecular collisions happen on distances that are comparable or longer than the characteristic length of the spatial gradient of a macroscopic variable. As the level of rarefaction increases, thermodynamic non-equilibria take place at first only in very localized regions close to the wall, where the velocity and temperature gradients are stronger, and, successively, in the whole domain. Four states of rarefaction of the gas flow can be identified: (i) the hydrodynamic regime, (ii) the slip flow regime, (iii) the transitional regime, and (iv) the free molecular regime. Each flow regime corresponds to a specific range of the Knudsen number and requires a specific mathematical model capable of reproducing its dynamics:

i. For $Kn < 0.001$, the gas flow is in the *hydrodynamic regime*, and it can be treated as a continuum medium. The rarefaction effects can be neglected since they do not have an important role in the dynamics of the gas flow. The compressible Navier-Stokes equations along with the classical no-slip boundary conditions accurately model the fluid dynamics in the hydrodynamic regime.

ii. For $0.001 < Kn < 0.1$, the gas flow is in the *slip regime*. The fluid can still be treated as a continuum matter, but a state of local thermodynamic non-equilibrium arises along the wall surfaces, since the intermolecular collision rate is decreased compared to the rate of collisions between gas molecules and the wall. The rarefaction state of the gas close to the wall produces macroscopic effects on the flow field in terms of velocity slip and temperature jump at the wall. While the Navier-Stokes equations can still be employed in the bulk flow, the classical no-slip boundary conditions must be substituted with new boundary conditions that can correctly model these macroscopic effects due to the rarefaction.

iii. For $0.1 < Kn < 10$, the gas is in the *transitional flow regime*, in which the collisions between molecules and the collisions between molecules and walls have equal importance. In this case, we cannot assume the gas to be in thermodynamic equilibrium, even in the points far from the walls, thus the continuum representation breaks down.

iv. For $Kn > 10$, the flow is in the free molecular regime, in which the high rarefaction level allows the molecules to freely move in the space without intermolecular collisions, so that the only existing interaction is between the molecules and the wall.

Figure 2.4 schematically represents the four flow regimes and the related mathematical model.

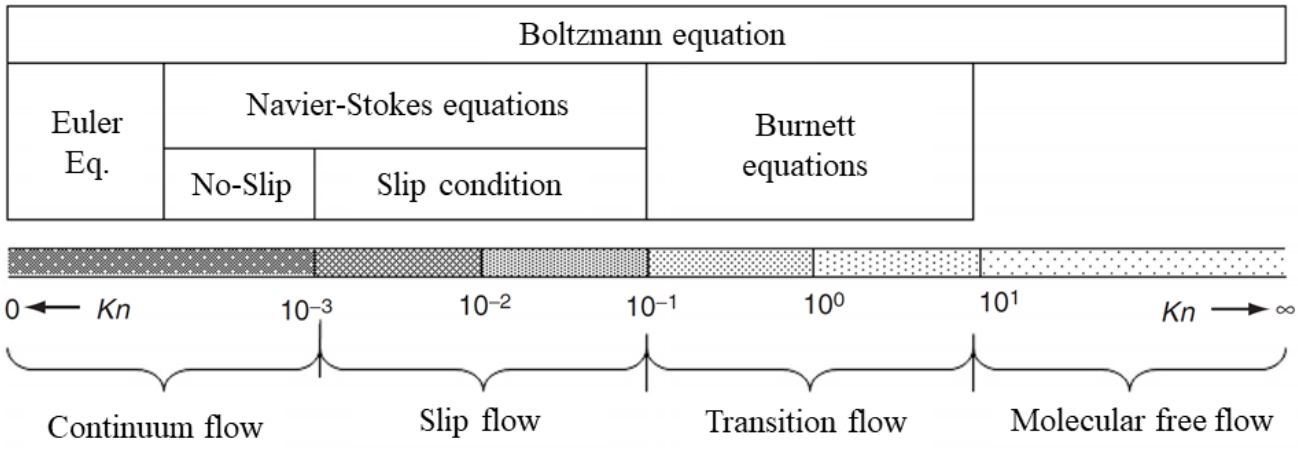

Figure 2.4. Flow regimes and corresponding mathematical models as a function of the Knudsen number. Figure from Agrawal (2012).

Even though the values of Kn that separate one gas regime from the other are not universal for every specific gas flow problem, this subdivision is useful and indicative of the order of magnitude that the Knudsen number has in a specific regime.

Note that the molecular models can be theoretically employed for any conditions along the entire rarefaction spectrum. However, their numerical solving in the case of low rarefied gases requires huge computational effort.

In the following sections, the theoretical models available for each of the above rarefaction regimes are briefly discussed.

i. Continuum regime

As discussed in Section 2.2, if a sample volume has a characteristic length that is much larger than the mean molecular spacing, the average macroscopic properties are subjected by negligible statistical fluctuations. When $Kn < 0.001$, this condition can be verified also for sample volumes that have a size that is much smaller

than the characteristic length of the fluid system. Therefore, the fluid can be modeled as a continuum medium, for which all the thermodynamic properties can be represented by means of continuous and derivable functions. Fluid flows in this rarefaction regime are accurately modeled by the well-known compressible Navier-Stokes (NS) equations.

ii. Slip flow regime

In this rarefaction regime, the continuum approach is still valid, but the no-slip boundary conditions at the wall are no longer suitable. As discussed in Section 2.4, there is a small region close to the solid surface, the Knudsen layer, that contains velocity and temperature gradients with spatial lengths comparable to the mean free path. This localized region of thermodynamic non-equilibrium in the neighborhood of the wall is always existing, even in the continuum regime. However, when the Knudsen number is in the range 0.001-0.1, the magnitude of the velocity slip and the temperature jump at the wall becomes comparable to that of the characteristic velocity and temperature of the macroscopic flow. For this reason, the no-slip boundary conditions need to be substituted by the boundary conditions presented in Section 2.4.

By applying a momentum balance at the wall, Maxwell derived the following boundary condition:

$$u_{slip} = \frac{2-\sigma}{\sigma}\lambda \left.\frac{\partial u}{\partial n}\right|_w + \frac{3}{4}\frac{\mu}{\rho T}\left.\frac{\partial T}{\partial s}\right|_w, \tag{2.15}$$

where *s* and *n* denote, respectively, the directions tangent and normal to the wall, and u the velocity of the gas. Figure 2.5 shows the physical meaning of the terms u_{slip} and $\frac{\partial u}{\partial n}$. The velocity gradient does not represent the gradient at the wall but the gradient at the outer boundary of the Knudsen layer, and the slip velocity neither represents the actual velocity jump of the gas at the wall nor the velocity at the outer boundary of the Knudsen layer. It derives, instead, from a linear extrapolation of the velocity profile outside the Knudsen layer towards the wall surface.

The boundary condition of Maxwell, Eq. (2.15), is still widely employed nowadays. However, numerical simulations (Albertoni *et al.*, 1963) demonstrated that a corrective coefficient β_{u1} slightly higher than unity should be added to the velocity slip proposed by Maxwell:

$$u_{slip} = \beta_{u1}\frac{2-\sigma}{\sigma}\lambda \left.\frac{\partial u_s}{\partial n}\right|_w. \tag{2.16}$$

A value on the order of 1.1 for β_{u1} seems to provide better predictions of the flow out of the Knudsen layer. Eq. (2.16) is considered a first-order slip boundary condition, since the slip velocity depends only on the first order derivative of the velocity. Other authors proposed values of the coefficient for the first-order boundary conditions based on different theoretical approaches, e.g., through the linearized Boltzmann equations based on the

Bhatnagar-Gross-Krook (BGK) model, lattice Boltzmann (LB) equations, or Direct Simulation Monte Carlo (DSMC).

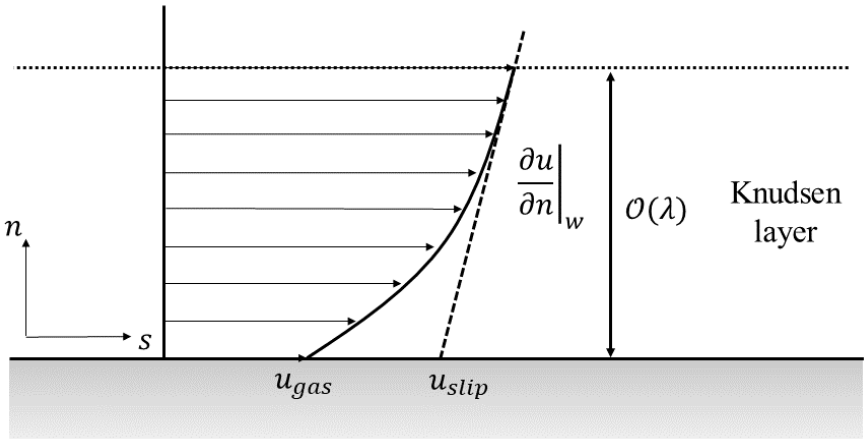

Figure 2.5. Illustrative representation of the velocity profile in the Knudsen layer: u_{slip} is the slip velocity and u_{gas} is the actual gas velocity at the wall.

	C_1	Approach
Maxwell (1879)	1	Momentum balance at the wall
Albertoni *et al*. (1963)	1.1455	BGK model
Loyalka (1971)	0.7252	BGK model
Loyalka *et al*. (1975)	1.0299	BGK model
Ohwada *et al*. (1989)	1.114	LB equations
Pan *et al.* (1999)	1.1254	DSMC simulations
Lockerby *et al*. (2005)	$\sqrt{\pi/2}$	Wall function approach

Table 2.2. Coefficients for the first-order slip boundary condition obtained by means of a theoretical approach and by assuming a fully diffusive reflection at the wall, i.e., σ = 1.

iii. Transitional regime

The coefficients listed in Table 2.2 refer to first-order slip boundary conditions that can be applied to gas flows with Knudsen numbers Kn < 0.1. When Kn is in the order of 0.1 or higher, Eq. (2.15) provides inaccurate predictions of the slip velocity at the wall. Alternative forms of Eq. (2.15) have been proposed for extending its validity to higher Knudsen number. For example, Beskok *et al*. (1999) suggested the following form for the velocity slip:

$$u_{slip} = \frac{2-\sigma}{\sigma}\frac{1}{1-B(Kn)Kn}\lambda\left.\frac{\partial u_s}{\partial n}\right|_w, \tag{2.17}$$

in which the coefficient $B(Kn)$ needs to be determined through experimental or numerical data. This form of the boundary condition does not introduce a second-order derivative for the velocity $\left.\frac{\partial^2 u}{\partial n^2}\right|_w$ and it is applicable for any Knudsen, as long as the coefficient B is determined for the Knudsen numbers of application.

However, higher-order slip boundary conditions have been proposed in the literature in order to extend to higher Knudsen numbers the validity of the continuum model with slip boundary conditions. The works of Colin (2005), Zhang *et al*. (2012), and Agrawal (2012) are only few of the reviews on the slip boundary conditions available in the literature. By defining a reference velocity u_0 and a reference length L_c, the general form of the non-dimensional second-order slip boundary condition at the wall is

$$u^*_{slip} = C_1 Kn\left.\frac{\partial u^*}{\partial n^*}\right|_w + C_2 Kn^2\left.\frac{\partial^2 u^*}{\partial n^{*2}}\right|_w, \tag{2.18}$$

where $u^*_{slip} = u_{slip}/u_0$, $u^* = u/u_0$, and $n^* = n/L_c$. There are some slip boundary conditions in which the second-order term depends on the tangential gradient of the velocity, $\partial^2 u/\partial s^2$, e.g., for the boundary condition proposed by Deissler (1964). However, for a gas flow in a channel, tangential gradients of the velocity are negligible with respect to the normal gradients if the gas can be assumed incompressible or, at least, locally incompressible. Therefore, most of the second-order slip boundary conditions proposed in the literature can be written in the form of Eq. (2.18). Table 2.3 lists, in a chronological order, some of the values of coefficients C_1 and C_2 proposed in the literature by means of theoretical considerations. The table provides also information on the way these two coefficients have been calculated. Extensions of the classical NS equations that take into account the gas rarefaction are provided by the quasi-gasdynamic (QGD) equations or the quasi-hydrodynamics (QHD) equations (Kandlikar *et al*., 2014).

	C_1	C_2	Method
Schamberg (1947)	1	$-\frac{5\pi}{12}$	?
Chapman & Cowling (1952)	$\frac{2-\sigma}{\sigma}\kappa_o \sim 1$	$\frac{2-\sigma}{\sigma}\frac{\kappa_o^2}{2} \sim 0.5$	Linearized Boltzmann
Cercignani (1963)	1.1466	-0.9756	BGK model
Deissler (1964)	$\frac{2-\sigma}{\sigma}$	-9/8	3D momentum balance at the wall
Cercignani (1988)	$\frac{2-\sigma}{\sigma}(1+0.1621\sigma)$	$\frac{2}{\pi}\left(\frac{1}{2}+c_C^2\right)$	Boltzmann equations, c_C is a parameter
Loyalka & Hickey (1989)	1.1019	0.0449	BGK model
Mitsuya (1993)	$\frac{2-\sigma}{\sigma}$	-2/9	2D momentum balance at the wall
Jie *et al.* (2000)	$\frac{2-\sigma}{\sigma}$	$\frac{2-\sigma}{\sigma}\frac{Re}{Kn}$	?
Hadjiconstantinou (2003)	1.1466	-0.647	BGK model
Lockerby *et al.* (2004)	$\frac{2-\sigma}{\sigma}$	$\frac{9}{4\pi}\frac{Pr(\gamma-1)}{\gamma}$	Boltzmann equations
Graur *et al.* (2006)	$1.012\frac{\sqrt{2}}{k_\lambda}$	$\frac{2}{k_\lambda^2}$	QGD equations
Wu (2008)	$\frac{2}{3}\left[\frac{3-\sigma f_w}{\sigma}-\frac{3}{2}\frac{3(1-f_w^2)}{Kn}\right]$	$-\frac{1}{4}\left[f_w^4+\frac{2}{Kn^2}(1-f_w^2)\right]$	Momentum balance at the wall $f_w = \min(1/Kn, 1)$
Roohi & Darbandi (2009)	$\frac{2-\sigma}{\sigma}$	$-\frac{2-\sigma}{\sigma}$	?
Li *et al.* (2011)	1	0.8	LB equations
Cercignani & Lorenzani (2010)	1.1366	-0.69261	Linearized Boltzmann, Cercignani-Lampis scattering kernel

Table 2.3. Coefficients for the second-order boundary conditions obtained by means of a theoretical approach.

iv. Free molecular regime

In the free molecular regime, the gas is so rarefied that the molecular interaction the Boltzmann equations are greatly simplified by the fact that the collision term is zero. In this case, even an analytical solution exists.

2.6 Analytical solution of gas flows in microchannels

The analytical solution of the 2D velocity distribution on a rectangular section is of significant importance for this experimental study, since it is required for comparing the velocity measurements of MTV with the mean velocity estimated by means of the constant volume technique. This idea will be further discussed in detail in Chapter 6. Moreover, the inlet over outlet pressure ratio employed in our MTV experiments is relatively high, thus the pressure distribution along the channel cannot be approximated as linear, as it usually happens in a standard non-compressible Poiseuille flow. The compressibility and rarefaction effects need to be both taken into account for obtaining a good estimation of the mean pressure and the pressure gradient along the channel. In Section 2.6.4, the different analytical solutions of the pressure distribution along the channel that are proposed in the literature are reviewed and discussed.

For these reasons, in this section, the mathematical problem for the steady gas flow in a channel with slip boundary conditions at wall is developed (Kandlikar *et al*., 2014). Since the experimental analysis of this work is applied to a channel with a rectangular section, the analytical approach here presented refers only to channels with this shape. A simplified model of the viscous and compressible gas flow is adopted for having a simple analytical solution in terms of mass flow rate and velocity profile at any cross-section of the channel. The hypotheses behind the model employed are thoroughly described and discussed in Section 2.6.1. Firstly, the ideal case of two infinite parallel plates is considered. Secondly, the real rectangular geometry of the channel section is taken into account in the mathematical problem. The different expressions of the mass flow rate are compared, and the contributions on the solution given by the velocity slip at the wall and the actual shape of the channel section are discussed.

Let us consider a channel with a length L and with a rectangular section as shown in Figure 2.6, where the smaller dimension H is the height and b is the width. Figure 2.6 also reports the Cartesian coordinates system employed. The section lies in the (y, z) plane, with the height H aligned in the y-direction, whereas the main axis of the channel points towards the x-direction. The origin of the coordinates system is placed at the center of the section, thus the walls of the channel are located at $y = \pm H/2$ and $z = \pm b/2$. The aspect ratio of the cross-section is defined as $a = H/b$. The characteristic length usually employed for characterizing the size of the channel cross-section is the hydraulic diameter D_h, defined as

$$D_h = \frac{4A}{P}, \tag{2.19}$$

where A is the area of the section, and P is its perimeter. For a rectangular section, the hydraulic diameter corresponds to

$$D_h = \frac{4Hb}{2(H+b)} = \frac{2H}{(1+a)}, \tag{2.20}$$

and if $a \ll 1$, it can be approximated as $D_h = 2H$. In the following sections, the local Knudsen number and the local Reynolds number in a cross-section are defined with respect to the hydraulic diameter as:

$$Kn = \frac{\lambda}{D_h}, \tag{2.21}$$

$$Re = \frac{\rho \bar{u} D_h}{\mu}, \tag{2.22}$$

where λ, ρ, μ, and $\bar{u}$ are the mean free path, the density, the dynamic viscosity, and the mean velocity at the considered cross-section along the channel. The Knudsen number and the Reynolds number based on the height H of the channel will be indicated differently, as Kn_H and Re_H. Finally, the local Mach number is defined as

$$Ma = \frac{\bar{u}}{c_s}, \tag{2.23}$$

with $c_S = \sqrt{\gamma R_s T}$ the speed of sound evaluated at the considered section. In the definition of the speed of sound, the parameter γ is the ratio of the specific heats of the gas considered.

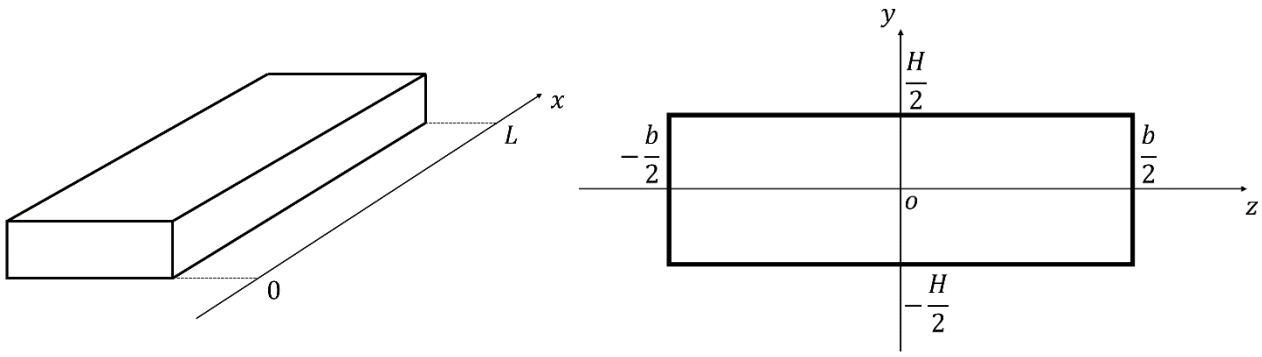

(a) (b)

Figure 2.6. Schematization of the channel geometry. The Cartesian coordinates system adopted is represented.

2.6.1 Discussion on hypotheses

The mathematical model employed for gas flows in microchannels is based on a series of hypotheses, which allows to avoid solving the full set of Navier-Stokes equations and to obtain analytical solutions of practical interest. The gas flow is assumed to be:

i. Ideal and Newtonian;
ii. Steady;
iii. Laminar;
iv. Locally-incompressible;
v. Isothermal;
vi. One-directional;
vii. Locally fully-developed.

The volume forces, e.g., gravitational forces or electromagnetic forces, are negligible in gas flows and, especially, in gas microflows, in which the surface-to-volume forces ratio is high. Understanding the field of validity of each of the hypotheses listed above is of fundamental importance for ensuring that the mathematical model employed is representative of the experimental flow.

i. Ideal and Newtonian gas

The equation of state relating the pressure, the density, and the temperature for an ideal gas is

$$p = \rho R_s T. \tag{2.24}$$

The ideal gas equation holds if the temperature is two times larger than the critical temperature T_{cr} or if the pressure is below the critical pressure p_{cr} of the gas considered. Moreover, if the gas is Newtonian, the constitutive equation that expresses the shear stresses tensor as a function of the rate of deformation is linear.

ii. Stationary flow

The steady state assumption guarantees that the thermodynamic properties and the velocity field do not depend on the time anywhere in the physical domain. This situation takes place if the boundary conditions on pressure, temperature, and velocity do not change in time as well. However, this hypothesis can still be applied even for slow-varying conditions at the inlet of the channel if the frequency response of the gas flow system is much higher than the frequency content of the external perturbation. As it will be discussed in Chapter 4, the experimental setup employed in this work is able of generating a quasi-steady gas flow, and the steady state hypothesis needs to be verified in relation to the variation rate of the inlet pressure.

iii. Laminar flow

In microchannels, laminar flows are the most common cases because of the reduced size of the channel. The problem of transition from laminar to turbulent flow is a quite complex problem. The linear stability of the laminar flow of the plane Poiseuille flow has been investigated by many authors with different methods. Orszag (1971) found a critical Reynolds number $Re_{H,cr}$ = 5772.22 by numerically solving the Orr-Sommerfeld equation, Shen (1954) and Lin (1955) found $Re_{H,cr}$ = 5360 by using the methods of asymptotic analysis, and Thomas (1953) found $Re_{H,cr}$ = 5780 using a finite-difference method. Tatsumi & Yoshimura (1990) extended the analysis of plane Poiseuille flow to flows in a rectangular duct of arbitrary aspect ratio. They demonstrated that by increasing the aspect ratio a the linear instability is delayed, and the critical Reynolds significantly increases to 10400 for an aspect ratio of 1/5. However, many experimental works (Schiller, 1923; Davies & White, 1928; Cornish, 1928) detected a transition for Reynolds much lower than the theoretical values found by Tatsumi & Yoshimura (1990). This is because, even though the flow is linearly stable, the flow transition is driven by a non-linear instability. Kao & Park (1970) were able to directly measure the instability by examining the growth or decay of controlled, artificial perturbations. They estimated Re_{cr} = 2600 for a = 1/8. Hanks & Ruo (1966) introduced a new generalized parameter for analytically predicting the laminar-turbulent transition in rectilinear flows. The application of this theory to rectangular ducts demonstrated a good agreement with the experiments. Tosun *et al*. (1988) applied this theory to rectangular ducts with different aspect ratios for numerically calculating the critical Reynolds number, which results to be Re_{cr} = 2800 for a = 0, and Re_{cr} = 1673 for a = 1. Experimental studies of water flows in rectangular micro-channels (Xu *et al.*, 2000; Pfund *et al*., 2000) confirmed critical Reynolds number $Re_{cr} \approx$ 1500-1900. The gas flows investigated in this work are characterized by Reynolds number in the order of 100 and, therefore, the hypothesis of laminar flow is largely satisfied.

iv. One-directional flow

For a steady flow, the assumption of one-directional flow brings the *y* and *z* components of the momentum conservation equation to give:

$$\frac{\partial p}{\partial y} = 0, \qquad \frac{\partial p}{\partial z} = 0. \tag{2.25}$$

If the transverse velocity components v and w are null or negligible, the pressure $p(x)$ is uniform on any cross-section of the channel and depends only on the *x* position. If the flow is isothermal, the density $\rho(x)$ is also uniform on the section and varies along the channel. Harley *et al*. (1995) tested the validity of these assumptions by solving numerically the full Navier-Stokes equations for the flow between two parallel plates with uniform wall temperature. These results demonstrated that the pressure is constant along the height even for high subsonic Mach numbers. The numerical results also showed that a transverse velocity v from the wall towards the center of the

channel is present. This velocity component exists because of the gas acceleration due to the gas compressibility. However, the numerical results of Harley *et al*. (1995) demonstrate that this velocity component is always smaller than 0.7% of the center axial velocity $u(x,0)$, even for high subsonic Mach.

Nevertheless, for gas in rarefied conditions, Arkilic *et al*. (1997) demonstrated through an analytical approach the presence of a transverse velocity in the opposite direction, from the center of the channel towards the wall. In that work, an asymptotic method is employed, in which the solution $\boldsymbol{u} = (u, v, w)$ and p are expanded with respect to the height-to-length ratio $\epsilon = H/L$, in the following way:

$$\begin{aligned} u &= u_0 + \epsilon u_1 + \epsilon^2 u_2 + \ldots \\ v &= v_0 + \epsilon v_1 + \epsilon^2 v_2 + \ldots \\ p &= p_0 + \epsilon p_1 + \epsilon^2 p_2 + \ldots \end{aligned} \tag{2.26}$$

The analytical solution for each terms of the expansion is found by introducing Eq. (2.26) in the 2D, compressible Navier-Stokes equations with first-order slip boundary conditions. They analytically demonstrated that the zeroth-order solution of the transverse velocity v_0 is null, and thus p_0 is uniform at any cross section. At first-order, the transverse velocity v_1 is a function of the Knudsen number Kn_H and of the zeroth-order pressure distribution p_0. By defining $\bar{u}_{out}$ the outlet mean axial velocity and $\bar{p}_{out}$ the outlet mean pressure, the expression of v_1 in non-dimensional form is

$$\tilde{v}_1 = \frac{\epsilon Re_H}{8\gamma Ma^2}\frac{1}{\tilde{p}_0}\left(\frac{1}{2}\frac{d^2\tilde{p}_0^2}{d\tilde{x}^2}\left(\tilde{y} - \frac{4}{3}\tilde{y}^3\right) + 4\,\frac{2-\sigma}{\sigma}Kn_H\tilde{y}\frac{d^2\tilde{p}_0}{d\tilde{x}^2}\right). \tag{2.27}$$

where $\tilde{v}_1 = v_1/\bar{u}_{out}$, $\tilde{p}_0 = p_0/\bar{p}_{out}$, $\tilde{x} = x/L$ and $\tilde{y} = y/H$. The application of the non-penetration boundary condition at the wall, that is $\tilde{v}_1|_{H/2} = 0$, results in a solvability condition for the pressure:

$$\frac{d^2\tilde{p}_0^2}{dx^2} + 12\frac{2-\sigma}{\sigma}Kn_H\frac{d^2\tilde{p}_0}{d\tilde{x}^2} = 0. \tag{2.28}$$

From Eq. (2.27) and (2.28) it can be noticed that if the $Kn_H \to 0$, v_1 goes to zero. This demonstrates that the existence of the first-order transverse velocity is due to rarefaction only. This mass transport towards the wall is necessary to maintain the mass conservation in the presence of an increasing slip velocity at the wall. However, when the channel is long, and the cross-section is small, i.e., when $\epsilon \to 0$, the transverse velocity ϵv_1 is negligible with respect to the axial velocity u_0, even for high inlet over outlet pressure ratio. This fact is shown in Figure 2.7, which shows the analytical result given by Arkilic *et al*. (1997) of $\tilde{u}_0$ and $\epsilon\tilde{v}_1$ for an inlet over outlet pressure ratio of 3 and Kn_H = 0.165. The magnitude of the transverse velocity increases while moving towards the channel outlet due to the rapid change of the pressure drop close to the exit of the channel. The non-dimensional first-order transverse velocity is 5 orders of magnitude smaller than the non-dimensional zeroth-order axial velocity. It is

interesting to notice that the mass migration towards the wall affects the molecules accordingly to their molecular weight, thus a gas-separation can take place in gas-mixture flows.

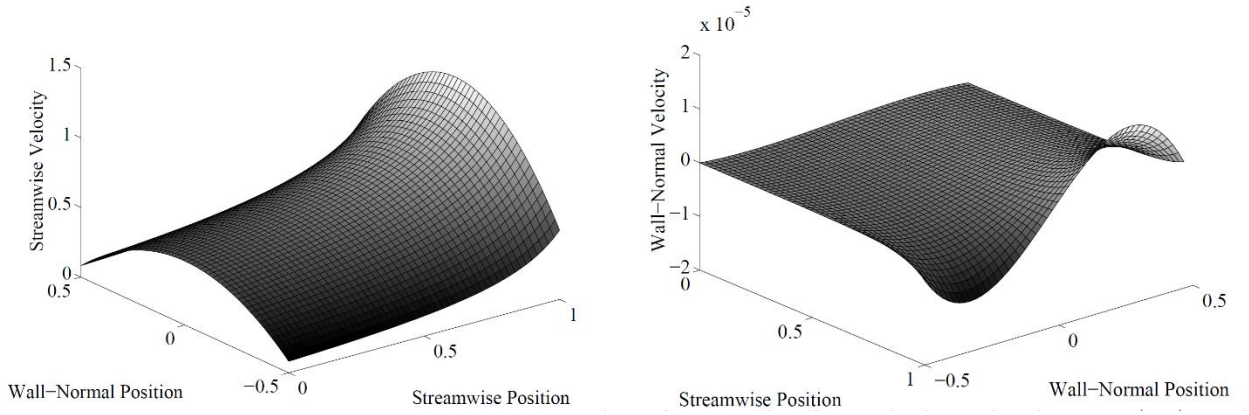

(a) (b)

Figure 2.7. Analytical solution from Arkilic *et al*. (1997) for Kn_H = 0.165 and an inlet-outlet pressure ratio of 3: (a) plot of the non-dimensional zeroth-order axial velocity $\tilde{u}_0$; (b) plot of the non-dimensional first-order transverse velocity $\epsilon\tilde{v}_1$.

v. Local incompressibility

The common criterion for incompressibility is based on verifying that the Mach number is always less than 0.3. This limit value for the Mach number comes from an evaluation of how much the gas density can vary in an isentropic flow, where no heat exchanges with the external environment and no irreversible phenomena are present. For a compressible, isentropic flow, the stagnation density ρ_0 is related to the static density ρ of the gas as

$$\rho_0 = \rho\left(1 + \frac{\gamma - 1}{2} Ma^2\right)^{1/(\gamma-1)}. \tag{2.29}$$

If Ma < 0.3, the increase in gas density due to decelerations of the flow are certainly less than 5%. This Mach number criterion for incompressibility check works for gas flows where pressure variations are due to velocity variations and not to viscous phenomena. This is the case of gas flows around aerodynamic bodies, such as airfoils, where the compression and expansion of the gas are caused by the presence of the solid object. In channel flows, a pressure drop along a channel is required for balancing the viscous stresses and for having a flowing gas. Here, viscous effects are dominant due to the relatively high velocity gradients at the wall, and the heat generation is relevant. Eq. (2.29) is, therefore, not valid in this situation, as the isentropic assumption does not hold anymore. Indeed, compressible behaviors of the gas can appear for Mach numbers even lower of 0.3. Especially in microchannels, high inlet over outlet pressure ratios can be obtained because of the small inner diameter, and the gas density can decrease considerably along the channel. Because of mass conservation, the gas expansion causes

an acceleration of the gas and, consequently, an increase in the local pressure gradient. If the pressure drop is less than 5% with respect to the inlet pressure, the density variation along the channel can be neglected, and the flow can be considered as globally incompressible. However, if the pressure drop is higher than 5% and the Mach number is not higher than 0.3, the local gradients of velocity and density are small in the flow direction, and the gas can be considered as locally incompressible (Morini *et al*., 2011). Harley *et al*. (1995) compared the analytical solution based on the hypothesis of local incompressibility with the numerical solutions of the full Navier-Stokes equations. They observed a discrepancy of less than 3% between the theoretical and numerical solutions only if $Ma < 0.3$ (see Figure 2.8b). The hypothesis of local incompressibility greatly simplifies the mathematical problem. In a one-directional flow, the incompressibility constraint yields

$$\boldsymbol{\nabla} \cdot \boldsymbol{u} = \frac{\partial u}{\partial x} + \frac{\partial v}{\partial y} + \frac{\partial w}{\partial z} = \frac{\partial u}{\partial x} = 0, \tag{2.30}$$

and $u = u(y, z)$ is, therefore, a function only of the position on the cross-section. The mass conservation law reads

$$\boldsymbol{\nabla} \cdot (\boldsymbol{u}\rho) = \boldsymbol{u} \cdot \boldsymbol{\nabla}\rho = u\frac{\partial \rho}{\partial x} = 0, \tag{2.31}$$

thus, the gas density ρ does not depend on *x*. This approximation has been demonstrated to work quite well in microchannel flows and to provide results in good match with experimental data, as it will be shown in Section 2.6.4.

vi. Isothermal flow

The isothermal hypothesis is widely used in microchannel flows, but its validity has been a matter of discussion in the past years. The work of Van den Berg *et al*. (1993) was addressed to verify the isothermal assumption for compressible gas flows in capillaries. Also, the work of Harley *et al*. (1995) and Cai *et al*. (2007) contributed to understand the scope of validity of this hypothesis in microchannel gas flows.

Actually, the temperature field is not uniform in the channel, but it is a good assumption for low subsonic Mach numbers. While the viscous dissipation can generate a considerable amount of heat, the gas expansion caused by the pressure drop in the flow direction tends to cool down the gas. As pointed out in Morini *et al*. (2012), since the viscous dissipation and the thermal cooling expansion are proportional, respectively, to $(\partial u/\partial y)^2$ and to u, a heat sink is located at the centerline of the channel, while the heat generation is dominant close to the walls. Van den Berg *et al*. (1993) were able to show analytically the separate contribution given by the viscous dissipation and the thermal expansion to the temperature distribution along a capillary. Moreover, they showed that, for the flow conditions under analysis, the net temperature distribution is decreasing in the flow direction, since the thermal cooling effect results to be dominant. Harley *et al*. (1995) numerically demonstrated the same effect in the two parallel plates configuration. In these numerical simulations, the channel was 4-μm deep and 100-μm long and no-

slip boundary conditions were employed. Figure 2.8 shows the evolution along the channel of the centerline temperature, velocity, and density, made non-dimensional with the conditions at the channel inlet, for a gas flow between parallel plates. Figure 2.8a and Figure 2.8b show the numerical solution for an outlet Mach number Ma_{out} of 0.15 and 0.84, respectively. Because of the compressibility, the density decreases and the velocity increases. The initial sharp temperature drop is due to the absence of velocity gradient, and, therefore, viscous dissipation at the entrance, as the inlet velocity is imposed to be uniform. While for the case of low Mach numbers the centerline temperature decreases of less than 0.5% on the channel's length, the temperature drop is of 12% for high subsonic Mach number. However, most of this drop occurs close the channel exit, and for the 80% of the channel's length the temperature varies of less than 3%.

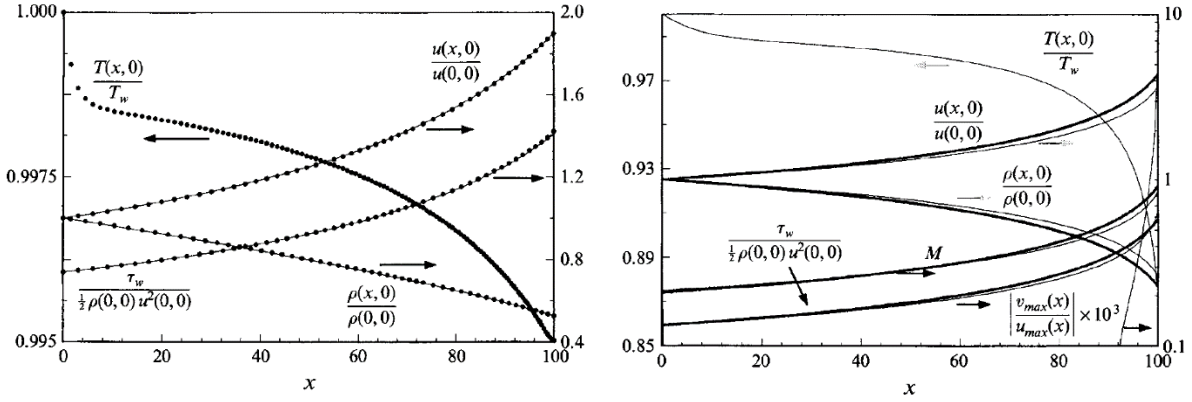

(a) (b)

Figure 2.8. Numerical solution provided by Harley *et al*. (1995) of the centerline temperature, velocity, and density distribution along the channel length, for a compressible, viscous gas between two parallel plates, with no-slip boundary conditions: (a) Ma_{in} = 0.07, and Ma_{out} = 0.15; (b) Ma_{in} = 0.21, and Ma_{out} = 0.85. The thin solid line represents the analytical solution based on an isothermal, locally incompressible model. In (b), the Mach number evolution is also shown.

The theoretical work of Van den Berg *et al*. (1993) and Harley *et al*. (1995) did not take into account neither slip velocity nor temperature jump at the wall. However, Cai *et al*. (2007) analytically investigated a non-isothermal gas flow in a parallel plates geometry by taking into account the rarefaction effects at the wall, and the temperature variations across the section and along the channel were seen to be always less than 0.2% for Ma_{out} less than 0.15. Even though the temperature variation on the cross-section is quite small, considering the small inner diameter of a microchannel, the temperature gradients can be large, and the heat fluxes can be quite significant. Some authors (Arkilic *et al*., 1995, Jang & Wereley, 2004) state that the isothermal hypothesis can be considered satisfied if $Ma \ll 1/\sqrt{\gamma}$, where, for a diatomic gas, γ = 1.4, and $1/\sqrt{\gamma} \approx 0.84$. This limitation on the Mach number is, anyway, less restrictive than that for guaranteeing local incompressibility.

vii. Locally, fully developed flow

As soon as the fluid enters the channel with a certain velocity, viscous effects tend to slow down the flow close to the wall, causing an acceleration of the flow at the center of the channel for maintaining the mass flow rate through the cross-section constant. In the first part of the channel, the fluid flow develops as the boundary layer thickness grows at the wall. In a steady, incompressible flow, the flow is considered as "fully-developed" when the viscous stresses and the pressure forces are in balance, and there is no variation of the momentum flux. In this situation, the velocity profile does not change neither in magnitude nor in shape. The fully-developed state is also associated to the unidirectionality of the flow, and the consequent uniformity of pressure and density on the cross-section. Mathematically, this condition corresponds to $\partial u/\partial x = 0$, and $v = w = 0$.

However, in a rarefied, compressible flow, this condition can never be satisfied. The velocity profile continuously develops along all the length of the channel since the decreasing density requires a gas acceleration for respecting mass conservation, and the increasing rarefaction level due to the pressure drop modifies the shape of the velocity profile. Moreover, as previously discussed, compressibility and rarefaction can generate transverse velocity components, even if the deviation from unidirectionality is negligible. A compressible flow cannot be, therefore, fully developed in the sense described for incompressible flows. Nevertheless, an entrance region with a certain length where the boundary layer forms exists even for a compressible flow. Moreover, even though the velocity profile keeps developing itself across all the channel length, the pressure and viscous forces locally balanced each other in first approximation. Therefore, a compressible flow can be approximated as locally, fully-developed as soon as the entrance effects disappear.

The hydrodynamic development length x_d is arbitrarily defined as the distance through the channel required for the centerline velocity to reach 99% of the fully-developed value. It is important to have an estimation of the entrance length in order to be aware of the percentage of the channel's length for which the fully-developed flow assumption is correct.

Many works have been dedicated to the theoretical and experimental evaluation of the entrance length in tubes and ducts of laminar incompressible flows. The results are always expressed in terms of x_d/D_h as a function of the Reynolds number. Although the absence of a universal formula, the data present in the literature are not widely scattered (Durst *et al*., 2005). Atkinson *et al*. (1969) proposed the following linear relationship between the non-dimensional development length and the Reynolds number for the parallel plates flow:

$$\frac{x_d}{D_h} = 0.3125 + 0.011Re. \tag{2.32}$$

Chen *et al*. (1973) proposed a similar formula:

$$\frac{x_d}{D_h} = \frac{0.3125}{0.0175Re + 1} + 0.011Re. \tag{2.33}$$

As the inner diameter of the channel reduces, the hydrodynamic development length becomes shorter as well. In microchannels, the entrance effects should be more limited for a chosen Reynolds number. The two terms in the right-hand side of Eq. (2.32) and Eq. (2.33) represent two different regimes of Reynolds numbers. From a mathematical point of view, the term proportional to the Reynolds number is the main contribution to x_d/D_h in the limit of high Reynolds numbers, while the other term is the main contribution in the low Reynolds number limit.

Interestingly, more recent studies pointed out that the presence of a slip velocity at the wall increases the hydrodynamic development length. Based on a numerical model, Barber & Emerson (2002) found the following relationship for an incompressible, laminar, slip flow between parallel plates:

$$\frac{x_d}{D_h} = \frac{0.332}{0.0271Re + 1} + 0.011Re\left[\frac{1 + 14.78(2 - \sigma)/\sigma Kn}{1 + 9.78(2 - \sigma)/\sigma Kn}\right], \tag{2.34}$$

which is quite similar to the formula of Chen *et al*. (1973) with the addition of a correcting factor depending on Kn. Another similar formula based on an analytical model was found by Duan *et al*. (2010):

$$\frac{x_d}{D_h} = \frac{0.315}{0.0175Re + 1} + 0.0112Re\left[1 + 6.7\frac{2 - \sigma}{\sigma}Kn - 37\left(\frac{2 - \sigma}{\sigma}Kn\right)^2\right]. \tag{2.35}$$

The difference between the results given by Eq. (2.34) and Eq. (2.35) is less than 8%, which is more than acceptable for having an estimation of the hydrodynamic development length. By considering full accommodation, i.e., σ = 1, Kn = 0.01, and Re = 100, Eq. (2.35) gives x_d/D_h = 1.3054. In a 1-mm deep channel, x_d = 2.6 mm.

Eqs. (2.34) and (2.35) provide an analytical expression for calculating the hydrodynamic development length in a parallel plates flow. These formulas are, therefore, valid if $a \to 0$. However, when the aspect ratio is close to unity, the presence of the lateral walls has an effect on the entry development of the flow. Han (1960) was the first to attempt a theoretical analysis of the flow development in rectangular ducts. By linearizing the axial momentum equation, a closed-form of the axial velocity was found for the entrance region. allowing for an evaluation of the development length. In this work, the computed non-dimensional entrance length $x_d/(D_h Re)$ was found to be 0.0752 and 0.0099 for a = 1 and a = 0, respectively. The value 0.0099 corresponding to the parallel plates case is similar to the coefficients 0.011 and 0.0112 of Eq. (2.34) and Eq. (2.35), respectively, namely the terms in the high Reynolds number limit. The general trend is that as the aspect ratio increases, the hydrodynamic development length is longer. The experimental studies of Sparrow *et al*. (1967) and of Beaver *et al*. (1969) demonstrated qualitatively the same result, even if some differences are present in the estimated entrance lengths. Beaver *et al*. (1969) tested water and light oil flows in seventeen channels with aspect ratios from 1.1 up to 51:1, for Reynolds

numbers between 400 and 3000. They concluded that for a < 0.5, $x_d/(D_h Re)$ is always about 0.015, whereas for a close to unity $x_d/(D_h Re) \sim 0.03$, which is more than the half the value estimated by Han (1960). Sparrow *et al*. (1967) carried out experiments with air flows in two channels, one with a = 0.5 and the other with a = 0.2. For the channel a = 0.2, they observed a developed flow for $x_d/(D_h Re) \geq 0.08$, while the channel a = 0.5 presented a slower development. Han (1960) estimated $x_d/(D_h Re)$ = 0.0427 for a = 0.25 and $x_d/(D_h Re)$ = 0.066 for a = 0.5, which are values smaller than those observed by Sparrow *et al*. (1967). By substituting the coefficient 0.0112 of Eq. (2.35) with the value 0.08 found by Sparrow *et al.* (1967) for a = 0.2, Eq. (2.35) can be still used for an estimation of the hydrodynamic development length in a channel with a rectangular cross-section. For σ = 1, Kn = 0.01, and Re = 100, the modified version of Eq. (2.35) gives x_d/D_h = 8.621, which corresponds to x_d = 14.4 mm, in a channel with a 1 × 5 mm^2 cross-section. This value of x_d is 7 times larger than the one previously calculated with the original form of Eq. (2.35) for the parallel plates.

It is important to underline that, while for an incompressible flow the definition of the Reynolds number to be used in the calculation of x_d/D_h is based on a constant density $\bar{\rho}$, for a compressible flow the gas density decreases. However, as it can be observed from the numerical results of Harley *et al*. (1995) shown in Figure 2.8, the density variation in the first few percentages of the channel length is quite small, even at high subsonic Mach numbers. Due to mass conservation, the mean velocity does not change much as well. The Reynolds number can be, therefore, calculated by taking the values of ρ, $\bar{u}$, and μ at the inlet.

2.6.2 Analytical solution of slip flow in parallel plates

When the aspect ratio a of the cross-section of the channel is very small, the gradients of the axial velocity in the direction of the smaller dimension, H, are much higher than the gradients in the other direction, so that:

$$\frac{\partial^2 u}{\partial y^2} \gg \frac{\partial^2 u}{\partial z^2}. \tag{2.36}$$

Hence, if $a \ll 1$, the momentum conservation equation for a locally-incompressible, locally fully-developed, laminar flow becomes:

$$\frac{d^2 u}{dy^2} = \frac{1}{\mu}\frac{dp}{dx}, \tag{2.37}$$

which represents the governing equation for the flow velocity between two infinite parallel plates. Eq. (2.37) is completed by the first-order slip boundary condition, Eq. (2.38), and the symmetry condition at the centerline of the channel, Eq. (2.39):

$$u(y = H/2) = -\beta_{u1}\frac{2-\sigma}{\sigma}\lambda\left.\frac{du}{dy}\right|_{y=\frac{H}{2}}, \tag{2.38}$$

$$\left.\frac{du}{dy}\right|_{y=0} = 0. \tag{2.39}$$

The application of second-order slip boundary conditions will be presented later in this section. In the previous section, the analytical work of Arkilic *et al*. (1997) has been introduced for discussing the presence of transverse velocity due to rarefaction effects in the flow between two parallel plates. The asymptotic method demonstrates that the zeroth-order axial velocity, u_0 in Eq. (2.26), solves exactly the same Eq. (2.37). This means that for long microchannels, i.e., when $\epsilon = H/L \to 0$, the hypothesis of local incompressibility is satisfied and the velocity and density gradient in the axial direction are negligible.

The mathematical problem formed by Eq. (2.37), (2.38), and (2.39), is applied to each section along the channel length. Since the pressure varies non-linearly with *x*, the pressure gradient is a function of *x*. For a dilute gas, the dynamic viscosity μ is only a function of the temperature. Since the flow is considered as isothermal, μ is everywhere constant. The analytical solution of the mathematical problem is:

$$u(x,y) = u_{slip}(x) + u_{cp}(x)\left(1 - \frac{y^2}{\frac{H^2}{4}}\right), \tag{2.40}$$

where

$$u_{cp} = -\frac{H^2}{8\mu}\frac{dp}{dx}, \tag{2.41}$$

$$u_{slip} = -\beta_{u1}\frac{2-\sigma}{\sigma}\lambda\frac{H}{2\mu}\frac{dp}{dx}. \tag{2.42}$$

The slip velocity u_{slip} translates forward the well-known plane Poiseuille velocity profile. u_{cp} is the centerline velocity of the plane Poiseuille velocity profile with no-slip at the wall. The dependence of u_{slip} and u_{cp} on *x* has been made explicit in Eq. (2.40). As discussed in the previous section, since the pressure decreases, and the gas accelerates while moving through the channel, the mean free path and the pressure gradient increases as well. Eq. (2.40) can be rewritten in a non-dimensional form by introducing the Knudsen number $Kn = \lambda/2H$ and by making the velocity non-dimensional with respect to u_{cp}:

$$u^* = \frac{u(x,y)}{u_{cp}} = \left(1 - y^{*2}\right) + 8\beta_{u1}\frac{2-\sigma}{\sigma}Kn, \tag{2.43}$$

in which $y^* = \frac{y}{H/2}$. The integration of the velocity profile over the height of the channel provides the mean velocity $\bar{u}(x)$ on each cross-section of the channel:

$$\bar{u}(x) = \frac{1}{H}\int_{-\frac{H}{2}}^{\frac{H}{2}} u(y)dy = u_{slip} + \frac{2}{3}u_{cp} = -\frac{H^2}{8\mu}\frac{dp}{dx}\left[\frac{2}{3} + 8\beta_{u1}\frac{2-\sigma}{\sigma}Kn\right]. \tag{2.44}$$

By using Eq. (2.44) and the equation of state of ideal gas, Eq. (2.24), the mass flow rate $\dot{m} = A\bar{u}(x)\rho(x)$ assumes the following expression:

$$\dot{m}_{plane,S1} = -\frac{bH^3}{8\mu}\frac{dp}{dx}\frac{p}{RT}\left[\frac{2}{3} + 8\beta_{u1}\frac{2-\sigma}{\sigma}Kn\right], \tag{2.45}$$

in which $A = bH$ is the area of the cross-section. The subscript "plane, S1" indicates that $\dot{m}_{plane,S1}$ is the expression for the mass flow rate in the parallel plates geometry and when the first-order slip boundary conditions are used. In a steady flow, the mass flow rate $\dot{m}_{plane,S1}$ is the same at any cross-section of the channel. Therefore, the pressure, the pressure gradient and Knudsen need to evolve along the channel accordingly to maintain the mass flow rate $\dot{m}_{plane,S1}$ constant. Eq. (2.45) requires the knowledge of the pressure gradient at a specific position *x* for calculating the mass flow rate through the channel. A more practical expression for $\dot{m}_{plane,S1}$ can be found by integrating Eq. (2.45) along the channel length L. In a dilute gas, the collision frequency ν is always proportional to the gas pressure, whatever is the collisional model chosen (see Eq. (2.12)), and, consequently, the mean free path and the Knudsen number are inversely proportional to the pressure. Hence, the product $Kn \cdot p$ is constant along the channel, and it can be set, arbitrarily, to $Kn_{out} \cdot p_{out}$. The integration of Eq. (2.45) yields to

$$\dot{m}_{plane,S1} = \frac{1}{L}\int_0^L \dot{m}_{plane,S1}dx = \frac{H^4 p_{out}^2}{4a\mu RTL}\left[\frac{\Pi^2-1}{6} + 4\beta_{u1}\frac{2-\sigma}{\sigma}Kn_{out}(\Pi-1)\right], \tag{2.46}$$

where the definition of the inlet-outlet pressure ratio $\Pi = p_{in}/p_{out}$ has been introduced. Eq. (2.46) is more interesting for practical applications, as it does not depend on the local thermodynamic conditions nor the local pressure gradient, but only on the thermodynamic conditions at the inlet at the outlet of the channel, which are much more accessible from an experimental point of view. By setting Kn_{out} to zero, the classical plane Poiseuille mass flow rate with no-slip at the wall is obtained:

$$\dot{m}_{plane,ns} = \frac{H^4 p_{out}^2}{4a\mu RTL}\frac{\Pi^2-1}{6}. \tag{2.47}$$

The mass flow rate $\dot{m}_{plane,S1}$ of Eq. (2.46) is commonly made non-dimensional with respect to $\dot{m}_{plane,ns}$ for a better quantification of the effect given by the slip at the wall on the mass flow rate:

$$\dot{m}^*_{plane,S1} = \frac{\dot{m}_{plane,S1}}{\dot{m}_{plane,ns}} = 1 + 24\beta_{u1}\frac{2-\sigma}{\sigma}\frac{Kn_{out}}{\Pi+1}. \tag{2.48}$$

These solutions are accurate for Knudsen numbers up to 0.1 (Colin, 2005). In order to improve the accuracy of the solution for higher Knudsen number, a slip boundary condition of higher order must be considered. By substituting the first-order slip boundary condition Eq. (2.38) with the general form of the second-order slip boundary condition

$$u(y = H/2) = -C_1\lambda\left.\frac{du}{dy}\right|_{y=\frac{H}{2}} - C_2\lambda^2\left.\frac{d^2u}{dy^2}\right|_{y=\frac{H}{2}}, \tag{2.49}$$

the resulting velocity profile has the same form as Eq. (2.42), but with a slip velocity that contains an additive term:

$$u_{slip} = -C_1\lambda\frac{H}{2\mu}\frac{dp}{dx} - C_2\lambda^2\frac{1}{\mu}\frac{dp}{dx}. \tag{2.50}$$

The non-dimensional velocity profile becomes

$$u^* = \left(1 - y^{*2}\right) + 8C_1Kn + 32C_2Kn^2, \tag{2.51}$$

and the mass flow rate in its dimensional and non-dimensional form, respectively, is

$$\dot{m}_{plane,S2} = \frac{H^4 p_{out}^2}{4a\mu RTL}\left[\frac{\Pi^2-1}{6} + 4C_1Kn_{out}(\Pi-1) + 16C_2Kn_{out}^2\ln\Pi\right], \tag{2.52}$$

$$\dot{m}^*_{plane,S2} = 1 + 24C_1\frac{Kn_{out}}{\Pi+1} + 96C_2Kn_{out}^2\frac{\ln\Pi}{\Pi^2-1}. \tag{2.53}$$

By setting $C_1 = \beta_{u1}\frac{2-\sigma}{\sigma}$ and $C_2 = 0$, the solutions for the first-order slip boundary condition is recovered.

2.6.3 Analytical solution of slip flow in a rectangular channel

When the aspect ratio a is higher than 0.01, the parallel plates assumption may provide mass flow rates that are substantially different from the correct value of the mass flow rate inside the rectangular channel (Colin, 2005). Actually, the magnitude of the velocity on the cross-section decreases while moving towards the lateral walls of the channel and it does not correspond to the same velocity profile. When the aspect ratio a > 0.01, the mean velocity calculated by Eq. (2.44) overestimates the mean velocity on the rectangular section, up to more than 40% when a = 1, i.e., for a square section.

In a rectangular cross-section channel, the gradients of the axial velocity u in the *z*-direction are not negligible with respect to those along the *y*-direction. Thus, the *x*-component of the momentum conservation equations takes the following form

$$\frac{d^2u}{dy^2}+\frac{d^2u}{dz^2}=\frac{1}{\mu}\frac{dp}{dx}, \tag{2.54}$$

where the axial velocity $u(y,z)$ is now a function of both *y* and *z*. The slip boundary conditions are now applied also to the lateral walls at $z=\pm b/2$. As it was done for the *y*-direction, one of the two slip condition is substituted with a condition of symmetry at $z=0$. Eq. (2.54) is then completed by the following set of boundary conditions:

$$u|_{y=\frac{H}{2}}=-\beta_{u1}\frac{2-\sigma}{\sigma}\lambda\left.\frac{\partial u}{\partial y}\right|_{y=\frac{H}{2}}, \tag{2.55}$$

$$u|_{z=\frac{b}{2}}=-\beta_{u1}\frac{2-\sigma}{\sigma}\lambda\left.\frac{\partial u}{\partial z}\right|_{z=\frac{b}{2}}, \tag{2.56}$$

$$\left.\frac{\partial u}{\partial y}\right|_{y=0}=0, \qquad \left.\frac{\partial u}{\partial z}\right|_{z=0}=0. \tag{2.57}$$

This mathematical problem is rewritten in a dimensionless form, so that Eq. (2.54) becomes

$$a^2\frac{\partial^2 u^*}{\partial y^{*2}}+\frac{\partial^2 u^*}{\partial z^{*2}}=-1, \tag{2.58}$$

where $y^*=y/(H/2)$, $z^*=z/(b/2)$, and $u^*=u/\left(2u_{cp}\right)$, with u_{cp} as defined in Eq. (2.41).

Different authors proposed a solution to this problem by means of different methods. Based on the linearity of Eq. (2.58), Ebert & Sparrow (1965) proposed to assume the following form for the velocity distribution:

$$u^*(y^*,z^*)=-\sum_{i=1}^{\infty}\Psi_i(z^*)\cos(\alpha_i y^*), \tag{2.59}$$

in which the dependence of u^* from y^* and z^* has been decomposed in the two base functions $\cos(\alpha_i y^*)$ and $\Psi_i(z^*)$, respectively. The choice of the function $\cos(\alpha_i y^*)$ allows to automatically satisfy the symmetry condition in the *y*-direction. The α_i are a set of eigenvalues, which possible values are found by substituting Eq. (2.59) in the slip boundary condition Eq. (2.55):

$$\sum_{i=1}^{\infty}\Psi_i(z^*)\left[\cos(\alpha_i)-2\alpha_i\beta_{u1}\frac{2-\sigma}{\sigma}Kn_H\sin\alpha_i\right]=0, \tag{2.60}$$

where the definition of the Knudsen number Kn_H based on the height of the channel has been employed. The non-trivial solutions α_i of Eq. (2.60) are given by the transcendental equation

$$\alpha_i \tan \alpha_i = \frac{1}{\beta_{u1}} \frac{\sigma}{2-\sigma} \frac{1}{2Kn_H}. \tag{2.61}$$

By substituting Eq. (2.59) in Eq. (2.58), the expression of the eigenfunctions Ψ_i is found:

$$\Psi_i = -\frac{\Omega_i}{\alpha_i^2}\left(1 - \frac{\cosh\left(\frac{\alpha_i z^*}{a}\right)}{\cosh\left(\frac{\alpha_i}{a}\right) + 2\beta_{u1}\left(\frac{2-\sigma}{\sigma}\right)Kn_H \alpha_i \sinh\left(\frac{\alpha_i}{a}\right)}\right), \tag{2.62}$$

with

$$\Omega_i = \frac{2\sin\alpha_i}{\alpha_i + \sin\alpha_i \cos\alpha_i}. \tag{2.63}$$

In Figure 2.9, the velocity distribution of Ebert & Sparrow has been calculated by taking into account the first 50 terms of the series. The solution is illustrated for a cross-section with a = 0.2 and for two Knudsen numbers: Kn_H = 0 (Figure 2.9a), and Kn_H = 0.01 (Figure 2.9b).

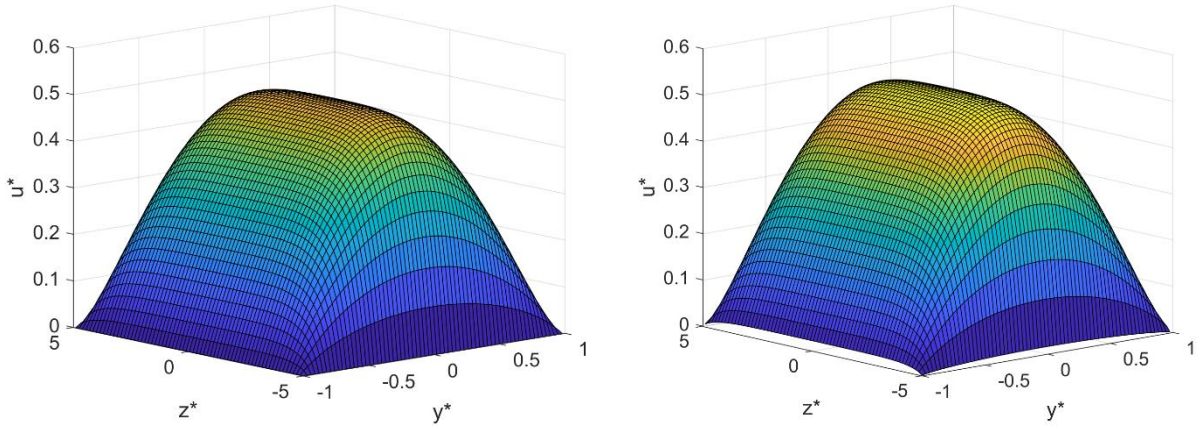

(a) (b)

Figure 2.9. Non-dimensional velocity distribution for β_{u1} = 1.1 and σ = 1, computed from the solution proposed by Ebert & Sparrow (1965): (a) Kn_H = 0; (b) Kn_H = 0.01. The first 50 terms of the series Eq. (2.59) have been considered.

The dimensional mean velocity is calculated by integrating on the cross-section the velocity distribution Eq. (2.59):

$$\bar{u}(x) = \left(-\frac{H^2}{4\mu}\frac{dp}{dx}\right)\frac{1}{4}\int_{-1}^{1}\int_{-1}^{1} u^*(x, y^*, z^*)dy^*dz^*, \tag{2.64}$$

with

$$\int_{-1}^{1}\int_{-1}^{1} u^*(x, y^*, z^*)dy^*\,dz^* =$$

$$4\left[\sum_{i=1}^{\infty}\left(\frac{\sin\alpha_i}{\alpha_i}\right)\left(\frac{\Omega_i}{\alpha_i^2}\right)\left(1-\frac{a/\alpha_i\sinh(\alpha_i/a)}{\cosh(\alpha_i/a)+2\beta_{u1}\dfrac{(2-\sigma)}{\sigma}Kn_H\alpha_i\sinh(\alpha_i/a)}\right)\right]. \tag{2.65}$$

The mass flow rate at any cross-section of the channel is provided by the following expression:

$$\dot{m}_{rect,S1}=-\frac{H^4}{4\mu a}\frac{dp}{dx}\frac{p}{RT}\left[\sum_{i=1}^{\infty}\left(\frac{\sin\alpha_i}{\alpha_i}\right)\left(\frac{\Omega_i}{\alpha_i^2}\right)\times\left(1-\frac{a/\alpha_i\sinh(\alpha_i/a)}{\cosh(\alpha_i/a)+2\beta_{u1}\dfrac{(2-\sigma)}{\sigma}Kn_H\alpha_i\sinh(\alpha_i/a)}\right)\right]. \tag{2.66}$$

The subscript 'rect,S1' indicates that the analytical expression of the mass flow rate is valid for first-order slip boundary conditions in a channel with rectangular section. As discussed in Section 2.6.2 for the parallel plates problem, the dependency of the mass flow rate from the pressure gradient is not desirable. From a practical point of view, an expression for $\dot{m}_{rect,S1}$ that only depends on the inlet-outlet pressure ratio is preferred. However, the analytical integration along the channel length of Eq. (2.66) is quite cumbersome. The calculation of the term in the brackets of Eq. (2.66) for Knudsen number in the range [0; 0.1] reveals a linear dependency with Kn_H. Therefore, the term in the bracket can be substitute by the polynomial fitting function $a_1 + a_2 Kn_H$ (Aubert & Colin, 2001), thus the mass flow rate takes the form

$$\dot{m}_{rect,S1}=-\frac{H^4}{4\mu a}\frac{dp}{dx}\frac{p}{R_sT}[a_1+a_2Kn_H]. \tag{2.67}$$

Coefficients a_1 and a_2 depend on the aspect ratio a of the channel cross-section, on the accommodation coefficient σ, and on the corrector factor β_{u1}. Table 2.4 shows the values of these coefficients for different values of the aspect ratio and for σ = 1 and β_{u1} = 1.1.

	$a=1$	$a=0.8$	$a=0.6$	$a=0.4$	$a=0.2$
a_1	0.1413	0.1724	0.2093	0.2499	0.2916
a_2	1.1881	1.3258	1.5016	1.7185	1.958

Table 2.4. Fitting coefficients a_1 and a_2 for the velocity distribution of Ebert & Sparrow (1965) with first-order boundary conditions, with σ = 1 and β_{u1} = 1.1.

An analytical solution for the mass flow rate in the no-slip problem can also be obtained, and its comparison with Eq. (2.67) for Kn_H = 0 provides the following analytical expression for the fitting coefficient a_1:

$$a_1 = 2\sum_{i=1}^{\infty} \frac{\sin^2 \alpha_{i,NS}}{\alpha_{i,NS}^4(\alpha_{i,NS} + \cos\alpha_{i,NS}\sin\alpha_{i,NS})}\left(\alpha_{i,NS} - a\tanh\frac{\alpha_{i,NS}}{a}\right), \tag{2.68}$$

where $\alpha_{i,NS} = (2i-1)\pi/2$. By reminding that the product $Kn_H p$ is not a function of *x*, the integration of Eq. (2.66) along the channel length gives

$$\dot{m}_{rect,S1} = \frac{H^4}{4\mu a}\frac{p_{out}^2}{R_s T L}\left[a_1\frac{\Pi^2-1}{2} + a_2(\Pi-1)Kn_{H,out}\right]. \tag{2.69}$$

The analytical mass flow rate and velocity distribution given by, respectively, Eqs. (2.69) and (2.59) are based on a first-order slip boundary conditions, and, for this reason, they are valid only for $Kn < 0.1$. The velocity expansion proposed by Ebert & Sparrow (1965) does not converge when higher-order slip boundary conditions are employed. However, the gas flows experimentally investigated in this work are characterized by Knudsen number that are much lower than this value, and, therefore, the analytical solution proposed by Ebert & Sparrow (1965) is employed in this work. Other authors proposed different approaches for solving Eq. (2.58) for which second-order boundary conditions can be implemented (Morini & Spiga, 1998; Auber & Colin, 2001; Jang & Wereley, 2004). These theoretical solutions are detailed in Appendix A.

2.6.4 Compressible and rarefaction effects on pressure distribution

Pong *et al*. (1994) were the first to provide experimental measurements of the pressure distribution along a rectangular micro-channel by means of pressure sensors on chip. The data revealed a non-linear evolution of the pressure across the micro-duct, but they did not measure any mass flow rate.

One year later, Liu *et al*. (1995) fabricated on a silicon substrate a microflow MEMS system integrating 250×250 μm^2 pressure sensors and a microchannel, 450-μm long and with a rectangular cross-section of 40×1.2 μm^2 area. By means of 13 distributed pressure sensors composed of polysilicon piezo-resistors, they have been able to provide accurate pressure distributions for different inlet pressures.

More recently, another research group has investigated the pressure distribution in micron-sized channels through integrated sensors. Zohar *et al*. (2002) fabricated microchannels of rectangular section with heights between 0.5 and 1 μm. The aspect ratio was designed to be very high, at least a = 40, for increasing the mass flow rate and the accuracy of its measurement, and for being able to compare the experimental data with the plane flow solution.

Jang & Wereley (2004) compared their experimental data with an analytical solution they developed for the pressure distribution in microchannels with a rectangular section. In their work, they fabricated rectangular microchannels with aspect ratios of about 0.3 using deep reactive ion etching (DRIE). This fabrication technique can dig hundred microns deep into the silicon with nearly vertical walls, a quite attractive feature in the manufacturing of microchannels with rectangular sections.

Even though the first experimental evidences of the real pressure distribution in channel gas flows are traced back to the 90s, the non-linear behavior of the pressure was theoretically predicted many years before. For example, Ebert & Sparrow, in 1965, pointed out how the gas compressibility has a significant effect on the pressure drop distribution. Especially in long ducts, the density reduction and the gas acceleration produce a significant change in the axial momentum flux along the channel. This term is not included in Eqs. (2.37) and (2.54), which only represents a balance between pressure and viscous forces. Nevertheless, the great interest in the locally-incompressible and locally fully-developed model derives from its simplicity of use, and the addition of the momentum flux term would provide a set of Navier-Stokes equations more difficult to be solved analytically. Starting from a simple momentum balance on a control volume that includes the momentum flux variation, Ebert & Sparrow (1965) analytically found an algebraic equation for the pressure distribution embedding compressibility effects:

$$\left[\left(\frac{p}{p_{out}}\right)^2 - 1\right] + 2\varrho Kn_H\left[\frac{p}{p_{out}} - 1\right] + 2Re^2\tilde{\phi}\tilde{\chi}\left\{\varrho Kn_H\left[\frac{p}{p_{out}} - 1\right] - \ln\frac{p}{p_{out}}\right\} = -\left[\left(C_f Re\right)_0 Re\tilde{\phi}\right]\frac{x-L}{D_h}. \tag{2.70}$$

Coefficient $\tilde{\phi}$, momentum-flux integral $\tilde{\chi}$, and friction coefficient C_f are defined as:

$$\tilde{\phi} = \frac{\mu^2 R_s T}{p_{out}^2 D_h^2}, \tag{2.71}$$

$$\tilde{\chi} = \frac{1}{A}\int_A \left(\frac{u}{\bar{u}}\right)^2 dA, \tag{2.72}$$

$$C_f = \frac{\bar{\tau}_w}{1/2\rho\bar{u}^2}, \tag{2.73}$$

where $\bar{\tau}_w$ is the shear stress at the wall and $\bar{u}$ is the mean velocity at a specific cross-section along the channel. All the three parameters are, indeed, dependent of the *x* coordinate. However, the momentum-flux integral is only slightly dependent on the Knudsen number, thus on the pressure. Therefore, in first approximation $\tilde{\chi}$ is considered constant. This means that the variation in the momentum flux is mainly determined by the density variation. The definition of coefficient ϱ comes from the relationship between the Poiseuille number $Po = C_f Re$ and the Knudsen number, which, in the case of circular tubes and parallel plates channel, takes the form

$$\frac{\left(C_f Re\right)}{\left(C_f Re\right)_0} = \frac{1}{1+\varrho Kn}. \tag{2.74}$$

Coefficient $\left(C_f Re\right)_0$ corresponds to the Poiseuille number with no-slip at the wall. Eq. (2.74) basically states that the friction forces decrease in the presence of slip, i.e., for $Kn > 0$. From the analytical solution of the parallel plates problem, it is found that $\left(C_f Re\right)_0 = 24$ and that $\varrho = 12$, if full accommodation is considered ($\sigma = 1$). Ebert & Sparrow (1965) provide the value of ϱ for different aspect ratio a of the rectangular cross-section, which are reported in Table 2.5.

a	0.0	0.05	0.1	0.15	0.2	0.25	0.3	0.5	1
ϱ	6	6.018	6.038	6.059	6.082	6.106	6.133	6.306	7.567

Table 2.5. Values of the coefficient ϱ of Eq. (2.74) for different aspect ratios $a = H/b$. Data from Ebert & Sparrow (1965).

In the left-hand side of Eq. (2.70) two terms of different origin can be identified: the first two terms derive from viscous dissipation, whereas the last term is given by the contribution to the momentum balance of the momentum flux variation.

Arkilic *et al*. (1997) developed a more sophisticated mathematical approach based on an asymptotic expansion method of the two-dimensional, isothermal gas flow solution between parallel plates. They demonstrated that the pressure distribution at zeroth-order with respect to the height-to-length ratio $\epsilon = H/L$ (see Eq. (2.26), in Section 2.6.1) is the solution of the following second-order, algebraic equation:

$$\left(\frac{p}{p_0}\right)^2 + 12\frac{2-\sigma}{\sigma}Kn_{H,out}\left(\frac{p}{p_0}\right) - \Pi\left(\Pi + 12Kn_{H,out}\right) + \left[\left(\Pi^2 - 1\right) + 12\frac{2-\sigma}{\sigma}Kn_{H,out}(\Pi - 1)\right]\frac{x}{L} = 0. \tag{2.75}$$

As suggested by Aubert & Colin (2001), the same result of Eq. (2.75) can be found in a much simpler way by comparing the expression of the mass flow rate dependent on the local pressure gradient, Eq. (2.45), with the one dependent on the inlet-outlet pressure ratio, Eq. (2.46). Eq. (2.75) can be rewritten in a more compact form in the following way

$$p^{*2} + c_1 p^* + c_2 + c_3 x^* = 0. \tag{2.76}$$

in which $p^* = p/p_{out}$ is the non-dimensional pressure, $x^* = x/L$ is the non-dimensional streamwise coordinate, and the coefficients are defined as

$$c_1 = 24\beta_{u1}\frac{2-\sigma}{\sigma}Kn_{out}, \qquad c_2 = -\Pi(\Pi + c_1), \qquad c_3 = (\Pi - 1)(\Pi + 1 + c_1). \tag{2.77}$$

Eq. (2.76) corresponds to a simple second order algebraic equation for each *x* location along the channel length, and it can be analytically solved. Since c_1 is always positive and p^* needs to be positive, the only physical solution of interest of Eq. (2.76) is

$$p^*(x^*) = \frac{-c_1 + \sqrt{c_1^2 - 4(c_2 + c_3 x^*)}}{2}. \tag{2.78}$$

This solution allows to investigate the individual effect on the pressure distribution given by compressibility and by rarefaction. High pressure ratios Π tends to increase the curvature of the pressure distribution, whereas the rarefaction phenomena at the wall have the contrary effect of reducing the non-linearity.

Arkilic *et al*. (1997) demonstrated a good match of this analytical solution with the experimental results of Pong *et al*. (1994), and, similarly, Zohar *et al*. (2002) found a good agreement with their experimental data as well. Figure 2.10 reports the comparison between the experimental pressure measurements and the corresponding analytical solution. Figure 2.10a shows that the effect of rarefaction on the pressure distribution at low Knudsen numbers is relatively weak. In Figure 2.10b, it can be observed how the increasing inlet over outlet pressure ratio amplifies the curvature of the pressure distribution.

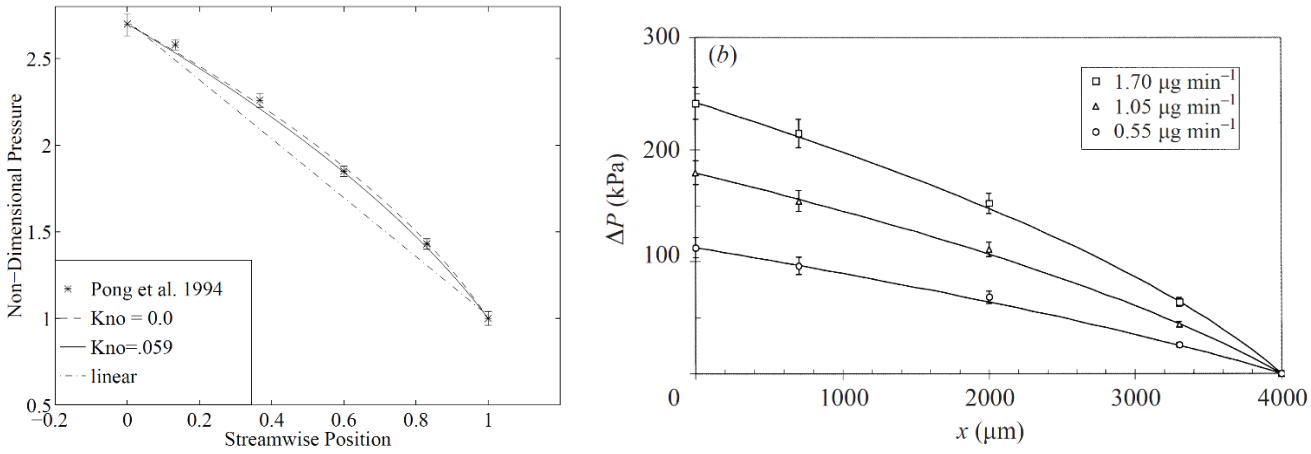

(a) (b)

Figure 2.10. Comparison of the analytical solution, Eq. (2.78), with the experimental data of (a) Pong *et al*. (1994) and (b) Zohar *et al*. (2002). In (b), the symbols are the pressure measurements and the curves are the analytical solutions. Figure (a) is taken from Arkilic *et al*. (1994) and (b) from Zohar *et al*. (2002).

A high inlet-outlet pressure difference produces an intense gas expansion along the channel and a consequent strong gas acceleration that generates higher shear stresses at the wall. The increasing viscous forces need to be balanced by higher pressure drop, hence the higher non-linearity of the pressure distribution. On the contrary, the rarefaction tends to reduce the friction forces at the wall, as Eq. (2.74) demonstrates, thus producing an effect opposite to the gas compressibility (Morini *et al*., 2004).

The governing equation for the pressure distribution Eq. (2.76) results from approximating the gas flow as locally, fully-developed, for which the pressure forces perfectly balance with the shear stresses at any cross-section of the channel. It does not take into account for any variation in the momentum flux along the channel, as the formula of Ebert & Sparrow, Eq. (2.70), does. Actually, Eq. (2.76) can be recovered from Eq. (2.70) by considering the parameters related to the plane flow model, namely by setting $\left(C_f Re\right)_0$ = 24 and ϱ = 12, and by dropping the last term of the left-hand side of Eq. (2.70), which comes from the variation of the momentum flux. The importance of the presence of the momentum flux term in the momentum balance was investigated by Ebert & Sparrow themselves. Figure 2.11 represents the analytical solution of the pressure distribution for a channel with rectangular cross-section. The results are shown for Kn = 0.01, for two, low Reynolds numbers, Re = 2 and Re = 10, and for two different aspect ratios, a = 0.2 and a = 1. Figure 2.11 demonstrates that the gas compressibility affects the pressure distribution mainly through the increase in the viscous forces. Neglecting the momentum flux term can provide an overestimation of the static pressure of more than 50% but only towards the outlet of the channel, that is in the region of high Mach numbers. The figure also shows the effect of the aspect ratio a for fixed outlet Knudsen number, Reynolds number, and, consequently, Mach number. High values of a increases the overall viscous forces, thus producing a more evident effect on the pressure distribution. For the same thermodynamic conditions, the reduction of a from 1 to 0.2 can drastically decrease the compressibility effects on the pressure drop.

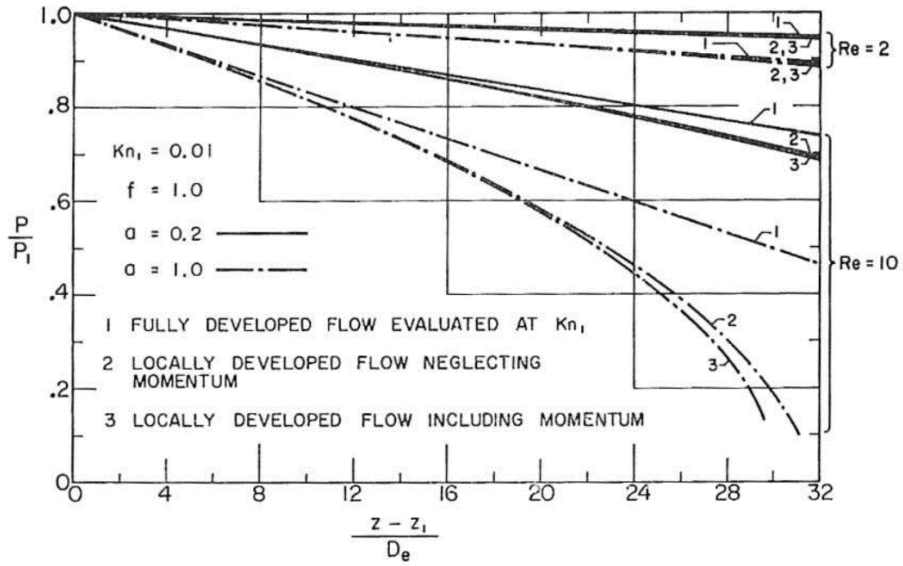

Figure 2.11. Non-dimensional pressure distribution $p(x)/p_{out}$ across a channel with a rectangular section of aspect ratio a = 1 (dashed line) and a = 0.2 (solid line), for $Kn_{H,out}$ = 0.01, and for σ = 1. The different curves refer to the pressure distribution characterizing the fully-developed flow (curve 1), the locally-developed flow neglecting the momentum flux in Eq. (2.70) (curve 2), and the locally-developed flow with the contribution of the momentum flux variation (curve 3). The figure is taken from Ebert & Sparrow (1965).

2.7 Conclusion

In this chapter, a review on the mathematical models available for rarefied gas flows in the slip flow regime has been presented. Particular focus has been dedicated in understanding the range of validity of the hypotheses that sustain the analytical approach for gas flows in microchannels with a rectangular cross-section. The effect of compressibility and rarefaction has been quantified as a function of the corresponding non-dimensional numbers. If Ma_{out} < 0.3 and Re_{out} < 1500, the gas flow can be considered everywhere in the channel as locally-incompressible, isothermal and laminar. The appropriate slip model to be used depends on the level of rarefaction. If Kn < 0.1, a first-order slip model may be accurate enough. However, if Kn > 0.1, a second-order boundary condition at the wall is necessary to not underestimate the slip velocity at the wall. The analytical solutions for the velocity profile and for the axial pressure distribution have been thoroughly discussed. The mathematical models for the laminar, locally-incompressible, isothermal, and locally, fully-developed flow are analytical tools that have been used for the experimental study of this work.

Section 2.5 demonstrates the lack of general agreement in the literature regarding the quantitative characterization of the gas-surface interaction. In the next chapter, it is pointed out that most of the experimental data available in the literature do not provide enough information to have a complete description of the phenomenon. Local experimental analysis for the investigation of the thermodynamic non-equilibrium at the solid wall are rare or almost absent and are of significant importance for the progress of this scientific research field.

References

Agrawal, A. (2012). A comprehensive review on gas flow in microchannels. *International Journal of Micro-Nano Scale Transport*.

Albertoni, S., Cercignani, C., & Gotusso, L. (1963). Numerical evaluation of the slip coefficient. *The physics of fluids*, *6*(7), 993-996.

Arkilic, E. B., Schmidt, M. A., & Breuer, K. S. (1997). Gaseous slip flow in long microchannels. *Journal of Microelectromechanical systems*, *6*(2), 167-178.

Atkinson, B., Brocklebank, M. P., Card, C. C. H., & Smith, J. M. (1969). Low Reynolds number developing flows. *AIChE Journal*, *15*(4), 548-553.

Aubert, C., & Colin, S. (2001). High-order boundary conditions for gaseous flows in rectangular microducts. *Microscale Thermophysical Engineering*, *5*(1), 41-54.

Barber, R. W., & Emerson, D. R. (2002). The influence of Knudsen number on the hydrodynamic development length within parallel plate micro-channels. *WIT Transactions on Engineering Sciences*, *36*.

Beavers, G. S., Sparrow, E. M., & Magnuson, R. A. (1970). Experiments on hydrodynamically developing flow in rectangular ducts of arbitrary aspect ratio. *International Journal of Heat and Mass Transfer*, *13*(4), 689-701.

Beskok, A., & Karniadakis, G. E. (1999). Report: a model for flows in channels, pipes, and ducts at micro and nano scales. *Microscale Thermophysical Engineering*, *3*(1), 43-77.

Bird, G. A. (1976). Molecular gas dynamics. *NASA STI/Recon Technical Report A*, *76*.

Bird, G. A. (1981). Monte-Carlo simulation in an engineering context. *Progress in Astronautics and Aeronautics*, *74*, 239-255.

Bird, G. A. (1994). Molecular gas dynamics and the direct simulation monte carlo of gas flows. Clarendon, Oxford, 508, 128.

Cai, C., Sun, Q., & Boyd, I. D. (2007). Gas flows in microchannels and microtubes. *Journal of Fluid Mechanics*, *589*, 305-314.

Cercignani, C. (1964). *Higher order slip according to the linearized Boltzmann equation* (No. AS64 19). California Univ. Berkeley, Inst. of Engineering Research.

Cercignani, C. (1988). The boltzmann equation. In *The Boltzmann Equation and Its Applications* (pp. 40-103). Springer, New York, NY.

Cercignani, C., Illner, R., & Pulvirenti, M. (2013). *The mathematical theory of dilute gases* (Vol. 106). Springer Science & Business Media.

Cercignani, C., & Lorenzani, S. (2010). Variational derivation of second-order slip coefficients on the basis of the Boltzmann equation for hard-sphere molecules. *Physics of Fluids*, *22*(6), 062004.

Chapman, S., Cowling, T. G., & Burnett, D. (1990). *The mathematical theory of non-uniform gases: an account of the kinetic theory of viscosity, thermal conduction and diffusion in gases*. Cambridge university press.

Chen, R. Y. (1973). Flow in the entrance region at low Reynolds numbers. *Journal of Fluids Engineering*, *95*(1), 153-158.

Colin, S. (2005). Rarefaction and Compressibility Effects on Steady and Transient Gas Flows in Microchannels. *Microfluidics and Nanofluidics*, 1(3), 268–279.

Cornish, R. J. (1928). Flow in a pipe of rectangular cross-section. *Proc. R. Soc. Lond. A*, *120*(786), 691-700.

Davies, S. J., & White, C. M. (1928). An experimental study of the flow of water in pipes of rectangular section. *Proc. R. Soc. Lond. A*, *119*(781), 92-107.

Deissler, R. G. (1964). An analysis of second-order slip flow and temperature-jump boundary conditions for rarefied gases. *International Journal of Heat and Mass Transfer*, *7*(6), 681-694.

Duan, Z., & Muzychka, Y. S. (2010). Slip flow in the hydrodynamic entrance region of circular and noncircular microchannels. *Journal of Fluids Engineering*, *132*(1), 011201.

Durst, F., Ray, S., Ünsal, B., & Bayoumi, O. A. (2005). The development lengths of laminar pipe and channel flows. *Journal of fluids engineering*, *127*(6), 1154-1160.

Ebert, W. A., & Sparrow, E. M. (1965). Slip flow in rectangular and annular ducts. *Journal of Basic Engineering*, *87*(4), 1018-1024.

Graur, I. A., Méolans, J. G., & Zeitoun, D. E. (2006). Analytical and numerical description for isothermal gas flows in microchannels. *Microfluidics and Nanofluidics*, *2*(1), 64-77.

Hadjiconstantinou, N. G. (2003). Comment on Cercignani's second-order slip coefficient. *Physics of Fluids*, *15*(8), 2352-2354.

Han, L. S. (1960). Hydrodynamic entrance lengths for incompressible laminar flow in rectangular ducts. *Journal of Applied Mechanics*, *27*(3), 403-409.

Hanks, R. W., & Ruo, H. C. (1966). Laminar-turbulent transition in ducts of rectangular cross section. *Industrial & Engineering Chemistry Fundamentals*, *5*(4), 558-561.

Harley, J. C., Huang, Y., Bau, H. H., & Zemel, J. N. (1995). Gas flow in micro-channels. *Journal of Fluid Mechanics*, *284*, 257-274.

Jang, J., & Wereley, S. T. (2004). Pressure distributions of gaseous slip flow in straight and uniform rectangular microchannels. *Microfluidics and Nanofluidics*, *1*(1), 41-51.

Jie, D., Diao, X., Cheong, K. B., & Yong, L. K. (2000). Navier-Stokes simulations of gas flow in micro devices. *Journal of Micromechanics and Microengineering*, *10*(3), 372.

Kandlikar, S., Garimella, S., Li, D., Colin, S., & King, M. R. (2014). *Heat transfer and fluid flow in minichannels and microchannels*. elsevier.

Kao, T. W., & Park, C. (1970). Experimental investigations of the stability of channel flows. Part 1. Flow of a single liquid in a rectangular channel. *Journal of Fluid Mechanics*, *43*(1), 145-164.

Kennard, E. H. (1938). Kinetic theory of gases, with an introduction to statistical mechanics.

Koura, K., & Matsumoto, H. (1991). Variable soft sphere molecular model for inverse-power-law or Lennard-Jones potential. *Physics of fluids A: fluid dynamics*, *3*(10), 2459-2465.

Lauga, E., Brenner, M. P., & Stone, H. A. (2006). Microfluidics: the no-slip boundary condition. *Perspective*, *17*(1).

Li, Q., He, Y. L., Tang, G. H., & Tao, W. Q. (2011). Lattice Boltzmann modeling of microchannel flows in the transition flow regime. *Microfluidics and nanofluidics*, *10*(3), 607-618.

Lin, C. C. L. (1955). Hydrodynamic stability. *Cambridge, UP*.

Liu, J., Tai, Y. C., & Pong, C. M. H. C. (1995, January). MEMS for pressure distribution studies of gaseous flows in microchannels. In *Micro Electro Mechanical Systems, 1995, MEMS'95, Proceedings. IEEE* (p. 209). IEEE.

Lockerby, D. A., Reese, J. M., Emerson, D. R., & Barber, R. W. (2004). Velocity boundary condition at solid walls in rarefied gas calculations. *Physical Review E*, *70*(1), 017303.

Lockerby, D. A., Reese, J. M., & Gallis, M. A. (2005). Capturing the Knudsen layer in continuum-fluid models of nonequilibrium gas flows. *AIAA journal*, *43*(6), 1391-1393.

Loyalka, S. K. (1971). Approximate method in the kinetic theory. *The Physics of Fluids*, *14*(11), 2291-2294.

Loyalka, S. K., & Hickey, K. A. (1989). Plane Poiseuille flow: near continuum results for a rigid sphere gas. *Physica A: Statistical Mechanics and its Applications*, *160*(3), 395-408.

Maxwell, J. C. (1879). VII. On stresses in rarefied gases arising from inequalities of temperature. *Philosophical Transactions of the royal society of London*, *170*, 231-256.

Morini, G. L., & Spiga, M. (1998). Slip flow in rectangular microtubes. *Microscale Thermophysical Engineering*, *2*(4), 273-282.

Morini, G. L., Yang, Y., Chalabi, H., & Lorenzini, M. (2011). A critical review of the measurement techniques for the analysis of gas microflows through microchannels. *Experimental Thermal and Fluid Science*, *35*(6), 849-865.

Morini, G. L., Yang, Y., & Lorenzini, M. (2012). Experimental analysis of gas micro-convection through commercial microtubes. *Experimental Heat Transfer*, *25*(3), 151-171.

Morini, G. L., Spiga, M., & Tartarini, P. (2004). The rarefaction effect on the friction factor of gas flow in microchannels. *Superlattices and microstructures*, *35*(3-6), 587-599.

Mitsuya, Y. (1993). Modified Reynolds equation for ultra-thin film gas lubrication using 1.5-order slip-flow model and considering surface accommodation coefficient. *Journal of Tribology*, *115*(2), 289-294.

Navier, C. L. M. H. (1823). Mémoire sur les lois du mouvement des fluides. *Mémoires de l'Académie Royale des Sciences de l'Institut de France*, *6*(1823), 389-440.

Orszag, S. A. (1971). Accurate solution of the Orr–Sommerfeld stability equation. *Journal of Fluid Mechanics*, *50*(4), 689-703.

Ohwada, T., Sone, Y., & Aoki, K. (1989). Numerical analysis of the shear and thermal creep flows of a rarefied gas over a plane wall on the basis of the linearized Boltzmann equation for hard-sphere molecules. *Physics of Fluids A: Fluid Dynamics*, *1*(9), 1588-1599.

Pan, L. S., Liu, G. R., & Lam, K. Y. (1999). Determination of slip coefficient for rarefied gas flows using direct simulation Monte Carlo. *Journal of Micromechanics and Microengineering*, *9*(1), 89.

Pong, K. C., Ho, C. M., Liu, J., & Tai, Y. C. (1994). Non-linear pressure distribution in uniform microchannels. *ASME-Publications-Fed*, *197*, 51-51.

Pfund, D., Rector, D., Shekarriz, A., Popescu, A., & Welty, J. (2000). Pressure drop measurements in a microchannel. *AIChE Journal*, *46*(8), 1496-1507.

Roohi, E., & Darbandi, M. (2009). Extending the Navier–Stokes solutions to transition regime in two-dimensional micro-and nanochannel flows using information preservation scheme. *Physics of fluids*, *21*(8), 082001.

Schamberg, R. (1947). *The fundamental differential equations and the boundary conditions for high speed slip-flow, and their application to several specific problems* (Doctoral dissertation, California institute of technology).

Schiller, L. (1923). Über den strömungswiderstand von rohren verschiedenen querschnitts und rauhigkeitsgrades. *ZAMM-Journal of Applied Mathematics and Mechanics/Zeitschrift für Angewandte Mathematik und Mechanik*, *3*(1), 2-13.

Shen, S. F. (1954). Calculated amplified oscillations in the plane Poiseuille and Blasius flows. *Journal of the aeronautical sciences*, *21*(1), 62-64.

Sparrow, E. M., Hixon, C. W., & Shavit, G. (1967). Experiments on laminar flow development in rectangular ducts. *Journal of Basic Engineering*, *89*(1), 116-123.

Tatsumi, T., & Yoshimura, T. (1990). Stability of the laminar flow in a rectangular duct. *Journal of Fluid Mechanics*, *212*, 437-449.

Taylor, G. I. (1923). Stability of a Viscous Liquid Contained between Two Rotating Cylinders Phil. Trans. R. Soc. Lond. A January.

Thomas, L. H. (1953). The stability of plane Poiseuille flow. *Physical Review*, *91*(4), 780.

Tosun, I., Uner, D., & Ozgen, C. (1988). Critical Reynolds number for Newtonian flow in rectangular ducts. *Industrial & engineering chemistry research*, *27*(10), 1955-1957.

Van den Berg, H. R., Ten Seldam, C. A., & Van der Gulik, P. S. (1993). Thermal effects in compressible viscous flow in a capillary. *International Journal of thermophysics*, *14*(4), 865-892.

Wu, L. (2008). A slip model for rarefied gas flows at arbitrary Knudsen number. *Applied Physics Letters*, *93*(25), 253103.

Xu, B., Ooti, K. T., Wong, N. T., & Choi, W. K. (2000). Experimental investigation of flow friction for liquid flow in microchannels. *International Communications in Heat and Mass Transfer*, *27*(8), 1165-1176.

Zhang, W. M., Meng, G., & Wei, X. (2012). A review on slip models for gas microflows. *Microfluidics and nanofluidics*, *13*(6), 845-882.

Zohar, Y., Lee, S. Y. K., Lee, W. Y., Jiang, L., & Tong, P. (2002). Subsonic gas flow in a straight and uniform microchannel. *Journal of fluid mechanics*, *472*, 125-151.

Chapter 3

Experimental techniques for rarefied gas flows

In this chapter, the state of the art on the measurement techniques for gas microflows is presented. The monitoring of the mass flow rate, pressure, temperature, and velocity fields is of key importance for the design, the control, and the understanding of microdevices that include gas microflows.

The mass flow rate is one of the most important parameters for the characterization of gas microflows. According to the classical continuum approach for fluid flows, an increase of the Knudsen number, that is a reduction of the average pressure or of the channel's dimension, would have resulted in a monotonically decreasing mass flow rate. However, it has been observed that the dimensionless mass flow rate has a minimum value at $Kn \cong 1$ before starting to slightly increase again at even higher Knudsen numbers. This phenomenon took the name of "Knudsen paradox", or "Knudsen minimum". Since the first experimental evidences observed by Knudsen in 1909, this topic is still nowadays at the center of the scientific investigation. Section 3.3 presents the experimental techniques for measuring the mass flow rate in channel gas flows.

With the development of the micromanufacturing techniques, the fabrication of pressure and temperature microsensors has been directly integrated in the fabrication process of the microdevices. Many microsensors adopt the same working principle as traditional macroscopic sensors, like diaphragm pressure sensors or thermocouples, even though new materials and fabrication processes are employed. In Sections 3.1 and 3.2, a brief review on pressure and temperature sensors for microdevices is presented. The measurement techniques described in these two sections are classified as intrusive, as the probe introduces inevitably some perturbations in the gas flow. The temperature of a gas is a measure of the average kinetic energy of the gas molecules. In kinetic theory, a scalar temperature is associated also to the energy stored in the rotational and vibrational modes of a polyatomic molecule. While specific techniques for investigating the rotational and vibrational temperatures exist, only the techniques for measuring the translation temperature of the gas are considered in this chapter.

The miniaturization of the already-existing macroscopic sensing techniques has been followed by the development of new experimental techniques able to provide more accuracy and a higher spatial resolution of the pressure, temperature, and velocity measurements. Most of the experimental data on gas microflows present in the literature are, up to now, related to measurements of average quantities, such as the mass flow rate, the average pressure or the average temperature at a specific cross-section in a microchannel. These experimental studies provided an indirect quantification of the velocity slip and the temperature jump that take place locally at the wall. The previous chapter was dedicated to the various mathematical models that have been proposed in the literature for describing

these rarefaction effects. All of them depend on the momentum and energy accommodation coefficients, which vary as a function of the wall properties and gas species, and which determination is still a difficult task. Local experimental data are required to evaluate these coefficients and to validate the proposed models. The urgency for direct measurements on the rarefaction phenomena pushed the research community to look for experimental techniques that could answer this demand.

Section 3.4 presents the most interesting visualization techniques for pressure, temperature, and velocity field measurements in confined and rarefied gases. These techniques are contactless and low-intrusive, which are features very appealing in gas microflows. A special section is dedicated to the molecular tagging velocimetry (MTV), since it is the technique employed in this work. Different implementations of this technique are presented, by discussing advantages and disadvantages of each one. Previous application of MTV for liquid and gas flows are discussed.

3.1 Pressure sensors

In the literature, measurements of gas pressure have been carried out at the inlet and the outlet of a microchannel by means of conventional pressure sensors, and/or along the microchannel by means of on-chip pressure sensors (Jang & Wereley, 2004). The inlet/outlet pressure monitoring is important in the characterization of the conductance of micro-ducts, while the distributed pressure sensors provided important information on the effect of compressibility and rarefaction, as already discussed in the previous chapter.

Many pressure sensors rely on sensing the pressure-induced deformation of a flexible structure, usually a diaphragm, but other types infer the gas pressure by tracking its influence on other properties of the system, such as the heat transfer to a solid surface. Both diaphragm-based and thermal pressure sensors introduce a perturbation in the gas system: the former requires a channel connection between the gas flow region and the pressure sensor cavity, the latter requires the introduction of heating elements.

Diaphragms in pressure sensors are usually square or circular clamped plates. In the linear elastic theory, the deflection $w(r)$ as function of the radial distance r from the center of the diaphragm is, for the circular plate,

$$w(r) = \frac{pR^4}{64E_D}\left[1 - \left(\frac{r}{R}\right)^2\right]^2, \tag{3.1}$$

where R is the radius of the diaphragm and E_D is the flexural rigidity. The proportionality between the pressure and the deflection is something desirable for having a sensor system simple to be calibrated. If the deflections become large, the proportionality is no longer true. Pressure sensors can be classified according to the transduction mechanism employed. The most common diaphragm-based pressure sensors in microdevices are piezo-resistive

and capacitive, but also optical and resonant sensors have very interesting properties for being applied in gas microflows.

While this type of pressure sensors can in principle be applied to liquids, other pressure sensors, such as the Pirani gauge, work specifically only for gas systems, since a relevant variation in thermal conductance with pressure is necessary.

3.1.1 Diaphragm-based piezo-resistive pressure sensors

The gas pressure measurement is inferred from the change in electrical resistance due to stresses in a piezo-resistor. Semiconductor-based sensors were born during the 1950s, when the piezo-resistivity of silicon and germanium was discovered. In these pressure sensors, piezo-resistors are mounted on or in the diaphragm. If the diaphragm deflections are small, the change of resistance is linear with pressure. The resistance variation can be due either to strain of the sensing element or to a resistivity change of the material. While in metal the first component is dominant, in semiconductors the second is much higher than the first one.

The first centimetric pressure sensors were made by a metal diaphragm with silicon strain gauges bonded to it by epoxies or eutectics. In the 1960s and 1970s, these early versions were quickly substituted by pressure sensors with silicon diaphragms, in which the strain gauges can be directly implanted through diffusion or ion implantation (Eaton & Smith 1954). Silicon diaphragms have the advantage of high mechanical stability and high reproducible elastic deformations. The development of the anisotropic chemical etching and the anodic bonding improved the precision in the size and the location of both diaphragms and strain gauges with respect to the common IC photolithography, allowing to reduce the diaphragms dimensions to hundreds of microns.

Other piezo-resistive materials have been used in pressure sensors, e.g., poly-Si, silicon carbide, carbon fiber, and carbon nanotubes. Silicon is excellent for its mechanical properties and its high sensitivity to applied stresses but suffers from degradation at high temperature. Piezo-resistors are often applied on the diaphragm in Wheatstone bridge configuration, in order to increase the sensitivity of the measurements and to compensate for possible temperature dilatation of the membrane. Figure 3.1 shows an example of disposition of piezo-resistors on a square diaphragm. More recent pressure sensors are based on MOFSET transistor, for which the transduction principle is different but very similar to the concept of change in resistance due to applied stresses (Kumar & Pant, 2014).

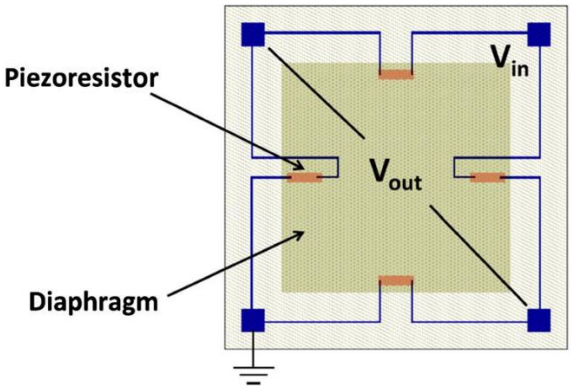

Figure 3.1. Piezo-resistors in a Wheatstone bridge configuration on a square diaphragm. Figure from Kumar & Pant (2014).

3.1.2 Diaphragm-based capacitive pressure sensors

Capacitive pressure sensors relate the diaphragm deformation to the change in capacitance of two parallel electrode plates. The advantages of these pressure sensors with respect to the piezo-resistive pressure sensors is the increased sensitivity, the decreased temperature sensitivity, and the higher adaptation to microfabrication. The sensitivity to the applied pressure can be increased by reducing the gap between the electrodes or by increasing the electrode surface.

Since the diaphragm deflection is not uniform across the plate, the capacitance does not vary linearly with the applied pressure. In order to achieve the desirable linearity, different modifications of the diaphragm structure are necessary. A first possibility is to employ a capacitive sensor in contact mode, in which the capacitance is proportional to the contact area between the two plates. However, the gain on linearity is accompanied by a loss of sensitivity. An alternative is to employ diaphragms with non-uniform cross-section. By making the central portion of the diaphragm thicker and, thus, stiffer with respect to the thinner parts on the sides (Figure 3.2), the vertical deflection of the plate becomes uniform under the applied pressure.

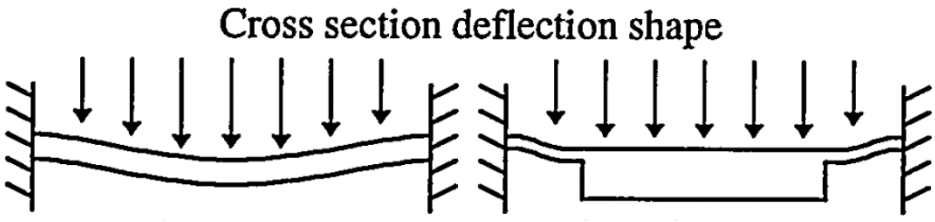

(a) (b)

Figure 3.2. Schematic of a diaphragm with (a) uniform and (b) non-uniform thicknesses.
Figure from Eaton & Smith (1997).

3.1.3 Diaphragm-based optical pressure sensors

The diaphragm pressure-induced deformations can be also detected through optical sensors. The diaphragm deformation is interrogated with a light source. Based on the change in the reflected light the gas pressure can be inferred. Kohl *et al*. (2005) fabricated a microchannel with integrated diaphragm pressure sensors distributed along its length. A laser source and a photodetector were employed off-chip for sensing the diaphragm deformation and, thus, the gas pressure in the channel.

An interferometric setup can also provide a high-sensitive optical detector system, e.g. with the Mach-Zehnder interferometry or the Fabry-Pérot (FP) interferometry. In the last years, many researchers combined optical fibers with diaphragm-based pressure sensors by employing FP interferometry (Lin *et al*., 2012; Zhu *et al*., 2017).

Abeysinghe *et* al. (2001) manufactured through anodic bonding a reflective diaphragm directly on a glass fiber tip. The Fabry-Pérot interferometry system is constituted by the diaphragm and a cavity-fiber interface at the tip. The deformation of the diaphragm modifies the Fabry-Pérot reflectivity, and, thus, the gas pressure can be measured. Quite interestingly, the authors noticed that the anodic bonding technique, which can "glue" glass and silicon, could not work on telecommunication glass fibers, as they are made out of pure silica, which does not contain a lot of alkali ions necessary for the anodic bonding mechanism. They specifically used borosilicate glass fibers that do contain alkali ions for bonding the silicon diaphragm to the tip of the fiber glass.

Diaphragm-based optical pressure sensors are quite interesting as they can work in harsh environment, e.g., high temperature, in which electronic components might not operate. Moreover, many works demonstrated a good linearity of the transduced signal and high sensitivity. However, its production cost is higher than for the piezo-resistive or capacitive pressure sensors because of the more complex experimental setup. Furthermore, the alignment of the optics and the calibration of the sensor is more challenging.

3.1.4 Diaphragm-based resonant pressure sensors

In this type of sensors, the pressure measurement is based on the monitoring of resonance frequency of a structural element that is embedded in the diaphragm. Similar to the piezo-resistive pressure sensors, the stresses applied to the diaphragm produce a state of strain that modifies the proper frequencies of vibration of the mechanical piece, which can be a beam, a bridge, or a diaphragm (Stemme, 1991). The excitation into resonance of the structural element can be carried out through different strategies, e.g., by means of piezo-electrics, resistive heating, or a magnetic field. The monitoring of the resonance frequency can be done through one of the sensing mechanisms above described, through piezo-resistors positioned on the vibrating beam (Petersen *et al*., 1991) or through capacitive electrodes. Figure 3.3 lists various examples of excitation and detection of resonant bridges. As an example of resonant pressure sensor with optical excitation and detection, Bartelt & Unzeitig (1993) fabricated a

micro-bridge made by silicon nitride mounted on a silicon diaphragm and employed a diode laser set at two different wavelengths for both the mechanical excitation and the interrogation of the resonance frequency of the bridge. The mechanical laser-excitation was based on the periodic generation of thermal stresses, as sketched in Figure 3.3. The optical detection was based on the Twyman-Green interferometry system.

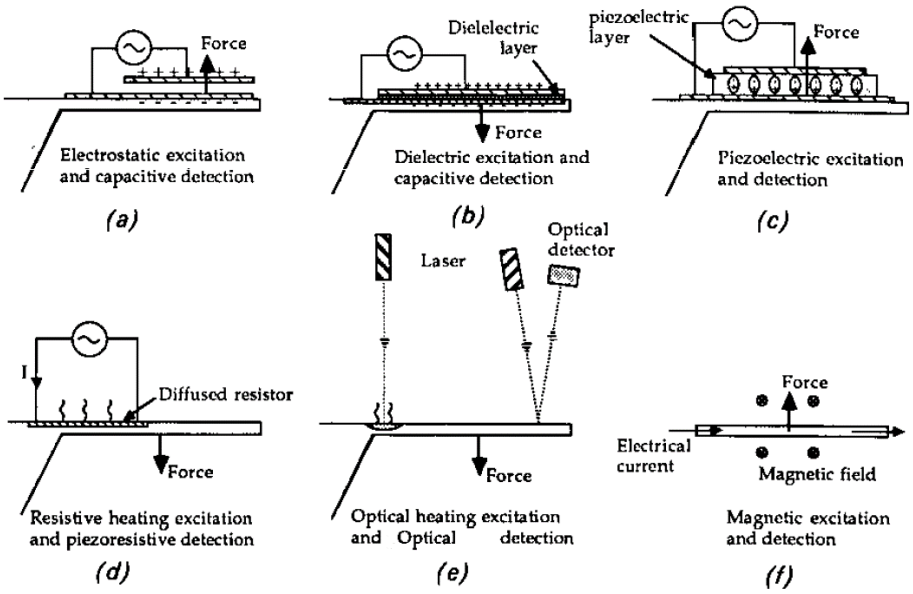

Figure 3.3. Possible excitation and detection systems for resonant beams in pressure sensors.
Figure from Stemme (1991).

Single-crystal silicon and quartz have excellent mechanical properties for being employed as resonator materials. Their high-level of purity provides elastic resonators with high-strength and high Q-factors, which guarantee a narrow resonant peak and, consequently, a high-resolution sensor. Resonant pressure sensors have higher sensitivity with respect to that of piezo-resistors, and, moreover, a frequency-based measurement is more immune to noise than analog signals from piezo-resistors or varying capacitance. The temperature dependence of the resonant material, a mismatch between the thermal expansion coefficient of different materials, and the type of excitation and detection can affect the resonance frequency, increasing the sensor temperature sensitivity.

3.1.5 Thermal pressure sensors

Thermal pressure sensors do not employ any diaphragm for measuring the gas pressure. Instead, the pressure measurement is inferred from the variation in heat loss of a heated metal wire suspended in the gas due to variation of the gas density. These devices are called Pirani gauges, and they have already been integrated in gas micro-circuits for measuring the gas pressure in vacuum systems (Shie *et al*., 1995) or in Knudsen pumps (Gupta *et al*., 2012). Chae *et al*. (2005) fabricated a miniaturized Pirani gauge, 2×2 mm^2 in size, with enhanced sensitivity and

dynamic range thanks to the novel dual heat sink configuration. In this work, the authors reported a minimal uncertainty of 50 μtorr and a working pressure range between about 10^{-2} and 5 Torr. The high sensitivity at low pressures, the simplicity, and the low-cost with respect to resonant or optical diaphragm-based pressure sensors make Pirani gauges very interesting for pressure measurements in gas flows in microdevices.

3.2 Temperature sensors

The temperature measurement techniques described in this section involve a contact between the sensing element and the gas. They provide information on the temperature only at a specific point inside the gas domain, where the sensitive material is located. The measurement of the bulk gas temperature requires a suspended probe. As an example, Peterson & Brown (1985) fabricated a thin-film resistor suspended inside the microchannel (Figure 3.4). However, measuring the bulk temperature is quite intrusive and introduces large disturbances in the flow. For minimizing this problem, it is often preferred to place the temperature sensitive elements on the wall of the channel flow.

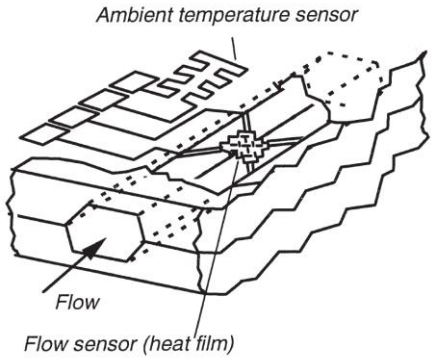

Figure 3.4. Suspended heat-film resistor in a microchannel. Figure from Nguyen (1991).

In rarefied gas condition, it is known that the temperature of the gas at the wall is different from the temperature of the probe surface. This aspect needs to be taken into consideration in the temperature measurements, especially when heating elements are present.

In the review of Morini *et al*. (2005), three main typologies of temperature sensors are recognized: the resistance temperature detectors (RTD), based on the temperature-dependence of material resistivity, the semiconducting sensors (SC), based on the CMOS technology, and the thin-film thermocouples (TFTC). From the review of Nguyen (1997), another alternative is given by resonant temperature sensors, which have a working principle similar to that of resonant pressure sensors previously described.

3.2.1 Resistance temperature detectors (RTD)

The functioning principle of RTDs is based on the dependency of the metal electrical resistivity from the temperature. The sensitive materials usually employed in this type of sensors are platinum (Park *et al*., 2003; Scholer *et al*., 2005), nickel (Weiping *et al*, 2005), poly-Si (Jiang *et al*., 1999), and others (Morini *et al*., 2011). Usually, pure metals, such as platinum and nickel, have a positive temperature coefficient of resistance (TCR), which means that the electrical resistance of the material increases with temperature. On the contrary, semiconductors like silicon or germanium have a negative TCR. The TCR factor is only slightly dependent on the temperature. RTDs are interesting for temperature measurements in microdevices because of their linear response and the ease of fabrication. µRTD sensors can be integrated in gas microsystems as thin films of the sensitive material applied directly on the substrate by using, e.g., chemical vapor deposition (CVD) for platinum and nickel or ion implantation in the case of poly-Si RTD. µRTDs based on platinum-film seem having some limitation in the working temperature, which needs to be not higher than 550 °C (Scholer *et al*., 2005). Poly-Si-based µRTDs can be a better and cheaper alternative in microfluidic applications.

3.2.2 Semiconducting sensors (SC)

MOS transistors, bipolar transistors and diodes can be employed as integrated temperature sensing elements. The base-emitter junction voltage of bipolar transistors and the voltage of silicon diodes are proportional to the temperature. Bipolar transistors and diodes have better performances in terms of temperature sensitivity and long-term stability with respect to MOS transistors, which have some limitations due to leaking current in the PN junction at high operational temperature (Li *et al*., 2012). The temperature range for these sensors could be -50 to 175 °C with accuracy between ±0.1 and ±3 °C (Bianchi *et al*., 1998). The low-cost, the integrability in silicon substrates, and the linear response make SCs interesting for temperature measurements in microsystems, even though, up to now, CMOS technology is not frequently used in microfluidic applications (Morini *et al*., 2011).

3.2.3 Thin film thermocouples (TFTC)

Thermocouple functioning is based on the Seebeck effect: when two metal materials are put in contact at two extremities, a difference in temperature between the junctions generate a voltage difference. The same physical but inversed principle is employed in the Peltier effect, which can generate a difference of temperature by imposing an electrical tension. This effect requires the use of two different metal materials for working. The most common conventional thermocouples are of type K, made of chromel and alumel, two alloys of nickel with chrome and aluminum, respectively. They have a wide operational temperature range, from -200 °C to 1250 °C, and high temperature sensitivity, on the order of 40 µV/°C.

The Seebeck effect can be exploited in microdevices by integrating thin film thermocouples. Zhang *et al*. (2006) embedded a thin film of chromel on a nickel substrate, obtaining a temperature sensor with same sensitivity characteristics as for usual K-thermocouples. Because of the wide working temperature range, TFTCs are preferable to RTDs and SCs in high-temperature environment.

3.3 Mass flow rate measurements

Mass flow rate measurements are quite challenging in microchannel flows. Flow sensors need to be capable of measuring very small flow rates, on the order of microliters per minute. As for pressure and temperature sensors, even flow sensors have been integrated in the micromachining process of microdevices since many years. In 1974, Van Putten and Middelhoek demonstrated the first integrated flow sensor based on silicon technology. The working principle of their flow sensor was based on the conventional hot-wire anemometry. The n-type silicon chip had dimensions of 1.5×1.5 mm^2, and the flow sensors was composed by 4 p-type diffused wire resistors disposed in a Wheatstone bridge configuration.

As Nguyen (1997) suggested, flow rate sensors can be classified in non-thermal and thermal flow sensors. The non-thermal sensors do not require any heating source and their working principle is electromechanical. The flow rate can be measured indirectly by sensing the distortion of a cantilever beam located in the flow field through a piezo-resistive element (Figure 3.5a). By knowing the relationship between the drag force and the flow velocity, the flow rate can be inferred (Gass *et al*., 1993). Another example of integrable non-thermal flow sensor is sketched in Figure 3.5b. The flow velocity can be calculated from the inlet-outlet pressure drop: a capacitive pressure sensor or any other pressure sensor described in Section 3.1 can be employed for measuring the difference of pressure. Another important and widely employed non-thermal flow sensor is the Coriolis mass flow resonator.

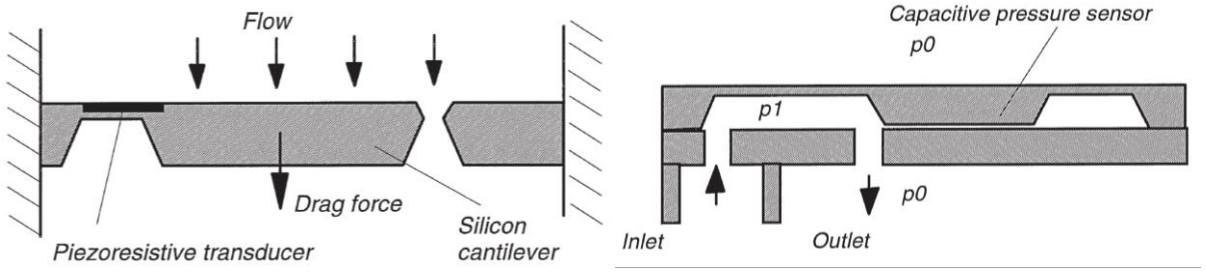

(a) (b)

Figure 3.5. (a) Piezo-resistive flow sensor based on the drag force on a silicon, cantilever beam. (b) Flow sensor based on a capacitive pressure sensor. Figure from Nguyen (1997).

The main drawback of non-thermal flow sensors is that the flow rate measurement depends on the gas density. Therefore, since the gas density depends on the temperature, this kind of sensors needs to be combined with temperature sensors for an accurate flow rate measurement. Because of the sensitivity of the measurements on the

gas density, some of these non-thermal sensors have been also employed as gas density sensor, e.g., the Coriolis density sensor of Enoksson *et al*. (1995).

One of the most common types of thermal flow sensor is the calorimetric sensor and it is usually made of a heat source and two temperature sensors. The mathematical expression that relates the mass flow rate to the heat power transferred to the gas, q_p, and two measured local temperatures, T_1 and T_2, is:

$$\dot{m} = \frac{q_p}{c_p(T_2 - T_1)}, \tag{3.2}$$

where c_p is the specific heat at constant pressure of the working fluid.

Depending on the type of heater and sensing technology, different thermal flow sensors can be built. Any of the temperature sensors described in Section 3.2 could be in principle applied for thermal flow sensors. Scholer *et al*. (2005) fabricated a flow sensor based on an RTD-platinum sensor and a platinum heater (Figure 3.6a), being able to measure flow rates as low as 10 nl/min with liquid flows. Diodes can be employed as heaters and temperature sensors in a flow meter, fabricated by means of CMOS-technology. Figure 3.6b illustrates an integrated thermo-electronic flow sensor fabricated by Yang & Søeberg (1991), who reported in their work flow measurement of 0.2 ml/min with an accuracy of 0.2%.

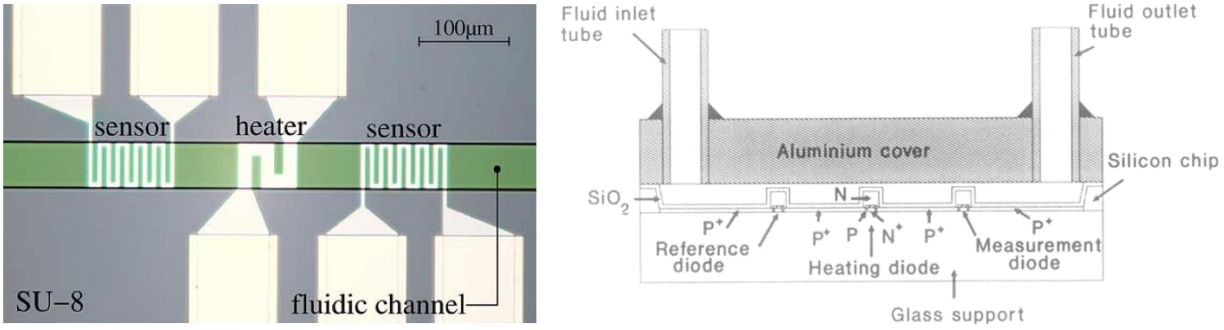

(a) (b)

Figure 3.6. (a) Microchannel with integrated thermo-resistive flow sensor made out of platinum. From Scholer *et al*. (2005). (b) Integrated thermo-electronic flow sensor on a silicon chip. From Yang & Søeberg (1991).

Thermal and non-thermal micro flow sensors are nowadays available in the market. Their precision in the flow rate measurement may be enough for characterizing some microfluidic chips performances. However, when the mass flow rate through the channel is lower than 10^{-8} kg/s, commercial mass flow rate sensors are not accurate enough (Morini *et al*., 2011). Especially in the experimental investigation of the rarefaction effects on the mass flow rates of gas flows, the average pressure inside the microchannel can be very low, when transitional and free molecular regime are achieved, and the mass flow rate can be very low as well. The mass flow rate of rarefied gas flows in microchannels can be as low as 10^{-14} kg/s, as measured, for instance, by Pitakarnnop *et al.* (2010). Even

though great advances in microfabrication provided flow rate microsensors with a resolution five orders of magnitude higher than most of the flow rate sensors nowadays available (Cho *et al*., 1992), these are not yet commercialized. For such low mass flow rates, there are more reliable and less expansive experimental techniques for carrying out flow measurements with acceptable uncertainty.

These experimental techniques indirectly measure the mass flow rate through a microchannel by tracking the rate of variation of gas mass inside reservoirs connected to the tested channel. The gas mass variation in the reservoirs, which have a volume considerably higher than that of the microchannel, is deduced by measuring the variation of pressure or volume in the reservoir. In particular, in the ideal gas case, the gas mass in a reservoir of volume V, at pressure p, and temperature T, is $m = pV/R_sT$, with R_s the gas specific constant. The rate of variation of gas mass in the reservoir is:

$$\frac{dm}{dt} = \frac{pV}{R_sT}\left(\frac{1}{V}\frac{dV}{dt} + \frac{1}{p}\frac{dp}{dt} - \frac{1}{T}\frac{dT}{dt}\right). \tag{3.3}$$

By keeping two of the three variables constant, the mass flow rate can be inferred by measuring the time evolution of the third variable. If the temperature fluctuations in the reservoirs can be maintained limited by a regulation system, the last term of Eq. (3.3) can be neglected as long as it is much smaller than the time variation of volume $\frac{dV}{dt}$ and the time variation of pressure $\frac{dp}{dt}$.

From Eq. (3.3), two main experimental techniques can be identified:

- the constant pressure technique,
- the constant volume technique.

These experimental techniques have been widely used in the past 30 years and allowed to provide a substantial amount of data on mass flow rate of rarefied gas flows in microchannels. The main uncertainty on the flow rate measurements of these techniques is due to untracked fluctuations of pressure, temperature, or volume.

Another possible experimental technique for measuring mass flow rate of gas microflows is the droplet tracking technique, which might be classified as constant pressure technique, depending on the way it is implemented.

3.3.1 Liquid-droplet tracking technique

In this method, a pipette with a liquid droplet inside is connected to the outlet of the microchannel. The gas flow pushes the droplet, and the tracking of the droplet position in time allows to measure the volume flow rate passing through the channel. Many authors have applied this technique for measuring mass flow rate in microchannels (Pong *et al*., 1994; Harley *et al*., 1995; Lalonde, 2001; Zohar *et al*., 2002; Maurer *et al*., 2003; Colin *et al*., 2004;

Ewart *et al*., 2006; Celata *et al*., 2007; Pitakarnnop *et al*., 2010). This technique can be employed when flow rates are not too high, otherwise the droplet might be sucked out from the pipette.

The liquid droplet in the pipette may be water, glycerin or oil (Maurer *et al*., 2003). At low operational pressures, water drops may result in substantial evaporation. Oil or glycerin drops have the advantage of a low saturation vapor at ambient temperature, which limits the droplet evaporation and, consequently, the contamination of the experimental section. The displacement of the droplet can be tracked with different approaches, e.g., by means of a series of opto-electrical sensors (Pitakarnnop *et al*., 2010), a microscope (Harley *et al*., 1995), or a CCD camera (Ewart *et al*., 2006).

Different implementations of this technique with different levels of complexity are possible. The simplest version of this approach requires only one pipette at the outlet of the tested channel.

This version can be classified as a constant-pressure technique, since the mass flow rate is simply deduced from a volume rate change at the channel outlet that is caused by the droplet movement without any substantial pressure variations. If the pipette has a diameter d_{pip}, the mass flow rate can be simply calculated as

$$\dot{m} = \frac{p}{R_s T}\frac{dV}{dt} = \frac{p\pi d_{pip}^2}{R_s T}\frac{\Delta l}{\Delta t}, \tag{3.4}$$

where Δl is the displacement of the droplet in a time interval Δt. A pressure sensor and a temperature sensor are required for measuring p and T at the channel outlet. The accuracy of the flow rate measurement is mainly limited by the precision of determination of the pipette diameter, which is the most sensitive parameter for the mass flow rate, as it can be noticed from Eq. (3.4). Other errors in the flow rate measurements are possibly introduced by the uncertainty in the distance between graduation lines of the pipette and/or between the opto-electronical sensors.

A technical problem that can be encountered is the pinning-depinning mechanism that makes the droplet stick on the surface and suddenly slip and jump. To reduce this problem, the inner surfaces of the pipette can be exposed to a hydrophobic treatment, which also reduces the probability of generation of a liquid-film as the droplet moves and/or a possible breakup of the droplet due to non-uniform friction forces.

If the flow rate is very low, the sensitivity and accuracy of the technique can be increased by mounting many identical microchannels in parallel. In this way, the mass flow rate to be measured is multiplied by the number of channels employed, and the droplet displacement is larger. Shih *et al*. (1996) adopted this idea using hundreds of microchannels in parallel and succeeded in measuring mass flow rates on the order of 10^{-12} kg/s in helium flows with an uncertainty of 3-4%.

In this implementation of the technique, the movement of the droplet allows equilibrium between the pressure at the outlet of the tested channel and the pressure at the outlet of the pipette. If the pipette outlet is exposed to

atmospheric pressure, the pressure at the pipette inlet cannot be lower than the atmospheric pressure. Thus, only gas flows at an average pressure higher than the atmospheric one can pass through the tested microchannel. For instance, Harley *et al*. (1995) employed this technique by maintaining the outlet channel at atmospheric pressure and the inlet pressures ranging from 3.4 MPa to 0.2 MPa, depending on the channel dimension and the gas used. They could obtain a maximum outlet Knudsen of about 0.36 with helium in a microchannel with a hydraulic diameter of about 1 µm.

An adaptation of this technique to gas flows with higher Knudsen numbers would require decreasing the pressure at the outlet of the pipette. This implementation requires a connection through a valve between the outlet and the inlet of the pipette for being able to reduce the pressure simultaneously on both sides of the pipette, thus avoiding the droplet being sucked out.

An advanced version of the droplet tracking technique has been employed by Colin *et al*. (2004) and Pitakarnnop *et al*. (2010), in which two pipettes are employed, both upstream and downstream the tested channel. Figure 3.7 illustrates the experimental apparatus employed by Pitakarnnop *et al*. (2010), in which the two droplet-tracking systems are indicated with OSA and OSB. Once the upstream and downstream reservoirs are filled up to the desired pressure, valves V2 and V1 are closed before valves V3 are open and the gas starts to flow through the tested microsystem.

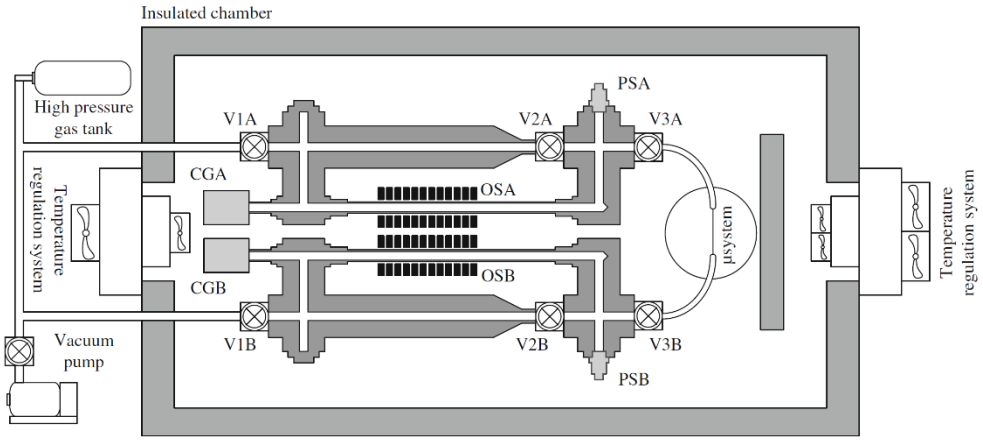

Figure 3.7. Experimental setup of Pitakarnnop *et al*. (2010) combining the constant volume technique with the droplet tracking technique based on opto-electronical sensors.

3.3.2 Constant pressure technique

This experimental technique is conceptually identical to the droplet tracking technique. The pressure in the upstream and/or the downstream reservoirs is maintained constant by adjusting the volume through a moving piston. As the gas flows through the channel, the piston moves accordingly to the intensity of the transfer of gas

mass. By measuring the displacement Δl of the piston in the time interval Δt, Eq. (3.4) can be employed for calculating the mass flow rate, if the diameter of the pipette is substituted with the diameter of the piston d_{cyl}. As for the droplet tracking technique, the uncertainty associated to the calculated mass flow rate is mainly dependent on the uncertainty on the value of d_{cyl}. However, the uncertainty on d_{cyl} can be definitely smaller with respect to the one on d_{pip} since the piston is bigger than the pipette. The discussion of Section 3.3.1 concerning the uncertainty introduced by the thermal fluctuations is applicable to this technique as well.

Moreover, as for the droplet tracking technique, the mass flow rate to be measured can be amplified by employing many identical microchannels in parallel. Colin *et al*. (2004), Pitakarnnop *et al*. (2010), and Bergoglio *et al*. (2015) analyzed gas flows in microfluidic chips made of hundreds of microchannels in a silicon wafer structure as the one sketched in Figure 3.8. The microchannels in the wafer cannot be perfectly identical due to limitations in the precision and repeatability of the microfabrication technique. Therefore, the measured mass flow rate corresponds to an average value of the mass flow rate through each microchannel.

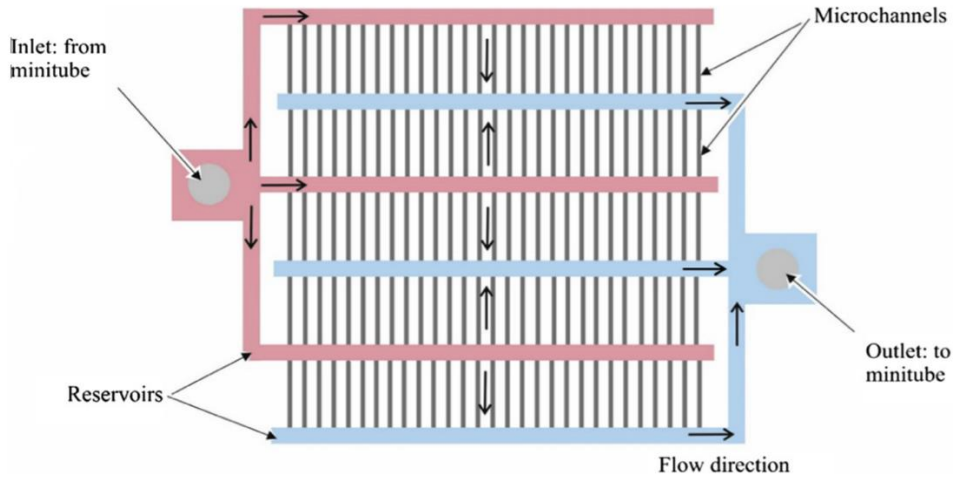

Figure 3.8. Structure of the microfluidic system employed by Colin *et al*. (2004), Pitakarnnop *et al*. (2010), and Bergoglio *et al*. (2015), composed by hundreds of microchannels on a silicon wafer. Figure from Bergoglio *et al*. (2015).

Figure 3.9 illustrates a scheme of the constant pressure experimental setup employed by Jousten *et al.* (2002). In their configuration, a volume displacer is used for maintaining constant the pressure at the inlet of the test section. Their experimental setup allowed to apply a more sophisticated implementation of the constant pressure technique, first described by Bennewitz and Dohmann (1965). In this method, the inlet pressure is allowed to vary in a sawtooth manner in a very small variation band, between $-5 \cdot 10^{-4}$ Pa and $5 \cdot 10^{-4}$ Pa around the initial pressure value. Valve V2 of Figure 3.9 opens and closes accordingly to the pressure difference between a reference pressure and the inlet pressure, which is measured by means of a capacitive differential pressure gauge (CDG). The authors

reported mass flow rate measurements of nitrogen flows between 10^{-14} and 10^{-8} kg/s and a relative uncertainty between 3% and 0.2%, respectively.

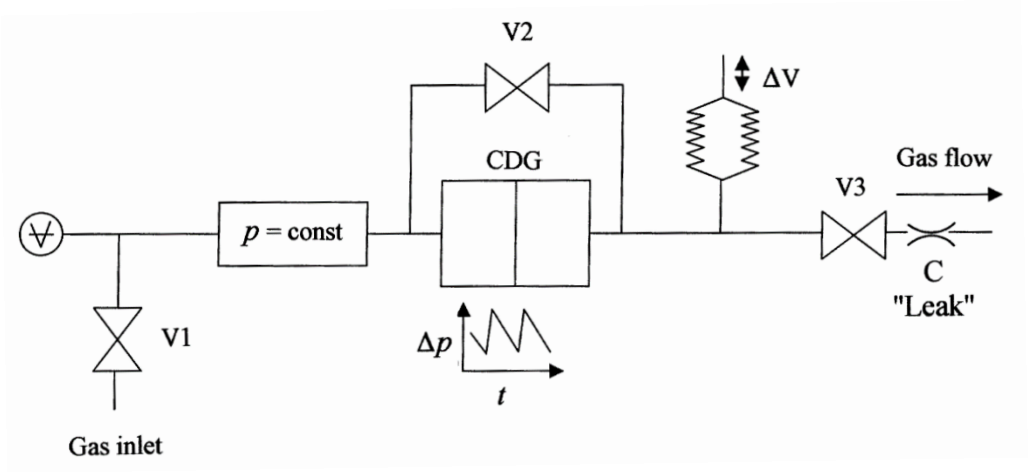

Figure 3.9. Schematic of the constant pressure experimental setup employed by Jousten *et al*. (2002).

3.3.3 Constant-volume technique

Among all the experimental techniques previously described, this is the simplest to be implemented as it does not require any moving parts such as liquid droplets or pistons. The most common version of this experimental setup is composed by two identical tanks at the two sides of the tested channel. As the gas flows from the high-pressure upstream tank to the low-pressure downstream tank through the tested channel, the upstream pressure, p_{in}, and downstream pressure, p_{out}, relax in time towards an equilibrium pressure. The mass flow rate can be indirectly calculated by tracking the pressure in the upstream and/or downstream reservoir by means of a conventional pressure sensor.

By taking into account for possible thermal fluctuations in the reservoir, the mass flow rate is calculated as:

$$\dot{m} = \frac{V}{R_s T}\frac{dp}{dt} - \frac{pV}{R_s T^2}\frac{dT}{dt} = \frac{V}{R_s T}\frac{dp}{dt} - \frac{m_g}{T}\frac{dT}{dt}. \tag{3.5}$$

where the gas mass in a tank has been defined as $m_g(t) = pV/R_s T$. Pressure variations can generally produce structural deformations of the reservoirs. However, they can usually be neglected and the reservoir volume V can be considered constant. The last term of Eq. (3.5) represents possible temperature fluctuations of the gas that generate fluctuations in the gas pressure. The mass flow rate passing through the tested channel corresponds to the rate of variation of the gas pressure that is only due to a gas mass transfer and not due to thermal instabilities. It can be noticed from Eq. (3.5) that the thermal fluctuations in a single tank are proportional to the mass of gas present in the tank. In order to quantify the contribution of the thermal instability to the calculation of the mass flow rate, Eq. (3.5) can be rewritten as (Ewart *et al*., 2006):

$$\dot{m} = \frac{V}{R_s T}\frac{dp}{dt}(1-\epsilon), \qquad \epsilon = \frac{dT/T}{dp/p}. \tag{3.6}$$

Most of the time, the temperature variation in a tank can be limited to half a degree (Ewart *et al*., 2006; Rojas-Cardenas *et al*., 2017), so that at ambient temperature $dT/T \cong 10^{-3}$. During the time a temperature variation of 0.5 K occurs, the pressure in the tank needs to vary of at least 10% of the absolute pressure for having $\epsilon \cong 10^{-2}$. Pitakarnnop *et al*. (2010) reduced the thermal fluctuations in the tanks by means of a system of Peltier modules. If the experimental setup can guarantee $\epsilon \ll 1$, the isothermal approximation holds, and the mass flow rate can be calculated as

$$\dot{m} = \frac{V}{R_s T}\frac{dp}{dt}. \tag{3.7}$$

The accuracy of the technique mainly depends on the precise measurements of the reservoir volumes. The measurement of the upstream or downstream reservoirs are composed also by the small volumes introduced by valves and connections. Different techniques for measuring the reservoir volumes are possible, e.g., the water balloon method used by Pitakarnnop *et al*. (2010), the method employed in the work of Rojas-Cardenas (2012), or the method employed in this work and described in Chapter 4. They all have in common the necessity of connecting to the system a reference reservoir with known volume.

One assumption that is usually implicitly accepted by many authors is that the gas flow through the tested channel is in a steady state, even if the conditions at the boundary vary in time. The gas system inside the channel is assumed to behave as a quasi-stationary dynamical system that instantly adapts to the time-dependent inlet and outlet pressures. This assumption is correct if the frequency content of the time-dependent pressure is inside the band pass of the microchannel frequency response. The works of Colin *et al*. (1998) on the frequency response of microchannels to oscillating inlet pressure may help in understanding if the rate of pressure variation at the channel inlet is slow enough for making valid the assumption of quasi-steady gas flow.

Equation (3.7) can be applied to one (Arkilic *et al*., 1997; Ewart *et al*., 2006; Rojas-Cardenas *et al*., 2017) or both (Colin *et al*., 2004; Pitakarnnop *et al*., 2010) tanks at the two side of the tested channel. The calculation of the mass flow rate in both upstream and downstream tanks helps in double-checking the measurement. The experimental setup is usually built symmetrically with respect the tested channel, such that the volumes of the upstream and downstream reservoirs are the same. This requires using also the same connecting pipes and the same valves on both sides of the test section. For this implementation of the constant volume technique, it can be demonstrated that the pressure evolution in the tank fits an exponential function and that the mean pressure inside the tested channel is constant (Silva *et al*., 2018). Figure 3.10a illustrates the typical pressure evolution in the two tanks. Differently, Figure 3.10b shows the pressure evolutions when the upstream tank is bigger the downstream one.

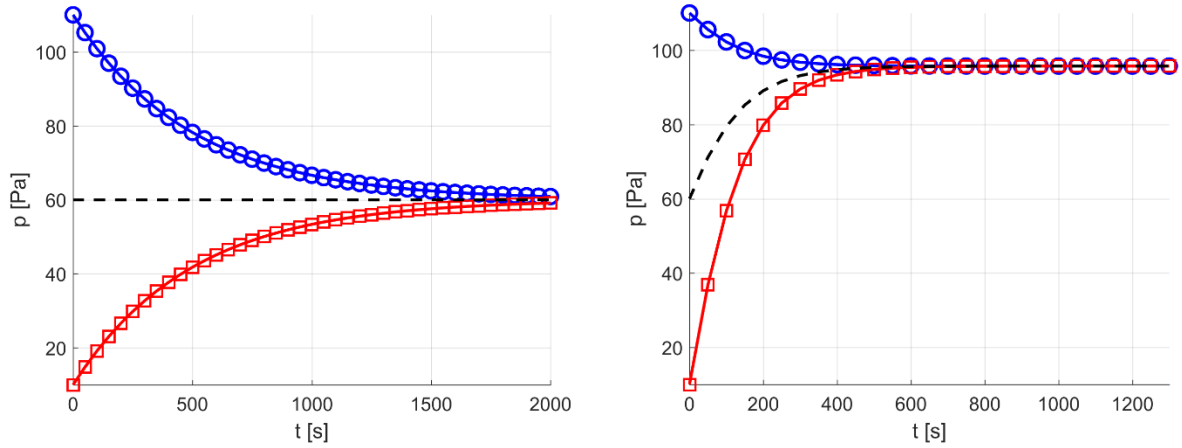

(a) (b)

Figure 3.10. Example of pressure evolution in the upstream tank (○) and the downstream tank (□), (a) when the reservoir volumes are equal, and (b) when the upstream reservoir is bigger than the downstream one. The dashed line represents the average of the upstream and downstream pressure.

Many authors employed a symmetric experimental setup, so that one experiment could associate the mass flow rate to a specific mean Knudsen number. As for the setup of Figure 3.7 used by Pitakarnnop *et al*. (2010), the experimental apparatus of Colin *et al*. (2004) combines the constant volume technique with the droplet tracking technique. In their work, the authors measured mass flow rates as low as 10^{-13} kg/s inside a series of microchannels etched by DRIE in a silicon wafer anodically bonded to a Pyrex cover. They demonstrated a good match with the theoretical mass flow rate computed by means of second-order boundary conditions up to outlet Knudsen numbers of 0.25. Pitakarnnop *et al*. (2010) measured a mass flow rate as low as 10^{-14} kg/s for an outlet Knudsen number of 1.4. The typical uncertainty in these experiments was of 4.5%.

Silva *et al*. (2017) proposed an analysis of rarefied gas flows in microchannels by using a non-symmetrical experimental setup. This configuration, which has been called the dynamic, constant volume technique, is characterized by a time-dependent mean pressure (as illustrated in Figure 3.10b). This experimental technique allows to obtain the mass flow rate through the tested microchannel at different Knudsen numbers by means of one single experiment. Moreover, it has the advantage of bigger pressure variation in the smaller reservoir, which makes the thermal fluctuations even less important in the calculation of the mass flow rate. Silva *et al*. (2018) analytically demonstrated that the pressure evolution in the tanks does not fit an exponential function anymore. The implementation of the constant volume technique adopted in this work is similar to the dynamic, constant volume technique described by Silva *et al*. (2018) since the gas circuit here employed is non-symmetric. However, the experimental setup of this work is inherently different from that used by Silva *et al*. (2018) because the gas flow through the tested channel is driven by a pumping system that maintains the downstream pressure low and

far from equilibrium with respect to the upstream pressure, as explained in Chapter 4. The procedure for carrying out the mass flow rate measurements in this type of gas circuit will be described in Chapter 6.

When the thermal stability in the tanks cannot be ensured, a symmetric experimental setup can also allow a different type of compensation of the temperature fluctuations. Arkilic *et al*. (1997) proposed a modified constant-volume technique, in which the mass flow rate measurement is based on pressure difference $\Delta p = p_T - p_r$ between the pressure p_T in a tank accumulating the gas flowing out the tested channel and a second, sealed tank attached to the first and at a reference constant pressure p_r. In this way, the mass flow rate is calculated as:

$$\dot{m} = \frac{V}{R_s T}\frac{d\Delta p}{dt} - \frac{\Delta p V}{R T^2}\frac{dT}{dt} = \frac{V}{R_s T}\frac{d\Delta p}{dt} - \frac{\Delta p}{p} m_g \frac{dT}{dt}. \tag{3.8}$$

Eq. (3.8) shows that the thermal fluctuation term is now proportional to the gas mass in the tank, as for Eq. (3.5), but, this time, also to the ratio of the pressure difference to the absolute pressure in the tank. Usually the possible thermal fluctuations in the tank make the mass flow rate computation problematic in the last seconds of the pressure relaxation, where the pressure variation in time is very slow (see Figure 3.10) and the factor ϵ of Eq. (3.6) increases. The approach proposed by Arkilic *et al*. (1997) drastically reduces the sensitivity of the mass flow measurement to thermal fluctuations since the pressure difference Δp is zero at the beginning of the experiment and remains very small with respect to the absolute pressure since the mass flow rate through microchannels is very small. This is true for experiments with gas flows at relatively high average pressure. When low-pressure conditions are employed, the pressure variation can be a substantial percentage of the absolute pressure, as illustrated, for instance, in Figure 3.10. Arkilic *et al*. (1997) applied this technique to gas flows in a rectangular channel with a height of 1.33 μm and a width of 52.25 μm, thus being able to obtain very small mass flow rates at atmospheric pressure. They reported a sensitivity of their technique as low as $7 \cdot 10^{-15}$ kg/s.

3.4 Optical techniques in gas flows

As many authors have stated in the past (Matsuda *et al*., 2011; Morini *et al*., 2011), the most suitable experimental technique for measurements in microflows should be based on sensing elements with characteristic sizes at the molecular level, or at least very close to this scale. As discussed in the previous sections, integrated microsensors in microdevices have been widely employed for the investigation of microdevices. However, they can provide only information on average properties of the flow, such as the mass flow rate through a section, and only at a specific location along the microfluidic device, such as the average pressure or temperature in a region close to the microsensor location. Many authors developed microfluidic chips in which a series of microsensors is integrated along the fluid circuit for providing measurements on the distribution of pressure, temperature, or average velocity along the microflow. However, the resolution of the measurements is always limited to a finite number of distributed measures. In microfluidic flows, the spatial gradients of the thermodynamic properties of

the flow may have characteristic lengths on the order of the micrometer, and the integration of an increasing number of microsensors inside the investigated system necessarily increases the amount of perturbation introduced in the fluid flow.

Therefore, the accurate investigation of the physical behavior of microdevices requires measurements techniques with high spatial resolution and that are low-intrusive. In this context, the research community focused in developing opto-chemical techniques that do not require the integration of intrusive micro-sensors. These advanced experimental techniques exploit the interaction of molecules with an incident light.

All the techniques that will be discussed in this section require, at least, a laser source for activating and a photodetector for interrogating the "molecular sensors" (Matsuda *et al*., 2007).

Because of the inherent optical nature of these experimental techniques, an optical access always needs to be present in the region of investigation. The integration of optical access may be a source of perturbation in the flow field. Microchannels made out of aluminum, silica or other materials would also need a portion of the inner surface made of a transparent material, resulting in inner surfaces characterized by quite different TMAC. For the experimental investigation carried out in this work, the requirement of integrating a small optical access in the testing channel resulted to be the most important source of perturbations, introducing air leakages and glass-plastic interfaces. Moreover, for whole-field measurement techniques such as molecular tagging techniques or particle image velocimetry, the investigated flow needs to be seeded with a sensing tracer, thus modifying the original composition of the gas flow.

Nevertheless, even though the visualization techniques are not completely non-intrusive, they can be classified as low-intrusive techniques.

The visualization techniques for pressure and temperature measurements are based on "molecular-sensors" that are introduced inside the flow field or distributed on the wall surfaces. To date, the most widely employed and successful method is provided by pressure- or temperature-sensitive paints applied on surfaces, which will be described in Sections 3.4.1 and 3.4.2. Whole-field measurements for pressure and temperature are, respectively, the molecular tagging manometry (MTM) and the molecular tagging thermometry (MTT), which are based on the same physical principle as for sensitive paints, that is a laser-induced photoluminescence, but the sensing molecules are introduced in the bulk of the flow. Important and promising optical techniques for temperature measurements in gas flows are also Raman thermometry techniques, such as coherent anti-Stokes Raman spectroscopy (Lutch *et al*., 2006).

The molecular tagging (MT) technique is at the core of this work. Among all the techniques here presented, MT technique is the most promising and versatile for pressure, temperature, concentration, and velocity field measurements in rarefied gas flows. They are whole-field optical techniques that exploit the laser-induced

photoluminescence properties of some molecular tracer. Photoluminescence is an intramolecular process that involves the electronic excitation of the absorbing molecule. Differently from other techniques such as Raman spectroscopy or PIV that are based on the elastic or inelastic scattering of the incident light, in molecular tagging techniques an electron of valence of the absorbing molecule jumps to a more external orbital with higher energy. Common molecular tracer employed in MT techniques for both liquid and gas flows are acetone and diacetyl. The photoluminescence of these molecules is characterized by two emission components: fluorescence and phosphorescence. In the past years, experimental techniques based on the fluorescence emission sensitivity to the fluid pressure and/or temperature have been specifically called as laser-induced fluorescence (LIF) techniques. Similarly, those techniques that exploit the phosphorescence component of the emission can be called as laser-induced phosphorescence (LIP) techniques. Although in the literature the nomenclature LIF is still adopted for the fluorescence-based techniques, LIF and LIP are considered here as two possible MT techniques, since they both work with the electronic excitation of the tracer molecules. MT measurements can also be carried out by exploiting the fluorescence and phosphorescence emissions simultaneously, as proposed, for instance, by Koochesfahani (2002).

Weather fluorescence or phosphorescence emission is considered, the total number S of photons collected by a photodetector from a volume ΔV of molecules excited by a laser beam of energy density I_{in} [J m^{-2}], can be calculated as

$$S = \eta_p \frac{I_{in}\sigma_{abs}(\lambda_{ex}, T)}{E_{ph}(\lambda_{ex})} n\phi(\lambda_{ex}, T, p)\Delta V, \tag{3.9}$$

where λ_{ex} [m] is the excitation wavelength, ϕ [-] is the quantum yield of the emission, σ_{abs} [m^2] is the absorption cross-section of the absorbing molecules, n [m^{-3}] is the molecular concentration of the emitting molecules, E_{ph} [J] is the photon energy, depending only on the excitation wavelength, and η_p [-] represents the capturing efficiency of the photodetector. The luminescence quantum yield ϕ is the percentage of excited molecules that re-emits a photon or, equivalently, the ratio of the re-emitted light to the absorbed light:

$$\phi = \frac{\text{Light emission}}{\text{Ligth absorption}}. \tag{3.10}$$

The luminescence quantum yield is strictly correlated to the characteristic times of radiative and non-radiative de-excitations that occur at the intramolecular level. The total number of photons that is emitted from a population of excited molecules is, indeed, higher if the occurrence of emission is faster than the occurrence of non-radiative de-excitations, i.e., transitions that de-excite the molecule with no photon emission. Non-radiative de-excitations can be enabled, for instance, by collisions of the excited molecule with other molecules, which is a phenomenon known as molecular quenching. By defining the emission rate k_r [s^{-1}], the non-radiative de-excitation rate k_{nr} [s^{-1}], and

the quenching rate k_Q[m^{3}s^{-1}] related to a specific molecular species Q with number density n_Q [m^{-3}], the quantum yield reads

$$\phi = \frac{k_r}{k_r + k_{nr} + k_Q n_Q} = \frac{\tau}{\tau_r}, \tag{3.11}$$

where $\tau_r = 1/k_r$ is the characteristic time of the radiative transition and $\tau = \left(k_r + k_{nr} + k_Q n_Q\right)^{-1}$ is the lifetime of the fluorescence or phosphorescence emission. Generally, all the constant rates, k_r, k_{nr}, and k_Q, may depend on the temperature. The origin and the significance of Eq. (3.11) will be further analyzed and discussed in Chapter 5. However, this brief introduction on the relationship between the quantum yield and the characteristic times of the intramolecular processes is very helpful for understanding the working principle of some of the optical techniques for pressure and temperature measurements.

3.4.1 Optical pressure measurements

i. Pressure-sensitive paints (PSP)

PSPs are opto-chemical sensors constituted by luminescent molecules embedded in a polymer binder. A UV-laser source is required for exciting the sensitive molecules towards a higher energy state, and the photon re-emission happens at a longer wavelength. Optical filters can be employed for separating the excitation light from the emitted light. The PSP principle is based on the oxygen quenching of the luminescence emitted by the paint. In particular, the luminescence quantum yield ϕ, and, equivalently, the lifetime τ of the light emission are inversely proportional to the oxygen concentration n_{O_2}, as described by Eq. (3.11) when oxygen is considered as the quencher species. This is mathematically described by the Stern-Volmert equation (Liu *et al*., 1997)

$$\frac{\phi_0}{\phi} = \frac{\tau_0}{\tau} = 1 + \tau_0 k_{O_2} n_{O_2}, \tag{3.12}$$

in which k_{O_2} is the oxygen quenching rate, and τ_0 and ϕ_0 are, respectively, the luminescent lifetime and the quantum yield when no oxygen quenching occurs. It is important to note that Eq. (3.11) and, thus, (3.12) implicitly assume an exponential decay of the luminescence emission rate, as it will be demonstrated in Chapter 5.

Hence, as the oxygen concentration increases, the intensity of the paint emission decreases. According to Henry's law (Liu *et al*., 2010), the oxygen concentration n_{O_2} in a polymer binder is proportional to the partial pressure p_{O_2} of oxygen. Under the assumption of uniform oxygen concentration, Eq. (3.12) can be rewritten by using Eq. (3.9) as a relationship between the gas pressure p and the luminescence intensity S:

$$\frac{S_{ref}}{S(p)} = A(T) + B(T)\frac{p}{p_{ref}}, \tag{3.13}$$

where S_{ref} is the luminescent intensity corresponding to the reference pressure p_{ref}. Coefficients $A(T)$ and $B(T)$ depend on the reference pressure p_{ref} employed for the calibration, the oxygen quenching rate, the luminescence constant rate, and the non-radiative de-excitation rate, which, in turn, depend on the gas temperature T. These rate constants and the Stern-Volmert equation will be further discussed in Chapter 5. The two coefficients A and B are usually calculated during the calibration process. Because the technique is based on oxygen quenching, PSPs have the advantage of being applicable to air flows, a feature that is not available in all optical techniques. However, for the same reason, it cannot be efficiently applied to liquid flows. The principle of the PSP technique is schematized in Figure 3.11.

Niimi *et al*. (2005) experimented the pressure/temperature sensitivity and the time response of luminescence of three different types of PSPs at pressures lower than 150 Pa. Their study demonstrated that the PtTFPP/poly(TMSP) paint is the most suitable PSP among the tested ones for application in the low-pressure range for its very high and linear sensitivity to oxygen pressure. They underlined, however, a non-negligible sensitivity to temperature, which necessarily requires a correction for accurate pressure measurements.

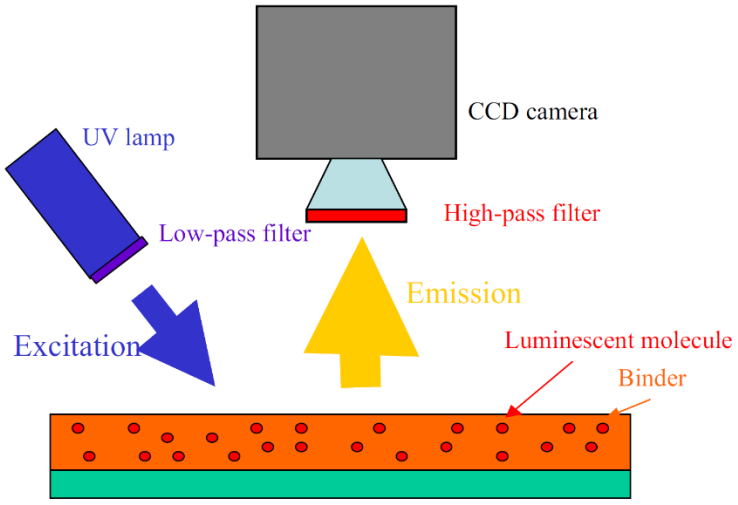

Figure 3.11. Schematic principle of the polymer-based pressure-sensitive paints. Figure from Huang & Sullivan (2005).

Huang & Sullivan (2005) applied the PtTFPP/TMSP paint on a glass slide covering a micromachined microchannel in aluminum with a height of 52 µm. They successfully demonstrated the application of PSPs to gas microflows for Knudsen numbers up to 0.8. The spatial resolution of the technique was enough to analyze the entrance effects on the pressure distribution, which is characterized by a rapid pressure drop. Figure 3.12a and Figure 3.12b represent, respectively, the pressure map at the channel entrance recorded by the CCD camera and the pressure distribution along the microchannel centerline for different pressures at the channel entrance.

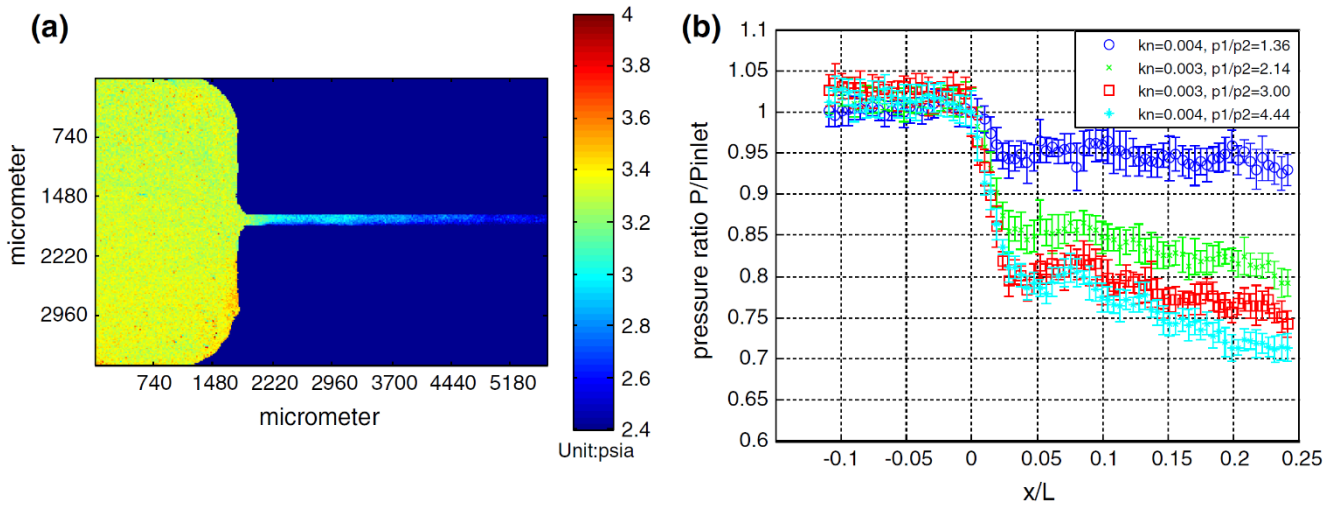

(a) (b)

Figure 3.12. (a) Pressure map at the channel entrance for a pressure ratio of 3.49. (b) pressure distribution along the channel centerline in the entrance region for different pressure ratios. Figures from Huang & Sullivan (2005).

PSPs applicability has been also investigated in unsteady flows. Gregory *et al*. (2007) verified the frequency response of PSPs by measuring the time-dependent pressure distribution of a sweeping jet generated by a microfluidic oscillator.

Even though the PSPs have been successfully used for sub-millimetric channels, their application in high Knudsen number flows is prevented by some limitations. Firstly, it is hard to produce a PSP with a thickness lower than 5 μm because of the necessity of a polymer binder. Moreover, the spatial resolution of PSP polymers is limited by the existence of molecular aggregation that makes the light emission distribution non-uniform when a uniform pressure is applied on the paint, as shown in Figure 3.13a.

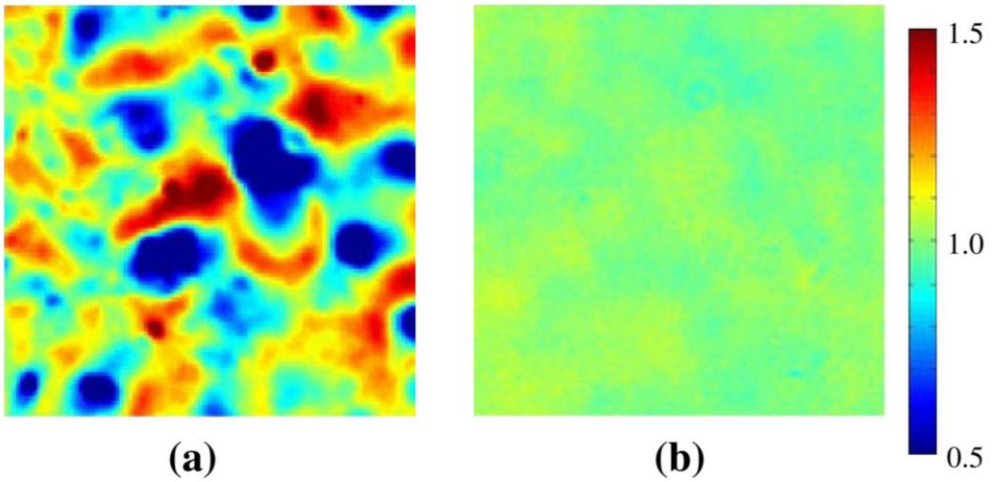

Figure 3.13. Relative intensity emission for (a) PSP and (b) PSFM. Figures from Matsuda *et al*. (2011).

The figure represents the PSP intensity distribution normalized with respect to the average intensity on a 160 × 160 μm^2 area, with polymer aggregations with size up to 40 μm (Matsuda *et al*., 2011). This non-uniformity can be partially reduced through a calibration based on the calculation of the intensity ratio S_{p_1}/S_{p2} at two different pressures p_1 and p_2. However, this problem cannot be completely solved because the polymer aggregations of the PSP result to be differently sensitive to the pressure.

An evolution of the polymer-based PSP has been provided by Matsuda *et al*. (2007), who developed the pressure-sensitive molecular film (PSMF). The fabrication technique is based on the Langmuir-Blodgett (LB) method, which is able to produce a nanometric film of ordered sensitive molecules. Beside the fact that PSMFs have a much smaller thickness with respect to conventional PSPs, they allow pressure measurements with a higher spatial resolution, since the molecular assembly of PSMF does not have the problematic linked to the formation of polymer aggregation, as shown in Figure 3.13b. For PSMF, the relationship between the luminescent intensity and the gas pressure is very similar to Eq. (3.13) but, since the adsorbed oxygen on the PSMF surface dominates the quenching process, the Stern-Volmert relation takes the form

$$\frac{S_{ref}}{S(\theta)} = A_{ads}(T) + B_{ads}(T)\frac{\theta}{\theta_{ref}}, \tag{3.14}$$

in which $\theta = n_{O_2}/n_{O_2,sat}$ provides the degree of oxygen saturation on the PSMF. The relation between the coverage θ of oxygen molecules and the partial pressure p_{O_2} of oxygen is described by the Langmuir adsorption isotherm equation:

$$\theta = \frac{A_\theta(T)p_{O_2}}{1 + A_\theta(T)p_{O_2}}, \tag{3.15}$$

where A_θ is a temperature-dependent coefficient. Matsuda *et al*. (2007) tested the temperature and the pressure sensitivities of different kinds of PSMF, based on different types of luminophores, e.g., PtMP, PtMPDME, PtPP, and CuMPDME. The application of PSMF to micro-nozzle flows revealed that the technique has enough spatial resolution and sensitivity for measuring pressure differences on a characteristic length of the order of 50 μm. Since the calibration coefficients of Eq. (3.13), (3.14) and (3.15) depend on the surface temperature, non-isothermal conditions would necessarily require measuring the local temperature on the PSPs.

ii. Molecular tagging manometry (MTM)

The PSPs can provide the distribution of pressure along the wall surfaces of a microchannel, but they cannot inform on the pressure in the bulk of the fluid flow. In this case, the sensing elements need to be introduced inside the fluid flow, as it happens in molecular tagging techniques. A MTM technique can be based on laser-induced fluorescence or phosphorescence.

Thurber & Hanson (1999) analyzed acetone fluorescence and its sensitivity to gas pressure and composition. The quantum yield of fluorescence ϕ_f increases with the external pressure. For higher pressure, the increase of the collisional rate increases the vibrational relaxation phenomena which reduce the internal energy of the molecule. Since the most important non-radiative path that competes with the fluorescence event, which is the intersystem crossing, is faster at higher internal energy levels, the fluorescence emission becomes more probable. This intramolecular mechanism is detailed in Chapter 5.

The feasibility of the application of MTM in gas flows based on LIP has been analyzed by Basu *et al*. (2010). As for the PSP-based sensors, the MTM technique proposed by Basu *et al*. is based on the oxygen quenching of molecular tracer luminescence. The same Stern-Volmert equation, Eq. (3.12), is, then, employed. However, instead of basing the pressure measurement on the total emitted light, Basu *et al*. applied the ratio-metric approach, a methodology developed by Hu & Kooschefahani (2003) for MTT in liquid flows.

As described by Eq. (3.11), the signal intensity is directly proportional to the laser energy. Fluctuations on the laser energy are always present and, sometimes, even their average value is subjected to unpredictable oscillations. Variations in the phosphorescence intensity can be due to instability in the laser source, and, thus, accurate pressure measurements require monitoring the laser energy. The ratio-metric approach eliminates the dependency of the phosphorescence signal from the laser energy in the following way.

By assuming an exponential decay for the phosphorescence emission rate $I_{ph}(t) = I_0 e^{-t/\tau}$, that is the number of photons emitted per unit time, the phosphorescence lifetime can be quantified by one single parameter, i.e., the constant lifetime τ, which generally depends on the pressure, the temperature and, especially, the oxygen concentration. The initial emission rate I_0 is proportional to the initial concentration of excited molecules, and, thus, its value could be, in theory, indirectly calculated by knowing the incident laser energy, the molecular tracer concentration and the molecular tracer absorption properties.

Under this assumption, the number of phosphorescent photons $S(t, \Delta t)$ collected by the CCD detector at a time t after the laser excitation and on an integration window Δt is

$$S(t, \Delta t) = \eta_p \int_t^{t+\Delta t} I_{ph}(\tilde{t}) d\tilde{t} = \eta_p I_0 \left(1 - e^{-\Delta t/\tau}\right) e^{-t/\tau}. \tag{3.16}$$

If signal S is available at two different times t_1 and t_2 after the laser excitation, the ratio S_R of the two intensities allows to eliminate the dependency from the laser energy through I_0. If two different integration windows are employed for the two intensities, it yields

$$S_R = \frac{S(t_1, \Delta t)}{S(t_2, \Delta t)} = \frac{\left(1 - e^{-\Delta t_1/\tau}\right)}{\left(1 - e^{-\Delta t_2/\tau}\right)} e^{-(t_1 - t_2)/\tau}. \tag{3.17}$$

By considering Eq. (3.12) and by assuming isothermal conditions and uniform oxygen concentration (Basu *et al*., 2010), a relationship between S_R and the gas pressure p can be found. The introduction of two different integration windows Δt_1 and Δt_2 provides an additive parameter that can be employed to control the sensitivity of the relationship between the ratio S_R and the pressure p, as demonstrated in Figure 3.14b. As it can be noticed, the theoretical predictions overestimate the experimental data.

It is important to underline that the ratio-metric approach of Hu & Kooschefahani (2003) requires collecting the phosphorescence emission at two different times but for the same laser pulse excitation. The measurement of S_{t_1} and S_{t_2} for two different excitations cannot account for energy variations between one laser pulse and the following.

Basu *et al*. (2010) analyzed the possible application of MTM based on acetone vapor phosphorescence and its sensitivity to oxygen concentration. Their experimental setup is shown in Figure 3.14a. A nitrogen-oxygen mixture was seeded by acetone molecules by bubbling the gas mixture inside a thermoregulated liquid-acetone bath. The acetone molecular concentration inside the gas mixture was determined from the temperature-dependence of the acetone vapor pressure. A XeCl excimer laser was employed for exciting the acetone vapor at 308 nm with a laser pulse duration of 20 ns and an energy of 135 mJ. Basu *et al*. did not report the diameter of the laser beam; therefore, the average laser energy density is not known.

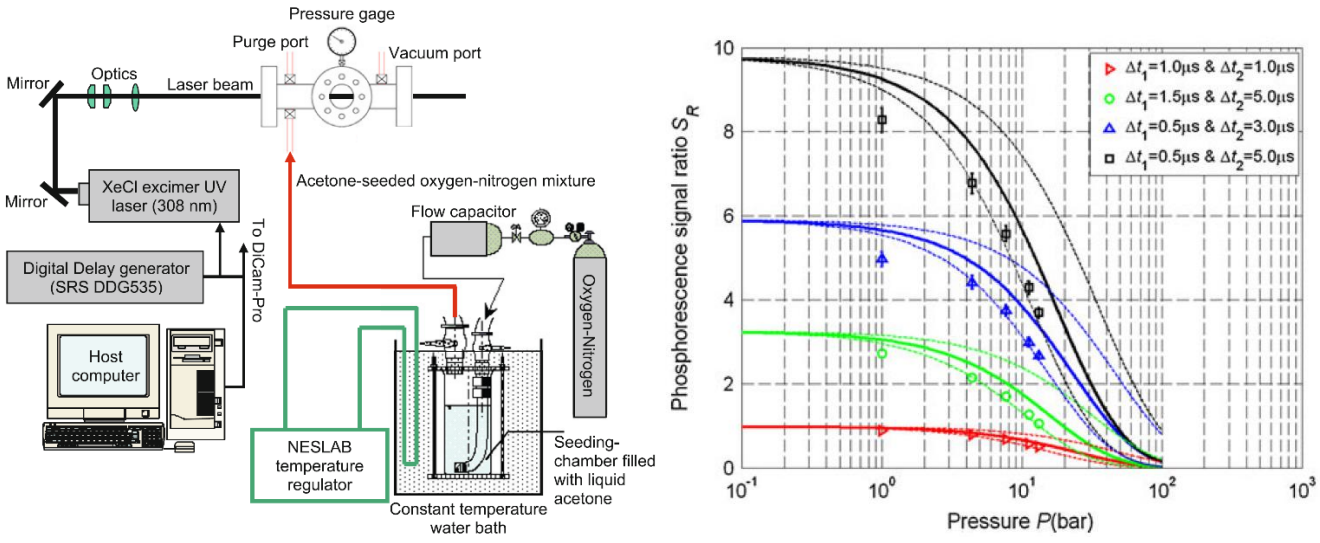

(a) (b)

Figure 3.14. (a) Schematic of the experimental MTM setup employed by Basu *et al*. (2010). (b) Comparison between the experimental data and theoretical predictions of S_R as a function of the gas pressure for a fixed oxygen concentration n_{O_2}. The different curves are related to different values Δt_1 and Δt_2 of the integration windows. The dashed lines represent the theoretical prediction for variation of the oxygen concentration of $\pm$50% with respect to the experimental condition.

As it will be discussed in Chapter 5, the experimental data of this work and others found in the literature corroborate the fact that the acetone emission at excitation wavelengths around 310 nm does not correspond to acetone phosphorescence but it is the result of phosphorescence of diacetyl, which forms following the decomposition of acetone molecules in radicals. Therefore, the results presented by Basu *et al*. on the phosphorescence sensitivity to oxygen pressure might be related to diacetyl vapor, for which oxygen quenching is more efficient than in the case of acetone.

For the application of this technique to gas flows different from air flows, such as nitrogen or helium flows, two extra gas species need to be added to the main one: the photoluminescent tracer, commonly acetone or diacetyl vapor, and the oxygen quencher. As thoroughly discussed in the next chapters, one of the main difficulties related to the application of the molecular tagging technique in rarefied gas flows is given by the reduced number of tracer molecules that provides light information. Especially in gas flows with low tracer concentration, small air leakages in the gas circuit may completely extinguish the tracer emission due to oxygen quenching, so that no information at all can be extracted from it. MTM is a very promising technique for whole-field pressure measurements in microflows but further analysis on the feasibility of its application to gas microflows is required.

3.4.2 Optical temperature measurements

i. Temperature-sensitive paints (TSP)

TSPs have been proposed as an optical-chemical mean for carrying out temperature measurements in gas microflows. As PSPs, TSPs are made of thin luminescent polymer coatings that are applied on a transparent surface in microdevices. The physical principle governing the function of TSPs is based on a different type of molecular quenching of the luminescent molecules. While PSPs principle is based on oxygen quenching, in TSPs the temperature sensitivity is provided by the thermal quenching. As stated in the review of Liu (2010), TSP cannot be sensitive to air pressure because the polymer binder for TSPs, which can be epoxy or a resin, is impermeable to oxygen molecules.

The quantum efficiency of the luminescence decreases with temperature. Since the frequency of intermolecular collisions increases with temperature, the thermal quenching is the result of the increasing probability of non-radiative de-excitations, which reduces the overall amount of re-emitted light. The relationship between the luminescence intensity S and the surface temperature T can be written as:

$$\frac{S}{S_{ref}} = f_{TSP}\left(T, T_{ref}\right). \tag{3.18}$$

Function $f_{TSP}(T, T_{ref})$ can be approximated by the Arrhenius equation (Liu, 2010), but in practical applications it is usually determined through a polynomial fitting of calibration data.

TSPs are very convenient temperature sensors when employed in combination with PSPs. As previously discussed, these pressure sensors need a temperature compensation for the application of the Stern-Volmert equation (3.13). The great advantage in the application in tandem of PSPs and TSPs is also given by the fact that they both require the same experimental equipment, i.e., a laser source, a photodetector, and an optical access on the microdevice. Liu *et al*. (2005) demonstrated the simultaneous application of TSPs and PSPs for the analysis of heat transfer in an impinging air jet. Figure 3.15 shows the contours of the temperature distribution measured with TSPs on the hot surface, for two different Reynolds numbers.

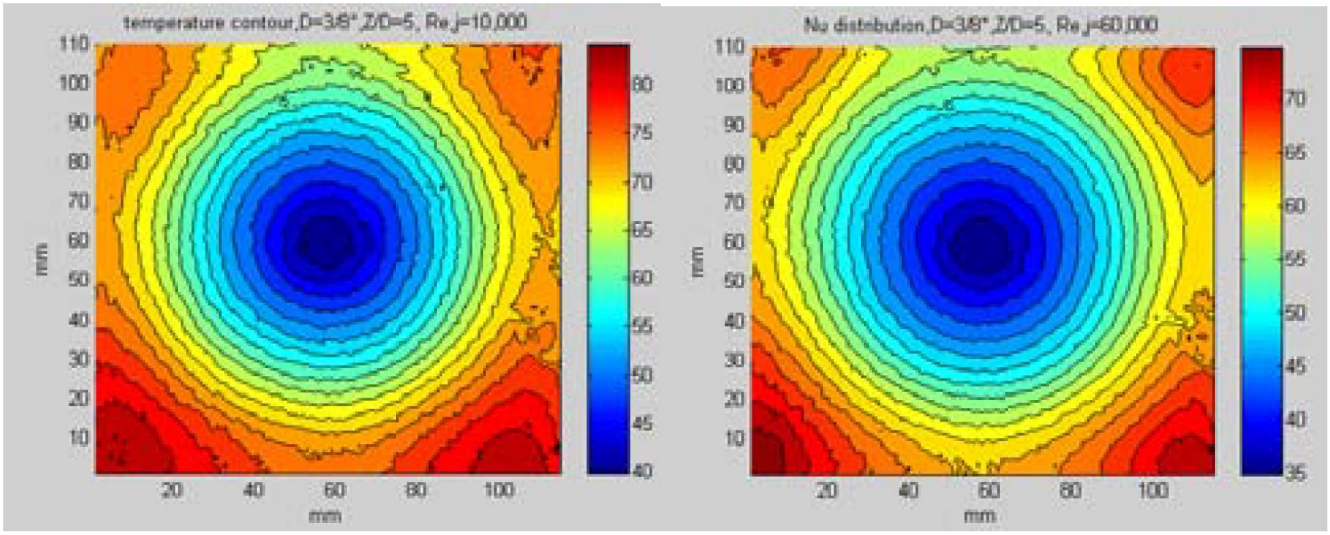

(a) (b)

Figure 3.15. Temperature distribution from TSP on a hot surface cooled by an impinging air jet for two Reynolds numbers: (a) Re = 10000 and (b) Re = 60000. Figure from Liu *et al*. (2005).

In another review of Liu *et al*. (1997), a useful table listing the main characteristics of TSPs with different luminophores and binders can be found. Its application on rarefied gas flows or gas microflows is still missing in the literature. It is not known at the current state, if the TPSs have the adequate sensitivity and spatial resolution for being applied to gas microflows.

ii. Molecular Tagging Thermometry (MTT)

Since the intensity of both short-lived fluorescence and long-lived phosphorescence depends on the temperature of the photoluminescent molecules, MTT can be based on either LIF or LIP. As it can be noticed from Eq. (3.9), if the molecular tracer concentration is constant, variation in temperature T can change the absorption cross-section $\sigma_{abs}(\lambda_{ex}, T)$ and/or the quantum yield $\phi(\lambda_{ex}, T, p)$ of the emission. The temperature sensitivity of these two parameters depends on the excitation wavelength λ_{ex}.

As in the case of MTV, applications of MTT to fluid problems started within liquid flows. Since oxygen quenching is very effective on phosphorescence emission, LIP for flow diagnostics in liquids flow has been much more limited than LIF until the apparition of new sophisticated molecular tracers. Ponce *et al*. (1993) designed a supramolecule based on 1-BrNp luminophore with a phosphorescence lifetime up to some milliseconds. They demonstrated that the quenching of the luminophore phosphorescence can be prevented by mixing alcohols ROH with an aqueous solution made of 1-BrNp luminphores and glucosyl-β-cyclodextrin (Gβ-CD).

Thomson & Maynes (2000) were among the firsts to analyze the possibility of extending the already existing MTV to an MTT technique. They reported that MTT based on the induced phosphorescence of the molecular complex 1-BrNp·Gβ·CD·ROH could provide temperature measurements over a range of 30° C and with 1.5° C of standard uncertainty. In their work, they employed laser pulses at 308 nm, with 16 ns pulse-width, an average energy density of 60 mJ/cm^2, and an intensified CCD camera capturing the phosphorescence emission between 200 and 300 μs after the laser excitation.

In gas flows, application of LIF-MTT with acetone vapor has been thoroughly investigated by Thurber & Hanson (1998). The results of Figure 3.16a demonstrates that for certain excitation wavelengths the fluorescence emission has an exploitable temperature sensitivity. The measurement resolution of this technique is very good between ambient temperature and 1000 K, but its sensitivity may be too low for applications in gas microflows. In the best case scenario, the curve of Figure 3.16a corresponding to an excitation wavelength of 248 nm shows a reduction of the fluorescence intensity of about 50% for a 100 K difference. LIF has been prevalently applied in gas combustion chambers where high temperatures and high temperature gradients are present (Dégardin *et al*., 2006). The experimental results of Figure 3.16a are relative to atmospheric pressure conditions. In real applications of LIF, variation of acetone concentration in the flow field makes the single-wavelength LIF technique not applicable for univocal temperature measurements, since the cause of fluorescence signal variations cannot be unambiguously identified. When the acetone partial pressure may vary inside the investigated domain, the dual-wavelength LIF is a possible alternative. By considering Eq. (3.9), if the fluorescence signals S_{λ_1} and S_{λ_2} are generated by two laser beams at two different excitation wavelengths λ_1 and λ_2, the ratio

$$\frac{S_{\lambda_2}}{S_{\lambda_1}} = \frac{\sigma_{abs}(\lambda_2, T)\phi_f(\lambda_2, T, p)}{\sigma_{abs}(\lambda_1, T)\phi_f(\lambda_1, T, p)} \tag{3.19}$$

does not depend on the local acetone molecular concentration. If the dependency of ϕ_f from pressure can be neglected with respect to the dependency from temperature, the ratio of the signal does not depend on the total gas pressure either. Figure 3.16b shows $S_{\lambda_2}/S_{\lambda_1}$ as a function of temperature for different excitation wavelength combinations. For having the best temperature sensitivity, the excitation wavelengths to be paired need to provide very different fluorescence signals, such as in the case of λ_2 = 320 nm and λ_1 = 248 nm.

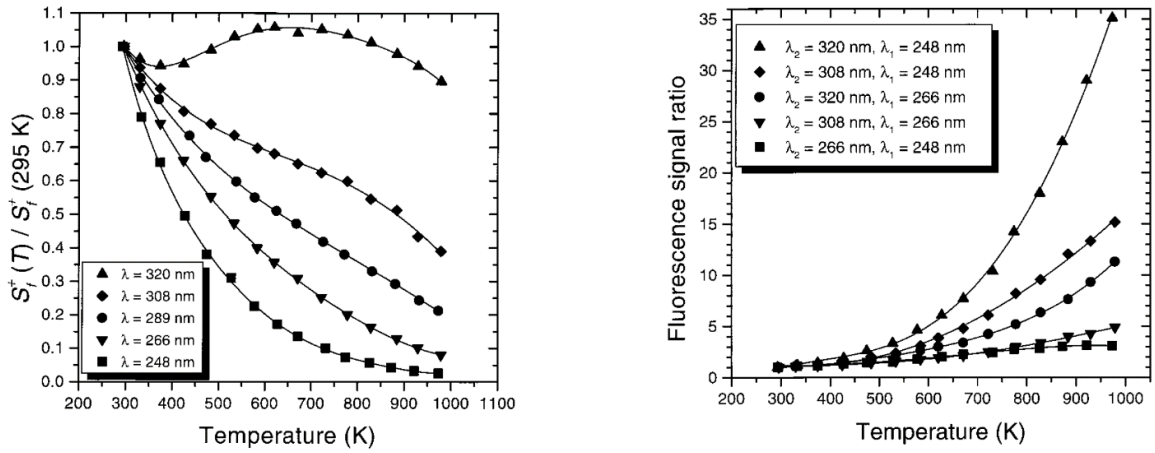

(a) (b)

Figure 3.16. (a) Fluorescence signal per unit acetone mole and per unit laser energy normalized to the room temperature and at atmospheric pressure as a function of temperature. (b) Fluorescence ratio $S_{\lambda_2}/S_{\lambda_1}$ for the dual-wavelength excitation normalized to the room temperature and at atmospheric pressure as a function of temperature.

Figure from Thurber & Hanson (1998).

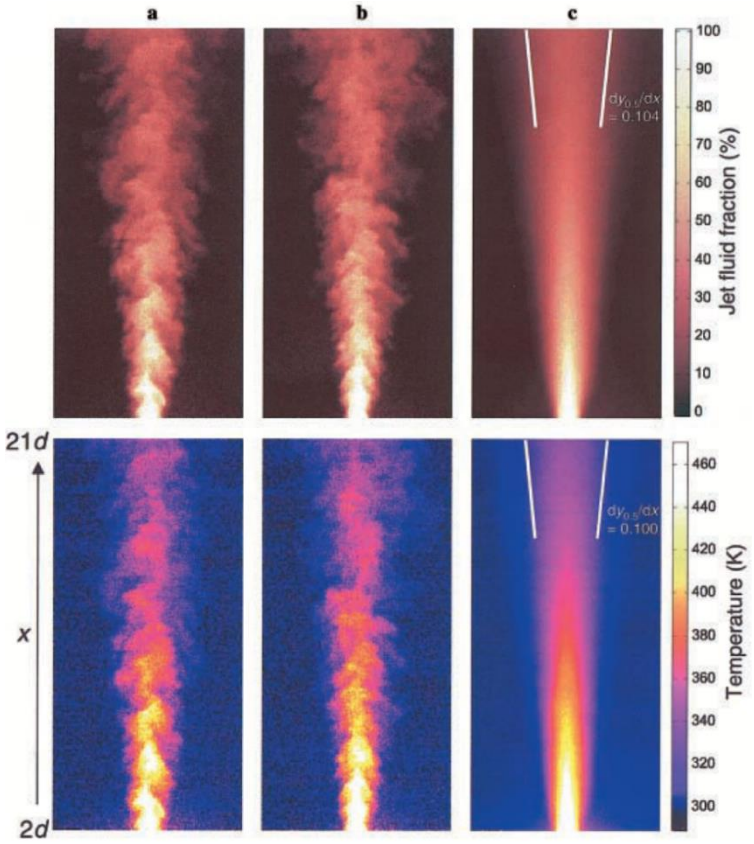

Figure 3.17. Mole fraction (top images) and temperature (bottom images) images of the heated air-acetone jet captured with the dual-wavelength LIF: (a) and (b) are representative instantaneous images; (c) corresponds to the average of 100 instantaneous images. Figure from Thurber & Hanson (2001).

Later, Thurber & Hanson (2001) applied the dual-wavelength-LIF MTT to a heated turbulent jet (Figure 3.17). While the signal ratio $S_{\lambda_2}/S_{\lambda_1}$ can inform on the temperature distribution in the air jet, the absolute value of the fluorescence emission can provide the distribution of the acetone concentration, enabling the possible investigation of the mixing properties of the jet. No applications of diacetyl LIF for temperature field measurements in gas flows have been found in the literature.

To the best of our knowledge, practical applications of MTT in gas flows based on LIP do not currently exist. Experimental studies on the temperature sensitivity of phosphorescence lifetime for diacetyl (Concheanainn & Sidebottom, 1979) and toluene (Kilmer & Spangler, 1971) vapors are available, but any experimental work related to acetone vapor has been found in the literature.

It has been observed that an increase in temperature makes the phosphorescence emission weaker and shorter. However, the application of LIP for temperature diagnostic in gas flows has not been carefully investigated yet. The control of the experimental conditions is the main difficulty for this type of analysis. By considering the relatively weak temperature sensitivity of the phosphorescence, the ratio-metric approach of Hu & Kooschefahani (2003) is necessary for cancelling the influences of laser energy fluctuations on the phosphorescence lifetime measurements. Small leakages in the experimental visualization cell may enable molecular quenching due to oxygen molecules, thus introducing perturbations in calibrating the relationship between temperature and phosphorescence lifetime. Especially at low pressure, the reduced number of tracer molecules and the increased molecular diffusion obliges to increment the laser excitation energy for producing an enough strong emission. However, this strategy produces side-effects that increases the complexity of the photoluminescence phenomenon and, thus, of the MTT technique. As it will be discussed in Chapter 5, high laser energy densities enable triplet-triplet annihilations that cause a non-exponential phosphorescence decay and a stronger dependency on small pressure variations.

3.4.3 Local velocity measurements

i. Particle Image Velocimetry (PIV)

One of the most widely used techniques for local investigation of the velocity field in both liquid and gas flows is the PIV. In this low-intrusive velocimetry technique, pre-seeded particles are irradiated by short laser sheet pulses. The scattered light or the fluorescence emission reveals the particle positions to a synchronized CCD camera, which focal plane coincides with the laser sheet plane, as sketched in Figure 3.18. The cross-correlation of two consecutive images capturing the particle positions between two laser shots allows the extraction of the velocity vectors in each interrogation window.

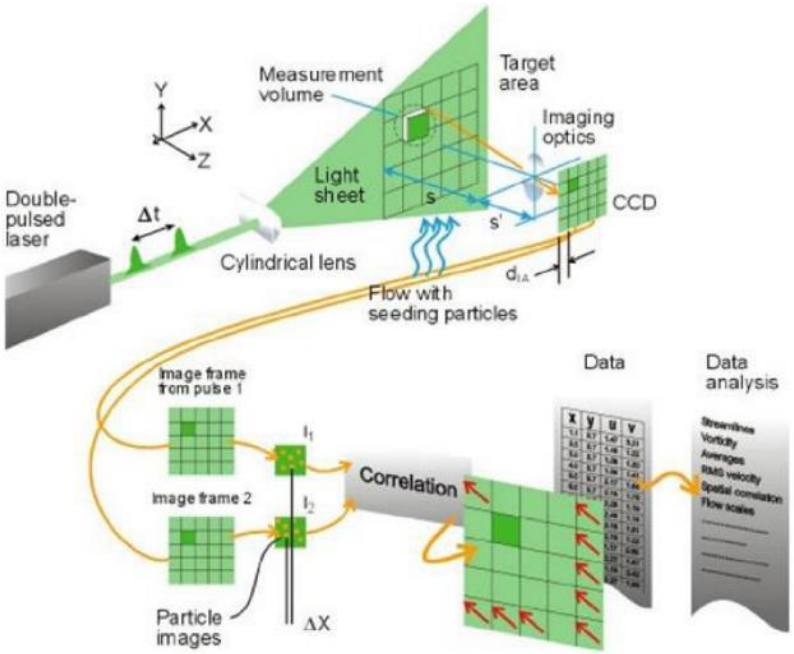

Figure 3.18. General scheme of PIV acquisition system. Figure from Jensen (2004).

More complex versions of PIV that use more than one camera allow flow visualization in a 3D domain (tomo-PIV) or of the three-dimensional velocity field on a 2D plane (stereo-PIV).

PIV can be applied in two different ways: the pattern matching velocimetry (PMV) and the particle tracking velocimetry. In the former case, the particle density in an interrogation window is high enough for the velocity vector to be inferred from the cross-correlation of two consecutive images. In the latter version, the velocity field is measured by tracking the displacement of single particles.

PIV application to microfluidic systems is known as µPIV. It has been demonstrated to be an accurate technique for measuring velocity fields in microfluidic devices, but only in the case of liquid flows (Santiago *et al*., 1998).

Tretheway & Meinhart (2002) and Joseph & Tabeling (2005) applied µPIV to investigate the slip length of apparent fluid slip on the hydrophobic walls of microchannels. Joseph & Tabeling measured velocity profiles of water flows in 30 × 300 μm^2 channels within 450 nm from the wall surface. Nd:YAG laser pulses of about 5ns at 532 nm were used for illuminating polystyrene spheres with 300-nm diameter, and were directed towards the tested microchannel by means of an inverted microscope. Fluorescence decay of the dye lasts a maximum of 10 ns, so that the motion of particles on an image was effectively frozen. A CCD camera allowed to capture two consecutive images separated by 150 µs. The out-of-plane measurement depth was very small, about 1.8 µm, so that the number of particles in one interrogation window was very low. In order to increase the signal-to-noise ratio, the authors cross-correlated about 50 pairs of images. In µPIV, very low particle image density is a common

problem due to the small depth of correlation (i.e., the depth over which particles significantly contribute to the correlation) characterizing microscope objectives (Olsen & Adrian, 2000).

µPIV has never been successfully applied to gas micro-flows or rarefied gas flows. The main problem is related to the tracer particle size. Besides the technological difficulties in generating particles with a diameter less than 1 µm in gas flows, the particle size should be (i) small enough to guarantee that the particles faithfully follow the fluid flow and (ii) big enough to reduce Brownian motion noise, which makes the cross-correlation operation inaccurate or impossible. The first requirement is translated in terms of time response of the accelerating particle, which characteristic time is (Lindken *et al*., 2009)

$$\tau_{p-PIV} = \frac{\rho_p}{\rho_f}\frac{d_p^2}{18\nu_f}, \tag{3.20}$$

where d_p is the particle diameter, ρ_p is the particle density, ρ_f the fluid density and ν_f its cinematic viscosity. The smallest time-scale of the fluid flow needs to be larger than the time response of the particle, which corresponds to a Stokes number, $St = \left(\rho_p d_p^2 U\right)/\left(\rho_f 18\nu_f L\right)$, as low as possible. It is evident that in rarefied gas flows, the reduced density ρ_f requires a decrease in the particle density and/or the particle diameter. For the second requirement, Santiago *et al*. (1998) provide the expression of the error ε of the Brownian motion $\langle s^2\rangle^{\frac{1}{2}}$ relative to the mean distance Δx travelled by a particle with velocity u_p and in a time interval Δt:

$$\varepsilon = \frac{\langle s^2\rangle^{\frac{1}{2}}}{\Delta x} = \frac{1}{u}\sqrt{\frac{2D}{\Delta t}}. \tag{3.21}$$

The Stokes-Einstein relation proves that the particle diffusion in the fluid is characterized by the diffusion coefficient $D = k_B T_f/\left(3\pi\rho_f \nu_f d_p\right)$, in which T_f is the temperature of the fluid and k_B the Boltzmann constant. In rarefied gas flows, particle diffusion is much faster with respect to the particle mean velocity, so that the error due to the Brownian motion is more relevant than in liquid flows.

The work of Yoon *et al*. (2006) is an emblematic demonstration of these limitations. They applied µPIV for measuring velocity fields of a gas flow in a U-shaped fuel cell with characteristic dimensions between 1 and 2 mm. They tested the technique with both smoked particle of 1 µm from a heated coil and water droplets with diameters between 1 to 8 µm. Figure 3.19a reports a µPIV visualization on a 180° switchback channel. The water seeding technique was considered by the authors as more appropriate than the smoked particles for in-situ measurements of operational combustion cells. By considering the range of possible water droplet diameters, the experimental results were corroborated by CFD simulations for analyzing the ability of the seeded particles to follow the gas flow trajectories. Figure 3.19b represents these results in a relatively high Reynolds number flow

for 3 different diameters of the water droplets. They concluded that particles smaller than 1 µm are required for accurately follow the gas flow.

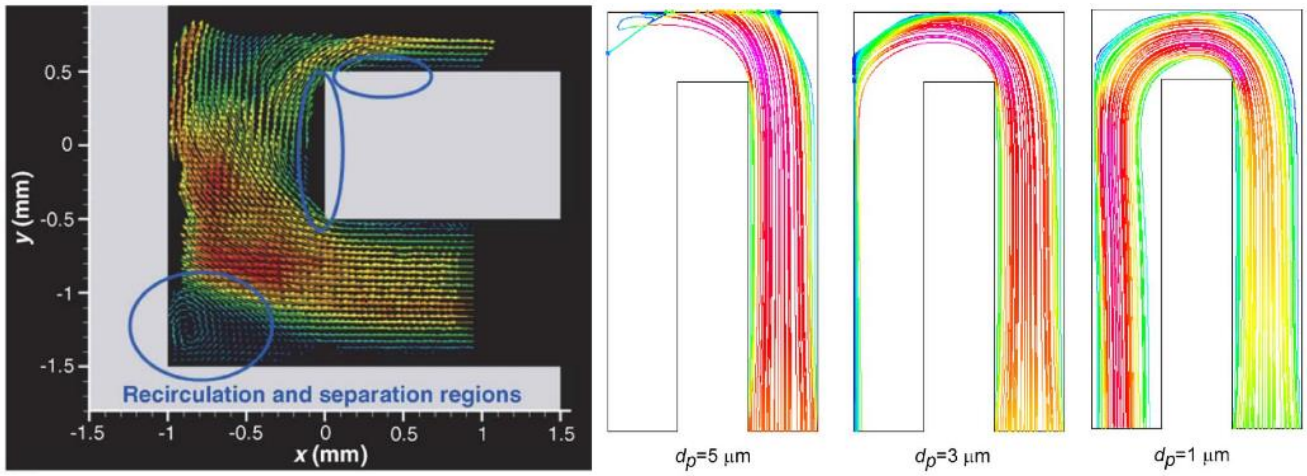

(a) (b)

Figure 3.19. (a) velocity distribution from µPIV measured with smoked particles in a gas flow. (b) CFD simulations at Re = 400, for different diameters d_p of the water droplets. From left to right: d_p = 5, 3, and 1 µm.

Figure from Yoon *et al.* (2006).

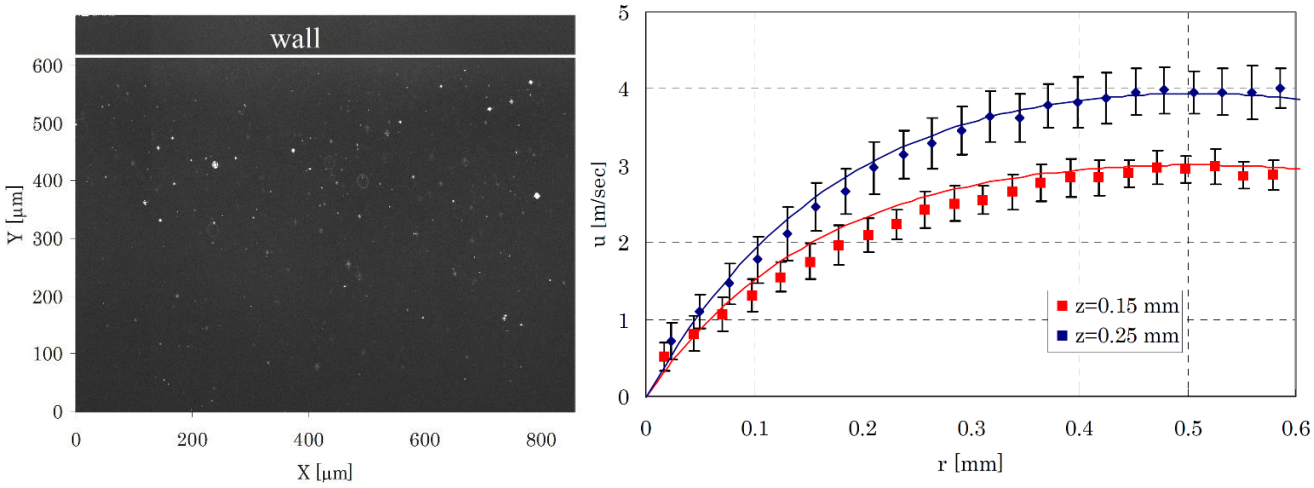

(a) (b)

Figure 3.20. (a) µPIV image of olive oil particles in air-water gas mixture flowing through a 0.5 × 5 mm^2 channel. (b) Axial velocity profile at Re = 130 for two focal planes at two positions in the depth direction.

Figure from Sugii & Okamoto (2006).

When the particle density is very low, PTV is preferred as analysis tool. Sugii & Okamoto (2006) showed its application for gas flows seeded with olive oil particles in a channel with 0.5 × 1 mm^2 cross section. By controlling inlet pressure and oil viscosity, they could generate oil droplets with a size of about 0.5 to 2 µm. Figure 3.20a

shows a typical image of fluorescent particles illuminated with a double-pulsed Nd:YAG laser. The microscope objectives allowed for a depth of correlation of about 18 μm. Out-of-focus particles appeared bigger than the estimated size. From one image, the authors could obtain only 10-20 velocity vectors due to the low number of particles present in the measurement window. For this reason, they integrated 155 images in order to produce the whole velocity distribution. Figure 3.20b reports the axial velocity profile measured by averaging along the flow direction. For a Reynolds number Re = 130, the maximum velocity registered was 3 and 4 m/s with a variance ranged between 0.17 and 0.25 and between 0.22 and 0.34 m/s, respectively for the two positions in the depth direction.

The application of μPIV to rarefied gas flows requires further improvements concerning the generation of micrometric particles in gases and the inaccuracies introduced by the noisy Brownian motion.

ii. Laser-Doppler anemometry (LDA)

The oldest laser-based velocimetry is the LDA. Differently from PIV and MTV which are "time-of-flight" technique, LDA can be categorized as a "Doppler-shift" method. As PIV, the velocimetry is carried out by seeding the flow with particles. Two monochromatic laser beams are crossed for creating an interference pattern. When particles cross the interference zone, the light is diffused at a different frequency with respect to that of the laser field. The particle velocity is then inferred from the frequency shift. All the problematics related to the choice of the particle size discussed for PIV holds also for LDA. Figure 3.21 schematizes the typical experimental setup of LDA.

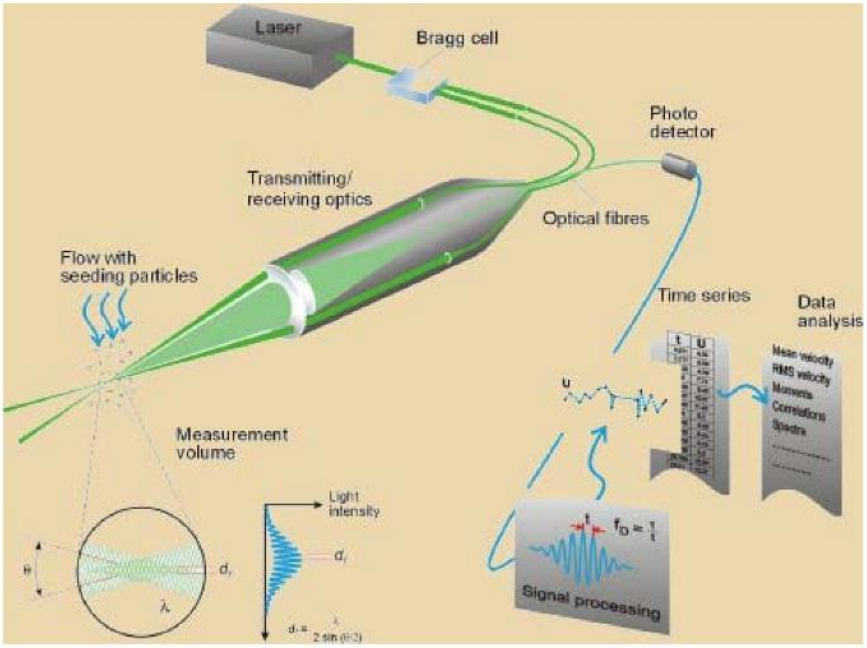

Figure 3.21. General scheme of LDA acquisition system. Figure from Jensen (2004).

The main difference with PIV and MTV is that LDA is not a field-measurement technique but a point-measurement technique. Moreover, the laser source is not pulsed but continuous, which reduces the complexity of the experimental setup with respect to PIV and MTV: no synchronization is required between the photodetector and the laser shots and less powerful, cheaper laser systems can be used. Yoon *et al*. (2006) refers to an application in gas flows in a U-shaped mini-fuel cell (Ladewig *et al*., 2004), but no complete velocity data were available for making any conclusion. Morini *et al*. (2011) concluded that LDA is not a possible candidate for velocity measurements in channels with size less than 1 mm.

iii. Molecular tagging velocimetry (MTV)

Molecular tagging velocimetry (MTV) can provide velocity fields in liquid and gas flows by tracking the luminescence emission of a molecular tracer. This flow visualization technique is often considered as the molecular counterpart of PIV. Because of the substantial difference in the nature of the tracer, MTV does not have the complications of the particle-based techniques. For this reason, it is, currently, the most promising technique for flow visualization in microdevices, even though other experimental challenges need to be faced.

In the simplest implementation of MTV, a pulsed laser source is required to tag a region of interest and a photodetector captures the light emitted by the tracer at two successive times. The tagged regions need to be interrogated on a time interval that is smaller than the lifetime of the tracer. The basic functioning principle of MTV is schematized in Figure 3.22 for the simplest scenario of 1D velocity field, e.g. fluid flow in a channel. At the reference time t_0, a pulsed laser beam tags the initial reference position of the tracer molecules. As the tracer moves by following the flow streamlines, the initial tagged line starts to deform accordingly to the velocity profile of the gas. The photodetector captures an image of the reference position at t_0 and an image of the deformed tagged line at a delay time $t_0 + \Delta t$. The velocity profile can be inferred from the mean molecular displacement $s_x(y)$ of the tagged line in the flow direction. For liquid and external 1D-gas flows, the velocity profile $u(y)$ can be successfully computed as

$$u(y) = \frac{s_x(y)}{\Delta t}. \tag{3.22}$$

Maynes & Webb (2002) demonstrated that 1D-MTV technique could be successfully applied to water flows in sub-millimetric tubes. A UV beam at 308 nm with a diameter focused down to 20 μm was employed for activating the phosphorescence emission of 1-BrNp·Gβ·CD·ROH supramolecules pre-seeded in the flow.

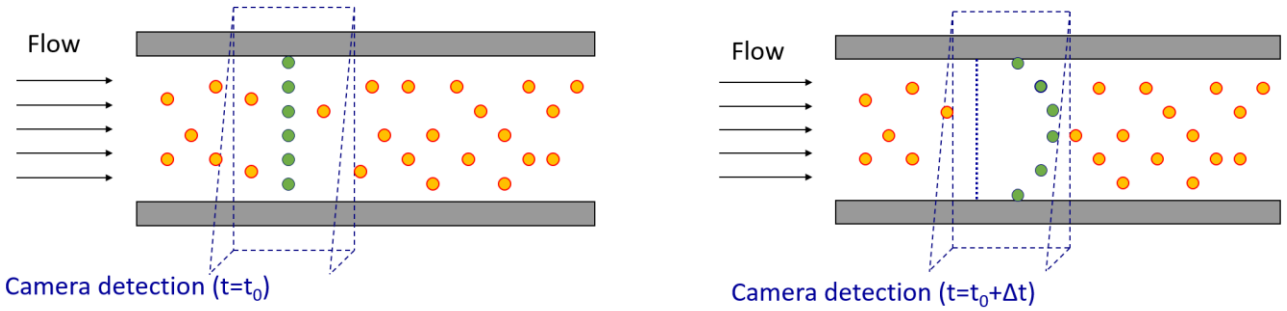

Figure 3.22. Basic principle of 1D-MTV by direct phosphorescence, for a gas flowing in a plane channel from left to right.

Previous works have demonstrated that in confined gas flows, such as in channel flows, the displacement profile cannot be simply calculated from Eq. (3.22). Samouda *et al*. (2015) applied MTV on pressure-driven argon flows seeded with acetone in a millimetric channel. By carrying out experiments at atmospheric pressure, they observed a displacement slip of the molecular tracer at the wall. The application of Eq. (3.22) would provide a velocity profile $u(y)$ with a non-zero velocity at the wall, something unexpected since the flow was not in rarefied conditions. Frezzotti *et al*. (2015) theoretically and numerically demonstrated that a combined mechanism of molecular diffusion of the tracer in the background gas together with the transversal velocity gradients at the wall generates a non-zero mean molecular displacement at the surface even if the average velocity of the flow at the wall is null. Frezzotti *et al*. (2015) provided a reconstruction method for correctly extracting the velocity profile from the displacement profile. Later, Si-Hadj Mohand *et al*. (2017) demonstrated the successful application of this method on MTV experimental data of argon flow in a 1 mm deep channel for non-rarefied gas conditions.

The flow visualization in 2D velocity field requires a more complex tagging system in order to have enough information for extracting the velocity vector. A laser excitation pattern can be employed for generating a grid of tagged lines. A possible strategy for measuring the velocity field is by tracking the displacement of the nodes of the tagging grid. Gendrich & Koochesfahani (1996) proposed a different approach based on a digital spatial correlation of the initial and the deformed tagging patterns. This methodology does not require any assumption on the intensity distribution of the emission, which can be affected by local quenching, laser energy fluctuations, non-uniformity of the tracer concentration, etc. Figure 3.23 shows an example of 2D-MTV application in gas flows. Stier & Koochesfahani (1999) applied the "grid-tagging" MTV with diacetyl tracer for visualizing the vorticity field in an intake gas flow. Because an oxygen-free environment is required for exploiting diacetyl phosphorescence, a high-pressure nitrogen flow was used.

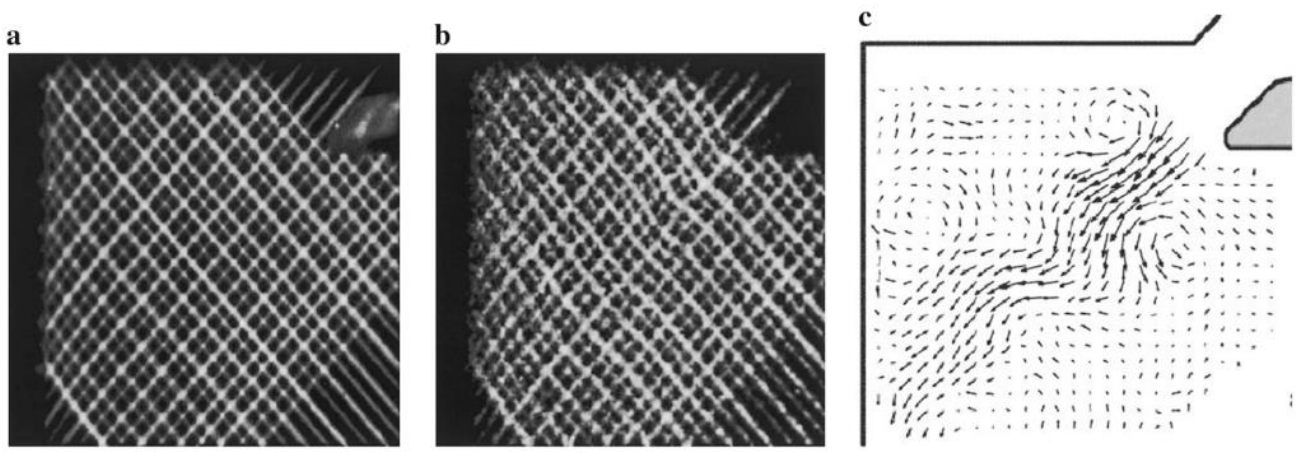

Figure 3.23. 2D-MTV applied to a nitrogen flow based on diacetyl phosphorescence: (a) Initial tagging pattern, (b) deformed tagging pattern after 50 μs, and (c) measured velocity vector field. Figure from Stier & Koochesfahani (1999).

MTV has also been applied for flow visualization in unsteady gas flows, e.g., for analyzing the vortex shedding of an oscillating airfoil (Figure 3.24). If the flow velocity is high in comparison to the rate of variation of the velocity itself, MTV technique could provide accurate unsteady velocity fields. Otherwise, if the velocity magnitude of the flow is not high enough for producing a relevant and measurable displacement in a time interval that is smaller than the characteristic time of the unsteadiness, MTV cannot be the right solution for this case.

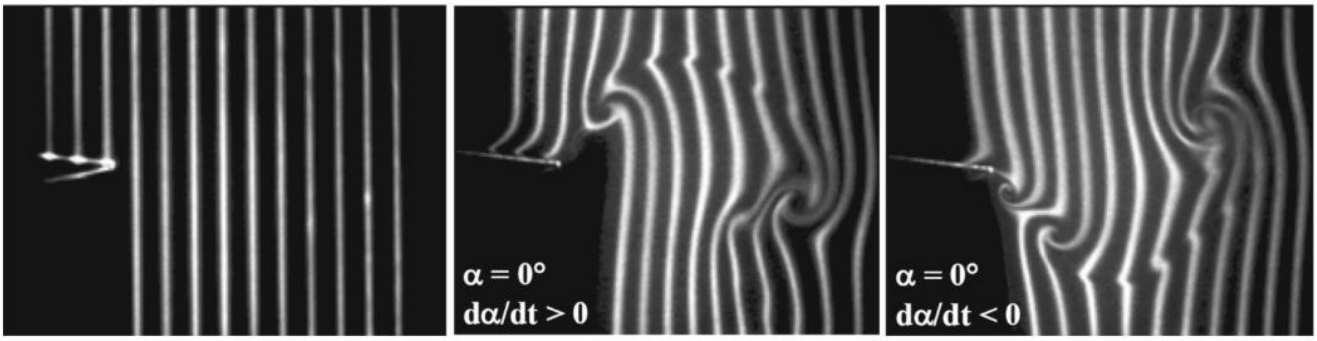

Figure 3.24. "Line-tagging" MTV for flow visualization in the wake of an oscillating airfoil.
Figure from (Koochesfahani *et al*., 2002).

In recent years, MTV with very high repetition rate, up to 1000 kHz, has been developed and widely applied to gas flows characterized by small length scale and high velocity magnitude, such as in supersonic/hypersonic, reacting and turbulent gas flows (Thurow *et al*., 2012). However, the frequency content of this type of gas flows can reach even 10^4-10^6 Hz, thus further development in pulsed laser technology is required for increasing the repetition rate. Laser sources with high repetition rates may also be fundamental for MTV applications to unsteady gas flows at low pressure, that is where the tracer emission is weak.

Different photoluminescent mechanisms can be employed for applying MTV. Based on the chemistry exploited for tracking the molecular tracer, the implementation of MTV can be very different: one or more laser sources may be necessary, and the molecular tracer might be premixed to the fluid flow or generated in-situ. Four different photoluminescent mechanisms are recognized in the literature:

(i) laser-induced photochemical anemometry (LIPA), or MTV by absorbance;

(ii) Raman excitation plus laser-induced electronic fluorescence (RELIEF), or MTV by vibrational excited-state fluorescence of oxygen;

(iii) photoactivated non-intrusive tracing of molecular motion (PHANTOMM), or MTV by photoproduct fluorescence;

(iv) MTV by direct phosphorescence.

(i) MTV by absorbance was originally introduced by Miller (1962) and then applied by Falco & Chu (1987), who introduced the acronym LIPA. In this technique, a laser excitation brings the tracer molecules (photochromes) to an electronically excited state. Afterwards, the excited molecules relax to lower energy levels through vibrational relaxation: part of the absorbed energy is released as heat and part of it is non-radiatively transferred into making or breaking chemical bonds of the molecule. This non-radiative energy transfer brings to the formation of a high-energy tautomer that has a different absorption spectrum with respect to the original tracer molecule. This newly formed chemical species is excited by white-light source and its position is revealed by analyzing the difference between the incident and transmitted light. This technique requires two laser sources, one for "writing", that is generating the tracer, and one for "reading", that is revealing the position of the tautomer molecules. In this scenario, the lifetime of the tracer is determined by the stability of the produced tautomer, which can persist even for several minutes. This is the only MTV technique that is based on the absorbance and not the emission of light from the tracer. Since the detection of emitted light is much easier and more accurate than the detection of transmitted light, the other versions of MTV are preferred from this point of view.

(ii) RELIEF is the most sophisticated implementation of MTV, as it is based on the stimulated Raman effect. The tracer for carrying out the velocity measurement needs to be oxygen. A first laser excitation brings the tagged oxygen molecules to a higher vibrational level. This long-lived state of the oxygen is then interrogated by a second laser excitation, which brings the molecule to an electronically excited state from which short-lived fluorescence is emitted. This technique has been developed by Miles *et al*. (1987) and successively applied for measuring velocity fields in air jet flows (Miles *et al*., 1989).

(iii) PHANTOMM is in principle similar to RELIEF and LIPA in the sense that the molecular tracer needs first to be somehow activated or produced with a first laser source, and, afterwards, interrogated. The "reading" excitation

electronically excites the activated tracer and the short-live luminescence is then captured for revealing the molecular displacement from the first laser excitation. It was originally developed by Lempert *et al*. (1995) for liquid flows by employing water-soluble caged dye fluorophores. While the version of Lampert *et al*. (1995) is specific for liquid flows, there are other variants of PHANTOMM that can be applied to gas flows and that are based on the same concept of (i) uncaging of the molecular tracer and (ii) excitation of its fluorescence emission, such as the hydroxyl tagging velocimetry (HTV), the ozone tagging velocimetry (OTV), the nitric oxide tagging velocimetry (NTV), or the photobleaching technique (Schembri *et al*., 2015). In all these techniques, the molecular tracer is "uncaged" by a photochemical dissociation of a specific molecular species inside the flow. In HTV (Pitz *et al*., 2000), OH radicals are generated by photon-dissociation at 193 nm of vibrationally excited water molecules. The OH radicals are then electronically excited at 248 nm and the consequent fluorescence emission is captured. In OTV (Pitz *et* al., 1996), ozone molecules are the long-lived tracer, which are uncaged from the dissociation of molecular oxygen at 193 nm through the following reaction chain:

$$\begin{aligned} O_2 + h\nu_{ex}(\lambda_{ex} = 193\text{nm}) &\rightarrow O + O, \\ O + O_2 &\rightarrow O_3. \end{aligned} \tag{3.23}$$

Again, a laser excitation at 248 nm reveals the displacement of the O_3 tagged region. Similarly, NTV relies on NO fluorescence. NO molecules are uncaged, for instance, by the molecular dissociation of NO_2 from a laser source at 308 nm (Orlemann *et al*., 1999).

(iv) The simplest implementation of MTV is MTV by direct phosphorescence, and it is the one adopted in this work. Differently from the other three versions of MTV, MTV by direct phosphorescence is the only technique that requires one single laser source. Therefore, its application is much simpler to put in place. The molecular tracer is previously added to the main flow and the laser source tags the molecules by exciting them to a higher electronic state. The light emission of the tagged molecules starts a few nanoseconds after the moment of excitation. A tracer with long phosphorescence lifetime is necessary to interrogate the molecular displacement after a delay time that is on the order of the characteristic time τ_{flow} of the fluid flow under consideration. By considering Eq. (3.11), a suitable long-living emission exists if the radiative decay rate k_r is smaller than $1/\tau_{flow}$ and, at the same time, the non-radiative decay rate k_{nr}, including quenching phenomena, is even smaller than k_r.

Diacetyl vapor has been used in oxygen-free gas flows by many authors (Stier & Koochesfahani, 1999). The first who proposed the use of diacetyl for flow visualization is Epstein (1974). Hiller *et al*. (1984) used diacetyl phosphorescence excited at about 430 nm in a nitrogen flow through a slit of 6 × 25 mm^2. Itoh *et al*. (1985) also applied the technique to nitrogen flows in a low-pressure chamber. The experiments were conducted for pressures in the range 50-250 Pa, and the authors reported a relevant molecular diffusion. Whereas the investigated pressures were very low, the flow visualizations were carried out quite far from the wall surface and for gas velocities limited to 6 m/s, so that no rarefied effects were observed.

In the introduction of this section, a distinction between LIF and LIP has been made as two possible implementations of the molecular tagging technique. By considering the very short characteristic time of fluorescence, on the order of tens of nanoseconds, this component of the light emission is hardly exploitable for velocimetry in gas flows. Actually, most of the gas flows of interest are characterized by characteristic fluid dynamic time much larger than tens of nanoseconds. Especially in microchannel flows, the flow rates are usually relatively small, and no molecular displacement of the molecular tracer can be identified before the fluorescence emission extinguishes. However, there are some applications of gas microflows that may deal with very high-speed flows and in rarefied conditions, such as in free jet flows typical of micro-propulsion systems, for which the strong intensity emission of acetone fluorescence has found a place in velocimetry measurements. Some authors employed acetone fluorescence for carrying out velocity measurements in supersonic flows. Lempert *et al*. (2002), for example, applied MTV based on acetone LIF for supersonic gas jet flows. The fluorescence emission was quite longer, on the order of 200-300 ns, than the usual characteristic fluorescence decay time on the order of tens of nanoseconds (Lozano *et al*., 1992). While the authors do not seem to have a clear idea of why such a "long"-living fluorescence was seen, it is believed that part of that emission was simply an early phosphorescence component of the emission. Beside the work of Lempert *et al*., the application of laser-induced acetone phosphorescence for MTV in gas flows have been quite limited in the past (Samouda *et al*., 2015, Si-Hadj Mohand *et al*., 2017).

3.5 Conclusions

In this chapter, a general review of the microsensors and the experimental techniques available for the analysis of gas microflows has been presented. Molecular tagging velocimetry by direct phosphorescence and the constant volume technique are the two experimental approaches employed in this work for analyzing gas flows in the slip flow regime. The possibility of employing both acetone and diacetyl vapors in MTV is explored and the constant volume technique provides a mass flow measurement that can be compared to the velocity field provided by MTV. In the next chapter, the experimental setups designed and built in this work are presented in detail.

References

Abeysinghe, D. C., Dasgupta, S., Boyd, J. T., & Jackson, H. E. (2001). A novel MEMS pressure sensor fabricated on an optical fiber. *IEEE Photonics Technology Letters*, *13*(9), 993-995.

Arkilic, E. B., Schmidt, M. A., & Breuer, K. S. (1997). Gaseous slip flow in long microchannels. *Journal of Microelectromechanical systems*, *6*(2), 167-178.

Bartelt, H., & Unzeitig, H. (1993). Design and investigation of micromechanical bridge structures for an optical pressure sensor with temperature compensation. *Sensors and Actuators A: Physical*, *37*, 167-170.

Basu, R., Naguib, A. M., & Koochesfahani, M. M. (2010). Feasibility study of whole-field pressure measurements in gas flows: molecular tagging manometry. *Experiments in Fluids*, *49*(1), 67-75.

Bergoglio, M., Mari, D., Chen, J., Mohand, H. S. H., Colin, S., & Barrot, C. (2015). Experimental and computational study of gas flow delivered by a rectangular microchannels leak. *Measurement*, *73*, 551-562.

Bianchi, R. A., Dos-Santos, F. V., Karam, J. M., Courtois, B., Pressecq, F., & Sifflet, S. (1998). CMOS-compatible smart temperature sensors. *Microelectronics Journal*, 627-636.

Celata, G. P., Cumo, M., McPhail, S. J., Tesfagabir, L., & Zummo, G. (2007). Experimental study on compressible flow in microtubes. *International Journal of Heat and Fluid Flow*, *28*(1), 28-36.

Chae, J., Stark, B. H., & Najafi, K. (2005). A micromachined Pirani gauge with dual heat sinks. *IEEE Transactions on Advanced Packaging*, *28*(4), 619-625.

Cho, S. T., Najafi, K., Lowman, C. E., & Wise, K. D. (1992). An ultrasensitive silicon pressure-based microflow sensor. *IEEE Transactions on Electron Devices*, *39*(4), 825-835.

Colin, S., Aubert, C., & Caen, R. (1998). Unsteady gaseous flows in rectangular microchannels: frequency response of one or two pneumatic lines connected in series. *European Journal of Mechanics series B Fluids*, *17*, 79-104.

Colin, S., Lalonde, P., & Caen, R. (2004). Validation of a second-order slip flow model in rectangular microchannels. *Heat transfer engineering*, *25*(3), 23-30.

Concheanainn, C. O., & Sidebottom, H. W. (1980). Temperature dependence of the triplet lifetime of biacetyl in the gas phase. *Journal of Photochemistry*, *13*(1), 55-66.

Degardin, O., Renou, B., & Boukhalfa, A. M. (2006). Simultaneous measurement of temperature and fuel mole fraction using acetone planar induced fluorescence and Rayleigh scattering in stratified flames. *Experiments in Fluids*, *40*(3), 452-463.

Eaton, W. P., & Smith, J. H. (1997). Micromachined pressure sensors: review and recent developments. *Smart Materials and Structures*, *6*(5), 530.

Enoksson, P., Stemme, G., & Stemme, E. (1995). Fluid density sensor based on resonance vibration. *Sensors and Actuators A: Physical*, *47*(1-3), 327-331.

Epstein, A. H. (1974). *Fluorescent gaseous tracers for three-dimensional flow visualization*. MIT Gas Turbine Laboratory.

Ewart, T., Perrier, P., Graur, I., & Méolans, J. G. (2006). Mass flow rate measurements in gas micro flows. *Experiments in fluids*, *41*(3), 487-498.

Falco, R. E., & Chu, C. C. (1988). Measurement of two-dimensional fluid dynamic quantities using a photochromic grid tracing technique. In *International Conference on Photomechanics and Speckle Metrology* (Vol. 814, pp. 706-710).

Frezzotti, A., Mohand, H. S. H., Barrot, C., & Colin, S. (2015). Role of diffusion on molecular tagging velocimetry technique for rarefied gas flow analysis. *Microfluidics and Nanofluidics*, *19*(6), 1335-1348.

Gass, V., Van der Schoot, B. H., & De Rooij, N. F. (1993, February). Nanofluid handling by micro-flow-sensor based on drag force measurements. In *Micro Electro Mechanical Systems, 1993, MEMS'93, Proceedings An Investigation of Micro Structures, Sensors, Actuators, Machines and Systems. IEEE.*(pp. 167-172). IEEE.

Gendrich, C. P., & Koochesfahani, M. M. (1996). A spatial correlation technique for estimating velocity fields using molecular tagging velocimetry (MTV). *Experiments in Fluids*, *22*(1), 67-77.

Gregory, J. W., Sullivan, J. P., Raman, G., & Raghu, S. (2007). Characterization of the microfluidic oscillator. *AIAA journal*, *45*(3), 568-576.

Gupta, N. K., An, S., & Gianchandani, Y. B. (2012). A Si-micromachined 48-stage Knudsen pump for on-chip vacuum. *Journal of Micromechanics and Microengineering*, *22*(10), 105026.

Harley, J. C., Huang, Y., Bau, H. H., & Zemel, J. N. (1995). Gas flow in micro-channels. *Journal of Fluid Mechanics*, *284*, 257-274.

Hiller, B., Booman, R. A., Hassa, C., & Hanson, R. K. (1984). Velocity visualization in gas flows using laser-induced phosphorescence of biacetyl. *Review of Scientific Instruments*, *55*(12), 1964-1967.

Hu, H., & Koochesfahani, M. M. (2003). A novel technique for quantitative temperature mapping in liquid by measuring the lifetime of laser induced phosphorescence. *Journal of visualization*, *6*(2), 143-153.

Huang, C. Y., & Sullivan, J. (2005). Psp measurement in microchannel flow. In *Instrumentation in Aerospace Simulation Facilities, 2005. iciasf'05. 21st International Congress on* (pp. 226-233). IEEE.

Huang, C. Y., Matsuda, Y., Gregory, J. W., Nagai, H., & Asai, K. (2015). The applications of pressure-sensitive paint in microfluidic systems. *Microfluidics and Nanofluidics*, *18*(5-6), 739-753.

Itoh, F., Kychakoff, G., & Hanson, R. K. (1985). Flow visualization in low pressure chambers using laser-induced biacetyl phosphorescence. *Journal of Vacuum Science & Technology B: Microelectronics Processing and Phenomena*, *3*(6), 1600-1603.

Jang, J., & Wereley, S. T. (2004). Pressure distributions of gaseous slip flow in straight and uniform rectangular microchannels. *Microfluidics and Nanofluidics*, *1*(1), 41-51.

Jensen, K. D. (2004). Flow measurements. *Journal of the Brazilian Society of Mechanical Sciences and Engineering*, *26*(4), 400-419.

Jiang, L., Wong, M., & Zohar, Y. (1999). Phase change in microchannel heat sinks with integrated temperature sensors. *Journal of microelectromechanical systems*, *8*(4), 358-365.

Joseph, P., & Tabeling, P. (2005). Direct measurement of the apparent slip length. *Physical Review E*, *71*(3), 035303.

Kilmer, N. G., & Spangler, J. D. (1971). Temperature Effects on the Phosphorescence of Benzene and Toluene. *The Journal of Chemical Physics*, *54*(2), 604-612.

Kohl, M. J., Abdel-Khalik, S. I., Jeter, S. M., & Sadowski, D. L. (2005). A microfluidic experimental platform with internal pressure measurements. *Sensors and Actuators A: Physical*, *118*(2), 212-221.

Koochesfahani, M. (2002). A novel method for instantaneous, quantitative measurement of molecular mixing in gaseous flows. *Experiments in fluids*, *33*(1), 202-209.

Koochesfahani, M. M., & Bohl, D. (2002). Molecular tagging visualization and velocimetry of the flow at the trailing edge of an oscillating airfoil. In *Proceedings of the 10th International Symposium on Flow Visualization*.

Kumar, S. S., & Pant, B. D. (2014). Design principles and considerations for the 'ideal' silicon piezoresistive pressure sensor: a focused review. *Microsystem technologies*, *20*(7), 1213-1247.

Ladewig, B., Blewitt, R., Shrimpton, J., & Kucernak, A. (2004). unpublished.

Lalonde, P. (2001). *Etude expérimentale d'écoulements gazeux dans les microsystèmes à fluides* (Doctoral dissertation, Toulouse, INSA).

Lempert, W. R., Ronney, P., Magee, K., Gee, K. R., & Haugland, R. P. (1995). Flow tagging velocimetry in incompressible flow using photo-activated nonintrusive tracking of molecular motion (PHANTOMM). *Experiments in Fluids*, *18*(4), 249-257.

Lempert, W. R., Jiang, N., Sethuram, S., & Samimy, M. (2002). Molecular tagging velocimetry measurements in supersonic microjets. *AIAA journal*, *40*(6), 1065-1070.

Li, X., Liu, Q., Pang, S., Xu, K., Tang, H., & Sun, C. (2012). High-temperature piezoresistive pressure sensor based on implantation of oxygen into silicon wafer. *Sensors and Actuators A: Physical*, *179*, 277-282.

Lin, C., Huang, Y. Q., Lei, W., & Ye, X. J. (2012). A Novel Fabry-Perot Cavity Fiber Sensor. *Physics Procedia*, *33*, 1939-1946.

Lindken, R., Rossi, M., Große, S., & Westerweel, J. (2009). Micro-particle image velocimetry (μPIV): recent developments, applications, and guidelines. *Lab on a Chip*, *9*(17), 2551-2567.

Liu, T. (2010). Pressure-and Temperature-Sensitive Paints. *Encyclopedia of Aerospace Engineering*.

Liu, Q., Sleiti, A. K., & Kapat, J. S. (2005, January). Application of pressure and temperature sensitive paints for study of heat transfer to a circular impinging air jet. In *ASME 2005 International Mechanical Engineering Congress and Exposition* (pp. 437-446). American Society of Mechanical Engineers.

Liu, T., Campbell, B. T., Burns, S. P., & Sullivan, J. P. (1997). Temperature-and pressure-sensitive luminescent paints in aerodynamics. *Applied Mechanics Reviews*, *50*(4), 227-246.

Lozano, A., Yip, B., & Hanson, R. K. (1992). Acetone: a tracer for concentration measurements in gaseous flows by planar laser-induced fluorescence. *Experiments in fluids*, *13*(6), 369-376.

Lucht, R. P., Roy, S., Meyer, T. R., & Gord, J. R. (2006). Femtosecond coherent anti-Stokes Raman scattering measurement of gas temperatures from frequency-spread dephasing of the Raman coherence. *Applied Physics Letters*, *89*(25), 251112.

Maurer, J., Tabeling, P., Joseph, P., & Willaime, H. (2003). Second-order slip laws in microchannels for helium and nitrogen. *Physics of Fluids*, *15*(9), 2613-2621.

Matsuda, Y., Mori, H., Niimi, T., Uenishi, H., & Hirako, M. (2007). Development of pressure sensitive molecular film applicable to pressure measurement for high Knudsen number flows. *Experiments in fluids*, *42*(4), 543-550.

Matsuda, Y., Uchida, T., Suzuki, S., Misaki, R., Yamaguchi, H., & Niimi, T. (2011). Pressure-sensitive molecular film for investigation of micro gas flows. *Microfluidics and Nanofluidics*, *10*(1), 165-171.

Maynes, D., & Webb, A. R. (2002). Velocity profile characterization in sub-millimeter diameter tubes using molecular tagging velocimetry. *Experiments in Fluids*, *32*(1), 3-15.

Miles, R., Cohen, C., Connors, J., Howard, P., Huang, S., Markovitz, E., & Russell, G. (1987). Velocity measurements by vibrational tagging and fluorescent probing of oxygen. *Optics Letters*, *12*(11), 861-863.

Miles, R. B., Connors, J., Markovitz, E., Howard, P., & Roth, G. (1989). Instantaneous supersonic velocity profiles in an underexpanded sonic air jet by oxygen flow tagging. *Physics of Fluids A: Fluid Dynamics*, *1*(2), 389-393.

Miller, S. (1962). Photochemical reaction for the study of velocity patterns and profiles. *BASc thesis, University of Toronto, Toronto*.

Mohand, H. S. H., Frezzotti, A., Brandner, J. J., Barrot, C., & Colin, S. (2017). Molecular tagging velocimetry by direct phosphorescence in gas microflows: correction of Taylor dispersion. *Experimental Thermal and Fluid Science*, *83*, 177-190.

Morini, G. L., Yang, Y., Chalabi, H., & Lorenzini, M. (2011). A critical review of the measurement techniques for the analysis of gas microflows through microchannels. *Experimental Thermal and Fluid Science*, *35*(6), 849-865.

Nguyen, N. T. (1997). Micromachined flow sensors—a review. *Flow measurement and Instrumentation*, *8*(1), 7-16.

Niimi, T., Yoshida, M., Kondo, M., Oshima, Y., Mori, H., Egami, Y., Asai, K., & Nishide, H. (2005). Application of pressure-sensitive paints to low-pressure range. *Journal of thermophysics and heat transfer*, *19*(1), 9-16.

Olsen, M. G., & Adrian, R. J. (2000). Out-of-focus effects on particle image visibility and correlation in microscopic particle image velocimetry. *Experiments in fluids*, *29*(1), S166-S174.

Orlemann, C., Schulz, C., & Wolfrum, J. (1999). NO-flow tagging by photodissociation of NO2. A new approach for measuring small-scale flow structures. *Chemical physics letters*, *307*(1-2), 15-20.

Park, H., Pak, J. J., Son, S. Y., Lim, G., & Song, I. (2003). Fabrication of a microchannel integrated with inner sensors and the analysis of its laminar flow characteristics. *Sensors and Actuators A: Physical*, *103*(3), 317-329.

Petersen, K., Pourahmadi, F., Brown, J., Parsons, P., Skinner, M., & Tudor, J. (1991, June). Resonant beam pressure sensor fabricated with silicon fusion bonding. In *Solid-State Sensors and Actuators, 1991. Digest of Technical Papers, Transducer'91., 1991 International Conference on* (pp. 664-667). IEEE.

Pitakarnnop, J., Varoutis, S., Valougeorgis, D., Geoffroy, S., Baldas, L., & Colin, S. (2010). A novel experimental setup for gas microflows. *Microfluidics and Nanofluidics*, *8*(1), 57-72.

Pitz, R. W., Brown, T. M., Nandula, S. P., Skaggs, P. A., DeBarber, P. A., Brown, M. S., & Segall, J. (1996). Unseeded velocity measurement by ozone tagging velocimetry. *Optics letters*, *21*(10), 755-757.

Pitz, R. W., Wehrmeyer, J. A., Ribarov, L. A., Oguss, D. A., Batliwala, F., DeBarber, P. A., ... & Dimotakis, P. E. (2000). Unseeded molecular flow tagging in cold and hot flows using ozone and hydroxyl tagging velocimetry. *Measurement Science and technology*, *11*(9), 1259.

Ponce, A., Wong, P. A., Way, J. J., & Nocera, D. G. (1993). Intense phosphorescence triggered by alcohols upon formation of a cyclodextrin ternary complex. *The Journal of Physical Chemistry*, *97*(42), 11137-11142.

Pong, K. C., Ho, C. M., Liu, J., & Tai, Y. C. (1994). Non-linear pressure distribution in uniform microchannels. *ASME-Publications-Fed*, *197*, 51-51.

Rojas-Cárdenas, M. (2012). Temperature Gradient Induced Rarefied Gas Flow. *Ecole Polytechnique Universitaire de Marseille*.

Rojas-Cárdenas, M., Silva, E., Ho, M. T., Deschamps, C. J., & Graur, I. (2017). Time-dependent methodology for non-stationary mass flow rate measurements in a long micro-tube. *Microfluidics and Nanofluidics*, *21*(5), 86.

Samouda, F., Colin, S., Barrot, C., Baldas, L., & Brandner, J. J. (2015). Micro molecular tagging velocimetry for analysis of gas flows in mini and micro systems. *Microsystem Technologies*, *21*(3), 527-537.

Santiago, J. G., Wereley, S. T., Meinhart, C. D., Beebe, D. J., & Adrian, R. J. (1998). A particle image velocimetry system for microfluidics. *Experiments in fluids*, *25*(4), 316-319.

Schembri, F., Bodiguel, H., & Colin, A. (2015). Velocimetry in microchannels using photobleached molecular tracers: a tool to discriminate solvent velocity in flows of suspensions. *Soft matter*, *11*(1), 169-178.

Schöler, L., Lange, B., Seibel, K., Schäfer, H., Walder, M., Friedrich, N., ... & Böhm, M. (2005). Monolithically integrated micro flow sensor for lab-on-chip applications. *Microelectronic Engineering*, *78*, 164-170.

Shie, J. S., Chou, B. C., & Chen, Y. M. (1995). High performance Pirani vacuum gauge. *Journal of Vacuum Science & Technology A: Vacuum, Surfaces, and Films*, *13*(6), 2972-2979.

Shih, J. C. (1996). Monatomic and polyatomic gas flow through uniform microchannels. *ASME MEMS DSC*, *59*, 197-203.

Si-Hadj Mohand, H., Frezzotti, A., Brandner, J. J., Barrot, C., & Colin, S. (2017). Molecular tagging velocimetry by direct phosphorescence in gas microflows: correction of Taylor dispersion. *Experimental Thermal and Fluid Science*, *83*, 177-190.

Silva, E., Deschamps, C. J., Rojas-Cárdenas, M., Barrot-Lattes, C., Baldas, L., & Colin, S. (2018). A time-dependent method for the measurement of mass flow rate of gases in microchannels. International Journal of Heat and Mass Transfer, 120, 422-434.

Stemme, G. (1991). Resonant silicon sensors. *Journal of Micromechanics and Microengineering*, *1*(2), 113.

Stier, B., & Koochesfahani, M. M. (1999). Molecular tagging velocimetry (MTV) measurements in gas phase flows. *Experiments in Fluids*, *26*(4), 297-304.

Sugii, Y., & Okamoto, K. (2006, January). Velocity measurement of gas flow using micro PIV technique in polymer electrolyte fuel cell. In *ASME 4th International Conference on Nanochannels, Microchannels, and Minichannels* (pp. 533-538). American Society of Mechanical Engineers.

Thomson, S. L., & Maynes, D. (2001). Spatially resolved temperature measurements in a liquid using laser induced phosphorescence. *Journal of fluids engineering*, *123*(2), 293-302.

Thurber, M. C., & Hanson, R. K. (1999). Pressure and composition dependences of acetone laser-induced fluorescence with excitation at 248, 266, and 308 nm. *Applied Physics B*, *69*(3), 229-240.

Thurber, M. C., & Hanson, R. K. (2001). Simultaneous imaging of temperature and mole fraction using acetone planar laser-induced fluorescence. *Experiments in Fluids*, *30*(1), 93-101.

Thurow, B., Jiang, N., & Lempert, W. (2012). Review of ultra-high repetition rate laser diagnostics for fluid dynamic measurements. *Measurement Science and Technology*, *24*(1), 012002.

Tretheway, D. C., & Meinhart, C. D. (2002). Apparent fluid slip at hydrophobic microchannel walls. *Physics of fluids*, *14*(3), L9-L12.

Van Putten, A. F. P., & Middelhoek, S. (1974). Integrated silicon anemometer. *Electronics Letters*, *10*(21), 425-426.

Yang, C., & Søeberg, H. (1992). Monolithic flow sensor for measuring millilitre per minute liquid flow. *Sensors and Actuators A: Physical*, *33*(3), 143-153.

Yoon, S. Y., Ross, J. W., Mench, M. M., & Sharp, K. V. (2006). Gas-phase particle image velocimetry (PIV) for application to the design of fuel cell reactant flow channels. *Journal of Power Sources*, *160*(2), 1017-1025.

Weiping, Y., Chong, L., Jianhua, L., Lingzhi, M., & Defang, N. (2005). Thermal distribution microfluidic sensor based on silicon. *Sensors and Actuators B: Chemical*, *108*(1-2), 943-946.

Zhang, X., Choi, H., Datta, A., & Li, X. (2006). Design, fabrication and characterization of metal embedded thin film thermocouples with various film thicknesses and junction sizes. *Journal of Micromechanics and Microengineering*, *16*(5), 900.

Zhu, J., Wang, M., Chen, L., Ni, X., & Ni, H. (2017). An optical fiber Fabry–Perot pressure sensor using corrugated diaphragm and angle polished fiber. *Optical Fiber Technology*, *34*, 42-46.

Chapter 4

Experimental setup

In this chapter, the experimental setups used in this work are presented. The overall experimental apparatus can be subdivided in three parts:

1) the laser system
2) the acquisition system
3) the gas circuit

The first two elements of the setup constitute the tagging system of MTV by direct phosphorescence and are described, respectively, in Sections 4.2 and 4.3. The third element is required to generate the experimental conditions of interest in a compatible way with the MTV features. In the following sections, each component of the experimental setup is described providing all the technical characteristics for defining the accuracy and the precision of the instrumentation. This information is necessary for a possible uncertainty analysis.

In this work, two experimental apparatus have been used. The first one is dedicated to the analysis of the photoluminescence properties of acetone and diacetyl vapors at low pressures and in gas mixtures of helium and argon. The second one has been designed for the application of MTV by direct phosphorescence to gas flows in the slip regime. While the tagging system is the same in the two cases, the gas system is specific for each experimental analysis, as described in Section 4.4.

Before describing all the components of the experimental apparatus, it is important to discuss some general properties of acetone and diacetyl vapors, such as the spectrum of absorption and the spectrum of emission of these two substances.

4.1 Absorption and emission spectra of tracers

The excitation wavelength of the laser source and the quantum efficiency of the photodetector need to be compatible, respectively, with the absorption spectrum and the emission spectrum of the employed tracer. Neither the absorption nor the emission spectrum have been measured in this work because of the lack of the necessary instrumentation: a long gas cell is necessary for carrying out absorption measurements to have a measurable difference between the incident irradiating energy and the transmitted energy, and a spectrometer is required for the analysis of the frequency content of the tracer emissions. Given the impossibility of directly measuring them, some data from the literature are here reported.

Thurber *et al*. (1998) measured the absorption spectrum $\sigma_{abs}(\lambda_{ex})$ of acetone vapor for different temperatures. The data are shown in Figure 4.1a. The authors did not find any substantial dependency on the vapor pressure. Acetone absorbs approximatively in the range 225-340 nm with a maximum absorption cross-section[1] of $4.7 \cdot 10^{-20}$ cm^2 at about 275 nm. To the best of our knowledge, data on phosphorescence emission spectra of acetone vapor are absent in the literature. This lack is mainly due to the fact that the main interest in acetone photoluminescence is related to its use in LIF diagnostic techniques. As discussed in the previous chapter, applications of acetone LIP in gas flow diagnostic are only a few. The only phosphorescence spectra found in the literature is given by Tran *et al*. (2005) but it is related to liquid acetone. Figure 4.1b shows both fluorescence and phosphorescence spectra for excitation wavelengths at 266 nm and 285 nm. Fluorescence spectra of acetone vapor for laser excitations at 266 nm and 308 nm are also provided by Bryant *et al*. (2000) and Lozano *et al*., (1992), respectively. These data are quite similar to those shown in Figure 4.1b. Fluorescence emission is in the range 350-550 nm, while phosphorescence has a wider spectrum, from 350 to 600 nm.

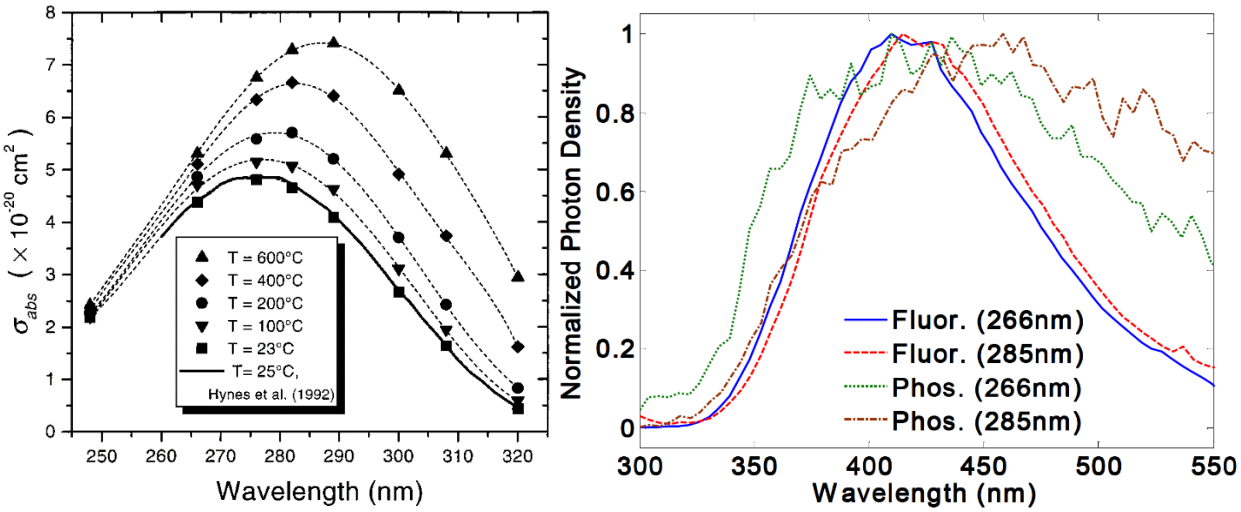

Figure 4.1. (a) Absorption spectrum of acetone at different temperatures (Thurber *et al*., 1998) and (b) emission spectrum of fluorescence and phosphorescence of liquid acetone (Tran *et al*., 2005).

Figure 4.2a and 4.2b show, respectively, the absorption spectrum and the phosphorescence emission spectrum of diacetyl vapor measured by Stier & Koochesfahani (1999) at ambient temperature. The maximum absorption cross-section is almost double of that of acetone, i.e., $8 \cdot 10^{-20}$ cm^2, corresponding to an excitation wavelength of about 417 nm (Lozano *et al*., 1992). The various curves in Figure 4.2b represent the phosphorescence spectra at different excitation wavelengths. The authors did not report the vapor pressure employed for measuring the phosphorescence spectra. Similar results on phosphorescence spectrum of diacetyl vapor can be found in Hiller *et al*. (1984). The spectral content of phosphorescence emission is in the range 500-700 nm, regardless of the

[1] the absorption cross-section is a measure of the probability of absorbing the incident light.

excitation wavelength employed. No data has been found related to the fluorescence spectra of diacetyl vapor. Parmenter & Poland (1969) reported that the fluorescence emission peak happens at 460 nm, and the phosphorescence emission peak at 510 nm, close to the value shown in Figure 4.2b.

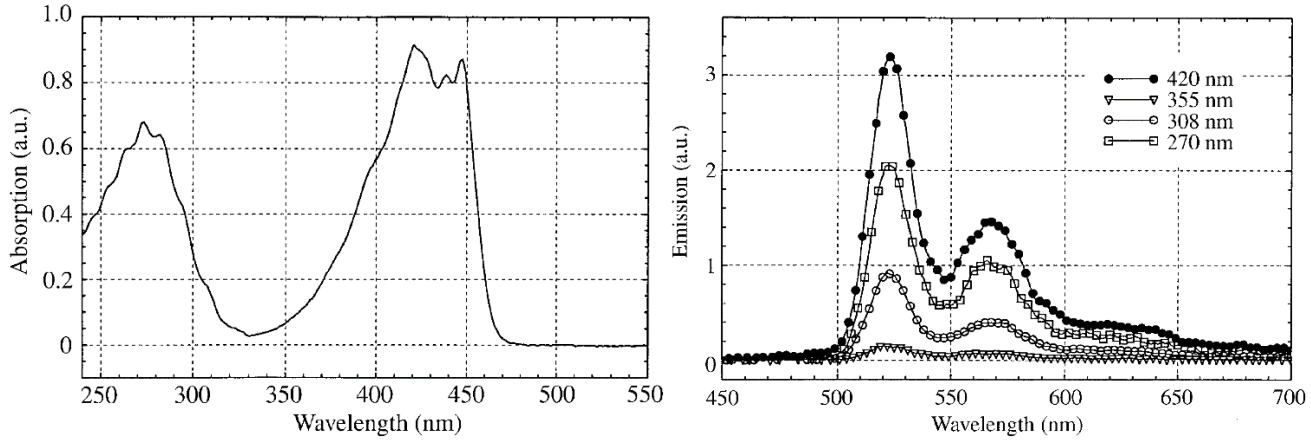

(a) (b)

Figure 4.2. (a) Absorption spectrum and (b) phosphorescence spectra for diacetyl vapor from Stier & Koochesfahani (1999).

Both for acetone and diacetyl vapors, the phosphorescence spectrum may actually be dependent on the vapor pressure and on the temperature. Higher pressures and temperatures increase the rate of collisions between molecules. In this situation, the absorbed laser energy is dissipated more efficiently, and the re-emitted energy is, therefore, less energetic, that is red-shift (Pringsheim, 1949). However, as it will be further discussed in Chapter 5, for the working pressure employed in this work and in the works related to data of Figure 4.1 and Figure 4.2, the vibrational relaxation is always faster than other radiative and non-radiative processes, thus the pressure dependency is lost. As an example, Parmenter & Poland (1969) experimentally demonstrated how the phosphorescence emission spectrum of diacetyl vapor excited at 435.8 nm does not vary from 15 to 2226 Pa. For the same reason, we believe that the phosphorescence spectrum of acetone vapor is not so different from the phosphorescence spectrum of liquid acetone of Figure 4.1b.

4.2 Laser system

The elements composing the laser system are:

1) the Nd:YAG Quantel twins laser;
2) the Opolette HE355 laser;
3) the laser beam optics;
4) the power meter.

In the course of this experimental study, two experimental campaigns have been conducted for the analysis of the tracer photoluminescence. In the first one, the Nd:YAG Quantel twins laser has been employed for studying the acetone phosphorescence excited at 266 nm. In the second experimental campaign, the Opolette HE355 laser has been used for studying the phosphorescence of acetone and diacetyl for different excitation wavelengths. In both laser systems, the laser (which stands for Light Amplification by Stimulated Emission of Radiation) technology is based on the stimulated emission of Nd:YAG crystals and the generation of laser pulses is made possible by the Q-switch technology. The basic structure of a laser cavity is shown in Figure 4.3. When the lamp pumps energy in the Nd:YAG gain medium, the light starts to bounce inside the resonator thanks to a mirror system and amplifies as it passes through the Nd:YAG crystals. At the moment of activation of the Q-switching, which is an opto-acoustic modulator, the energy is released from the cavity and the laser pulse is generated.

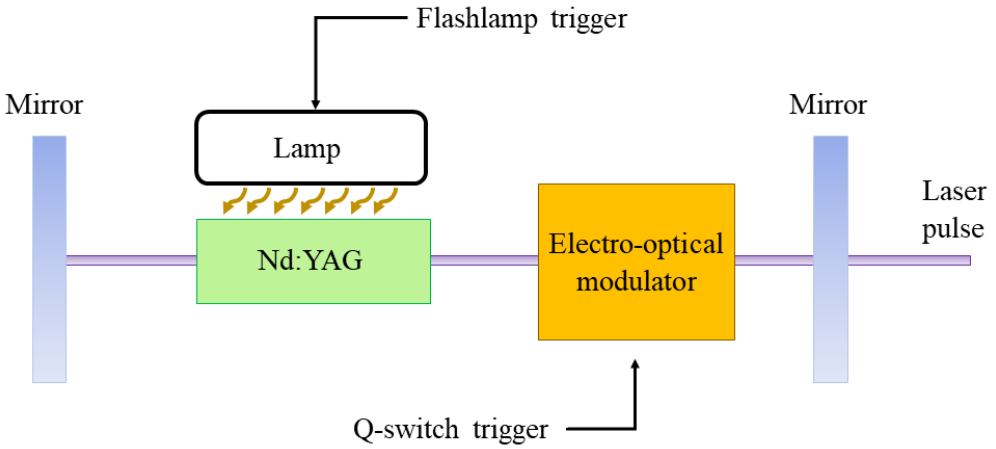

Figure 4.3. Typical laser resonator with Q-switching.

The pumping lamp and the activation of the Q-switching are electronically controlled, respectively, by the Flashlamp trigger signal and the Q-switch trigger signal. Because of the resonator losses, the energy in the cavity tends to decrease in time. If the Q-switch is activated later, the laser pulse energy is lower. For this reason, the delay between the Flashlamp trigger and the Q-switch trigger can be used to control the laser pulse energy. Higher delays would provide less energy.

Because the laser shots need to be synchronized with the acquisition system, the Flashlamp and the Q-switch trigger signals are externally generated. The duration and the delay of these signals need to be carefully controlled to avoid damaging the laser cavity. The delay between them can reach a minimum of 150 µs and a maximum of 300 µs. The Flashlamp and the Q-switch signals have been, therefore, analyzed at the oscilloscope. A diode has also been used for detecting the arrival of the laser pulse in the domain of investigation. A delay between the activation of the Q-switch and the laser pulse arrival has been noticed. Depending on the energy delivered, this delay varies from about 90 to 60 ns, respectively, for a Q-switch delay of 300 µs and 150 µs (Figure 4.4).

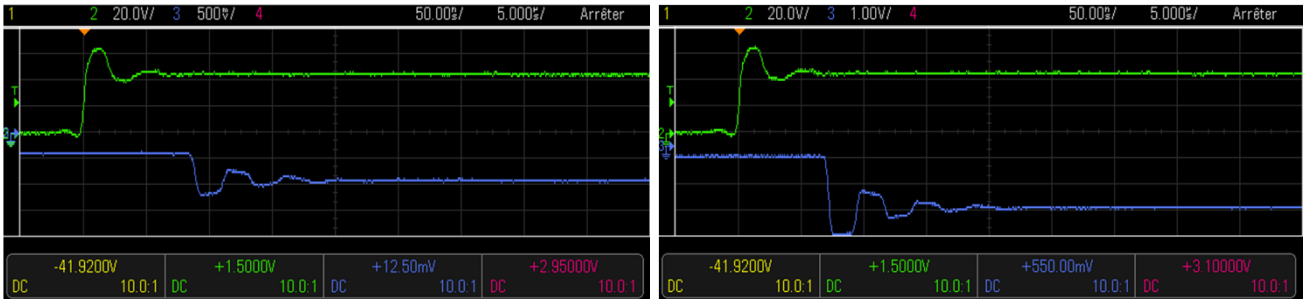

(a) (b)

Figure 4.4. Q-switch (green) and diode (blue) signals on the oscilloscope. The diode signal represents the arrival of the laser pulse at the domain of investigation. (a) Q-switch delay of 300 µs; (b) Q-switch delay of 150 µs.

4.2.1 Nd:YAG Quantel Twins laser

The Q-switched Nd:YAG Quantel Twins (Brilliant®) solid state laser is a IV class laser. It is combined with two sequential second-harmonic generator (SHG) for quadrupling the laser beam frequency. The Nd:YAG crystals provides a laser beam at 1064 nm and the frequency-quadrupling modules allows to produce laser beams at 266 nm. Figure 4.5 shows the overall apparatus. A mechanical attenuator is also present at the exit of the second SHG for reducing the laser pulse energy delivered. Reducing the laser energy by increasing the Q-switch delay with respect to the Flashlamp has as drawback of decreasing the stability of the energy delivered. The mechanical attenuator helps in producing laser beams with low and stable energy.

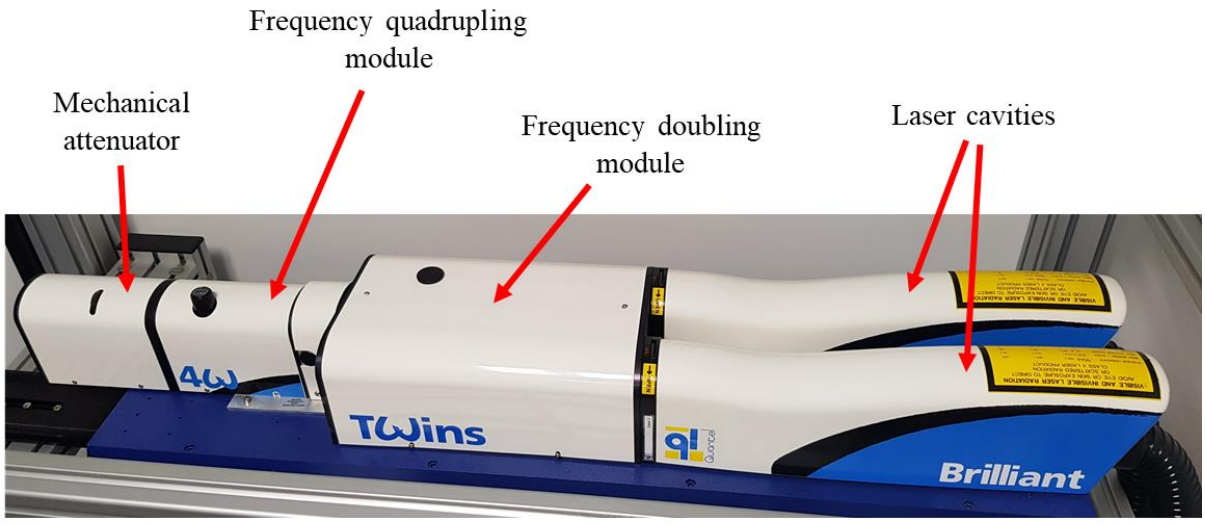

Figure 4.5. Nd:YAG Quantel Twins (Brilliant®).

The most important characteristics of the laser pulses are summarized in Table 4.1.

Wavelength	266 nm
Pulse duration	9 ns
Repetition rate	10 Hz
Beam diameter at the exit	7 mm
Highest energy per pulse	30 mJ
M^2	4
Beam divergence	< 0.7 mrad

Table 4.1. Specifications of the Nd:YAG Quantel Twins laser.

In order to carry the laser beam from the exit of the laser system to the domain of investigation, the laser arm of Figure 4.6 is used. The double-coated mirrors mounted in the arm allow to transmit laser beam with wavelengths of 266, 355, and 532 nm. Its use is not compatible with other wavelengths.

Figure 4.6. Laser arm used with the Nd:YAG Quantel Twins laser.

4.2.2 OPOlette laser

The OPOlette HE355 LD (Figure 4.7) is a tunable laser system that can provide laser pulses with wavelengths in the range 210-355 nm and 410-710 nm. In order to generate these ranges of frequency, nonlinear crystals are pumped at 355 nm with an Nd:YAG laser coupled with a third-harmonic generator (THG).

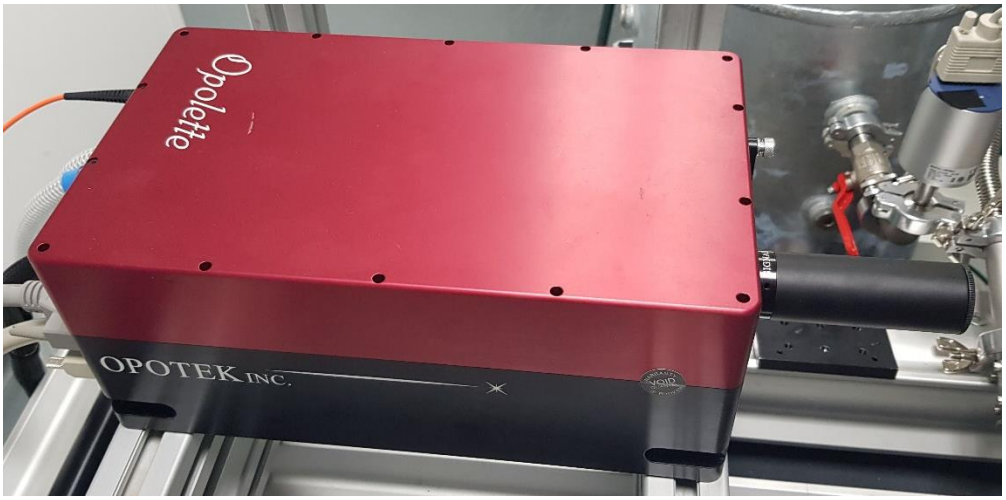

Figure 4.7. OPOlette HE355 LD from Opotek Inc.

In comparison to the frequency-quadrupled Nd:YAG laser, the OPOlette is a much more compact system that does not require any laser arm and the repetition rate can be set to 10 or 20 Hz. Table 4.2 summarizes the main specifications of the system. The beam quality factor, M^2, is provided by the manufacturer only for laser beam at 500 nm. The highest laser pulse energy depends on the laser wavelength and is, in general, much lower than the energy density provided by the Nd:YAG laser. Figure 4.8 reports the laser energy as a function of the laser wavelength for Q-switch delay of 174 µs. A mechanical attenuator is available only for the range 410-2200 nm. Because of the low energy values of the laser pulses delivered by the OPOlette in the range 210-355 nm, the energy stability is lower than in other operational ranges. In Section 4.2.4, the statistical fluctuations of the laser energy are better characterized.

Wavelength	210-355 / 410-2200 nm
Pulse duration	7 ns
Repetition rate	10 or 20 Hz
Beam diameter at the exit	4 mm
Highest energy @ 450 nm	8 mJ
M^2 @ 500 nm	3.94
Beam divergence	< 0.5 mrad

Table 4.2. Specifications of the OPOlette HE355 laser.

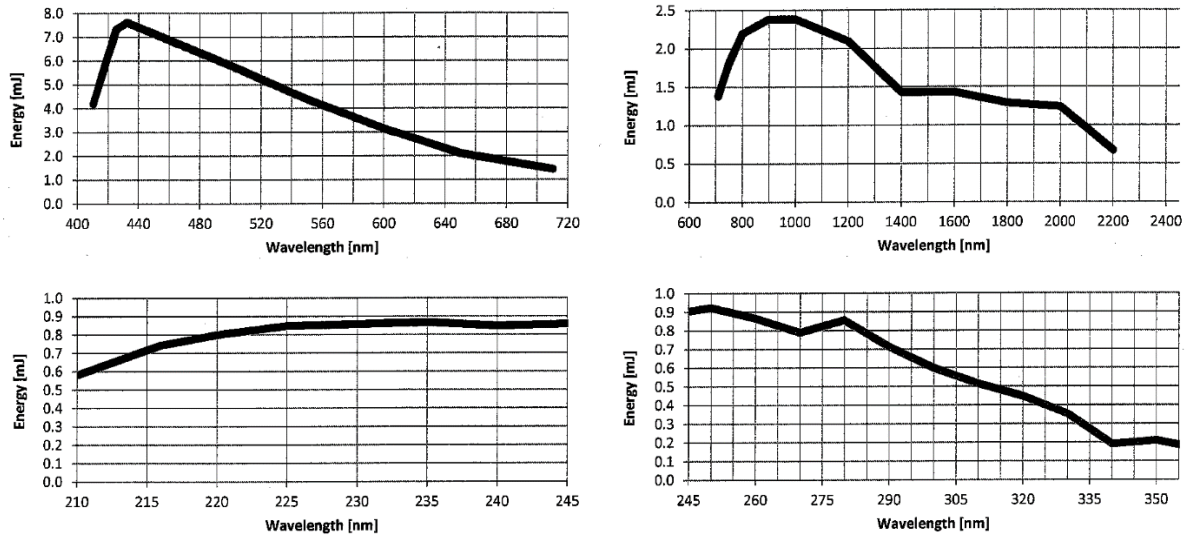

Figure 4.8. Energy delivered by the OPOlette HE355 as a function of the laser wavelength for a Q-switch delay of 174 µs.

4.2.3 Optics for laser beam focusing

The application of MTV to fluid flows in a small physical space requires the laser excitation to be localized on a region that is smaller than the characteristic size of the investigated domain. In particular, the laser beam diameter should be quite smaller than the mean displacement of the tagged molecules. In a rectangular channel with a height of 1 mm, laser beams with a diameter of about 10 to 100 µm have been estimated to be small enough for an accurate measurement of the gas velocity profile. Since the laser beam delivered by the laser system has a diameter of about 5 mm, optical elements are required to focus the laser beam.

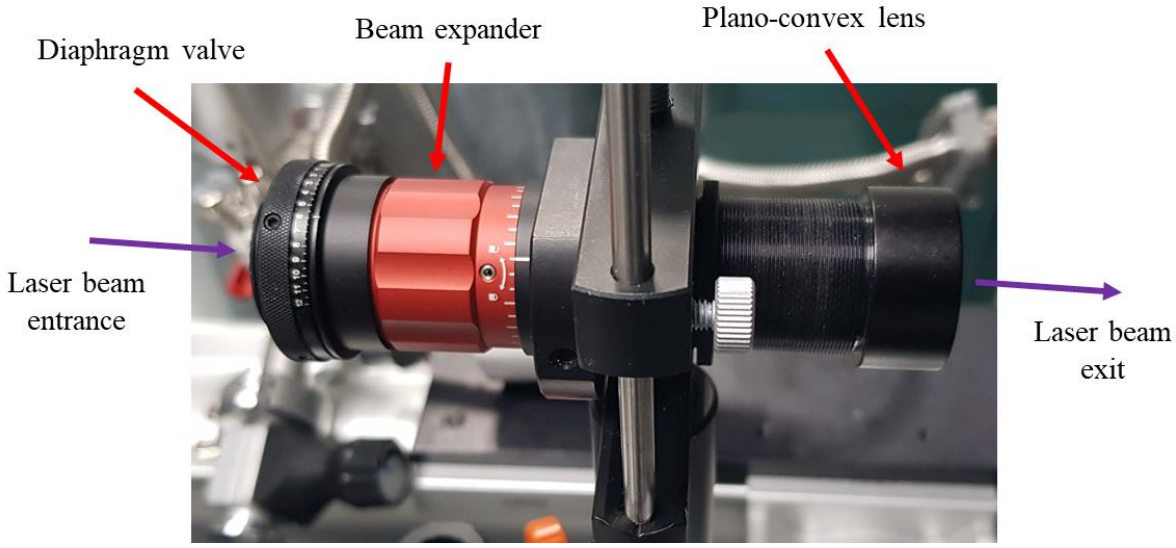

Figure 4.9. Optical system for focusing the laser beam.

Figure 4.9 shows the optical system mounted in front of the laser exit. It is composed (in this order) by (i) a diaphragm valve, (ii) a beam expander, and (iii) a plano-convex lens.

In order to avoid the laser beam to be possibly reflected back into the laser cavity, which can produce irreversible damages to the laser system, the optical system is suspended far enough from the laser system exit. In this way, even small inclinations of the optics prevent dangerous reflections.

The most important element of the optical system is the plano-convex lens, as it allows to reduce the laser beam diameter. Plano-convex lenses are usually cheaper than biconvex lenses and their asymmetry reduces spherical aberrations. An anti-reflective (AR) coating is applied on the lens surface, which maximizes the transmission of UV light. The manufacturer of the plano-convex lens provided that the focal length is 150 mm for λ_{ex} = 266 nm. However, because of possible chromatic aberrations, the focal distance increases with the beam wavelength. This effect is a consequence of the light dispersion produced by the dependence of the refraction index from the beam wavelength. It is assumed that variations of the focal length at different laser wavelengths are negligible for the following calculations.

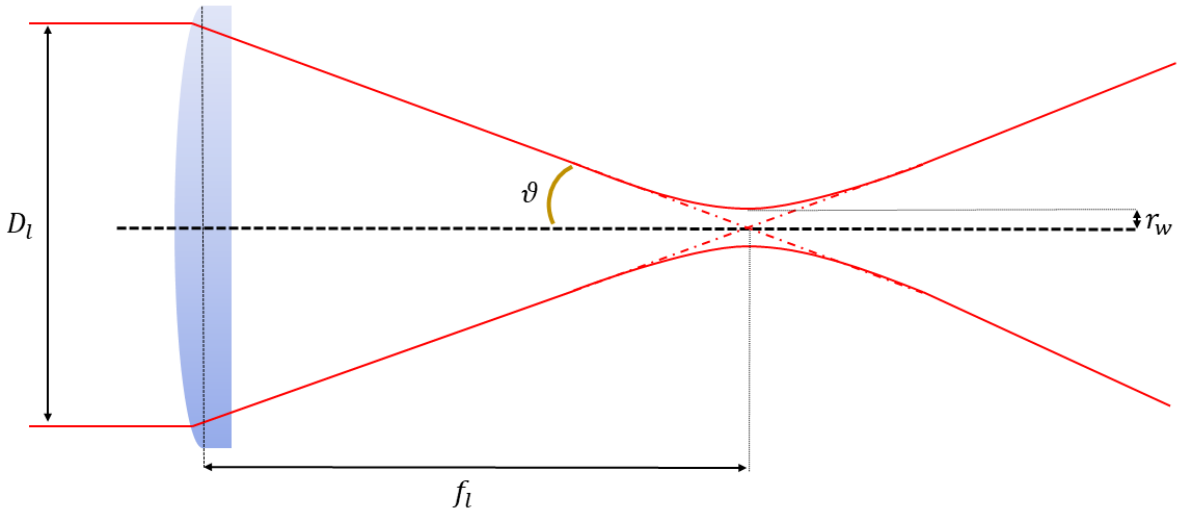

Figure 4.10. Focusing of the laser beam through the plano-convex lens.
The beam waist r_w and the divergence half-angle ϑ are represented.

Figure 4.10 schematized the focusing of a laser beam with diameter D_l into a beam of radius r_w. The divergence half-angle ϑ of the beam after passing the lens is

$$\vartheta = \operatorname{atan}\left(\frac{D_l}{2f_l}\right), \tag{4.1}$$

where f_l is the focal length of the plano-convex lens. While the definition of laser diameter is trivial for a cylindrical intensity distribution, real laser beams have a transverse shape that makes the definition more arbitrary.

The diameter D_l is here defined by considering the full width at half-maximum (FWHM), that is the width of the laser energy distribution in correspondence of an energy intensity that is the half of the maximum value.

Because of diffraction, there is a physical limit in the minimum laser beam diameter that it can be achieved by focusing with lenses. The minimum possible beam waist $r_{w,min}$, i.e., the radius of the beam at the focus spot, depends on the laser wavelength λ_{ex} and on the divergence half-angle ϑ:

$$r_{w,min} = \frac{\lambda_{ex}}{\pi\vartheta}. \tag{4.2}$$

Therefore, higher laser wavelengths and lower divergence angles make the theoretical smallest beam waist bigger. This physical limit can be obtained only for laser beams with the highest quality, which are known as diffraction-limited Gaussian beams. The practical beam waist that can be obtained is thicker for lower beam qualities. The quality of a laser beam is usually given by the laser manufacturer in terms of M^2, but it can also be expressed in terms of the beam product parameter (BPP), which is defined as the product between the divergence half-angle ϑ and the beam waist r_w. By considering Eq. (4.2), a diffraction-limited Gaussian beam has

$$BPP_{min} = r_{w,min}\vartheta = \frac{\lambda_{ex}}{\pi}. \tag{4.3}$$

Laser beams with lower quality have higher BPP values. M^2 is defined as the ratio between the BPP of the laser beam and the BPP for the diffraction-limited Gaussian beam:

$$M^2 = \frac{BPP}{BPP_{min}} = \frac{BPP}{\lambda_{ex}/\pi}. \tag{4.4}$$

Therefore, the minimum value of M^2 can be 1, and laser beams with lower quality are characterized by higher M^2 numbers. By the definition of M^2 and BPP, the real beam waist r_w can be calculated if the M^2 value is known:

$$r_w = \frac{M^2\lambda_{ex}}{\pi\vartheta}. \tag{4.5}$$

Table 4.3 lists the theoretical minimum beam diameter $2r_{w,min}$ and the beam diameter $2r_w$ for M^2 = 4 and 8 at the focus spot for three wavelengths of interest, i.e., 266 nm, 310 nm, and 410 nm. These values have been calculated for a laser beam diameter D_l at the lens entrance of 4 mm, as provided by the OPOlette HE355 laser. Table 4.4 lists the values of the same parameters but for a beam diameter D_l at the lens entrance of 7 mm, as provided by the frequency-quadrupled Nd:YAG laser.

Laser wavelength	$2r_{w,min}$	$2r_w$ at $M^2 = 4$	$2r_w$ at $M^2 = 8$
266 nm	12.7 µm	50.8 µm	101.6 µm
310 nm	14.8 µm	59.2 µm	118.4 µm
410 nm	19.6 µm	78.3 µm	156.6 µm

Table 4.3. Minimum beam diameter $2r_{w,min}$ and beam diameter $2r_w$ for M^2 = 4 and 8, and for λ_{ex} = 266, 310, and 410 nm. The values are calculated for D_l = 4 mm (OPOlette laser) and f_l = 150 mm.

Laser wavelength	$2r_{w,min}$	$2r_w$ at $M^2 = 4$	$2r_w$ at $M^2 = 8$
266 nm	7.3 µm	29 µm	58.1 µm

Table 4.4. Minimum beam diameter $2r_{w,min}$ and beam diameter $2r_w$ for M^2 = 4 and 8, and for λ_{ex} = 266 nm. The values are calculated for D_l = 7 mm (Nd:YAG laser) and f_l = 150 mm.

The value of M^2 for the laser beam of the OPOlette is provided by the manufacturer only at 500 nm, and it is 3.94. Based on the experimental results of fluorescence emission, it seems that M^2 at 266, 310, and 410 nm is higher than 4 since the observed focused beam diameter $2r_w$ is not as small as 50-70 µm as calculated in Table 4.3.

The value of M^2 provided by the manufacturer for the Nd:YAG laser is 4 at 266 nm and, indeed, it seems to be the correct value since the observed focused beam diameter appears to be only slightly bigger that the calculated value, 29 µm. Because the Nd:YAG laser delivers laser pulses with a beam diameter that is almost twice the laser beam diameter delivered by the OPOlette, the beam waist w that can be obtained with the Nd:YAG laser is almost half of the beam waist that can be obtained with the OPOlette.

Actually, the beam can be focused more if the beam diameter D_l at the entrance of the lens is bigger. For this reason, a beam expander has been placed before the plano-convex lens for doubling the laser beam diameter. Two beam expanders are available for this experimental setup: the BE02-UVB Thorlabs® is AR coated for wavelengths in the range 240-360 nm, while the GBE02-A Thorlabs® is AR coated for the range 400-650 nm. For both of them, the diameter of the laser beam at the entrance is doubled at the exit. The two beam expanders also allow an adjustment of the collimation of the laser beam at the exit.

There are mainly two categories of refracting beam expanders: Keplerian and Galilean. While the former uses two lenses with positive focal lengths, the latter uses two lenses, one with positive and the other with negative focal length. Keplerian beam expanders are characterized by a focus spot (shown in Figure 4.11a) of in the middle of the two lenses that may heat up the air inside the system if the laser energies are high enough. This yields possible variations of the refraction index and distortion of the beam wavefront. The beam expanders here used are Galilean, and they do not have this problematic (Figure 4.11b).

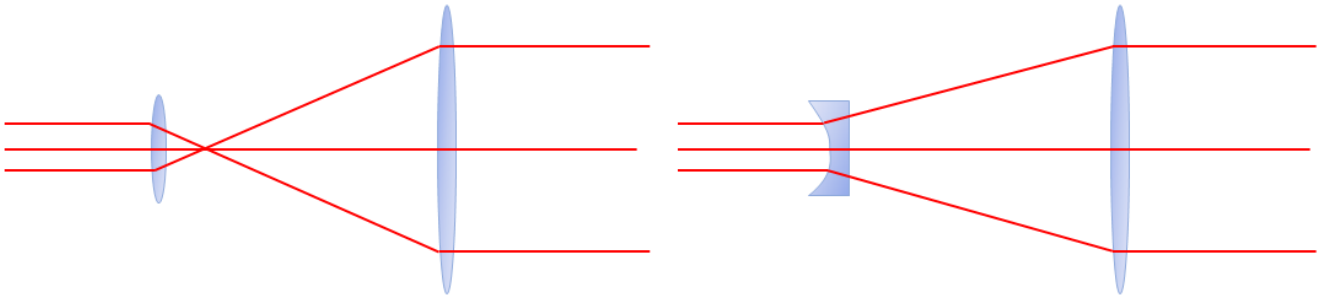

(a) (b)

Figure 4.11. (a) Keplerian and (b) Galilean beam expander structure.

The last piece of the optical system is the diaphragm valve, which provides a mechanical control on the diameter of the focused beam. Closing the valve makes the diameter of the beam passing through the plano-convex lens smaller, thus the beam waist is bigger.

4.2.4 Energy detector and statistical fluctuations

The laser pulse energy is monitored by means of a QE12LP-S-MB-D0 Gentec-EO® energy detector (Figure 4.12). The maximum admissible energy density varies from 8 to 1 J/cm^2 at 1064 and 266 nm, respectively. The energy densities employed in this work are much lower than this limit. The energy detector sensitivity is about 103 V/J at 1064 nm, with an uncertainty of ±3% with 95% level of confidence. A measured energy of 30 µJ has a standard deviation of about 0.2 µJ.

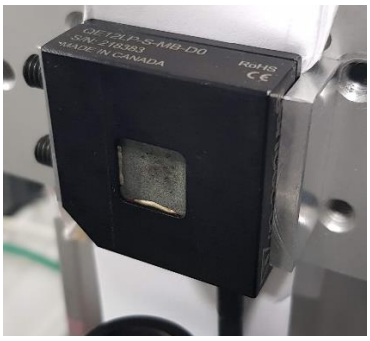

Figure 4.12. Energy detector QE12LP-S-MB-D0 Gentec-EO®.

Therefore, the uncertainty on the laser energy is not dominated by instrumental fluctuations but by statistical fluctuations of the energy delivered by the laser system. Especially when low energy levels are obtained without a mechanical attenuator, like in the case of OPOlette laser in the range 210-355 nm, the energy variations can be even 10 times higher than the uncertainty in the measure provided by the energy detector. Figure 4.13a shows the measured laser energy on 100 consecutive laser pulses at 310 nm. The data refers to an average pulse energy of 30 µJ, which is the lowest value employed in this work. The standard deviation of the laser pulse energy has been

calculated for different group of 100 laser pulses, and it is about 10 µJ, which is 33% of the average energy. Figure 4.13b shows the average energy calculated on groups of 100 laser pulses at 310 nm. The standard deviation on the average energy of 100 laser pulses is less than 1 µJ but anyway higher than the instrumental uncertainty.

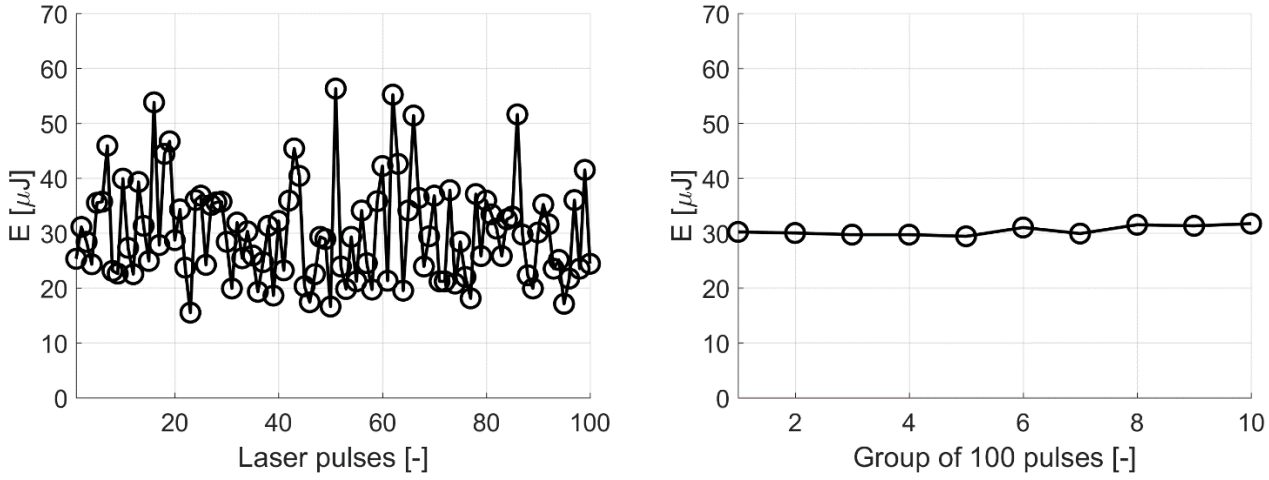

(a) (b)

Figure 4.13. (a) Laser energy fluctuation on 100 laser pulses; (b) Average laser energy of 10 groups of 100 laser pulses each.

4.3 Acquisition system

The acquisition system is composed by a series of lens that direct the light into a photodetector composed by a 25-mm intensified relay optics (IRO) and a 12-bit *Imager Intense* (LaVision®) progressive scan charge-coupled device (CCD). The overall system is defined as ICCD and is shown in Figure 4.14. The IRO is an electro-optical device which allows (i) the amplification of the light received and (ii) high-speed gating imaging. It is an essential element for the detection of phosphorescence of acetone and diacetyl vapors at low pressures, since the low tracer concentration and the high molecular diffusion make the signal intensity weak. While the minimum exposure time of a CCD is usually of the order of milliseconds, the image intensifier can reduce the exposure to a hundred of nanoseconds by means of an electronic shutter device.

Figure 4.14. Acquisition system ICCD.

4.3.1 Internal structure of the ICCD

The internal structure of the ICCD is schematized in Figure 4.15. The acquisition system can be subdivided in 6 parts:

1) the *external objectives* for collecting the emitted light;
2) the *photocathode*, which converts the incident photons in electrons;
3) the *micro channel plate* (MCP), which amplifies the electron flux generated by the photocathode;
4) the *phosphor plate*, which reconverts in "green" photon the electron bombarding coming from the MCP;
5) the *lens coupling system*, which collects the light emitted by the phosphor plate;
6) the *CCD*, which accumulates electrical charges proportionally to the light received.

The final step of the acquisition process is the *digitalization* of the accumulated electrons on the CCD cells. The photocathode, the MCP, the phosphor plate, and the internal lens system constitute the IRO.

The IRO and the CCD shutter are piloted by two trigger signals synchronized with the trigger signals for activating the laser system.

Since the first light sensitive element of the ICCD is the photocathode, it is its spectral quantum efficiency that needs to be compared to the spectra of the laser-induced tracer emissions. The objective of this section is to describe the internal structure of the ICCD and to provide information on instrumental uncertainty and time response of the acquisition system.

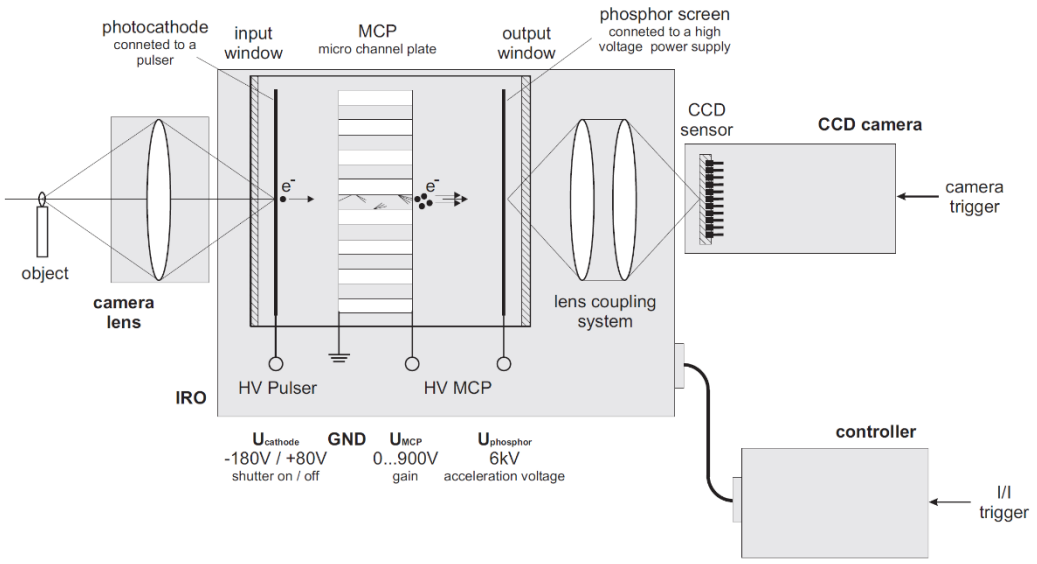

Figure 4.15. Schematic of the internal structure of the ICCD. The voltages reported on the figure are only typical values but not necessarily the one characterizing the ICCD employed in this work.

i. External objectives

The external objectives have the function of collecting the light emitted from the observed source, which is in this case the photoluminescence of the tracer. The optical system is composed by a primary objective, which is an inverted 28 mm Nikkor lens, combined with a secondary objective, that is a 105 mm Nikkor objective (Figure 4.16). Since they are both set to the maximum aperture, f/2.8, the diameter of the entrance pupil is then $D_{o,1}$ = 10 mm and $D_{o,2}$ = 37.5 mm, respectively, for the two objectives.

Figure 4.16. Optical collector mounted on the ICCD. In the picture, the IRO is on the left.

Each objective can be schematized as a thin symmetric biconvex lens, for which all the rays that starts from the focal point will be parallel rays on the back of the lens. This simplification of the optical system does not represent all possible compensations of spherical aberration, chromatic aberration, vignetting, or astigmatism that the two objectives are able to guarantee. However, it is sufficient to provide the most important characteristics of the optical system.

Figure 4.17 schematizes the overall optical system. The two lenses are represented with their own aperture, namely $D_{o,1}$ and $D_{o,2}$, $d_{o,1}$ is the distance between the two lenses, $d_{o,2}$ is the distance between the 105 mm Nikkor lens and the photocathode, L_o is an object on the focal plane of the first lens, and L'_o is the image of the object projected on the IRO photocathode.

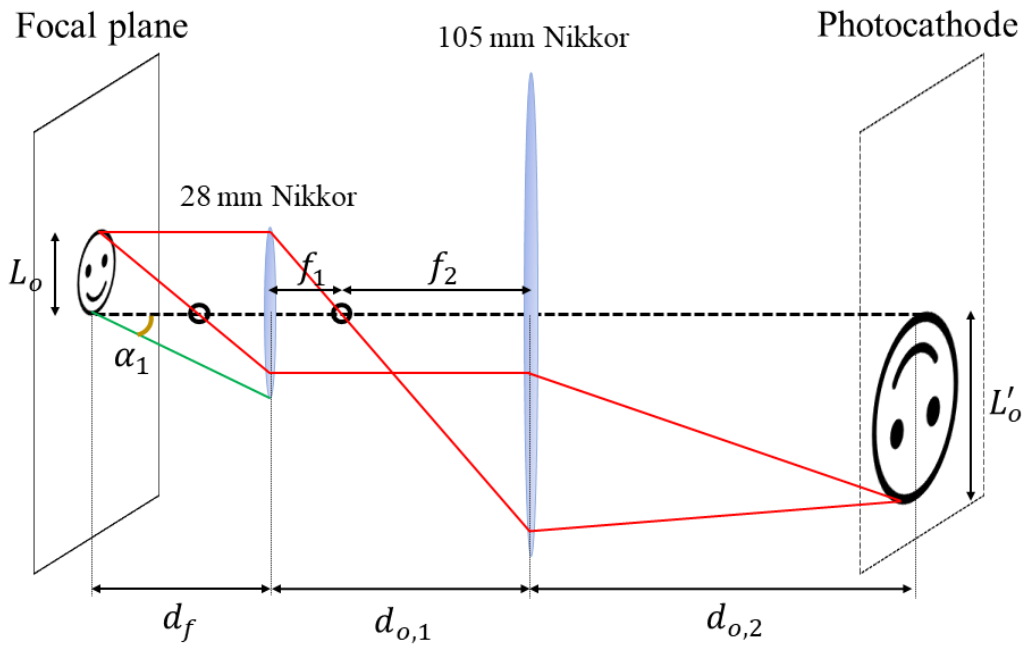

Figure 4.17. Schematization of the combined Nikkor lenses system. The lens on the left represents the primary objective, 28 mm Nikkor, with an aperture $D_{o,1}$ = 10 mm, and the lens on the right represents the secondary objective, 105 mm Nikkor, with an aperture $D_{o,2}$ = 37.5 mm. The image on the focal length of the primary objective is magnified and inverted on the photocathode plate.

Photographic lenses are usually equipped with a regulation of the distance between the lens and the film of the camera. When this parameter is set to “infinity”, this distance corresponds to the focal length of the lens, so that a far object is focused on the sensitive film. In the optical system here employed, the 105 mm Nikkor can control the distance of the lens from the photocathode surface, while the regulation on the inverse-mounted 28 mm Nikkor controls the distance $d_{o,1}$ between the lenses of the primary and the secondary objectives. The 105 mm Nikkor is set to “infinity” but, because of the type of mounting on the CCD camera, the distance $d_{o,2}$ between the lens and

the photocathode does not correspond to the focal length f_2 and is approximately 46.5 mm. The 28 mm Nikkor is set to "infinity", so that the distance between the two lenses corresponds to the sum of the focal lengths of the two objectives, which are f_1 = 28 mm and f_2 = 105 mm.

With this configuration, the magnification factor m_e can be calculated by the thin lens theory as

$$m_e = -\frac{L_o'}{L_o} = -\frac{f_2}{f_1} = -3.75. \tag{4.6}$$

The minus sign derives from the fact that the image of the object is inverted. The fact the that distance between the two lenses is the sum of the focal lengths makes the magnification of the system always the same independently of the distance of the object with respect to the 28 mm Nikkor. However, the object image is focused on the photocathode only at a specific distance d_f from the primary objective. By applying the thin lens formula to the system of two lenses, the focusing distance can be calculated as

$$d_f = \frac{\left(d_{o,1} + \frac{d_{o,2} f_2}{d_{o,2} - f_2}\right) f_1}{d_{o,1} + \frac{d_{o,2} f_2}{d_{o,2} - f_2} - f_1} = 32.16 \text{ mm}. \tag{4.7}$$

The actual focusing distance is higher than the theoretical value calculated in Eq. (4.7) of almost 6 mm. This discrepancy is probably due to the fact that the Nikkor objectives are not simple biconvex lenses, but they have a more complex internal structure. Nevertheless, even though the schematization of Figure 4.17 is not able to predict the correct value of the focusing distance, it is, instead, able to provide the correct magnification factor. In Section 4.3.5, both the magnification factor and the focusing distance are measured by recording images with the ICCD. In the following calculations, the real value d_f = 38 mm is considered.

The aperture is set to its maximum value, corresponding to f/2.8, for maximizing the light gathered by the objective. The fraction of light collected from a point source that is on the axis of the lens system can be estimated as the solid angle of the lens Ω divided by the solid angle of the sphere, 4π steradians (unit abbreviated as sr). By considering the sketch of Figure 4.17, angle α_1, where index 1 refers to the primary objective, is equal to

$$\alpha_1 = \tan^{-1} \frac{D_{o,1}/2}{d_f} \approx 0.131 \text{ rad}, \tag{4.8}$$

which corresponds to about 7.5°. The solid angle of the cone is $\Omega = 2\pi(1 - \cos\alpha_1) = 0.0537$ sr, therefore, the fraction of collected light is

$$\eta_o = \frac{\Omega}{4\pi} = 0.0043 = 0.43\%. \tag{4.9}$$

Increasing the collected light would require a bigger aperture $D_{o,1}$. The classical rule says that multiplying by $\sqrt{2}$ the aperture of the lens, or, equivalently, dividing by $\sqrt{2}$ the f-number would double the collected light. It is

important to underline that Eq. (4.9) gives the fraction of light gathered from a point source that lies on the axis of the lens system. The amount of light captured from point sources on other positions on the focal plane would depend also on the aperture $D_{o,2}$ of the second objective and the distance d between the lenses.

The final overall magnification of the ICCD needs to take into account also the effect of the internal optics of the IRO (see Section 4.3.5). For application of MTV to millimetric channel, high magnification is desired for better exploiting the CCD resolution on the detection of the tracer molecular displacement. By looking at Eq. (4.6), higher magnification can be obtained either by reducing the focal length of the first objective, f_1, or by increasing the focal length of the second objective, f_2.

In the first case, an objective with a minimum f-number f/2.8 would have a smaller aperture $D_{o,1}$, with the drawback of reducing the amount of light collected. For maintaining the same aperture while reducing the focal length, an objective with lower f-number should be used, e.g., with f/2 or f/1.4. However, this type of objective is more expansive. In the second case, the second objective can be substituted for example with 200 mm f/4.0, and the aperture would be even higher $D_{o,2}$ = 50 mm. In both cases, even if the amount of light gathered can be maintained, as the magnification increases the brightness, namely the light intensity per unit surface, necessarily decreases, because the same quantity of light is spread on a bigger surface on the CCD sensor.

No light filters are used on the objectives for avoiding further reduction of the amount of captured light. The laser beam and its possible reflection, as well as the ambient light, might be sources of noise during the photoluminescence acquisition. However, the tracer emission is investigated at times that are far from the moment of laser excitation, which lasts only between 4 and 7 ns. During the acquisition process, no other additional light source was present in the acquisition room.

ii. The photocathode

The photocathode is a metal plate that emits electrons from the surface when it is hit by electromagnetic waves. This physical phenomenon is the photoelectric effect and it takes place only if the incident photon is energetic enough. For this reason, the conversion efficiency Q_e [%] depends on the wavelength λ_e of the incident photons. Figure 4.18 shows the frequency response of the photocathode S20 mounted on the ICCD. The photocathode acts as a high-band pass on the frequency spectrum of the light emitted by the tracer.

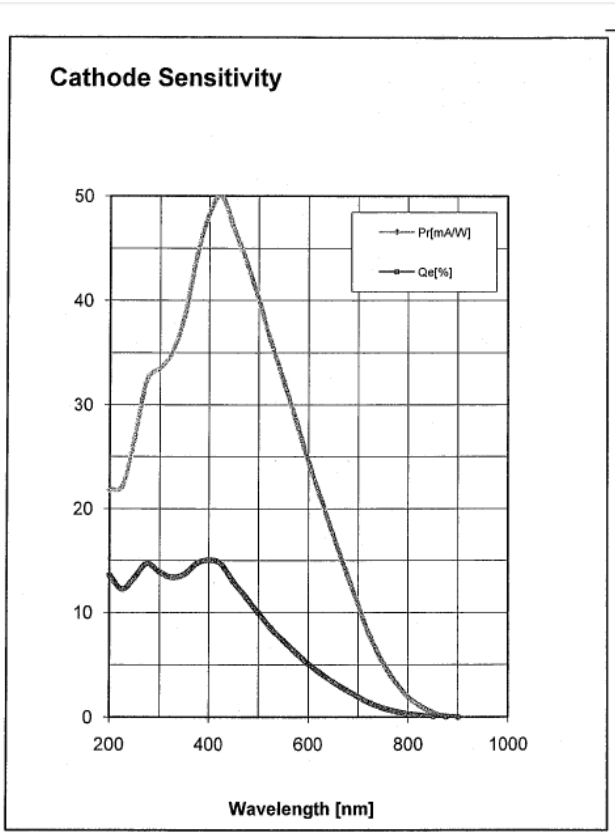

[nm]	Pr [mA/W]	Qe[%]
200	21,8	13,6
225	22,1	12,3
250	26,8	13,4
275	32,5	14,7
300	33,4	13,9
325	35,0	13,4
350	38,3	13,7
375	44,2	14,7
400	48,2	15,0
425	50,1	14,7
450	47,0	13,0
475	43,8	11,5
500	40,1	10,0
525	36,1	8,6
550	32,3	7,3
575	28,4	6,2
600	24,5	5,1
625	21,1	4,2
650	17,6	3,4
675	14,1	2,6
700	10,8	1,9
725	7,7	1,3
750	5,2	0,9
775	3,3	0,5
800	1,9	0,3
825	1,0	0,2
850	0,4	0,1
875	0,1	0,0
900	0,0	0,00

Figure 4.18. Quantum efficiency Q_e of the photocathode S20 as a function of the incident photon wavelength. Pr is the generated current per unit power which can be calculated as $Pr = Q_e\lambda_e/k$, where k = 1.24 J µm C^{-1}, and λ_e is in µm. The table on the right provides some values of Pr and Q_e for certain incident photon wavelength λ_e.
Figure from LaVision® documentation.

The quantum efficiency moves from 15% at 400 nm down to about 5% at 700 nm, which means that the photocathode needs to receive, respectively, between 6 and 20 photons for emitting one electron. The spectra of acetone and diacetyl emissions, shown respectively in Figure 4.1 and Figure 4.2, can be compared with the sensitivity of the S20 plate. The emission peak for diacetyl phosphorescence happens at 525 nm, at which the photocathode has a conversion efficiency of 8.6%. Acetone's emission is maximum for wavelengths around 450 and 500 nm, at which Q_e is between 13% and 11%. It is worthwhile noticing that any information related to the frequency content of the tracer emission is lost at the level of the photocathode.

A voltage difference is applied between the photocathode and the MCP for accelerating the electrons from the former to the latter element. Actually, the opening/closing system of the IRO is controlled by commuting the voltage at the level of the photocathode. By considering the MCP as the reference potential, a voltage of -180 V on the photocathode moves the electrons towards the MCP, while a voltage of +50 V forces the electrons to stay on the photocathode. The commutation time of the voltage is of the order of 1 to 2 ns. However, the minimal gate

time is determined by the physical properties of the photocathode material and by its capacity to adapt quickly to the voltage commutation. When the photocathode has high conductivity, the minimal gate time of the IRO can be very small but the quantum efficiency is reduced. The S20 plate mounted on the ICCD employed in this work allows for a minimal gate time of 100 ns. The adjustment of gate time Δt_{gate} is provided by controlling the square-wave trigger signal for commuting the voltage from +50 to -180 V and vice versa.

It is worthy underlining that the lifetime of the ICCD is mainly determined by the deterioration of the photocathode. Because of gas molecules present inside the IRO, the electron bombardment generates positive ions that are accelerated back towards the photocathode. This effect damages the metal plate and reduces its lifetime. The manufacturer manual guarantees an expected lifetime higher than 1000 hours, but it does not inform on the maximal working time.

iii. The MCP

The electrons emitted by the photocathode are then multiplied by the MCP, which is a circular plate of 25-mm diameter, of 400-µm thickness, and formed by more than 1 million microchannels of 6 µm in diameter (Figure 4.19a). A voltage difference is applied between the entrance and the exit of the MCP for accelerating the electrons. As sketched in Figure 4.19b, each collision of one electron with the internal walls of the microchannels generates secondary electrons in cascade. The regulation of the MCP voltage difference provides the control on the intensity of the light amplification, that is the *gain* G of the IRO. Every microchannel of the MCP has a finite number of available electrons for the amplification. If the number of electrons that enter the microchannel multiplied by the amplification factor corresponding to a certain MCP potential exceeds the total capacity of the microchannel, the MCP is discharged. Some milliseconds are needed for recharging. Since the laser repetition rate is limited to a maximum of 20 Hz, even if the total capacity of the MCP is exceeded for one gated acquisition of the laser-induced emission, the MCP has the necessary time to recharge.

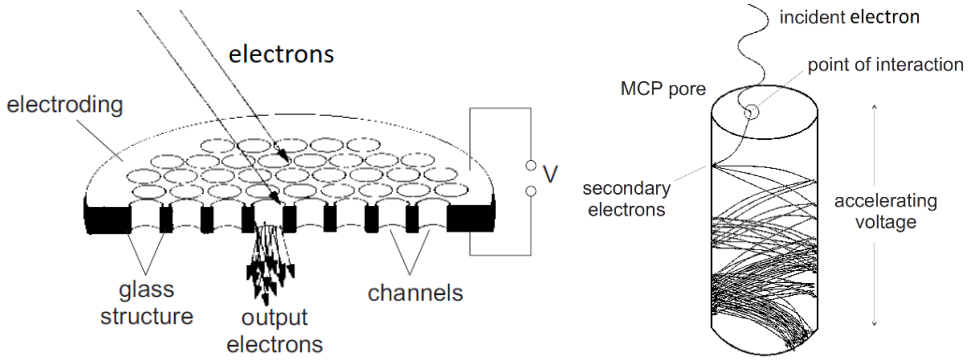

(a) (b)

Figure 4.19. (a) Illustration of the micropores composing the MCP; (b) sketch of the electron cascade inside the MCP microchannels. Figure from LaVision® documentation.

iv. The phosphor plate

The electrons coming out from the MCP micropores are accelerated towards the phosphor plate by means of a strong potential difference of 3-5 kV with respect to the voltage at the exit of the MCP. Each electron that hits the phosphor plate surface produces the emission of many "green" photons, that is photons with a wavelength between 500-550 nm. The electron acceleration is necessary for making the electron-photon conversion more efficient. Differently from the photon-electron conversion of the photocathode or of the CCD, the electron-photon conversion provided by the phosphor plate amplifies the signal. Its quantum efficiency depends on the type of phosphor employed and on the intensity of the acceleration. For instance, the phosphor plate P20 is characterized by an electron-photon conversion factor of about 66 ph/e^- for each kV of potential difference between the exit of the MCP and the phosphor plate. Moreover, once the IRO gate is closed, the phosphor plate keeps glowing for a certain time, even if no electron hits its surface anymore. If the IRO gate is open again before the complete decay of the residual glowing, the emitted phosphor light sent to the CCD at the second exposure will contain also a "ghost" emission from the first exposure, as illustrated in Figure 4.20.

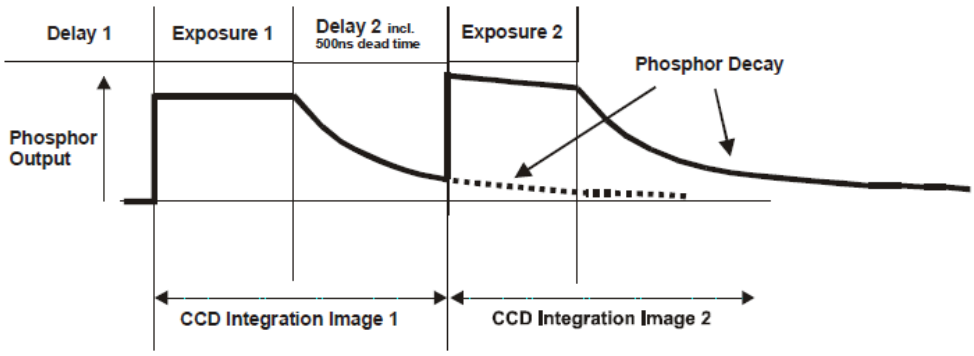

Figure 4.20. After-exposure decay of phosphor emission and effect of the "ghost" glowing on the light integrated in the CCD. Figure from LaVision® documentation.

Table 4.5 lists some characteristics of different phosphor plates, namely the "color" of the emitted photons, the conversion efficiency relative to that of the phosphor plate P20, and the after-exposure phosphor decay time to 10%. The phosphor plate P46 is the one mounted on the ICCD employed in this work. The P46 has 30% of the quantum efficiency of the P20, that is an electron-photon conversion factor of about 20 ph/e^-/kV, but it has a much shorter phosphor decay time of 300 ns. This characteristic makes P46 more suitable than P20 for gating rate higher than 15 Hz. However, the P43 would have been a better choice since it provides a quantum efficiency 3 times higher than that of P46 and has a decay time 50 times lower than the highest laser repetition rate employed in this work, that is 20 Hz.

Phosphor plate	Photon color	Relative efficiency	Decay time to 10%
P20	Green	100%	70 ms
P43	Green	90%	1 ms
P46	**Green**	**30%**	**300 ns**
P47	Blue	25%	100 ns

Table 4.5. Characteristics of some phosphor plates. The one mounted on the ICCD employed in this work is the P46.

The phosphor light emission is only partially captured by the internal optical collector and sent to the CCD. Since the phosphor plate has two faces, only the photons that are emitted from the face directed toward the CCD are collected. The electron-photon conversion needs, therefore, to take into account a loss of 50% of the photons emitted by the phosphor plate. However, the amplification given by this conversion guarantees that for each received electron, more than one photon is generated.

v. The internal optical collector

The photons emitted by the phosphor plate are collected by a system of lenses and directed towards the cells of the CCD. This optical transmission reduces considerably the intensity of the acquired signal. In the ICCD employed in this work, the integrated coupling-lens system is able to collect only 10% of the photons coming from the phosphor plate. An alternative, more efficient optical system would have been given by a transmission through optic fibers, which could save 70% of the light.

In order to fit the intensity distribution coming out from the IRO into the CCD sensor, the coupling-lens system needs to reduce the size of the image. A de-magnification m_i = 2.17 is used for the 25-mm IRO combined with the CCD *imager intense*. Differently from the external optical collector, the projected image is not inverted. This magnification factor needs to be taken into account for calculating the overall magnification given by the ICCD.

vi. The charged-couple device (CCD)

Finally, the photons emitted by the phosphor plate reach the CCD and are re-converted in electrons by means of the photoelectric effect. The CCD consists of a rectangular array of semiconducting cells able to accumulate charges and with a dimension of 6.45 × 6.45 μm^2. The resolution of the CCD *imager intense* is 1376 (horizontal) × 1040 (vertical) pixels and, therefore, covers an actual area of 8.87 × 6.7 mm^2. As in the case of the conversion made by the photocathode, the photon-electron conversion involves a de-amplification of the signal. Figure 4.21 represents the quantum efficiency Q_{CCD} of the CCD *imager intense* as a function of the incident photon wavelength. The maximum efficiency is about 65% and corresponds to a wavelength of 500 nm, which is close, unsurprisingly, to the wavelength of the "green" photons emitted by the phosphor plate.

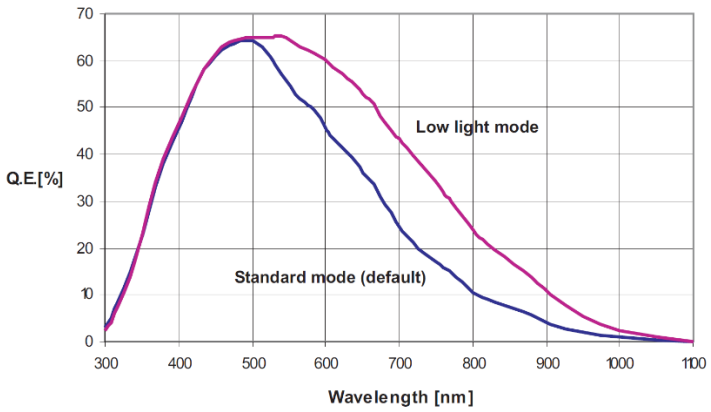

Figure 4.21. Quantum efficiency of the CCD *imager intense* as a function of the incident photon wavelength. Figure from LaVision® documentation.

vii. Digitalization of the charges

The last step of the acquisition chain is the analog-digital conversion of the accumulated charges in each CCD cell. The charges of each pixel are flushed in a specific order into the register cells and are digitalized one by one, as sketched in Figure 4.22. An average noise corresponding to μ_{RON} = 5 e$^-$ is introduced on each pixel during this conversion. This so-called readout noise (see Section 4.3.4) defines the digital unit of the acquisition:

$$1 \text{ count} = 5\ e^-, \tag{4.10}$$

so that N_{e^-} charges on a pixel corresponds to N_{e^-}/μ_{RON} counts.

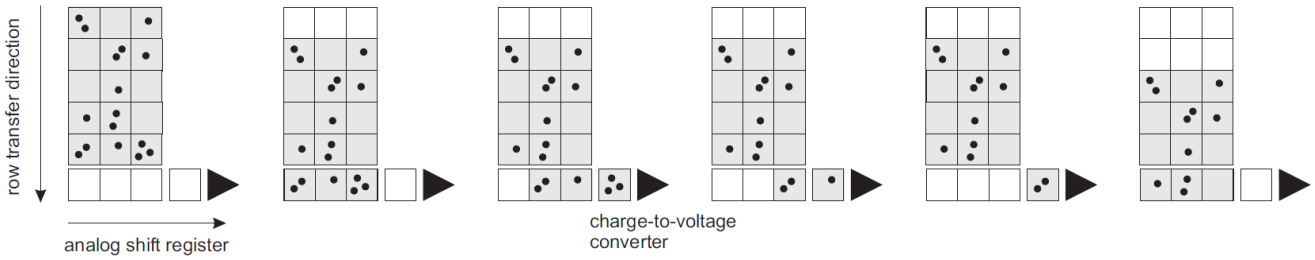

Figure 4.22. Readout process of the accumulated charges of each CCD pixel. Figure from LaVision® documentation.

4.3.2 ICCD sensitivity

The understanding of the role and characteristics of each element in the acquisition chain allows estimating the number of photons emitted by an observed light source from the number of counts recorded on a CCD pixel.

The photocathode has a low threshold limit on the number of incident photons that can generate an electron. This threshold defines the minimum light intensity the ICCD is sensitive to. As discussed in the previous section, the

quantum efficiency of the photocathode is about 10% in the wavelength range of interest. This would require 10 incident photons on a point of the photocathode surface for generating one single electron.

By reminding that the external objectives of the camera have a collection factor of 0.78%, an isotropic light point source needs to emit about 1230 photons for the photocathode to receive at least 10 photons. This represents the order of magnitude of the weakest light source that the ICCD is able to capture.

The number of counts on one CCD pixel for each electron emitted by the photocathode can be estimated through the following calculation:

1) the manufacturer states that at the maximum amplification gain, G = 100%, about 500 electrons are produced by the MCP for each received electron. $G_{MCP}(G)$ is defined as the number of electrons generated by the MCP per electron received and it is a function of the parameter G;

2) the phosphor screen P46 has a conversion efficiency Q_{P46} of about 20 photons per electron received per kV;

3) only half of the phosphor emission is directed towards the CCD sensor and the coupling-lens system gathers only 10% of the phosphor plate photons. The percentage of photons emitted by the phosphor screen that are sent towards the CCD is defined as η_{IO};

4) the quantum efficiency Q_{CCD} of the CCD corresponding to the "green" photon wavelength can be approximated to 65%;

5) finally, the conversion in digital units provides the number of counts, which corresponds to the number of accumulated electrons on the CCD divided by the average read out noise μ_{RON}.

By considering a voltage difference ΔU = 4 kV between the MCP exit and the phosphor screen and by setting the IRO at maximum amplification, G = 100%, the number of counts per electron generated by the photocathode is

$$\frac{G_{MCP}(G = 100\%)\Delta U Q_{P46}\eta_{IO}Q_{CCD}}{\mu_{RON}} = 260 \text{ counts} \tag{4.11}$$

where $G_{MCP}(G = 100\%)$ = 500, Q_{P46} = 20 kV^{-1}, η_{IO} = 0.05, Q_{CCD} = 0.65, and μ_{RON} = 5. The ICCD sensitivity $S_{ICCD}(G)$ can be calculated for different amplification gains, and the curve of Figure 4.23 can be obtained. This sensitivity curve represents the effect of all the components of the ICCD from the photocathode to digitalization of the accumulated charges on the CCD.

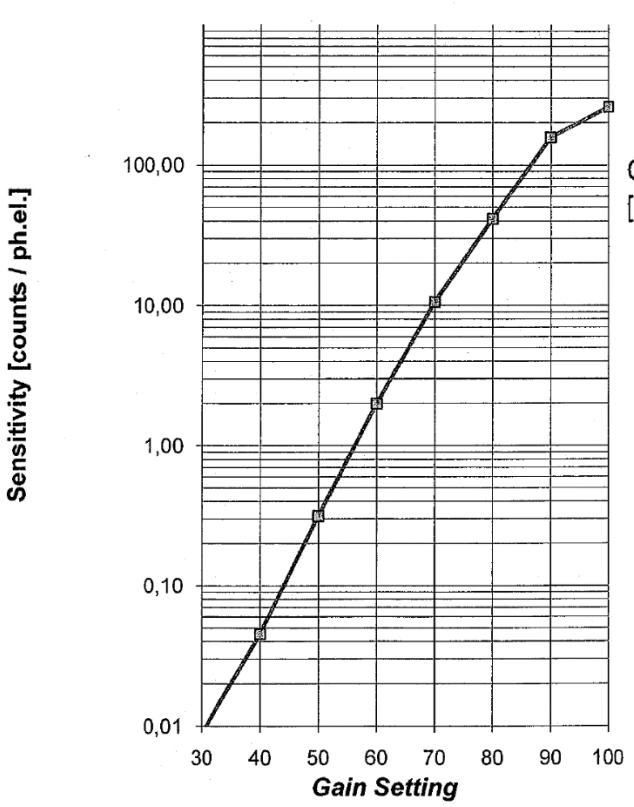

Gain [Scale]	Umcp [V]	Sensitivity [cnts/photoelectron]
20	220	0,002
30	330	0,009
40	440	0,05
50	550	0,31
60	660	1,99
70	770	10,6
80	880	41,4
90	990	157,3
100	1100	260,0

Figure 4.23. Sensitivity curve of the ICCD: it provides the number of counts per electron generated by the photocathode for different values of the amplification gain. On the right, a table providing the values of gain, sensitivity, and voltage difference applied between the entrance and the exit of the MCP. Figure from LaVision® documentation.

If the gain is set to 100%, it seems that whenever an electron is generated by the photocathode, at least 260 counts should be recorded on the CCD pixel. If no electrons are generated, no counts are recorded. This scenario means that an image recorded at G = 100% should have no values between 0 and 260 counts, something that does not happen in real application. It can be explained as follows.

Firstly, the values of Figure 4.23 are only estimations and may vary according to the probability of amplification of the MCP, the probability of electron-photon conversion of the phosphor plate, the probability of collecting light by the coupling-lens system, and the probability of photon-electron conversion of the CCD.

Secondly, while in the calculation it is assumed that all the photons that reach a CCD cell produce charges exclusively on that CCD pixel, in practice the charge accumulation is distributed among adjacent pixels, as shown in Figure 4.24. It is, therefore, difficult to estimate the values of counts recorded on a single pixel, but the total number of charges accumulated over all the CCD sensor should provide a value close to the theoretical expectation given by the ICCD sensitivity of Figure 4.23.

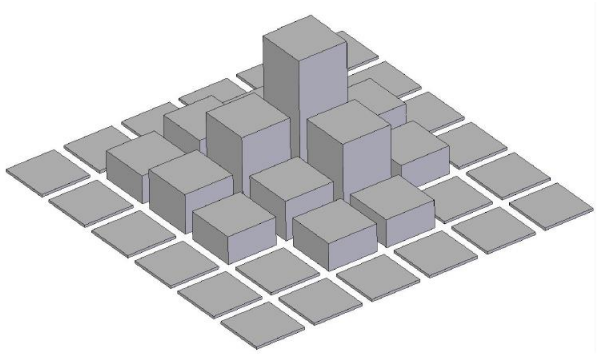

Figure 4.24. Sketch of the intensity distribution of charges spread over an area of pixels.
Figure from LaVision® documentation.

The overall efficiency conversion η_{ICCD} of the acquisition system that gives the number of counts registered on the CCD sensor of an isotropic light point source is provided by

$$\eta_{ICCD}(G) = \eta_o Q_e S_{ICCD}(G), \tag{4.12}$$

where η_o is the fraction of collected light of the external optical system and Q_e is the quantum efficiency of the photocathode.

4.3.3 The on-chip integration technique

The main parameters that can be controlled for each recorded image are:

1) the delay time t between the IRO trigger and the laser Q-switch trigger;
2) the IRO gate Δt_{gate}, i.e., the time interval of light integration;
3) the IRO amplification gain G;
4) the exposure time t_{CCD} of the CCD detector.

The IRO gate is controlled by a trigger signal generated by the IRO controller. The laser trigger, the camera shutter trigger, and the IRO trigger are all synchronized by a programmable timing unit (PTU) with a precision of 5 ns.

Since this study involves low tracer concentrations and requires limited laser energy levels to preserve the integrity of the access window, the amount of light that one single laser excitation can provide is very low. As a matter of fact, recording on the CCD the phosphorescence emission given by one pulse laser excitation results in a more or less blank image. For this reason, the on-chip integration technique is used. This technique allows to collect in one single image the light generated by more than one laser excitation. By keeping open the CCD camera exposure, the IRO gate Δt_{gate} is open always at the same delay time after each laser excitation. This concept is illustrated in Figure 4.25.

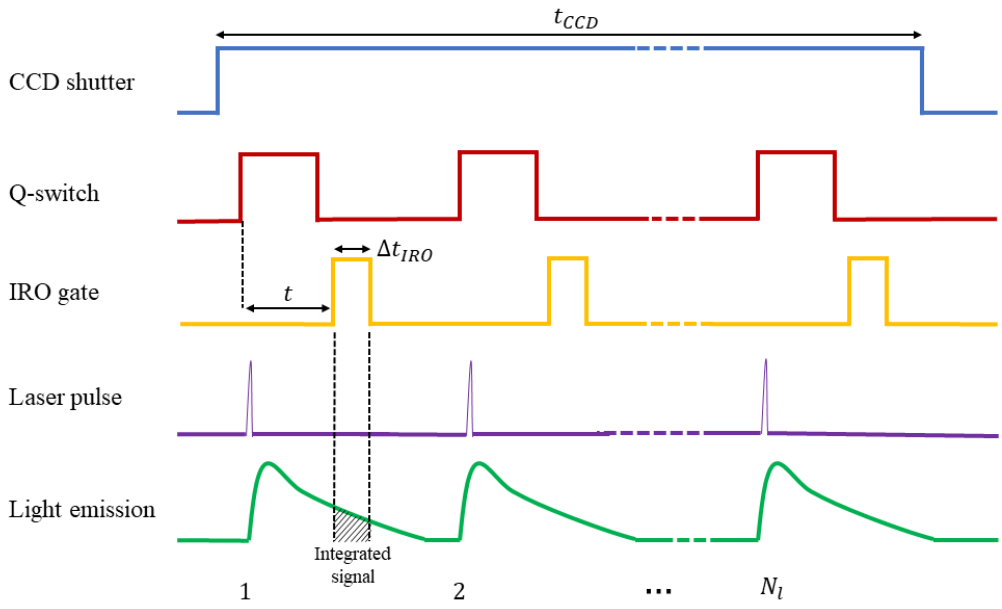

Figure 4.25. Train of signals related to one image acquisition by means of the on-chip integration technique.

Since the phosphorescence emission is weak, the IRO amplification is always exploited at its maximum, thus G is fixed to 100%. The final image is given by the average of N_i images that are each the result of the integration of N_l laser pulses. The definition of the CCD exposure time t_{CCD} is, therefore, made indirectly by defining N_l and setting the laser repetition rate. A common number of laser pulses per image employed in this work is N_l = 100, which gives t_{CCD} = 10 s and t_{CCD} = 5 s for laser repetition rates of 10 Hz and 20 Hz, respectively.

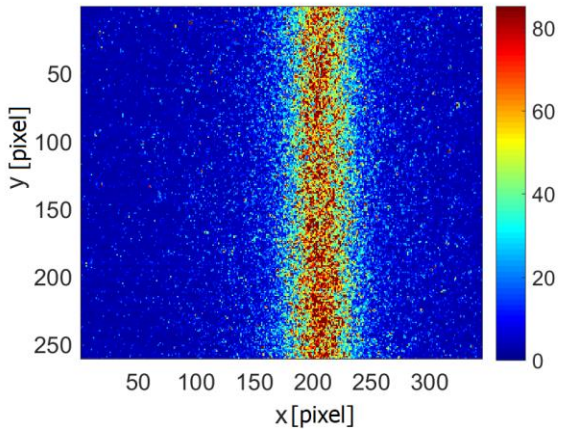

Figure 4.26. Example of raw image of tracer light emission induced by a laser beam.

Figure 4.26 shows a typical recorded image showing the laser-induced phosphorescence emission of the tracer diffusing in a quiescent background gas. The laser beam comes from the top side to the bottom side of the image and its axis belongs to the focal plane of the optical collector. The image is the result of averaging N_i = 10 images,

each of them with N_l = 100 integrated laser pulses. The recorded emission represents phosphorescing diacetyl molecules diffusing in helium.

4.3.4 Instrumental uncertainties of ICCD

Along the acquisition chain, different sources of noise affect the final value of the recorded signal intensity. From the point of view of MTV application, the evaluation of the statistical uncertainties on the emitted light intensity is not of direct interest. In fact, the velocimetry technique requires precision in evaluating the molecular displacement and the time separation between two images. Differently, the quantitative analysis of the photoluminescence lifetime requires a characterization of the precision of the measured light intensity. However, the statistical fluctuations on the absolute value of the recorded light in one point of the space certainly determine the precision in measuring the mean molecular displacement.

For this analysis, the signal-to-noise ratio SNR on the measured light intensity is defined as the ratio between the number of counts registered on a CCD cell, or on the entire CCD sensor, with respect to its standard deviation. It is worthy noticing that this definition will change in the next chapters accordingly to the quantity of interest for the considered problem.

Each element of the ICCD gives a source of noise. The main instrumental uncertainty is given by

1) the *shot noise* of photocathode,
2) the *CCD dark noise*,
3) the *photocathode dark noise*,
4) the *readout noise.*

The CCD dark noise, the photocathode dark noise, and the readout noise are relevant only for low signal intensities and at low gain amplification, while the dominant source of noise at high intensifier gain is the shot noise of the photocathode. For the experimental investigation of the minimum gas pressures that can be used while still detecting exploitable phosphorescence signals, all these noise sources are relevant. Differently, for the quantitative experimental analysis of the phosphorescence lifetime and molecular tracer diffusion and the application of MTV, the external light emission, which can come from, for example, the tracer phosphorescence, the glass wall fluorescence, or possible light reflections, is so strong that the only relevant noise source is the shot noise of the photocathode. The sources of noise introduced by the ICCD above listed are further described in the following sections.

i. Photocathode shot noise

An emitting source is usually described by a Poisson distribution. The main characteristics of this distribution is that its standard deviation is equal to the root square of the mean emission. This noise is called photonic shot. The photocathode emission can be described by this probability function. Therefore, if there is a mean value of μ_{e^-} electrons emitted by the plate (in one point or the total emission), the statistical fluctuation on the number of emitted electrons is $\sigma_{e^-} = \sqrt{\mu_{e^-}}$. Although also the CCD, the MCP, and phosphor plate are affected by the photonic noise, fluctuations of the photocathode emission are amplified by the IRO. The fluctuations on the accumulated charges on one pixel strongly depends on the amplification gain G. If N_c counts have been recorded, the corresponding number of electrons emitted by the photocathode is $N_c/S_{ICCD}(G)$, where $S_{ICCD}(G)$ is the ICCD sensitivity function of the amplification gain (see Section 4.3.2). The statistical fluctuations on the emitted electrons is $\sigma_{e^-} = \sqrt{N_c/S_{ICCD}(G)}$, which produces an uncertainty on the recorded counts of:

$$\sigma_{shot} = \sigma_{e^-} S_{ICCD}(G) = \sqrt{N_c S_{ICCD}(G)}. \tag{4.13}$$

ii. CCD dark noise

The thermal distribution of the electrons in the CCD silicon cells produces a "dark" current that is accumulated during the CCD exposure. This noise is drastically reduced by cooling down the CCD camera to about -11° C. However, relatively long camera exposition heats the CCD cells to a level such that the dark-noise pattern is clearly visible on the acquired image. Figure 4.27 represents the dark images of the CCD for increasing exposure time. The recording of the dark image happens with the IRO shutter off, so that no external light affects the CCD acquisition. The images in the figures are only the result of the dark current in the CCD sensor. The exposure time is defined indirectly by setting the number of integrated laser pulses per image, even if no laser shots are produced for real. Each figure is the result of averaging 5 dark images.

As it can be noticed, a strong non-uniform signal distribution is present at the up-right corner of the CCD sensor. This problem may be caused by the cooling system that does not cool correctly that zone of the CCD sensor. As the exposure time increases, the signal intensity in the problematic region increases as well. The average dark image intensity is about 45 counts.

This issue is easily solved by subtracting the dark image from the real acquisition of the tracer emission. Because the dark image pattern may vary from one day to another, a new dark image was captured before any acquisition made during the experimental work.

The generation of thermal electrons is characterized by its own statistical fluctuations. As for the photon noise, the dark noise exhibits a Poisson distribution. From the images of Figure 4.27, an average dark noise of 35 counts is

observed, which corresponds to an average number of 175 thermal electrons generated in the CCD. The uncertainty in the number of counts given by the dark noise is then characterized by $\sqrt{175} \cong 13$ e$^-$. Therefore, the standard deviation of the dark noise in counts is $\sigma_{dark} \cong 3$ counts. This noise source is important for low light intensity acquisitions.

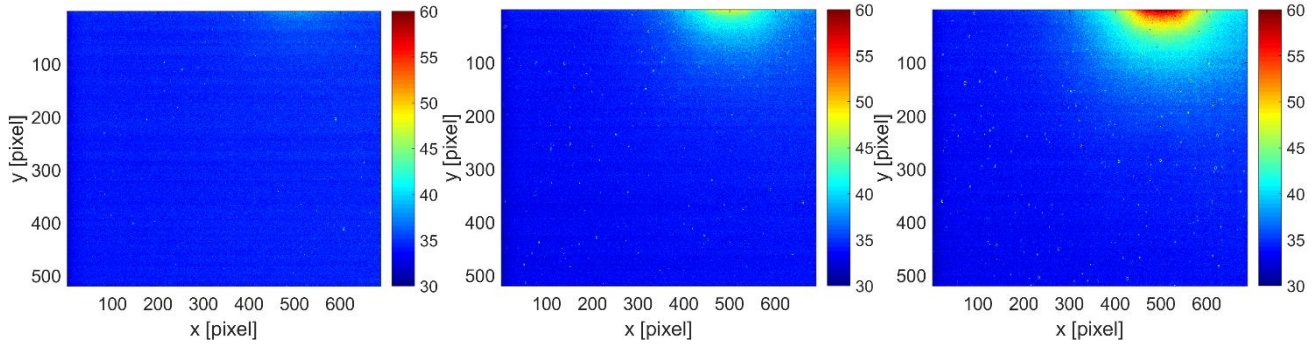

(a) (b) (c)

Figure 4.27. Dark images for (a) t_{CCD} = 10 s, (b) t_{CCD} = 50 s, (c) t_{CCD} = 100 s. For a laser repetition rate of 10 Hz, the three exposition times correspond, respectively, to N_l = 100, 500, and 1000.

iii. Photocathode dark noise

As for the CCD sensor, the electrons inside the photocathode are characterized by a thermal energy distribution. Because the electrons energy may overcome the threshold energy level required for the emission to occur, the randomly emitted electrons from the photocathode provide a dark noise on the final signal intensity. It can be reduced by cooling the photocathode, as for the case of the CCD dark noise. However, this noise source is usually negligible when the acquisition is done with an IRO gate of the order of microseconds. Since most of the image acquisitions made in this work have been produced with IRO gates between 100 ns and 2 µs, the photocathode dark noise is neglected.

iv. Readout noise

The readout noise is generated at the moment of converting the charges accumulated on each CCD pixel into a digital unit. Because the read noise is added to every pixel when they are read out, it is applied uniformly across the CCD. Usually this noise is in average μ_{RON} = 5 e$^-$, which means that every light source that produces on the CCD pixel a number of charges lower than this value is not detected. The readout noise defines, indeed, the noise floor and the quantization error of the CCD sensor. By considering the quantization error as uniformly distributed, its standard deviation is $\sigma_Q = \sqrt{1/12} = 0.3$ counts. The real readout noise has its own probability distribution, which is not known a priori. Its standard deviation can be assumed to be $\sigma_{RON} = 1.5$ counts.

Since the photocathode dark noise is negligible and since the readout noise and the quantization noise are smaller than the CCD dark noise, the main noise sources are the shot noise of the photocathode and the dark noise of the CCD. While the last is independent of the signal intensity recorded, the shot noise depends on the gain amplification and on the signal intensity. The overall instrumental uncertainty on the recorded counts is

$$\sigma_{ICCD} = \sqrt{\sigma_{shot}^2 + \sigma_{dark}^2} = \sqrt{N_c S_{ICCD}(G) + \sigma_{dark}^2}. \tag{4.14}$$

At high amplification gain or high signal level, the uncertainty given by the dark noise becomes negligible. The standard deviation given by Eq. (4.14) is, actually, an overestimation of the noise on the signal recorded on one pixel, because the photocathode shot noise is distributed on more than one pixel, as previously explained. However, when all the light intensity recorded on an image is integrated, the value σ_{ICCD} is a good estimation of the uncertainty on the total number of counts. In this perspective, Figure 4.28 reports the relative uncertainty on the total number N_c of counts collected on one image as a function of N_c when the maximum gain G = 100% is employed. This is the condition where the random electrons emissions from the photocathode are amplified the most. The figure shows that for a total signal in the range 10^7-10^6 counts the uncertainty is between 0.5% and 1.5%. In this work, the lowest total signal recorded from acetone and diacetyl phosphorescence emission is on the order of 10^6.

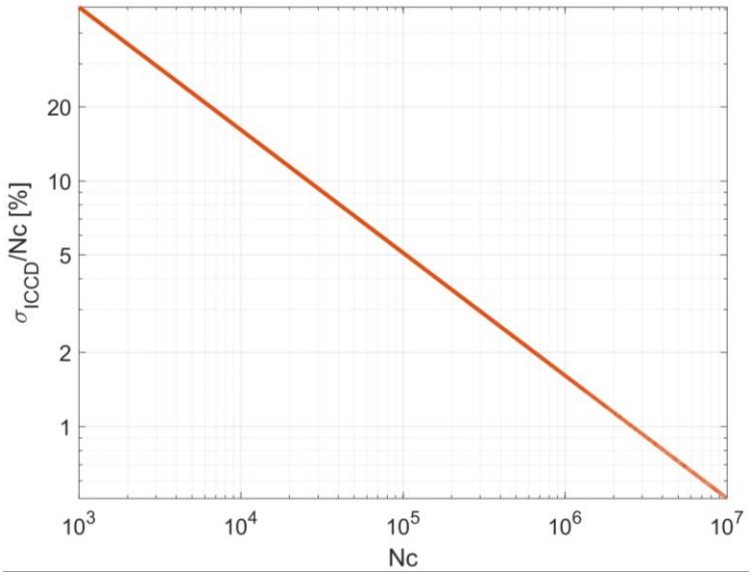

Figure 4.28. Uncertainty given by ICCD noise on the total number N_c of collected counts on an image.

4.3.5 Magnification, focusing distance and depth of focus

The primary magnification can be defined as the ratio between the sensor size and the field of view (FOV) of the camera. The external and internal optical systems provide together an overall magnification m of the observed object. The external collecting lenses provide a magnification of m_e = -3.75, while the internal coupling-lens system de-magnifies of a factor m_i = 2.17. The overall magnification $m = m_e m_i$ given by the external optical system and the internal optical collector of the IRO and CCD is about 1.7. As the CCD covers an actual area of 8.87 mm × 6.71 mm, the FOV is 5.29 mm × 4 mm. Consequently, each photosite of the CCD (physically 6.45 μm in width) corresponds to a pixel imaging a physical area in the focal plane of 3.8 μm × 3.8 μm without binning and of 15.2 μm × 15.2 μm with a 4 × 4 binning.

The focusing distance d_f and the depth of focus (DOF) of the ICCD have been measured by varying the relative position of an object in front of the camera. Figure 4.29 shows four images of a sample grid. The optimal focusing distance between the image and the primary objective has been considered to be at 38 mm (Figure 4.29c). With respect to this reference position: in Figure 4.29a, the objectives are moved closer of 150 μm; in Figure 4.29b, the objectives are moved closer of 50 μm; in Figure 4.29d, the objectives are moved further of 150 μm: it is possible to see that the three cases show an image which is slightly out of focus.

The measured focusing distance is, therefore, 6 mm higher than the theoretical values calculated in Eq. (4.7). In the images (Figure 4.29), each square has a real area of 200 × 200 μm^2. The number of pixels that composes one side of these squares is about 50. This provides a pixel size of 4 μm, which is close to the theoretical value 3.8 μm. The theoretical magnification m_e of the external optical system calculated in Eq. (4.6) corresponds, therefore, to the measured value.

While images that are 50 μm distant from the focal plane seem to be still on focus, higher distances produce images that are too blurred. Therefore, the measured DOF is about 100 μm.

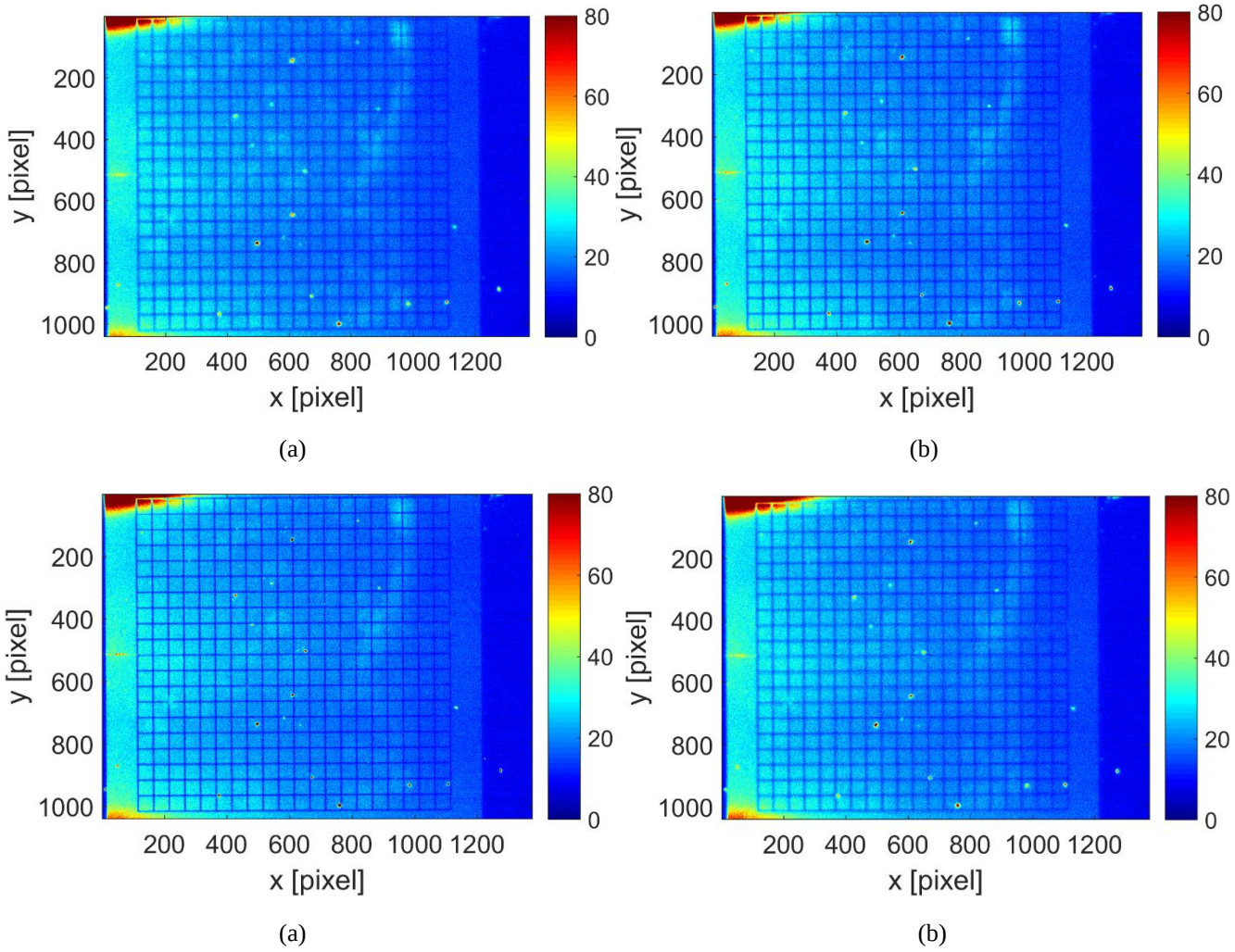

Figure 4.29. Images of a sample grid recorded at different distances from the ICCD objectives.
The distances are (a) d_f, = d_f - 150 µm, (b) d_f, = d_f - 50 µm, (c) d_f = 38 mm, and (d) d_f, = d_f + 150 µm.

4.3.6 Binning

Binning is the process of grouping adjacent pixels in a single mega pixel at the moment of the CCD readout procedure. The charges collected in each CCD photosite of the group are integrated to provide a mega pixel. Figure 4.30 illustrates this idea for a 2 × 2 and 4 × 4 arrays, but matrices of photosites with different dimensions in the two directions can also be used, e.g., 1 × 2 or 4 × 1. This feature is very interesting for getting benefits of binning without losing the spatial resolution in a specific direction of interest.

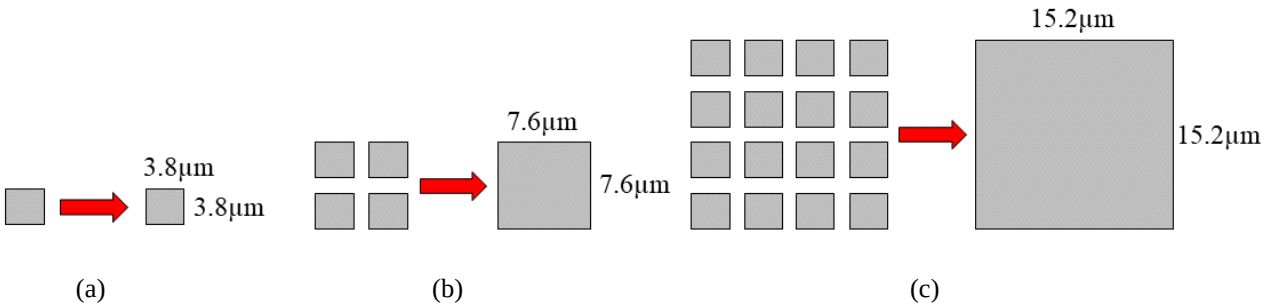

Figure 4.30. Grouping of photosites by binning: (a) 1 × 1, (b) 2 × 2, and (c) 4 × 4.

The reason why the binning operation is different than simply using a lower resolution relies on the hardware strategy employed for reading out the charges of the CCD cell into the on-chip registers. Binning has mainly two advantages: (i) improving the signal-to-noise ratio and (ii) increasing the readout speeds. The charges of a group of photosites are gathered together on-chip, and they are read-out all together. For this reason, there is only one single readout noise associated to the group of charges, instead of having a readout noise for each pixel. Moreover, the readout process is faster because it does not happen for each single photosite. While the faster readout speed is not very interesting in our application, binning is here employed for improving the signal-to-noise ratio SNR. For example, a binning 4 × 4 improves the SNR by a factor 16. It must be understood that binning can improve SNR only with respect to the readout noise, which is not negligible only at very low light emissions. Any other possible noise that increases the accumulated charges on the CCD cells, e.g., other light sources in the field of view, shot noise of the photocathode etc., cannot be separated from the light emission of interest by the binning operation, which does not improve the signal-to-noise ratio in this sense.

Most of the experimental data presented in this work have been acquired by employing a 4 × 4 binning. The resolution of the CCD is, thus, reduced from 1376 × 1040 to 344 x 260 pixels, and the pixel size increases from 3.8 × 3.8 μm^2 to 15.2 × 15.2 μm^2. The application of a 4 × 4 binning should provide ideally a signal 16 times more intense with respect to the acquisition without binning. This aspect has been directly verified on the laser-induced tracer emission. Figure 4.31a and Figure 4.31b show the same emission with the same acquisition parameter without and with binning, respectively. The ratio of the signal intensity with binning over the signal intensity without binning is of about 15, which is close to the expected value. By keeping this in mind, even though most of the experimental data here presented refer to acquisitions made with a 4 × 4 binning, it is ascertained that an image with higher resolution and 16 times less bright can be obtained.

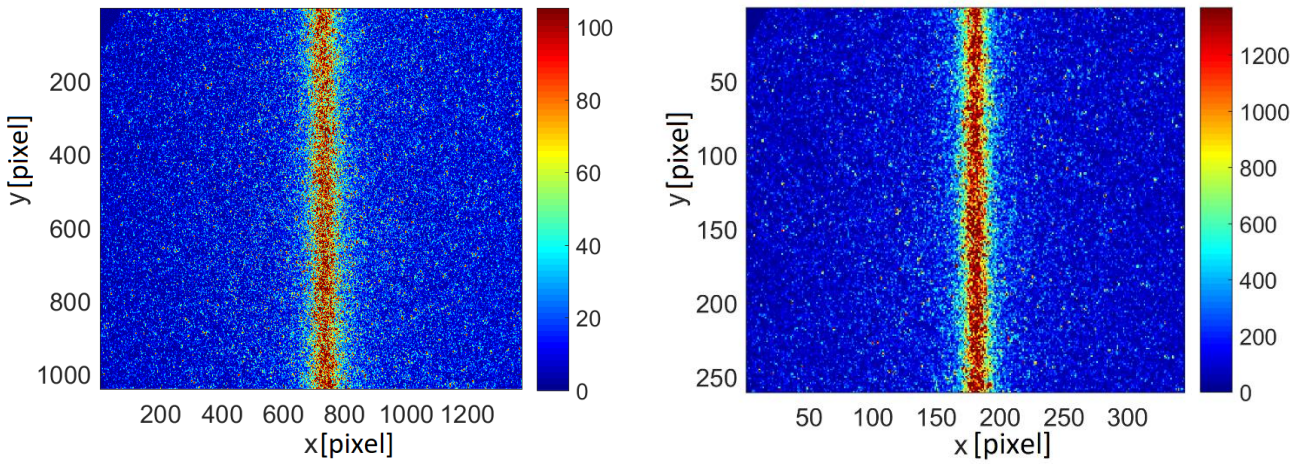

(a) (b)

Figure 4.31. Raw images of diacetyl phosphorescence emission at p = 5 kPa, T = 293 K, and for t = 2 µs after the excitation. The images represent the collection of N_l = 100 laser pulses, (a) without binning and (b) with 4 × 4 binning.

4.3.7 Signal intensity with IRO gate and N_l

Statistical fluctuations are produced during all phases of the acquisition process, namely the excitation, the photon emission, and the acquisition phase. A higher number N_i of averaged images can increase the quality of the resulting image by reducing the data fluctuations. It cannot, however, increase the light intensity. Differently, a higher number N_l of laser pulses increases the recorded light intensity and reduces the statistical fluctuations. Figure 4.32a shows the light intensity amplification due to an increasing number N_l of laser pulses, from 10 to 2000. The data refer to the phosphorescence emission of acetone vapor at a pressure p = 3 kPa, excited by a laser beam at 266 nm. The relationship is not exactly linear: as the number of laser pulses integrated in one image grows, the light amplification tends to decrease. The main limitation in increasing the number of laser pulses N_l or averaged images N_i is given by the recording time, which linearly increases with these two parameters. Alternatively, the IRO gate can be increased. In this way, the acquisition time does not change. In the view of the application of the MTV to gas flows, the IRO gate should be kept lower than the characteristic time of the flow in order to be able to accurately evaluate the molecular displacement. The relationship between the amount of light recorded and the size of the IRO gate is linear, as proved by the data of Figure 4.32b.

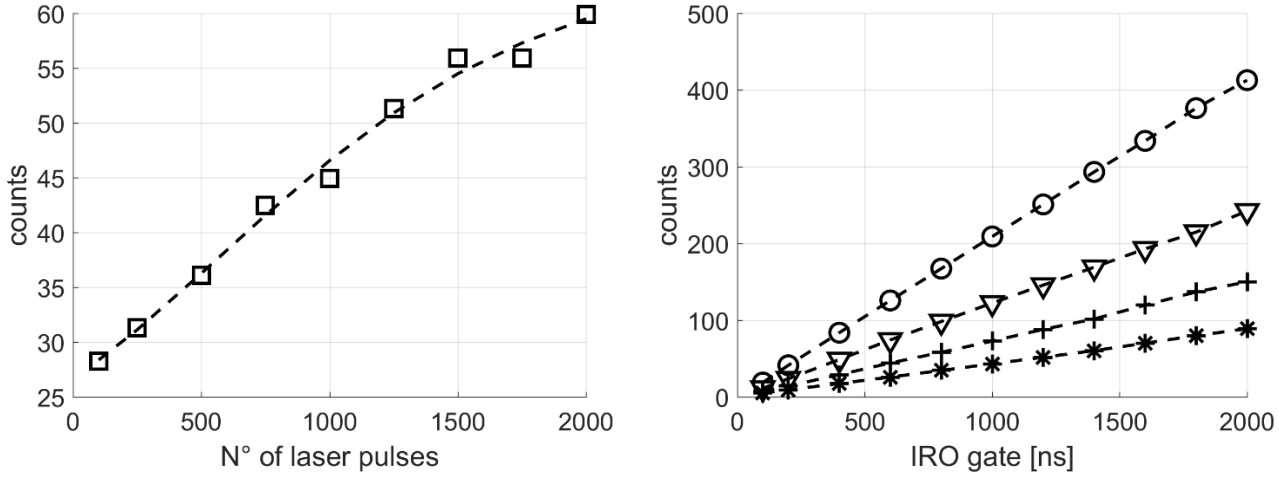

(a) (b)

Figure 4.32. (a) Emission intensity of acetone vapor at $p = 3$ kPa, $T = 293$ K, and $\lambda_{ex} = 266$ nm as a function of the number of laser pulses N_l integrated in one image. The data refer to the phosphorescence emission at t = 50 μs after the excitation and result from the average of 10 images; (b) phosphorescence emission of acetone vapor at $p = 5$ kPa, $T = 293$ K, and $\lambda_{ex} = 266$ nm as a function of the IRO gate. Data shown are for t = 50 μs, N_l = 100 (○); t = 100 μs, N_l = 100 (▽); t = 50 μs, N_l = 50 (+); t = 100 μs, N_l = 50 (✱).

Since our experiments deal with a weak source of light, a high number of laser pulses and a limited number of averaged images is preferred. However, when the main noise source is not instrumental but comes from other light sources in the field of view of the camera, such as the fluorescence of the optical access for the laser beam, increasing N_l does not improve the ratio of the signal intensity to the background noise. In this situation, increasing the number of integrated laser pulses or the number of averaged images does not make any difference.

4.4 Gas system

The final objective of this work is the application of MTV technique for directly measuring the slip velocity at the wall characterizing rarefied gas flows in a rectangular channel. The first task is guaranteeing the feasibility of this project by exploring the limitations of the intensity and the lifetime of the laser-induced emission of the tracer at low pressures. Afterwards, a suitable experimental setup must be designed to develop experimental flows in a channel that are characterized by (i) a measurable slip velocity at the wall and (ii) suitable conditions for the successful application of MTV. The simultaneous satisfaction of these two requirements is at the origin of the complexity in designing an optimal experimental setup.

In this section, the gas systems employed in this work are described. Section 4.4.1 describes the gas system used for carrying out experiments on phosphorescence emission of acetone and diacetyl vapors at low pressures. In

Section 4.4.2, the gas circuit for generating flows in the channel that can be analyzed by MTV is described. In this work, gas-vapor mixtures with helium and argon have been investigated.

4.4.1 Experimental setup for photoluminescence analysis

The first part of this work aims to analyze the intensity and the lifetime of the phosphorescence emission of the molecular tracers in different thermodynamic conditions. For this study, the laser excitation was carried out on gas-vapor mixture at rest in a small visualization chamber. Figure 4.33a shows the disposition of the ICCD and of the laser with respect to the static cell. Figure 4.33b represents a schematic view of the same experimental setup. As previously said, two experimental campaigns have been conducted for the analysis of the photoluminescence at low pressure. In the first one, the Nd:YAG laser was employed for analyzing acetone phosphorescence at 266 nm, whereas in the second, the OPOlette was used for exciting both acetone and diacetyl at excitation wavelengths in the range 240-355 nm and 410-480 nm. When the Nd:YAG was used, the positions of the camera and of the laser beam were switched with respect to the illustration of Figure 4.33: the camera was positioned horizontally and the laser beam was transmitted from Nd:YAG system exit to the top window of the visualization chamber through a laser arm. For the second experimental campaign, the configuration of the setup was changed as shown in Figure 4.33 because the mirrors mounted in the laser arm reflect light beams only with wavelengths around 266 nm or 532 nm.

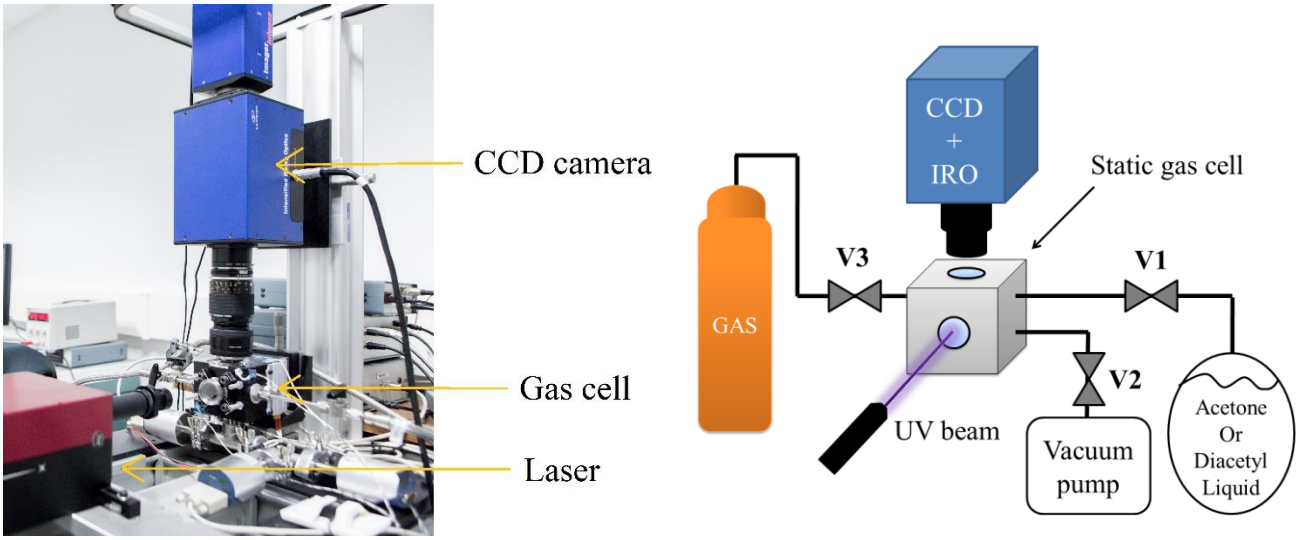

(a) (b)

Figure 4.33. (a) experimental setup. (b) schematic of the experimental setup.

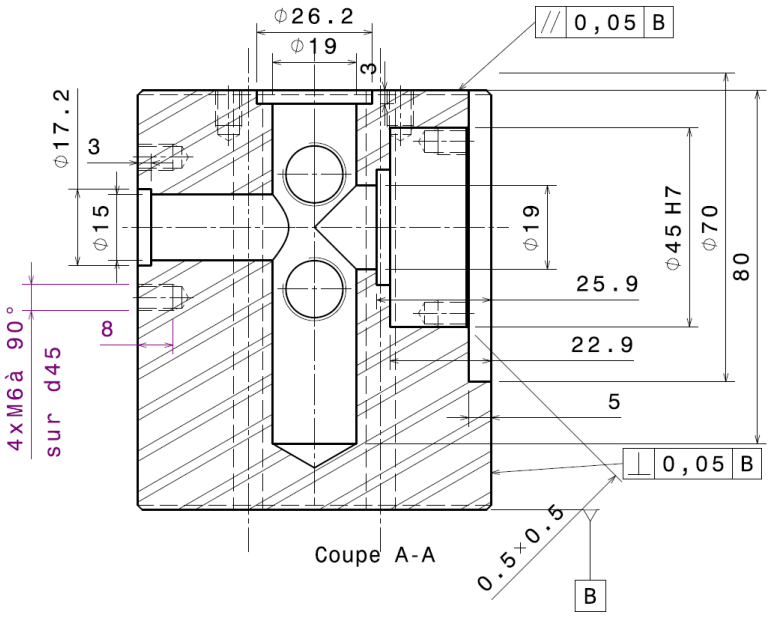

Figure 4.34. Internal dimensions of the visualization chamber.

The analysis of the phosphorescence emission has been conducted for gas mixtures with pressures from 15000 to 10 Pa. Such experimental study requires a static cell that provides a leakage-free environment while being able to guarantee the optical accesses for the excitation and the phosphorescence acquisition. Figure 4.34 shows a sketch of the chamber, providing all dimensions. The total internal volume, including the volume added by the optical windows, is about 70 ml.

The static gas cell is equipped with two optical accesses: an optical window in Suprasil® for the laser beam access, and an optical window in Borofloat® that is transparent to the light emitted by the tracer. Suprasil® glass has been chosen for the laser beam access window due to its limited fluorescence emission under UV excitation, thus reducing the background light noise in phosphorescence acquisitions. Unfortunately, the chamber does not have an exit window for the laser beam. Therefore, the energy could not be monitored during an image acquisition but only just before or after it. A third access is available on the visualization chamber for connecting one or more pressure sensors. Kalrez® O-rings have been used as joints for placing the optical windows and for the pressure sensor connection. This material has an excellent chemical resistance to acetone or diacetyl, differently from the cheaper Viton® O-rings.

The chamber is also equipped with a Swagelok® connection for introducing an RTD thermocouple and monitoring the mixture temperature. However, no variation in the temperature was registered in the chamber during the experiments. Since any useful information were obtained from it and since the Swagelok® connection was an important source of leakages, no internal temperature sensor was employed, and the connection was closed with a cap.

The leakages have been quantified by monitoring the pressure growth inside the chamber starting from pressures of about 5 Pa. Once the chamber is completely outgassed, the pressure increases of about 6 Pa in 1 hour.

Three gas lines are connected to the static cell: one for channeling acetone or diacetyl vapor, one for channeling the background gas, and one for vacuuming the cell by means of a vacuum pump. These three gas-vapor lines are regulated by Swagelok® valves. In Figure 4.33b, V1 is the valve regulating the tracer pressure in the chamber, V2 is the valve on the pumping line, V3 is the valve regulating the gas pressure in the chamber.

The acetone or diacetyl vapor is generated from a bottle containing the fluid in its liquid form. The bottle is directly connected to the cell and its vertical position ensures that only vapor is aspired. The cell is vacuumed during 2-days in order to have a complete outgassing of the unwanted molecules adsorbed by the inner walls. This procedure is repeated every time before a new type of vapor or gas could be used inside the cell.

Working with a static gas cell rather than a flowing gas cell makes the experimental setup much simpler, permits an easier and better control of pressure and temperature conditions of the mixture, and reduces the waste of gas and vapors, since the same mixture can be employed for more than one acquisition. The relative concentrations of gas and vapor can be accurately controlled, since the mixing is directly done inside the cell by simply adding the right amount of partial pressure.

While acetone has a saturated vapor pressure of 24 kPa at 20 °C and has relatively low toxicity, diacetyl has a lower saturated vapor pressure, about 6 kPa at 20 °C, and its toxicity is quite higher, such that some precautions must be taken during its handling. Although the highest diacetyl pressure at ambient temperature that can be employed is relatively low, this is not a limitation for the current work, as the targeted rarefied regime requires even lower pressures. For all the experiments carried out in this analysis, the vapor pressure employed in the chamber was always enough lower than the saturated vapor pressure at ambient temperature in order to prevent possible vapor condensations.

Since the bottle of liquid tracer is connected to the static cell, all the air present in the connections and dissolved in the liquid must be outgassed. This is mandatory for having an oxygen-free environment since oxygen quenching negatively affects the phosphorescence lifetime. In order to guarantee the complete elimination of air from the bottle, the following procedure is repeated several times:

1) valve V2 is opened and vacuum is made in the chamber;
2) valve V2 is closed and valve V1 is fully opened, filling the chamber with vapors and air;
3) once the pressure inside the chamber is stable, valve V1 is closed and valve V2 is opened to vacuum again the chamber.

These operations are carried out until the highest pressure in the chamber provided by the bottle does not exceed the expected saturated vapor pressure of the tracer under use. This is a guarantee that the vapor provided by the bottle is only made of tracer. Once the highest pressure provided by the bottle corresponded to the estimated saturated pressure vapor, the same procedure was repeated other 10-20 times to ensure the removal of oxygen from the bottle. Moreover, the small but inevitably present leakages reintroduce in the bottle line some oxygen that in the long term can become a relevant percentage with respect to the tracer pressure. For this reason, this procedure is repeated before starting any experimental measurements.

Although the simplicity of using a static cell, this setup requires, however, attention on some issues, such as gas mixing time, inner wall adsorption of acetone and diacetyl, and the occurrence of molecular photolysis following laser excitation. The mixing process is relatively fast, considering the small volume of the cell. Moreover, for checking the absence of significant photolysis, it has been verified that, for the laser intensities used, the signal intensity did not vary in time during a series of many successive laser shots. The main issue is the adsorption of the tracer molecules on the inner walls, which causes a monotonic drop of the nominal pressure in the cell. However, a stable pressure condition is easily attained by refilling the cell with acetone or diacetyl in order to saturate the adsorption phenomenon towards a stationary state.

A gas-tracer mixture with tracer partial pressure p_2 and gas partial pressure p_1 is formed by following this procedure:

1) the chamber is vacuum for several hours for complete outgassing;
2) valve V2 is partially open to fill the chamber with acetone or diacetyl vapor at the desired partial pressure p_2 and then closed;
3) valve V3 is partially open to fill the chamber with gas up to the total pressure $p_2 + p_1$ and then closed.

Because the gas line is always maintained at a pressure of 1 bar, the lower tracer pressure p_2 in the chamber guarantees that during step 3 the gas is flowing inside the chamber and no tracer vapor is flowing in the opposite direction.

4.4.2 Experimental setup for MTV and CV techniques at low pressures

In this section, the experimental setup employed for generating a gas mixture flow through a rectangular channel is described. The successful application of MTV to gas flows at low pressures relies on the existence of a gas circuit that can generate and maintain optimal experimental conditions. The gas system needs to fulfill the following requirements:

1) all the components need to have chemical compatibility with acetone and diacetyl vapors;

2) it needs to be functioning at low pressures with no leakages;

3) the thermodynamic conditions (i.e., pressure, temperature, and tracer concentration) of the gas-vapor mixture in the test channel need to be regulated;

4) high flow rates need to be generated for producing a measurable displacement profile that MTV can detect;

5) the mass flow rates passing through the channel needs to be stable in time or, at least, slowly varying with respect to the acquisition times required by MTV technique.

As it will be discussed in Chapter 6, the relatively high molecular diffusion of the tracer in the background gas at low pressures heavily distorts the tagging line. The resulting displacement profile assumes a shape that can be detected by the ICCD resolution only if the flow rate in the channel is high enough. As the average pressure in the channel decreases, the necessary flow rate increases. For instance, the required flow rate at an average pressure of 500 Pa is at least about 4-5 liters per minute.

In addition to the requirements listed above, the gas system should also preferably integrate an alternative technique to measure the mass flow rates inside the channel for verification of the results provided by MTV technique.

The initial idea was to design a closed-loop gas system as the one depicted in Figure 4.35. The gas-vapor mixture can be formed inside the gas circuit with a similar procedure to the one described in the previous section, and a pump or a fan can control and maintain the flow rate inside the loop.

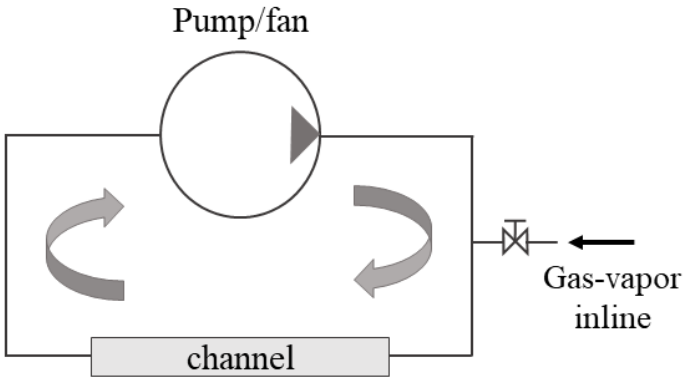

Figure 4.35. Closed-loop gas system. This concept has not been implemented in this work.

The advantages of such a gas system are:

1) the possibility of easily preparing the gas-vapor mixture inside the system with desired average pressure and tracer concentration;

2) the possibility of defining the desired flow rate through the channel by adjusting the pump or the fan power;

3) the reduced consumption of gas and tracer vapor;

4) the stability of the pressure conditions at the inlet and the outlet of the channel thus guaranteeing a steady mass flow rate through the test section.

Despite these advantages, this gas system could not be, however, realized mainly for two reasons:

1) no commercially available oil-free pumps or a fans chemically resistant to acetone or diacetyl vapors and, at the same time, capable of working at low pressure conditions without leakages and providing the required flow rates could be found;

2) the leakages in the tested channel are still too important for applying MTV to a recycled gas-vapor mixture.

Especially because of the second reason, a closed-loop gas system cannot be a solution at this stage of the project. The channel still has some leakages at the level of the laser access windows, so that some oxygen molecules are inevitably added to the gas flow. If fresh gas-vapor mixture is not employed through the channel, the amount of oxygen in the recycled gas mixture increases to an extent that oxygen quenching completely extinguish the tracer phosphorescence and no MTV measurements are possible. For these reasons, the gas system needs to be an open circuit, in which the gas flowing through the channel comes from an upstream source of oxygen-free gas-tracer mixture.

The gas system designed and built in this work for applying MTV to gas flows at low pressures is illustrated in Figure 4.36. The basic working principle of this gas system relies on (i) preparing the gas-tracer mixture in a big reservoir at desired pressure p_1 and tracer concentration χ and (ii) forcing the gas mixture to pass through the channel by pumping it into the atmosphere.

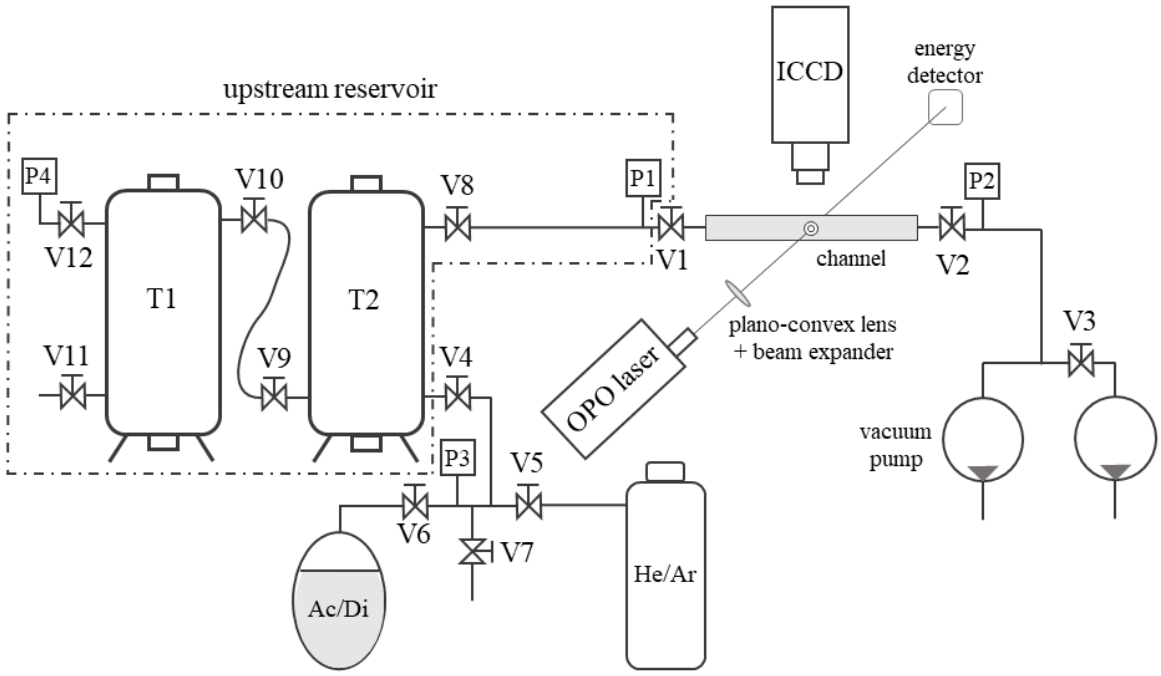

Figure 4.36. Gas system for application of MTV to gas-vapor mixture flows at low pressures. T1 and T2 are the two tanks; P are pressure sensors; V1 is the inlet channel valve; V2 is the outlet channel valve.

The upstream reservoir is composed by two tanks of about 90 liters each. The two tanks are connected by a pipe with a diameter of about 1.5 cm and a length of 1.3 m. All the valves are Pfeiffer® ball valves except for valves V5, V6, and V7, which are Swagelok® valves. The system of valves V4, V5, V6, and V7 allows for preparing the gas-vapor mixture in the reservoir with the same procedure used for the visualization chamber. Valves V11 and V7 are supplementary entries for vacuuming the big tanks.

At the outlet of the channel, two GEFI® rotary vacuum pumps of the same model are used in parallel to achieve the highest mass flow rate through the channel. The two pumps need to be identical for assuring that neither of the two pumps suck oil vapor from the other. For the same reason, Valve V3 is necessary for switching on, firstly, the pump on the left and, successively, the pump on the right (see Figure 4.36) The pumping at the channel outlet is required for exhausting the gas from the tanks into the atmosphere since the experimental flow conditions are at pressures lower than the atmospheric one.

The signals from pressure sensors P1, P2, P3, and P4 are processed by a National Instruments® DAQ card. The digital data are then displayed and managed with NI Signal Express® software. Pressure sensors P1 and P2 are used for monitoring the pressure, respectively, at the inlet and the outlet of the channel. Pressure sensor P3 on the mixing line is necessary for assuring the complete outgassing of air in the acetone/diacetyl bottle by following the procedure explained in the previous section. Pressure sensors P4 and P1 can be both used for measuring the pressure in the tanks. Moreover, pressure sensor P4 has been introduced for comparison with P1 during gas flows

from the tanks through the channel. This allows to check for any possible difference of pressure in two far locations inside the two-tanks system.

Pressure sensors P1 and P2 are inserted in the circuit through a T-junction, so that they provide a measure of the static pressure of the gas flow at those locations. Pressure sensor P4 provides both the static and the total pressures of the gas in the reservoir because the gas velocity at its location is always negligible even when the gas flow is passing through the channel. For this reason, a difference between pressure p_1 measured by sensor P1 and pressure p_4 measured by sensor P4 would correspond to the dynamic pressure of the gas flow at the position of P1. However, for all the experiments carried out during this work, no difference was recorded between the measured given by P1 and that given by P4. This fact demonstrates that the dynamic pressure of the gas flowing in the pipe connecting the reservoir to the channel is negligible for the gas pressures and velocities employed in the analysis. As a matter of fact, for the experimental flow generated at low pressure, the highest mass flow rate is on the order of 5×10^{-6} kg/s at an average pressure of 5000 Pa. By considering that the pipeline connecting the tanks to the channel inlet has a diameter of 15 mm, the average velocity of the gas in this tube is about 1 m/s, and its dynamic pressure is $\frac{1}{2}\rho V^2 \sim 0.015$ Pa, which is 6 orders of magnitude smaller than the static pressure. The sensor P1 always provides the static and total pressure in the tanks, which justifies the fact that the pipe connecting the channel to the tanks can be considered part of the upstream reservoir.

The channel

The main requirements that the design of the channel needs to fulfill for being adapted to MTV measurements are:

1) an optical access for the UV laser excitation of the tracer seeded in the gas flow;
2) an optical access for capturing the phosphorescence emission of the tracer by means of the ICCD;
3) materials that are chemically resistant to acetone and diacetyl vapor;
4) good sealing properties for preventing leakage.

The first three requirements make the channel be an assembly of elements of different materials.

The channel used in this work is shown in Figure 4.37. It is 20-cm long and has an internal rectangular section with a width of 6 mm and a height of 913.5 µm. The main body is composed by two long pieces made out of PEEK®, a material with good mechanical properties (e.g., stiffness and machinability) and good chemical resistance to acetone and diacetyl. The channel is grooved along the first piece of PEEK® and the second one covers it (Figure 4.37b). A planar joint made of Kalrez® is in between the two pieces of PEEK®, to enable excellent sealing characteristics at these locations.

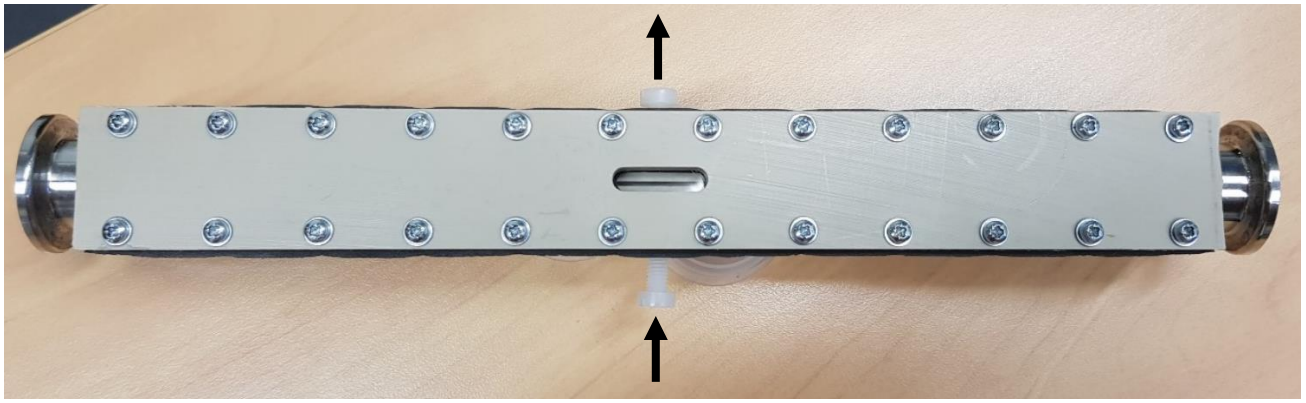

(a)

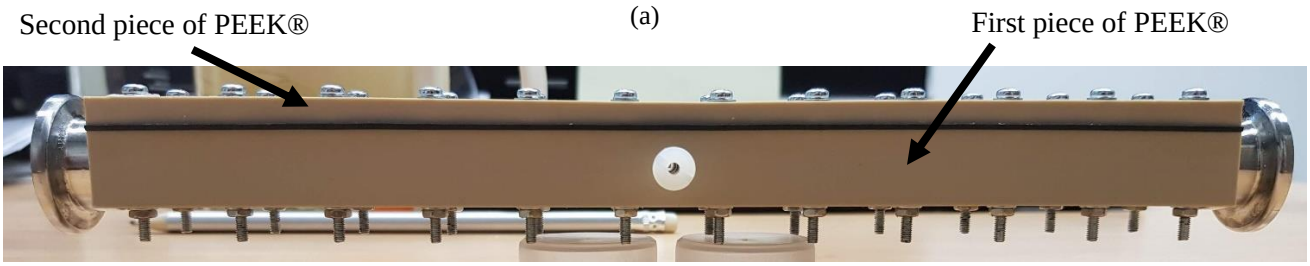

(b)

Figure 4.37. (a) Channel from the point of view of the ICCD camera. The arrows indicate the optical access for the laser beam; (b) channel from the point of view of the laser beam. The black rubber in between the two pieces of PEEK® is the planar joint in Kalrez®.

The channel is equipped with optical accesses that allows MTV velocity measurements only at the middle position along the channel length. Two Suprasil® small windows (Figure 4.38a) are inserted in two lateral cavities of the first piece of PEEK®. Their positioning inside the cavity is regulated by a perforated plastic screw. A small Kalrez® O-ring is used for better sealing properties in these locations of the channel. The double-window system allows a continuous monitoring of the laser energy by means of the energy detector, as sketched in Figure 4.36. The gap in the second piece of PEEK® accommodates a small rectangular window in borosilicate (Figure 4.38b), for providing the required transparency of the channel to the tracer emission.

In the previous version of this channel, the cover for the first piece of PEEK® was made of glass. The structure of this cover was much simpler than the current one, as the transparency to phosphorescence emission was automatically guaranteed by the cover itself. However, the fragility of the glass made this version of the channel impossible to be used at low pressures. The screws for connecting the glass cover to the piece of PEEK® needed to be well tightened to prevent air leakage inside the channel but the stresses weakened the glass cover until

breakup. The non-homogenous cover combining PEEK® with borosilicate glass windows solved this problem while providing very good sealing properties.

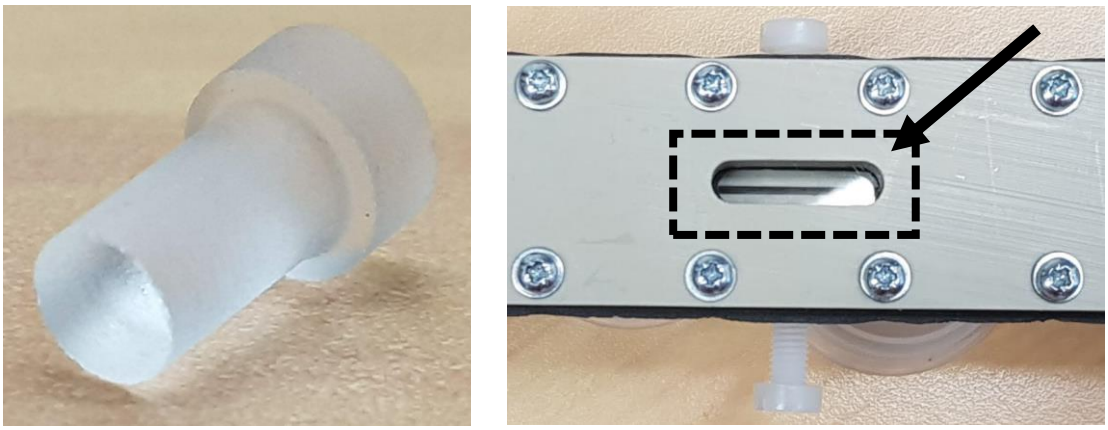

(a) (b)

Figure 4.38. (a) Suprasil® window; (b) Borosilicate optical access for ICCD acquisition. The smaller dimension of the rectangular gap that can be seen through the window corresponds to the height of the channel.

The most delicate components of the assembly are the Suprasil® windows. Random high-energy-density laser pulses can sometimes generate small circular cracks on the surface of the windows. These small surface irregularities can diffuse the laser energy inside the investigated section, thus increasing the background noise.

A great issue of this design is that the insertion of the Suprasil® windows inside the cavities need to simultaneously guarantee good sealing properties and a good positioning with respect to the inner wall of the channel. In other words, pushing the windows deeper inside the holes would make the channel more leakage-proof but at the same time the windows could exceed the channel wall level, thus creating a small obstacle for the gas flow. A future design may try to separate these two functionalities with two different elements.

Finally, good sealing properties may be achieved by using vacuum grease at the level of the O-rings. However, vacuum conditions inside the channel slowly move the grease inside the tested channel and, therefore, its use has been judged to be incompatible with investigations of gas flows in a millimetric channel. Other sources of perturbations in the gas flow are given by surface imperfections at the Suprasil®-PEEK® interface and residual fibers of PEEK® that results from the machining of the piece.

Channel dimensions

The channel length L = 20 cm has been easily measured with a ruler. The characterization of the section dimensions is, instead, more difficult to be carried out precisely. The only dimension of the channel section that could be directly measured is the height of the channel, which is the most important geometric parameter for the velocity

reconstruction by means of MTV. Figure 4.39 represents a picture taken with the ICCD of a portion of the channel gap that can be seen in Figure 4.38b through the borosilicate window, which is the region investigated by MTV.

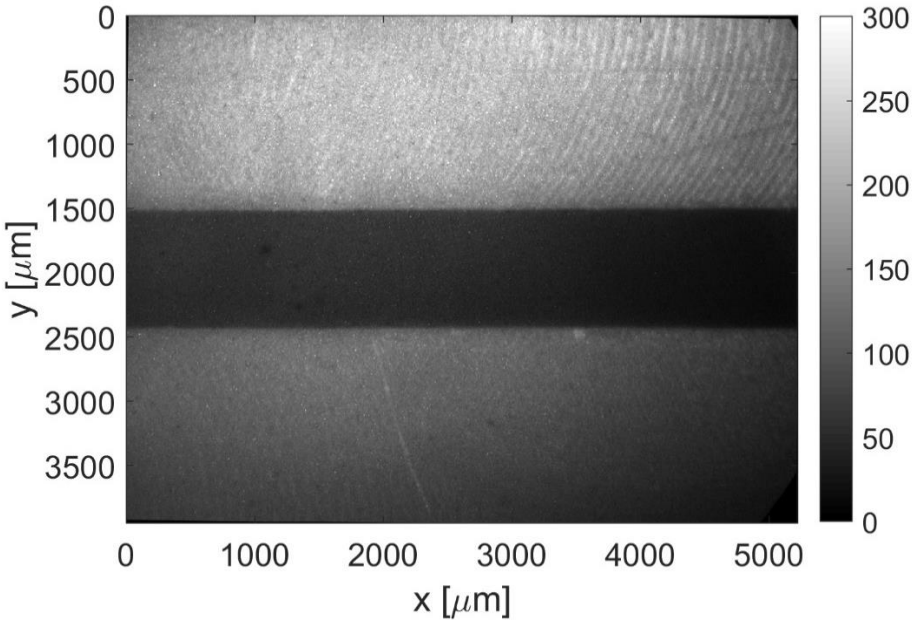

Figure 4.39. Image recorded with the ICCD of the channel gap in the region of interest for MTV. The image represents the outermost channel height in the direction of the channel width.

The image has been recorded without binning, in order to exploit the best resolution of the CCD, which is 3.8 μm. By considering different locations on the image in the *x* direction, the top and bottom positions of the gap have been repeatedly measured. Because the localization of the wall position is made by eye, the repeated measurements take also into account the statistical fluctuations generated by the visual perception. From 40 measurements, a mean value of H = 913.5 μm with an uncertainty of 0.98 μm has been calculated. The measured height represents the channel height at the outermost section in the direction of the width. Pictures in the interior region could not be recorded with sufficient clarity for detecting the top and bottom wall position. Therefore, the only measure available is the channel height in the outermost transversal section. The channel height has also been observed with a microscope at the entrance and at the exit sections of the channel. These observations confirmed that the height is less than 1 mm and close to 910 μm. However, even though this value of the height is probably characteristic of most of the cross-sections along the channel length, the height of the cross-section at the middle position $x = L/2$ along the channel length, that is the section investigated by MTV, may vary with the actual position of the Suprasil® windows inside the cavities. If the glass windows are not pushed inside the cavities enough, the wall distance will be larger than the measured value of H. Actually, the velocity reconstruction from MTV data, which will be explained in Chapter 6, requires the actual channel height at the section of investigation, which is not necessarily 913.5 μm. In Chapter 6, a post-processing procedure for detecting the real positions of

the walls in the channel region investigated by MTV is presented. From this methodology, the channel height has been measured to be 1003 µm. Therefore. while the characteristic height along the channel is considered to be H = 913.5 µm, the channel height used for MTV velocity measurements is, instead, H_{MTV} = 1003 µm.

The width b of the section could not be directly measured. The inlet and outlet of the channel did not allow enough visual access for observing with the microscope the entire channel width, but only a part of it. Even though the mass flow rate measurement by CV technique does not depend on the section dimensions and even though MTV technique requires only a precise measurement of the channel height, an accurate measurement of the channel width is necessary for a correct calculation of the average flow speed from the mass flow rate measurements. Fortunately, the uncertainty on the averaged flow speed given by the uncertainty on the width are not so important, as it will be discussed in detail in Chapter 6.

The channel width b has been indirectly defined by trying to fit the experimental mass flow rate measurements with the theoretical solution of the mass flow rate given by Eq. (2.69). The characterization of the section width has been done by considering argon-acetone gas flows driven by a moderate inlet-outlet pressure ratio, in order to minimize the compressibility effects. The gas flow has been generated through the channel by pumping out the argon-acetone mixture from the upstream reservoir. As the pressure inside the reservoir decreases, the average pressure inside the channel varies from about 13 kPa to 5.5 kPa and the mass flow rate decreases in time as well. Figure 4.40 reports a comparison between the measured mass flow rate $\dot{m}$ and the numerical solution $\dot{m}_{rect,S1}$ of Ebert & Sparrow (1965). The reader is directed to Chapter 6 for further information regarding the procedure for measuring the mass flow rate by means of CV technique. By setting the channel width to b = 5800 µm, the difference between the experimental and the numerical mass flow rates is reduced to less than 1.5%.

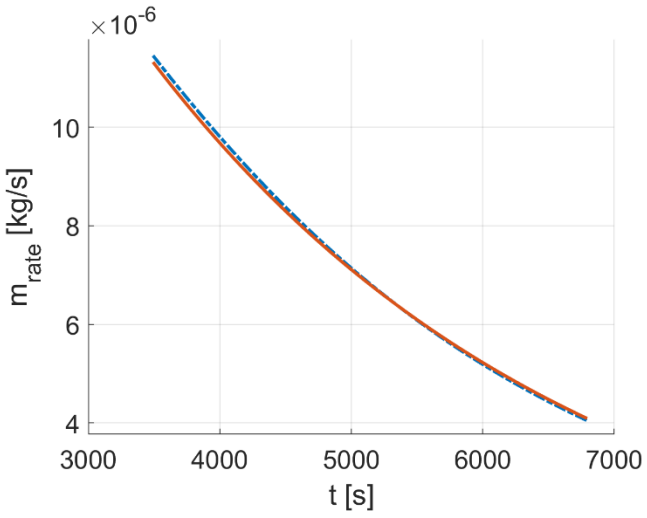

Figure 4.40. Comparison of the experimental mass flow rate $\dot{m}$ (solid red line) and the theoretical solution $\dot{m}_{rect,S1}$ (dashed blue line) of Ebert & Sparrow (1965).

As it will be discussed in Chapter 6, because of the distributed and concentrated head losses from the pressure sensor to the inlet/outlet section of the channel, the upstream and downstream pressure measurements do not correspond exactly to the inlet and outlet pressures. The numerical solution $\dot{m}_{rect,S1}$ depends on the pressure ratio applied at the channel ends, and, therefore, the precision in estimating the width b with this strategy depends on the precision of estimating the actual inlet and outlet pressures. Moreover, any imprecision on the value of H affects the calculated width b for matching the theoretical mass flow rate to the experimental mass flow rate. In order to take into account all these uncertainties, the uncertainty on b is overestimated to be ±200 μm. As it will be discussed in detail in Chapter 6, the calculation of the average velocity from the experimental mass flow rate will be carried out by taking into account these uncertainties on the width.

The experimental procedure

The procedure for generating the experimental flow is the following:

1) valve V1 is closed, and the two tanks are vacuumed through valves V11 and/or V4-V7.
2) the gas-tracer mixture is prepared inside the two tanks. The channeling of the tracer vapor and of the gas is made through valve V4: the tracer vapor is introduced first in the tanks at the desired pressure through valve V5, and, afterwards, the gas from the pressurized bottle is added through valve V5 to reach the total gas pressure of interest. Once the mixture is prepared, valve V4 is closed;
3) valve V2 is open, and the two pumps are activated. Valve V3 can be completely or only partially open to control the pumping power;
4) valve V1 is open and the gas flows through the channel.

At step 2, the prepared mixture is left in the tank for at least 1 hour for assuring a perfect mixing between gas and tracer vapor. Once valve V1 is open, the pressure inside the tanks starts to decrease, and the inlet-outlet pressure conditions applied to the channel vary in time. Sensors P1 and P2 monitor the pressure evolution at the two sides of the channel. P1 and P2 may not correspond exactly to the pressures, respectively, at the inlet and the outlet of the channel because of the distributed head losses provided by valves V1 and V2 and the concentrated head losses provided by the section variation at the inlet or outlet of the channel. The data recording of pressure measurements P1 and P2 starts just before step 4.

One experiment starts at the moment of opening valve V1 and ends whenever the data recording is terminated. In the following of this work, one of this experiment is indicated as “experimental run”.

Combined application of MTV and CV techniques

Because of the pressure inside the tanks decreases in time, the pressure difference $\Delta p = p_1 - p_2$ applied at the channel ends and the average pressure inside it decreases in time as well. The result is an unsteady gas flow rate that decreases as the time passes.

MTV technique requires, however, a steady gas flow for being applied. More precisely, the velocity profile to be measured needs to be the same during the image acquisition. While the physical phenomenon observed, namely the molecular displacement of tagged molecules, takes place on characteristic times of the order of 100 μs, the image acquisition requires more time, of the order of 10 seconds. As discussed in Section 4.3.3, more than one laser excitation is needed to produce sufficient light on the CCD sensor and to provide an image that contains exploitable information on the molecular displacement. The rapidity of the acquisition of one image is limited by the repetition rate of the laser system. For the highest available repetition rate, 20 Hz, one image of 100 laser pulses required 5 seconds to be recorded. If the investigated velocity profile varies slowly and in an acceptable range during at least 5 seconds, the recorded image is representative of one physical condition.

In order to slow down the rate of variation of the pressure conditions and, thus, maintaining as steady as possible the experimental conditions for applying MTV technique, the gas system is composed by very large tanks. For a given mass flow rate, the decrease of pressure in the upstream reservoir is much slower as the volume of the reservoir increases. While on the one hand tanks that are as big as possible are preferred from this point of view, on the other hand evident limitations in space and costs require the prior identification of the minimal volume required for guaranteeing a stable flow rate for at least one MTV image acquisition. The dimensioning of the gas system passed through numerical simulations governing the evolution of the pressure in the upstream and downstream reservoirs.

The use of two vacuum pumps at the outlet of the channel is justified by a much better stability of the experimental conditions for MTV. Actually, a simpler gas circuit with similar time-dependent experimental conditions could be developed from the current one by simply substituting the pumping system with one of the two tanks. For this setup, the pressure drop of the upstream tank would be accompanied by a correspondent pressure increase in the downstream tank. Differently from the setup of Figure 4.36, this concept would have had the additional advantage of having an experimental flow with a constant average pressure in the channel and only a varying inlet-outlet pressure difference. Nevertheless, a more stable velocity profile can be achieved if the downstream pressure is maintained low and far from the upstream pressure. This result is mainly due to the fact that the velocity profile is much more sensitive to the inlet-outlet pressure difference than to the average pressure. The simple pressure relaxation of the gas from the upstream tank to the downstream tank results in a too rapid drop of the pressure difference and too rapid variation of the velocity profile, making the MTV application not possible.

While from one side, the non-stationarity of the flow rate makes the MTV acquisitions more complicated, on the other side this unsteadiness turns to be favorable for a simultaneous application of the constant volume technique. The details on the application of the technique are discussed in Chapter 6.

The upstream-reservoir volume

The application of the constant volume technique for measuring the mass flow rate passing through the channel from the pressure variation inside the tanks requires an accurate evaluation of the upstream reservoir volume V_R. The total volume takes into account the volume of the two tanks, the small volume of the valves, and the volume of the connecting pipes. With reference to Figure 4.36, the reservoir volume corresponds to the zone limited by the dashed line.

The methodology here used for measuring the reservoir volume is based on a simple thermodynamic experiment. At first, the reservoir is vacuumed through valve V11 until reaching a pressure between 10 to 500 Pa. Here, valves V8, V9, V10, and V12 are kept open, while V1 and V4 are closed. Once the desired pressure in the reservoir has been attained, valve V11 is closed and a bottle with known volume V_b is attached to the connection at V11. At this stage, the pressure in the reservoir is p_R and the pressure in the bottle is p_b, which corresponds to the atmospheric pressure. By opening valve V11, the reservoir-bottle system relaxes towards a thermodynamic equilibrium attaining an equal pressure p_{eq}. Since the initial and the final state are at steady state certainly at the same temperature, the reservoir volume V_R can be calculated from

$$p_R V_R + p_b V_b = p_{eq}(V_R + V_b). \tag{4.15}$$

This same procedure has been applied for measuring volumes V_{T1} and V_{T2} of tanks T1 and T2.

The accuracy on the value of V_b is crucial for the accurate measurement of volume of interest. Its value has been calculated by filling the bottle with water and by measuring its weight with a balance. The empty bottle has a mass of m_b = 1270 g. As the bottle is completely filled with water, the mass is $m_{b,filled}$ = 1755 g. By considering a water density of ρ_{H_2O} = 0.997 kg/m^3, the volume of the bottle is calculated as

$$V_b = \frac{m_{b,H_2O} - m_b}{\rho_{H_2O}} = 486.5 \text{ ml}. \tag{4.16}$$

The experience described above has been repeated several times and the results are reported in Table 4.6, Table 4.7, and Table 4.8, respectively for the reservoir volume, T1 tank volume, and T2 tank volume. In the tables, the pressures in the bottle and in the reservoir before connecting the two systems and the pressure at equilibrium are reported as well for each experiment.

The average volumes are V_R = 175.98 l, V_{T1} = 87.72 l, and V_{T2} = 87.71 l, with corresponding standard deviation σ_{V_R} = 138.8 ml, $\sigma_{V_{T1}}$ = 143 ml, $\sigma_{V_{T2}}$ = 241.5 ml, and relative uncertainty 0.08%, 0.16%, and 0.3%.

p_b[Pa]	p_R[Pa]	p_{eq}[Pa]	V_R[l]
99643.08	23.92	298.92	175.74
99652.72	298.73	572.57	176.02
99659.74	572.22	845.29	176.10
99642.76	839.39	1111.69	176.04

Table 4.6. Measurement of the reservoir volume by relaxation of pressure p_b and p_R towards the equilibrium pressure p_{eq}.

p_b[Pa]	p_{T1}[Pa]	p_{eq}[Pa]	V_{T1}[l]
100005.5	19.95	570.12	87.93
99264.73	10.56	559.19	87.53
99088.32	32.68	579.36	87.66
99654.62	101.03	650.89	87.59
99645.25	299.03	846.08	87.86
99647.37	500.11	1046.61	87.77

Table 4.7. Measurement of tank T1 volume by relaxation of pressure p_b and p_{T1} towards the equilibrium pressure p_{eq}.

p_b[Pa]	p_{T2}[Pa]	p_{eq}[Pa]	V_{T2}[l]
99165.85	17.51	564.63	87.68
99113.23	22.01	568.64	87.70
99204.89	24.48	572.03	87.63
99290.56	101.23	651.03	87.28
99639.38	298.45	844.83	87.97
99649.41	496.51	1041.61	88.01

Table 4.8. Measurement of tank T2 volume by relaxation of pressure p_b and p_{T2} towards the equilibrium pressure p_{eq}.

4.4.3 Pressure sensors

The pressure in the gas systems is monitored by means of Inficon® capacitance diaphragm gauges. Depending on the pressure range investigated, pressure sensors with full scale reading value between 13.3 Pa and 133000 Pa have been used. The pressure sensor with the smallest full scale has been used for quantifying the leakages inside the visualization chamber, the tanks, or the channel. The resolution of the pressure sensors is 0.03% of the full scale, and the uncertainty on the measure is 0.15% of the reading. The characteristic time response of these sensors is 30 ms, and it is definitely smaller than the characteristic time of pressure variations recorded during MTV experiments, which is on the order of hours.

4.5 Conclusions

In this chapter, the experimental setups used in this work have been described in detail. The instrumental uncertainties of the ICCD, the energy detector, and the pressure sensors have been discussed in relation to the statistical fluctuations of the experimental conditions. In the next chapter, the first of the two gas systems presented is used for investigating the phosphorescence emission of acetone and diacetyl vapors.

References

Bryant, R. A., Donbar, J. M., & Driscoll, J. F. (2000). Acetone laser induced fluorescence for low pressure/low temperature flow visualization. *Experiments in Fluids*, *28*(5), 471-476.

Ebert, W. A., & Sparrow, E. M. (1965). Slip flow in rectangular and annular ducts. *Journal of Basic Engineering*, *87*(4), 1018-1024.

Hiller, B., Booman, R. A., Hassa, C., & Hanson, R. K. (1984). Velocity visualization in gas flows using laser-induced phosphorescence of biacetyl. *Review of Scientific Instruments*, *55*(12), 1964-1967.

Lozano, A., Yip, B., & Hanson, R. K. (1992). Acetone: a tracer for concentration measurements in gaseous flows by planar laser-induced fluorescence. *Experiments in fluids*, *13*(6), 369-376.

Parmenter, C. S., & Poland, H. M. (1969). Fluorescence, Phosphorescence, and Triplet Formation in Biacetyl at Low Pressures. *The Journal of Chemical Physics*, *51*(4), 1551-1558.

Pringsheim, P. (1949). Fluorescence and phosphorescence.

Stier, B., & Koochesfahani, M. M. (1999). Molecular tagging velocimetry (MTV) measurements in gas phase flows. *Experiments in Fluids*, *26*(4), 297-304.

Thurber, M. C., Grisch, F., Kirby, B. J., Votsmeier, M., & Hanson, R. K. (1998). Measurements and modeling of acetone laser-induced fluorescence with implications for temperature-imaging diagnostics. *Applied optics*, *37*(21), 4963-4978.

Tran, T., Kochar, Y., & Seitzman, J. (2005). Measurement of Liquid Acetone Fluorescence and Phosphorescence for Two-Phase Imaging. In *43rd AIAA Aerospace Sciences Meeting and Exhibit* (p. 827).

Chapter 5

Experimental analysis of acetone and diacetyl phosphorescence

This chapter presents the experimental results on the phosphorescence emission of acetone and diacetyl vapors at low pressures. In the first section, the motivations behind the necessity of this experimental analysis are presented. The first part of the chapter provides a qualitative analysis of the phosphorescence intensity and lifetime of the tracer vapors of interest. In the second part of the chapter, a mathematical model is formulated for providing an explanation and a quantification of the observed experimental results. The interest in acquiring a more in-depth knowledge of the physical processes happening at the intramolecular level is motivated in the context of MTV applications. The quantitative analysis reported in Section 5.4 also revealed information that are of key importance even for other molecular tagging techniques, such as MTT.

5.1 Motivation of this experimental analysis

This work aims to apply MTV technique to gas flows in the slip regime through a channel with a rectangular section. For attaining these rarefied conditions, the Knudsen number of the flow $Kn_H = \lambda/H$ should be increased at least up to values of the order of 0.01. This can be done, in theory, by reducing the height of the channel H or by increasing the mean free path λ of the gas. However, the precision of the MTV measurement decreases with the channel size mainly because of the bigger size of the laser beam with respect to the magnitude of molecular displacement to be measured.

Because of the limitations in reducing the channel height, attainting the slip flow regime necessarily requires increasing the mean free path of the gas, that is decreasing its average pressure. However, low-pressure conditions reduce the light signal intensity generated by the excited molecular tracer because of three reasons:

1) the number of tracer molecules present in the gas mixture is lower, thus reducing the amount of light emitted;

2) the molecular diffusion of the tracer molecules through the background gas increases, thus spreading in the space the emitting molecules and destroying the tagged line signal;

3) the relative importance of oxygen quenching increases, thus reducing the phosphorescence quantum yield.

While the third issue can be solved by an experimental setup with good sealing properties, the first two phenomena cannot be avoided and are inevitably present in low-pressure MTV analysis. The reduction in the light intensity limited until now the application of MTV to gas flows in the slip regime. In this context, the experimental analysis

presented in this chapter aimed to the exploration of the phosphorescence emission of acetone and diacetyl vapors at low pressures in order to reveal the feasibility of MTV application to the aimed experimental conditions.

5.1.1 Digital spatial resolution: the CCD and the optical system

For a given magnification power of the optical system and for a given spatial resolution of the CCD sensor, reducing the height of the channel reduces the number of CCD pixels available for representing the gas velocity gradients in the direction perpendicular to the channel walls and for capturing the molecular displacement of the tagged molecules in the flow direction. The current ICCD provides between 263 and 66 pixels, respectively without binning and with a 4 × 4 binning, for representing the 1-mm height of the channel used in this experimental work. For a smaller channel, maintaining the same spatial resolution would require either increasing the spatial resolution of the CCD sensor or increasing the magnification power of the optical system. While the former requires a more expensive sensor, the latter option has the drawback of reducing the amount of light collected, which, in the experimental conditions of interest, is a factor of fundamental importance. More expensive objective lenses are necessary for increasing the magnification without losing too much light. From this point of view, the minimum channel height is limited by the characteristics of the CCD and the optical system employed.

5.1.2 Uncertainty on the tagged line position: the laser beam size

The precision of the MTV technique is not only limited by the spatial resolution of the acquisition system but also, and mainly, by the uncertainty on the identification of the tagged line position. In this regard, the size of the laser beam has a fundamental role. Figure 5.1 shows two gaussian distributions, one thinner the other thicker, that can represent the light emission produced by a laser excitation, respectively, with a focused energy distribution and a more spread energy distribution.

In the absence of any noise in the light intensity distribution, the position of the intensity peak can be identified with the maximum precision for both the distributions. However, because of the fluctuations in the light distribution, there is an uncertainty associated with the localization of the Gaussian peak. This uncertainty is determined by the relationship between the SNR of the light emission and the standard deviation of the Gaussian profile. It can be imagined that, if the distribution is flatter in the peak region, the fluctuations in the intensity distribution can hide easier the position of the peak.

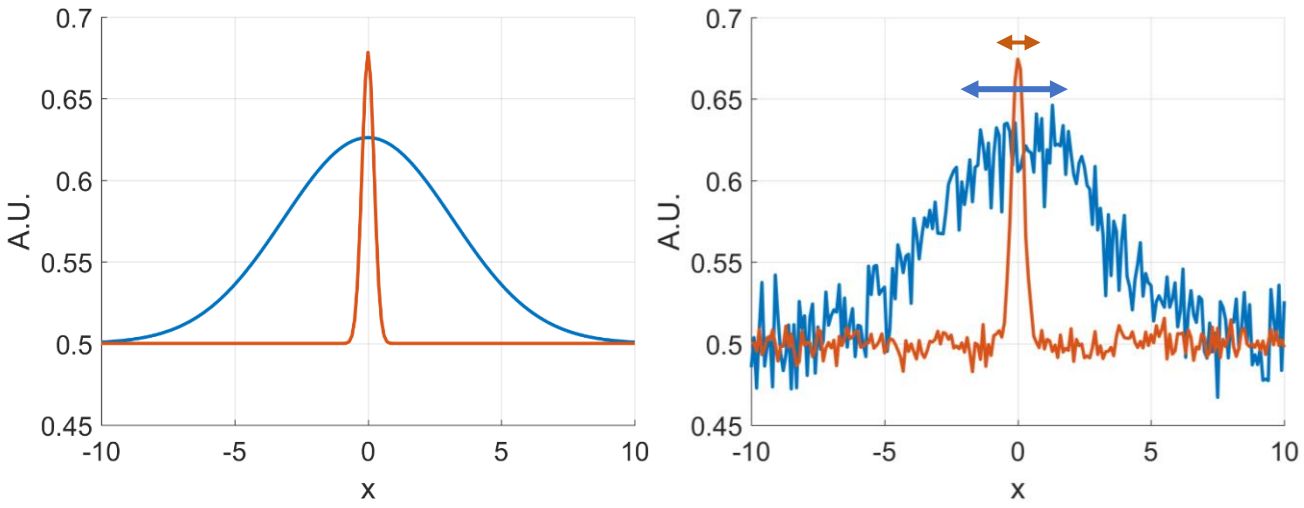

(a) (b)

Figure 5.1. Illustration of the role of the laser beam diameter in the determination of the intensity peak position. The red and the blue curves are two Gaussian distributions, respectively, with small standard deviation and large standard deviation: (a) distribution with unlimited SNR; (b) distribution with limited SNR.

Nevertheless, the ultimate evaluation of the precision of MTV measurements does not depend only on the absolute uncertainty in the tagged line position but on the ratio of this uncertainty to the mean molecular displacement that needs to be measured. Therefore, the reason why the laser beam diameter needs to be smaller enough with respect to the channel height is only indirectly related to this fact. In first approximation, the average velocity $\bar{u}$ through the channel section is proportional to H^2 and to dp/dx. If, for instance, the channel height is halved, the pressure gradient needs to be quadrupled for maintaining the same flow speed. Because for the same inlet-outlet pressure differences a reduction in the channel height provides lower average gas velocities through the channel section, the resulting mean displacement of the tagged molecules is smaller and, thus, the relative uncertainty on the tagged line position increases. However, if the pressure gradient can be increased accordingly to the reduction of the channel height, no reduction in the laser beam diameter is required for maintaining the same uncertainty in the measurement of the molecular displacement.

Regardless of the channel height employed, for a given SNR a thinner tagged line can provide higher precision in the measurement of the mean molecular displacement than a thicker tagged line can do. As it will be further discussed in Section 5.3.8, the precision in measuring the molecular displacement is dominated by the SNR of the intensity distribution and not by the spatial resolution provided by the ICCD.

5.2 Intramolecular processes in photoluminescence phenomena

Photoluminescence represents the ensemble of intramolecular processes that occur when a molecule that absorbs a photon resends part of the energy back, after some time, in the form of light. Differently from other processes such as Rayleigh or Raman scattering, the absorption process in photoluminescence necessarily involves an electronic transition to a higher energetic state. More precisely, an electron of valence, that is an electron of the most external orbitals that belongs to a specific chemical bond in a molecule, jumps to a higher energetic orbital.

A good tool for representing the possible intramolecular processes that follow the photon absorption is the Jablonski's diagram, which is illustrated in Figure 5.2. In this representation, each horizontal line corresponds to a specific energy level: as the stocked energy increases, the molecule state goes up in the diagram. However, not all the horizontal black lines in the Jablonski's diagram represent the same form of energy. The thick lines refer to different electronic states, while the thinner lines represent mechanical energy that is stocked in activated vibrational and rotational modes of the molecule.

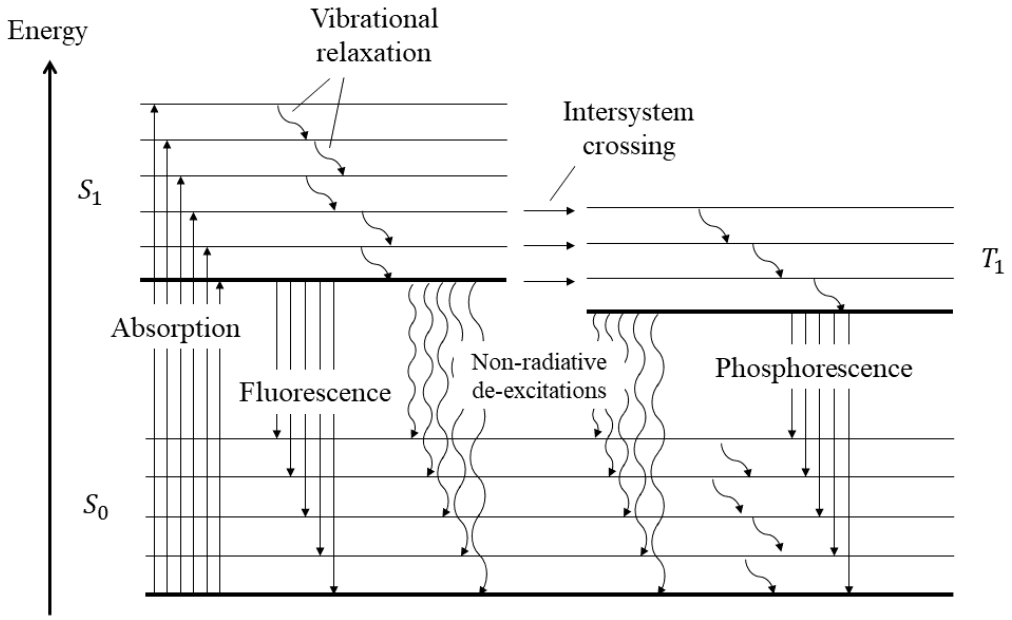

Figure 5.2. Jablonski energy-level diagram. The straight lines represent radiative processes, the wavy lines represent non-radiative processes. The non-radiative de-excitations include both internal and external conversions.

S_0 is the singlet ground state of the molecule, that is when the electron of valence is in its stable orbital. At the moment of the photon absorption, the electronic transition $S_0 \rightarrow S_1$ occurs, where S_1 is the excited singlet state and in which the electron of valence jumps to the higher orbital. In a singlet state, the spins of the two electrons are paired and, thus, they exhibit no magnetic field. Singlet molecules are diamagnetic, that is they are neither attracted nor repelled by a magnetic field. In the singlet excited state, the molecule may go through a changing in

the spin of the excited electron. This possible internal conversion is known as inter-system crossing (ISC), which produces the transition $S_1 \rightarrow T_1$, with T_1 the excited triplet state. The direct transition $S_0 \rightarrow T_1$ is not allowed as it would also require a change in the spin of the electron. This process is known as a "forbidden transition" in quantum mechanics. Because triplet molecules have unpaired electrons, they are paramagnetic. This means that triplet molecules can interact with a magnetic field and can be subjected to either an attracting or a repelling force. The terms "singlet" and "triplet" derive from the definition of multiplicity of an energy level. By defining Γ_S the total spin angular momentum, the multiplicity of the energy state is given by $2\Gamma_S + 1$. In a singlet state, the electrons have the opposite spin, so that $\Gamma_S = 0$ and its multiplicity is one. The triplet state, instead, has two unpaired electrons which provides $\Gamma_S = 1$ and a multiplicity of 3.

A molecule in its excited state is a metastable system, as it tends, after some time, to de-excite back to its stable electronic configuration, namely the ground state. As it will be discussed in detail in the next section, the transition of an excited molecule to the ground state can happen through various intramolecular processes. When the de-excitation takes place by means of a radiative process, the molecule loses energy by emitting a photon. Because of the different nature of the electronic configuration between S_1 and T_1, the radiative decay of a singlet molecule has very different characteristics in terms of lifetime and probability with respect to those of the radiative decay of a triplet molecule. The radiative de-excitation $S_1 \rightarrow S_0$ is called *fluorescence*, while the radiative transition $T_1 \rightarrow S_0$ is called *phosphorescence*.

For each electronic configuration, that is S_0, S_1, and T_1, the molecule can assume different vibrational-rotational states. As the complexity of the molecule structure increases, the number of possible vibrational-rotational modes increases, so the possible energetic levels in each electronic state. The number of possible vibrational modes N_v corresponds to

$$N_v = 3N_{atom} - 6. \tag{5.1}$$

Since the number of atoms for acetone (C_3H_6O) and diacetyl ($C_4H_6O_2$) are N_{atom} = 10 and N_{atom} = 12, the two molecules have, respectively, N_v = 24 and N_v = 30 vibrational modes. The number of vibrational-rotational modes that are activated in a gas system in thermodynamic equilibrium depends on its temperature T. The initial energy level E_{S_0} of a molecule in the singlet ground state S_0 is given by

$$E_{S_0} = E_{S_0-0} + \Delta E_{thermal}(T), \tag{5.2}$$

where E_{S_0-0} is the lowest energy level in the ground state and $\Delta E_{thermal}(T)$ is the energy stored in the activated vibrational-rotational modes, which is a function of the temperature T. By assuming that the vibrations are modelled as simple harmonic oscillators, the thermal energy at a temperature T can be determined as the sum of the vibrational energies:

$$\Delta E_{thermal}(T) = \sum_{i=1}^{N_v} \frac{h\nu_i}{e^{h\nu_i/k_B T} - 1}, \tag{5.3}$$

where ν_i is the vibrational frequency of each mode. Once a molecule absorbs a quantum of light, the photon energy may both modify the electronic configuration and activate new vibrational-rotational modes or deactivate some of them. A transition that simultaneously produces a change in the electronic level and in the vibrational level is called *vibronic transition*.

By considering a photon with frequency ν_{ex} and energy $E_{ph} = h\nu_{ex}$, the energy level of the molecule in the singlet excited state S_1 corresponds to:

$$E_{S_1} = E_{S_0} + h\nu_{ex} = E_{S_1-0} + \Delta E_{thermal}(\tilde{T}), \tag{5.4}$$

where E_{S_1-0} is the lowest energy level in the singlet excited state and $\tilde{T}$ is the new temperature of the molecule, which can be higher or lower than T_0. Immediately after the photon excitation, the gas is in thermodynamic non-equilibrium and, thus, the vibrational and rotational temperatures are different from the translational temperature. Because of the quantum nature of the molecule, the transition $S_0 \rightarrow S_1$ can occur only if the energy $h\nu_{ex}$ of the absorbed photon is high enough for $E_{S_0} + h\nu_{ex}$ being equal or higher than the energy jump E_{S0-S1} between S_0 and S_1. Since the lowest energy level in the triplet state is lower than the lowest energy level in the excited singlet state, the energy separation between S_0 and T_1 is smaller than that between S_0 and S_1. Therefore, the phosphorescence spectrum is usually composed by photons with higher wavelength with respect to those of fluorescence spectrum. The spectrum properties of fluorescence and phosphorescence emissions of acetone and diacetyl vapors are reported in the previous chapter.

During the absorption process, the energy excess, that is $\left(E_{S_0} + h\nu_{ex}\right) - E_{S0-S1}$ may be high enough to excite the electron to an even higher orbital, for instance S_2, or even to break the chemical bond thus enabling photodissociation. From S_2, it is common that the internal conversion $S_2 \rightarrow S_1$ occurs, in which the energy electronically stored is converted in vibrational-rotational energy. In the following section, only the intramolecular processes that occur from the singlet state S_1 towards the de-excitation to the ground state S_0 are discussed.

5.2.1 Radiative and non-radiative de-excitations

The Jablonski's diagram of Figure 5.2 illustrates the most important intramolecular transitions. These processes can be classified in radiative transitions,

i) *fluorescence* and

ii) *phosphorescence*,

and non-radiative transitions,

iii) *vibrational-relaxation*,

iv) *molecular quenching*,

v) *intersystem crossing*, and

vi) *internal non-radiative de-excitation*.

In the case of radiative transitions, the spontaneous de-excitation produces the emission of a photon with a frequency ν_e, which value depends on the energy jump of the transition. The emitted photon can produce an energy jump that brings the molecule to an energy level higher, equals to, or lower than the initial energy level E_{S_0}:

- if the emitted photon has less energy than the absorbed one, the energy difference is known as *Stokes shift*;
- if the emitted photon has more energy than the absorbed one, the energy difference is known as *anti-Stokes shift;*
- if the emitted photon has the same energy of the absorbed one, this process is known as *Rayleigh's resonance*.

Therefore, the final energy level that the molecule acquires in the ground state after the de-excitation will depend on the frequency of the emitted photon. The determination of the probability of having a de-excitation from a certain vibrational-rotational state of the electronically excited state to a specific vibrational-rotational state in the ground state follows the *Frank-Condon principle*, which states that the highest probability of absorption or emission occurs when the starting and the final vibrational state wave functions overlap the most.

In the case of non-radiative transitions, no photon emission occurs, and, instead, modifications in the electronic configuration and/or in the vibrational-rotational state of the molecule are accompanied by internal or external energy transfers. Internal conversions happen spontaneously without involving the interaction with the environment. These intramolecular processes can result in a phenomenon where a molecule relaxes from a higher electronic state to an upper vibrational energy level of a lower electronic state. This can happen in a singlet-singlet transition where no change in electron spin occurs, like $S_2 \rightarrow S_1$, or in the intersystem crossing transition $S_1 \rightarrow T_1$ with electronic spin inversion. While in these cases the internal energy in the molecules does not change but only transforms from the electronic form to the vibrational-rotational form, there exist other internal non-radiative de-excitations that produce a loss of the internal energy and that is transferred into the translational energy of the molecule. The radiative processes can be considered as internal conversions as well, since they happen spontaneously without any external trigger. External conversions, such as vibrational-relaxation or molecular quenching, involve, instead, the interaction with the environment, i.e., another molecule, with a consequent energy transfer. Depending on the type of interaction, the excited molecule loses energy by electronic de-excitation or by de-activation of vibrational-rotational modes. The decrease in internal energy of the considered excited molecule is always accompanied by an increase of energy of the environment. All the energy losses that the molecule encounters are dissipated in heat, which increases the internal or translational temperature of the surrounding

molecules. Because of the energy dissipation that occurs between the absorption and the re-emission, an absorbed photon with energy $h\nu_{ex}$ is sent back with an energy $h\nu_e$ that is always equal or, more likely, lower. External conversions other than vibrational-relaxation and molecular quenching exist, such as the photosensitization, also called the Forster resonance energy transfer (FRET), but they are not discussed in the following sections.

The quantum yield of fluorescence or phosphorescence represents the percentage of excited molecules that radiatively decays. However, this simple definition of the quantum yield hides the fact that its value is strictly dependent on the singlet or triplet lifetime and on the single characteristic times of the intramolecular processes. More precisely, the value of the quantum yield ϕ is determined by the competition between the radiative and non-radiative processes. A simple example can clarify this idea. Consider 100 excited molecules, a radiative transition that is characterized by a rate of 10 photons per second, and a non-radiative transition that produces the de-excitation of 10 molecules at each second. In this scenario, all molecules de-excite in 5 seconds: 50 molecules de-excite by emitting a photon, and 50 molecules de-excite without emitting a photon. Therefore, in this case, the lifetime of the excited molecule population corresponds to 5 seconds and the quantum yield is equal to 50%. If now we consider the same initial number of excited molecules, that is 100, the same radiative rate, i.e., 10 photons per second, but a non-radiative transition that produces the de-excitation of 90 molecules per second, the lifetime of the excited molecules population is reduced to 1 second and the quantum yield is reduced to 10%.

In the following sections, each of the intramolecular processes above listed are discussed and characterized by a rate k or, equivalently, a characteristic time $\tau = 1/k$. In some contexts, the use of the rate k makes the description of the intramolecular process easier; in other contexts, the characteristic time τ is more useful for comparing the rapidity of different intramolecular processes. In Section 5.2.4, experimental values found in the literature of the characteristic times and of the quantum yields characterizing acetone and diacetyl vapors are reported and summarized in tables.

i. Fluorescence

Fluorescence is the radiative spontaneous de-excitation from the excited singlet state S_1 to the singlet ground state S_0. Fluorescence emission is, usually, strong and very fast. The occurrence of this radiative transition is, indeed, very improbable. The rate of fluorescence emission k_f is very high in comparison, for instance, to the rate of phosphorescence emission, but because the non-radiative transitions that take place from the excited singlet state are even faster and more probable, the fluorescence quantum yield, that is the percentage of excited singlet molecules that produce fluorescence, is very low. The main non-radiative transition that limits the fluorescence quantum yield is the inter-system crossing, which transforms a singlet into a triplet. However, even though very few excited singlets radiatively decay to the ground state, fluorescence intensity is usually stronger with respect to the phosphorescence emission because of the relatively high k_f. Acetone vapor is characterized by a characteristic

time of fluorescence $\tau_f = 1/k_f$ of about 1 μs, but its low quantum yield ϕ_f = 0.2% makes the observed fluorescence lifetime τ_{S_1} as fast as 4 ns (Breuer & Lee, 1971). In diacetyl vapor, the non-radiative transition to the triplet state is slightly slower than in acetone, but the characteristic time of fluorescence emission is even higher than that of acetone, of the order of 10 μs. Even though its fluorescence quantum yield is 0.25%, even slightly higher than that of acetone, diacetyl fluorescence intensity is weaker than acetone fluorescence, since the photons are emitted at a rate that is an order of magnitude slower than that of acetone. For some molecules, the non-radiative transition is very much faster than the rate of fluorescence emission, so that no fluorescence is shown at all, even though phosphorescence is exhibited. For instance, this is the case of benzophenone, in which the energy separation between the lowest energy level in the excited singlet state S_1 and the lowest energy level in the triplet state T_1 is so small that the transition $S_1 \rightarrow T_1$ is essentially complete (Backstrom & Sandros, 1960).

ii. Phosphorescence

Phosphorescence is the radiative transition of the triplet molecules to the ground singlet state. It is believed that because a change in electron spin is required during this transition, the rate of occurrence of this radiative transition is much lower than that of fluorescence. Because the internal non-radiative transitions happening in the triplet state are generally slower than the non-radiative transitions happening in the singlet state, the phosphorescence quantum yield is between one to two orders of magnitude higher than the fluorescence quantum yield. The characteristic time of phosphorescence is about $\tau_{ph} = 1/k_{ph}$ = 10 ms for both acetone (Heicklen, 1959) and diacetyl (Sidebottom *et al*., 1972). However, the resulting lifetime τ_{T_1} of the phosphorescence emission and, equivalently, of the triplet population is about 200 μs for acetone and 1.5 ms for diacetyl (Lozano *et al*., 1992). This is because the internal non-radiative rate of the diacetyl triplet is one order of magnitude slower than that of acetone triplet, and, therefore, the phosphorescence quantum yield of diacetyl is ϕ_{ph} = 15%, that is one order of magnitude higher than that of acetone, which is ϕ_{ph} = 1.8%. These values are representative of the competition between radiative and internal non-radiative transitions. However, in presence of external conversions, that is molecular quenching, the observed quantum yield and emission lifetime are lower.

iii. Vibrational-relaxation

When an excited molecule collides with another molecule, an energy transfer between the two molecules may occur. In this eventuality, the excited molecule relaxes to a lower vibrational energy level in the same electronic configuration and the loss in energy is transferred to the other molecule, by increasing its vibrational or translation temperature. This process is called vibrational-relaxation and its rate of occurrence is proportional to the rate of intermolecular collision. By considering a HS collisional model, the rate of collisions between the excited molecules E, singlet or triplet, and molecules of another species M is expressed as (Bird, 1994)

$$\nu_{EM} = n_M \pi d_{EM}^2 \sqrt{\frac{8k_B T}{m_{EM}}}, \tag{5.5}$$

with d_{EM} and $m_{EM} = m_E m_M/(m_E + m_M)$ the average molecular diameter and the reduced molecular mass of the two species, respectively. There is a certain probability $\langle p_{vr} \rangle$ of occurrence of vibrational-relaxation following the intermolecular collision (Brown & Phillips, 1973). The rate of vibrational-relaxation k_{vr} can be calculated then as

$$k_{vr} = \langle p_{vr} \rangle \nu_{EM}. \tag{5.6}$$

The probability of vibrational-relaxation after a collision is very close to unity, so that the rate of vibrational-relaxation and the rate of collision coincides (Thurber *et al*., 1998). In acetone and diacetyl vapor at a pressure of the order of 1 kPa, the rate of vibrational-relaxation is of the order of 10^8 s^{-1}.

The rapidity of vibrational-relaxation is then proportional to the gas pressure. If the pressure is high, vibrational-relaxation is fast and brings the excited molecule down to lower energy level in the singlet or triplet state. Differently, if the pressure is extremely low, the intermolecular collisions and, thus, the vibrational-relaxations occur very rarely. This is known as "isolated molecule" condition (Parmenter & Poland, 1969; Copeland & Crosley, 1985; Anderson & Parmenter, 1970), an environment free from external perturbations that is, indeed, optimal for the quantitative analysis of internal non-radiative processes, such as internal conversions $S_1 \rightarrow S_0$ and inter-system crossing $S_1 \rightarrow T_1$. However, this condition can be obtained only at very low pressures of the order of 0.1 Pa. For higher pressures, the vibrational-relaxation is so fast that the excited molecule is brought to the lowest energy level of that electronic state before any other radiative or non-radiative processes occur. It is worth to precise that, when the gas temperature is high enough that some vibrational-rotational modes are activated at thermodynamic equilibrium, the fast vibrational-relaxation brings the excited molecule not to the lowest energy level but to the corresponding thermalized energy level, that is $\Delta E_{thermal}(T)$, Eq. (5.3). For the pressure and temperature ranges used in this experimental work, the condition of fast vibrational-relaxation is always satisfied.

Vibrational-relaxation can have an influence on the fluorescence and phosphorescence quantum yield if radiative and/or non-radiative processes show a dependency from the vibrational energy level of the molecule. If this happens, a dependency from the excitation wavelength should also be observed. In the literature, most of the works did not report any important dependency of the fluorescence rate (Breuer & Lee, 1971), phosphorescence rate (Lee & Lewis, 1980), or inter-system crossing rate (Shortridge *et al*., 1970) from the vibrational energy level. More recently, Thurber *et al*. (1998) and Yuen *et al*. (1997) experimentally observed an increase of 30-50% of the fluorescence quantum yield by increasing the pressure from 1 atm to 8 atm, that they explained by assuming a dependency of the intersystem crossing rate from the vibrational energy. Yuen and co-workers wrote:

"It is also frequently assumed that the vibrational transfer rate is fast relative to the intersystem crossing rate and that the system is vibrationally relaxed. However, the pressure dependence of the acetone LIF signal that we observe indicates that the assumption that the vibrational population distribution in the excited singlet has relaxed completely to a thermal (Boltzmann) distribution may not be valid."

iv.Inter-system crossing (ISC)

As previously introduced, the inter-system crossing $S_1 \rightarrow T_1$ is the internal conversion that produces a change in the electron spin, thus bringing the excited singlet to the triplet state. Even though non-radiative transitions of the type $S_1 \rightarrow S_0$ may exist, the intersystem crossing is the main internal process that inherently limits the fluorescence quantum yield. The probability of this transition is very close to unity because the intersystem crossing rate k_{ISC} is much higher than the fluorescence rate k_f. In diacetyl vapor, the characteristic time $\tau_{ISC} = 1/k_{ISC}$ is estimated to be of the order of 10 ns (Parmenter & Poland, 1969; Sidebottom *et al*., 1972), which is about 1000 times faster than its fluorescence rate. Similarly, acetone vapor has τ_{ISC} of the order of 1 ns (Breuer & Lee, 1971), about 500 times higher than the fluorescence characteristic time. These values for τ_{ISC} are essentially identical to the lifetime of excited singlet τ_{S1} in acetone and diacetyl. A related quantum yield for the intersystem crossing transition can be defined as

$$\phi_{ISC} = \frac{k_{ISC}}{k_f + k_{ISC}}, \tag{5.7}$$

which results being about 99.75%.

v. Molecular quenching

Molecular quenching is the non-radiative de-excitation to the ground state S_0 caused by molecular collision with a quencher species. This external conversion is similar to the vibrational-relaxation in the sense that involves an energy transfer due to intermolecular collisions. However, the transfer of energy involved in the molecular quenching is more important, since it causes the dissipation of the energy jump from an excited state to the ground state. The rate of molecular quenching is directly proportional to the quencher concentration. By considering Eq. (5.5) and that the probability of quenching after a collision with a quencher molecule of species Q is $\langle p_Q \rangle$, the quenching rate is

$$K_Q = n_Q \langle p_Q \rangle \pi d_{EQ}^2 \sqrt{\frac{8k_B T}{m_{EQ}}} = n_Q k_Q. \tag{5.8}$$

The characterization of the quenching efficiency is usually provided in terms of k_Q because it is independent of the quencher concentration. It represents the quenching rate per unit volume of quencher and has dimensions m^3/s.

The presence of a quencher reduces the quantum yield of the emission. By defining k_r and k_{nr} as the radiative and non-radiative rate, the quantum yield in absence of molecular quenching is defined as $\phi_0 = k_r/(k_r + k_{nr})$. When quenching molecules are introduced, the quantum yield $\phi(n_Q) = k_r/(k_r + k_{nr} + n_Q k_Q)$ is a decreasing function of the quencher concentration n_Q. The ratio between the ϕ and ϕ_0 provides the well-known Stern-Volmert relationship:

$$\frac{\phi}{\phi_0} = 1 + n_Q k_Q \tag{5.9}$$

The quenching constant rate k_Q is calculated by experimentally measuring the reduction of the quantum yield as a function of the quencher pressure.

Triplet molecules are more sensitive to molecular quenching than singlet molecules. In particular, oxygen quenching is very efficient in extinguishing the phosphorescence emission. It is possible that because the stable state of oxygen molecule is the triplet state, its paramagnetic property makes the quenching of paramagnetic triplets more efficient. Thurber *et al*. (1999) provided a probability of oxygen quenching of $\langle p_{O_2} \rangle$ = 0.00399 for acetone vapor, which provides a quenching rate of k_{O_2} = 3.94×10^{-18} m^3/s. Kaskan & Duncan (1950) and Sidebottom *et al*. (1972) measured from the triplet lifetime of diacetyl a quenching rate of k_{O_2} = 8.5×10^{-19} m^3/s, from which a quenching probability of $\langle p_{O_2} \rangle$ = 0.0012 is calculated. The kinetic properties of acetone and diacetyl used in these calculations have been taken from Table 5.3.

vi. Internal non-radiative de-excitation

Internal non-radiative transitions of the type $S_1 \rightarrow S_0$ or $T_1 \rightarrow S_0$ can occur in absence of any external perturbations. It is because of these internal conversions that not all molecules exhibit fluorescence or phosphorescence emissions. If the non-radiative de-excitation mechanisms happen much quicker than radiative emission, the absorbed light energy is converted in translational or roto-vibrational energy. In acetone and diacetyl vapours, singlet lifetime is dominated by the intersystem crossing transition. Triplet lifetime is dominated by the non-radiative transition $T_1 \rightarrow S_0$. The non-radiative rate k_{nr,T_1} can be calculated from the phosphorescence rate k_{ph} and the phosphorescence quantum yield ϕ_{ph} in absence of any other external non-radiative decays. Sidebottom *et al*. (1972) estimated $\tau_{nr,T1} = 1/k_{nr,T_1}$ between 1.4 and 2.3 ms for diacetyl, which is unsurprisingly close to the triplet lifetime τ_{T_1} measured by many authors (Parmenter & Poland, 1969; Almy & Anderson, 1940; Kaskan & Duncan, 1950). Similarly, τ_{nr,T_1} for acetone vapor can be estimated from the data τ_{T_1} = 200 µs and ϕ_{ph} = 1.8% as τ_{nr,T_1} = 204 µs, which, again, is very close to the measured triplet lifetime.

5.2.2 The Beer-Lambert law

This section aims to provide the excited molecule density $n_{ex,0}(x,y,z)$ generated by a laser pulse. The laser excitation is represented as a stream of photons propagating in the y-direction. The incident photon flux $N_{in}(x,y,z,t)$ [$m^{-2}s^{-1}$] provides the number of photons crossing a section perpendicular to the direction of propagation per unit time. By assuming that all the photons have energy $E_{ph} = hc/\lambda_{ex}$, where λ_{ex} is the photon wavelength, h = 6.626·10^{-34} [$m^2s^{-1}kg$] is the Plank's constant and c = 299.79·10^6 m/s is the speed of light, the laser beam can be completely defined by the irradiance function $J_{in}(x,y,z,t)$ [$m^{-2}s^{-1}J$]. In general, the laser beam can have an irradiance distribution that can evolve in time. In this work, the laser excitation is represented by a pulse lasting between 4 and 7 ns. Because the characteristic time of the excitation is much faster than the photoluminescence processes under analysis, the laser excitation is modeled as an instantaneous event characterized by an intensity function $I_{in}(x,y,z)$ [$m^{-2}J$] representing the energy density distribution on each cross-section along the direction of propagation.

The differential version of the Beer-Lambert law provides the infinitesimal variation of the laser energy density produced by the presence of an absorbing species with molecular density $n(x,y,z,t)$ along an infinitesimal path dy:

$$dI_{in} = -n\sigma_{abs}dyI_{in}, \tag{5.10}$$

where $\sigma_{abs}(x,y,z,T,\lambda_{ex})$ [m^{-2}] is the absorption cross-section of the absorbing species, which mainly depends on the excitation wavelength λ_{ex} and the vapor temperature T. In Eq. (5.10), the volume $\sigma_{abs}dy$ represents the effective volume of molecules that is going to absorb the laser energy. In the following, the absorption cross-section $\sigma_{abs}(T,\lambda)$ and the molecular density n are considered uniform in space and constant in time. During one laser pulse excitation, the light absorption may in theory reduce the number of molecules that can absorb a photon. However, since the percentage of molecules that transit to the excited singlet state is very low, the molecular concentration n is practically constant in time during the laser excitation. Moreover, depending on the photon wavelength and the laser energy density, different photolysis reactions may occur following the laser excitation. However, since the quantum yield associated to the photodecomposition is very low and since chemical recombination is possible, the occurrence of photolysis is even less important for what concerns the possibility of reducing the number of absorbers. An easy calculation demonstrates that even if all the excited molecules decompose and never recombine, laser pulses at 20 Hz can excite the same sample of vapor for 5 days in a row without substantially change the concentration n of absorbing molecules.

The integration of Eq. (5.10) along a path L_y yields to the integral form of the Beer-Lambert law, which provides the variation of laser energy density $\Delta I = I_{in}(x,0,z) - I_{in}(x,L_y,z)$ due to the energy absorption of the tracer

$$I_{in}(x, L_y, z) = I_{in}(x, 0, z)e^{-n\sigma L_y}. \tag{5.11}$$

The quantity $\ell = 1/n\sigma$ [m] is defined as the optical length of the medium. If $L_y \ll \ell$, the medium is defined as optically thin, and the laser intensity can be assumed constant along the absorption path L_y. For instance, acetone vapor at p = 15 kPa, T = 293 K, and with $\sigma_{abs}(\lambda_{ex} = 266\,nm)$ = 4.34·10^{-24} m^2 has an optical length of about 63 mm. Because the FOV of the camera has a dimension in the laser beam direction of 4 mm, the laser intensity does not vary substantially along the absorption path. The experimental observations confirm this fact as the photoluminescence intensity provided by tracer is uniform along the laser beam. Therefore, the laser excitation is described by an energy density distribution $I_{in}(x, z)$ that depends only on the position (x, z) on a cross-section perpendicular to the laser propagation direction and it is always the same for every section along all the laser beam. The resulting density distribution $n_{ex,0}(x, z)$ of excited molecules is characterized by the same invariance in the *y*-direction. The integration on a section of the laser energy distribution provides the total energy of a laser pulse

$$E_l = \int_{-\infty}^{\infty}\int_{-\infty}^{\infty} I_{in}(x, z)\, dx\, dz, \tag{5.12}$$

which is the only property of the laser pulses that is directly measured by means of the energy detector. The energy density function $I_{in}(x, z)$ cannot be directly measured but it can be inferred from the early light emission distribution of the tracer, as explained in Section 5.3.3.

Even though the laser intensity is assumed to not vary along the direction of propagation, a variation in the laser energy density dI_{in} in the *y*-direction needs to be allowed for estimating the amount of molecule excitation. The number of excited singlet molecules dN_{ex} generated in an infinitesimal volume $dV = dAdy$ is equal to the number of absorbed photons dN_{ph}, which can be expressed as

$$dN_{ex} = dN_{ph} = -\frac{dA \cdot dI_{in}}{E_{ph}} = n\sigma_{abs}\frac{I_{in}}{E_{ph}}dydA, \tag{5.13}$$

where dA is an infinitesimal area on the cross-section of the laser beam. Finally, the distribution of excited molecule density $n_{ex,0}(x, z)$ that follows the laser excitation can be calculated as

$$n_{ex,0}(x, z) = n\sigma_{abs}\frac{I_{in}(x, z)}{E_{ph}}. \tag{5.14}$$

5.2.3 Singlet and triplet lifetime

The lifetime of singlet and triplet molecules is determined by both the radiative and non-radiative processes. By considering the intramolecular processes described in Section 5.2.1, the transitions from the photon absorption to the return to the ground state are:

1) $Ac + h\nu_{ex} \rightarrow {}^1Ac^*$,
2) ${}^1Ac^* \rightarrow {}^1Ac$,
3) ${}^1Ac \rightarrow Ac$ (or Ac^*),
4) ${}^1Ac \rightarrow Ac$ (or Ac^*) + $h\nu_f$,
5) ${}^1Ac + Q \rightarrow Ac$ (or Ac^*),
6) ${}^1Ac \rightarrow {}^3Ac^*$,
7) ${}^3Ac^* \rightarrow {}^3Ac$,
8) ${}^3Ac \rightarrow Ac$ (or Ac^*),
9) ${}^3Ac \rightarrow Ac$ (or Ac^*) + $h\nu_{ph}$,
10) ${}^3Ac + Q \rightarrow Ac$ (or Ac^*).

in which ${}^1Ac$ is the excited singlet, ${}^3Ac$ is the excited triplet, and the sign * accounts for excitation of vibrational-rotational modes. The term Ac stands for acetone molecule, but the same equations listed above are valid for diacetyl as well, which will be indicated as Di. All the following considerations are valid also for a diacetyl molecule.

Transition (1) corresponds to photon absorption. This is a the fastest among all the intramolecular processes. The electron excitation to the upper orbital has characteristic times of the order of picoseconds. Therefore, absorption can be considered as instantaneous with respect to all the other intramolecular processes.

Transitions (2) and (7) represent the vibrational-relaxation to the lowest energy level, respectively, in the singlet and the triplet state. The experimental analysis here presented has been carried out at ambient temperature, therefore, it is assumed that no vibrational-rotational modes are activated at the thermalized condition. Moreover, because the gas pressure employed in the experiments is not lower than 250 Pa, the condition of fast vibrational-relaxation can be considered as fully satisfied. This means that vibrational-relaxations in the singlet state (2) occur certainly before transitions (3), (4), (5), and (6), and vibrational-relaxations in the triplet state (7) occur before transitions (8), (9), and (10).

Transitions (4) and (9) are, respectively, fluorescence and phosphorescence emissions.

Transitions (5) and (10) represent the molecular quenching caused by a generic quencher species Q, respectively, in the singlet and in the triplet state.

Transitions (3) and (6) correspond, respectively, to the internal non-radiative de-excitation in the singlet state and the intersystem crossing transition. As previously discussed, the dominant internal conversion in the excited singlet state is the non-radiative transition to the triplet state. Transition (3) can then be neglected in this representation. The internal non-radiative de-excitation in the triplet state, that is transition (8), is faster than phosphorescence and, therefore, cannot be neglected. Depending on the concentration of the quencher Q, the triplet lifetime can be dominated by either internal or external conversions.

For all those transitions that bring an excited molecule to the ground state, that is the processes (3), (4), (5), (8), (9), and (10), the de-excitation might result in a molecule Ac^* with some of the vibrational-rotational modes excited. However, for the thermodynamic conditions employed in this work, this residual energy is quickly

dissipated in the surrounding environment through intermolecular collisions, and all de-excited molecules will eventually reach the lowest energy level in the ground state.

From these considerations, the singlet and triplet lifetimes are essentially determined by the following transitions:

1) $^1\text{Ac} \rightarrow \text{Ac} + h\nu_f$,
2) $^1\text{Ac} + \text{Q} \rightarrow \text{Ac}$,
3) $^1\text{Ac} \rightarrow {}^3\text{Ac}$,
4) $^3\text{Ac} \rightarrow \text{Ac}$,
5) $^3\text{Ac} \rightarrow \text{Ac} + h\nu_{ph}$,
6) $^3\text{Ac} \rightarrow \text{Ac} + \text{Q}$.

The differential equations that govern the time decay of the singlet $n_{S_1}(x,y,z,t)$ and triplet $n_{T_1}(x,y,z,t)$ molecule concentration are, therefore,

$$\frac{\partial n_{S_1}}{\partial t} = -k_f n_{S_1} - k_{Q,S_1} n_Q n_{S_1} - k_{ISC} n_{S_1} + D\nabla^2 n_{S_1}\,, \tag{5.15}$$

$$\frac{\partial n_{T_1}}{\partial t} = -k_{ph} n_{T_1} - k_{nr,T_1} n_{T_1} - k_{Q,T_1} n_Q n_{T_1} + k_{ISC} n_{S_1} + D\nabla^2 n_{T_1}, \tag{5.16}$$

in which the diffusion term takes into account of the molecular diffusion of the excited molecules in space. The two equations are completed by the initial conditions $n_{S_1}(t=0) = n_{S_1,0} = n_{Ac}\sigma_{abs} I_{in}/E_{ph}$ and $n_{T_1}(t=0) = n_{T_1,0} = 0$. Because the de-excitation processes here considered are all linear with respect to the excited molecule concentration, the molecular diffusion does not affect the singlet and triplet lifetime. By assuming a uniform quencher concentration n_Q, the integration on a domain of volume V of Eq. (5.15) and (5.16) provide the governing equations for the total number of excited singlet $N_{S_1}(t)$ and triplet $N_{T_1}(t)$:

$$\frac{dN_{S_1}}{dt} = -k_f N_{S_1} - k_{Q,S_1} n_Q N_{S_1} - k_{ISC} N_{S_1}, \tag{5.17}$$

$$\frac{dN_{T_1}}{dt} = -k_{ph} N_{T_1} - k_{nr,T_1} N_{T_1} - k_{Q,T_1} n_Q N_{T_1} + k_{ISC} N_{S_1}, \tag{5.18}$$

As it can be observed from Eq. (5.15) and (5.16), the intersystem crossing couples the two equations, being a sink for the singlets and a source for the triplets. However, as already discussed in the Section 5.2.1, the quantum yield of the intersystem crossing is close to 1 and much faster than all the intramolecular processes that occur in the triplet state. In first approximation, the equations can be solved separately. The equation for the singlet population remains

$$\frac{dN_{S_1}}{dt} = -k_f N_{S_1} - k_{Q,S_1} n_Q N_{S_1} - k_{ISC} N_{S_1}, \qquad N_{S_1,0} = \int_V n_{Ac}\sigma_{abs}\frac{I_{in}}{E_{ph}}\,dV, \tag{5.19}$$

while the equation for the triplet population simplifies in

$$\frac{dN_{T_1}}{dt} = -k_{ph}N_{T_1} - k_{nr,T_1}N_{T_1} - k_{Q,T_1}n_Q N_{T_1}, \qquad N_{T_1,0} = \int_V n_{Ac}\sigma_{abs}\frac{I_{in}}{E_{ph}}dV. \tag{5.20}$$

In the absence of non-linear quenching, the analytical solutions of the two equations provide an exponential decay of the singlet and triplet molecule concentration:

$$N_{S_1} = N_{S_1,0}e^{-(k_f+k_{Q,S_1}+k_{ISC})t}, \qquad N_{T_1} = N_{T_1,0}e^{-(k_{ph}+k_{Q,T_1}+k_{nr,T_1})t}, \tag{5.21}$$

in which $\tau_{S_1} = 1/(k_f + k_{Q,S_1} + k_{ISC})$ and $\tau_{T_1} = 1/(k_{ph} + k_{Q,T_1} + k_{nr,T_1})$ are, respectively, the singlet and the triplet lifetime. The terms $-k_f N_{S_1}$ and $-k_{ph}N_{T_1}$ represent the number of singlet and triplet molecules that de-excite by emitting a photon. Fluorescence $I_f(t) = k_f N_{S_1}$ and phosphorescence $I_{ph}(t) = k_{ph}N_{T_1}$ emission rates are proportional, respectively, to the singlet and the triplet populations, and, thus, they are exponentially decaying as well. The time evolution of the emitted light is, then, representative of the lifetime of the excited molecule. The total emitted fluorescence light S_f and the total emitted phosphorescence light S_{ph} are, respectively,

$$S_f = \int_0^{+\infty} I_f(t)dt = \frac{k_f}{k_f + k_{ISC} + k_q n_Q}N_{S_1,0}, \tag{5.22}$$

$$S_{ph} = \int_0^{+\infty} I_{ph}(t)dt = \frac{k_{ph}}{k_{ph} + k_{nr,T_1} + k_q n_Q}N_{T_1,0}. \tag{5.23}$$

Because the quantum yields are defined as the percentage of excited molecules that de-excited by emitting a photon, $S_f = \phi_f N_{S_1,0}$ and $S_{ph} = \phi_{ph}N_{T_1,0}$. The comparison of these definitions with Eq. (5.22) and (5.23) provide the expression of the quantum yields:

$$\phi_f = \frac{k_f}{k_f + k_{ISC} + k_q n_Q}, \qquad \phi_{ph} = \frac{k_{ph}}{k_{ph} + k_{nr,T_1} + k_q n_Q}. \tag{5.24}$$

Finally, by considering Eqs. (5.19) and (5.20), the total emitted light can be expressed as

$$S_f = \phi_f n_{Ac}\sigma_{abs}\frac{I_{in}}{E_{ph}}, \qquad S_{ph} = \phi_{ph}n_{Ac}\sigma_{abs}\frac{I_{in}}{E_{ph}}. \tag{5.25}$$

5.2.4 Literature data on radiative and non-radiative rates

Table 5.1 and Table 5.2 summarize the values found in the literature of the characteristic times $\tau = 1/k$ and the quantum yields ϕ related to the intramolecular processes discussed in the previous sections, respectively for acetone and diacetyl vapors. Some authors did not provide the parameters for all the intramolecular processes. However, in some cases, it is possible to infer the missing data from the available data. In these tables, the values in bold have been calculated from the available data by means of Eqs. (5.7) and (5.24). The characteristic times

and the quantum yields of the intramolecular processes are in general dependent of the vapor temperature, the excitation wavelength, and the vapor concentration. The values of τ and ϕ here reported refer to vapor at ambient temperature, unless otherwise specified, and the excitation wavelength used in each work is reported. While the intrinsic characteristic times of radiative and non-radiative transitions to the ground state do not substantially vary as a function of the vapor concentration, the singlet and triplet population lifetime, τ_{S_1} and τ_{T_1}, might depend on the vapor pressure. This can happen if the vibrational-relaxation rate is comparable with other intramolecular characteristic rates and/or if molecular quenching is present. Nevertheless, the values of the quantum yields and of the excited molecules lifetime reported in Table 5.1 and Table 5.2 correspond to vapor conditions for which the hypothesis of fast vibrational-relaxation discussed in Section 5.2.1 holds and for which the effects of external molecular quenching or molecular self-quenching are negligible.

	λ_{ex}	τ_{S_1}	τ_f	τ_{ISC}	τ_{T_1}	τ_{ph}	τ_{nr,T_1}	ϕ_f	ϕ_{ph}	ϕ_{ISC}
Hunt & Noyes (1948)	313 nm	30 ns	33 ns	-	10 µs	10 µs	-	-	-	-
Kaskan & Duncan (1950)	?	-	-	-	244 µs	-	-	-	-	-
Heicklen (1959)	313 nm	-	-		200 µs	**11.1 ms**	**204 µs**	0.21%	1.8%	-
Breuer & Lee (1971)	313 nm	2.6 ns	1.25 µs	2.7 ns	-	-	-	0.21%	-	**97.2%**

Table 5.1. Values of the characteristic times and quantum yields of each intramolecular process for the case of acetone vapor at ambient temperature. The experimental data from the Heicklen (1959) are referred to vapor at T = 40° C.

	λ_{ex}	τ_{S_1}	τ_f	τ_{ISC}	τ_{T_1}	τ_{ph}	τ_{nr,T_1}	ϕ_f	ϕ_{ph}	ϕ_{ISC}
Rawcliffe (1942)	?	-	-	-	1.4 ms	-	-	-	-	-
Almy & Gillette (1943)	404.7 & 435.8 nm	-	-	-	1.4 ms	**9.6 ms**	**1.6 ms**	-	14.5%	-
Kaskan & Duncan (1950)	?	-	-	-	1.8 ms	-	-	-	-	-
Okabe & Noyes (1957)	435.8 nm	19 ns	10 µs	16-25 ns	1.5 ms	10 ms	1.8 ms	0.25%	15%	**95%**
Parmenter & Poland (1969)	435.8 nm	10-21 ns	4-8.5 µs	10 ns	1.82 ms	**12.6 ms**	**2.13 ms**	0.25%	14.5%	99.7%
Sidebottom *et al*. (1972)	436.5 nm	20-28 ns	7-14 µs	19.6-28.5 ns	1.26-1.78 ms	8-12.5 ms	1.45-2.33 ms	0.23%	14.9%	**99.8%**
Concheanainn & Sidebottom (1980)	440 nm	-	-	-	1.8 ms	-	-	-	-	-

Table 5.2. Values of the characteristic times and quantum yields of each intramolecular process for the case of diacetyl vapor at ambient temperature.

Note that, even though the characteristic time of fluorescence decay τ_f is of the order of 1 or 10 μs, the resulting lifetime τ_{S_1} of fluorescence radiation is much lower and of the order of some nanoseconds. This is because the non-radiative transitions in the excited singlet state, which are mainly dominated by the intersystem crossing transition, are much faster than the radiative decay.

The data available in the literature are much more complete for the case of diacetyl vapor than for the case of acetone vapor. The data on acetone fluorescence are provided mainly for a laser excitation at 313 nm and the data on acetone phosphorescence are almost absent in the literature. To the best of our knowledge, the work of Heicklen (1959) is the only one that provides a quantum yield for acetone phosphorescence, even for excitation wavelengths lower than 313 nm. Differently, diacetyl photoluminescence has been more widely studied. The values of the characteristic times and quantum yields reported by different experimental works are relatively consistent with each other. It is important underlining that in the earliest experimental works, such as those of Almy & Gillette (1943) or Kaskan & Duncan (1950), the difference between fluorescence and phosphorescence emission was not yet clear, thus these authors discuss about a 'fluorescence' emission, even though the observed light emission was actually phosphorescence.

5.3 Phosphorescence analysis for MTV applications

In this section, the experimental study of phosphorescence emission of acetone and diacetyl vapors at low pressures is presented. The experimental data are analyzed in the perspective of applying MTV to gas flows in the slip regime. The main objective of this analysis is directed towards understanding the minimal gas-tracer mixture pressure that can be achieved and, consequently, the maximum level of rarefaction achievable in a 1-mm height channel while still obtaining an exploitable phosphorescence signal.

In the following analysis, the level of rarefaction is quantified by means of the Knudsen number defined as

$$Kn_H = \frac{\lambda}{H}, \tag{5.26}$$

where H is the height of the channel and λ is the mean free-path of the gas-tracer mixture. The calculations are made by considering the internal dimensions of the channel used on the experimental setup, that is with H = 1 mm. The mean free path λ depends on the temperature T, the pressure p, the tracer concentration χ, and the kinetic properties of each gas component, that is the molecular mass m_i and the molecular diameter d_i. By using the HS model, the mean free path of the gas mixture is calculated as

$$\lambda = \sum_{i=1}^{2} \frac{\chi_i}{\sum_{j=1}^{2} n_j \pi d_{ij}^2 \sqrt{\frac{m_i + m_j}{m_j}}}, \tag{5.27}$$

where the indices 1 and 2 refer to the gas and the tracer species, respectively (Bird, 1994). The molecular concentration of each species is defined as $\chi_i = n_i/n$, with n the total molecular density of the mixture. Helium is the best candidate for application of MTV at low pressures, since it is the species with the smallest molecular diameter and the lower molecular mass. By using helium, Knudsen numbers in the slip regime can be achieved with pressures of the order of 1.5 kPa. Other gases with bigger molecular diameters, like argon or nitrogen, require pressures that are on the order of 500 Pa for achieving the same rarefaction regime. While the mean free path of a single species does not depend on the molecular mass, the mean free path in a mixture varies as a function of the ratio between the molecular masses of the two gas components. The presence of a tracer vapor in the gas mixture makes the Knudsen number even lower for a given total pressure since acetone or diacetyl are bigger and heavier molecules than helium. Figure 5.3 allows to graphically identify the range of pressure required for achieving the Knudsen number in the slip regime. The curves represent the Knudsen number as a function of the pressure for helium, argon, and acetone-helium mixture at χ = 20%.

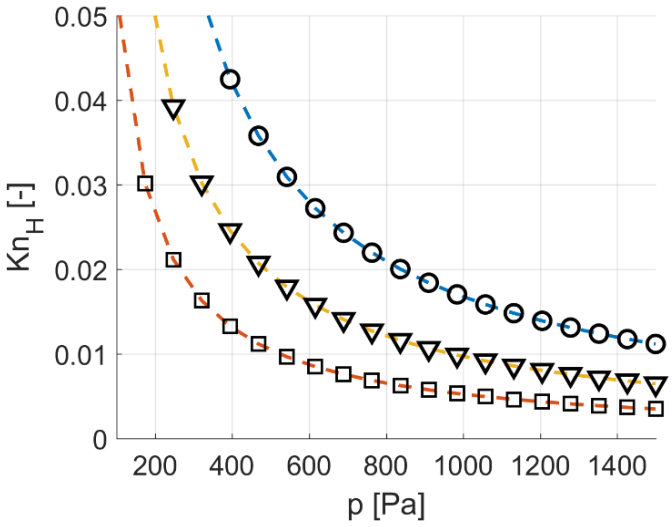

Figure 5.3. Knudsen number Kn_H as a function of the pressure p: helium (○ - -), argon (□ - -), and acetone-helium at χ = 20% (▽- -).

Reducing the tracer concentration would provide higher Knudsen numbers but to the expense of a less intense phosphorescence signal. Moreover, the molecular diffusion in helium is higher than in argon, thus reducing the signal lifetime. Higher percentage of tracer vapor in the mixture would provide the further advantage of reducing the molecular diffusion. The experimental analysis proposed in this section aims to identify the optimal

thermodynamic conditions that satisfy both requirements of low tracer concentration and low pressure for increasing the Knudsen number and of high tracer concentration and high pressure for increasing the signal intensity and lifetime.

The kinetic properties used in Figure 5.3 and in the future calculations are reported in Table 5.3.

Gas/Vapor	M [kg/mol·10^3]	d [pm]
Helium	4.0026	233
Argon	39.95	417
Acetone	58.08	730
Diacetyl	86.09	590

Table 5.3. Molar mass M and molecular diameter d of different gases. The data on helium and argon have been taken from Bird (1994). Acetone and diacetyl data have been taken, respectively, from Frezzotti *et al*. (2015) and Almy & Anderson (1940).

During this experimental campaign, no beam expander was employed on the optics for the laser beam. The diaphragm valve was partially closed for reducing the laser beam diameter to about 1-2 mm at the entrance of the plano-convex lens and, thus, reducing the focusing of the beam in the visualization chamber. Depending on the laser system and the laser wavelength employed, the focused laser beam diameter in the FOV of the camera was between 200-400 µm. The experiments were carried out without focusing at the maximum capability of the laser optics in order to better exploit the spatial resolution of the camera. In this way, more information could be extracted on the molecular diffusion of the emitting tracer in the background gas.

In Section 5.3.1, the post-processing procedure applied to each recorded image for providing the quantity of interest is explained. Section 5.3.4 is dedicated to the analysis of the acetone phosphorescence that follows the 266-nm laser excitation. Afterwards, Section 5.3.5 presents the experimental study on acetone and diacetyl phosphorescence at different excitation wavelengths. A comparison between acetone and diacetyl phosphorescence is proposed in Section 5.3.6 to identify the best tracer in terms of signal intensity and lifetime, while Section 5.3.7 demonstrates the existence of a durable and intense phosphorescence signal in gas-tracer mixtures with Knudsen numbers Kn_H in the slip regime. Finally, a preliminary statistical analysis on the position of the tagged line is presented in Section 5.3.8.

5.3.1 Image processing procedure

In the experimental analysis, the raw image is averaged along the direction of the laser beam and, then, a Gaussian fitting is carried out, as shown in Figure 5.4.

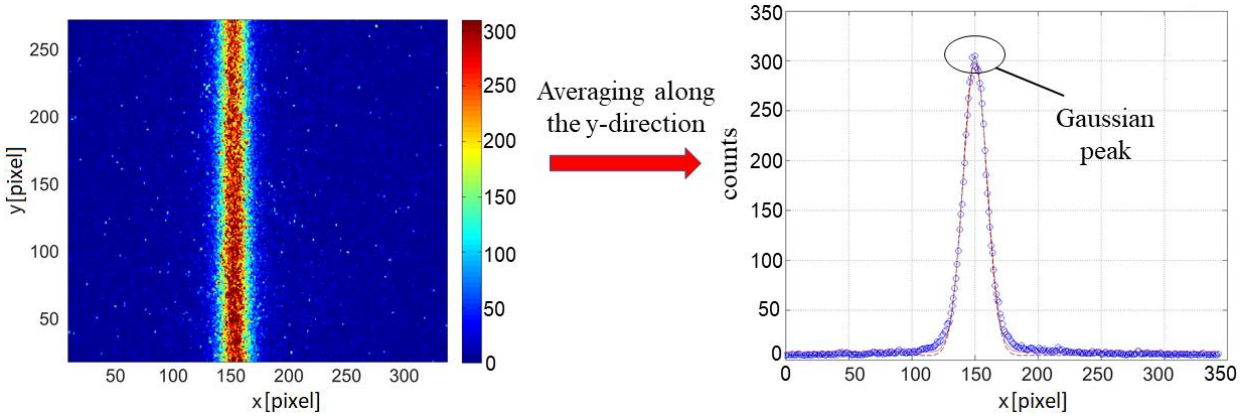

(a) (b)

Figure 5.4. Example of raw image and image processing procedure; (a) phosphorescence emission of pure acetone 10 μs after the laser excitation at 5 kPa for $N_l = 100$, $N_i = 10$, $\Delta t_{gate} = 100$ ns, and $G = 100\%$; (b) Gaussian fitting (red line) of the emission profile (blue circles) that results from the averaging along the y-direction of the raw image shown in (a).

The employed fitting function has the following expression:

$$f(x,t) = a_1(t) + \frac{a_2(t)}{\sqrt{2\pi a_3(t)}} e^{-\frac{(x-a_4)^2}{2a_3(t)}}, \tag{5.28}$$

where $a_1, a_2, a_3,$ and a_4 are the fitting coefficients.

The degree of freedom, $a_1(t)$, is introduced to take into account the background emission, which is never zero and decreases in time. This background offset does not come from a noise source generated by the acquisition system, such as the CCD dark noise or the photocathode shot noise. Firstly, the average dark noise distribution does not depend on time and, moreover, is always subtracted from the recorded image. Secondly, the photocathode shot noise or other noise sources that produce instrumental uncertainties on the recorded number of counts do not contribute in generating an average signal in the background. Instead, the background noise is mainly the result of reflections on the walls of the visualization chamber of the light emitted by the tracer. Indeed, the background offset $a_1(t)$ decreases with time following the phosphorescence decay. The UV-light itself is not considered as a possible source of background noise because, even though no filters are used on the ICCD objectives, the IRO gate is open only after the end of the laser pulse, which lasts only about 5 ns. However, it is possible that reflection and diffusion of the UV light inside the visualization chamber may excite tracer molecules that are out-of-beam or adsorbed by the internal walls, thus contributing to the background emission. Diacetyl vapor is particularly

sensitive to the adsorption phenomenon and its emission is stronger than acetone. As a result, the background emission in the case of diacetyl vapor is more intense than in the case of acetone vapor. Parameter $a_2(t)$ represents the amplitude of the Gaussian signal. More precisely, its time evolution is strictly linked to the phosphorescence lifetime of the excited tracer. Since this parameter is not affected by the diffusion mechanisms, the analysis of $a_2(t)$ can provide important information about the photoluminescence process. Coefficient $a_3(t)$ corresponds to the variance of the Gaussian and its evolution in time gives information about the diffusion rate of the excited tracer molecules inside the background gas mixture. Finally, coefficient a_4 represents the position of the Gaussian peak. Due to possible small perturbations in the position of the laser beam and to fluctuations in the laser energy pattern, this value can be slightly different from one acquisition to the other. While this last parameter is not of much interest for the experimental analysis presently described, the MTV technique is based on the accurate measurement of a_4.

The averaging operation of the collected light along the laser beam direction reduces the statistical fluctuations of the emission distribution. The same result could have been achieved by simply averaging more images, but at the expense of a higher amount of time for the acquisition. As for the application of the MTV, the operation of averaging along the laser beam cannot be applied, since the tagged line deforms as the excited tracer molecules follow the gas flow direction. An independent Gaussian fitting must be applied on each row of pixels for detecting the Gaussian peak position and thus tracking the molecular displacement along the tagged line. In this scenario, the reduction of the statistical fluctuations necessarily requires averaging more images.

The fact that the signal can be approximated by a Gaussian is not as straightforward as it seems. The shape of the laser energy distribution that excites the molecular tracer is more complex than a simple Gaussian. Even if the light beam at the exit of the laser has a Gaussian intensity pattern, this distribution is modified by a circular obturator positioned before the focalization lenses. Therefore, the final energy distribution of the light beam takes the form of a circularly-truncated Gaussian. Thus, the acquired signal cannot be precisely described by a Gaussian profile. However, the molecular diffusion smooths the distribution of excited molecules towards a Gaussian distribution quite quickly after the laser excitation. Furthermore, if the IRO gate, i.e., the integration time, is small enough with respect to the luminescence and diffusion rates, the Gaussian fitting can be considered as a good approximation of the signal.

The Gaussian peak value is then taken as the main characterization of the signal intensity at a given instant *t* after the laser excitation and for the thermodynamic conditions under consideration. From Eq. (2), the Gaussian peak corresponds to the following expression:

$$S_{gp}(t) = f(a_4, t) = a_1(t) + \frac{a_2(t)}{\sqrt{2\pi a_3(t)}}. \tag{5.29}$$

As it can be seen from Eq. (5.29), the Gaussian peak value is determined by $a_1(t)$, $a_2(t)$, and $a_3(t)$, which can be affected both by phosphorescence lifetime and/or diffusion. The Gaussian peak is an interesting quantity for characterizing the time evolution of the signal, as it contains information related to both phenomena. Moreover, in MTV the Gaussian peak is used for tracking the displacement of the tagged line and, thus, is a fundamental quantity for carrying out velocimetry measurements. The background component $a_1(t)$ is kept and not subtracted from the signal intensity because it does not influence, in any matter, the signal-to-noise ratio of the peak intensity $S_{gp}(t)$, which depends only on the statistical fluctuations of the recorded light. Moreover, it is something that is inevitably present also during MTV acquisitions in channel flows.

For a desired thermodynamic condition, i.e., desired total pressure p of the mixture and tracer concentration χ, the spreading phosphorescence distribution is recorded at different delay times t after the laser excitation. An example of a group of data gathered during one set of experiments is shown in Figure 5.5. Figure 5.5a illustrates the time evolution of the signal intensity $S_{gp}(t)$, where each data is calculated from one image recorded at defined N_l and N_i. Figure 5.5b shows the time evolution of the Gaussian phosphorescence distribution corresponding to the data of Figure 5.5a. This particular set of data shown corresponds to phosphorescence emitted by acetone vapor excited at 266 nm in a helium mixture at p = 10 kPa and χ = 75%. In the following sections, the datum $S_{gp}(t)$ is indicated with S and is referred to as "signal intensity" or "phosphorescence emission" interchangeably.

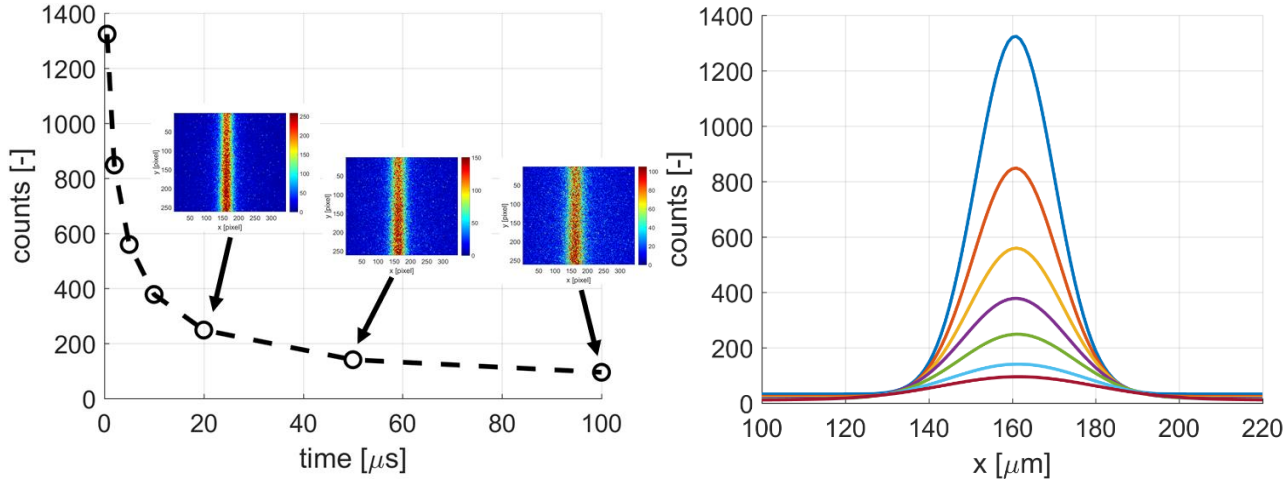

(a) (b)

Figure 5.5. Example of data set on time evolution of phosphorescence emission. The data corresponds to phosphorescence emitted by acetone vapor excited at 266 nm in a helium mixture at p = 10 kPa and χ = 75%. The average laser intensity is $\bar{I}_{in}$ = 0.08 J/cm^2, and the recording parameters are: $N_l = 500$, $N_i = 10$, $G = 100\%$, and $\Delta t_{gate} = 500$ ns: (a) signal intensity $S_{gp}(t)$ in time; (b) Gaussian profiles associated to the data point in (a). The distributions in (b) corresponds to t = 0.55, 2, 5, 10, 20, 50, 100 μs, respectively, from the highest Gaussian profile to the lowest one.

5.3.2 Signal transformation for different IRO gains

Since the phosphorescence emission at low pressures is relatively weak, the IRO gain is set, for most of the image acquisitions, at its maximum, that is G = 100%. However, in the first microseconds following the laser excitation the signal intensity can be strong enough that a maximum IRO amplification may dangerously saturate the CCD sensor. The maximum number of counts per pixel is about 4000, and if this limit is overcome the CCD cells may be irreversibly damaged. Avoiding this eventuality requires using appropriate IRO gains as a function of the signal intensity. However, if low gains are used in the first microseconds of the emission and high gains are used for the later weak phosphorescence emission, the reconstruction of the complete time evolution of the light emission requires somehow to convert the signal recorded at low gain into the corresponding signal at high gain or vice-versa. If I is defined as the amount of light reaching the IRO photocathode, the two signals recorded are

$$S_1 = S_{ICCD}(G_1)I, \tag{5.30}$$

$$S_2 = S_{ICCD}(G_2)I, \tag{5.31}$$

where $S_{ICCD}(G)$ is the ICCD sensitivity that depends on the IRO gain. The ratio between Eq. (5.30) and (5.31) determines the relation between the two signals recorded at different gains:

$$S_2 = \frac{S_{ICCD}(G_2)}{S_{ICCD}(G_1)} S_1 = C_{ICCD} S_1. \tag{5.32}$$

The conversion factor C_{ICCD} may be calculated by considering the curve shown in Section 4.3.2. However, as previously discussed, the sensitivity curve reported does not take into account of possible redistribution over the CCD pixels of the accumulated charges. Its application is valuable for converting the total signal accumulated by the CCD sensor at two different gains, but it cannot be applied to convert the signal $f(a_4, t)$ as defined in Eq. (5.29). Instead, a practical way to compute the conversion factor is by recording twice the same light emission $I(t)$ at a certain delay time t with both low G_1 and high G_2 gain. The ratio between the two recorded signals, S_1 and S_2, provides the value of C_{ICCD}. Even though this conversion factor is calculated for a signal at a delay time for which low and high gains can be used, the same conversion factor can be used to convert other signals at other delay times. Figure 5.6 demonstrates that this conversion technique works.

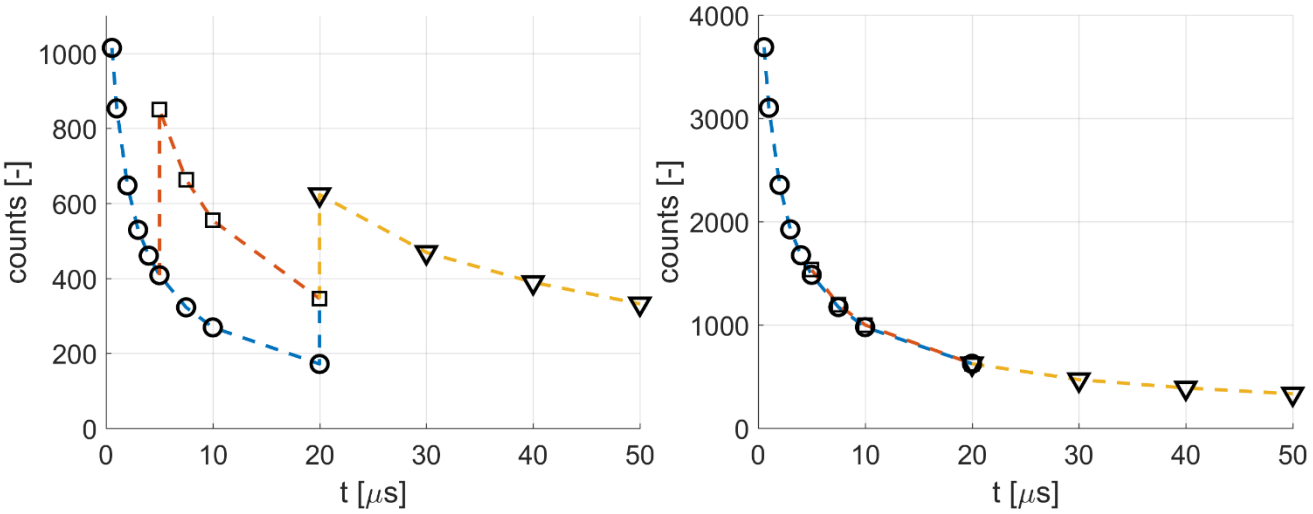

Figure 5.6. Signal transformation for different IRO gains: (a) time evolution of phosphorescence emission $S_{gp}(t)$ recorded at G = 85% (○ - -), G = 90% (□ - -), and G = 100% (▽ - -); (b) conversion of all the data in (a) to G = 100%. The phosphorescence data refer to acetone vapor excited at 266 nm in helium mixture at p = 98 kPa and χ = 20%. The average laser intensity is about $\bar{I}_{in}$ = 0.06 J/cm^2, and the recording parameters are: $N_l = 100$, $N_i = 10$, and $\Delta t_{gate} = 500$ ns.

In Figure 5.6a, the circle data are recorded at G_1 = 85%, for t between 1 µs and 20 µs, the square data are recorded at G_2 = 90% for t between 5 µs and 20 µs, and the triangle data are recorded at G_3 = 100% for t between 20 µs and 50 µs. The signals at t = 20 µs corresponding to G_3 = 100 % and G_2 = 90% are used to calculate the conversion factor C_{ICCD} from 90% to 100% of gain. The conversion factor can be also calculated for gain variations from 85% to 90% or from 85% to 100%, respectively, with the signals at t = 5 µs and t = 20 µs. Figure 5.6b illustrates how the conversion makes all the curves overlapping in time, thus providing the whole phosphorescence lifetime at the same gain 100%. It is worthy to notice that the combination of multiple conversions provides the same result. For instance, the circle data can be converted to 100% by using the conversion factor from 85% to 100% or by using a double conversion, from 85% to 90% and, then, from 90% to 100%.

5.3.3 Average laser energy density

The comparison of phosphorescence data from different experiments requires knowing the average energy density of the laser pulses employed. The energy detector can provide a measurement of the average pulse energy E_l but it does not provide the spatial distribution of energy on the laser cross section. For measuring the average laser energy density, an estimation of the laser beam diameter is required. In this work, the diameter of the energy distribution is taken as the full width at half maximum (FWHM)[1]. This estimation is done by considering the

[1] FWHM is the width of the laser energy distribution in correspondence of an energy intensity that is the half of the maximum value.

phosphorescence emission distribution captured some nanoseconds after the laser excitation, when the molecular diffusion did not change yet the spatial distribution of the excited molecules. Therefore, the light pattern is a good representation of the laser energy distribution. For a Gaussian function, the relationship between FWHM and the standard deviation a_3 of Eq. (5.28) is

$$FWHM = 2\sqrt{2\ln 2}\, a_3 \approx 2.633 a_3. \tag{5.33}$$

The average energy density $\bar{I}_{in}$ is then estimated as

$$\bar{I}_{in} = \frac{E_l}{\left(\pi \frac{FWHM^2}{4}\right)}. \tag{5.34}$$

A more complete characterization of the laser energy density distribution $I_{in}(x, y)$ is provided in Appendix B. The range of average laser pulse energies employed in this experimental analysis is between 20 to 100 µJ. Eq. (5.14) states that the phosphorescence intensity is linear with the laser energy if no saturation is attained. This fact has been verified and is shown in Figure 5.7.

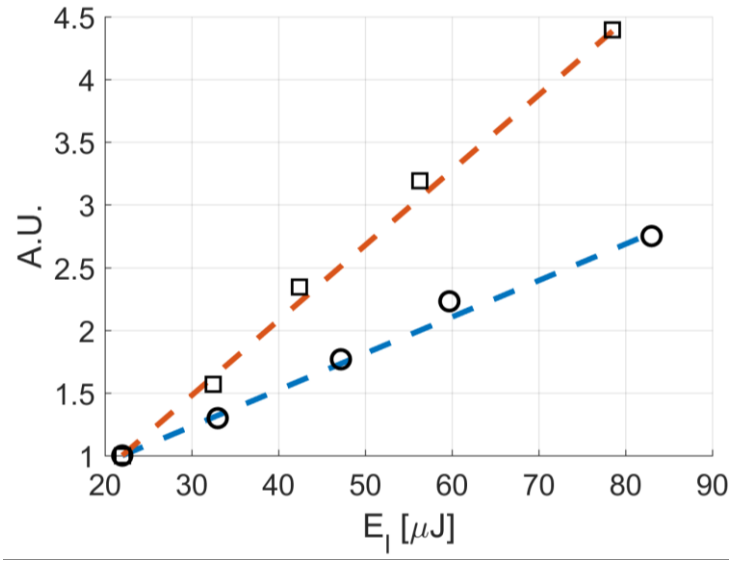

Figure 5.7. Fluorescence (□ - -) and phosphorescence (○ - -) intensity S_{gp} of acetone excited at 266 nm and at p = 10 kPa as a function of the average laser pulse energy E_l. Each point results from the integration of N_l = 100 laser pulses and averaging N_i = 10 images. The IRO gate Δt_{gate} is 100 ns for the fluorescence data and 500 ns for the phosphorescence data. The FWHM of the laser energy distribution is estimated to be about 400 µm.

The curves represent the signal intensity provided by acetone vapor at p = 10 kPa and excited at 266 nm as a function of the average laser pulse energy E_l. Both fluorescence and phosphorescence emissions are collected by the ICCD: the square data points correspond to light emission integrated at few nanoseconds after the laser

excitation, while the circle data points represent the phosphorescence emission integrated at t = 600 ns. The data are normalized with respect to the intensity corresponding to the lowest energy used, which is about 20 µJ.

5.3.4 Acetone emission at 266 nm

In this section, the first experimental results on phosphorescence emission of acetone vapor excited at 266 nm are presented. The following data have been produced by using the Nd:YAG Quantel twins, which specifications are reported in Section 4.2.1. Acetone phosphorescence has been tested in gas mixture of argon and helium for experimenting the influence of the gas species on the phosphorescence lifetime and intensity. Figure 5.8 reports the phosphorescence data in an acetone-argon mixture at p = 10 kPa for different tracer concentration χ, from 100% to 25%. As observed in Figure 5.8a, lowering the acetone concentration reduces the overall intensity of the signal, because the number of excited molecules is evidently reduced. Figure 5.8b shows the same data of Figure 5.8b but normalized with respect to the first delay time, t = 550 ns. The lifetime of the signal does not show particular dependency on the partial pressure of acetone vapor but seems to be mainly determined by the total pressure of the mixture. Acetone diffusion increases as the percentage of acetone present in the mixture decreases. This is because argon molecules are lighter and smaller than acetone molecules. Since the normalized curves of Figure 5.8b do not vary substantially with χ, it might be that the signal lifetime is dominated by the decay of the phosphorescence emission, which depends only weakly on the partial pressure of acetone.

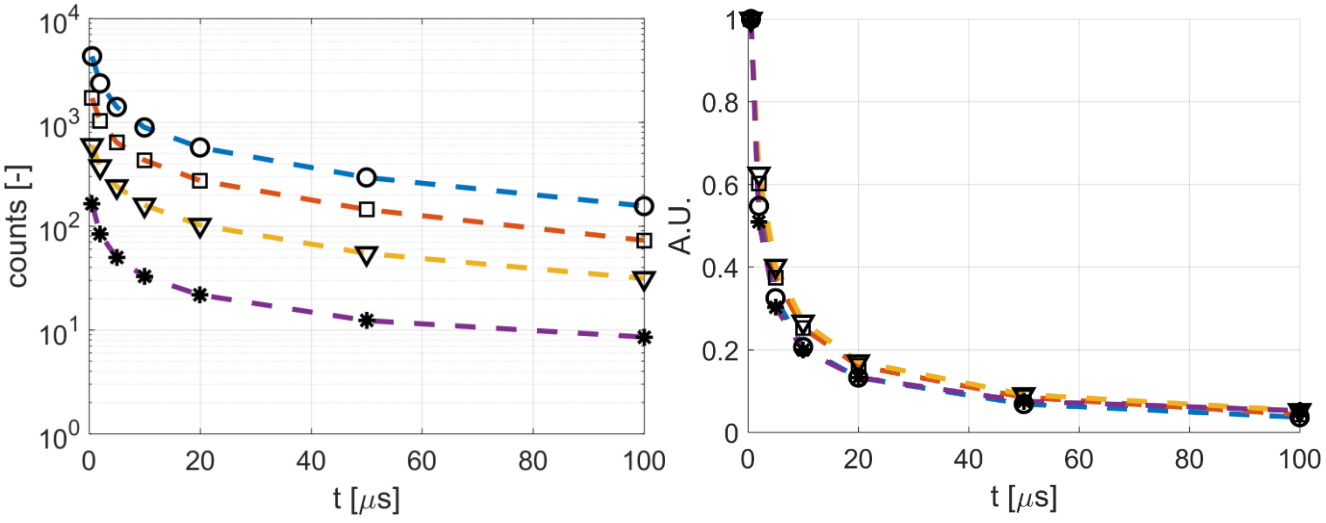

(a) (b)

Figure 5.8. Time evolution of phosphorescence emission $S_{gp}(t)$ for acetone vapor excited at 266 nm in argon mixture at p = 10 kPa, T = 293 K, and χ = 100% (○ - -), 75% (□ - -), 50% (▽- -), and 25% (✱- -): (a) logarithmic of the signal intensity; (b) data normalized at the first delay time t = 550 ns. The average laser intensity is about $\bar{I}_{in}$ = 0.08 J/cm^2, and the recording parameters are: $N_l = 500$, $N_i = 10$, $G = 100\%$, and $\Delta t_{gate} = 500$ ns.

Similar results are shown in Figure 5.9 for acetone-helium mixtures at p = 10 kPa. The normalized curves of Figure 5.9b reveals a stronger, even though still weak, dependency of the signal lifetime with the acetone partial pressure. It seems that the signal decay is higher for higher acetone partial pressure. This may be explained as the result of decreasing phosphorescence quantum yield due to self-quenching mechanisms.

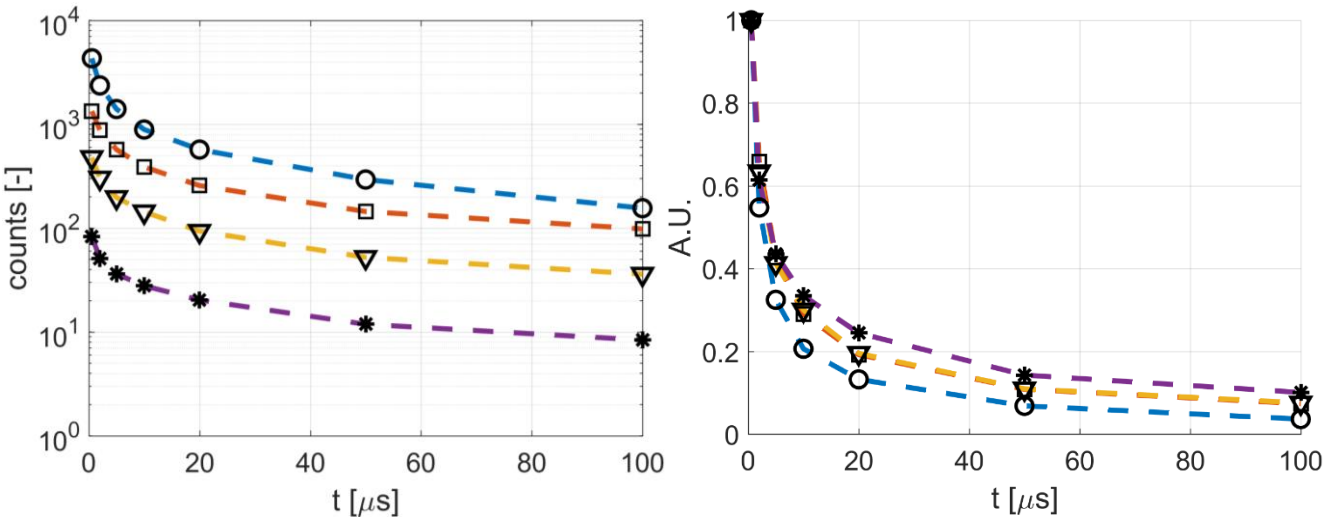

(a) (b)

Figure 5.9. Time evolution of phosphorescence emission $S_{gp}(t)$ for acetone vapor excited at 266 nm in helium mixture at p = 10 kPa, T = 293 K, and χ = 100% (○ - -), 75% (□ - -), 50% (▽ - -), and 25% (✱ - -): (a) logarithmic of the signal intensity; (b) data normalized at the first delay time t = 550 ns. The average laser intensity is about $\bar{I}_{in}$ = 0.08 J/cm^2, and the recording parameters are: $N_l = 500$, $N_i = 10$, $G = 100\%$, and $\Delta t_{gate} = 500$ ns.

For the acetone-argon and acetone-helium emission data of Figure 5.8 and Figure 5.9, the acetone partial pressure is p_{Ac} = 2.5 kPa, 5 kPa, 7.5 kPa, and 10 kPa, respectively, for the tracer concentration χ = 25%, 50%, 75%, and 100%. For better understanding the role of molecular diffusion in the signal intensity decay, these data can be compared with the time evolution of acetone phosphorescence provided by pure acetone at the same partial pressures. Because the presence of helium or argon does not seem to have any strong influence on the phosphorescence quantum yield of acetone excited at 266 nm, the same amount of acetone vapor with or without additive gas should provide the same phosphorescence lifetime only if the molecular diffusion does not have a determining role in the signal intensity decay. In Figure 5.10 the time evolution of phosphorescence emitted by pure acetone vapor at p = 2.5 kPa and 5 kPa is compared with the emission provided by acetone vapor in helium mixture with the same partial pressure, p_{Ac} = 2.5 kPa and 5 kPa. The data related to the acetone-helium mixture are the same of Figure 5.9.

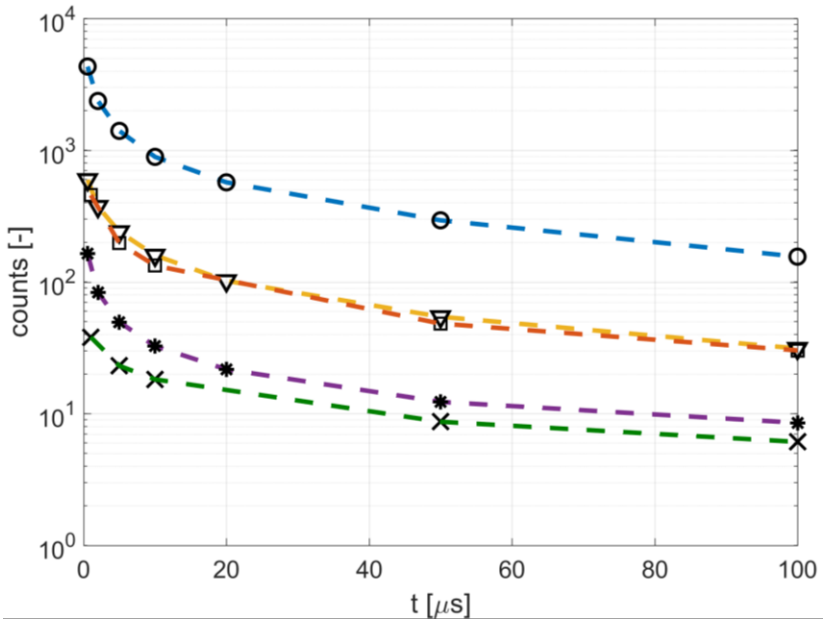

Figure 5.10. Time evolution of phosphorescence emission $S_{gp}(t)$ for acetone vapor excited at 266 nm at T = 293 K: pure acetone at p = 10 kPa (○ - -), 5 kPa (□ - -), and 2.5 kPa (× - -); acetone-helium mixture at p = 10 kPa and χ = 50% (▽ - -) and 25% (✱ - -). The data related to acetone-helium mixture are the same of Figure 5.9. For all the data shown, the average laser intensity is about $\bar{I}_{in}$ = 0.08 J/cm^2, and the recording parameters are: $N_l = 500$, $N_i = 10$, $G = 100\%$, and $\Delta t_{gate} = 500$ ns.

The signal decay provided by acetone vapor at p_{Ac} = 5 kPa results to be almost identical whether 5 kPa of helium are added or not. Even though the tracer molecular diffusion in pure acetone at 5 kPa is two times higher than in acetone-helium at p = 10 kPa and χ = 50%, the signal intensity in time is the same. Evidently, the effect of molecular diffusion on the signal decay is negligible with respect to that given by the radiative and non-radiative de-excitations of the acetone triplet population. Differently, pure acetone at p = 2.5 kPa provides a signal intensity that is lower than that provided by the same amount of acetone molecules in helium at a total pressure of p = 10 kPa. In this case, the molecular diffusion in pure acetone is four times higher than in helium and contributes in reducing the signal intensity. Moreover, the lower pressures in the visualization chamber favorizes the possibility of air-leaking and, consequently, of oxygen quenching.

By having a better look to the quality of the light signal provided by pure acetone, it can be understood if this tracer excited at 266 nm can be practically exploited for MTV applications in rarefied gas flows. For the typical gas velocity magnitudes employed in this work through a channel with a section area of 1 × 5 mm^2, a measurable displacement of the tagged line is obtained for delay time from the laser excitation of the order of 50 µs. Figure 5.11a, Figure 5.11b, and Figure 5.11c represent the phosphorescence emission provided by pure acetone, respectively, at p = 10 kPa, 5 kPa, and 2.5 kPa after 50 µs from the laser excitation. The images result from

averaging N_i = 10 images each integrating N_l = 500 laser pulses. For a channel of 1 mm in height and for a helium-acetone mixture with a molar fraction $\chi = 5\%$ of acetone vapor, an average total pressure of about 1400 Pa is required to get a gas flow at $Kn_H = 0.01$. This thermodynamic condition requires an acetone partial pressure of only 70 Pa. Figure 5.11c demonstrates that even at 2500 Pa of pure acetone the signal intensity at t = 50 µs is almost vanished. The results presented in this section demonstrate that for these thermodynamic conditions, the phosphorescence signal provided by the acetone molecules when excited by a 266 nm laser beam is not enough intense and durable in time for being used in MTV applications in rarefied conditions.

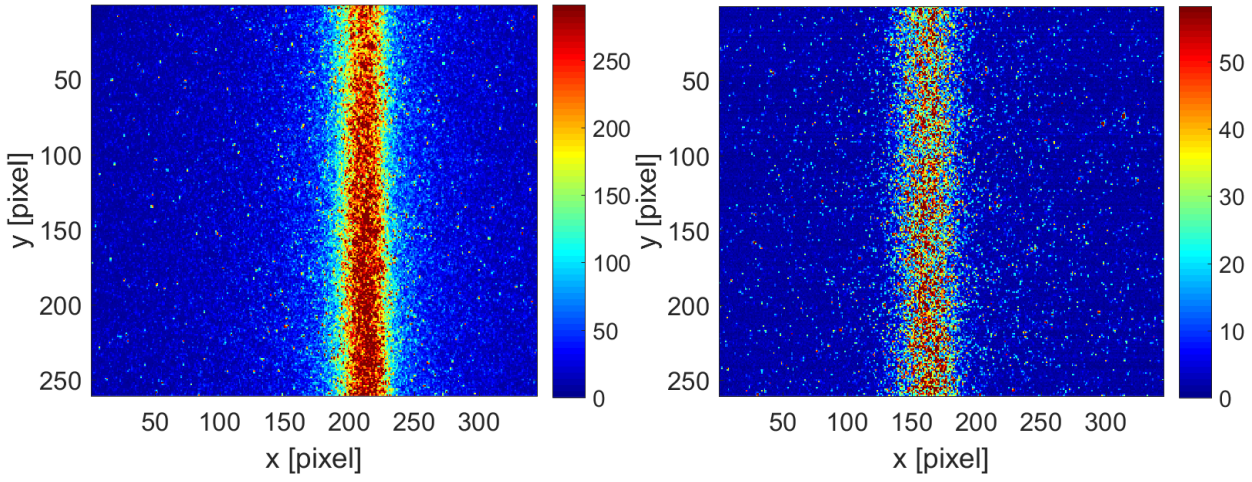

(a) (b)

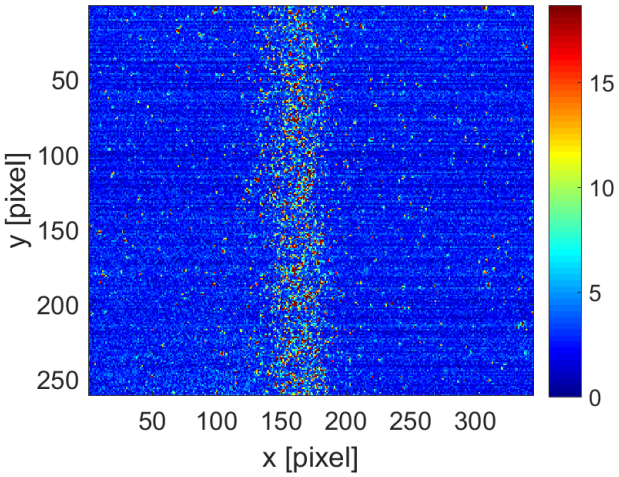

(c)

Figure 5.11. Phosphorescence emitted by acetone vapor excited at 266 nm at t = 50 µs and (a) p = 10 kPa, (b) p = 5 kPa, and (c) p = 2.5 kPa. The average laser intensity is about $\bar{I}_{in}$ = 0.08 J/cm^2, and the recording parameters are: $N_l = 500$, $N_i = 10$, $G = 100\%$, and $\Delta t_{gate} = 500$ ns.

5.3.5 Optimization of the phosphorescence intensity with the excitation wavelength

The results of the previous section showed that acetone vapor at a partial pressure of about 2500 Pa produces an emission that is too weak for making the tracking of the tagged line in a gas flow possible. The application of MTV to gas flows in the slip regime requires a molecular tracer that provides an exploitable tagged signal at partial pressures that are about one order of magnitude lower. However, the data of Figure 5.10 showed that the duration of the signal intensity at the investigated pressure range was mainly limited by the low quantum yield ϕ_f of acetone phosphorescence at 266 nm and not by the deteriorating effect given by the molecular diffusion. Confident of this fact, an investigation of the phosphorescence emission provided by acetone vapor at excitation wavelengths different from the usual 266 nm and by a new tracer, i.e., diacetyl vapor, has been carried out. This experimental exploration has been made possible by the OPOlette laser, which can generate laser pulses at different wavelengths.

In this second experimental campaign, it has been observed that acetone vapor can provide higher phosphorescence emissions when excited at a different excitation wavelength. Even if the absorption spectrum of acetone has a peak at 271 nm and goes rapidly down at 340 nm, the strongest emission is obtained for an excitation wavelength between 300 and 310 nm. Figure 5.12 and Figure 5.13 show this result, demonstrating that the phosphorescence intensity can be more than 12 times its value obtained at 260 nm. In Figure 5.12a and Figure 5.13a, data represent the phosphorescence emission of pure acetone vapor at p = 15 kPa and p = 1.5 kPa, respectively. For all the excitation wavelengths, the pulse energy was set to 30 μJ and the laser beam diameter was kept to about 310 μm. The average energy density is thus estimated to be 0.04 J/cm^2. The different curves refer to different delay times after laser excitation. For a better analysis of the amplification factor that can be obtained by modifying the excitation wavelength, phosphorescence data are normalized with respect to the highest value of the light intensity emission. In Figure 5.12b, the emission provided by acetone vapor at 15 kPa is maximum for excitation wavelengths between 305 and 310 nm, regardless of the considered delay time. At 1.5 kPa (Figure 5.13b), no visible signal for excitation wavelengths equal or lower than 270 nm could be recorded. Figure 5.13b demonstrates that even at low pressure the highest amplification is given for excitation wavelengths between 305 and 310 nm.

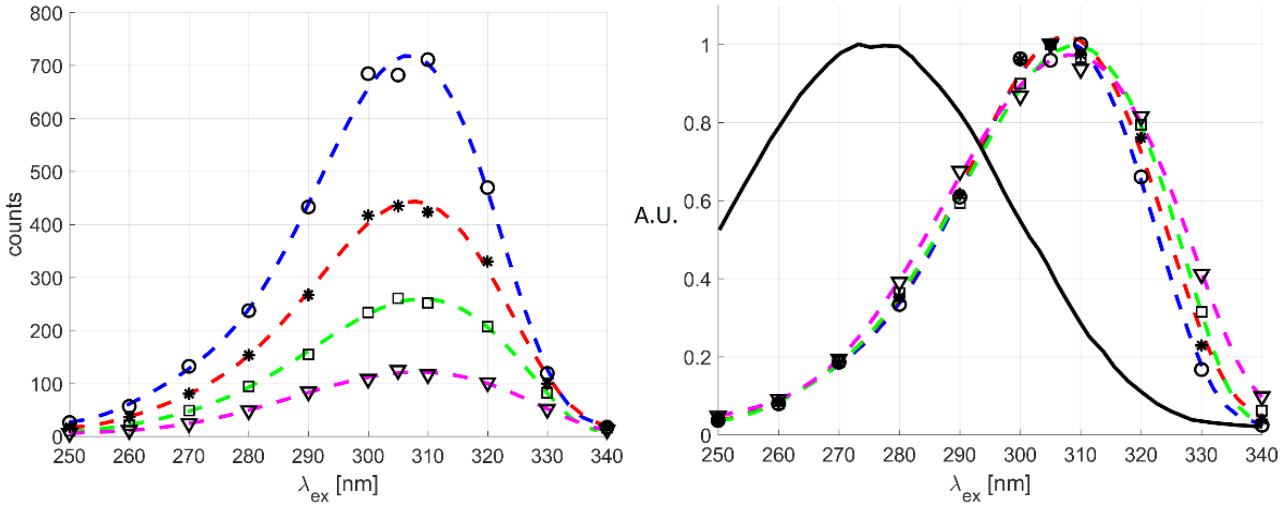

(a) (b)

Figure 5.12. (a) Phosphorescence emission S_{gp} of acetone vapor at $p = 15$ kPa and $T = 293$ K as a function of the excitation wavelength and for t = 5 μs (○ - -), 10 μs (✱- -), 20 μs (□ - -), and 50 μs (▽- -) after the laser excitation. In (b) the same data as in (a) are normalized with respect to the highest light intensity recorded for each delay time. The average laser intensity is 0.04 J/cm^2, and the recording parameters are: $N_l = 100$, $N_i = 10$, $G = 100\%$, and $\Delta t_{gate} = 100$ ns. The black solid line is the absorption spectrum of acetone, taken from Lozano *et al*. (1992).

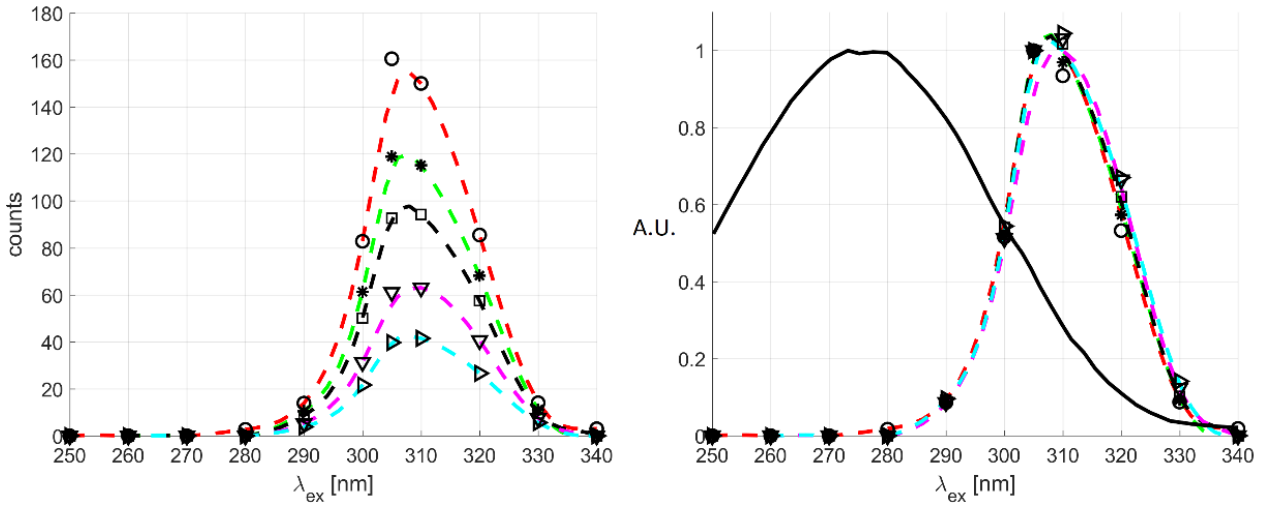

(a) (b)

Figure 5.13. (a) Phosphorescence emission S_{gp} of acetone vapor at $p = 1.5$ kPa and $T = 293$ K as a function of the excitation wavelength and for t = 1 μs (○ - -), 5 μs (✱- -), 10 μs (□ - -), 25 μs (▽- -), and 50 μs (▷- -) after the laser excitation. In (b) the same data as in (a) are normalized with respect to the highest light intensity recorded for each delay time. The average laser intensity is 0.04 J/cm^2, and the recording parameters are: $N_l = 100$, $N_i = 10$, $G = 100\%$, and $\Delta t_{gate} = 100$ ns. The black solid line is the absorption spectrum of acetone, taken from Lozano *et al*. (1992).

This non-intuitive experimental result can be explained by the fact that, even if acetone vapor absorbs much less photons at these wavelengths, the quantum yield of phosphorescence, namely the percentage of excited acetone molecules that effectively produce phosphorescence, is higher. This behavior results in a higher number of photons re-emitted by the acetone molecules and received by the CCD sensor. Even if this phenomenon can be summarily explained by means of an overall quantum yield coefficient that describes the molecule's journey from the excitation to the phosphorescence emission, the intramolecular transition processes that are involved in the light emission observed for an excitation at 310 nm are more complex than a simple excitation and de-excitation process. During the '40s and '50s, several chemistry oriented publications discussed about a "green" phosphorescence emitted by acetone molecules for an excitation wavelength of 313 nm almost identical to the emission bands of the diacetyl's spectrum (Almy *et al*., 1940). Furthermore, Almy and Anderson (1940) stated that they observed chemical evidences of diacetyl's presence in acetone. Several authors hypothesized that the observed "green" phosphorescence, which increases the overall intensity of the signal recorded in the present work, is directly emitted by diacetyl molecules that form after a decomposition of acetone molecules and a subsequent recombination of two free acetyl radicals CH_3CO (Heicklen & Noyes, 1959; Dorfman & Noyes, 1948). However, diacetyl molecules do not emit when excited at 310 nm, a fact that was verified in the present work. In fact, the diacetyl's excitation to the triplet electronic state that foreruns the phosphorescence emission is caused by molecular collisions with excited acetone molecules, following a molecular energy-transfer process known as photosensitization (Yip *et al*.,1994). The laser excitation produces, therefore, two groups of chemical reactions. In the first one, the diacetyl formation is described by the following equations:

$$CH_3COCH_3 + h\nu_{ex}(\lambda_{ex} = 310\text{nm}) \rightarrow CH_3CO + CH_3, \tag{5.35}$$

$$2CH_3CO \rightarrow CH_3(CO)_2CH_3. \tag{5.36}$$

As discussed by Lozano *et al*. (1999), the diacetyl formation reduces as the excitation wavelength decreases from 310 nm because other photodecomposition reactions take place and become dominant. The second group of laser-induced chain reactions starts from the acetone singlet excitation and generates the triplet diacetyl emission through the following equations:

$$Ac + h\nu_{ex}(\lambda_{ex} = 310\text{nm}) \rightarrow {}^1Ac^*, \tag{5.37}$$

$${}^1Ac^* \rightarrow {}^1Ac, \tag{5.38}$$

$${}^1Ac \rightarrow {}^3Ac, \tag{5.39}$$

$${}^3Ac + Di \rightarrow Ac + {}^3Di, \tag{5.40}$$

$${}^3Di \rightarrow Di + h\nu_p, \tag{5.41}$$

in which, Eq. (5.38) represents the vibrational relaxation towards the lowest energy level in the singlet excited state, Eq. (5.39) represents the intersystem crossing from singlet to triplet acetone, and Eq. (5.40) corresponds to the triplet-energy-transfer mechanism that allows triplet diacetyl formation. In Eq. (5.41), ν_p is the frequency of the emitted phosphorescent photon.

Similarly, we investigated the phosphorescence emission of pure diacetyl vapor at 5 kPa for excitation wavelengths ranging from 410 to 470 nm. The results are shown in Figure 5.14. As for the data in Figure 5.12, the pulse energy was set to 30 µJ and the average energy density was about 0.04 J/cm^2 for all the excitation wavelengths used. In this range, the emission has a maximum at 410 nm. It can be ascertained that the phosphorescence intensity does not follow the absorption spectrum as a function of the excitation wavelength. By moving from 410 to 470 nm, the signal tends to decrease, even if higher absorption can be found from 420 up to 450 nm. It is possible that a lower wavelength excitation could provide higher emission. Unfortunately, the OPOlette laser cannot provide excitation wavelengths between 355 nm and 410 nm, and, therefore, we could not investigate this part of the spectrum. In Figure 5.14b, the light intensity is normalized with respect to that provided by an excitation at 410 nm. Further investigations on the dependency of diacetyl phosphorescence from the excitation wavelength were carried out also at lower pressures. These experimental results are not here presented, since they only confirm, once again, that the excitation wavelength at which the signal intensity is maximized is 410 nm, at least in the range 410 to 470 nm.

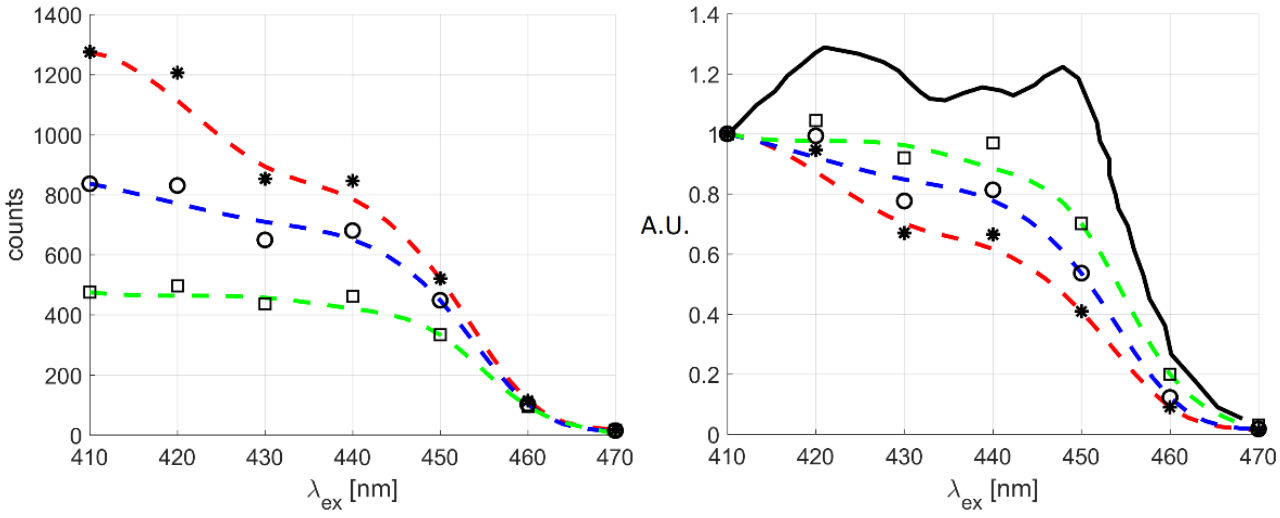

(a) (b)

Figure 5.14. (a) Phosphorescence emission S_{gp} of diacetyl vapor at $p = 5$ kPa and $T = 293$ K as a function of the excitation wavelength and for t = 5 µs (✱- -), 10 µs (○ - -), 25 µs (□ - -) after the laser excitation. In (b) the same data as in (a) are normalized with respect to the light intensity emitted for an excitation at 410 nm. The average laser intensity is 0.04 J/cm^2, and the recording parameters are: $N_l = 100$, $N_i = 10$, $G = 100\%$, and $\Delta t_{gate} = 100$ ns. The black solid line represents the absorption spectrum of diacetyl, taken from Stier and Koochesfahani (1999).

5.3.6 Phosphorescence emission of pure tracers at low pressure

In the light of the results shown in Section 5.3.5, the wavelengths 310 and 410 nm have been chosen as optimum values for exciting the acetone and the diacetyl vapors, respectively. A direct comparison between the phosphorescence intensity given by acetone excited at 310 nm and that of diacetyl excited at 410 nm is shown in Figure 5.15. It represents the phosphorescence intensity of both tracers with respect to the delay time, from 1 to 100 μs, at p = 5 kPa. Each point in the figure corresponds to an average of 10 images, each image resulting from the integration of 100 excitations. The IRO gain and gate were 100 % and 100 ns, respectively. Figure 5.15 shows that the diacetyl signal can be from 2 to 5 times higher than the acetone signal, between 1 and 100 μs after the laser excitation. As previously discussed, since the growth of acetone emission intensity resulting from moving the excitation wavelength from 266 to 310 nm is probably due to diacetyl's emission, it was expected that from a direct excitation of diacetyl vapor a stronger signal intensity could be obtained.

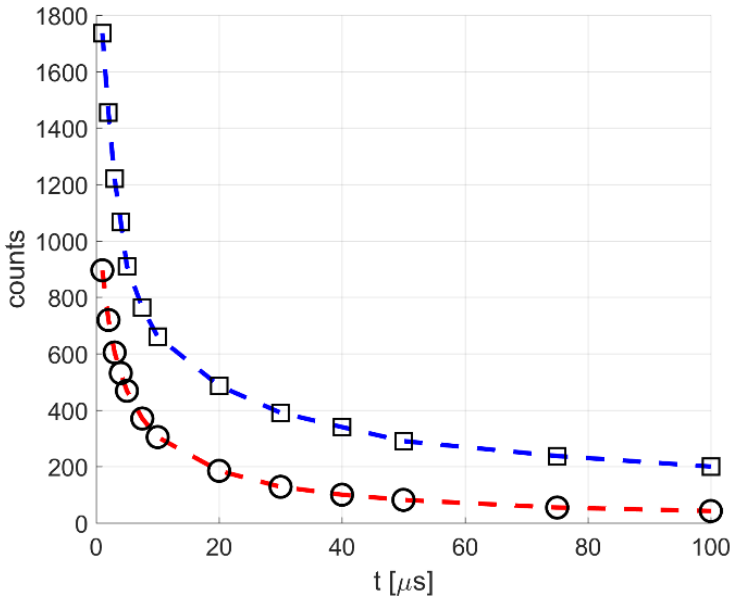

Figure 5.15. Time evolution of phosphorescence emission $S_{gp}(t)$ for acetone (○ - -) and diacetyl (□ - -) at p = 5 kPa and T = 293 K, respectively excited at 310 and 410 nm. For all data shown in the figure, the average laser intensity is 0.08 J/cm^2, and the recording parameters are: N_l = 100, N_i = 10, G = 100%, and Δt_{gate} = 100 ns.

5.3.7 Phosphorescence emission of acetone and diacetyl in helium mixture

The phosphorescence lifetime of acetone excited at 310 nm and diacetyl excited at 410 nm have been analyzed in helium mixtures at low pressures and relatively low tracer concentrations. Figure 5.16 shows the time evolution of phosphorescence emission for acetone and diacetyl in helium at p = 1 kPa and with a tracer molar fraction χ = 5% and χ = 2% for the case of acetone and diacetyl, respectively. At this low acetone partial pressure level of 50 Pa, it is necessary to further increase the number of laser excitations integrated in each image for collecting

enough light when the highest delay times are used. The data on acetone phosphorescence in Figure 5.16 have been recorded for $N_l = 500$, $N_i = 10$, $G = 100\%$, and $\Delta t_{gate} = 500$ ns and shows an exploitable signal that lasts at least 100 µs. In a 1-mm deep channel, these conditions correspond to $Kn_H = 0.015$, which is within the slip flow regime.

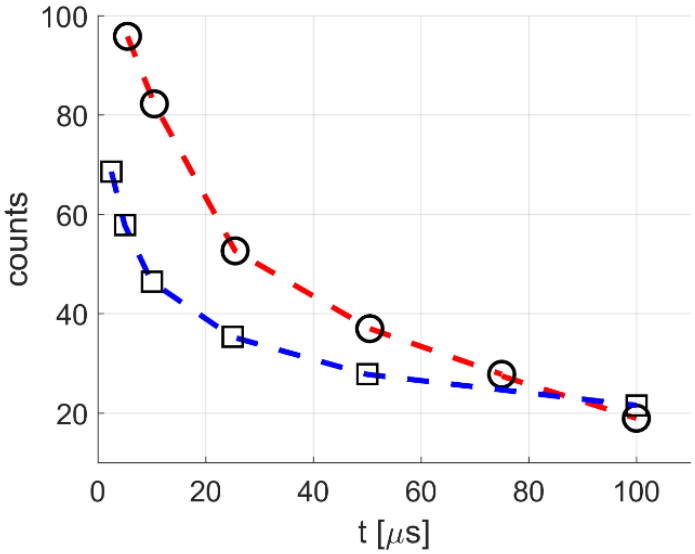

Figure 5.16. Time evolution of phosphorescence emission $S_{gp}(t)$ in helium for acetone (○ - -) and diacetyl (□ - -) at $p = 1$ kPa and $T = 293$ K. For the data on acetone emission: $\lambda_{ex} = 310$ nm, $\chi = 5\%$, $N_l = 500$, $N_i = 10$, $G = 100\%$, and $\Delta t_{gate} = 500$ ns. For the data on diacetyl emission: $\lambda_{ex} = 410$ nm, $\chi = 2\%$, $N_l = 100$, $N_i = 10$, $G = 100\%$, and $\Delta t_{gate} = 500$ ns. For all the data shown in figure, the average laser intensity is 0.08 J/cm^2.

By mixing helium with diacetyl, a signal intensity comparable to that of acetone can be obtained, even for lower molecular tracer concentration and number of excitations per image. The data on diacetyl phosphorescence in Figure 5.16 have been recorded for $N_l = 100$, $N_i = 10$, $G = 100\%$, and $\Delta t_{gate} = 500$ ns. In a 1-mm deep channel, these thermodynamic conditions provide a Knudsen number $Kn_H = 0.015$. A comparison of the data of Figure 10 shows that the two mixtures generate about the same absolute signal intensity. For instance, both tracers provide an intensity around 20 counts at 100 µs. However, a diacetyl-helium mixture with a concentration of $\chi = 5\%$ and 500 excitations per image would result in a signal almost 10 times higher than that provided by the acetone-helium mixture.

By increasing the diacetyl molar fraction, a strong signal can be obtained even at lower pressures. Figure 5.17 shows the phosphorescence emission in time for a diacetyl-helium mixture with a total pressure of 500 Pa and with 10 % and 20 % of diacetyl molar concentration. In a 1 mm deep channel, these thermodynamic conditions

correspond to $Kn_H = 0.027$ and 0.022, respectively. The acquisition parameters are the same as those used for the data of Figure 5.17.

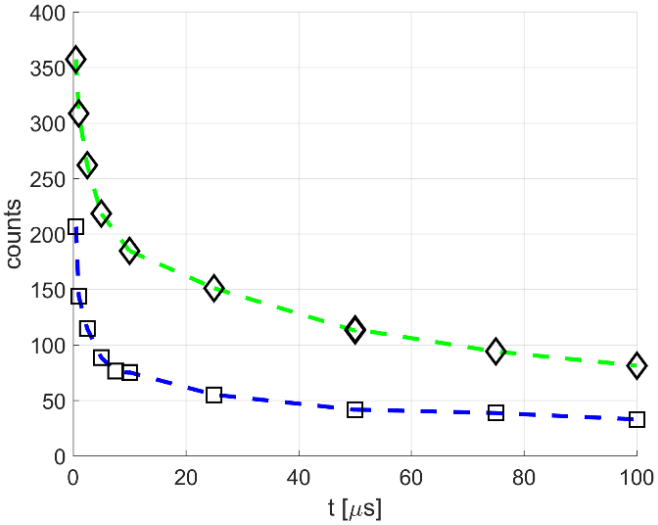

Figure 5.17. Time evolution of diacetyl phosphorescence $S_{gp}(t)$ in helium at p = 500 Pa and $T = 293$ K for diacetyl molar fractions $\chi = 10\%$ (□ - -) and $\chi = 20\%$ (◇ - -). The recording parameters are $N_l = 100$, $N_i = 10$, $G = 100\%$, and $\Delta t_{gate} = 500$ ns. For all data shown in the figure, the average laser intensity is 0.08 J/cm^2, and the excitation wavelength is 410 nm.

However, by comparing the data of Figure 5.16 and Figure 5.17, it can be noticed that the signal intensity is far higher in Figure 5.17, even if the mixture has lower pressure. This is because the data of Figure 5.16 refer to a diacetyl-helium mixture at 1 kPa with only 2 % of diacetyl, that is a diacetyl partial pressure of 20 Pa. In Figure 5.17, although the gas mixture has a total pressure two times lower, diacetyl partial pressure is 50 Pa and 100 Pa for molar fractions of 10 % and 20 %, respectively. shows the raw images acquired for the mixture at $\chi = 10\%$ for t = 10, 25, and 50 μs. It is worthy to remind that these images have been taken with the minimum effort in terms of laser pulses and averaged images. Clearly, higher quality images can be obtained by increasing N_l and N_i, which are here set to 100 and 10, respectively. The comparison of Figure 5.18 with Figure 5.11 is representative of how this experimental study provided an evident improvement of the signal quality at low pressures.

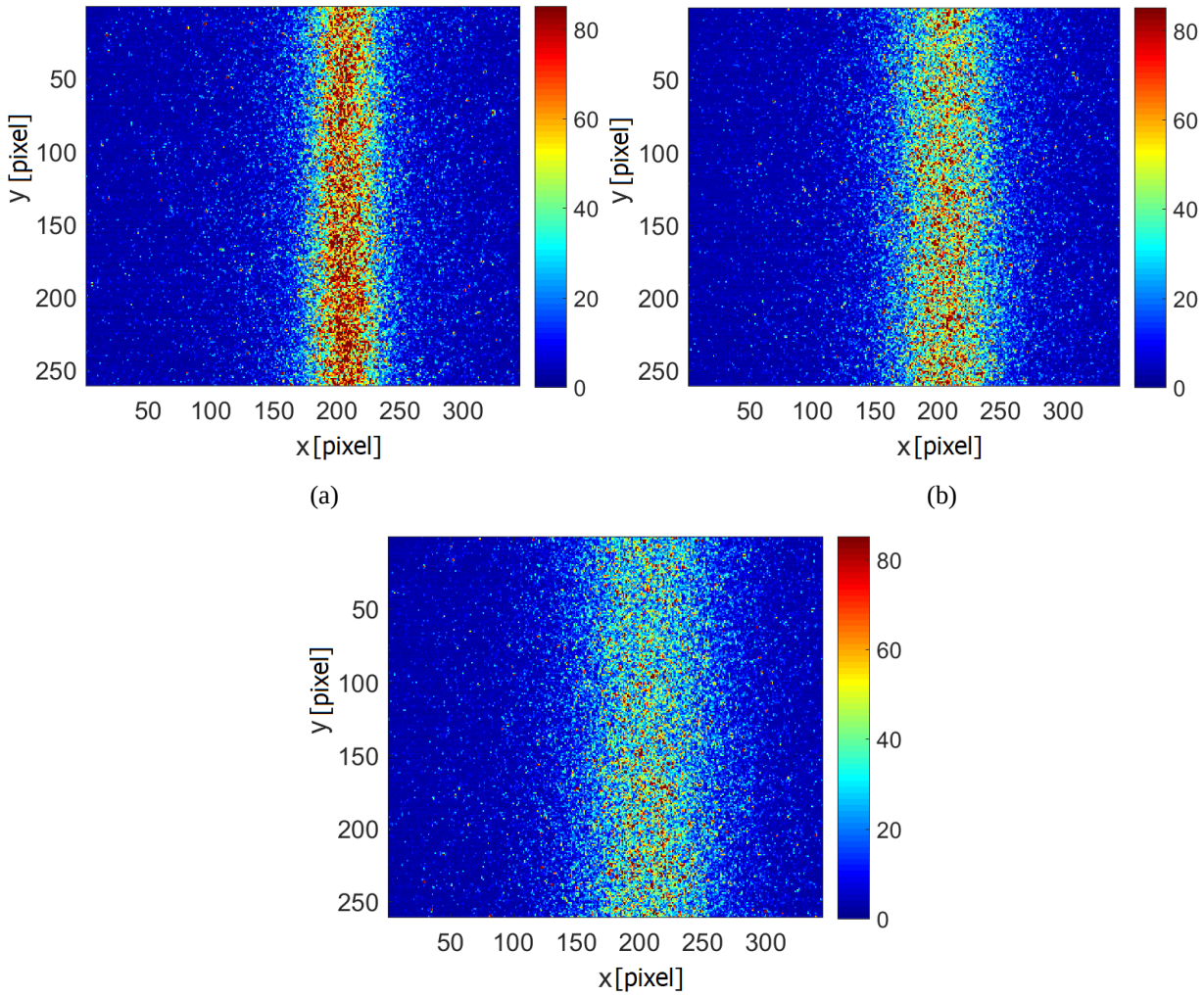

Figure 5.18. Raw images of diacetyl phosphorescence emission in helium at p = 500 Pa and T = 293 K for a diacetyl molar fraction χ = 10% at (a) t = 10 μs, (b) t = 25 μs, and (c) t = 50 μs. The images refer to the data from Figure 5.17 at χ = 10%.

5.3.8 Statistical analysis on Gaussian peak position

In MTV technique, the velocity profile of the investigated gas flow is extracted by measuring the molecular displacement of the tagged tracer molecules. The position of the tagged line is identified with the peak of intensity of the phosphorescence emission distribution. The same Gaussian fitting function employed in this analysis for quiescent gas mixtures is used in gas flows for the identification of the deformed tagged line. The estimation of the uncertainty on the measured molecular displacement is of fundamental importance for estimating the precision on the velocity measurement. A first preliminary analysis on this regard can be based on the images of the diffusing phosphorescing molecules that have been collected during this experimental study.

For instance, Figure 5.19a shows diacetyl phosphorescence excited at 410 nm in helium at p = 1 kPa and χ = 10%. The light distribution corresponds to the emission at 50 μs after the laser excitation for Δt_{gate} = 1 μs, N_l = 100,

and N_i = 10. Figure 5.19b shows the peak position $s_{x,i}$ at each line i along the beam of phosphorescent molecules, identified by applying the Gaussian fitting per line. The bars represent one standard deviation $\sigma_{sx,i}$ of the Gaussian distribution on each line. $\sigma_{sx,i}$ is representative of the thickness of the Gaussian profile at each line, but it does not provide directly the uncertainty on the peak position related to one horizontal line of pixels. The definition of $s_{x,i}$ and $\sigma_{sx,i}$ is substantially identical, respectively, to that of the fitting parameters a_4 and a_3 defined in Section 5.3.1. The only difference is that the parameters a_4 and a_3 are related to a Gaussian function that fits the data distribution that results from the vertically averaging the whole image.

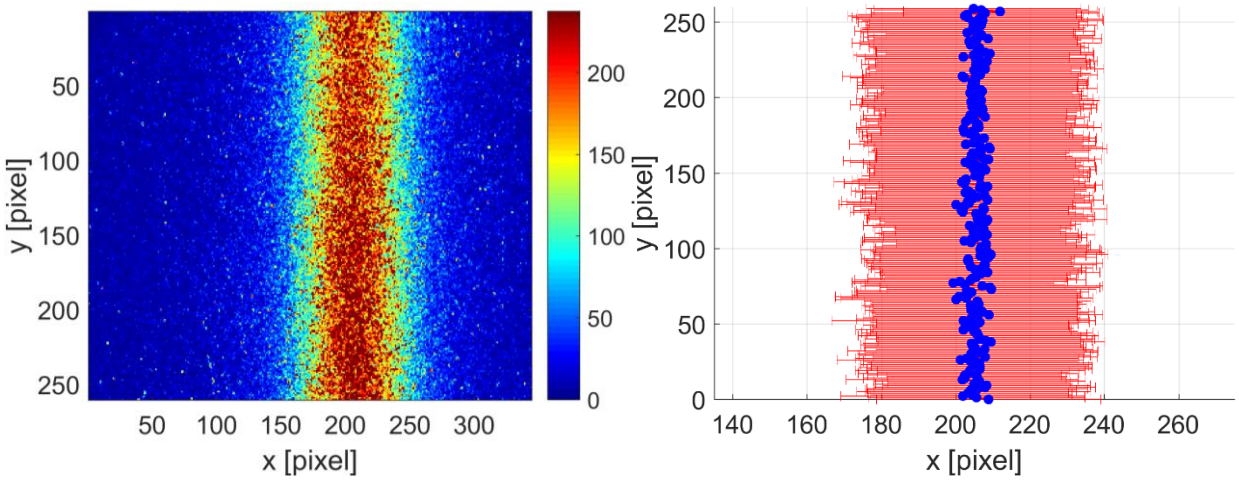

(a) (b)

Figure 5.19. (a) Raw image of diacetyl phosphorescence emission in helium at p = 1 kPa, T = 293 K, for a diacetyl molar fraction χ = 10% at t_d = 50 µs, ; (b) the blue dots correspond to the peak position $s_{x,i}$ of the Gaussian fitting function applied at each line along the laser beam direction, while the red bars represent one standard deviation σ_{sx} of the Gaussian profile on each horizontal line of pixels.

The mean position of the tagged line μ_x in one image is calculated as

$$\mu_x = \frac{\sum_{i=1}^{N_y} s_{x,i}}{N_y}. \tag{5.42}$$

and its physical meaning is identical to that of the fitting parameter a_4 defined in Section 5.3.1. The uncertainty on $s_{x,i}$ can be estimated by calculating the standard deviation around the mean position of the tagged line as

$$\sigma_{\mu_x} = \frac{\sum_{i=1}^{N_y} (s_{x,i} - \mu_x)^2}{N_y - 1}. \tag{5.43}$$

In MTV, the precision in evaluating the molecular displacement also depends on the precision of measuring the position of the initial tagged line, which can be affected by fluctuations due to small accidental movements of the

laser beam. The statistical fluctuations on the position of the tagged line can be estimated by calculating the standard deviation on μ_{sx} measured from different images recorded in one day.

Table 5.4 lists the mean of the standard deviation $\overline{\sigma_{sx}}$ of the Gaussian profile, the tagged line position μ_x, and the standard deviation σ_{μ_x} on the tagged line position for images at different delay times t, different IRO gain G, and different IRO gate Δt_{gate}. The data refers to diacetyl phosphorescence excited at 410 nm in a mixture of helium at p = 1 kPa and χ = 10%. Because the images were recorded with a binning 4 × 4, one pixel corresponds to 15.2 μm. In the table, two sections of data are highlighted: in the first one, only the IRO gain is modified, while in the second one the IRO gate is modified. The rest of the data represents how the time of acquisition with respect to the laser excitation influences the statistical quantities under consideration.

t_d [ns]	Gain G [%]	Gate Δt_{gate} [ns]	$\overline{\sigma_{sx}}$ [pixels]	μ_x [pixels]	σ_{μ_x} [pixels]
5	85	100	61.57	205.08	0.43
500	85	100	62.72	204.91	1.23
1000	85	100	72.33	205.23	1.45
2500	85	100	100.61	205.55	1.53
5000	**85**	100	138.99	205.43	1.83
5000	**100**	100	138.08	205.19	2.88
7500	100	100	181.74	205.13	3.12
10000	100	100	223.36	205.25	3.43
25000	100	100	428.98	205.34	4.71
50000	100	**100**	813.35	204.82	5.43
50000	100	**500**	861.78	205.13	2.69
50000	100	**1000**	872.35	205.41	2.04

Table 5.4. Mean value $\overline{\sigma_{sx}}$ of the standard deviation of the Gaussian profiles along the laser beam direction, tagged line position μ_x, and standard deviation σ_{μ_x} characterizing the peak position on each horizontal line of pixels for different recording parameters. The data refers to images of diacetyl phosphorescence excited at 410 nm in helium at p = 1 kPa and χ = 10%. All the images were recorded by setting N_l = 100 and N_i = 10. The statistical quantities are given in pixels, and one pixel corresponds to 15.2 μm. The two highlighted sections show the effect of variation in the IRO gain or in the IRO gate.

As expected, $\overline{\sigma_{sx}}$ increases with time because of the diffusion of the tagged molecules. For the same reason, increasing the IRO gate makes $\overline{\sigma_{sx}}$ larger. Differently, the IRO gain does not seem to have any particular effect on the shape of the distribution. It is worth noting that $\overline{\sigma_{sx}}$ has the same meaning of the fitting parameter a_3 defined in Section 5.3.1. Because they are calculated differently, their values are slightly different, but almost identical.

The position of the tagged line μ_{sx} does not vary substantially. The standard deviation on the value μ_x of all the images considered is about 0.2 pixel, that is about 3 μm. This means that the uncertainty on the tagged line position produced by possible fluctuations in the laser beam position is dominated by the CCD resolution.

The uncertainty on the peak position σ_{μ_x} is mainly determined by the quality of the signal, i.e., on the signal-to-noise ratio of the phosphorescence intensity, and not by the resolution of the CCD. As the time passes after the laser excitation, the SN ratio decreases because of the molecular diffusion and of the phosphorescence decay, thus σ_{μ_x} increases. For the same reason, increasing the IRO gate reduces the uncertainty on the peak position, as shown in the second group of data highlighted in the Table 5.4. Instead, increasing the IRO gain makes the uncertainty on the peak position higher but does not increase $\overline{\sigma_{sx}}$. These observations demonstrate that the uncertainty on the peak position identification depends more on the SN of the phosphorescence intensity than on the thickness of the tagged line. It is important to underline that, however, the decreasing uncertainty σ_{μ_x} with increasing IRO gate is due to the fact that the gas mixture is quiescent. In gas flows, the peak position moves in the flow direction proportionally to the gas velocity magnitude and, therefore, the IRO gate integrates different positions of the peak on the same image. In this case, the gain in reducing the uncertainty σ_{μ_x} must be compared to the region covered by the moving peak in order to assess the benefits of increasing the IRO gate.

It should be kept in mind that the final deformed tagged line used for extracting the velocity profile is not based directly on the mean displacement data, but it is based on a fitting function that is numerically generated from a mathematical model that describes the advection-diffusion of the tracer in the background gas. This reconstruction method, which is described in the next chapter, helps, therefore, in filtering the fluctuations on the displacement data and in reducing the uncertainty on the deformed tagged line used for computing the velocity profile.

5.4 Quantification of phosphorescence lifetime and molecular diffusion

The experimental data reported in the previous section are sufficient to proceed in analyzing the feasibility of MTV applications to gas flows in the slip regime. Nevertheless, the qualitative analysis above presented on the time evolution of the phosphorescence intensity does not allow to clearly understand which ones are the most important intramolecular mechanisms that determine the phosphorescence decay experimentally observed.

Most of the experimental data found in the literature demonstrates an exponential decay of the triplet lifetime for both acetone (Kaskan & Duncan, 1950; Copeland & Crosley, 1985) and diacetyl (Sidebottom *et al*., 1972; Parmenter & Poland, 1969). The mathematical model that well represents the experimental observations made by these authors is given by Eq. (5.16), in which the triplet molecule concentration $n_{T1}(x, y, z, t)$ decays in time as a consequence of linear radiative and non-radiative de-excitations. Differently, all the experimental results of this work demonstrate a non-exponential decay of the phosphorescence emission and, thus, the mathematical model Eq. (5.16) cannot explain the observed phenomenon. A large part of this work has been focused in shedding light on the reasons of these observations.

In the light of MTV technique, the interest in acquiring a more in-depth knowledge of the photoluminescence processes taking place after the laser excitation derives from different reasons.

Because of the relatively strong molecular diffusion and the interactions of the tagged molecules with the channel walls, MTV requires a numerical post-processing treatment of the measured molecular displacement for correctly extracting the gas velocity profile. The accuracy of the velocity measurements strongly depends on the accuracy in modeling the molecular diffusion of the tracer through the background gas. The reconstruction method is based on an advection-diffusion equation that governs the evolution of the tagged line from its initial position. In this mathematical representation, the diffusion coefficient D_{12}, which represents the diffusion of tracer molecules through a gas-tracer mixture, needs to be calculated a priori. As it will be discussed in Chapter 6, the velocity profile computed by means of the reconstruction method is very sensitive to the value of D_{12} introduced in the advection-diffusion equation, especially for measurements at low pressures. In the previous work of Si-Hadj Mohand *et al*. (2017), the diffusion coefficient D_{12} used for the velocity reconstruction has only been theoretically estimated. In first approximation, the Chapman-Enskog formula for binary gas mixture (Marrero & Mason, 1972) provides:

$$D_{12} = \frac{3\sqrt{\pi}}{8}\sqrt{\frac{k_B T}{m_{12}}}\frac{1}{\sqrt{2}\pi d_{12}^2 n}, \tag{5.44}$$

where $d_{12} = \frac{d_1+d_2}{2}$ is the average molecular diameter, k_B is the Boltzmann constant, n is the overall density number of the mixture, and $m_{12} = \frac{m_1 m_2}{m_1+m_2}$ is the reduced molecular mass. For the notation here adopted, d_1 and m_1 are, respectively, the molecular diameter and the molecular mass of the carrier gas, whereas d_2 and m_2 are the same quantities characterizing the tracer vapor, i.e., acetone or diacetyl. Even though more accurate formulas for estimating D_{12} are available and have been used (see Chapter 6), the accuracy of the diffusion coefficient depends on the accuracy of estimating the kinetic properties of the tracer. While the molecular mass can be trivially calculated once the chemical composition of the molecule is known, the estimation of the molecular diameter d_2 is a more cumbersome task. The literature reports very few rough estimations of the kinetic diameter of acetone and diacetyl molecules. Moreover, the few values found are not consistent. The only data related to the kinetic diameter of acetone and diacetyl molecules that could be found in the literature are listed in Table 5.5.

Almy and Anderson (1940) estimated the kinetic diameter of diacetyl to be $d_{Di} \cong$ 590 pm from experimental data on phosphorescence lifetime. Mirzaei *et al*. (2012) estimated from experimental measurements of the self-diffusion coefficient a kinetic diameter two times bigger, $d_{Di} \cong$ 1180 pm. For acetone molecules, the estimated values of its kinetic diameter d_{Ac} are in the range 460-730 pm. Because the diffusion coefficient depends on the square of the molecular diameter, this range of uncertainty on d_2 can lead to uncertainties on the diffusion coefficient of Eq. (5.44) of more than 50%.

References	Kinetic diameter of acetone	Kinetic diameter of diacetyl
Frezzotti *et al*. (2015)	730 pm	-
Nadykto & Yu (2003)	616 pm	-
Gales *et al*. (2000)	460 pm	-
Bowen *et al*. (2004)	469 pm	-
Almy & Anderson (1940)	590 pm	590 pm
Mirzaei *et al*. (2012)	-	1180 pm

Table 5.5. Data in the literature on kinetic diameter of acetone and diacetyl molecules.

For this reason, the experimental data obtained in this work on phosphorescence emission of acetone and diacetyl can be useful for measuring the diffusion coefficient at different pressures and, by means of a kinetic model such as Eq. (5.44), new data on the kinetic diameter can be provided. Indeed, the images recorded during this experimental work represents both the diffusion in space and the phosphorescence decay of the excited molecules. A mathematical model capable of providing analytical or numerical solutions that can fit well the evolution of the light distributions experimentally observed can be a tool for extracting parameters of interest, such as the diffusion coefficient. Indeed, this work demonstrates that the extraction of the coefficient diffusion from the experimental results cannot be separated from the correct modeling of the most important intramolecular processes taking place during the phosphorescence emission.

Moreover, the development of such mathematical model is the first step towards a reconstruction method for MTV that is able to process the whole 2D light distribution collected in the images. In Chapter 6, it is demonstrated that an evolution of the post-processing tools for extracting the velocity profile from the molecular displacement is an urgent need for finally measuring a slip velocity at the wall and directly quantifying the effects of thermodynamic non-equilibrium. The current reconstruction method extracts the velocity profile only from the evolution of the mean molecular displacement in the flow direction of the light distribution on the image, but it does not exploit the information related to how the molecular diffusion spreads in space the tagged tracer. The combination of an advanced 2D reconstruction method and a proper 2D fitting function of the image data might be in the future a key technique for simultaneous measurements of velocity profiles and tracer diffusion coefficient.

The experimental and theoretical analysis presented in this section is, therefore, of crucial importance for the progress of MTV application to gas flows. Indeed, the theoretical explanations of these experimental observations and the numerical tools here developed are also necessary for the development of other molecular tagging techniques, such as MTT and MTM. In Section 5.4.3, it is demonstrated that the phosphorescence lifetime strongly depends on the laser energy excitation and the vapor partial pressure employed because of the triplet-triplet annihilation (TTA) mechanism, a phenomenon that is not described in the model presented in Eq. (5.20). In the perspective of developing thermometry and manometry techniques based on phosphorescence emission, a correct

description of the intramolecular processes is of fundamental importance for establishing a relationship between the phosphorescence decay time and, respectively, the gas temperature and the gas pressure.

In Section 5.4.1, the image processing procedure for computing the quantities of interest is explained. Section 5.4.2 presents the experimental results in terms of these quantities that have been considered for this theoretical analysis. In Section 5.4.4, the parameter identification algorithm for extracting the TTA rate and the diffusion coefficient from the experimental data is briefly described. Finally, the results provided by the parameter identification algorithm are presented and discussed.

5.4.1 Image processing procedure

The Gaussian peak intensity $S_{gp}(t)$ defined in Section 5.3.1 for analyzing the time evolution of the signal includes information on both the molecular diffusion and the triplet population lifetime. An analysis that allows to shed light on the intramolecular mechanisms and a quantification of the molecular diffusion requires instead the definition of quantities that represent separately the two phenomena. For each image recorded at a certain time t, two parameters are calculated: the total light (TL) and the variance σ_x^2 of the light distribution.

TL represents the simple integration of the all the counts collected in each pixel of the CCD. The TL related to an image recorded at time t is:

$$\mathrm{TL}(t) = \sum_{i=1}^{N_{x,pixel}} \sum_{j=1}^{N_{y,pixel}} S_{ij}(t), \tag{5.45}$$

where S_{ij} is the signal in counts collected on the (i, j) pixel, $N_{x,pixel}$ is the number of pixels in the *x*-direction, and $N_{y,pixel}$ is the number of pixels in the *y*-direction. Because the noise floor for each pixel oscillates between 2 and 5 counts when a 4 × 4 binning is used, the minimum TL detectable for a CCD resolution of 344 × 260 pixels is between 178880 and 357760 counts, respectively. The TL is usually of the order of 10^6 counts. As discussed in Chapter 4, the relative uncertainty provided by instrumental noise of the ICCD is less than 2%. Indeed, the dominant uncertainty on the TL value is given by oscillations in the laser energy density and unpredictable oxygen quenching. Differently from the Gaussian peak intensity, TL is not directly affected by the molecular diffusion and the only information that provides is related to the time evolution of the tracer triplet population $N_{T1}(t)$. Because the light emitted per unit volume is proportional to the excited molecule concentration, the time evolution of the total light collected by the ICCD corresponds to the time evolution of the number of excited molecules except for possible non-linearities introduced by the acquisition system, e.g., the optical collector. Moreover, TL is representative of the excited molecules lifetime only if the light distribution remains inside the FOV of the camera. The invariance of the physical phenomenon along the laser beam direction guarantees that the tagged molecules that diffuse through the top and the bottom boundaries of the FOV are substituted by tagged molecules

that comes from outside to the inside of the FOV. Differently, if the molecular diffusion moves the tagged molecules out of the FOV through its lateral boundaries, TL decreases but not because of triplet de-excitations. Therefore, if it is guaranteed that the light distribution, or at least most of it, remains inside the FOV, TL is representative of the time evolution of the triplet population. However, as it will be discussed in Section 5.4.3, the triplet lifetime and, thus, TL is dependent of the molecular diffusion through non-linear, non-radiative de-excitations.

The variance σ_x^2 of the signal distribution is calculated with the same procedure of Section 5.3.1. The image is averaged along the laser beam direction providing a 1D signal distribution $\tilde{S}(x,t)$ and a fitting function is used for filtering the noise. An improvement of the procedure introduced in Section 5.3.1 is given in Appendix B, where a sum of Gaussian functions is used for better representing the signal distribution. Whatever is the function employed for fitting $\tilde{S}(x,t)$, the variance of the 1D signal distribution is calculated σ_x^2 by applying the following definition

$$\sigma_x^2(t) = \frac{\sum_{i=1}^{N_{x,pixel}} (x_i - \mu_x)^2 \tilde{S}(x_i,t)}{\sum_{i=1}^{N_{x,pixel}} \tilde{S}(x_i,t)}, \tag{5.46}$$

in which x_i is the position of the i-th pixel along the x axis of the CCD sensor, and μ_x is the average position of the excited molecules, as defined in Eq. (5.42). This quantity represents how the excited molecules are distributed in the space and increases because of the molecular diffusion. However, as discussed in Section 5.4.3, non-linear non-radiative de-excitation mechanisms can modify the shape of the distribution, so that the time evolution of $\sigma_x^2(t)$ is affected also by the number of molecules present in a specific location.

Figure 5.20 and Figure 5.21 schematizes how the recorded images are processed for computing the evolution of TL and σ_x^2 in time. In order to compare the experimental data with the numerical data provided by the chosen mathematical model for representing the excited molecules lifetime, TL data are normalized with respect to the value at the first delay time available. For a similar reason, the variance at the first time $\sigma_{x,0}^2$ is subtracted from $\sigma_x^2(t)$.

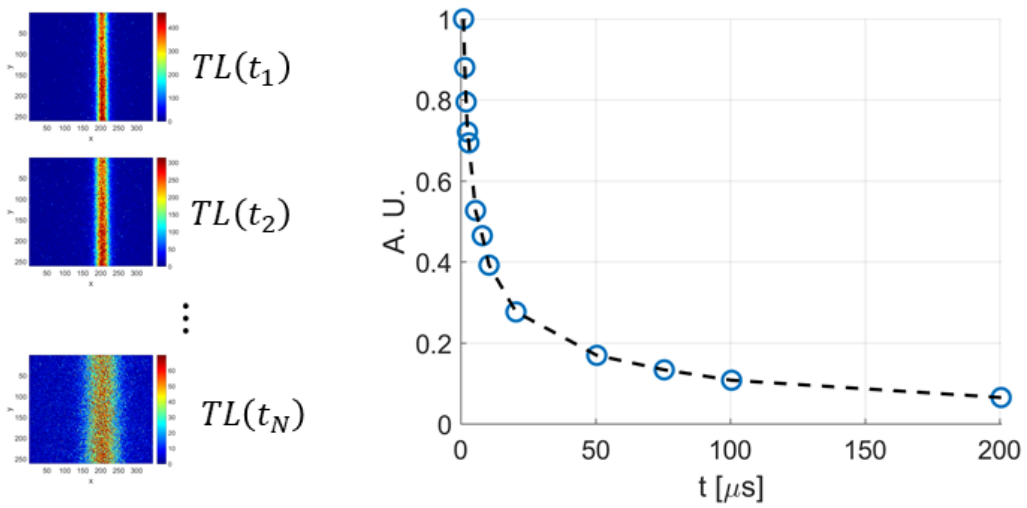

Figure 5.20. Computation of TL from recorded images and representation in time of the excited molecule population.

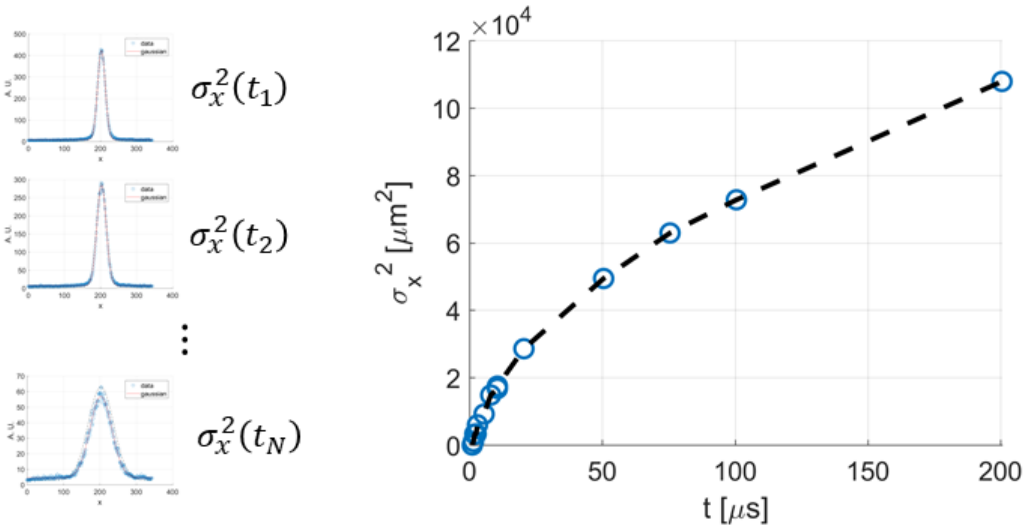

Figure 5.21. Computation of the variance σ_x^2 from 1D signal distribution $\tilde{S}(x,t)$ and representation in time of the spatial distribution of the excited molecules.

5.4.2 Experimental data on TL and σ_x^2

The mathematical analysis has been applied to experimental data that refer to the phosphorescence emission of only pure acetone and diacetyl vapors. This is the starting point for shedding light on which are the intramolecular processes that determine the evolution in time of the observed light emission. No data related to acetone and diacetyl phosphorescence in gas mixture has been treated, but the following considerations and numerical tools developed in this work are still applicable.

Figure 5.22a and Figure 5.22b report the evolution in time of the TL normalized with respect to the value of TL at the first time. The data shown are related to some of the experimental data collected, respectively, for acetone

vapor excited at 310 nm and for diacetyl vapor at 410 nm. Experimental data on acetone vapor excited at 266 nm have also been collected but they are not shown in this work. At this excitation wavelength, the low phosphorescence quantum yield does not allow to extract quantitative information at pressures lower than 5 kPa. However, the experimental data of acetone excited at 266 nm have the same trend of those here presented for the case of acetone at 310 nm and diacetyl at 410 nm.

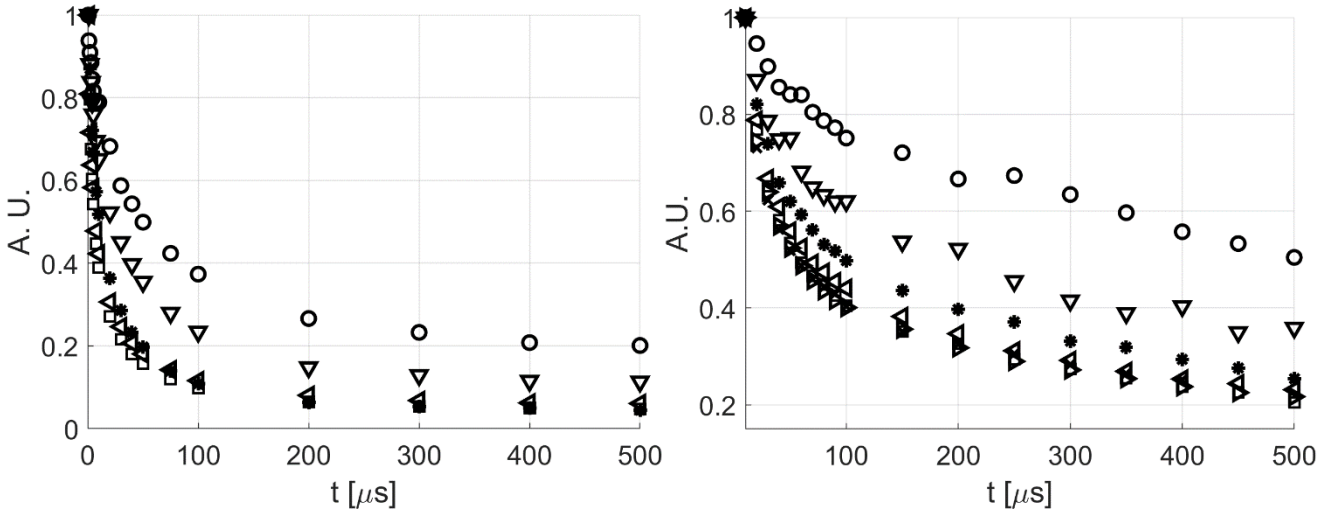

(a) (b)

Figure 5.22. Time evolution of the TL normalized at the first time for (a) acetone vapor excited at 310 nm and (b) diacetyl vapor excited at 410 nm at different pressures: (a), p = 1 kPa (○), p = 2 kPa (▽), p = 5 kPa (✱), p = 10 kPa (◁), p = 15.1 kPa (□); (b), p = 250 Pa (○), p = 500 Pa (▽), p = 750 Pa (✱), p = 1 kPa (◁), p = 1.5 kPa (□), p = 2 kPa (▷), p = 2.5 kPa (×). The recording parameters are $N_l = 100$, $N_i = 10$, $G = 100\%$, and $\Delta t_{gate} = 100$ ns. For all data shown in the figure, the average laser energy density is 0.08 J/cm^2.

The phosphorescence decay observed never follows an exponential function, and, therefore, the identification of a triplet lifetime τ_{T_1} constant from the experimental data cannot be done in a straightforward way. The amount of tracer molecules that absorb the light energy increases with the pressure, thus the absolute value of the TL increases as well. The normalized values of the TL shown in Figure 5.22 demonstrate, however, that the triplet population lifetime decreases with an increase of the vapor pressure, both for the case of acetone and diacetyl. This observation reveals the possibility of an intramolecular mechanism that depends on the collision rate between the molecules and that non-radiatively de-excites the triplet molecules to the ground state. Moreover, a closer look to the data of Figure 5.22 shows that the decrease of the triplet lifetime slows down as the pressure increases.

In order to highlight the physical dependence of phosphorescence lifetime from the rate of collision ν_{rate}, the time coordinate is made non-dimensional by means of the characteristic time of collision $1/\nu_{rate}$. For the pressure range investigated, acetone and diacetyl vapors can be assumed as dilute gases, for which only binary collisions

take place. Under this assumption and for a general IPL collisional model, the collision rate ν_{rate} can be expressed as a function of the vapor pressure p as

$$\nu_{rate} = \frac{p}{\mu} k_\nu, \tag{5.47}$$

where μ is the vapor dynamic viscosity and k_ν is the collision rate coefficient, which value depends on the collisional model employed. Data on viscosity of acetone and diacetyl vapors are absent in the literature but it can be estimated from the value of the mean free path as

$$\mu(T) = \frac{p}{k_\lambda \sqrt{RT}} \lambda. \tag{5.48}$$

with λ calculated as in Eq. (5.27). For a HS model, k_λ = 1.2766 and the viscosity at ambient temperature T = 293 K is $\mu = 0.666\times10^{-5}$ Pa s and $\mu = 1.244\times10^{-5}$ Pa s for acetone and diacetyl, respectively. The calculated collisional rates are reported in Table 5.6 and Table 5.7, respectively for acetone and diacetyl vapors. The normalized TL as a function of the non-dimensional time $t^* = t \cdot \nu_{rate}$ is shown in Figure 5.23.

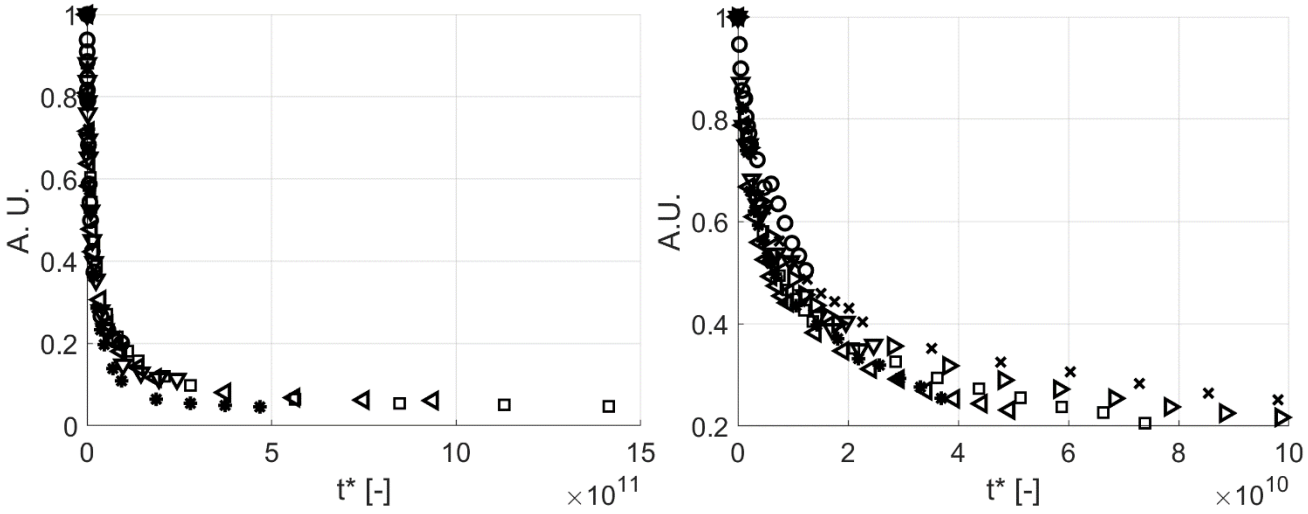

(a) (b)

Figure 5.23. TL normalized at the first time as a function of the non-dimensional time $t^* = \nu_{rate}(p)t$ for (a) acetone vapor excited at 310 nm and (b) diacetyl vapor excited at 410 nm at different pressures. The reported data are the non-dimensional version of the data of Figure 5.22: in (a), p = 1 kPa (○), p = 2 kPa (▽), p = 5 kPa (✱), p = 10 kPa (◁), p = 15.1 kPa (□); in (b), p = 250 Pa (○), p = 500 Pa (▽), p = 750 Pa (✱), p = 1 kPa (◁), p = 1.5 kPa (□), p = 2 kPa (▷), p = 2.5 kPa (×).

p [kPa]	1	2	5	10	15.1
ν_{rate}[$\times 10^{-9}$ s^{-1}]	0.2	0.5	0.9	1.9	2.8

Table 5.6. Collisional rates at different pressures for acetone vapor used for the non-dimensional time.

p [Pa]	250	500	750	1000	1500	2000	2500
ν_{rate} [$\times 10^{-8}$ s^{-1}]	0.25	0.5	0.75	1	1.5	2	2.5

Table 5.7. Collisional rates at different pressures for diacetyl vapor used for the non-dimensional time.

As a consequence of the dilute gas approximation, the collisional rate is proportional to the pressure, independently of the collisional model employed. Uncertainties in the estimated viscosity μ or the coefficient k_λ may produce errors in the characteristic time of collision but do not affect the scaling of the curves of Figure 5.23. For a better comparison of the non-dimensional lifetime at different pressures, the curves are all translated back of $t_0 \cdot \nu_{rate}$, where t_0 is the first time at the which the experimental datum is available. Both for the case of acetone and diacetyl, the curves tend to collapse into a single curve. The triplet lifetime $\tau_{T_1}(p)$ is, evidently, a decreasing function of the pressure, even though this dependency does not follow a perfect inversed proportionality. At high pressures, the collisional-dependent mechanism behind the decrease in the triplet lifetime reaches its saturation, and thus the non-dimensional decay shown in Figure 5.23 becomes slower.

The second quantity of interest is the variance σ_x^2 of the light distribution as a function of time. Figure 5.24 reports the values of σ_x^2 extracted from the same images processed for calculating the TL of Figure 5.22. The data of Figure 5.24 demonstrate that the variance evolves quite linearly in time only at the lowest pressures employed, that is at 1 kPa for acetone vapor and between 250-500 Pa for diacetyl vapor. Surprisingly, as the pressure increases, the time evolution of σ_x^2 becomes non-linear: in the first times after the laser excitation the variance of the distribution grows faster, whereas, at later times, it slows down towards a linear evolution. This effect is clearer for the data related to acetone vapor because of the higher pressures employed. The highest pressure used for diacetyl vapor is 3000 Pa, while acetone has been tested for pressures up to 15 kPa. Diacetyl vapor could not be tested at the same high pressures because of its lower saturated vapor pressure, which is limited to about 6 kPa at ambient temperature. As for the TL, the evolution of σ_x^2 demonstrates a non-linear dependency from the vapor pressure.

The non-linear behavior of σ_x^2 was not expected at all. As it will be demonstrated in the next section, in the absence of non-linear effects on the triplet de-excitation, the molecular diffusion of the triplet molecules should make the variance of the molecules distribution evolve linearly in time and with a growth rate proportional to the diffusion coefficient D, as described by the Einstein's formula:

$$\sigma_x^2(t) = 2Dt + \sigma_{x,0}^2. \tag{5.49}$$

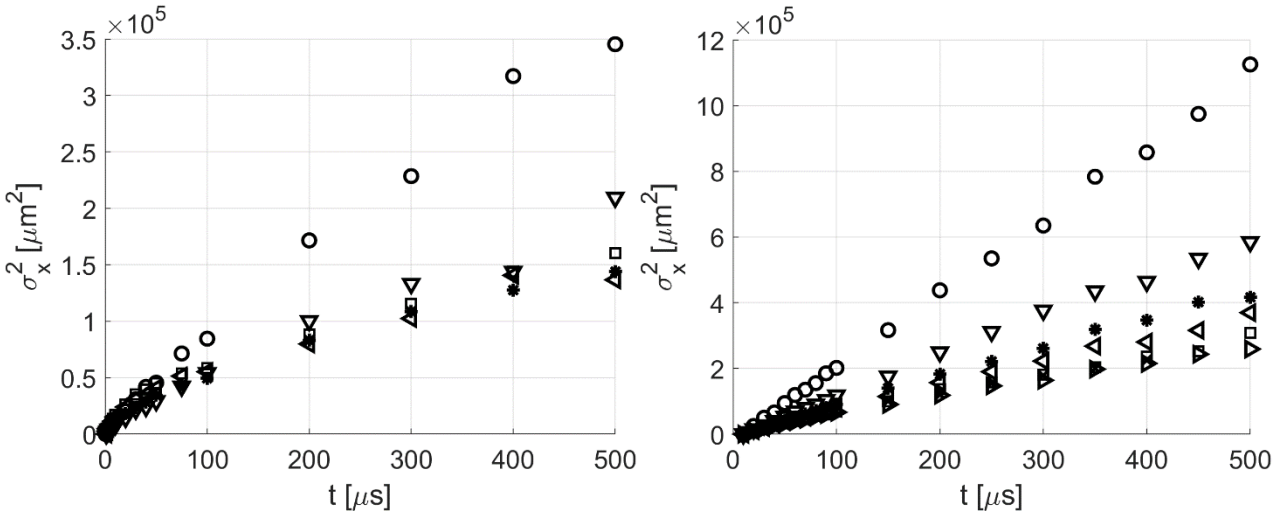

(a) (b)

Figure 5.24. Time evolution of the variance $\sigma_x^2(t) - \sigma_{x,0}^2$ for (a) acetone vapor excited at 310 nm and (b) diacetyl vapor excited at 410 nm at different pressures. In (a), p = 1 kPa (○), p = 2 kPa (▽), p = 2 kPa (✱), p = 5 kPa (◁), p = 10 kPa (□), p = 15.1 kPa (▷); in (b), p = 250 Pa (○), p = 500 Pa (▽), p = 750 Pa (✱), p = 1 kPa (◁), p = 1.5 kPa (□), p = 2 kPa (▷), p = 2.5 kPa (×). The recording parameters are $N_l = 100$, $N_i = 10$, $G = 100\%$, and $\Delta t_{gate} = 100$ ns. For all data shown in the figure, the average laser energy density is 0.08 J/cm^2.

The fact that the experimental data of Figure 5.24 do not follow Eq. (5.49) can be made clearer by expressing the same experimental data in a non-dimensional form. From the Chapman-Enskog theory, the diffusion coefficient at first order can be written as

$$D = D^* \lambda^2 \nu_{rate}, \tag{5.50}$$

where the constant $D^* = \frac{3\sqrt{\pi}}{8}$ for the case of HS model. Therefore, Eq. (5.50) can be made non-dimensional in the following manner:

$$\frac{\left(\sigma_x^2(t) - \sigma_{x,0}^2\right)}{\lambda^2} = 2D^*(\nu_{rate} t) \quad \rightarrow \quad \sigma_x^{2*}(t) = 2D^* t^*. \tag{5.51}$$

Eq. (5.51) states that if the experimental data follows the Einstein relationship, the non-dimensional variance should evolve linearly in time with the same slope $2D^*$, where D^* corresponds to the non-dimensional diffusion coefficient. Figure 5.24 reports the non-dimensional version of the data of Figure 5.25. This operation makes evident the fact that the variance is a non-linear function of time and grows faster at higher pressures in both acetone and diacetyl vapors.

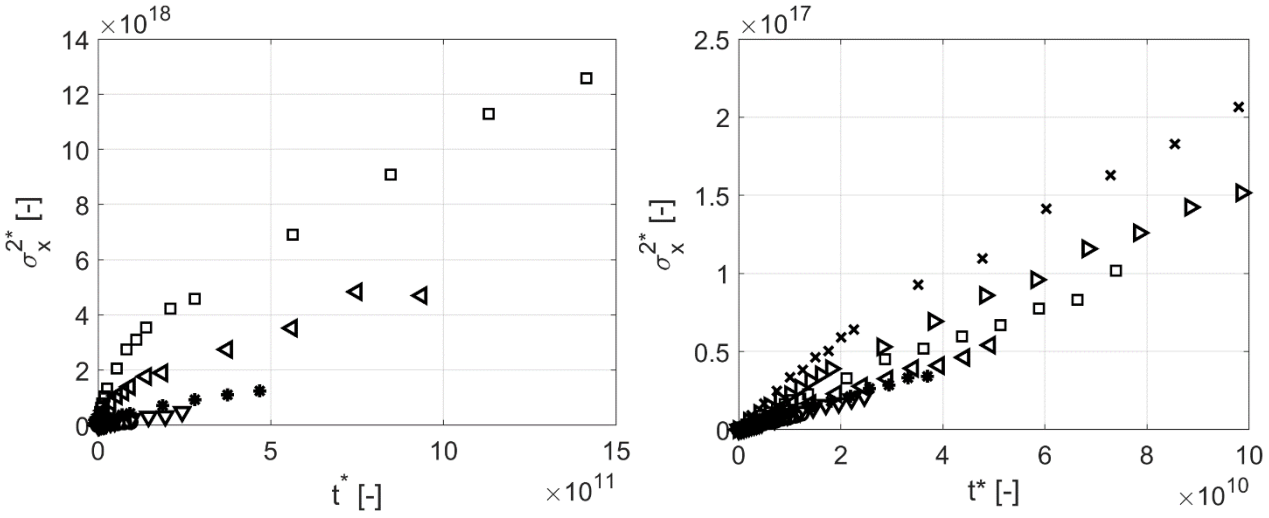

(a) (b)

Figure 5.25. Non-dimensional variance $\sigma_x^{2*}(t)$ as a function of the non-dimensional time t^* for (a) acetone vapor excited at 310 nm and (b) diacetyl vapor excited at 410 nm at different pressures. The reported data are the non-dimensional version of the data of Figure 5.24: in (a), p = 1 kPa (○), p = 2 kPa (▽), p = 5 kPa (✱), p = 10 kPa (◁), p = 15.1 kPa (□); in (b), p = 250 Pa (○), p = 500 Pa (▽), p = 750 Pa (✱), p = 1 kPa (◁), p = 1.5 kPa (□), p = 2 kPa (▷), p = 2.5 kPa (×).

5.4.3 The triplet-triplet annihilation (TTA)

The identification of the most important intramolecular processes involved in the triplet de-excitation observed in the experimental data of this work should explain:

1. the non-exponential decay of the triplet population;
2. the decreasing triplet lifetime with increasing pressure;
3. the non-linear evolution of the variance of the light distribution.

A possible explanation is given by the triplet-triplet annihilation (TTA) process, for which the collision of two excited triplet produces a non-radiative de-excitation to the ground state. As oxygen molecules are efficient quencher because of their paramagnetic nature, acetone or diacetyl triplet produce an efficient molecular self-quenching. By considering Eq. (5.16), the substitution of the quencher concentration n_Q with n_{T_1} provides a non-linear triplet de-excitation that depends on the triplet concentration itself. As discussed in Section 5.2.3, by considering that the intersystem crossing quantum yield is closed to unity and that the intersystem crossing rate is much faster than all the radiative and non-radiative processes in the triplet state, the governing equation for the triplet population $n_{T_1}(x, y, z, t)$ is

$$\frac{\partial n_{T_1}}{\partial t} = -\left(k_{ph} + k_{nr,T_1} + n_Q k_Q\right) n_{T_1} - k_{TTA} n_{T_1}^2 + D\nabla^2 n_{T_1}. \quad (5.52)$$

Because of the existence of a non-linear de-excitation, the time evolution of the triplet population strongly depends on the initial distribution $n_{T_1,0}(x,y,z)$. From Eq. (5.14), it is known that the initial distribution of triplet concentration is proportional to the vapor pressure p and to the laser energy density distribution $I_{in}(x,y,z)$. If the laser energy density is high, the triplet concentration is denser and thus the non-linear TTA mechanism assumes importance. For the same reason, higher pressures enable the TTA which makes the triplet molecules de-excite faster. The dependency of the triplet lifetime from the pressure is also indirectly related through the molecular diffusion. As a matter of fact, at low pressures, the quadratic term $k_{TTA} n_{T_1}^2$ becomes smaller faster because the molecular diffusion is quicker. The presence of a non-linear term in Eq. (5.52) allows also to predict a non-linear evolution of the variance of the distribution $n_{T_1}(x,y,z,t)$, as illustrated by the experimental results of Figure 5.24. If the TTA was not present, the application of the mathematical definition of the variance to Eq. (5.52) would provide the Einstein formula, Eq. (5.49). Any other linear intramolecular process would not affect the linearity of the time evolution of σ_x^2. The presence of the TTA process is, therefore, essential for providing the observed non-linear behavior.

The TTA mechanism is, therefore, able to explain all the three observations listed above: the non-exponentiality of the phosphorescence emission, the pressure dependency of the triplet lifetime, and the non-linear evolution of the variance.

Contrarily to the experimental observations reported in the previous section, most of the experimental work that can be found in the literature did not report a non-exponential decay. Moreover, there are already several gas flow applications of molecular tagging thermometry techniques in the literature that are explicitly based on the exponentiality of the acetone triplet lifetime (Hu & Koochesfahani, 2002) and diacetyl triplet lifetime (Kuhni *et al*., 2017).

Almy & Anderson (1948), Parmenter & Poland (1969), Sidebottom *et al*. (1972) have been able to measure a diacetyl triplet lifetime τ_{T_1} of about 1.5 ms from an exponentially decaying light emission. Moreover, they did not observe any substantial dependency of the diacetyl triplet lifetime from the pressure. However, the possibility of the TTA mechanism was already clear at that time. For instance, Sidebottom *et al*. wrote:

"The fully intensity of the laser beam at the three wavelengths employed created a sufficient concentration of triplet molecules so that the bimolecular triplet-triplet annihilation reaction was very important. The deviation of the triplet emission intensity from the simple exponential decay gave evidence of this. At the low intensities employed in the present work, decays of phosphorescence and fluorescence emission were clearly exponential in character over several lifetimes."

Furthermore, there are also few works (Garabedian & Dows, 1968; Badcock *et al*., 1972; Hunter & Stock, 1973; Mirzaei *et al*., 2012) on the experimental characterization of the TTA process in diacetyl. To the best of our knowledge, the work of Mirzaei *et al*. is the only to report a non-linear evolution in time of the distribution variance in diacetyl vapor, while associating this behavior to the TTA mechanism.

Experimental studies on acetone phosphorescence are fewer in the literature. Kaskan & Duncan (1950) observed a decreasing lifetime of acetone triplet by increasing the pressure from about 2 kPa to 25 kPa, which have been associated to a non-radiative de-excitation caused by collisions with non-excited acetone molecules. They measured a triplet lifetime varying between 200 and 250 μs. Copeland & Crosley (1985) also observed that the triplet population from acetone excited at wavelengths between 305 to 325 nm has a lifetime that decreases with the pressure. However, this study was conducted in the "isolated molecule" condition, that is at very low pressures, between about 0.1 and 30 Pa.

5.4.4 Parameter identification of k_{TTA} and D

Eq. (5.52) is numerically solved and the solution is compared to the experimental data collected in this work. A parameter identification algorithm has been developed in order to find the best set of parameters (k_{ph}, k_{nr,T_1}, k_{TTA}, D) that makes the numerical solution fits the experimental data in terms of TL and σ_x^2. In order to make the comparison between the numerical solution and the experimental data possible, the experimental conditions must be reproduced in the numerical approach as accurate as possible. Firstly, the solution $n_{T_1}(x,y,z,t)$ must be properly processed to produce the numerical data TL and σ_x^2 (Section 5.4.5). Secondly, because the triplet lifetime depends on the triplet distribution, the initial triplet distribution $n_{T_1,0}(x,y,z)$ needs to be accurately estimated from the available experimental measurements. A rigorous procedure for estimating the initial triplet concentration distribution is reported in Appendix B. Because of the axisymmetry and the invariance in the laser beam direction of the initial condition, the solution $n_{T_1}(r,t)$ is axisymmetric as well. Therefore, Eq. (5.52) is solved in polar coordinates as

$$\frac{\partial n_{T_1}}{\partial t} = -k_{ph,tot} n_{T_1} - k_{TTA} n_{T_1}^2 + D \frac{1}{r} \frac{\partial}{\partial r}\left(r \frac{\partial n_{T_1}}{\partial r} \right), \tag{5.53}$$

in which $k_{ph,tot} = k_{ph} + k_{nr,T_1} + n_Q k_Q$. An implicit Euler time-marching method and second-order finite difference for the diffusion term have been used to numerically solve Eq. (5.53). A convergence analysis on the TL and σ_x^2 with respect to the mesh and the time step demonstrated that a first-order scheme in time and second-order scheme in space are enough for providing a converged solution with a grid of 100 points in space and 100 in times.

Once the numerical solution can be generated and compared to the experimental data, the optimization problem is defined. As discussed at the beginning of Section 5.4, the main interest is to extract the self-diffusion coefficient D at different pressures and thus provide new measurements of the kinetic diameter of acetone and diacetyl molecules. However, because of the importance of the non-linear TTA process, the diffusion coefficient cannot be extracted independently from the constant rates k_{ph}, k_{nr,T_1}, and k_{TTA}. The values of these coefficients must be defined a priori or introduced as optimization parameters. In any case, k_{ph}, k_{nr,T_1}, and $n_Q k_Q$ cannot be identified separately in this formulation, and only the sum $k_{ph,tot}$ can be in theory extracted from the experimental data. The single contribution in $k_{ph,tot}$ given by k_{ph} and k_{nr,T_1} require measuring the phosphorescence quantum yield. Even though this has not been done in this work, the experimental data are sufficient for a first estimation. A sensitivity analysis of the numerical solution with respect to the parameters demonstrated that:

1. the numerical solution $\widehat{\mathrm{TL}}$ is very sensitive to k_{TTA}, sensitive to D, but not much sensitive to $k_{ph,tot}$;
2. the numerical solution $\hat{\sigma}_x^2$ is very sensitive to D, sensitive to k_{TTA}, but not much sensitive to $k_{ph,tot}$.

Because of the importance of the TTA mechanism, the first instants of the triplet de-excitations are dominated by k_{TTA}. However, at later times, when the TTA process has extinguished, the triplet de-excitation through internal conversion $k_{ph,tot}$ dominates. In this time region the light recorded is less intense and the number of data point available is not enough. From this sensitivity analysis, it has been concluded that the parameter $k_{ph,tot}$ cannot be accurately extracted from the experimental data, and, therefore, it has been fixed. From the literature, $k_{ph,tot}$ is about 666.7 s^{-1} for diacetyl (Sidebottom *et al*., 1972) and 5000 s^{-1} for acetone (Kaskan & Duncan, 1950) in absence of external molecular quenching. These two values are used in the parameter identification of k_{TTA} and D, even though the actual value of $k_{ph,tot}$ that characterizes the experimental data might be higher because of oxygen quenching $n_{O_2} k_{O_2}$. Moreover, for enhancing the convergence stability, the optimization algorithm employed is the following:

1) an initial guess for the parameter (k_{TTA}, D) is provided;
2) while keeping constant D, the parameter k_{TTA} is varied in order to minimize the following objective function:

$$\varepsilon_{\mathrm{TL}}(k_{TTA}) = \sum_{i=1}^{N_t} \left(\mathrm{TL_i} - \widehat{\mathrm{TL}}(t_i, k_{TTA}, D)\right)^2; \tag{5.54}$$

3) while keeping constant k_{TTA}, the parameter D is varied in order to minimize the following objective function:

$$\varepsilon_{\sigma_x^2}(D) = \sum_{i=1}^{N_t} \left(\sigma_{x,i}^2 - \hat{\sigma}_x^2(t_i, k_{TTA}, D)\right)^2; \tag{5.55}$$

4) step 3 and 4 are repeated until convergence.

In Eq. (5.54) and (5.55), $\widehat{\mathrm{TL}}$ and $\hat{\sigma}_x^2$ are, respectively, the numerical TL and the numerical variance. In the following section, the procedure for calculating the numerical $\widehat{\mathrm{TL}}$ and $\hat{\sigma}_x^2$ is presented.

5.4.5 Numerical calculation of TL and σ_x^2

The theoretical solution $n_{ex}(x, y, z, t)$ must be processed to correctly produce the data TL and σ_x^2 that can be finally compared with the experimental data of Figure 5.22 and Figure 5.24. Because the laser energy density distribution $I_{in}(x, z)$ is assumed to not vary along the laser beam direction, the initial concentration of triplet molecules $n_{T_1,0}(x, z)$ and, thus, the solution in time $n_{T_1}(x, z, t)$ are invariant with respect to the *y*-direction.

The total number of excited molecules $N_{T_1}(t)$ at time t that is inside the FOV of the acquisition system is

$$N_{T_1}(t) = \int_0^{L_y} \int_0^{L_x} \int_{-\infty}^{\infty} n_{T_1}(x, z, t) dz\, dx\, dy = L_y \int_{\infty}^{\infty} \int_{-\infty}^{\infty} n_{T_1}(x, z, t) dz\, dx. \tag{5.56}$$

The integral in the *x*-direction has been arbitrarily extended to infinity because it is assumed that all the excited molecules stay inside the FOV of the camera for all their lifetime. The double integral in Eq. (5.56) corresponds to integrate the excited molecule concentration on a section perpendicular to the direction of propagation of the laser beam. The rate of photon emission provided by the phosphorescence is

$$I_{ph}(t) = k_{ph} N_{T_1}(t). \tag{5.57}$$

The phosphorescence emission, Eq. (5.57), is integrated at time t on a time interval Δt_{gate} corresponding to the IRO gate used. However, because not all the photons emitted by the excited molecules that are in the FOV of the camera will reach the optical collector, only a percentage η_o is collected:

$$N_{ph}(t) = \eta_o \int_t^{t+\Delta t_{gate}} I_{ph}(\hat{t}) d\hat{t}, \tag{5.58}$$

where the sign $\widehat{\ }$ is used for differentiating the integration variable from the time of integration t. The optical phenomenon of photon collection is, in reality, more complex and the introduction of the coefficient η_o is only a simplification. Depending on the position of the excited molecules with respect to the focusing plane of the optical collector at the moment of the photon emission the percentage of collected light can vary accordingly. More precisely, group of molecules that are closer to the optical lenses have more probability of sending a photon through the ICCD system, since the solid angle Ω is bigger. Vice-versa, molecules that are further from the optical

collector have less probability of sending a photon in the direction of the objectives. Nevertheless, it is assumed that this effect does not vary substantially the total light collected.

The conversion of the photon received by the photocathode into counts is done through the conversion factor $Q_e S_{ICCD}(G)$, where Q_e is the quantum efficiency of the photocathode and $S_{ICCD}(G)$ is the ICCD sensitivity at the IRO gain G. Finally, the relationship between the total light TL and the excited molecule concentration $n_{T_1}(x, y, z, t)$ is

$$\mathrm{TL}(t) = \eta_o Q_e S_{ICCD}(G) k_{ph} L_y \int_t^{t+\Delta t_{gate}} \int_{\infty}^{\infty} \int_{-\infty}^{\infty} n_{T_1}(x, z, \hat{t}) dz\, dx\, d\hat{t}. \tag{5.59}$$

The normalization of the function $\mathrm{TL}(t)$ with respect to the value $\mathrm{TL}(t_0) = \mathrm{TL}_0$ at time t_0 allows to cancel the dependency on the parameters η_o, Q_e, $S_{ICCD}(G)$, and k_{ph} and on their relative uncertainties:

$$\frac{\mathrm{TL}(t)}{\mathrm{TL}_0} = \frac{\int_t^{t+\Delta t_{gate}} \int_{\infty}^{\infty} \int_{-\infty}^{\infty} n_{T_1}(x, z, \hat{t}) dz\, dx\, d\hat{t}}{\int_{t_0}^{t_0+\Delta t_{gate}} \int_{\infty}^{\infty} \int_{-\infty}^{\infty} n_{T_1}(x, z, \hat{t}) dz\, dx\, d\hat{t}}. \tag{5.60}$$

Eq. (5.60) is based on the following assumptions:

1) the total number of tagged molecules in the FOV of the camera, which corresponds to the initial number of excited molecules $N_{T_1,0}$, does not vary in time.

2) the photon collection does not depend on the *z*-direction, the principal axis of the optical collector;

3) the ICCD has a linear response to the amount of light collected.

Eq. (5.60) can be further simplified with further assumptions. All the experimental results showed that the light distribution is perfectly symmetric with respect to the laser beam axis. It is legit, therefore, to assume that the laser energy density distribution $I_{in}(r)$ and, thus, the excited molecule concentration $n_{T_1}(r, t)$ are axisymmetric, with r the radial coordinate. Hence, the spatial integral in Eq. (5.60) can be rewritten as

$$\frac{\mathrm{TL}(t)}{\mathrm{TL}_0} = \frac{\int_t^{t+\Delta t_{gate}} \int_0^{\infty} n_{T_1}(r, \hat{t}) r dr\, d\hat{t}}{\int_{t_0}^{t_0+\Delta t_{gate}} \int_0^{\infty} n_{T_1}(r, \hat{t}) r dr\, d\hat{t}}. \tag{5.61}$$

While the assumption of axisymmetry of excitation distribution is not required for the double-exponential model (5.21), it is essential for the application of the TTA model. Finally, a last simplification can be made by assuming that the IRO gate is small enough that the excited molecule concentration does not vary during the light integration:

$$\frac{\mathrm{TL}(t)}{\mathrm{TL}_0} = \frac{\int_0^\infty n_{T_1}(r,t) r dr}{\int_0^\infty n_{T_1}(r,t_0) r dr} = \frac{N_{T_1}(t)}{N_{T_1}(t_0)}, \tag{5.62}$$

which makes the normalized TL correspond to the normalized total number of excited molecules at time t.

In a similar way, the variance σ_x^2 of the light distribution can be related to the theoretical solution $n_{T_1}(x,z,t)$. By assuming that the ICCD system does not produce any distortion of the spatial distribution of the signal, the 1D signal distribution $\tilde{S}(x,t)$ can be calculated by integrating the excited molecule distribution $n_{T_1}(x,z,t)$ in the *z*-direction. As done for the calculation of TL, the conversion efficiency of the ICCD can be taken into account and $\tilde{S}(x,t)$ is calculated as

$$\tilde{S}(x,t) = \eta_o Q_e S_{ICCD}(G) k_{ph} \int_t^{t+\Delta t_{gate}} \int_{-\infty}^{\infty} n_{T_1}(x,z,\hat{t}) dz\, d\hat{t}. \tag{5.63}$$

If the assumption of axisymmetry for the excitation distribution is enabled, the integral operation in the *z*-direction corresponds to the known Abel transform

$$\int_{-\infty}^{\infty} n_{T_1}(x,z,\hat{t}) dz = \int_0^\infty \frac{n_{T_1}(r,t)}{\sqrt{r^2 - x^2}} r dr. \tag{5.64}$$

The variance of the distribution $\tilde{S}(x,t)$ is then calculated as

$$\sigma_x^2 = \frac{\int_{-\infty}^{\infty} (x-\mu_r)^2 \tilde{S}(x,t) dx}{\int_{-\infty}^{\infty} \tilde{S}(x,t) dx} = \frac{\int_{-\infty}^{\infty} (x-\mu_r)^2 \int_t^{t+\Delta t_{gate}} \int_0^\infty \frac{n_{T_1}(r,t)}{\sqrt{r^2-x^2}} r dr\, d\hat{t} dx}{\int_{-\infty}^{\infty} \int_t^{t+\Delta t_{gate}} \int_0^\infty \frac{n_{T_1}(r,t)}{\sqrt{r^2-x^2}} r dr\, d\hat{t} dx}, \tag{5.65}$$

where the mean position of the light distribution can be calculated simply as

$$\mu_r = \frac{\int_0^\infty n_{T_1}(r,t) r dr}{\int_0^\infty n_{T_1}(r,t) dr}, \tag{5.66}$$

because of the axisymmetry of the excited molecule distribution. Notice how, as for the case of TL, the efficiency conversion of the ICCD and the phosphorescence constant rate k_{ph} does not appear in the computation of the variance. Since $n_{T_1}(r,t)$ is numerically calculated by solving Eq. (5.53), Eq. (5.65) is solved numerically as well.

5.4.6 Results of the parameter identification

Figure 5.26 presents the results of the parameter identification algorithm applied on the experimental data of diacetyl vapor. Figure 5.26a reports the value of k_{TTA} extracted at different vapor pressures. The TTA rate does not show any particular dependency on the pressure, and its average value is k_{TTA} = 0.983×10^{-16} m^3/s. Garabedian

& Dows (1968), Badcock *et al*. (1972) and Hunter & Stock (1974) reported, respectively, k_{TTA} = 1.18×10^{-16}, 1.39×10^{-16} and 7.6×10^{-16} m^3/s. The result here measured is quite close to the data reported by the first two works. Figure 5.26b shows the extracted diffusion coefficient at different pressures. Because for the pressure employed the vapor can be considered as a dilute gas, the diffusion coefficient should be inversely proportional to the pressure. However, the measured diffusion coefficient does not show this behavior. Eq. (5.44) is also used for estimating the kinetic diameter of diacetyl molecule, which results are reported in Figure 5.26b. Because D is not inversely proportional to the pressure, it is expected that the calculated kinetic diameter varies with the pressure. Its value ranges between 727.2 and 425.3 pm from the lowest to highest pressure. The average value d = 594 pm is very close to the estimated 590 pm of Almy & Anderson (1940).

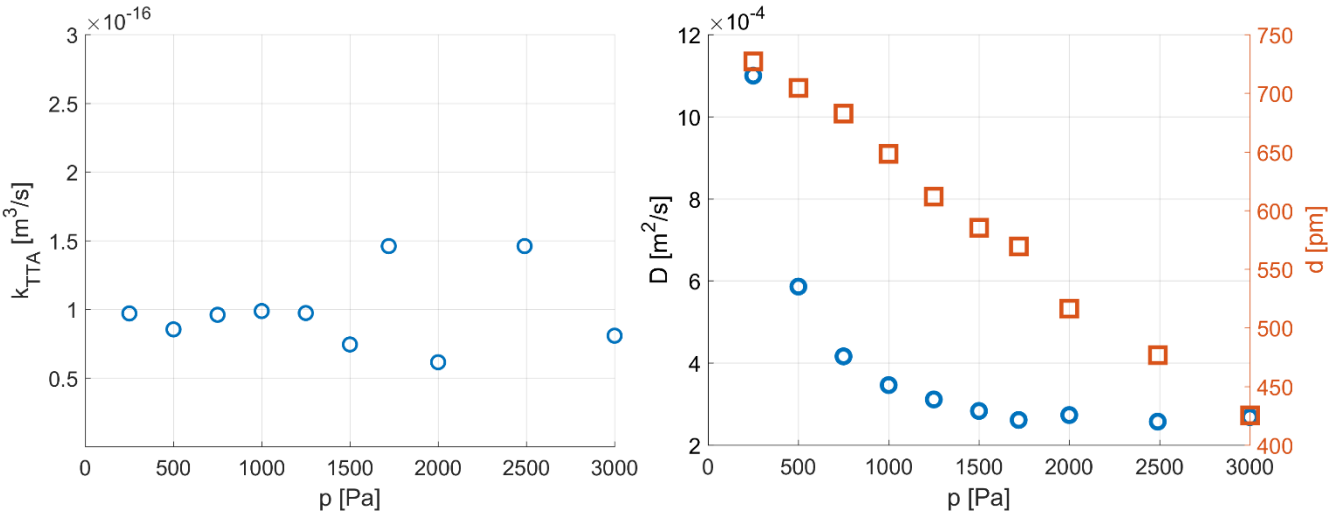

Figure 5.26. (a) TTA rate k_{TTA} at different pressures extracted from the experimental data of diacetyl; (b) diffusion coefficient D (○) at different pressures extracted from the experimental data of diacetyl. The kinetic diameter (□) calculated from the measured diffusion coefficient by means of Eq. (5.44) is also reported.

It is very surprising that the kinetic diameter decreases linearly with the pressure. This observation could be explained by considering that the real temperature at which the triplet molecules diffuse does not correspond to the ambient temperature. Indeed, the mathematical model developed is able to predict the triplet lifetime of acetone and diacetyl, but it does not take into account of how the non-radiative processes influence the vapor thermodynamic. As shown in Eq. (5.44), because D depends on the root square of the temperature, the temperature should increase as T^2 as the vapor pressure increases for maintaining the kinetic diameter constant. As a matter of fact, the TTA term is proportional to $n_{T_1}^2$, and thus the amount of energy dissipated by TTA is proportional to p^2. When triplet-triplet annihilation occurs, the triplet de-excitation transfers the lost energy into vibrational, rotational, or translational energy of the other triplet. Because the vibrational-relaxation is very fast, it can also be assumed, in first approximation, that at all the dissipated energy increases the translation temperature of the

molecules. In this way, the temperature would increase with the pressure as p^2, which would explain why the measured diffusion coefficient is not inversely proportional to the pressure.

5.5 Conclusions

In this chapter, an experimental study on the phosphorescence emission of acetone and diacetyl vapor has been carried out.

In the first part of this chapter, a qualitative analysis of the light signal lifetime at low pressures and in helium and argon mixtures has been presented in the perspective of MTV applications. The first preliminary data showed that the phosphorescence emission provided by acetone vapor excitation at 266 nm is too short and weak at pressures lower than 5 kPa. However, the second experimental campaign demonstrated that the phosphorescence emission provided by acetone vapor excited at 310 nm and diacetyl vapor excited at 410 nm is sufficiently durable and intense for being used in helium mixtures with Knudsen numbers in the slip regime. In the next chapter, these results are exploited in discussing the feasibility of MTV application to gas flows in the slip regime.

In the second part of this chapter, a quantitative analysis of the acetone and diacetyl triplet lifetime have been presented. The unusual non-exponential decay of the phosphorescence emission and its dependency on the vapor pressure have been compared to the experimental works in the literature. The main intramolecular process determining the observed triplet concentration evolution has been identified in the non-radiative triplet-triplet annihilation.

The awareness of the existence of the TTA process is of fundamental importance in molecular tagging applications. First of all, molecular tagging thermometry technique is based on the temperature dependency on the phosphorescence lifetime. However, if the pressure and/or the laser energy density is high enough, TTA mechanism is activated and phosphorescence lifetime is directly dependent on the pressure and the laser energy employed. In this scenario, MTT cannot associate to a temperature a specific lifetime of the emission. Especially in micro gas flows, where the laser excitation is usually focalized in a small region, TTA may be quite important. The correlation between temperature and phosphorescence lifetime is possible only by taking into account the non-radiative de-excitation provided by triplet collisions. The numerical tools developed in this work may be a good starting point for the development of a more complete and robust MTT technique.

References

Anderson, L. G., & Parmenter, C. S. (1970). Effect of Phase on the Fluorescence Lifetime and on the Intersystem Crossing Rate in Biacetyl. The Journal of Chemical Physics, 52(1), 466-468.

Almy, G. M., & Anderson, S. (1940). Lifetime of fluorescence in diacetyl and acetone. *The Journal of Chemical Physics*, 8(10), 805-814.

Almy, G. M., Fuller, H. Q., & Kinzer, G. D. (1940). The Fluorescence of Diacetyl. *The Journal of Chemical Physics*, 8(1), 37-45.

Almy, G. M., & Gillette, P. R. (1943). The quantum yield of diacetyl fluorescence. *The Journal of Chemical Physics*, 11(4), 188-195.

Backstrom, H. L., & Sandros, K. (1960). Transfer of triplet state energy in fluid solutions. Acta Chemica Scandinavica, 14(1), 48-62.

Badcock, C. C., Sidebottom, H. W., Calvert, J. G., Rabe, B. R., & Damon, E. K. (1972). Triplet-triplet annihilation reaction in biacetyl vapor excited at 4365 A and 25°. *Journal of the American Chemical Society*, 94(1), 19-24.

Bird, G. A. (1994). Molecular gas dynamics and the direct simulation monte carlo of gas flows. Clarendon, Oxford, 508, 128.

Bowen, T. C., Noble, R. D., & Falconer, J. L. (2004). Fundamentals and applications of pervaporation through zeolite membranes. *Journal of Membrane Science*, 245(1-2), 1-33.

Breuer, G. M., & Lee, E. K. (1971). Fluorescence decay times of cyclic ketones, acetone, and butanal in the gas phase. *The Journal of Physical Chemistry*, 75(7), 989-990.

Concheanainn, C. O., & Sidebottom, H. W. (1980). Temperature dependence of the triplet lifetime of biacetyl in the gas phase. *Journal of Photochemistry*, 13(1), 55-66.

Copeland, R. A., & Crosley, D. R. (1985). Radiative, collisional and dissociative processes in triplet acetone. *Chemical physics letters*, 115(4-5), 362-368.

Dorfman, L. M., & Noyes Jr, W. A. (1948). The Photo-Chemical Decomposition of Acetone at 3130A. *The Journal of Chemical Physics*, 16(6), 557-560.

Frezzotti, A., Mohand, H. S. H., Barrot, C., & Colin, S. (2015). Role of diffusion on molecular tagging velocimetry technique for rarefied gas flow analysis. *Microfluidics and Nanofluidics*, 19(6), 1335-1348.

Gales, L., Mendes, A., & Costa, C. (2000). Hysteresis in the cyclic adsorption of acetone, ethanol and ethyl acetate on activated carbon. *Carbon*, 38(7), 1083-1088.

Garabedian, M. E., & Dows, D. A. (1968). Vapor-phase bimolecular quenching of the triplet state of biacetyl. Journal of the American Chemical Society, 90(10), 2468-2470.

Kaskan, W. E., & Duncan, A. F. (1950). Mean lifetime of the fluorescence of acetone and biacetyl vapors. *The Journal of Chemical Physics*, 18(4), 427-431.

Kuhni, M., Storace, R., Vena, P., Galizzi, C., Mauger, C., & Escudié, D. (2017). Simultaneous optical diagnostic velocity and scalar field by molecular tagging technique. *Digital proceedings of the 8th European Combustion Meeting*, pp. 1372-1377.

Heicklen, J. (1959). The Fluorescence and Phosphorescence of Biacetyl Vapor and Acetone Vapor1. *Journal of the American Chemical Society*, 81(15), 3863-3866.

Heicklen, J., & Noyes Jr, W. A. (1959). The Photolysis and Fluorescence of Acetone and Acetone-Biacetyl Mixtures. *Journal of the American Chemical Society*, 81(15), 3858-3863.

Hu, H., & Koochesfahani, M. (2002). A novel method for instantaneous, quantitative measurement of molecular mixing in gaseous flows. *Experiments in fluids*, 33(1), 202-209.

Hunt, R. E., & Noyes Jr, W. A. (1948). Photochemical studies. XXXIX. A further study of the fluorescence of acetone. *Journal of the American Chemical Society*, 70(2), 467-476.

Hunter, T. F., & Stock, M. G. (1974). Photophysical processes in the vapour-phase measured by the optic-acoustic effect. Part 2. Triplet state yield and lifetime in high pressure biacetyl vapour. *Journal of the Chemical Society, Faraday Transactions 2: Molecular and Chemical Physics*, 70, 1022-1027.

Lee, E. K., & Lewis, R. S. (1980). Photochemistry of simple aldehydes and ketones in the gas phase. *Adv. Photochem*, 12(1).

Marrero, T. R., & Mason, E. A. (1972). Gaseous diffusion coefficients. *Journal of Physical and Chemical Reference Data*, 1(1), 3-118.

Mirzaei, M., Dam, N. J., & van de Water, W. (2012). Molecular tagging velocimetry in turbulence using biacetyl. *Physical Review E*, 86(4), 046318.

Mohand, H. S. H., Frezzotti, A., Brandner, J. J., Barrot, C., & Colin, S. (2017). Molecular tagging velocimetry by direct phosphorescence in gas microflows: correction of Taylor dispersion. *Experimental Thermal and Fluid Science*, 83, 177-190.

Nadykto, A. B., & Yu, F. (2003). Uptake of neutral polar vapor molecules by charged clusters/particles: Enhancement due to dipole-charge interaction. *Journal of Geophysical Research: Atmospheres*, 108(D23).

Okabe, H., & Noyes Jr, W. A. (1957). The Relative Intensities of Fluorescence and Phosphorescence in Biacetyl Vapor1. *Journal of the American Chemical Society*, 79(4), 801-806.

Parmenter, C. S., & Poland, H. M. (1969). Fluorescence, Phosphorescence, and Triplet Formation in Biacetyl at Low Pressures. *The Journal of Chemical Physics*, 51(4), 1551-1558.

Lozano, A., Yip, B., & Hanson, R. K. (1992). Acetone: a tracer for concentration measurements in gaseous flows by planar laser-induced fluorescence. *Experiments in fluids*, 13(6), 369-376.

Rawcliffe, R. D. (1942). An Electronic Method of Measuring Molecular Lifetimes. *Review of Scientific Instruments*, 13(10), 413-418.

Résibois, P., & De Leener, M. (1977). Classical kinetic theory of fluids.

Sidebottom, H. W., Badcock, C. C., Calvert, J. G., Rabe, B. R., & Damon, E. K. (1972). Lifetime studies of the biacetyl excited singlet and triplet states in the gas phase at 25. deg. *Journal of the American Chemical Society*, 94(1), 13-19.

Stier, B., & Koochesfahani, M. M. (1999). Molecular tagging velocimetry (MTV) measurements in gas phase flows. *Experiments in Fluids*, 26(4), 297-304.

Thurber, M. C., Grisch, F., Kirby, B. J., Votsmeier, M., & Hanson, R. K. (1998). Measurements and modeling of acetone laser-induced fluorescence with implications for temperature-imaging diagnostics. *Applied optics*, 37(21), 4963-4978.

Thurber, M. C., & Hanson, R. K. (1999). Pressure and composition dependences of acetone laser-induced fluorescence with excitation at 248, 266, and 308 nm. Applied Physics B, 69(3), 229-240.

Yip, B., Lozano, A., & Hanson, R. K. (1994). Sensitized phosphorescence: a gas phase molecular mixing diagnostic. *Experiments in fluids*, 17(1-2), 16-23.

Yuen, L. S., Peters, J. E., & Lucht, R. P. (1997). Pressure dependence of laser-induced fluorescence from acetone. *Applied optics*, 36(15), 3271-3277.

Chapter 6

Application of MTV to gas flows in the slip regime

In this final chapter, MTV is applied to gas flows in the slip regime. At first, Section 6.1 presents a numerical analysis of the rarefied thermodynamic conditions identified by the experimental analysis presented in the previous chapter. The reconstruction method is introduced and applied to numerical experiments carried out at the Knudsen numbers of interest for demonstrating the feasibility of MTV application. A preliminary analysis is also dedicated to understanding the required pressure difference and flow rate and how to generate them in a compatible manner with MTV technique. A new version of the reconstruction method based on time-correlated displacement data is also presented in the light of the sensitivity analysis of the velocity reconstruction with respect to variation in the diffusion coefficient. Section 6.2 presents the experimental flow conditions that can be generated with the current gas circuit. CV technique is described and applied to the time-dependent pressure measurements. Afterwards, an average velocity is extracted through a specific procedure from the measured mass flow rate for comparison with MTV results. In Section 6.3.1, the post-processing procedure applied to the image data collected by MTV is discussed in detail. In Section 6.3.2 and 6.3.3, MTV technique is applied, respectively, to argon-acetone flow in non-rarefied conditions and to helium-acetone flow in the slip regime.

6.1 Feasibility analysis of MTV application to gas flows in the slip regime

The analysis presented above demonstrates that both acetone and diacetyl gas tracers can provide a durable and intense phosphorescence signal in slip flow regime conditions. It has been observed, in particular, that, in a gas mixture of helium at 1 kPa with a tracer concentration of about 5%, the phosphorescence emission lasts even for 100 μs after the laser excitation. For a channel with a height H = 1 mm, this thermodynamic condition corresponds to a Knudsen number Kn_H = 0.015, whether acetone or diacetyl is used. It has also been shown that by further reducing the pressure to 500 Pa and by increasing the tracer concentration to 10%, a strong signal can be obtained up to Kn_H = 0.025. Knudsen numbers in the range [0.015; 0.025], which are within the slip flow regime, correspond, therefore, to rarefaction conditions that can be experimentally investigated by means of MTV.

However, the fact that an exploitable phosphorescence signal is still present in these thermodynamic conditions cannot demonstrate by itself the feasibility of the application of the MTV technique to internal gas flows in the slip regime. The data presented in Section 5.3 on the phosphorescence lifetime of acetone and diacetyl have been carried out for a quiescent gas mixture in a non-confined environment. These data take into account the weakening effect of the signal due to the diffusion of the tracer molecules inside the background gas, but they do not take into account the conjugated effects of advection and diffusion on the molecular tracer in a confined environment.

The diffusion process combined with the velocity gradient perpendicular to the wall deforms the tagged line in such a way that a derivation of the velocity profile from the simple measurement of the streamwise tracer displacement does not provide correct results. As a matter of fact, Frezzotti *et al.* (2015) demonstrated that a specific reconstruction method is needed to correctly extract the velocity profile from the measurement of the displacement profile of the tagged gas molecules, which are subjected to Taylor dispersion (see Section 6.1.11). Even for nonrarefied gas conditions, in which no slip velocity is expected at all, a displacement slip at the wall is measured by the MTV technique. This displacement slip has already been experimentally observed by Samouda *et al.* (2015) and analyzed by Si-Hadj Mohand *et al.* (2017) for gas flows at atmospheric and sub-atmospheric pressures, respectively. At lower pressures, the advection-diffusion process can distort the displacement profile to such an extent that even the reconstruction method could not be sufficient to accurately measure the gas-mixture velocity profile. For the limit case scenario of high Knudsen numbers, the displacement profile of excited molecules tends asymptotically to an almost flat profile, from which the velocity information cannot be retrieved. Even though the magnitude of the displacement is definitely large and measurable by means of the MTV technique, the reconstruction method may fail to provide the correct velocity profile in the case where the shape of the displacement profile is hidden by the CCD resolution and/or experimental inaccuracies. It is, therefore, necessary to carefully verify our ability to accurately measure the displacement profile that should form in specific rarefied conditions where a durable and intense phosphorescence emission is still present.

In this perspective, numerical experiments of the molecular advection and diffusion of the gas mixture are carried out by DSMC. These numerical results allow (i) to predict the shape of the displacement profile in the thermodynamic conditions of interest and (ii) to verify if an accurate reconstruction of the velocity profile of the gas flow is possible.

6.1.1 Calculation of binary gas mixture properties

Both the numerical study and the experimental analysis require the computation of the most important thermodynamic properties of the tracer-gas mixture. The mean free path is calculated as in Eq. (5.27). In this numerical analysis, the Knudsen number Kn_H is defined based on the smaller dimension of the channel section, that is H = 1 mm. By knowing the molar mass M_i of each species, the molar mass of the mixture M is computed as

$$M = \sum_{i=1}^{2} \frac{n_i}{n} M_i, \tag{6.1}$$

with n_i the molecular density of each species and $n = n_1 + n_2$ the molecular density of the gas mixture. In the following analysis, indices 1 and 2 refer to the gas and the tracer species, respectively. The specific ideal gas constant of the mixture is then calculated as $R_s = R_{univ}/M$, with R_{univ} = 8.314 J mol^{-1} K^{-1}. The definition of the

Reynolds number Re and of the Mach number Ma require the calculation, respectively, of the dynamic viscosity μ and of the speed of sound c_s for the gas mixture. The dynamic viscosity can be calculated through the definition of the mean free path λ of the gas mixture, as done in Eq. (5.48) for the estimation of the viscosity of the acetone and diacetyl vapors. The calculation of the speed of sound requires instead to pass by the calculation of the specific heat ratio $\gamma = c_P/c_V$ of the mixture, where c_p is the specific hear at constant pressure and c_V is the specific heat at constant volume. Because the internal energy of a gas mixture is equal to the sum of the internal energies of each species, the equivalent specific heats of the gas mixture can be calculated as

$$c_p = \sum_{i=1}^{2} \frac{n_i}{n} c_{p,i}, \tag{6.2}$$

$$c_V = \sum_{i=1}^{2} \frac{n_i}{n} c_{V,i}, \tag{6.3}$$

with $c_{p,i}$ and $c_{V,i}$ the specific heats of each species. Thus, the specific heat ratio of the mixture can be expressed as a function of the specific heat ratio γ_i and the specific ideal gas constant $R_{s,i} = R_{univ}/M_i$ of each species as

$$\gamma = \frac{\sum_{i=1}^{N_i} \frac{n_i}{n} \frac{\gamma_i}{\gamma_i - 1} R_{s,i}}{\sum_{i=1}^{N_i} \frac{n_i}{n} \frac{1}{\gamma_i - 1} R_{s,i}}. \tag{6.4}$$

Complex molecules such as acetone and diacetyl are characterized by a γ closer to unity than the case of monoatomic or diatomic molecules. In the following calculations, γ_2 = 1.11 for both acetone and diacetyl molecules (Bird, 1994).

The Reynolds number and the Mach number are defined with respect to the average velocity on the section or with respect to the maximum velocity reached on the velocity profile. In the latter case, the two non-dimensional numbers are indicated as Re_{max} and Ma_{max}.

6.1.2 Generation of numerical experiments by DSMC simulations

DSMC simulations of the gas-tracer mixture flow in a channel with a height $H = 1$ mm are carried out for Knudsen numbers in the range [0.015; 0.025] for the case of a plane laminar pressure-driven flow. The domain of the mathematical problem is defined by two parallel infinite plates perpendicular to the *y*-direction. The gas flows in between the two plates along the *x*-direction. The computational domain has open boundaries in the streamwise *x*- and spanwise *z*-directions. Since the 2D steady pressure-driven flow is invariant along these two directions, the computational cells are distributed only along the *y*-direction, which corresponds to the direction of the height of the channel. The axis of the channel is positioned at $y = 0$. For all considered cases, 500 cells along the height of the channel and 1 million test particles are employed. The steady pressure-driven flow is obtained as a result of

the equilibrium between the viscous stresses and a uniform force applied to all particles in the computational domain. The force has been adjusted so that the maximum value of velocity of the attained steady state velocity profile is $u_{max} =$ 40 m/s for all numerical experiments here shown. The corresponding Mach number is $Ma_{max} = 0.078$, so that the compressibility effects could be considered as negligible. Once the steady velocity profile is attained, the tracer molecules are tagged along a line perpendicular to the channel walls. The streamwise displacement $s_x(y,t)$ of the tagged molecules is calculated by averaging their position in the (x, z) plane for each value of y. By defining the number density $n_{T1}(x,y,z,t)$ of the tagged molecules, the displacement function $s_x(y,t)$ can thus be defined as follows:

$$s_x(y,t) = \frac{\int x n_{T1}(x,y,z,t)\, dxdz}{\int n_{T1}(x,y,z,t)\, dxdz}. \tag{6.5}$$

6.1.3 Definition of the test case

In the previous chapter, thermodynamic conditions that guarantee the existence of an exploitable phosphorescence signal and that provide a Knudsen number Kn_H in the slip regime have been identified. The numerical analysis is, then, carried out for three representative test cases in the range of these thermodynamic conditions, which are of interest for the application of MTV. An acetone-helium flow with an acetone concentration $\chi = 5\%$ at $Kn_H =$ 0.015, 0.02 and 0.025 is considered. The molar mass and molecular diameter are $M_1 = 4{\cdot}10^{-3}$ kg mol^{-1} and $d_1 = 233$ pm, for helium (Bird, 1994), and $M_2 = 58{\cdot}10^{-3}$ kg mol^{-1} and $d_2 = 730$ pm, for acetone (Frezzotti *et al.*, 2015). Since the Knudsen number and the diffusion coefficient characterizing these thermodynamic conditions do not change much whether acetone or diacetyl is used, the numerical analysis is carried out for acetone-helium mixtures only. By considering $M_2 = 89{\cdot}10^{-3}$ kg mol^{-1} and $d_2 = 590$ pm for diacetyl vapor (Almy & Anderson, 1940), a diacetyl-helium mixture is characterized by almost the same Knudsen numbers as for an acetone-helium mixture at the same thermodynamic conditions in terms of pressure, temperature and tracer concentration. For instance, a diacetyl-helium mixture at $T = 293$ K, $\chi = 5\%$ and $p = 750$ Pa is characterized by a Knudsen number $Kn_H = 0.02$, while for an acetone-helium mixture it would be $Kn_H = 0.0193$.

6.1.4 Numerical experiment analysis

Figure 6.1 shows the displacement data along the channel at different times t after the acetone molecules were tagged for two different rarefaction conditions, $Kn_H = 0.015$ and $Kn_H = 0.025$. Eq. (6.5) has been used to evaluate the average displacement $s_{x,j}$ at each computational cell j along the channel height. These data are fitted with a 4th order polynomial function providing a displacement profile $s_x(y)$. The results are shown at 10, 25, 50, and 100 μs after the initial molecular tagging.

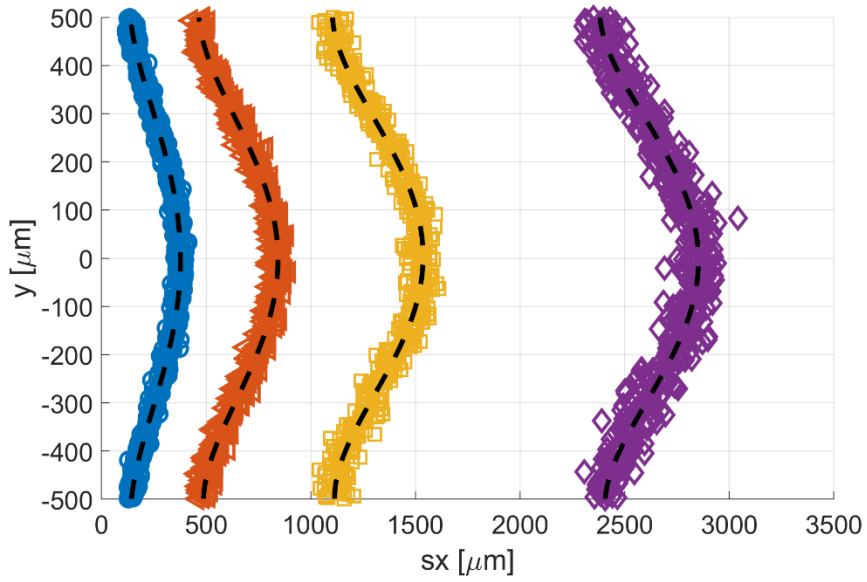

(a)

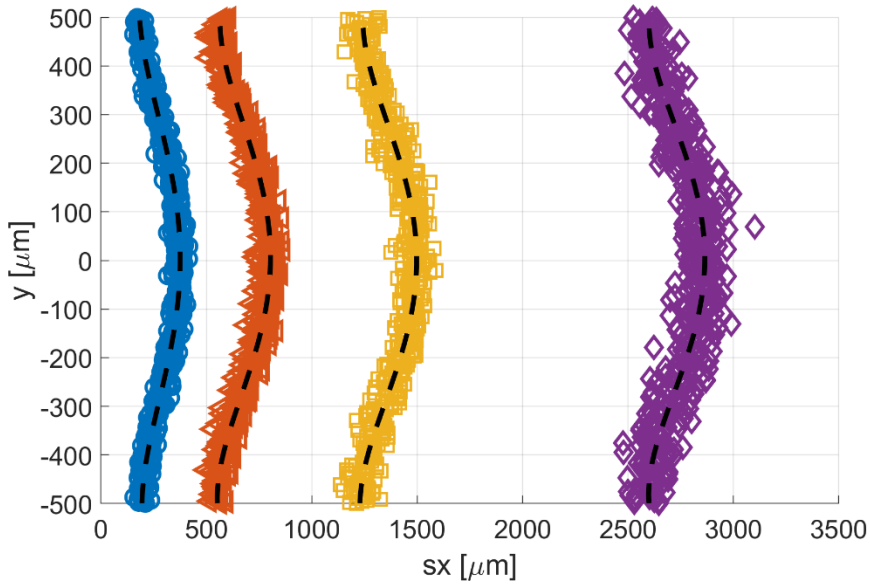

(b)

Figure 6.1. Displacement data $s_{x,j}$ from DSMC simulation (symbols) of acetone-helium mixture with χ = 5% for (a) Kn_H = 0.015 and (b) Kn_H = 0.025, at times t = 10 μs (○), 25 μs (◁), 50 μs (□), 100 μs (◇) after the acetone molecules tagging. The black dashed line is the displacement profile $s_x(y)$ given by the data polynomial fitting.

As the tagged molecules move along the channel, the displacement line is deformed by the advection and the diffusion mechanisms. After a few tens of microseconds, the shape of the displacement profile reaches a steady state: the profile simply translates in the flow direction with the same fixed shape.

The comparison between Figure 6.1a and Figure 6.1b shows that higher rarefaction levels produce more dispersed data and a flatter displacement profile as a consequence of higher molecular diffusion. The dispersion of the average displacements s_{x_j} can be reduced by increasing the number of particles employed in the simulation or by averaging more than one numerical experiment.

The mean displacement of the tagged line is almost the same for the two considered rarefied conditions, since the bulk velocity is almost the same in each numerical experiment. As described in Section 4.1, the uniform force applied to the particles is adjusted to generate a steady pressure-driven velocity profile characterized by a maximum value of 40 m/s at the center line of the channel. The bulk velocity is only slightly increased by the slip velocity at the wall, which increases with the Knudsen number. For all considered rarefied conditions, the tagged line moves after 50 μs of about 1.5 mm, a displacement that is clearly detectable by means of a CCD in which every pixel corresponds to 15.2 μm on the image. 50 μs is a representative time interval since an appreciable phosphorescence signal is still obtained from the tagged molecules at the pressure conditions of interest.

However, even if the overall displacement of the tagged line is detectable by the resolution of the CCD, this does not guarantee a correct measurement of the velocity profile. The success of the reconstruction method designed by Frezzotti *et al*. (2015) depends on the accuracy of the measurements of the displacement profile. The spatial resolution of the CCD must be high enough to accurately measure the actual shape of the molecular displacement. It is convenient to define the difference between the maximum and the minimum displacement of the tagged line at a certain time *t* as:

$$\Delta s_x(t) = \max\big(s_x(y)\big) - \min\big(s_x(y)\big). \tag{6.6}$$

Figure 6.2 shows the evolution of $\Delta s_x(t)$ for three different Knudsen numbers. Δs_x is trivially zero at the beginning of the experiment and it reaches a maximum value Δs_∞ after a characteristic time interval which depends on the flow rarefaction.

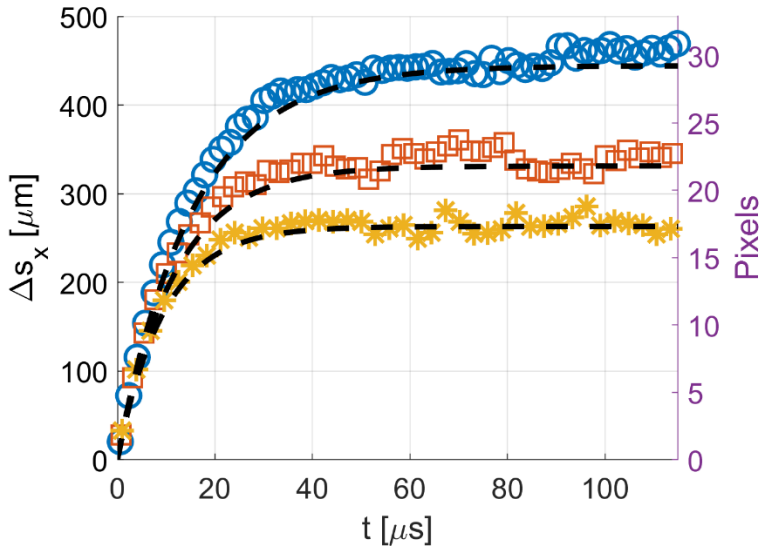

Figure 6.2. Time evolution of $\Delta s_x(t)$ in an acetone-helium mixture with acetone molar concentration at χ_2 = 5 %, T = 293 K, and for Kn_H = 0.015 (○), Kn_H = 0.02 (□), and Kn_H = 0.025 (✱).

The asymptotic displacement profile is reached after about 60, 50, and 40 µs for Kn_H = 0.015, 0.02, 0.025, respectively. After this transition time, the displacement profile remains the same, as the overall group of tagged molecules moves on through the channel. On the basis of these results (Figure 6.2), one can estimate at what instant an appropriate profile measurement can be realized. Furthermore, it is noticed that once the asymptotic value Δs_∞ is reached, there is no reason to further delay the image acquisition of the frozen displacement profile, whose quality is deteriorated by the increasing statistical noise due to the molecular diffusion. Moreover, the experimental data on phosphorescence emission shown in Section 5.3 demonstrate the evidence of an exploitable phosphorescence signal for times higher than 60 µs after laser excitation. Therefore, the phosphorescence signal intensity, for the considered thermodynamic parameters, is not an obstacle for measuring a precise molecular displacement.

In order to verify that the displacement profile can be accurately resolved by the CCD, Figure 6.2 also shows the number of available pixels for measuring $\Delta s_x(t)$ when a 4 × 4 binning is activated. In this configuration, Δs_∞ corresponds to about 18, 24, and 30 pixels for Kn_H = 0.025, 0.02, and 0.015, respectively. Even though the displacement profile is flatter at higher rarefied conditions, the time necessary to reach the Δs_∞ is lower than for less rarefied cases. Therefore, since the acetone emission is stronger for shorter delay times, a compromise between CCD resolution and amount of collected light needs to be reached. This is possible by modifying the binning operation. In particular, a 2 × 2 binning or no binning at all can be chosen for increasing the available pixels up to 72 and 120, for Kn_H = 0.025 and Kn_H = 0.015 cases, respectively. Indeed, instead of decreasing the binning in both directions, the same improvement in available pixels for measuring Δs_∞ can be obtained by using a 4 × 2 or 4 × 1 binning, which would reduce the collected light only of a factor 2 and 4, respectively, and not of a factor 4

and 16 as in the case of 2 × 2 and 1 × 1 binning. The highest spatial resolution can be employed at Kn_H = 0.025 even for delay times up to 100 μs, since the reduction of signal intensity can be easily recovered by increasing the number of laser pulses per image from 100 to 500.

6.1.5 Advection-diffusion equation for the displacement profile

In Chapter 5, the governing equation for the triplet distribution $n_{T1}(x,z)$ has been introduced by taking into account of the molecular diffusion, the linear radiative and non-radiative terms, and the non-linear triplet deactivation. In the channel flow scenario, the triplet distribution $n_{T1}(x,y,z)$ is also dependent of the *y* coordinate as a velocity gradient along the channel height is generated by the gas advection and the shear stresses at wall surfaces. By considering the coordinate system introduced in Section 2.6, the complete governing equation that describes the evolution in time and space of $n_{T1}(x,y,z)$ is

$$\frac{\partial n_{T1}}{\partial t} + u(x,y,z)\frac{\partial n_{T1}}{\partial x} = D_{12}\nabla^2 n_{T1} - \left(k_{ph} + k_{nr}\right)n_{T1} - k_{TTA}n_{T1}^2, \tag{6.7}$$

in which $u(x,y,z)$ is the axial velocity distribution on the cross-section (*y*, *z*) at the location *x* along the channel, and the Laplacian operator $\nabla^2 = \frac{\partial^2}{\partial x^2} + \frac{\partial^2}{\partial y^2} + \frac{\partial^2}{\partial z^2}$. In an infinite-long channel with rectangular section $H \times b$, the coordinates are defined for $-H/2 \le y \le H/2$, $-b/2 \le z \le b/2$, and $-\infty \le x \le \infty$. Eq. (6.7) is completed by the following initial and boundary conditions:

$$n_{T1}(x,y,z,t=0) = n_{T1,0}(x,z), \tag{6.8}$$

$$\left.\frac{\partial n_{T1}}{\partial y}\right|_{-H/2} = 0, \qquad \left.\frac{\partial n_{T1}}{\partial y}\right|_{H/2} = 0, \tag{6.9}$$

$$\left.\frac{\partial n_{T1}}{\partial z}\right|_{-b/2} = 0, \qquad \left.\frac{\partial n_{T1}}{\partial z}\right|_{b/2} = 0. \tag{6.10}$$

Because the initial condition $n_{T1,0}(x,z)$ is bounded in *x*, n_{T1} and $\frac{\partial n_{T1}}{\partial x}$ are both zero at $x \to \pm\infty$. The initial condition $n_{T1,0}(x,z)$ is independent of the *y* coordinate since the excitation is uniform along the laser beam. Eq. (6.9) and (6.10) represent the condition of non-penetration of the tagged molecules into the wall. The expression of the boundary conditions is a direct consequence of the first Fick law for which the diffusive flux $\boldsymbol{J}$ is proportional to the concentration gradient by means of the diffusion coefficient D_{12}:

$$\boldsymbol{J} = -D_{12}\boldsymbol{\nabla} n_{T1}. \tag{6.11}$$

Because the diffusive flux $\boldsymbol{J}$ needs to be null in the direction perpendicular to the wall surfaces, Eq. (6.9) and (6.10) hold.

The tracer molecules are tagged at a location *x* close to half the length L of the channel. The application of the definitions (6.5) to Eq. (6.7) allows to find the governing equation for the displacement profile $s_x(y,t)$. However, some assumptions are needed in order to be able to develop the advection-diffusion equation for $s_x(y,t)$.

As discussed in Chapter 2, the compressibility and rarefaction of the gas mixture makes the axial velocity increases in the flow direction. However, if the pressure gradients are not too high, the velocity gradient $\frac{\partial u}{\partial x}$ can be neglected, and the $u = u(y,z)$ can be approximated as independent of the *x* position.

The non-linear term in Eq. (6.7) provided by the TTA rate can in theory have an important effect on the spatial distribution of the light emitted by the tagged molecules., whereas at $y = 0$ the tagged molecule concentration can reduce because of the molecular diffusion, the gradient velocity at the wall spreads the tagged molecules much faster, so that regions of lower concentration are formed closed to the channel surfaces. This non-uniformity in the tagged molecules distribution makes the TTA process act differently in the space, so that the resulting displacement profile s_x, which is inferred from the light distribution and not from the tagged molecules position, may be distorted by this non-linear triplet de-excitation. However, in the following analytical formulation, the TTA term is dropped. The effect of the non-linear TTA mechanism on the displacement of the tagged line has been investigated by numerically solving Eq. (6.7). This preliminary analysis showed that the TTA terms has a negligible influence on the shape of the tagged line. Eq. (6.7) reduces, then, to

$$\frac{\partial n_{T1}}{\partial t} + u(y,z)\frac{\partial n_{T1}}{\partial x} = D_{12}\nabla^2 n_{T1} - \left(k_{ph} + k_{nr}\right)n_{T1}. \tag{6.12}$$

The concentration of excited molecules on each plane (*x*, *z*) is defined as

$$n_{T1,y}(y,t) = \int_{-b/2}^{b/2}\int_{-\infty}^{\infty} n_{T1}\,dx\,dz \tag{6.13}$$

By integrating Eq. (6.12) in the *x* and *z* directions, an equation for $n_{T1,y}$ is obtained:

$$\frac{\partial n_{T1,y}}{\partial t} = D_{12}\frac{\partial^2 n_{T1,y}}{\partial y^2} - \left(k_{ph} + k_{nr}\right)n_{T1,y}, \tag{6.14}$$

which is completed by the conditions $n_{T1,y}(y, t=0) = \bar{n}_{T1,y}$ and $\frac{\partial n_{T1,y}}{\partial y} = 0$ at $y = \pm H/2$. Because the initial condition $\bar{n}_{T1,y}$ does not depend on *y*, the diffusion term is always zero, Eq. (6.14) is then solved by the analytical solution:

$$n_{T1,y}(t) = \bar{n}_{T1,y}e^{-\left(k_{ph}+k_{nr}\right)t}. \tag{6.15}$$

This result states that the concentration of triplet molecules on each plane (*x*, *z*) decay in the same manner along the channel height. This would have not been true if the TTA term was kept. By multiplying Eq. (6.12) by *x*, by integrating in the *x* and *z* directions, and by using Eq. (6.15), the governing equation for $s_x(y,t)$ is obtained (Frezzotti *et al*., 2015):

$$\frac{\partial s_x}{\partial t} = \bar{u}(y) + D_{12}\frac{\partial^2 s_x}{\partial y^2}, \tag{6.16}$$

in which the average velocity is

$$\bar{u}(y) = \frac{\int_{-b/2}^{b/2}\int_{-\infty}^{\infty} u(y,z) n_{T1} dx\, dz}{n_{T1,y}(t)}. \tag{6.17}$$

Therefore, the evolution of the displacement profile $s_x(y,t)$ is both subjected by the gas advection $\bar{u}(y)$ and the molecular diffusion in the *y*-direction. It is, indeed, the molecular diffusion perpendicular to the wall surfaces that prevents from computing the velocity profile by simply dividing the displacement by the time of flight t. The average velocity $\bar{u}(y)$ is determined both by the velocity profile $u(y,z)$ and by the excited molecules distribution $n_{T1}(x,y,z,t)$. As it has been analyzed in Chapter 2, the velocity function $u(y,z)$ far from the later walls, that is at $z = \pm b/2$, is substantially flat in the *z*-direction. Therefore, if the excited molecules remain in the central region for which $\frac{\partial u}{\partial z} \approx 0$, it holds that $\bar{u}(y) \approx u(y)$.

Finally, the advection-diffusion equation governing the displacement function $s_x(y,t)$ is:

$$\frac{\partial s_x}{\partial t} = u(y) + D_{12}\frac{\partial^2 s_x}{\partial y^2}, \tag{6.18}$$

which is completed by the following boundary and initial conditions:

$$\left.\frac{\partial s_x}{\partial y}\right|_{y=\pm H/2} = 0, \qquad s_x(y, t=0) = 0. \tag{6.19}$$

The boundary conditions Eq. (6.19) are a direct consequence of Eq. (6.9).

6.1.6 Velocity reconstruction method

In order to extract the velocity profile from the displacement of the tagged line, the advection-diffusion equation governing the evolution of the displacement profile $s_x(y,t)$ needs to be employed. This necessity derives from the fact that the computation of the velocity profile from the molecular displacement cannot be done without taking into account the combined effect of molecular diffusion in the *y*-direction and advection in the *x*-direction.

The velocity reconstruction method is a parameter identification technique in which the solution $s_x(y,t)$ of Eq. (6.18) is compared to the measured displacement data $s_{x,j}$ available from MTV for determining the velocity profile

$u(y)$. By assuming that the velocity function $u(y)$ can be written as a linear combination of N_u basis functions $U_i(y)$, that is:

$$u(y) = \sum_{i=1}^{N_u} b_i U_i(y), \tag{6.20}$$

the fitting coefficients b_i are modified in order to make the solution $s_x(y,t)$ fit the displacement data. In this procedure, the diffusion coefficient D_{12} is a given parameter. The linearity of the advection-diffusion equation assures that the displacement solution $s_x(y,t)$ is:

$$s_x(y,t) = \sum_{i=1}^{N_u} b_i S_{x,i}(y,t), \tag{6.21}$$

where each displacement basis function $S_{x,i}(y,t)$ is the solution of Eq. (6.18) when the advection-diffusion equation is applied to the corresponding velocity basis function $U_i(y)$. By defining the Green function $G(y,y',t)$ associated to Eq. (6.18), the analytical expression of the displacement basis function is:

$$S_{x,i}(y,t) = \int_{-H/2}^{H/2} G(y,y',t) U_{x_i}(y') dy'. \tag{6.22}$$

Practically, the displacement functions $S_{x,i}(y,t)$ are computed by numerically solving Eq. (6.18) for each velocity function $U_i(y)$. An implicit Euler scheme is used for the discretization in time, and second-order finite differences are employed for the discretization of the diffusion term. The use of an implicit time-marching method makes the numerical problem unconditionally stable, thus no constraints in the time step used exist. Since the coefficients $\boldsymbol{b} = \left(b_1, b_2, \dots, b_{N_u}\right)^T$ of the linear combinations of Eqs. (6.20) and (6.21) are the same, the velocity profile can be reconstructed by simply fitting the displacement experimental data with the fitting functions $S_{x_i}(y,t)$. For a given set of N_y displacement data $\boldsymbol{s}_x = \left(s_{x,1}, s_{x,2}, \dots, s_{x,N_y}\right)^T$ that corresponds to a time t from the initial tagged line position, the fitting procedure is based on the minimization of the error function

$$\varepsilon_{s_x}(\boldsymbol{b}) = \frac{1}{2}\sum_{j=1}^{N_y} \left(s_{x,j} - s_x\left(y_j, t, \boldsymbol{b}\right)\right)^2 = \frac{1}{2}(\boldsymbol{s}_x - \boldsymbol{\Lambda b})^T(\boldsymbol{s}_x - \boldsymbol{\Lambda b}), \tag{6.23}$$

in which the matrix $\boldsymbol{\Lambda} = \left[\boldsymbol{S}_{x,1} \quad \boldsymbol{S}_{x,2} \quad \cdots \quad \boldsymbol{S}_{x,N_u}\right]$ contains the basis function vectors $\boldsymbol{S}_{x_i} = \left(S_{x,i}(y_1,t) \quad S_{x,i}(y_2,t) \quad \dots \quad S_{x,i}\left(y_{N_y},t\right)\right)^T$. The application of the least mean square optimization method provides the following algebraic linear system for the fitting coefficients $\boldsymbol{b}$**:**

$$\boldsymbol{\Lambda}^{\mathrm{T}}\boldsymbol{\Lambda}\boldsymbol{b} = \boldsymbol{\Lambda}^{\mathrm{T}}\boldsymbol{s}_x \rightarrow \begin{bmatrix} \boldsymbol{S}_{x,1}^T\boldsymbol{S}_{x,1} & \boldsymbol{S}_{x,1}^T\boldsymbol{S}_{x,2} & \cdots & \boldsymbol{S}_{x,1}^T\boldsymbol{S}_{x,N_u} \\ \boldsymbol{S}_{x,2}^T\boldsymbol{S}_{x,1} & \boldsymbol{S}_{x,2}^T\boldsymbol{S}_{x,2} & \cdots & \boldsymbol{S}_{x,2}^T\boldsymbol{S}_{x,N_u} \\ \vdots & \vdots & \ddots & \\ \boldsymbol{S}_{x,N_u}^T\boldsymbol{S}_{x,1} & \boldsymbol{S}_{x,N_u}^T\boldsymbol{S}_{x,2} & \cdots & \boldsymbol{S}_{x,N_u}^T\boldsymbol{S}_{x,N_u} \end{bmatrix} \begin{Bmatrix} b_1 \\ b_2 \\ \vdots \\ b_{N_u} \end{Bmatrix} = \begin{bmatrix} \boldsymbol{S}_{x,1}^T \\ \boldsymbol{S}_{x,2}^T \\ \vdots \\ \boldsymbol{S}_{x,N_u}^T \end{bmatrix} \begin{Bmatrix} S_{x_1} \\ S_{x_2} \\ \vdots \\ S_{x_{N_y}} \end{Bmatrix} \tag{6.24}$$

If not differently specified, the velocity basis functions used for the results presented in this chapter are:

$$U_1(y) = 1, \qquad U_2(y) = \left(1 - \frac{y^2}{H^2/4}\right). \tag{6.25}$$

By choosing only even basis functions, the reconstructed velocity profile is necessarily symmetric with respect to y = 0. However, in the application of MTV to real experimental data, the position of the walls in the images is not precisely known, and the displacement data can be not symmetric with respect to y = 0, in which case the addition of an odd basis function $U_i(y) = y/(H/2)$ is necessary for generating a non-symmetric displacement profile.

6.1.7 Evaluation of the diffusion coefficient

Besides the precision of the performed experimental measurements, the success of the reconstruction method depends on the accurate estimation of the diffusion coefficient, D_{12}, used for generating the displacement basis functions $S_{x,i}(y,t)$. The diffusion coefficient depends on the thermodynamic properties of the gas mixture, i.e. the mean free path λ of the mixture, the temperature T of the mixture, the molecular tracer concentration χ, the molecular mass m_i and diameter d_i of each component species. The mutual-diffusion coefficient can be estimated by means of the Chapman-Enskog equation (Marrero & Mason, 1972) for a binary gas mixture:

$$\overline{D}_{12} = \frac{3\sqrt{\pi}}{8}\sqrt{\frac{k_B T}{m_{12}}}\frac{1}{\sqrt{2}\pi d_{12}^2 n}, \tag{6.26}$$

where $d_{12} = \frac{d_1+d_2}{2}$ is the average molecular diameter, k_B is the Boltzmann constant, n is the overall density number of the mixture, and $m_{12} = \frac{m_1 m_2}{m_1+m_2}$ is the reduced molecular mass. As discussed in Section 5.3.5, the photochemical process behind the phosphorescence emission of acetone vapor excited by a laser beam at 310 nm is quite complex. The decomposition/recombination process produces diacetyl molecules. Thus, in principle, the background gas could not be considered as a binary mixture anymore. Nevertheless, the percentage of excited acetone molecules that recombine into diacetyl molecules is very low (Almy & Anderson, 1940), so it can be considered that the emitting diacetyl molecules still diffuse in a binary background medium only made of acetone and helium. Eq. (6.26) gives, therefore, a good representation of the tagged tracer diffusion, even for the case of acetone excited at 310 nm.

However, it can be noticed that Eq. (6.26) does not depend on the molecular tracer concentration χ, and only provides a first order approximation of the diffusion coefficient, which is accurate only if χ is small enough. By considering that the molecular mass and the molecular diameter of acetone or diacetyl are considerably different from those of helium, the molecular tracer concentration χ considered in the numerical experiments is high enough to imply that Eq. (6.26) will not give a good estimation of the diffusion coefficient. A better estimation of the diffusion coefficient is provided by the Blanc's law (Blanc, 1908):

$$D_{12} = \frac{1}{\frac{\chi_2}{D_{22}} + \frac{\chi_1}{D_{12}}}, \tag{6.27}$$

in which D_{22} is the self-diffusion coefficient of tracer vapor. Eq. (6.27) represents the tracer diffusion in a background gas that is a mixture of gas and vapor. The self-diffusion coefficient D_{22} weighted by the tracer concentration takes into account the fact that the tagged molecules are diffusing also through the tracer vapor. It can be computed as

$$D_{22} = \frac{3\sqrt{2\pi}}{8}\sqrt{\frac{k_B T}{m_2}}\frac{1}{\sqrt{2}\pi d_2^2 n} = \frac{3\sqrt{2\pi}}{8}\lambda_2^2 \nu_{rate,2} \tag{6.28}$$

in which λ_2 is the mean free path of the tracer molecules and the characteristic collision rate $\nu_{rate,2}$ of the tracer is defined as

$$\nu_{rate,2} = \frac{\sqrt{\frac{k_B T}{m_2}}}{\lambda_2}. \tag{6.29}$$

The Blanc's law can provide a satisfactory estimation of the coefficient D_{12} in the advection-diffusion equation (6.18), but it does not represent a complete description of the tracer diffusion in the channel. Eq. (6.27) provides the diffusion coefficient of the tracer in a binary mixture when the diffusion happens in a non-confined space. The gas-wall interactions affect the diffusion process in such a way that the effective diffusion coefficient D_{eff} is a decreasing function of the Knudsen number. Even though the presence of diffusive walls only slightly modifies the effective diffusion coefficient in the considered range of Knudsen numbers (Frezzotti *et al*., 2015), an accurate evaluation of D_{eff} requires taking into account of this local phenomenon at wall. Therefore, for each considered mixture composition and Knudsen number, the diffusion coefficient D_{12} of Eq. (6.18) must be substituted with the effective diffusion coefficient D_{eff}.

For accurately estimating this effective diffusion coefficient, DSMC simulations were carried out in the channel for the mixture at rest (without any advection). Its value was computed by means of the Einstein's formula (Résibois & De Leener, 1977), which provides a linear relationship between the variance

$$\sigma_x^2(t) = \frac{\int x^2 n_2(x,y,z,t)\,dx}{\int n_2(x,y,z,t)\,dx}, \tag{6.30}$$

of the tracer molecules positions and the time t:

$$\sigma_x^2(t) = \sigma_{x,0}^2 + 2D_{eff}t, \tag{6.31}$$

where σ_0^2 is the variance at the initial condition. For instance, Figure 6.3 represents the time evolution of the variance $\sigma_x(t)^2$ for acetone-helium and diacetyl-helium mixtures at χ = 5 % and Kn_H = 0.02. The effective diffusion coefficient is D_{eff} = 2.263·10^{-3} and 2.899·10^{-3} m^2/s for the cases of the acetone-helium and diacetyl-helium mixtures, respectively. This calculation takes into account both the molecular tracer concentration χ and the influence of diffusive walls on the molecular diffusion. The Chapman-Enskog Eq. (6.26) provides $\overline{D}_{12}$ = 2.9·10^{-3} m^2/s for the acetone-helium mixture and $\overline{D}_{12}$ = 3.78·10^{-3} m^2/s for the diacetyl-helium mixture, which differ from the effective diffusion coefficients by 28% and 30.5%, respectively. Since the tracer-gas molecular mass ratio, m_2/m_1, is higher for the diacetyl-helium mixture than for the acetone-helium mixture, the difference between the first order approximation of the diffusion coefficient $\overline{D}_{12}$ and the effective diffusion coefficient D_{eff} is higher for the diacetyl-helium mixture than for the acetone-helium mixture. The Blanc's law provides D_{12} = 2.297·10^{-3} m^2/s and 2.936·10^{-3} m^2/s, respectively, for the acetone-helium and the diacetyl-helium mixture, which are slightly higher, of about 1.5% than the values of D_{eff}, as expected. Aware of the fact that the most accurate diffusion coefficient can be calculated by DSMC simulations, the Blanc's law is chosen for the computation of the coefficient D_{12} to be used in the reconstruction method because of its simplicity and its satisfying accuracy.

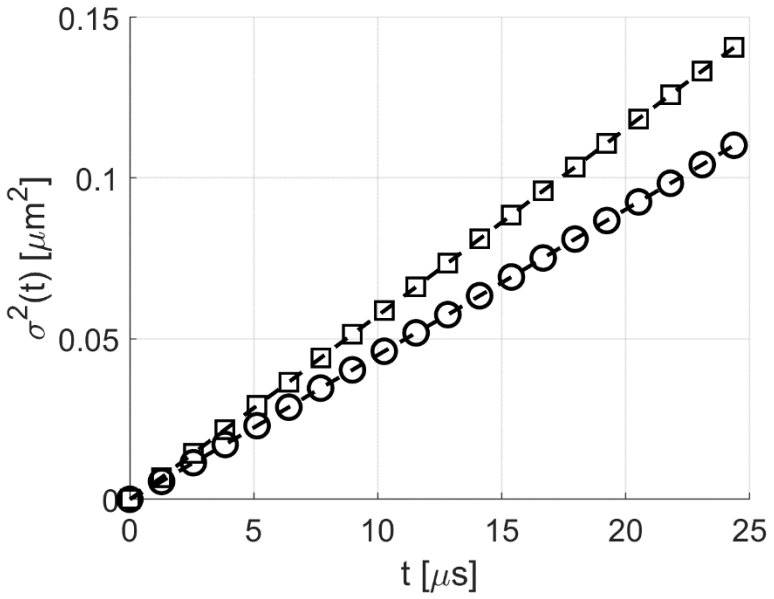

Figure 6.3. Evolution in time of the variance $\sigma_x^2(t)$ of the tracer molecules position, as defined in Eq. (13), for (○) acetone-helium and (□) diacetyl-helium mixtures with a tracer concentration $\chi = 5$ % and Kn_H = 0.02.

The analytical solution of the Navier-Stokes equations for a channel with rectangular cross-section shows that the velocity profile $u(y,z)$ varies along the width of the channel. However, if $b \gg H$, the solution $u(y,z)$ can be considered as two dimensional when the fluid is far enough from the lateral walls. Therefore, if the tracer molecules are tagged in the center part of the channel, the velocity profile solution can be obtained by treating the problem as 2D, thus $u(y,z) \approx u(y)$. It must be, therefore, verified that, for the degree of molecular diffusion that characterizes the thermodynamic conditions of interest, the excited tracer molecules remain in the region where $u(y,z) \approx u(y)$ during the time necessary to measure the molecular displacement in the flow direction. From Eq. (6.31), the characteristic time for an excited molecule to move from the center of the channel $z = 0$ to a distance $z = \tilde{z}/2$ can be estimated as:

$$t_z = \frac{\tilde{z}^2}{2D_{eff}}. \tag{6.32}$$

By considering the velocity solution of Ebert & Sparrow (1965) presented in Chapter 2, the variations of the velocity profile $u(y)$ in a channel with a section defined for $y \in [-H/2, H/2]$ and $z \in [-b/2, b/2]$ are less than 1% in the central region, for $z \in$ [-1 mm, 1 mm] (see Section 6.2.5). For a diffusion coefficient of the order of 0.002 m^2/s and for $\tilde{z}$ = 2 mm, the characteristic time t_z is 1 ms, which is about 20 times higher than the time for reaching the steady shape of the displacement profile and about 10 times higher than the lifetime of the phosphorescence signal.

6.1.8 Application of the reconstruction method to numerical experiments

As demonstrated in Figure 6.4 for the case $Kn_H = 0.02$, the estimation of the velocity profile by simply dividing the computed displacement $s_x(t)$ by the delay time t provides wrong results.

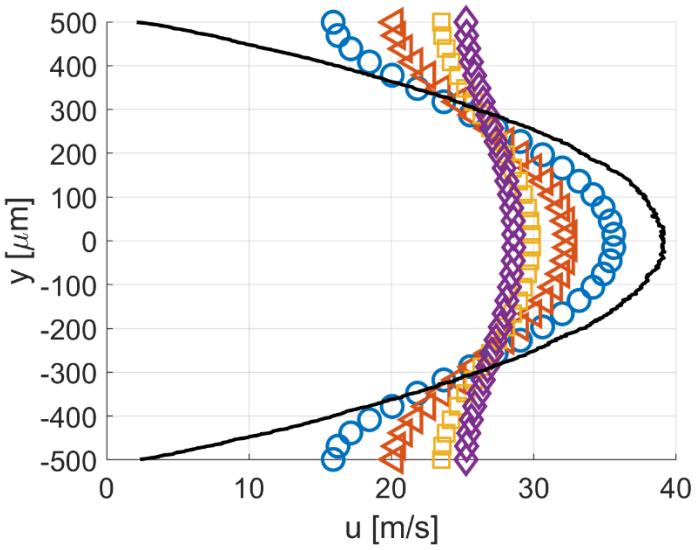

Figure 6.4. Comparison between DSMC velocity profile (black solid line) and profiles resulting from the division of the computed displacement by the corresponding delay time, for t = 10 μs (○), 25 μs (◁), 50 μs (□), 100 μs (◇) and for Kn_H = 0.02.

The reconstruction method is, therefore, necessary to correctly extract the velocity profile from the displacement data. Figure 6.5 compares the velocity fields of an acetone-helium mixture computed with DSMC, with the velocity profiles reconstructed from the displacement data of the tagged molecules obtained by numerical experiments. The comparison was performed at delay times of 10, 25, 50, and 100 μs, for the three test cases previously defined. The displacement basis functions $S_{x,1}(y,t)$ and $S_{x,2}(y,t)$ corresponding to the velocity basis functions $U_1(y)$ and $U_2(y)$ defined in Eq. (6.25) are computed by setting the diffusion coefficient of equation Eq. (4) to $D_{eff} = 1.71\times10^{-3}$, 2.28×10^{-3}, and 2.85×10^{-3} m^2/s for $Kn_H = 0.015$, 0.02, and 0.025, respectively. Figure 6.5 demonstrates that the method is successful in extracting the velocity profiles for all the displacement data at every considered delay time and for the three tested Knudsen numbers.

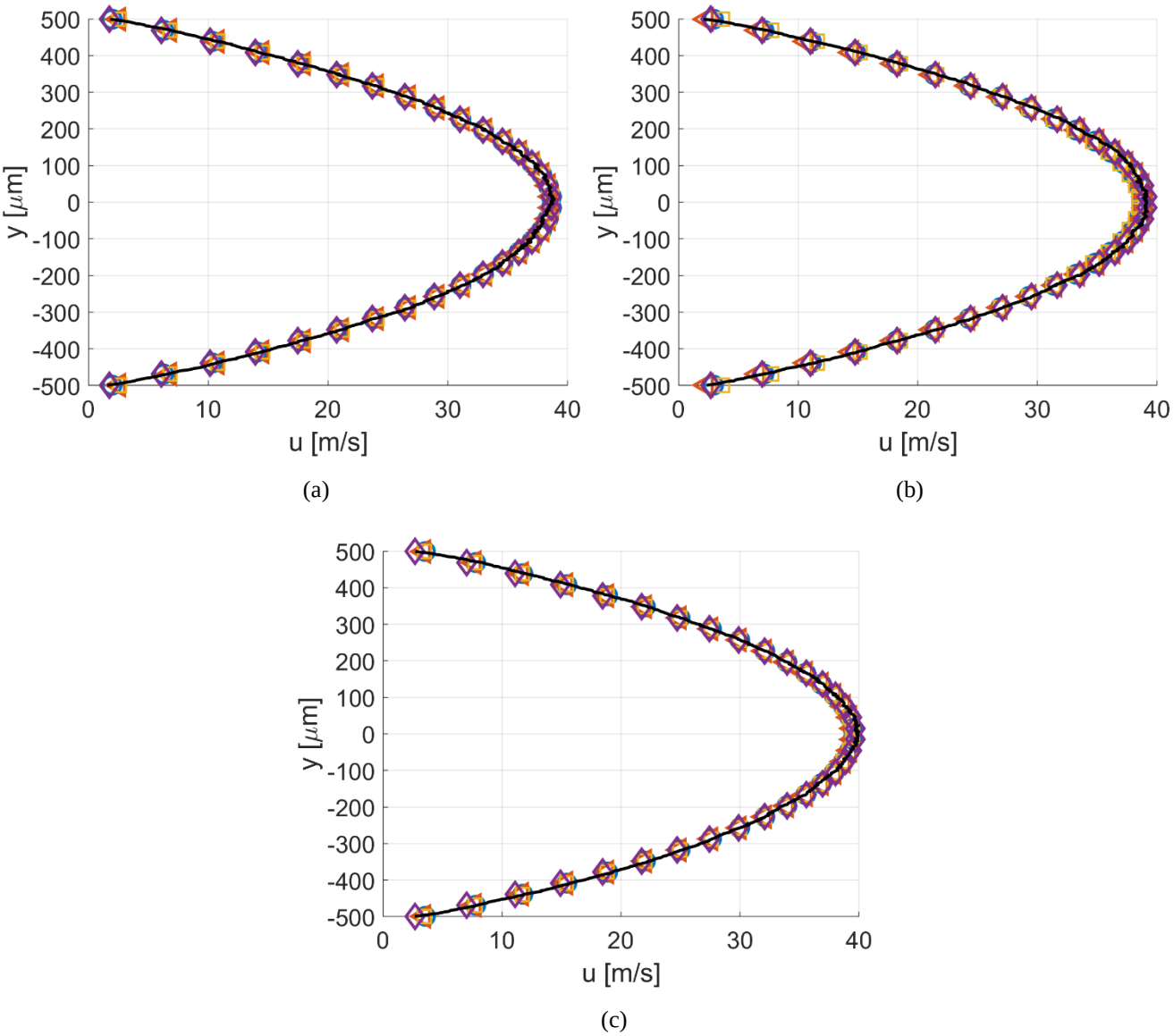

Figure 6.5. Comparison between DSMC (black solid line) and reconstructed velocity profiles for times t = 10 μs (○), 25 μs (◁), 50 μs (□), 100 μs (◇) and for (a) Kn_H = 0.015, (b) Kn_H = 0.02, and (c) Kn_H = 0.025.

In order to quantitatively evaluate the accuracy of the reconstruction, the cumulative error ε_v^k on the velocity $u^k(y)$ measured from the displacement data corresponding to delay time t_k is defined as follows:

$$\varepsilon_v^k = \frac{1}{u_{DSMC}(0)} \frac{1}{H} \int_{-\frac{H}{2}}^{\frac{H}{2}} \left| u^k(y) - u_{DSMC}(y) \right| dy, \tag{6.33}$$

where $u_{DSMC}(y)$ is the velocity profile of the gas mixture computed by DSMC.

Table 6.1 reports the errors ε_v^k for each considered Knudsen number and delay time t_k. As it can be ascertained, there is no a clear trend of the error ε_v^k with respect to the Knudsen number or the delay time. In average, the error on the velocity reconstruction is around 0.65 %. The reconstruction method is, therefore, accurate to extract the velocity profiles of helium-acetone mixture flows in the slip regime.

	$t = 10$ µs	$t = 25$ µs	$t = 50$ µs	$t = 100$ µs	$\langle\varepsilon_v\rangle$
$Kn_H = 0.015$	0.23 %	0.6 %	0.88 %	1.34 %	0.76 %
$Kn_H = 0.020$	0.67 %	0.41 %	0.88 %	0.27 %	0.56 %
$Kn_H = 0.025$	0.41 %	0.58 %	0.39 %	1.04 %	0.6 %

Table 6.1. Cumulative error ε_v^k on the reconstructed velocity relative to different delay time and Knudsen number. $\langle\varepsilon_v\rangle$ is the average error.

The accuracy of the velocity reconstruction depends on the correct estimation of the diffusion coefficient. For Knudsen numbers in the range [0.015; 0.025], variations of 10% and 20% in the diffusion coefficient provide velocity reconstructions with an average error $\langle\varepsilon_v\rangle$ of 2% and 3%, respectively. While the reconstruction error is in average still limited even for high variations of the diffusion coefficient, the local error close to the wall drastically increases from a few percentage up to 100% for variations of 20% on the diffusion coefficient, as it is demonstrated in the following section.

6.1.9 Sensitivity of the reconstructed velocity to D_{12}

For the theoretical analysis above presented, the diffusion coefficient D_{12} characterizing the numerical experiment is known with the best accuracy. However, even in this favorable case, the local relative error

$$\varepsilon_r^k = \frac{\left|u^k(y) - u_{DSMC}(y)\right|}{u_{DSMC}(y)}, \tag{6.34}$$

of the reconstruction can be even more than 20% close to the wall. Figure 6.6 shows this fact for the velocity reconstruction of the acetone-helium flow at Kn_H = 0.015.

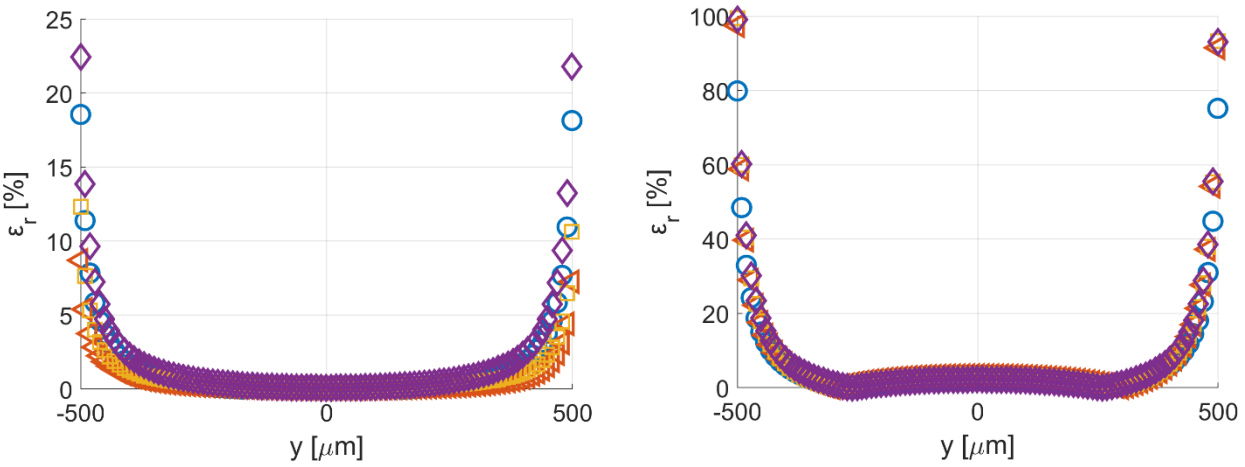

(a) (b)

Figure 6.6. Local relative error ε_r^k of the velocity reconstruction for times t = 10 μs (○), 25 μs (◁), 50 μs (□), 100 μs (◇), and for the acetone-helium flow at Kn_H = 0.015 of Figure 6.5a. In (a), the diffusion coefficient D_{12} employed for the reconstruction is the accurate effective diffusion coefficient D_{eff}; in (b), the diffusion coefficient D_{12} employed for the reconstruction is 20% more of the one used in (a).

Because in the definition of ε_v^k, the integral of the error between the reconstruction $u^k(y)$ and the DSMC velocity profile $u_{DSMC}(y)$ is divided by $u_{DSMC}(0)$, which is the highest velocity along y, the local error given by the reconstruction at the wall has very low relative importance. Therefore, ε_v^k is always limited to 1.5% even if the local error can go up to 20%. As demonstrated by Figure 6.6, there is not a clear tendency of the error on the slip velocity with respect to the time of reconstruction t.

In the case where the diffusion coefficient D_{12} for the velocity reconstruction does not correspond to the correct value, the local error drastically increases close to the wall. Figure 6.6b reports the local relative error on the reconstructed velocity when D_{12} is increased of 20% from its correct value D_{eff}. The modification of D_{12} gives rise to reconstruction error close to the wall up to 100%.

A variation of 20% on the diffusion coefficient is, actually, an underestimation of the error that can be made on the value of D_{12} in a real experimental analysis. In practical applications of MTV, the thermodynamic properties of the investigated experimental flow are known with limited accuracy. By considering the expression of D_{12} provided by the Blanc's law, errors in the calculation of the diffusion coefficient can be due to imprecisions of the pressure p, the temperature T, the tracer concentration χ, the molecular diameter d_i and the molecular mass m_i of the species.

Because the average pressure of the investigated gas mixture flow is based on direct measurements of the upstream and downstream pressures and because the dependency of D_{12} from the temperature is limited by the root square,

the thermodynamic parameter that produces the largest uncertainty on the diffusion coefficient is the tracer concentration χ, which cannot be directly measured. Even though the gas mixture is properly prepared in the reservoir with a controlled tracer concentration, the value of χ may, a priori, vary along the channel flow. Szalmas *et al*. (2010) numerically demonstrated the possible variation of relative molar concentration in helium-argon rarefied gas flows in long microchannels. Even though the results reported show variations only of few percentages in χ, this effect is expected to increase in magnitude as the molecular mass ratio m_2/m_1 of the two species increases, as for the case of an acetone-helium mixture.

Anyway, as already discussed in the previous chapter, the main source of error in the calculation of the diffusion coefficient is given by the uncertainty on the molecular diameter d_2 of the tracer. For instance, for an acetone-helium mixture at p = 1 kPa and χ = 5%, d_2 = 460 pm (Gales *et al*., 2000) and d_2 = 730 pm (Frezzotti *et al*., 2015) provide, respectively, D_{12} = 1.66×10^{-3} m^2/s and D_{12} = 3.4×10^{-3} m^2/s, that is a variation of 50-100%.

Moreover, Eq. (6.28) and Eq. (6.26) employed for the calculation of, respectively, the mutual-diffusion coefficient and the self-diffusion coefficient provide good results for molecules that can be kinetically modeled as hard spheres. This may be a good approximation for helium molecules, but it does not capture the complex structure of acetone and diacetyl molecules.

The impossibility of computing the correct value of D_{12} makes the velocity reconstruction method really inaccurate when a non-zero slip velocity is present.

6.1.10 The time-correlation (TC) reconstruction method

From the sensitivity analysis presented in the previous section, an evolution of the reconstruction method is here proposed in order to overcome the problem related to the fact that the diffusion coefficient cannot be accurately known in an experimental investigation.

By modifying the diffusion coefficient employed in the reconstruction algorithm, the fitting coefficients b_i of the velocity profile of Eq. (6.20) varies accordingly to make the numerical displacement $s_x(y, t, \boldsymbol{b})$ fit the displacement data $s_{x,j}$ at the best. Because the quality of the fitting of the displacement data remains unaffected by the variation in the diffusion coefficient, there is not a unique set of parameters $(b_1, b_2, b_3, \dots, b_{N_u}, D_{12})$ that can well fit a set of displacement data $s_{x,j}$ at a specific time t. In other words, there is more than one combination $(u(y), D_{12})$ that can generate the same displacement profile at time t. It is, indeed, this mathematical property that prevents to extract an accurate velocity profile independently from the accuracy of the diffusion coefficient.

This problem is overcome by considering that there exists only one set of parameters $(b_1, b_2, b_3, \dots, b_{N_u}, D_{12})$ able to generate a solution $s_x(y, t)$ that can simultaneously fit N_t group of displacement data $s_{x,j}^k$ that corresponds to a

different t_k, with k = 1, 2, …, N_t. In this way, because there is a unique combination $(u(y), D_{12})$ that minimizes the error between the synthetic solution $s_x(y,t)$ and the displacement data $\boldsymbol{s}_x = \left(s_{x,1}^1, s_{x,1}^1, \dots, s_{x,N_y}^1, s_{x,1}^2, s_{x,1}^2, \dots, s_{x,N_y}^2, \dots, s_{x,1}^{N_t}, s_{x,1}^{N_t}, \dots, s_{x,N_y}^{N_t}\right)^T$, the diffusion coefficient D_{12} can be inserted in the reconstruction method as an optimization parameter along with the fitting coefficient $\boldsymbol{b}$. The time correlation of the available displacement data $\boldsymbol{s}_x$ in the optimization algorithm is done by minimizing the error function

$$\varepsilon_{s_x}(\boldsymbol{p}) = \frac{1}{2}\sum_{k=1}^{N_t}\sum_{j=1}^{N_y}\left(s_{x,j}^k - s_x(y_j, t_k, \boldsymbol{p})\right)^2 = \frac{1}{2}|\boldsymbol{s}_x - \mathbf{Z}(\boldsymbol{p})|^2, \tag{6.35}$$

with respect to the optimization parameters $\boldsymbol{p} = \left(b_1, b_2, b_3, \dots, b_{N_u}, D_{12}\right)^T$. By considering the definition of $\boldsymbol{\Lambda}$ that has been introduced in Section 6.1.6, $\mathbf{Z}(\boldsymbol{p}) = \left(\boldsymbol{\Lambda}(D_{12}, t_1)\boldsymbol{b}, \boldsymbol{\Lambda}(D_{12}, t_2)\boldsymbol{b}, \dots, \boldsymbol{\Lambda}\left(D_{12}, t_{N_t}\right)\boldsymbol{b}\right)^T$ contains the synthetic solution $s_x(y,t)$ evaluated at each time t_k and at each position y_j. In the reconstruction method introduced in Section 6.1.6, the diffusion coefficient is a fixed parameter, and the displacement basis functions $S_{x,i}$ need to be numerically generated only one time. In that case, the optimization problem reduces to the resolution of a system of algebraic linear equations for the fitting parameters $\boldsymbol{b}$. Differently, because D_{12} varies during the minimization of Eq. (6.35), the basis displacement functions $S_{x,i}(y,t,D_{12})$ that corresponds to each basis velocity functions $U_i(y)$ needs to be recalculated at each iteration of the optimization algorithm. In this context, the problem of finding the global minimum of the error function $\varepsilon_{s_x}(\boldsymbol{p})$ is preferably solved by using the Gauss-Newton algorithm. By defining $\boldsymbol{p}_i = \left(b_{1,i}, b_{2,i}, \dots, b_{N_u,i}, D_{12,i}\right)^T$ the optimization parameters at the i-th iteration, the update $\Delta\boldsymbol{p}_i$ is calculated by solving the following linear system:

$$\boldsymbol{J}(\boldsymbol{p}_i)^T\boldsymbol{J}(\boldsymbol{p}_i)\,\Delta\boldsymbol{p}_i = \boldsymbol{J}(\boldsymbol{p}_i)^T\left(\boldsymbol{s}_x - \mathbf{Z}(\boldsymbol{p}_i)\right), \tag{6.36}$$

in which the Jacobian matrix assumes the form

$$\boldsymbol{J}(\boldsymbol{p}_i) = \left[\left.\frac{\partial\mathbf{Z}}{\partial b_1}\right|_{\boldsymbol{p}_i} \quad \left.\frac{\partial\mathbf{Z}}{\partial b_2}\right|_{\boldsymbol{p}_i} \quad \dots \quad \left.\frac{\partial\mathbf{Z}}{\partial b_{N_u}}\right|_{\boldsymbol{p}_i} \quad \left.\frac{\partial\mathbf{Z}}{\partial D_{12}}\right|_{\boldsymbol{p}_i}\right]. \tag{6.37}$$

While the gradient of $\mathbf{Z}$ with respect to the fitting coefficients b_i can be analytically calculated as

$$\left.\frac{\partial\mathbf{Z}}{\partial\boldsymbol{b}}\right|_{\boldsymbol{p}_i} = \left[\boldsymbol{\Lambda}(D_{12}, t_1) \quad \boldsymbol{\Lambda}(D_{12}, t_2) \quad \dots \quad \boldsymbol{\Lambda}\left(D_{12}, t_{N_t}\right)\right], \tag{6.38}$$

the Jacobian with respect to the diffusion coefficient D_{12} needs to be calculated numerically. By introducing a small perturbation δD_{12}, the Jacobian is calculated by finite differences

$$\left.\frac{\partial \mathbf{Z}}{\partial D_{12}}\right|_{\boldsymbol{p}_i} \approx \frac{\mathbf{Z}\left(\boldsymbol{b}_i, D_{12,i} + \delta D_{12}\right) - \mathbf{Z}\left(\boldsymbol{b}_i, D_{12,i}\right)}{\delta D_{12}}. \tag{6.39}$$

The existence of a global minimum for the optimization problem above formulated and, thus, the uniqueness of the solution $(u(y), D_{12})$ have not been mathematically demonstrated. Nevertheless, the application of the time-correlation (TC) reconstruction method to the numerical experiments presented in the previous section is successful in reconstructing the correct velocity profile and in finding the correct diffusion coefficient D_{12}.

As an example, the application of the TC reconstruction method to the numerical experiment at Kn_H = 0.015 is demonstrated in Figure 6.7. The displacement data $s_{x,j}$ at t = 10 μs, 25 μs, 50 μs, and 100 μs of Figure 6.1 are used all together in the optimization algorithm. Figure 6.7a shows the reconstructed velocity and the initial guess used for the velocity profile. By choosing an initial guess for the diffusion coefficient of $D_{12,0}$ = 1×10^{-2} or 1×10^{-4} m^2/s, it quickly converges to the value D_{12} = 1.683×10^{-3} m^2/s, which is very similar to the D_{eff} = 1.71×10^{-3} m^2/s. The TC method is, therefore, robust in converging towards the desired solution, while maintaining the local relative error ε_r^k limited to 4% close to the walls (Figure 6.7b). The numerical displacement profiles generated by the reconstructed velocity perfectly fit all the displacement data of Figure 6.1a.

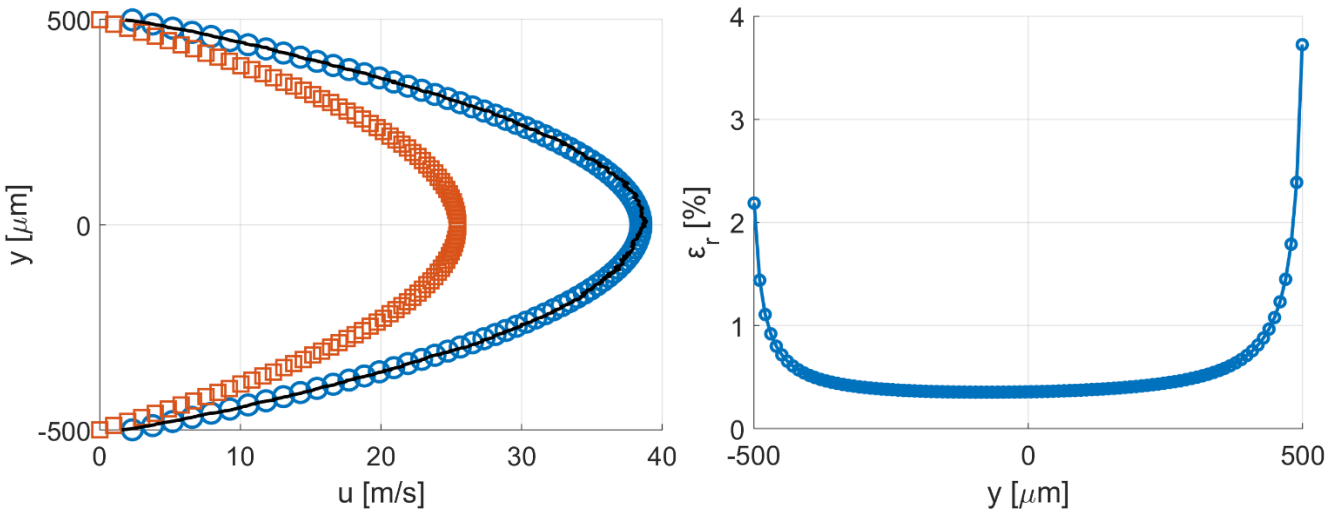

(a) (b)

Figure 6.7. Application of the TC reconstruction method to the numerical experiment at Kn_H = 0.015. In (a), it is represented the reconstructed velocity (○), the initial guess of the velocity profile (□), and the DSMC velocity profile (black solid line); in (b), the local relative error ε_r^k of the reconstruction.

6.1.11 Taylor dispersion and theoretical maximum velocity slip

The mechanism that makes the molecular displacement at the wall different from zero even in cases where no slip velocity at the wall occurs lies on the interaction of the molecular diffusion with the gas advection. Figure 6.8

sketches a possible trajectory of a tagged molecule close to the wall. By considering the case of non-rarefied conditions, the gas velocity at the wall is zero and thus the tagged molecule does not move in the flow direction. However, because of the molecular diffusion, the observed molecule can migrate further from the wall and enter in flow regions in which the velocity is not zero anymore. Hence, the molecule is advected by the gas in the flow direction, and, afterwards, the molecular diffusion can bring it back again close to the wall. The final position of the molecule is shifted forward, thus providing an artificial molecular displacement at the wall. The combined advection-diffusion mechanism is known as Taylor dispersion and represents the phenomenological explanation for the appearance of a flattened displacement profile.

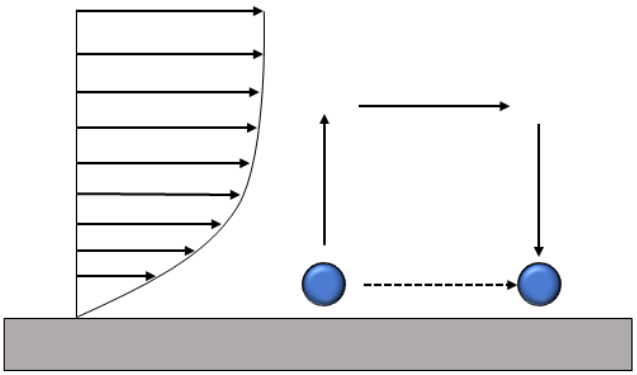

Figure 6.8. Illustration of the advection-diffusion of a molecule close to the wall by Taylor dispersion.

In Section 6.1.4, the evolution in time of the displacement profile thickness $\Delta s_x(t)$, defined in Eq. (6.6), has been analyzed for different rarefied conditions. As reported in Figure 6.2, when the Knudsen number increases, the displacement profile $s_x(y,t)$ tends to be flatter and the asymptotic thickness $\Delta s_x(t \to \infty) = \Delta s_\infty$ results to be smaller. As a matter of fact, at lower average pressures, the molecular diffusion is higher and, consequently, the Taylor dispersion is stronger.

The shape of the displacement profile does not depend only on the molecular diffusion. Frezzotti *et al*. (2015) provides an analytical expression of the asymptotic thickness for a gas flow between parallel plates:

$$\Delta s_\infty = \frac{u_{cp}}{D_{12}} H^2 = \frac{H^4}{8\mu D_{12}} \left|\frac{dp}{dx}\right|, \tag{6.40}$$

in which $u_{cp} = -\frac{H^2}{8\mu}\left|\frac{dp}{dx}\right|$ is the maximum velocity of the Poiseuille velocity profile with no-slip at the wall. For a given flow velocity u_{cp}, the velocity gradient at the wall increases when the channel height H is reduced. This is because the velocity gradient at the wall is stronger, and the advection in the flow direction of molecules diffusing from the wall is stronger, thus the Taylor dispersion effect is enhanced. Eq. (6.40) demonstrates the thickness of the displacement profile is very sensitive to the channel height. Since $\Delta s_\infty \propto H^4$, the velocity reconstruction is

very sensitive to uncertainties in the channel height. Eq. (6.40) also reveals that increasing the pressure gradient and, thus, the flow speed makes the displacement profile thickness larger. For this reason, high flow velocities are desired for MTV applications, especially in low-pressure gas flow, in which the high molecular diffusion tends to flatten the displacement profile.

While, from one hand, increasing the pressure gradient is desired for generating high flow speeds, on the other hand, decreasing the average pressure for reaching the rarefied conditions limits the maximum pressure difference that can be applied to the channel ends. The current experimental channel allows MTV investigations only at the middle position $x = L/2$ along the channel length. For a given upstream pressure p_1, the highest pressure gradient can be obtained by setting the downstream pressure p_2 as close as possible to zero. By assuming a linear pressure distribution along the channel, the average pressure and the pressure gradient at the position $x = L/2$ are, respectively, $(p_1 + p_2)/2$ and $(p_1 - p_2)/L$. It is evident that, once the lowest downstream pressure p_2 is obtained, the pressure gradient cannot be increased without increasing the average pressure. For this reason, there is a theoretical maximum limit for the slip velocity. By considering a first-order slip boundary condition, an HS model, and full accommodation σ = 1, the velocity slip of a gas flow in parallel plates at its middle position $x = L/2$ can be expressed as

$$u_{slip} = 1.277 \frac{2\mu\sqrt{R_s T}}{(p_2 + p_1)} \frac{H}{2\mu} \frac{p_1 - p_2}{L} = 1.277\sqrt{R_s T} \frac{H}{L} \frac{p_1 - p_2}{p_1 + p_2}. \tag{6.41}$$

The highest theoretical slip velocity that can be investigated by MTV with the current experimental channel is, therefore,

$$u_{slip,max} = \lim_{p_2 \to 0} 1.277\sqrt{R_s T} \frac{H}{L} \frac{p_1 - p_2}{p_1 + p_2} = 1.277\sqrt{R_s T} \frac{H}{L}, \tag{6.42}$$

which depends only on the channel geometry, the temperature, and the gas mixture properties. It is worthy underlining that the real maximum slip velocity that can be obtained is, actually, lower than the one given by Eq. (6.42) because of the compressibility of the gas that tends to decrease the pressure gradient and to increase the average pressure at $x = L/2$.

6.2 Experimental flow conditions

In this section, the gas circuit described in Chapter 4 is employed for generating the experimental flow to be investigated by MTV. The post-processing procedure employed for the complete characterization of the gas flow properties from the time-dependent pressure measurements is presented in detail.

Later in this chapter, velocity measurements by MTV are reported for both non-rarefied gas flows and gas flows at low pressures in the slip regime. Because the main interest and novelty of this work is the application of MTV

to gas flows in the slip regime, the detailed analysis of the thermodynamic conditions generated in the channel is here presented only for the experimental data related to helium-acetone flows at low pressures. However, the post-processing procedure described in this section is general and can be applied to non-rarefied gas flows as well.

The acetone-helium mixture used in the experimental results here presented has a tracer concentration of χ = 20%. The increased tracer concentration with respect to the 5% employed in the previous numerical analysis is dictated by the still non-negligible air-leakages in the tested channel, which make oxygen-quenching relevant. The use of 20% of tracer in the mixture helps in increasing the SNR of the tagged line, thus, providing more exploitable displacement data at low pressures.

The preparation of an experimental run conducted at low pressure is done by filling the upstream reservoir with gas mixture at a pressure p_1 of about 5 kPa and by vacuuming at maximum pumping power the downstream volume to the minimum pressure. At the moment of opening the valve at the channel inlet, the gas mixture starts flowing through the channel and the downstream pressure p_2 quickly grows up to about 1.2 kPa, as a consequence of the limited maximum mass flow rate that the two pumps can sustain at the working pressure p_2.

Figure 6.9 shows the typical evolution in time of the pressure conditions applied to the tested channel during one experimental run at low pressure.

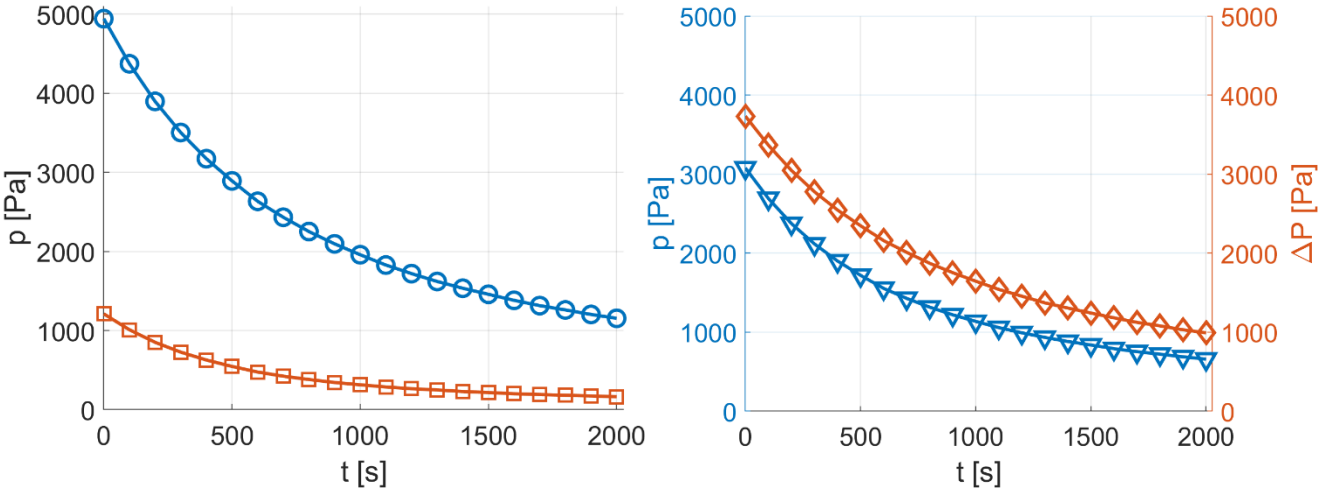

(a) (b)

Figure 6.9. Evolution in time of the experimental pressure conditions generated at low pressures: (a) upstream p_1 (○) and downstream p_2 (□) pressure measurements; (b) mean pressure $p_m = \frac{p_1+p_2}{2}$ (▽) and pressure difference $\Delta p = p_1 - p_2$ (◇).

The pressure data p_1 and p_2 shown in Figure 6.9a represent the pressure measurement provided by the pressure sensors P1 and P2, which position in the experimental setup is illustrated in Figure 4.37 of Chapter 4. The pressure data are recorded with a sample frequency of 10 Hz, and a zero-phase digital filter is applied for cutting off the

noise on the voltage signal. In Figure 6.9b, the mean pressure $p_m = \frac{p_1+p_2}{2}$ and the pressure difference $\Delta p = p_1 - p_2$ are reported. The average pressure in the channel varies between 3000 Pa and 700 Pa with a corresponding pressure difference of 4000 Pa down to 1000 Pa at the lowest pressure obtained. The decrease of p_m and Δp slows down as the average pressure in the upstream reservoir decreases since the mass flow rate through the channel decreases as well. The slowly decreasing downstream pressure is beneficial for the stability of the velocity profile to be measured. The magnitude of the velocity profile is strongly dependent on the pressure gradient, and the fact that the upstream and the downstream pressure decrease simultaneously makes the pressure gradient varying slower, even though the average pressure varies faster than in the case of two constant volumes at the two sides of the channel without any pumping work. At the lowest average pressure, the flow speed is much more stable, which is a suitable experimental condition for the application of MTV. Even though the experimental run could continue towards even lower pressures than those reported in Figure 6.9, MTV has been applied for average pressures only down to about 700 Pa. The MTV results shown in Section 6.3.3 demonstrate new difficulties in the reconstruction of the velocity profile from the displacement data. At the current stage of this project, MTV investigations did not go further down in pressure because of the priority of solving these new issues.

As discussed in the previous numerical analysis, the application of MTV to gas flows at low pressures requires the highest flow rates in the limit of incompressibility for making the thickness of the deformed tagged profile as large as possible. Reducing the pumping power would decrease the inlet over outlet pressure ratio and, thus, the velocity magnitude through the channel, for which the tracer displacement profile would be even more flattened by the Taylor dispersion. Consequently, the experimental run shown in Figure 6.9, which is generated at the maximum pumping power, represents the best experimental conditions for MTV application at low pressures that the current gas circuit can provide. MTV acquisitions in the slip flow regime are, therefore, carried out on these flow conditions, which are thoroughly investigated in the following sections. An even more suitable experimental flow for MTV investigations would require a stronger pumping force for reducing to the minimum the downstream pressure and, thus, increasing to the maximum the pressure difference on the channel.

Because the two pumps work in parallel at full regime and the valves connecting the upstream reservoir with the vacuum system are fully open, the upstream and downstream pressure evolutions do not change substantially when the experimental run is repeated. The repeatability of the experimental conditions that the gas circuit is able to provide is assessed in Section 6.2.1.

As discussed in Section 6.2.3, the constant volume (CV) technique is applied for measuring the mass flow rate along the tested channel at any time during the experimental run. The theoretical solutions presented in Chapter 2 related to the fully-developed, isothermal, locally incompressible, laminar flow are here employed for a complete characterization of the thermodynamic properties of the flow inside the channel. In particular, the analytical

solutions for the pressure distribution along the channel and the velocity distribution on the rectangular cross-section are combined with the mass flow rate measurements provided by CV technique for estimating the average axial velocity that can be compared with MTV velocity measurements.

6.2.1 Repeatability of the experimental conditions

The experimental run described in the previous section has been repeated several times. The repeatability of the experimental conditions is important for both the mass flow rate measurements provided by CV technique and the velocity measurements provided by MTV. For the former technique, the possibility of reproducing the same pressure evolution in the upstream reservoir allows to repeat the mass flow rate measurements, thus helping in characterizing the statistical uncertainty of the measure. For MTV, the fact that the same experimental flow can be reproduced with the highest accuracy is, instead, a real necessity for comparing velocity measurements that come from displacement profile recorded at different delay times and for having the possibility of averaging images that belong to different experimental runs. Figure 6.10a reports the pressure measurements p_1 and p_2 for three experimental runs. For all the three cases, the gas mixture is acetone-helium at χ = 20% and the starting pressure in the upstream reservoir is about p_1 = 5000 Pa. The corresponding evolution in time of the average pressure p_m and of the pressure difference Δp_{12} are reported in Figure 6.10b. As it can be observed, the gas circuit is able to reproduce the same flow conditions for all the duration of the experimental run and no appreciable differences are present from one experiment to another.

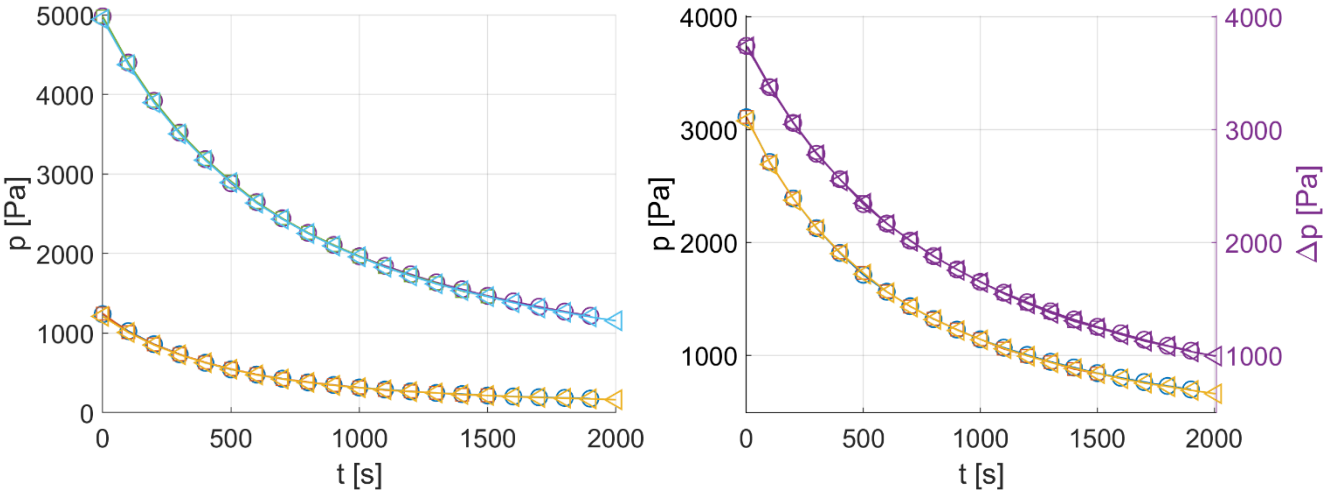

(a) (b)

Figure 6.10. Repetition of the experimental flow three times: experimental run 1 (○), experimental run 2 (□), experimental 3 (◁). In (a), the evolution in time of the upstream p_1 and the downstream p_2 pressures; in (b), the evolution in time of the pressure difference $\Delta p_{12} = p_1 - p_2$ and the average pressure $p_m = (p_1 + p_2)/2$.

6.2.2 Minor head losses

The theoretical estimation of the axial distribution of the gas flow properties along the channel requires knowing the pressures p_{in} and p_{out}, respectively, at the inlet and the outlet of the duct. The available upstream p_1 and downstream p_2 pressure measurements do not correspond directly to p_{in} and p_{out} because of (i) the minor head losses caused by the sudden section contraction at the inlet and the sudden section expansion at the outlet and of (ii) the pressure drop along the pipe connecting the pressure sensors to the channel inlet/outlet. The total pressure difference $\Delta p_{12} = p_1 - p_2$ can be written as

$$\Delta p_{12} = \Delta p_{in} + (p_{in} - p_{out}) + \Delta p_{out}, \tag{6.43}$$

in which Δp_{in} and Δp_{out} are the pressure drops, respectively, at the inlet and the outlet of the channel that are due to both localized and distributed head losses. The pipe system connecting the pressure sensors P1 and P2 to, respectively, the channel inlet and outlet is sketched in Figure 6.11.

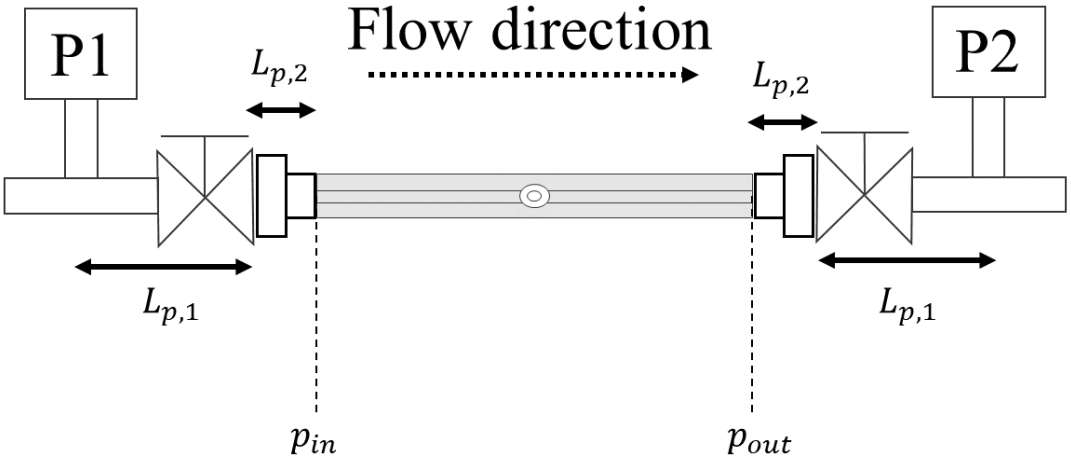

Figure 6.11. Schematization of the connections between the pressure sensors and the channel inlet/outlet.

The pressure sensor is connected to the channel inlet through, in this order, an ISO-KF T-junction, a valve, and an ISO-KF Swagelok® adapter, which all have a circular inner diameter. When the Pfeiffer® ball valve is in its fully open position, it is possible to consider it just as a straight tube with, approximatively, the same inner diameter of the T-junctions, which is 15 mm. The ISO-KF Swagelok® adapter has, instead, a smaller diameter of 5 mm. Therefore, the connection between the pressure sensor and the channel/inlet outlet is modeled as the composition of two elements. The first element is a tube with a diameter $D_{p,1}$ = 15 mm and a length $L_{p,1}$ = 130 mm, which represents both the ISO-KF T-junction and the fully-open ball valve, and the second. The second element is another tube that represents only the ISO-KF Swagelok ® adapter and that has a diameter of $D_{p,2}$ = 5 mm and length $L_{p,2}$ = 17.4 mm.

The pressure drop $\Delta p_{d,i}$ along each element of the connection is estimated by means of the analytical expression of the mass flow rate through a circular tube, that is

$$\dot{m} = \frac{\pi D_{p,i}^4}{128\mu}\rho_p \frac{\Delta p_{p,i}}{L_{p,i}} \quad \rightarrow \quad \Delta p_{d,i} = \dot{m}\frac{128\mu}{\pi D_{p,i}^4}\frac{L_{p,i}}{\rho_{p,i}}, \tag{6.44}$$

where the gas density $\rho_p = p_1/(R_s T)$ in the connections is estimated from the pressure measurement p_1. The overall distributed pressure drop along the ISO-KF T-junction, the valve, and the ISO-KF Swagelok® adapter is $\Delta p_d = \Delta p_{p,1} + \Delta p_{d,2}$.

The head losses $\Delta p_{in,c}$ and $\Delta p_{out,e}$ produced, respectively, by the sudden section contraction at the channel inlet and the sudden section expansion at the channel outlet are calculated as

$$\Delta p_{in,c} = \frac{1}{2}K_c\left(\frac{\dot{m}}{A}\right)\left(\frac{R_s T}{p_{in}}\right), \tag{6.45}$$

$$\Delta p_{out,e} = \frac{1}{2}K_e\left(\frac{\dot{m}}{A}\right)\left(\frac{R_s T}{p_{out}}\right). \tag{6.46}$$

The calculation of the head losses from Eq. (6.45) and Eq. (6.46) would require calculating the gas density from the pressure p_{in} and p_{out}, which are not known. The head losses are then approximated by using instead p_1 and p_2 respectively. The value of the coefficients K_c and K_e depend on the geometry that produces the head loss. For the case of sudden contraction and sudden expansion, they can be approximated as K_c = 0.5 and K_e = 1.

The overall pressure drops at the inlet, $\Delta p_{in}(t) = \Delta p_{in,c}(t) + \Delta p_{in,d}(t)$, and at the outlet, $\Delta p_{out}(t) = \Delta p_{out,c}(t) + \Delta p_{out,d}(t)$, depend on the mass flow rate $\dot{m}(t)$ and varies in time. Their calculation is, therefore, carried out in the next section, in which CV technique is used for calculating the mass flow rate passing through the channel at any time during the experimental run.

6.2.3 Dynamic-constant volume technique

CV technique allows to measure the mass flow rate $\dot{m}(t)$ at any time during the experimental run from the rate of variation of the pressure in the upstream reservoir. As already discussed in Chapter 4, two pressure sensors, P1 and P4, monitor the pressure in the tanks. The double-pressure measurements at two different and far locations in the reservoir reveal that the pressure variation in time of p_1, which is close to the channel entrance, and of p_4, which is directly connected to the inlet tank, are the same for all the duration of the experimental run. This demonstrates that the dynamic pressure in correspondence of the pressure sensor P1 is negligible, and that the measurement p_1 is representative of the pressure inside the upstream reservoir. By assuming that the pressure

variation caused by thermal fluctuations in the big tanks are negligible with respect to the pressure variation caused by the reduction in the gas mass, the mass flow rate is calculated as

$$\dot{m} = \frac{V_R}{R_s T}\frac{dp_1}{dt}, \tag{6.47}$$

where V_R = 175.98 l is the upstream reservoir volume, which has been measured in Chapter 4. For the experimental setup here employed, the downstream pressure p_2 cannot be used for inferring a mass flow rate measurement. The decrease in time of p_2 is the result of the unbalance between the mass flow rate $\dot{m}$ that passes through the tested channel, which tends to increase p_2, and the mass flow rate $\dot{m}_p$ imposed by the pumping system, which depends on the working pressure p_2 and reduces the mass of gas in the downstream volume V_D. If the pressure variation due to the thermal fluctuations are neglected, the relationship between the downstream pressure variation and the mass flow rates is:

$$\dot{m} - \dot{m}_p = \frac{V_D}{R_s T}\frac{dp_2}{dt}. \tag{6.48}$$

Because the mass flow rate provided by the vacuum pumps is always higher than the mass flow rate passing through the channel, pressure p_2 keeps decreasing in time. Since the mass flow rate $\dot{m}_p(t)$ is not known a priori, a measurement of $\dot{m}$ cannot be extracted from the rate of variation of p_2. Contrarily, the measurement of $\dot{m}$ from the rate of variation of the upstream pressure combined with Eq. (6.48) could provide a characterization of the mass flow rate generated by the two pumps as a function of the working pressure. Even though this type of analysis would increase the understanding of the gas circuit functioning, the characterization of the pumping system is out of the scope of this work.

The evaluation of the derivative $\frac{dp_1}{dt}$ in Eq. (6.47) is carried out by fitting the pressure data $p_1(t)$ with a proper analytical function. The best fitting function is usually identified by means of a mathematical description of the experimental system. For instance, in the classical version of CV technique with two identical closed volumes at the two sides of the tested channel, it can be analytically demonstrated that the upstream and downstream pressure both evolve exponentially with time. Differently, when the upstream and downstream volumes are not equal in dimensions, like in the gas circuit employed in this work, the pressure $p_1(t)$ and $p_2(t)$ do not follow an exponential decay. This is because the average pressure in the system decreases in time during the pressure relaxation, the conductance of the channel varies accordingly. Silva *et al*. (2018) analytically solved the problem of pressure relaxation with two different volumes and found the most appropriate fitting function for the evolution in time of the pressures in the reservoirs. The experimental setup of this work has, indeed, two different volumes at the two sides of the tested channel, but the fitting function found by Silva and co-workers does not fit well the pressure data of Figure 6.9a. As a matter of fact, the gas circuit is not a "constant-volume" setup because of the pumping

force applied to the downstream volume. The evolution in time of the reservoir pressure depends inherently on the characteristic curve of the two pumps, which determines the mass flow rate $\dot{m}_p$ as a function of the working pressure. An analytical solution of the upstream and downstream pressure functions $p_1(t)$ and $p_2(t)$ can be found only if an analytical expression of the pumping mass flow rate is available. In this context, the characterization of the pumping system by means of Eq. (6.48) gains significant importance.

Since the most suitable fitting function for the pressure relaxation characterizing the type of experimental setup employed in this work is not known a priori, the fitting function that works the best for pressure data p_1 has been determined to be a series of N exponential functions:

$$p_1 = \sum_{i=1}^{N} a_i e^{-t/\tau_i}. \tag{6.49}$$

A possible theoretical explanation of the suitability of Eq. (6.49) is provided by the following reasoning: as the conductance of the tested channel varies as the average pressures decreases, the characteristic time of pressure relaxation changes accordingly. The evolution in time of the reservoir pressure can then be described by a series of exponential with characteristic times τ_i that can take into account of the evolution of the channel conductance. The most appropriate number N of exponential functions to be used depends on the duration of the experiments. For short experiments that last about 500 seconds, two or three exponentials are enough for fitting well the pressure data p_1. Longer experiments, such as the one shown in Figure 6.9, require between 5 to 7 exponentials. If the number of exponential functions employed is higher than what is actually needed for representing the pressure evolution in time, the resulting fitting function assumes spurious oscillations, similarly to what happens for polynomial fittings. Once the fitting parameters a_i and τ_i have been determined, the rate of variation of the upstream pressure is analytical calculated as:

$$\frac{dp_1}{dt} = \sum_{i}^{N} -\frac{a_i}{\tau_i} e^{-t/\tau_i}. \tag{6.50}$$

Figure 6.12a reports the time evolution of the mass flow rate $\dot{m}(t)$ for the entire duration of the experimental run. From the highest to the lowest values of p_m and Δp, the mass flow rate decreases of one order of magnitude, ranging between 6×10^{-6} kg s^{-1} and 5×10^{-7} kg s^{-1}.

From the measured mass flow rate, the head losses described in the previous section can be evaluated. Figure 6.12b reports the evolution in time of the effective pressure difference $\Delta p = p_{in} - p_{out}$ acting on the channel, the pressure losses Δp_c and Δp_e due to the sudden change in cross-section at the inlet and the outlet, and the pressure drop Δp_d in the connections between the pressure sensors at the entrance/exit of the channel. At the beginning of the experiment, when the mass flow rate is the highest, the pressure losses are the highest, as expected from Eq.

(6.44), (6.45) and (6.46). The distributed head losses are mainly due to the ISO-KF Swagelok® adapter, since its inner diameter of 5 mm is comparable to the hydraulic diameter of the channel D_h = 1.6 mm. While the pressure drops along the ISO-KF T-junction and the ball valve is limited to a maximum of 0.5 Pa at the inlet and 2 Pa at the outlet., the pressure drop along the ISO-KF Swagelok® adapter assumes maximum values of 5 Pa and 20 Pa. In any case, the distributed pressure losses are between 3 to 4 orders of magnitude smaller than the inlet-outlet pressure difference Δp on the channel. The distributed pressure losses are, therefore, always negligible, even though they are taken into account in the calculation of the inlet and outlet pressure. Instead, the main source of pressure losses are given by the head losses due to the sudden change in cross-section. While the head losses at the entrance, $\Delta p_{in,c}$, are 3 orders of magnitude lower than Δp, varying from 10 Pa to 0.1 Pa, at the exit, the cross-section expansion produces a pressure drop $\Delta p_{out,e}$ that is between 100 Pa and 5 Pa. When the mass flow rate reaches values of the order of 2×10^{-6} kg/s, the concentrated pressure losses are comparable to the distributed pressure drop.

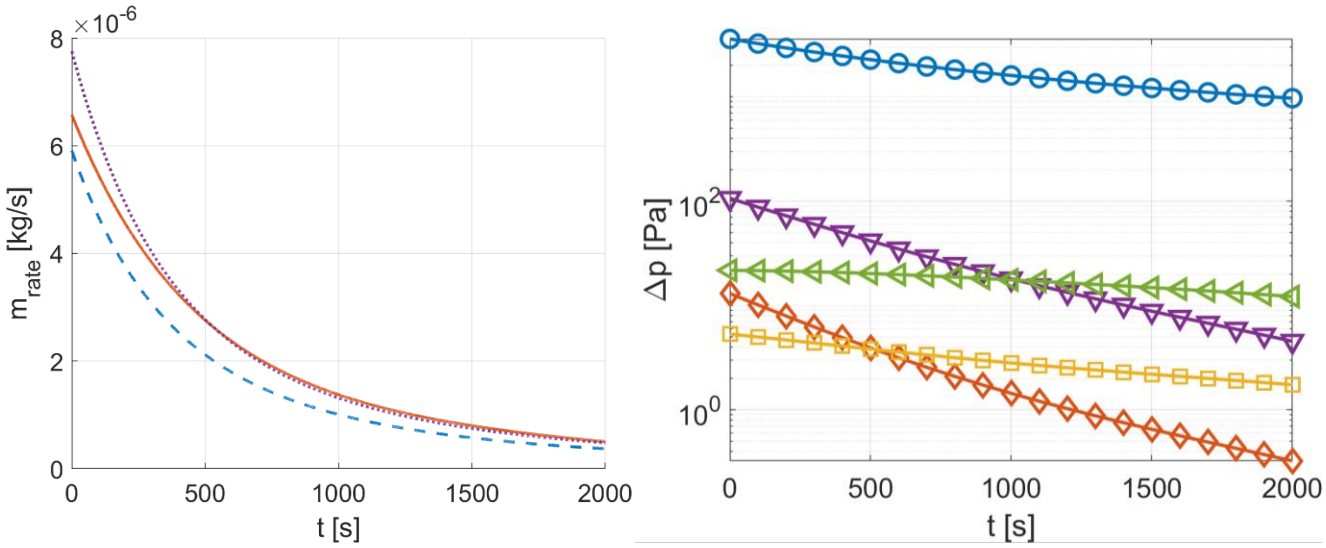

(a) (b)

Figure 6.12. (a) Mass flow rate $\dot{m}(t)$ during the experimental run: measured mass flow rate (solid line) from CV technique and theoretical mass flow rate from the velocity solution proposed by Ebert & Sparrow (1965) for H = 913.5 µm (dashed line) and H = 1 mm (dotted line); (b) Pressure drops taking place between the pressure sensor measurements p_1 and p_2: inlet-outlet pressure drop, $\Delta p_e = p_{in} - p_{out}$ (○), outlet head losses due to the sudden cross-section expansion, $\Delta p_{out,e}$ (▽), inlet head losses due to the sudden cross-section contraction, $\Delta p_{in,c}$ (◇), and pressure drop on the connections at the inlet, $\Delta p_{in,d}$ (◁), and at the outlet, $\Delta p_{out,d}$ (□).

The actual pressure at the inlet and at the outlet of the channel are, therefore, calculated as

$$p_{in} = p_1 - \left(\Delta p_{in,c} + \Delta p_{in,d}\right), \tag{6.51}$$

$$p_{out} = p_2 + \left(\Delta p_{out,e} + \Delta p_{out,d}\right). \tag{6.52}$$

By knowing the pressure ratio $\Pi(t) = p_{in}/p_{out}$ acting on the tested channel at each time during the experimental run, the measured mass flow rate can be compared to the theoretical solution. Because of the relatively low Knudsen numbers, the theoretical mass flow rate is calculated from the velocity distribution of Ebert & Sparrow (1965), which is based on first-order slip boundary conditions and which expression is reported here:

$$\dot{m}_{rect,S1}(t) = \frac{bH^3}{4\mu}\frac{p_{out}^2}{R_s T L}\left[a_1\frac{\Pi^2 - 1}{2} + a_2(\Pi - 1)Kn_{H,out}\right]. \tag{6.53}$$

The values of the width b = 5800 ± 200 μm and of the height H = 913.5 μm have been measured by means of the methodology discussed in Chapter 4. With these dimensions, the aspect ratio is $a = H/b$ = 0.152, and the fitting coefficients in Eq. (6.53) are a_1 = 0.3 and a_2 = 2.02, which have been calculated with full accommodation, σ = 1, and β_{u1} = 1.1. As it can be observed in Figure 6.12a, there is not a perfect match between mass flow rate measured from CV technique and the theoretical value provided by Eq. (6.53). The difference $\left|\dot{m}_{rect,S1} - \dot{m}\right|$ varies between 10% at the beginning of the experiment to a maximum of 30% when the average pressure in the channel reaches about 1.5 kPa. In the same figure, it is shown how the numerical mass flow rate fits better the experimental data by modifying the height channel to H = 1 mm. While the reason of these discrepancies is not clear, it is believed that the theoretical solution does not capture correctly all the features of the experimental flow inside the channel.

The width b = 5800 μm has been set in order to fit other experimental data, which are related to argon-acetone flow at pressures between 13 kPa and 6 kPa. Those experiments have been chosen for calibrating the numerical mass flow rate to the experimental one (reported in Figure 4.41 of Chapter 4) because characterized by a relatively low inlet over outlet pressure ratio and, thus, negligible compressibility effects. The inlet-outlet pressure difference and the resulting flow speed in the experiments used for determining b are one order of magnitude lower than those of the acetone-helium flow here analyzed. Higher flow rates make the thermodynamic conditions and the mass flow rate vary faster in time. A first possible explanation of the considerable error between the numerical and experimental data is that the hypothesis of quasi-stationarity of the gas flow is not satisfied. The theoretical solution given by Eq. (6.53) represents, indeed, the mass flow rate that would pass through the channel if the flow field is always in steady state with respect to the instantaneous inlet over outlet pressure ratio $\Pi(t)$. If the pressure boundary conditions at the channel inlet and outlet vary too fast with respect to the time response of the channel gas flow, the mass flow rate $\dot{m}(t)$ stays far from the steady flow solution $\dot{m}_{rect,S1}(t)$.

A second factor that could make the analytical mass flow rate different from the measured one is related to the hypothesis of locally fully-developed gas flow. The hydrodynamic development length might be long enough to make the entry region of developing flow not negligible with respect to the total length of the channel. In this scenario, the assumption of locally fully-developed flow cannot be applied to all the channel length, and Eq. (6.53) does not hold anymore. The following equation can be used for estimating the hydrodynamic development length:

$$x_d = \left(\frac{0.315}{0.0175Re + 1} + 0.08Re\left[1 + 6.7\frac{2-\sigma}{\sigma}Kn_{in}\right]\right)D_h, \tag{6.54}$$

which derives from Eq. (2.35) with the coefficient 0.08 proposed by Sparrow *et al*. (1967) for a rectangular channel with aspect ratio 0.2, close to that of the tested channel. $x_d(t)$ varies from 1.3 cm to 0.14 cm from the highest to the lowest Reynolds number $Re = 4\dot{m}/\mu\pi D_h$ along the experimental run. In Eq. (6.54), Kn_{in} is calculated by considering the inlet pressure p_{in}. The understating of the importance of an entry length of about 1.3 cm in a 20-cm long channel would require a numerical investigation that has not been accomplished in this work.

As it will be presented in the following of this chapter, the measured mass flow rate combined with the theoretical pressure distribution inside the channel provide average velocity measurements that are similar to those provided by MTV. The theoretical solution $\dot{m}_{rect,S1}$, instead, provides, with the same procedure, an average velocity that diverges more from those experimentally measured by MTV and CV techniques.

6.2.4 Thermodynamic conditions along the channel

From the measured inlet and outlet pressure p_{in} and p_{out}, the axial pressure distribution along the channel can be predicted from the analytical solution, Eq. (2.76), discussed in Chapter 2. Figure 6.13a reports $p(x,t)$ at three different times during the experimental run, that is t = 30, 900, and 1800 s from the beginning of the experiment. Since the pressure ratio Π is relatively high, ranging from 4 to 6.5, the compressibility effect on the pressure distribution are not negligible for all the duration of the experimental run. As shown in Figure 6.13b, even though the pressure difference $p_{in} - p_{out}$ decreases in time, the pressure ratio $\Pi = p_{in}/p_{out}$ increases and, thus, the gas compressibility assumes even more importance at the lowest pressures.

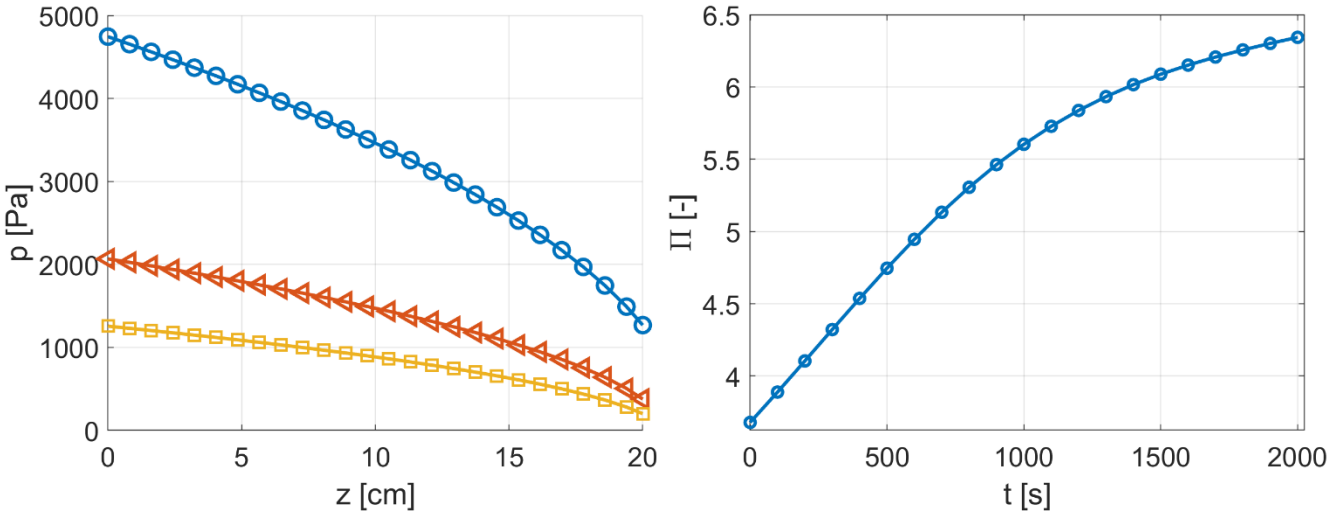

(a) (b)

Figure 6.13. (a) Pressure distribution $p(x,t)$ along the channel length at three different times t = 0, 1000, and 2000 s during the experimental run, which correspond to the pressure ratios Π = 4 (O), 6 (◁), and 7 (□); (b) Time evolution of the pressure ratio Π(t) during the experimental run.

The mass flow rate measurement $\dot{m}(t)$ provided by CV technique and the theoretical pressure distribution $p(x,t)$ inferred from the pressure measurements $p_{in}(t)$ and $p_{out}(t)$, respectively, at the inlet and the outlet can, together, provide an estimation of the flow rate $\dot{V}(x,t)$ and of the average velocity $\overline{u_{2D}}(x,t)$ on the cross-section at each position x along the channel and at each time t during the experimental run. By considering that $\dot{m}(t) = \dot{V}(x,t)p(x,t)/R_sT$, the volume flow rate $\dot{V}$ can be calculated from Eq. (6.47) as

$$\dot{V} = \frac{V_R}{p}\frac{dp_1}{dt}. \tag{6.55}$$

Differently from $\dot{m}$, $\dot{V}$ does not depend on the estimation of R_sT in the reservoir. The specific ideal gas constant R_s of the gas mixture depends on the molar mass M of the mixture, which is calculated from Eq. (6.1). Therefore, the accuracy in $\dot{m}$ depends on the precision of controlling χ. The volume flow rate $\dot{V}$, instead, does not depend on χ but the uncertainty on its measurement is related to the accuracy of the theoretical model, Eq. (2.76), of representing the real distribution of pressure $p(x)$ along the channel.

The average velocity $\bar{u}_{2D}(x,t)$ of the axial velocity distribution on the cross-section is

$$\bar{u}_{2D} = \frac{\dot{V}}{Hb} = \frac{V_R}{Hbp}\frac{dp_1}{dt}, \tag{6.56}$$

The uncertainty on $\bar{u}_{2D}$ is also determined by the uncertainty on the dimensions of the cross-section H and b along the channel. Because the gas flow is assumed to be isothermal, the speed of sound c_s, which only depends on the gas temperature, is constant along the channel. Figure 6.14a and Figure 6.14b report, respectively, the distribution of the Mach number $Ma(x,t) = \bar{u}_{2D}/c_s$ and the Knudsen number $Kn(x,t) = \lambda(x,t)/D_h$ at different times t during the experimental run.

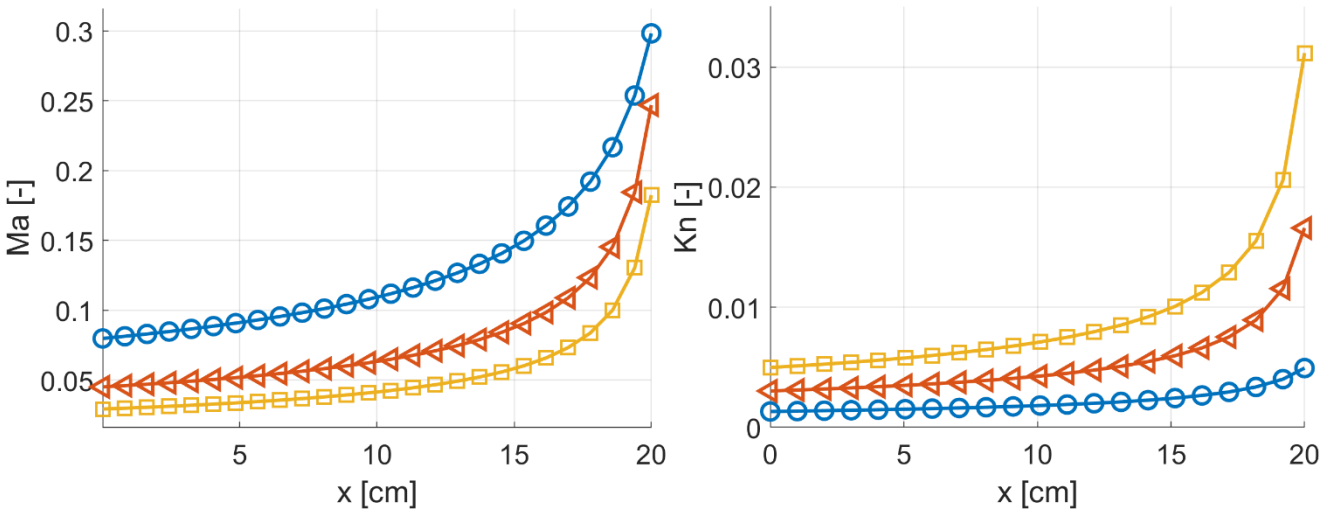

(a) (b)

Figure 6.14. (a) Mach number $Ma(x,t) = \bar{u}_{2D}/c_s$ distribution along the channel length at three times; (b) Knudsen number $Kn(x,t) = \lambda(x,t)/D_h$ distribution along the channel length at three times. For both Ma and Kn, the three times are t = 0 (○), 1000 (◁), and 2000 s (□) correspond to the three pressure distributions $p(x,t)$ of Figure 6.13a, for which the pressure ratios are Π = 4, 6, and 7.

As expected, the gas expansion and the consequent gas acceleration in the flow direction make the Knudsen number and the Mach number increase towards the channel outlet. The outlet region is more interesting for MTV application to gas flows in rarefied conditions, since, for a given pressure difference applied on the channel, the Knudsen numbers are higher. Moreover, as the average pressure in the gas system decreases, the Mach number and, thus, the average velocity remain relatively high in the channel region close to its exit. From the point of view of MTV analysis, because the higher diffusion at higher Knudsen number tends to flatten the displacement profile of the tagged molecules, higher gas velocities are desired for increasing the displacement profile thickness Δs. Unfortunately, the current experimental channel is equipped with optical accesses for the laser excitation and the ICCD acquisitions only at the center position. Future developments of the experimental setup may take into considerations the outlet region of the channel for investigating gas flows characterized by higher rarefaction and higher flow speed.

The theoretical solution $p(x,t)$ that takes into account of the gas density variation along the channel is of fundamental importance for the accurate estimation of the average pressure $p_c(t) = p(x = L/2, t)$ at the central cross-section at x = 10 cm, that is where MTV analysis is applied. The curves of Figure 6.14 correspond to the three pressure distributions of Figure 6.13a, for which the central pressure is, respectively, p_c = 3462, 1470, and 885 Pa.

From the pressure function $p_c(t)$, the time evolution of the average velocity $\bar{u}_{2D}$ at the center position $x = L/2$ can be known at every time during the experimental run. The Mach number $Ma = \bar{u}_{2D}/c_s$ and the Knudsen number $Kn = \lambda/D_h$ characterizing the flow conditions investigated by MTV are reported in Figure 6.15. The non-dimensional numbers are expressed as a function of the mixture pressure p_c. Since the Mach number is always lower than 0.3, the flow can be considered as the central section as locally incompressible. When the pressure p_c reaches values lower than 1.5 kPa, the flow is considered entering the slip flow regimes, where $Kn \geq 0.004$, or, equivalently, $Kn_H \geq 0.008$. The Reynolds number Re, which is constant along the channel, varies in time from 100 to 5, and, therefore, the flow can be certainly considered as laminar.

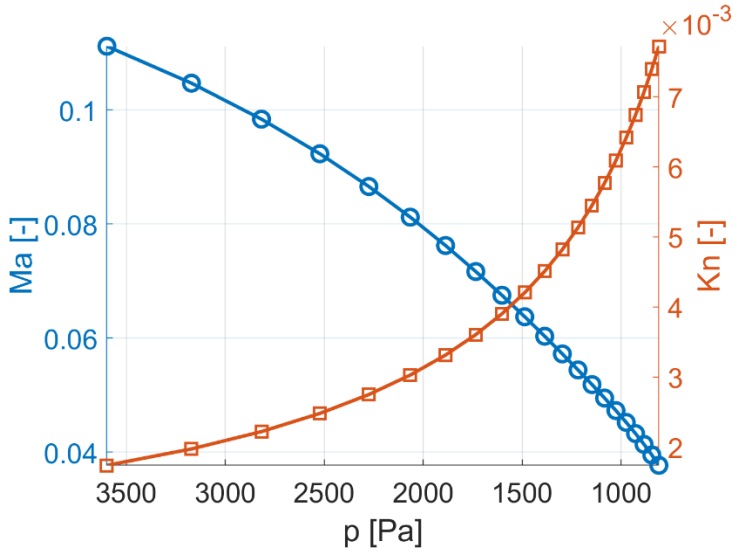

Figure 6.15. Mach number Ma (○) and Knudsen number Kn (□) as a function of the average pressure $p_c(t)$ at the middle position $x = L/2$ during one experimental run. The Mach number is calculated from the average velocity $\bar{u}_{2D}$ and the Knudsen number is based on the hydraulic diameter D_h. The Knudsen number Kn_H based on the channel height has values that are approximatively double of those of Kn.

6.2.5 Velocity measurement for comparison with MTV results

In order to be able to compare the flow rate measurements provided by CV technique with the velocity measurements provided by MTV technique, the axial velocity distribution $u_{2D}(x,y,z,t)$ on the cross-section at the center position $x = L/2$ along the channel needs to be theoretically estimated. As a matter of fact, the average

velocity $\bar{u}_{2D}(x,t)$ of Eq. (6.56) represents the average value of the 2D distribution $u_{2D}(x,y,z,t)$ on the cross-section, while the average velocity that MTV can provide is related to a velocity profile $u(y,t)$, that is only a transversal section at a specific z. The location z at which MTV is applied is not known exactly but, as already discussed in Section 6.1.7, for $z \in$ [-1 mm, 1 mm], the velocity profile $u(y,t)$ is not dependent of the z coordinate. Because the range of Knudsen numbers Kn_H under investigation are very below 0.1, the velocity solution with first-order slip boundary conditions proposed by Ebert & Sparrow (1965) is a suitable prediction of the velocity distribution on the cross-sections of the experimental channel. The non-dimensional solution $u^*_{2D}(y^*,z^*)$ calculated from Eq.(2.59) for Kn_H = 0.01 is shown in Figure 6.16a, where $z^* = z/(b/2)$ and $y^* = y/(H/2)$. For these calculations, full accommodation is assumed, i.e., σ = 1 and β_{u1} = 1.1. On the same figure, three velocity profiles $u^*_{z^*}(y^*)$ are highlighted at three different locations, z^* = -0.5, 0, and 0.5, which, for b = 5 mm, delimitate a central region $z \in$ [-1 mm, 1 mm]. The three velocity profiles are reported in Figure 6.16b to demonstrate the independency with respect to z.

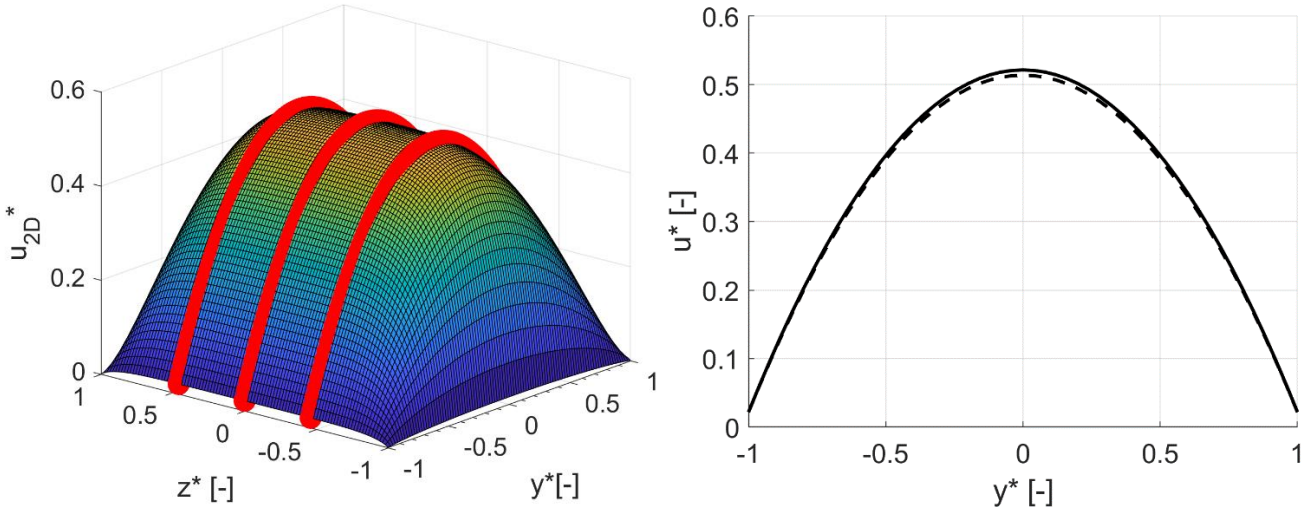

(a) (b)

Figure 6.16. (a) Non-dimensional velocity distribution $u^*_{2D}(y^*,z^*)$ for Kn_H = 0.01, σ = 1 and β_{u1} = 1.1, calculated from the solution of Ebert & Sparrow (1965). The red thick lines highlight the velocity profiles $u^*_{z^*}(y^*)$ at the locations z^* = -0.5, 0, and 0.5; (b) velocity profile at z^* = 0 (solid line) and at z^* = ±0.5 (dashed line).

The average $\bar{u}$ of the velocity profile at $z = 0$ along the width of the cross-section located at $x = L/2$ is calculated from the measured $\bar{u}_{2D}$ as

$$\bar{u}_{CV}(t) = \frac{\overline{u^*}_{z^*=0}}{\overline{u^*}_{2D}} \bar{u}_{2D}\left(x = \frac{L}{2}, t\right). \tag{6.57}$$

In a similar way, the theoretical slip velocity u_{slip} can be inferred from the measured average velocity $\bar{u}_{2D}$ and the theoretical velocity distribution $u^*_{2D}(y^*, z^*)$ as

$$u_{slip,CV}(t) = \frac{u^*_{z^*=0}(y^* = \pm 1, t)}{\overline{u^*}_{2D}} \bar{u}_{2D}\left(x = \frac{L}{2}, t\right). \tag{6.58}$$

The non-dimensional velocity distribution $u^*_{2D}(y^*, z^*)$ and, thus, the non-dimensional velocity profile $u^*_{z^*=0}(y^*)$ evaluated at the center location $z^* = 0$ weakly depend on the value of $Kn(x = L/2, t)$, which can vary in time. For Kn_H between 0.001 and 0.01, the ratio $\overline{u^*}_{z^*=0}/\overline{u^*}_{2D}$ of Eq. (6.57) varies from 1.1432 to 1.1412. However, the ratio $u^*_{z^*=0}(y^* = \pm 1, t)/\overline{u^*}_{2D}$ of Eq. (6.58) varies from 0.0083 to 0.0708 for the same Kn_H. The average velocity $\bar{u}_{CV}(t)$ of the velocity profile is, therefore, about 14% higher than the measured 2D average velocity $\bar{u}_{2D}$, almost independently of the Knudsen number of the investigated flow. Figure 6.17 represents the evolution in time of $\bar{u}_{CV}(t)$ and $u_{slip,CV}(t)$ during one experimental run.

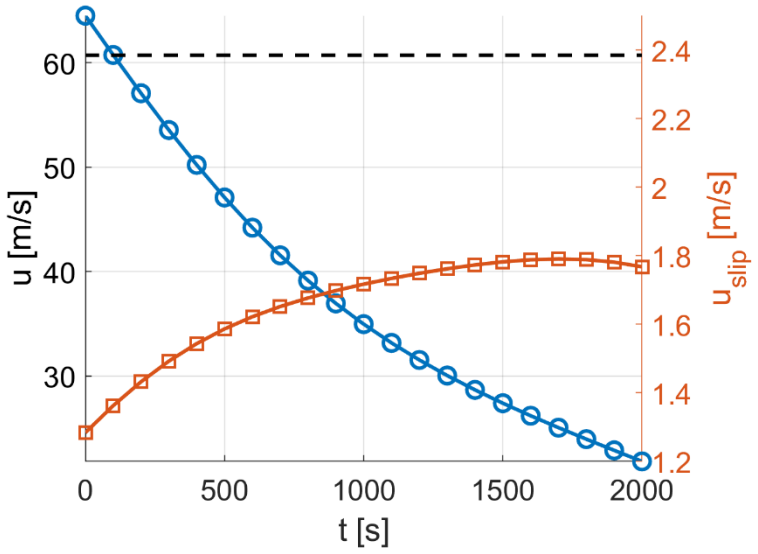

Figure 6.17. Evolution in time during the experiment of the average velocity $\bar{u}_{CV}(t)$ (○) and the slip velocity $u_{slip,CV}(t)$ (□) characterizing the velocity profile investigated by MTV. The dashed line represents the theoretical maximum velocity slip $u_{slip,max} = 1.277\sqrt{R_s T}\frac{H}{L}$ introduced in Section 6.1.11.

In the same figure, the theoretical maximum slip velocity $u_{slip,max} = 1.277\sqrt{R_s T}\frac{H}{L}$ = 2.38 m/s that can be obtained at the middle cross-section $x = L/2$ in the best conditions is also reported for comparison. The velocity slip does not vary substantially during the experiment, and its value remains between 1.2 and 1.8 m/s. These predictions derive from a combination of the mass flow rate $\dot{m}(t)$ measured by CV technique, the theoretical pressure distribution $p(x, t)$ and the theoretical velocity distribution $u^*_{2D}(y^*, z^*)$. The comparison of MTV velocity

measurements with the average velocity $\bar{u}_{CV}$ of this semi-empirical formulation will provide a validation and verification of the two experimental techniques and of the analytical solutions.

6.2.6 Velocity profile stability for MTV application

As previously discussed, the application of MTV for the investigation of the velocity field requires the gas flow to be steady or at least slowly-varying in time. From the semi-empirical analysis presented in the previous sections, the evolution in time of the investigated velocity profile during one experimental run can be predicted and its rate of variation can be compared with the time requirements of the acquisition system. The recording of one image with N_l = 100 and with a laser repetition rate of 20 Hz takes 5 seconds. From the mass flow rate and pressure measurements, it has been calculated that the velocity profile $u(y,t)$ and the pressure $p_c(t)$ varies of less than 0.5% during the recording of one single image at any time along the experimental run. This fact confirms that the experimental setup is able to generate experimental flow conditions that are in the slip regime and that are stable enough for MTV acquisitions.

The SNR of one single recorded image is too low for providing an accurate measurement of the tagged line displacement. The realization of an exploitable image mandatorily requires averaging more images representing the same flow conditions. As it will be discussed in Section 6.3.1, a possible strategy consists in averaging consecutive images recorded along one experimental run by taking advantage of the slow variation in time of the investigated flow conditions. In this perspective, it is of fundamental importance assessing how much the experimental conditions vary from one image to the other.

By considering that the time between two consecutive image acquisitions is 5 seconds, the recording of N_i = 10, 20, and 30 images takes, respectively, 50, 150, and 200 seconds. By following the analysis described in the previous sections, the velocity profiles have been calculated at times t = 0, 1000, and 2000 s along the experimental run, at which the gas mixture pressure and the average velocity at the cross-section investigated by MTV are, respectively, p_c = 3462 Pa, 1470 Pa, and 885 Pa and $\bar{u}_{CV}$ = 60.8 m/s, 38.3 m/s, and 23.2 m/s. The thermodynamic conditions along the channels at these three instants are described by Figure 6.13 and Figure 6.14. At each of these times, the velocity profile $u(y,t)$ has also been evaluated at 50, 150, and 200 seconds after t for showing how the velocity function varies from the first image to the last one recorded in a group of 10, 20, and 30 images. Figure 6.18a and Figure 6.18b report the variation in time of the velocity profiles for the cases of N_i = 20 and 30, respectively. The figures also report the average velocity profiles (the solid black lines) at each time t that an average image of a group of 20 or 30 images would represent. At t = 0, variations of 1, 2, and 3 m/s on the maximum value of the velocity profile occur in group of N_i = 10, 20, and 30 images. At lower pressures, at t = 2000 s, the variations in time are halved, with 0.5, 1, and 1.5 m/s at the peak velocity. At the first times of the experimental run, the mass flow rate is the highest and the inlet over outlet pressure ratio varies faster.

Consequently, the time stability of the velocity profile is lower. As the average pressure in the system decreases and the slip regime is approached, the velocity profile varies slower. At the wall, the velocity slip varies of less than ±0.05 m/s in a group of N_i = 30 images.

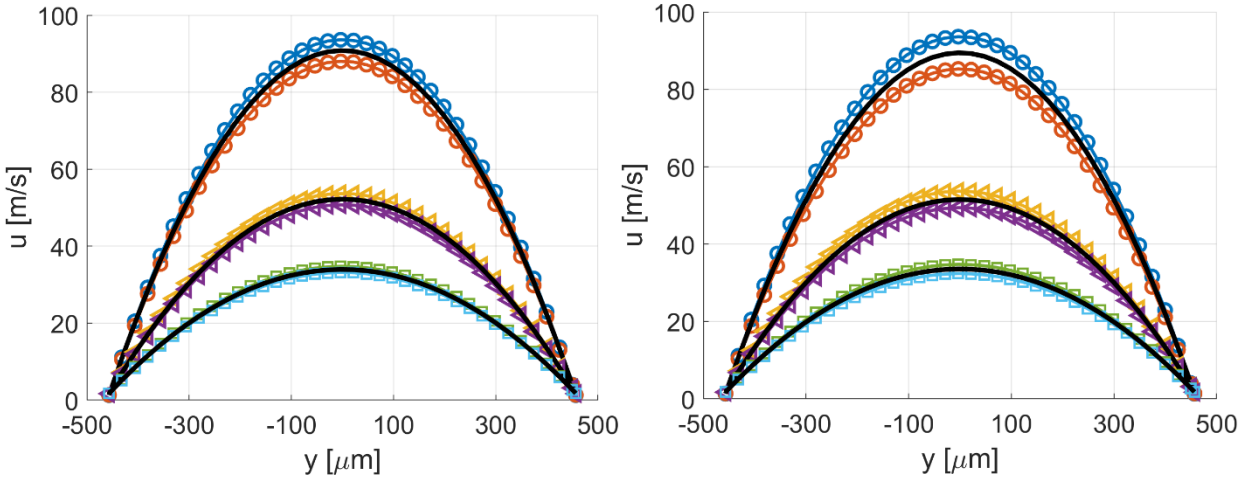

Figure 6.18. Velocity profiles $u(y,t)$ at t = 0 s (○), 1000 s (◁), and 2000 s (□) during the experimental run. The evolution of $u(y,t)$ during the recording of (a) N_i = 20 and (b) N_i = 30 consecutive images is illustrated. At each time t, it is reported: the velocity profile captured by the first image of the group; the velocity profile captured by the last image of the group; the average velocity profile (the solid black lines) that the image resulting from the average of the N_i images would represent.

Figure 6.19 reports the relative variation of $u(y,t)$ along the channel height with respect to the average velocity profile for the three times t along the experimental run. For N_i = 20, the variation of the velocity profile is always less than ±3.5% at any position along the channel height. For N_i = 30, the velocity profile varies from ±3.5% at low pressures to less than ±5% at the high pressures. At low pressures, the mass flow rate and, thus, the rate of variation of the inlet and outlet pressure conditions are than at high pressures.

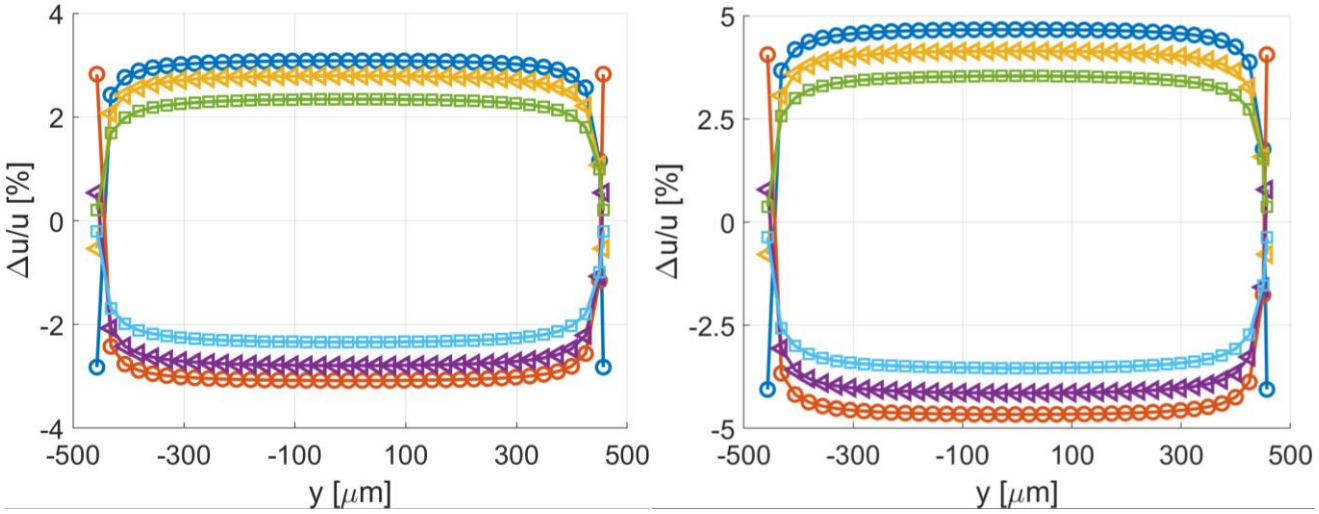

(a) (b)

Figure 6.19. Relative variation of the velocity profile with respect to the average velocity profile (solid lines in Figure 6.18) in groups of (a) N_i = 20 and (b) N_i = 30, and at t = 0 s (○), 1000 s (◁), and 2000 s (□) during the experimental run.

As already highlighted in the previous section, because of the simultaneous decreasing of the average pressure and of the pressure gradient, the variation in time of the slip velocity is quite limited during the experiment even though the overall velocity profile varies consistently. This peculiarity of the experimental flow conditions is of great help for the validation of MTV velocity reconstructions. Indeed, the experimental results from MTV should, in theory, provide velocity profile that varies in time but with very small variations of the slip velocity. Moreover, because the slip velocity does not vary a lot in time, all the experimental data gathered during the entire experiment might be correlated for extracting an accurate measurement of it.

6.3 Molecular tagging velocimetry

In this section, MTV is applied to non-rarefied and slightly rarefied flows of acetone-argon and helium-acetone mixtures. The procedure for generating an experimental run has been defined in Section 4.4.2. Once the valve upstream from the tested channel is open, the gas mixture starts flowing through the channel, from the upstream reservoir into the atmosphere by means of the two pumps working in parallel. Some seconds after the beginning of the experimental run, the image recording is launched. The image acquisition keeps going on for all the duration of one experimental run. One set of recording parameters is, therefore, used for each experimental run: the delay time t_d, the IRO gate Δt_{gate}, the IRO gain G, and the number of laser pulses per image N_l are fixed, and a big amount of images is collected as the pressure in the upstream reservoir decreases. Since one experimental run lasts about 30 mins and the laser repetition rate is 20 Hz, a group of about 360 images is collected when N_l = 100 per image is employed.

Because of the low intensity and the statistical fluctuations of the light emission, the SNR of one single image is relatively poor and the average of more than one image is mandatory for carrying out the velocity measurement. Figure 6.20 shows an example of one single image collecting 100 laser pulses with an IRO gate Δt_{gate} = 100 ns.

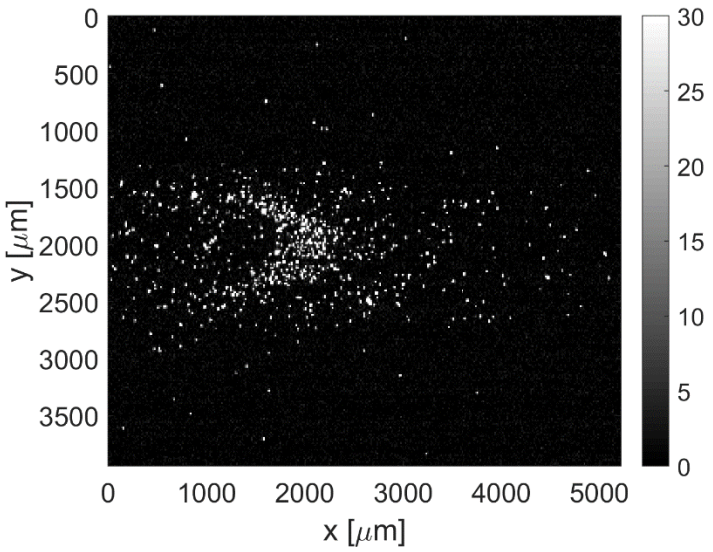

Figure 6.20. Example of a raw image acquisition of the tracer emission in a gas flow with Δt_{gate} = 100 ns and N_l = 100.

Because of the unsteady experimental flow conditions, a suitable averaging strategy needs to be put in place for producing a final image from which the velocity profile can be extracted. The procedure described in the previous sections provides a measurement of all the most important thermodynamic parameters of the gas mixture flow at the central cross-section along the channel, which is the location investigated by MTV. The measurement of the evolution in time of the inlet and the outlet pressures provides the average pressure p_c, the pressure gradient $\frac{\partial p}{\partial x}$, and the Knudsen number Kn at the central cross-section of the channel at every time during the experimental run. In particular, the correct estimation of the average pressure is essential for obtaining accurate MTV measurements, because the reconstruction method requires the definition of the diffusion coefficient characterizing the investigated gas flows. Each image of 100 laser pulses represents the integration of time-varying thermodynamic conditions during 5 seconds. While for a time frame of this duration the thermodynamic conditions are substantially the same, different images recorded along one experimental run are related to different average pressures and flow rate conditions. Depending on the averaging operation employed for producing the final image, the associated thermodynamic conditions must be processed accordingly.

In Section 6.3.1, each step of the post-processing procedure applied to the set of recorded images is discussed in detail, from the averaging operation to the production of the displacement data $s_{x,j}$ to be provided in input to the reconstruction method. In Section 6.3.2, MTV is applied to argon-acetone flow in non-rarefied conditions for

demonstrating the ability of the experimental setup of providing correct measurements at sub-atmospheric pressures. In Section 6.3.3, MTV is applied to helium-acetone flow and the very first results in terms of molecular displacement in the slip flow regime are illustrated. The application of the reconstruction method reveals new difficulties for the accurate measurements of the slip velocity at wall surface. In the light of the experimental results presented in Chapter 5, MTV measurements here presented have been carried out by using acetone vapor excited at 310 nm.

6.3.1 Post-processing procedure

In this section, the post processing procedure applied to the set of recorded images is described. The main objective is to identify the position and the shape of the deformed tagged line. A series of steps is necessary for accurately extracting the displacement profile from a noisy image.

The flow chart in Figure 6.21 shows the sequence of post-processing operations, which are:

a) image averaging;

b) wall detection and image cutting;

c) detection of the tagged line initial position;

d) filtering of the background noise;

e) gaussian fitting by line;

f) 2D fitting of the whole image (facultative);

g) extracting the displacement data $s_{x\,j}$.

In Figure 6.21, the image at step (a) represents an example of image resulting from averaging some images. Steps (b) and (c) are grouped as they are operations that simply modify the size of the image or the Cartesian coordinate system origin. Operations (e) and (f) are gathered in the group of fitting procedure. At step (g), two examples of possible displacement data are shown, depending on the type of image fitting employed.

All the operations described below have been implemented by means of the Matlab® software and have been systematically applied to all the image data recorded.

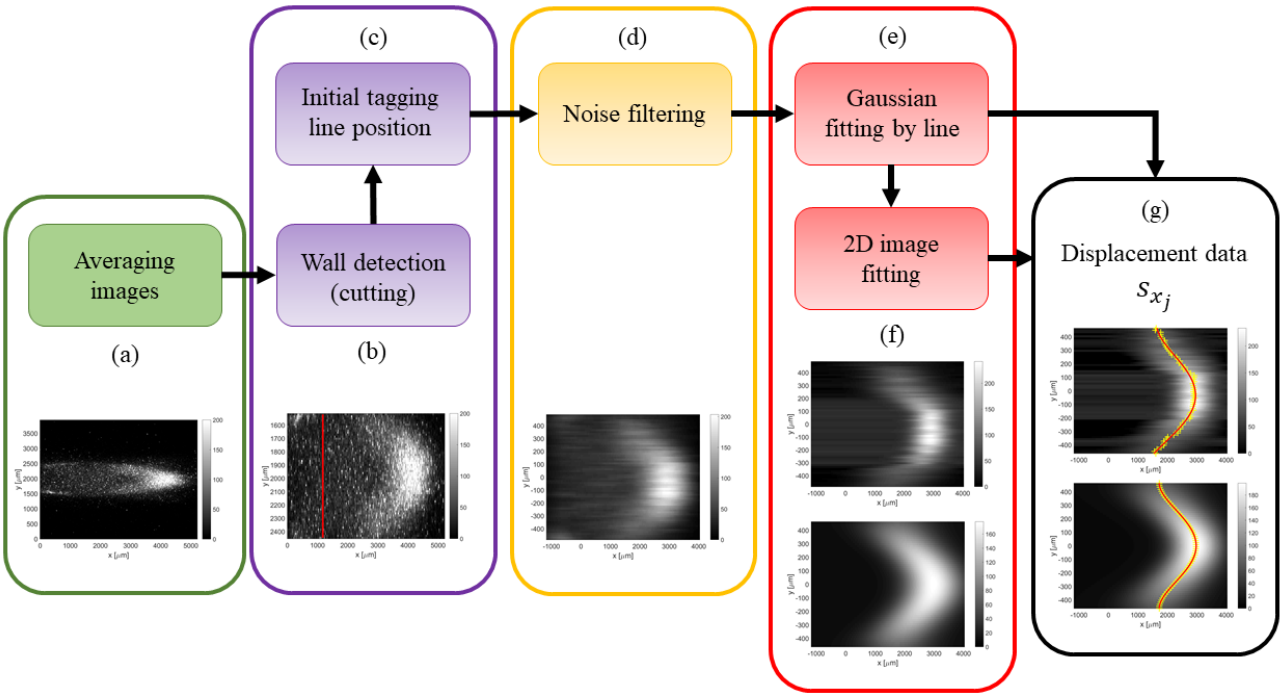

Figure 6.21. Flow chart of the image post-processing: a) image averaging; b) detecting wall position and image cutting; c) detecting tagged line position; d) filtering background noise; e) Gaussian fitting per each horizontal line of pixels; f) 2D fitting of the whole image (facultative step); g) extraction of the displacement data s_{x_j}.

a. Averaging operation

Since the experimental condition is inherently unsteady, the averaging operation needs a specific strategy for providing an image with enough high SNR and that is representative of a specific experimental flow condition. Two possible strategies have been identified in this work.

The first way consists in repeating the same experiments many times and averaging "vertically" along the different experimental runs in correspondence of an instant when the flow conditions, that is the average pressure and the inlet-outlet pressure difference, are the same. For instance, if the average of N_i images is desired, the experimental run must be repeated N_i times and the image acquisition needs to occur at the same moment along the experimental run. A schematic representation of this concept is shown in Figure 6.22.

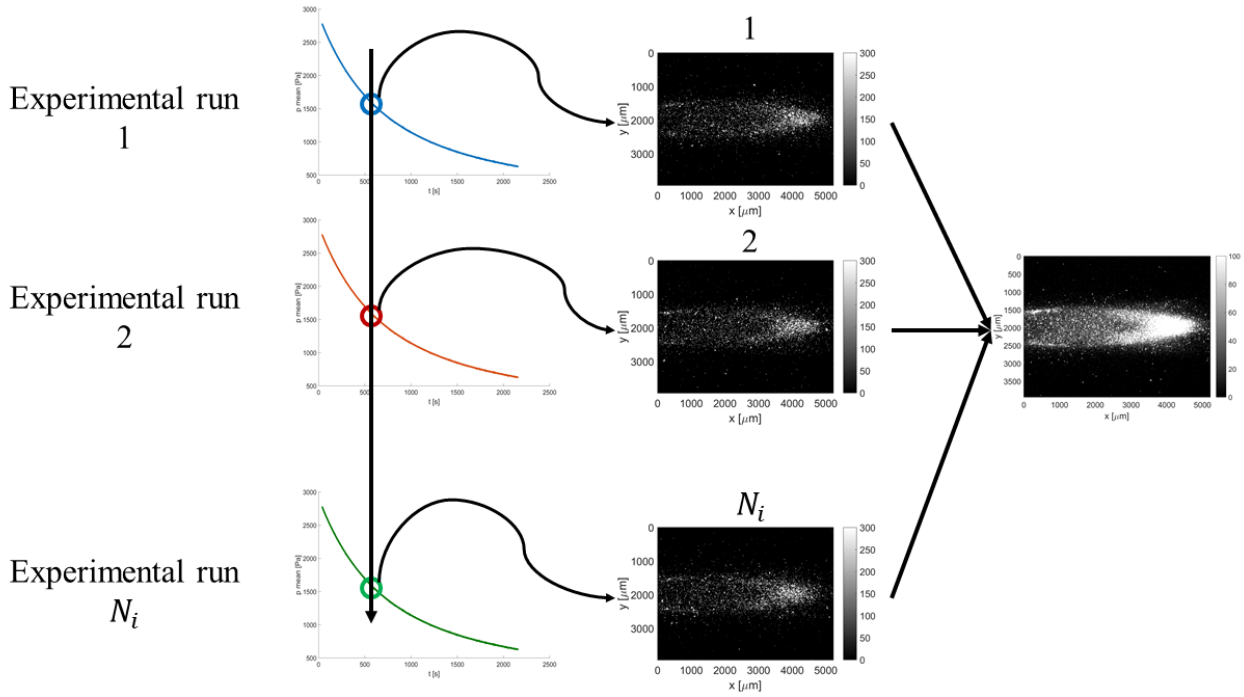

Figure 6.22. Illustration of the first strategy for producing an averaged image from a group of N_i images. The average is made "vertically" through N_i different experimental runs. The colored curves show the evolution of the pressure in the investigated section with time.

This is the most proper way to compute the average of a statistical property at a specific time in an unsteady process.

The image acquisition and the experimental run are not launched in a synchronized manner: the moment at which the image acquisition occurs does not always correspond to the same time along the experimental run. However, at N_l = 100, a new image is recorded every 5 seconds. Therefore, the maximum time interval between two images that come from two different experimental runs is, at maximum, 5 seconds, during which the thermodynamic conditions are substantially the same.

The success of this strategy is mainly determined by the ability of reproducing the same experimental conditions during the different experimental runs. In Section 6.2.1, it has been demonstrated that the gas circuit is able to reproduce the same average pressure and corresponding pressure difference with high repeatability. This is, however, true only for low-pressure flows, for which the vacuum pumps can be employed at the maximum of their pumping power. At high pressure, the flow rate through the tested channel needs to be limited for limiting the mass flow rate and thus guaranteeing an enough slow-varying experimental condition inside the channel. This requires controlling the mass flow rate imposed by the vacuum pumps by partially closing a valve, which is quite difficult to be accurate in repeating this operation several times for different experimental runs without

electronically controlled valves. A future experimental setup will be designed by considering this experimental necessity.

The second strategy consists in applying the averaging over images that belong to the same experimental run. Figure 6.23 illustrates this idea, in which, differently from the first strategy, the images are averaged "horizontally".

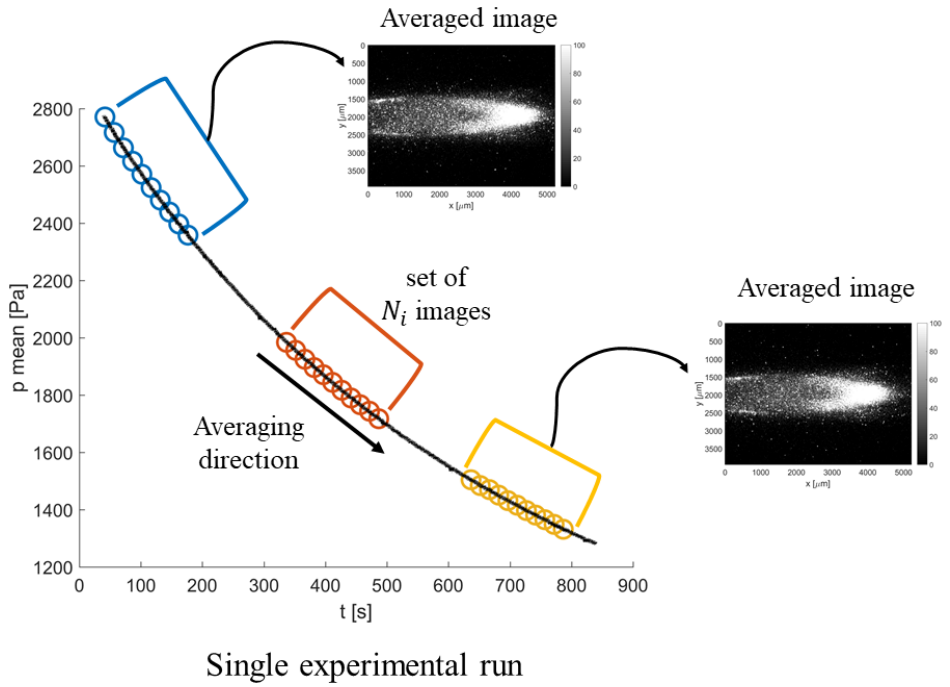

Figure 6.23. Illustration of the second strategy for producing an averaged image from a group of N_i images. The average is made "horizontally" on N_i images recorded on the same experimental run.

By recording images with the same delay time t for all the duration of one experimental run, the average can be applied to any group of N_i images that belongs to a time window centered to the experimental condition of interest. By moving the averaging window along the experimental run, a great number of averaged images that represent a multitude of thermodynamic conditions can be obtained from one single experiment.

With respect to the previous averaging procedure, this averaging strategy is much less time-consuming. In the first strategy, the production of one image that results from the average of N_i images requires repeating the experiments N_i times. While the experimental run itself can last in this case also only 10 mins, the preparation of the gas mixture for each experiment require other 20 mins. If N_i = 10, one averaged image corresponding to one specific delay time t is obtained in 5 hours. In this second strategy, many averaged images at a specific delay time t and for different average pressure and pressure difference can be obtained in 25 mins. The repetition of the experimental run can be done, instead, at a different delays. In this case, the repeatability of the experimental conditions is

exploited for capturing the displacement profile of the same flow but at different times after the laser excitation. Therefore, a data set full of information that characterizes a single flow conditions is produced in 5 hours.

The drawback of this strategy is, evidently, the fact that the group of N_i images used for producing one averaged image corresponds to different thermodynamic conditions. The group of images cannot be, therefore, arbitrary large. The size of the averaging window needs to be small enough, so that the experimental conditions of the investigated flow vary only in an acceptable range. This problematic has been analyzed in detail in Section 6.2.6.

b. Wall detection

The channel gap takes only a small portion of the field of view of the ICCD. The scope of the following operation is to identify which region of the image is going to be considered for the velocity reconstruction. In principle, it is desired to localize the position of the top and the bottom channel wall. In this way, the region where the tagged line develops is identified, and the fitting procedure is applied only to this region of interest.

The strategy employed in this work for the identification of the channel walls is based on the investigation of the light emission provided by the top and the bottom Suprasil® windows. The fluorescence of the silica is short-lived but very strong in the first few nanoseconds after the laser excitation. By recording the light emission of the silica with no tracer vapor inside the channel, the spots of maximum intensity on the windows correspond to the locations of entrance and exit of the laser beam, and, therefore, they represent the position on the image of the intersection between the tagged line and the channel walls. As illustrated in Figure 6.24, a region of interest is identified around the two spots and the pixels providing the maximum intensity are identified. The average *y*-position of the light peaks is associated to the position of the channel walls on the image. By assuming that the channel does not move with respect to the ICCD camera for the subsequent acquisitions, the images recording the tagged line displacement are cut at the level of the wall lines previously detected, as shown in Figure 6.25. By indicating with y_t and y_b the *y*-coordinates of, respectively, the top and the bottom walls, the position of the channel centerline corresponds to $y_c = (y_t + y_b)/2$. Finally, the *y*-coordinate system is redefined so that the origin $y = 0$ corresponds to the channel centerline.

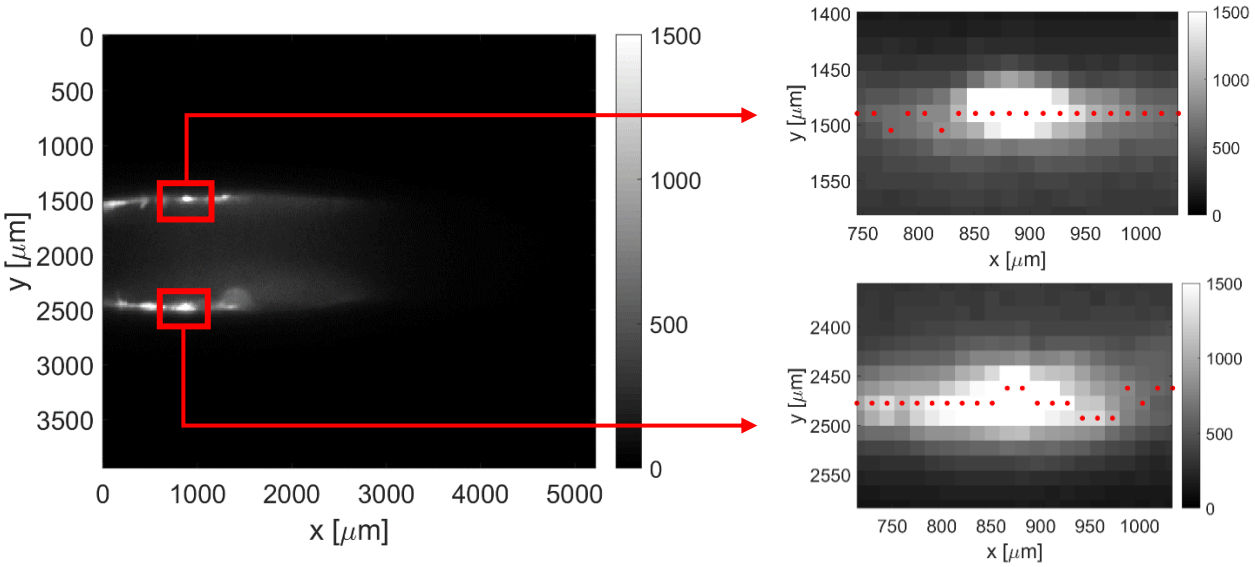

Figure 6.24. Post-processing procedure for detecting the position of the channel walls on the image: (a) raw image of the light re-emission of the Suprasil® windows and definition of the region of interest (red squares); (b) detection of the position of maximum light intensity.

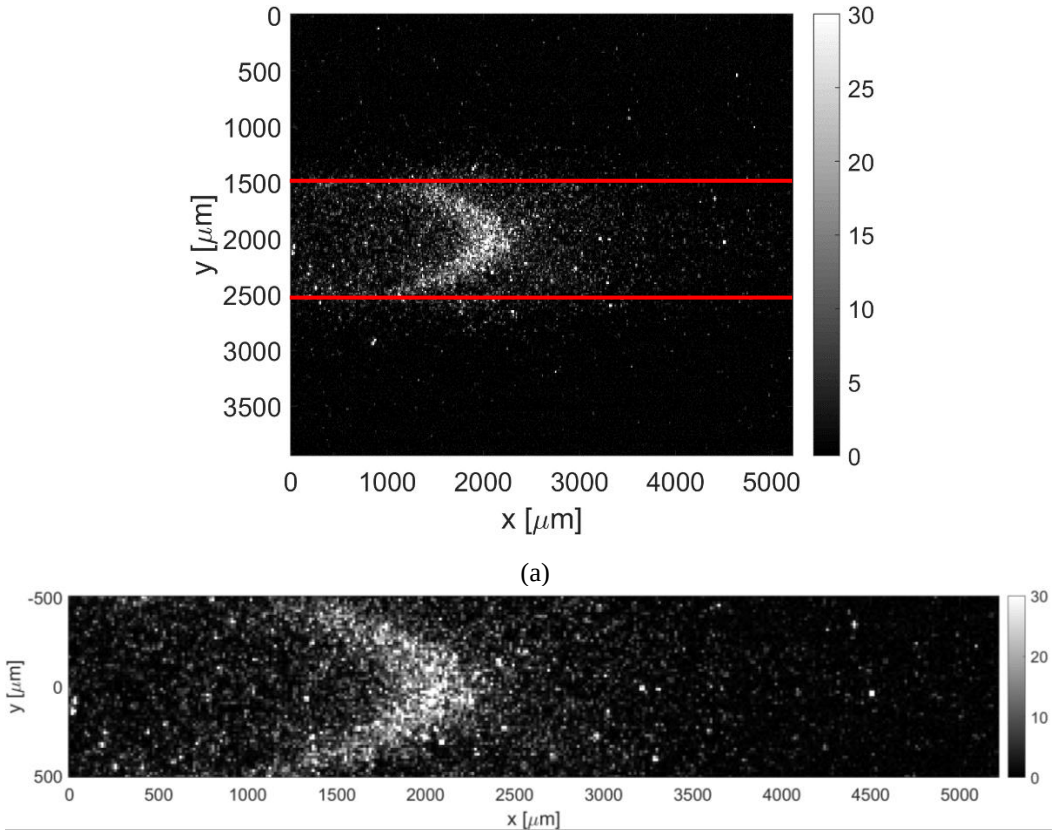

Figure 6.25. (a) Original image and wall lines (red lines) detected in Figure 6.24; (b) cut image with re-definition of the origin of the *y* coordinate system.

The procedure described above has a limited precision in localizing the channel walls. Firstly, the lowest possible uncertainty is determined by the pixel size. Secondly, the maximum intensity emission on the Suprasil® windows represents only an indication of where the wall is located. The identified wall lines may correspond to the solid surface that is just before or just after the plane where the tagged line is developing.

Moreover, imperfections in the calibration of the laser beam position and of the channel orientation with respect to the ICCD can make the distance between the identified wall lines slightly larger or smaller with respect to the measured height value.

The positioning of the laser beam inside the focal plane of the ICCD is not an easy task and it may happen that the laser beam is finally positioned just in front or just behind the focal distance. Because the external optical system mounted on the ICCD is not telecentric, the lens magnification can slightly vary as a function of the working distance. This means that the distance between the channel walls identified from the Suprasil® emission may appear closer or further than reality because the laser beam may lie, respectively, further or closer with respect to the focal distance. This optical distortion of the distances also affects the recorded molecular displacement. For instance, if the detected channel wall distance is smaller than expected, the average molecular displacement and the thickness of the displacement profile appear smaller than reality as well. In this case, the reconstruction method would then provide a smaller average velocity and a bigger slip velocity at the wall. From this point of view, a precise localization of the wall lines on the image and its comparison with the measured value of the channel height is of fundamental importance for understanding if the recorded tagged line displacement requires a rescaling.

Similar effects on the identified wall positions are caused by imprecisions in the calibration of the channel orientation with respect to the ICCD. Rotations around the channel main axis modify the relative position of the spot of maximum light intensity on the Suprasil® windows. It is worth noticing that, because the ICCD objectives are not telecentric, the top or bottom walls of the channel are not hidden even if the channel is rotated. The distortions of the identified wall distance caused by this effect should be discerned from that given by imprecisions in the laser beam positioning. A possible way of separating the two causes is based on the fact that a rotation of the channel with respect to the ICCD objectives would also cause slight asymmetries in the displacement profile with respect to the center line. In this scenario, the point of maximum displacement might not perfectly correspond to the position $y = 0$, which is defined as the middle point between the identified channel walls.

If the dimensions of the channel cross-section investigated by MTV could be measured directly and with precision, all these optic effects could be corrected by comparing the wall distance detected on MTV images and the measured channel height. However, a direct measurement of the channel height between the Suprasil® windows could not be possible during this work and, thus, these corrections could not be applied. Fortunately, the optic

deformations are quite limited, require only small adjustments, and do not prevent from applying MTV with enough accuracy. In future developments, the correction of these optic effects would certainly improve the velocimetry technique accuracy.

c. Initial tagged line position

The measurement of the displacement profile along the channel height requires firstly the identification of the initial position of the tagged molecules. The simplest strategy for detecting the initial position of the tagged line would be carrying out the laser excitation in a quiescent gas mixture. Unfortunately, the air-leakages at the level of the Suprasil® windows are important enough that oxygen quenching quickly extinguishes the light signal, even a few nanoseconds after the laser excitation. Moreover, fluorescence emission of diacetyl vapor or of acetone vapor excited at 310 nm is very weak and, therefore, the light emission is mainly provided by triplet molecules, which are much more sensitive to oxygen quenching than excited singlet molecules. This fact obliges to detect the vertical tagged line when the gas mixture is flowing through the channel. Even small flow rates are enough to provide fresh oxygen-free gas mixture. Generally, stronger flow rates make the oxygen leakages even less important, thus increasing the SNR of the light emission. While increasing the flow rate is interesting for the accurate capture of the displacement profile, it is not a necessity for the detection of the initial position of the tagged line. In order to minimize possible displacements of the vertical tagged line from its original position, the flow rate needs to be low enough with respect to the delay time of acquisition chosen. For a gas flow with an average velocity of 30 m/s, the delay time cannot be higher than 100 ns or 500 ns, depending on the dimension of the binning operation. The interest in slightly delaying the time of acquisition with respect to the laser excitation derives from the idea of getting rid of the intense short-lived emission of Suprasil®.

The post-processing procedure for the computation of the tagged line position is quite trivial. Figure 6.26 illustrates an example of early-emission from the tagged molecules. Firstly, a region of interest is defined around the tagged line and, secondly, the position of the maximum light intensity is localized along the tagged line. A linear fitting of the light peaks provides the mean abscissa μ_x of the tagged line and possible inclinations of the laser beam with respect to the wall surface. Because the SNR is relatively high, it is preferred to avoid the use of binning for obtaining the highest precision in the evaluation of μ_x.

By assuming that the laser beam position does not move with respect to the ICCD, the abscissa μ_x is considered as the starting position of the tagged molecules for the images representing the deformed tagged line. The x coordinate system of these images is translated so that the origin $x = 0$ corresponds to the initial position of the tagged line.

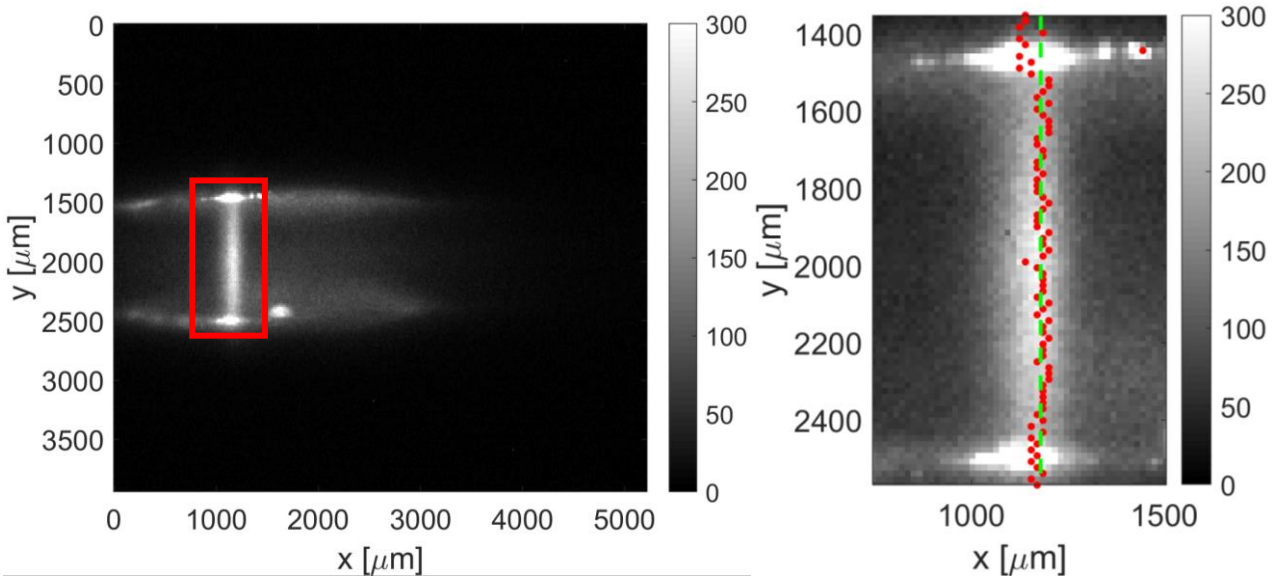

(a) (b)

Figure 6.26. Post-processing procedure for detecting the initial position of the tagged line: (a) raw image and definition of the region of interest (red square); (b) fitting of the maximum intensity along the *y* coordinate detected on the region of interest.

d. Noise filtering

The identification of the deformed tagged line is based on the application of appropriate fitting functions on the recorded image. The fitting procedure is a tool for extracting the most important information out of the background noise. Nevertheless, the SNR of the image is sometimes so low that the background noise prevents the convergence of the fitting optimization. In these cases, it is necessary to first pre-treat the image with a noise filter for improving its SNR.

A first strategy of reducing the background noise is based on the application of a 2D filter, that is a filter function that is applied on the whole image. The type of 2D filter employed in this work is the median filter. This non-linear digital filter is based on the application of the median operator on a small window of pixels around each pixels of the image. It is very efficient in removing granular noise while preserving sharp edges. Figure 6.27 illustrates an example of noise reduction by means of the 2D median filter.

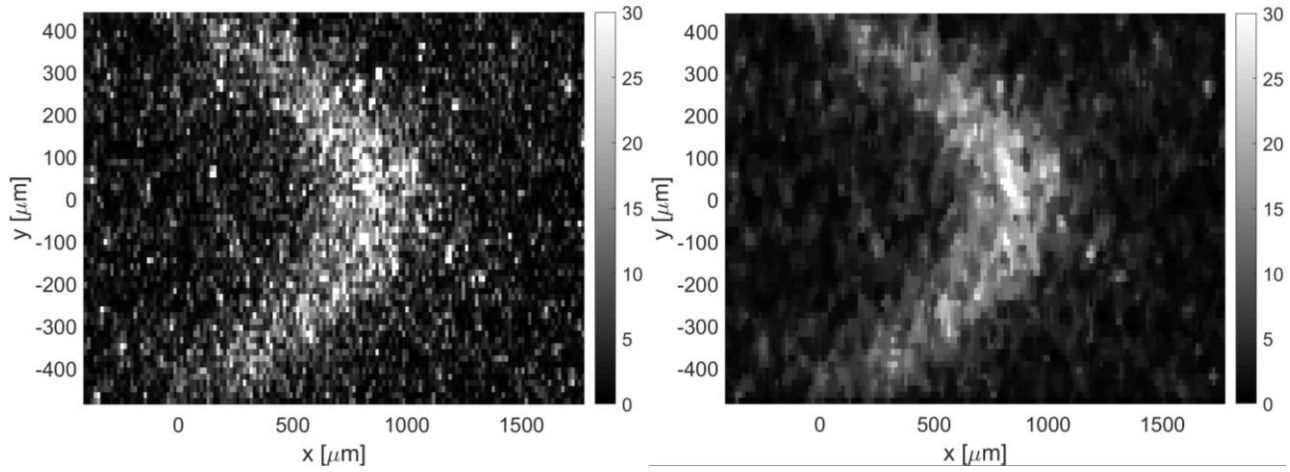

(a) (b)

Figure 6.27. (a) Raw image; (b) Median filter applied to the image in (a).

A second possibility consists in applying a 1D noise filter on each horizontal line of pixels. A family of digital filters that can be employed for this purpose is the finite impulse response (FIR) filters family. The basic idea of this type of filters is using the signal to be filtered as an input for a dynamical system with a finite response to the impulse. The moving average filter is an example of FIR filters, which is based on a kernel filter that is a squared-box window. An alternative option is using a kernel filter that is a Gaussian function, which provides the well-known Gaussian filter. These filters are implemented by applying the convolution of the signal on a horizontal line of pixel with the squared-box or the Gaussian window. For instance, Figure 6.28 illustrates the filtering effect of the moving average filter and the Gaussian filter with $N = 20$ on the same raw image of Figure 6.27a.

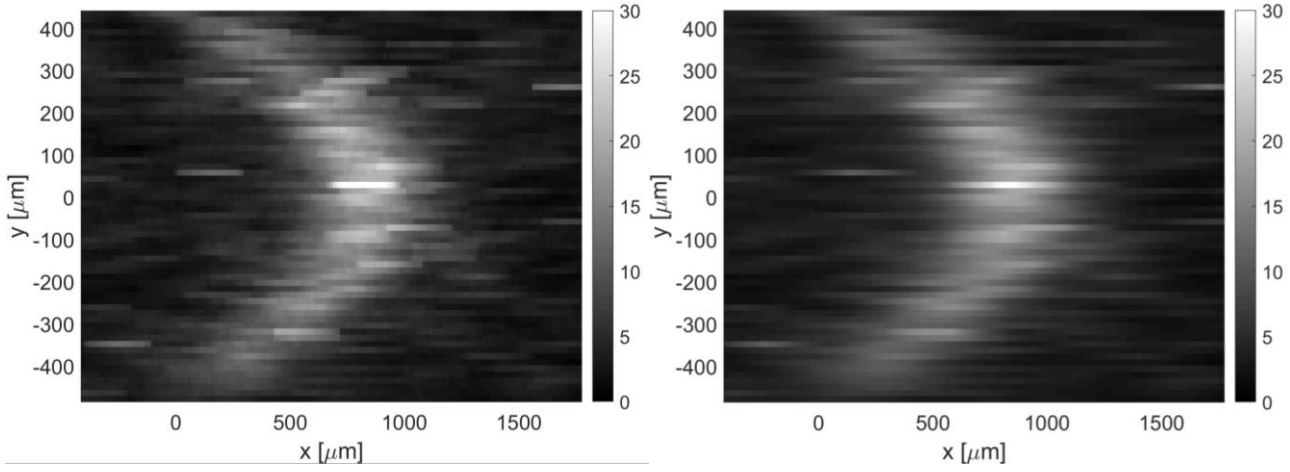

(a) (b)

Figure 6.28. (a) Moving-average filter with a window of 20 points; (b) Gaussian filter with a window of 20 points. The filters have been applied to the image of Figure 6.27a.

Both the 2D median filter and the 1D FIR filters have been used to imrpove the SNR of the image. However, the median filter has resulted to be more efficient in improving the convergence of the fitting procedure while maintaining the sharpness of the tagged line. From this point of view, the FIR filters smooth the light intensity peak more, thus increasing the uncertainty in detecting the displacement profile.

e. Gaussian fitting per line

In order to track the molecular displacement at different times from the initial position, an appropriate criterion for identifying the tagged line profile is required. In Chapter 5, the analysis of the molecular diffusion of the tracer vapor through a quiescent background gas mixture showed that the best fitting function that represents the evolution in time of the light distribution is the Gaussian function. In a channel gas flow, the light distribution spreads because of the molecular diffusion but it is also transported by the gas flow. The combined mechanism of the gradient velocity and the molecular diffusion in the direction perpendicular to the wall may affect, in principle, the shape of the tagged molecule distribution, thus differing from the Gaussian distribution characterizing the free molecular diffusion in a quiescent gas. However, the image data revealed that these effects are negligible, and the Gaussian function is still representative of the light distribution in the gas flow direction. As it has been done in previous works (Lempert *et* al., 2003; Samouda *et al*., 2015; Si-Hadj Mohand *et al*., 2017), the Gaussian fitting applied to each horizontal line of pixels at any position $y = y_j$ is

$$f(x) = \frac{a_2}{\sqrt{2\pi a_3}} e^{-\frac{(x-a_4)^2}{2a_3}} + a_1, \tag{6.59}$$

where the fitting parameters a_1, a_2, a_3, and a_4 represent, respectively, the offset, the amplitude, the variance, and the peak position. Figure 6.29a illustrates the application of this fitting procedure to the image shown in Figure 6.27. Figure 6.29b shows, for instance, the Gaussian function and the relative MTV data that correspond to the horizontal line of pixels indicated in Figure 6.29a. If no further image fitting is applied, as the one proposed in the next section, the data $a_{4,j}$ correspond to the displacement data $s_{x,j}$ at each location y_j. The set of data $s_{x,j}$ is then processed by the reconstruction method. As it can be observed in the example of Figure 6.29b, the statistical fluctuations characterizing the signal distribution on one horizontal line of pixels are significant with respect to the peak of intensity. This certainly increases the uncertainty in localizing the tagged line profile. Lempert *et al*. (2003) states that a general rule of thumb is that the uncertainty on the position of the peak is between 3% to 10% of the full width of the intensity profile, depending upon its SNR. Anyway, since the whole set of displacement data $s_{x,j}$ along the channel height will be afterwards fitted by the numerical solution of Eq. (6.18), the uncertainty on the tagged line position at each location y_j is mainly represented by the ratio of the deviation between the displacement data and the displacement profile, $s_{x,j} - s_x(y_j)$, to the value of the displacement profile $s_x(y_j)$ itself.

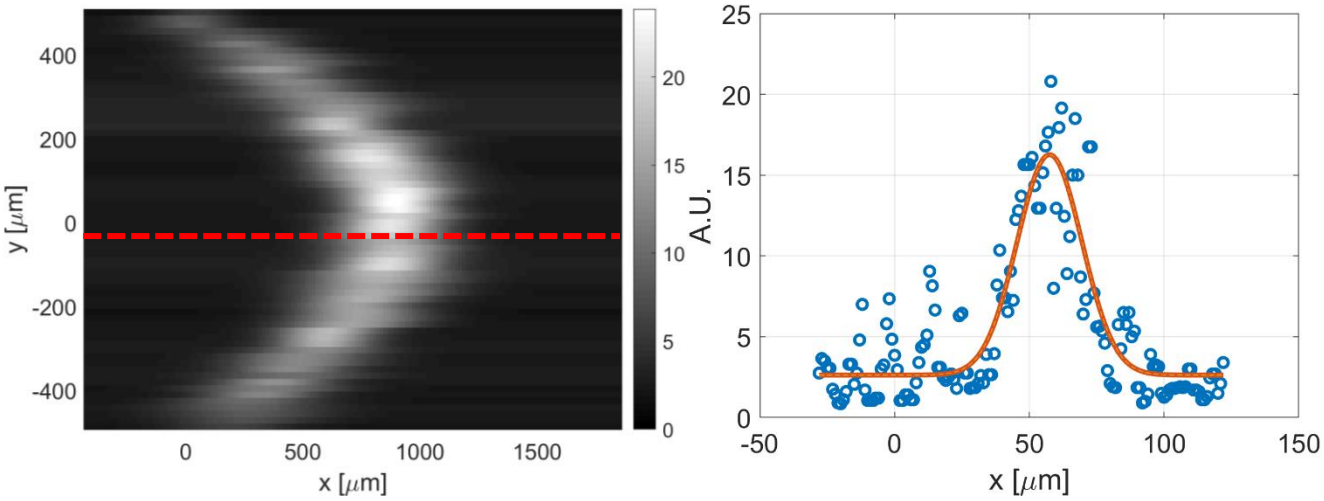

Figure 6.29. (a) Image resulting from the application of the Gaussian fitting per line to the image of Figure 6.27; (b) example of data distribution along a horizontal line of pixels, indicated by the red dashed line in (a), and corresponding Gaussian fitting.

f. 2D fitting function

Another strategy for identifying the profile of the deformed tagged line consists in finding a 2D function able of fitting the whole image. In this way, instead of trying to find the displacement of the intensity peak at each location *y* along the channel height separately, all the information collected on an image is used with the idea of extracting a more accurate displacement profile. Moreover, a 2D fitting is the first step towards a possible future reconstruction method for extracting the velocity profile from a 2D molecular displacement.

The expression of the 2D fitting function $f_{2D}(x,y)$ proposed in this work is based on the assumption of the previous section, i.e., that the light distribution can be described through Gaussian functions in the *x* direction at each position *y*. However, differently from the fitting strategy explained in the previous section, the fitting coefficient of the Gaussian distribution are now functions of the *y* coordinate. The 2D fitting function has the expression

$$f_{2D}(x,y) = \frac{a_2(y)}{\sqrt{2\pi a_3(y)}} e^{-\frac{1}{2}\left(\frac{x-a_4(y)}{a_3(y)}\right)^2} + a_1(y), \tag{6.60}$$

in which the dependency of the fitting parameters $\boldsymbol{a}(y) = (a_1, a_2, a_3, a_4)$ from the *y* coordinate is assumed being:

$$a_1 = p_{1,1}, \tag{6.61}$$

$$a_2(y) = p_{2,1} + p_{2,2}(y - y_0)^2, \tag{6.62}$$

$$a_3(y) = p_{3,1} + p_{3,2}(y - y_0)^2, \tag{6.63}$$

$$a_4(y) = p_{4,1} + p_{4,2}(y - y_0)^2 + p_{4,3}(y - y_0)^4. \tag{6.64}$$

The above assumptions on the shape of each coefficient a_i with respect to *y* is based on observations of the usual distribution of the same parameters on the recorded images. The variance $a_3(y)$ of the Gaussian distribution usually has a minimum close to the centerline $y = 0$ and tends to increase towards the walls, where the SNR of the light intensity is lower. The fact that the phosphorescence emission is weaker close to the walls than at the centerline y = 0 of the channel may be due to different factors. It is possible that the collisions of the triplet molecules with the wall surface give rise to efficient molecular quenching (Parmenter & Poland, 1969) or, similarly, that the leakages at the level of the interfaces between the Suprasil® windows and the PEEK cause oxygen quenching close to the walls. The amplitude $a_2(y)$ of the Gaussian is, for the same reason, a parabolic function as well, with lower values in the region close to the wall. The assumption of a 4-th order polynomial function for the displacement profile $a_4(y)$ corresponds to assume that the velocity profile is symmetric and parabolic. Indeed, the diffusion term of Eq. (6.18) converts the second-order source term $U_{x_2}(y) = \left(1 - \frac{y^2}{H^2/4}\right)$ into a 4-th order distribution for the displacement profile solution $s_x(y, t)$. For asymmetric displacement data distribution, an odd term needs to be added to the polynomial expression of $a_4(y)$ in order to well fit the 2D light distribution. Although the form of $a_4(y)$ is here assumed to be as in Eq. (6.64), the following numerical procedure can be easily extended to any form of the function $a_4(y)$. Finally, the offset a_1 does not have any particular trend along the channel height, and, therefore, it has been considered as a constant.

The central position y_0 of functions a_2, a_3, a_4 can be either fixed to 0, that is the centerline of the channel, or considered as a free parameter that will be determined by the fitting procedure. In the following of this section, the latter case is considered for the sake of generality, so that there are 9 fitting parameters to be identified, which are $\boldsymbol{p} = \left(p_{1,1}, p_{2,1}, p_{2,2}, p_{3,1}, p_{3,2}, p_{4,1}, p_{4,2}, p_{4,3}, y_0\right)^T$.

The image data is described by a matrix of values F_{ij} representing the light intensity recorded on the pixel at position (x_i, y_j). The problem of finding the optimal values of parameters $\boldsymbol{p}$ that make the function fit at best the set of data F_{ij} is solved in a least mean square sense, by minimizing the objective function

$$\varepsilon_{2D}(\boldsymbol{p}) = \frac{1}{2}\sum_{i=1}^{N_x}\sum_{j=1}^{N_y}\left(F_{ij} - f_{2D}(x, y, \boldsymbol{p})\right)^2. \tag{6.65}$$

In Appendix C, the details of the optimization algorithm are reported.

Figure 6.30 illustrates the result of the 2D fitting applied to the image of Figure 6.27b. The fitting function could have also been applied to the non-filtered version (Figure 6.27a). However, since the background noise makes the convergence of the fitting algorithm more difficult, the filtered image is preferred. In Figure 6.30b, offset a_1, amplitude $a_2(y)$, variance $a_3(y)$, and displacement $a_4(y)$ provided by the optimization algorithm are displayed along with the same data that come from the Gaussian fitting per line.

Finally, if the 2D fitting procedure is adopted, the set of displacement data $s_{x,j}$ that is going to be employed for the velocity reconstruction correspond to the values of the function $a_4(y)$ evaluated at all positions y_j of each pixel along the channel height.

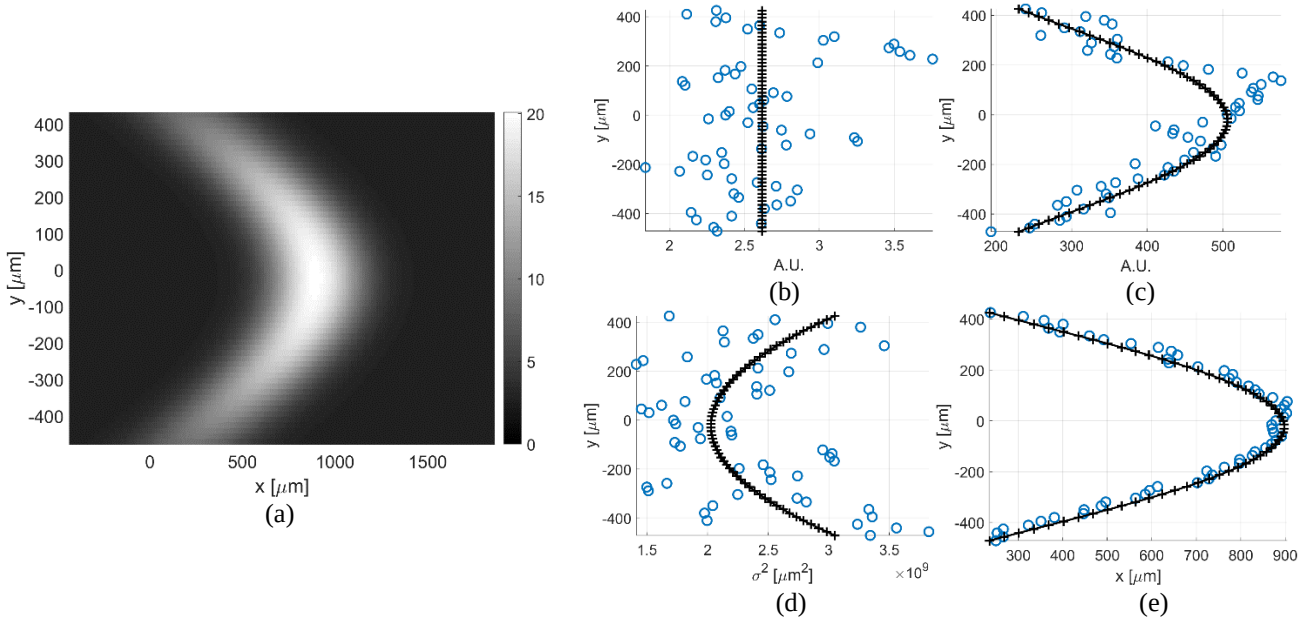

Figure 6.30. (a) 2D fitting based on Eq. (6.60) of the image data in Figure 6.27b; (b) the offset a_1, (c) the amplitude $a_2(y)$, (d) the variance $a_3(y)$, and (e) the displacement $a_4(y)$ functions. The same data from the Gaussian fitting per line (O) are displayed for comparison with the 2D fitting function data (+).

g. Displacement data

Once the set of displacement data $s_{x,j}$ has been defined, the final step before the application of the velocity reconstruction algorithm is the correct positioning of the displacement data inside the mathematical domain.

The velocity reconstruction is sensitive to the channel height H employed for generating the numerical solution $s_x(y)$. Indeed, for a given velocity profile $u(y)$ and a given diffusion coefficient D, the displacement profile $s_x(y)$ at a certain time t has a thickness Δs that is proportional to H^4 (see Section 6.1.11). The value of the wall distance H used in defining the mathematical domain needs, therefore, to be as accurate as possible in order to have a correct velocity reconstruction. As previously discussed, the localization of the channel walls on the image cannot

be done with the highest accuracy and is affected by possible imperfections in the calibration of the positioning of the channel and the laser beam with respect to the ICCD. The best approach to face this aspect would be, once again, to measure directly the internal dimensions of the channel cross-section, and, then, setting the height of the mathematical domain equal to the measured channel height. Because direct measurements of H are not available, the only solution is employing the channel wall distance identified on the image from the Suprasil® fluorescence. The positioning of the displacement data is, in this case, straightforward, because the mathematical domain is directly defined by the region of interest identified on the MTV images. Appendix D describes the rigorous post-processing procedure that would be required if the channel height was known a priori by direct measurements.

6.3.2 MTV application to argon-acetone flows in non-rarefied conditions

In this section, MTV technique is applied to argon-acetone flows in non-rarefied conditions. The previous works of Samouda *et al*. (2015) and Si-Hadj Mohand *et al*. (2017) already demonstrated the successful application of MTV for velocity measurements in channel gas flow in non-rarefied conditions by using as a tracer acetone vapor excited at 266 nm. In the work of Si-Hadj Mohand *et al*., the lowest gas pressure they could employ was about 42 kPa. They could not apply MTV for lower pressures because of the low signal intensity due to the limited phosphorescence quantum yield of acetone excited at 266 nm. In the light of the experimental results presented in Chapter 5, MTV is here based on acetone vapor excited at 310 nm, which guarantees a detectable and long-lived tagged line even for pressures lower than 1 kPa.

In this section, MTV is applied to gas flows at pressures between 30 and 6 kPa, in order to demonstrate that the novel experimental setup, combining MTV and CV techniques, provides accurate results in non-rarefied conditions. Moreover, these results demonstrate, for the first time, the successful application of MTV technique to confined gas flows at pressures lower than 42 kPa.

In these experiments, the pumping power is controlled by partially opening the downstream valve. The mass flow rate and, thus, the inlet over outlet pressure ratio are maintained low in order to make the upstream pressure vary slowly enough for MTV applications. From the highest to the lowest average pressure inside the channel during this experimental run, the mass flow rate varies between about 3×10^{-5} to 1×10^{-5} kg/s and the inlet-outlet pressure difference ranges between 560 and 445 Pa. The Mach number and the Knudsen number at the section $x = L/2$ along the channel length, i.e., the one investigated by MTV, do not vary substantially during the experimental run and their average values are, respectively, of the order of Ma = 0.03 and Kn = 1×10^{-4}. In these thermodynamic conditions the compressible and the rarefaction effects are negligible, and, as a matter of fact, the theoretical pressure distribution along the channel is practically linear.

Figure 6.31a, Figure 6.31b, and Figure 6.31c show the molecular displacement of the tagged line through the channel, respectively, for t = 10, 25, and 50 μs after the laser excitation. Each image represents the average of 20

images integrating 100 laser pulses. The acquisitions have been carried out by setting the gain at maximum, G = 100%, the IRO gate at minimum, Δt_{gate} = 100 ns, and by using a 4 × 4 binning. A 2D median filter has been applied to each image for increasing its SNR. A comparison of the images of Figure 6.31 with the MTV acquisitions reported in the work of Si-Hadj Mohand *et al*. (2017) demonstrates the great improvement in the quality of the light signal provided by the experimental analysis of phosphorescence emission presented in Chapter 5. Acetone vapor excited at 310 nm is characterized by a phosphorescence emission that is much stronger and durable than that following an excitation at 266 nm.

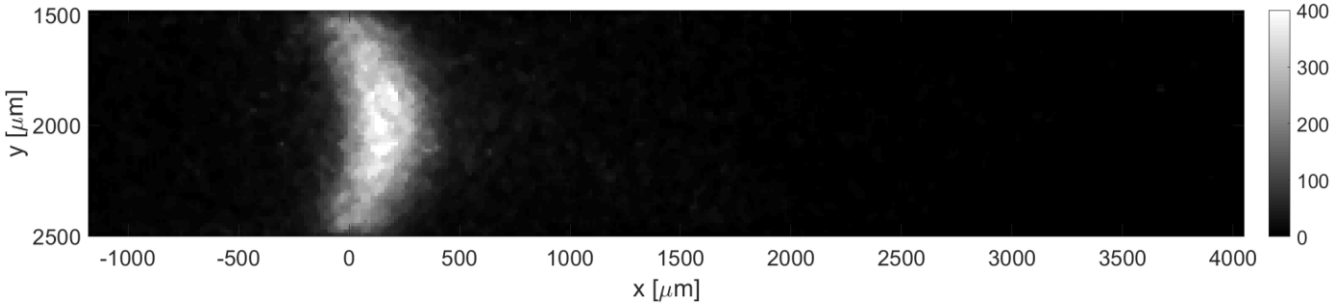

(a)

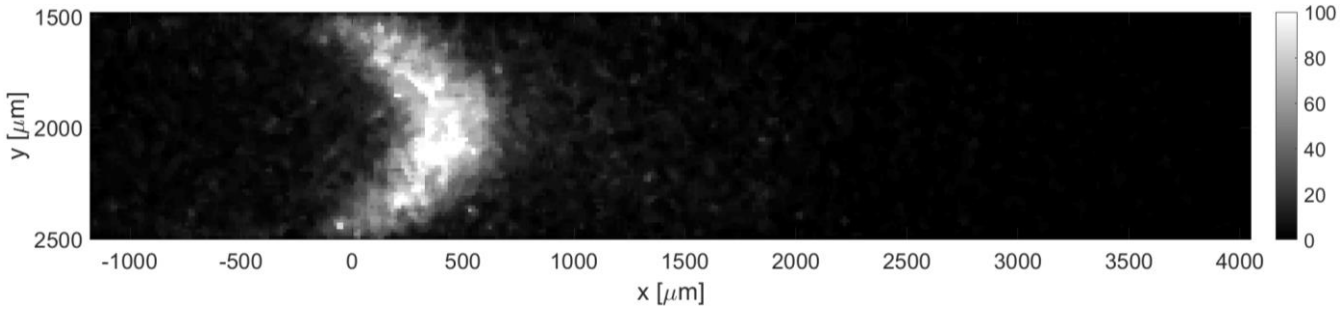

(b)

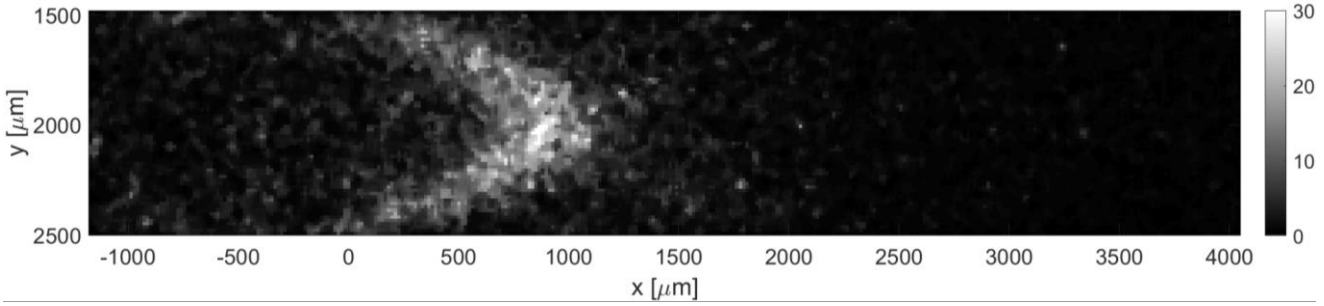

(c)

Figure 6.31. MTV acquisitions of argon-acetone flow with χ = 20%: (a) t = 10 µs, p_c = 27.38 kPa, and Δp = 527.2 Pa; (b) t = 25 µs, p_c = 28.83 kPa, and Δp = 537.5 Pa; (c) t = 50 µs, p_c = 30.36 kPa, and Δp = 548.5 Pa. The recording parameters are: N_l = 100, N_i = 20, G = 100%, and Δt_{gate} = 100 ns. The acquisitions are made with a 4 × 4 binning. The laser pulse energy was varying between 30 and 40 µJ.

The three images belong to the same experimental run and have been recorded at different instants as the average pressure in the system decreases. Therefore, the three images do not correspond exactly to the same thermodynamic conditions. Nevertheless, the average pressure and the inlet-outlet pressure difference are quite similar for the three cases and are in average p_c = 28 kPa and Δp = 520 Pa. Therefore, the comparison of the molecular displacement at different times is still representative of how the tagged line evolves as it moves through the channel. The average pressure p_c, the inlet-outlet pressure difference Δp, the Mach number, and the Knudsen number that characterize each image of Figure 6.31 are summarized in Table 6.2. For gas flows at high pressures, variations in the average pressure have little influence on the investigated velocity profile. However, the average velocity profile varies substantially even for variations of 10 Pa on the pressure difference. For the image at t = 50, 25, and 10 µs, the inlet-outlet pressure difference is, respectively, 520, 510, 505 Pa. The corresponding average velocities $\bar{u}_{CV}$ calculated from the mass flow rate measurements of CV technique are also reported in Table 6.2.

	t [µs]	p_c [kPa]	Δp [Pa]	Ma [-]	Kn [-]	$\dot{m}$ [kg/s]	$\bar{u}_{CV}$ [m/s]
Figure 6.31a	10	27.38 ± 1.5%	527.2 ± 0.6%	0.036 ± 0.2%	9.8×10^{-5} ± 1.5%	2.63×10^{-5} ± 1.7%	11.5 ± 0.2%
Figure 6.31b	25	28.83 ± 1.5%	537.5 ± 0.6%	0.036 ± 0.2%	9.3×10^{-5} ± 1.5%	2.79×10^{-5} ± 1.7%	11.56 ± 0.2%
Figure 6.31c	50	30.36 ± 1.5%	548.5 ± 0.6%	0.036 ± 0.2%	8.8×10^{-5} ± 1.5%	2.95×10^{-5} ± 1.7%	11.61 ± 0.2%

Table 6.2. Flow properties associated to the images of Figure 6.31. The reported percentage change indicates how much the properties vary inside the group of averaged images.

Each image results from averaging 20 images, each integrating 100 laser pulses. The average is carried out along one single experimental run, and, therefore, the experimental flow conditions vary inside the group of 20 images. Table 6.2 also reports the variations in percentage with respect to the average value of each property.

The procedure presented in Section 6.3.1 for the identification of the wall positions on the image provides a channel height H = 1003 µm, which is higher than the value 913.5 measured in Chapter 4. The images in Figure 6.31 demonstrate that the evolution of the light distribution is, indeed, confined in between the detected walls. This is quite evident especially for MTV acquisitions at low delay times, such as in Figure 6.31a and Figure 6.31b, in which the SNR of the light emission is relatively high. Most likely, the Suprasil® windows were not perfectly positioned inside the cavities but were slightly below the channel wall level, thus providing a larger wall distance.

Figure 6.32a reports the displacement data $s_{x,j}$ provided by the Gaussian fitting per line applied to the images of Figure 6.31. The application of the reconstruction method to these data provides the velocity profiles shown in Figure 6.32b. The diffusion coefficient D employed for the velocity reconstruction has been estimated by means

of the Blanc's law, Eq. (6.27), and has been set to 3.197×10^{-5}, 3.368×10^{-5}, and 3.546×10^{-5} m^2/s, respectively, for the data at t = 50, 25, and 10 µs. Because argon and acetone have similar molecular mass and kinetic diameter, variation in the tracer concentration χ does not modify much the estimated diffusion coefficient used in the reconstruction. The uncertainty on the actual tracer concentration characterizing the gas flow at the investigated channel section, therefore, does not influence the velocity reconstruction. The reconstruction algorithm is successful in accurately extracting the distribution of the axial velocity. As expected, the slip velocity at the wall is very close to zero, with values ranging between 0.006 and 0.2 m/s.

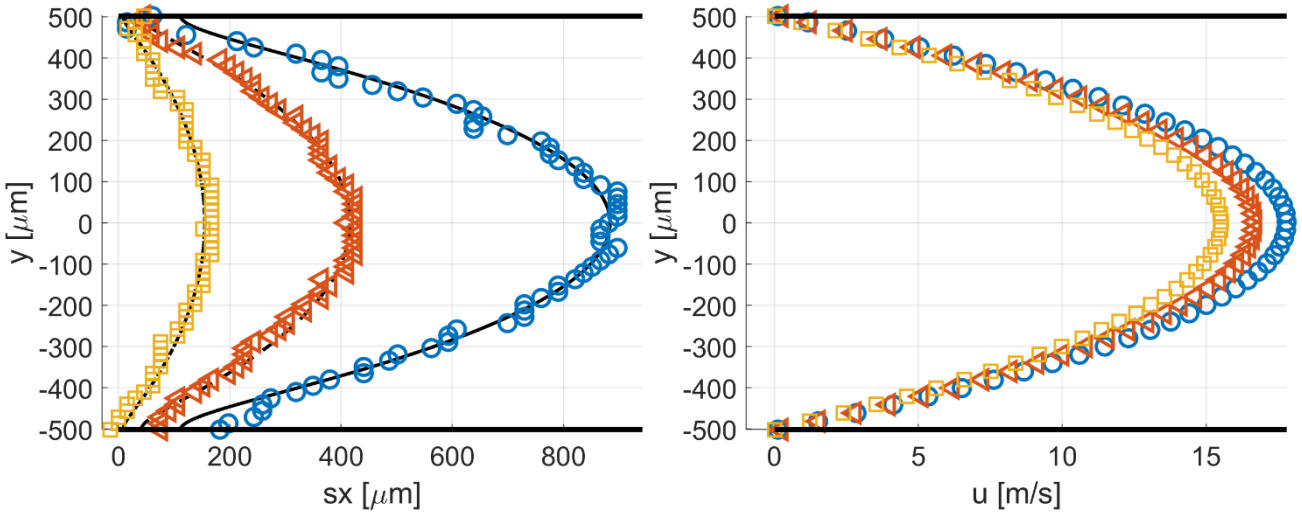

(a) (b)

Figure 6.32. (a) Displacement data computed by applying the Gaussian fitting per line to the images of Figure 6.31; velocity reconstruction from the displacement data in (b): t = 10 µs (□), 25 µs (◁), and 50 µs (○).

The average velocities of the velocity profiles corresponding to the displacement data at t = 50, 25, and 10 µs are, respectively, $\bar{u}_{MTV}$ = 11.85, 11.15, and 10.34 m/s. These values differ from the average velocities $\bar{u}_{CV}$ estimated from the mass flow rate measurements of 3.67%, 1.76%, and 8.25%. These discrepancies can be understood by analyzing the incertitude that characterizes $\bar{u}_{CV}$ and $\bar{u}_{MTV}$.

The main uncertainty in the calculation of the velocity $\bar{u}_{CV}$ is associated to the uncertainties on the dimensions of the channel cross-section, which could not be directly measured. Because the channel height could be at least estimated from the MTV acquisitions, the most important uncertainty is given by the channel width b, which could only be estimated by reducing the error between the theoretical mass flow rate and the mass flow rate measured by CV technique. By assuming that the channel width b has values between 5800±200 µm, the average velocity $\bar{u}_{CV}$ varies of no more than ±4%. This incertitude is higher than the error between $\bar{u}_{CV}$ and $\bar{u}_{MTV}$ for the data related to the acquisitions at t = 25 µs and t = 50 µs. Differently, the error related to the data at t = 10 µs is twice

the estimated uncertainty on $\bar{u}_{CV}$. Therefore, the origin of this discrepancy should be due to inaccuracies in the MTV measurements.

When the magnitude of the displacement is comparable to the size of the tagged line diameter, the relative uncertainty on the displacement data is higher. As already discussed in Chapter 4, the uncertainty in the measured molecular displacement depends on the SNR of the light distribution. However, because the SNR of the images of Figure 6.31 is relatively high, the uncertainty on the displacement measurement is, in this case, dominated by the CCD resolution, that is 15.2 μm since a 4 × 4 binning is used. The average displacement $\bar{s}_x$ related to the data shown in Figure 6.32a is 102.5, 276.5, and 587.8 μm. Therefore, the relative uncertainty on the measurement of $\bar{s}_x$ due to the CCD resolution is 14.8%, 5.5%, and 2.6%, respectively, for the data at t = 10, 25, and 50 μs. The accuracy on the "time of flight" t is mainly determined by the PTU capability, which guarantees a synchronization between the ICCD acquisition and the laser excitation with a precision of the order of 5 ns. The relative uncertainty on the average velocity $\bar{u}_{MTV} = \bar{s}_x/t$ is, therefore, determined by the relative uncertainty on the mean molecular displacement $\bar{s}_x$. The uncertainty on $\bar{u}_{MTV}$ is calculated to be ±1.53, ± 0.61, and ± 0.31 m/s, respectively, for t = 10, 25, and 50 μs. Table 6.3 reports the value and the calculated uncertainties of $\bar{u}_{CV}$ and $\bar{u}_{MTV}$. It can be noticed that at high delay times, the uncertainty on the average velocity $\bar{u}_{MTV}$ is comparable or lower than that on $\bar{u}_{CV}$. Differently, MTV acquisitions at low delay times provide less accurate average velocity than CV technique. In all cases, the range of values of $\bar{u}_{MTV}$ is always overlapped to that of $\bar{u}_{CV}$.

t [μs]	10	25	50
$\bar{u}_{CV}$ [m/s]	11.5 ± 0.4	11.56 ± 0.4	11.61 ± 0.4
$\bar{u}_{MTV}$ [m/s]	10.34 ± 1.53	11.15 ± 0.61	11.85 ± 0.31

Table 6.3. Average velocities $\bar{u}_{CV}$ and $\bar{u}_{MTV}$ calculated, respectively, from CV technique and MTV technique for the image data of Figure 6.31. The reported uncertainty on $\bar{u}_{CV}$ has been calculated by considering variations of the channel width of ±200 μm with respect to the estimated value 5800 μm. The uncertainty on $\bar{u}_{MTV}$ is calculated from the relative uncertainty of the measured mean molecular displacement due to the CCD resolution.

Argon-acetone mixture flows have also been investigated by MTV at lower pressures, in order to verify the reconstruction method in non-rarefied conditions but with higher molecular diffusion. The images of Figure 6.33 illustrate MTV acquisitions carried out at a pressure of 6500 Pa and at t = 20, 30, 40, and 50 μs. All the characteristics of the observed experimental flow are reported in Table 6.4.

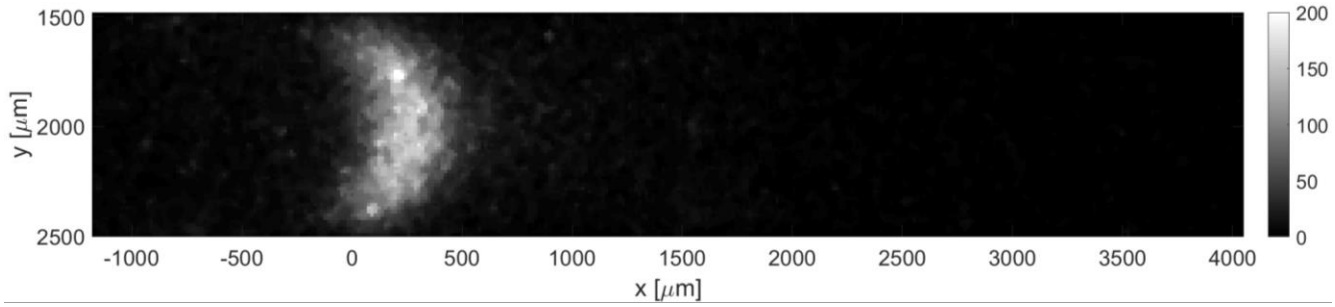

(a)

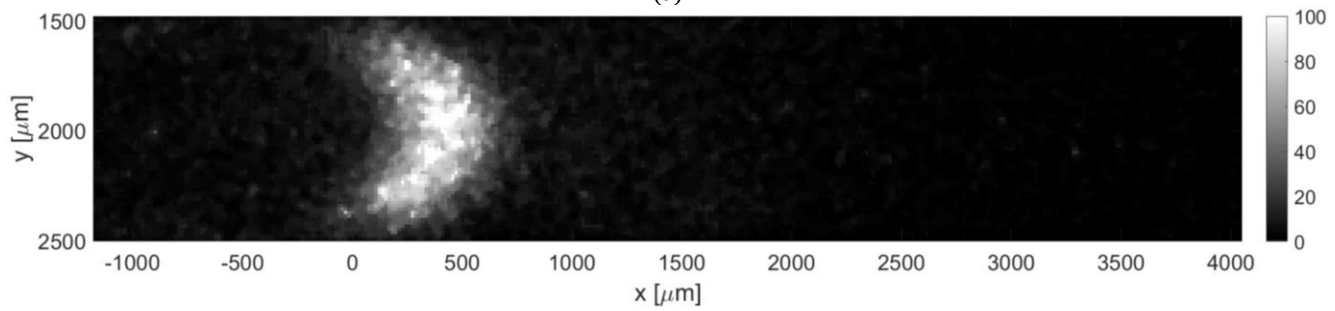

(b)

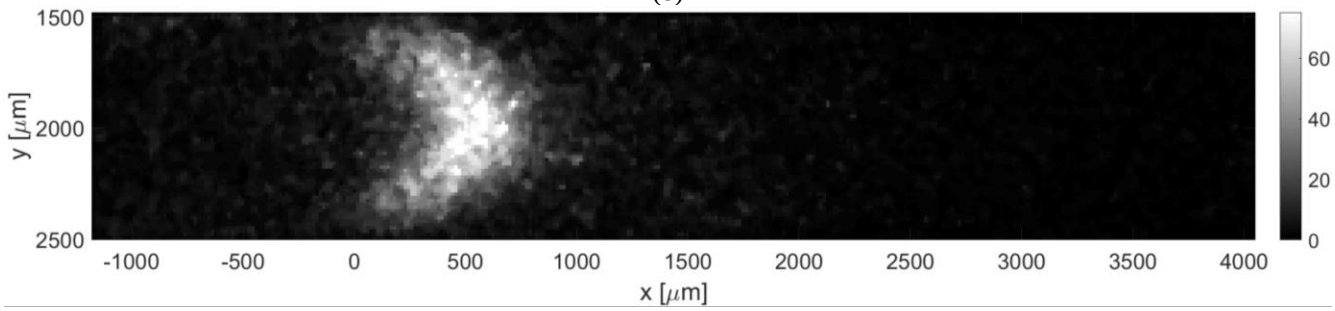

(c)

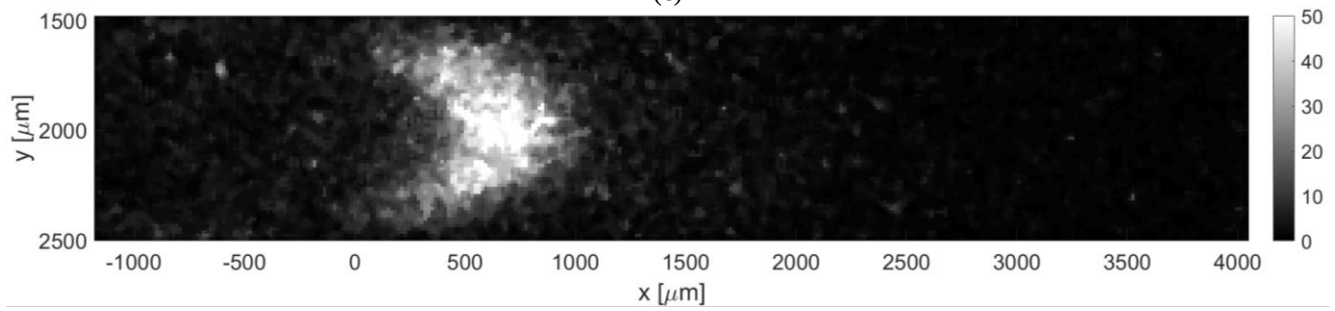

(d)

Figure 6.33. MTV acquisitions of argon-acetone flow with χ = 20%: (a) t = 20 µs, p_c = 6904 Pa, and Δp = 372.7 Pa; (b) t = 30 µs, p_c = 6620 Pa, and Δp = 368.4 Pa; (c) t = 40 µs, p_c = 6336.5 Pa, and Δp = 364 Pa; (d) t = 50 µs, p_c = 6071 Pa, and Δp = 359.5 Pa The recording parameters are: N_l = 100, $N_i = 20$, $G = 100\%$, and $\Delta t_{gate} = 100$ ns. The acquisitions are made with a 4 × 4 binning. The laser pulse energy was varying between 20 and 30 µJ.

	t [μs]	p_c [Pa]	Δp [Pa]	Ma [-]	Kn [-]	$\dot{m}$ [kg/s]	$\bar{u}_{CV}$ [m/s]
Figure 6.33a	20	6904 ± 1.5%	372.7 ± 0.3%	0.03 ± 0.25%	3.8×10^{-4} ± 1.5%	5.41×10^{-6} ± 1.5%	9.41 ± 0.2%
Figure 6.33b	30	6620 ± 1.2%	368.4 ± 0.3%	0.03 ± 0.3%	4×10^{-4} ± 1.2%	5.14×10^{-6} ± 1.5%	9.32 ± 0.2%
Figure 6.33c	40	6336.5 ± 1.2%	364 ± 0.3%	0.029 ± 0.3%	4.2×10^{-4} ± 1.2%	4.87×10^{-6} ± 1.5%	9.22 ± 0.2%
Figure 6.33d	50	6071 ± 1.5%	359.5 ± 0.3%	0.029 ± 0.3%	4.4×10^{-4} ± 1.1%	4.61×10^{-6} ± 1.5%	9.12 ± 0.2%

Table 6.4. Flow properties associated to the images of Figure 6.33. The reported percentage change indicates how much the properties vary inside the group of averaged images.

As for the case at higher pressure, because the MTV images have been recorded along the same experimental run, the thermodynamic properties associated to each image are not exactly the same but, again, quite similar. In particular, the images have been recorded first at t = 20 μs after the laser excitation, and afterwards at 30, 40, and 50 μs, in this order. For this reason, the pressure and the mass flow rate decrease from t = 20 μs to t = 50 μs. Because the gas pressure is one order of magnitude lower than the case presented in Figure 6.31, the mass flow rate is one order of magnitude lower and the Knudsen number is one order of magnitude higher.

Figure 6.34a and Figure 6.34b reports, respectively, the displacement data with the corresponding numerical displacement profile and the reconstructed velocity. The diffusion coefficients used for the reconstructions are 1.4×10^{-4}, 1.46×10^{-4}, 1.53×10^{-4}, and 1.6×10^{-4} m^2/s, respectively, for the data at t = 20, 30, 40, and 50 μs. As it can be observed, the reconstruction method is not able to provide an accurate velocity profile. The slip velocity at the wall, which was expected to be limited to a maximum of 0.05 m/s, ranges between 1 and 2.6 m/s, depending on the delay time of the displacement data used. Figure 6.34a shows that the displacement data are well fitted by the numerical solution. Except for the case at t = 50 μs, the dispersion of displacement data around the numerical solution is qualitatively limited. However, while the relatively high SNR at the channel centerline y = 0 makes the identification of the deformed tagged line quite accurate, there might be an uncertainty on how the displacement profile should be close to the wall. With respect to the displacement profiles at 30 kPa reported in Figure 6.32, the molecular displacement at the wall is, in this case, definitely larger as a consequence of the higher molecular diffusion. The accurate evaluation of the molecular slip at the wall appears to be of fundamental importance for extracting a correct velocity profile.

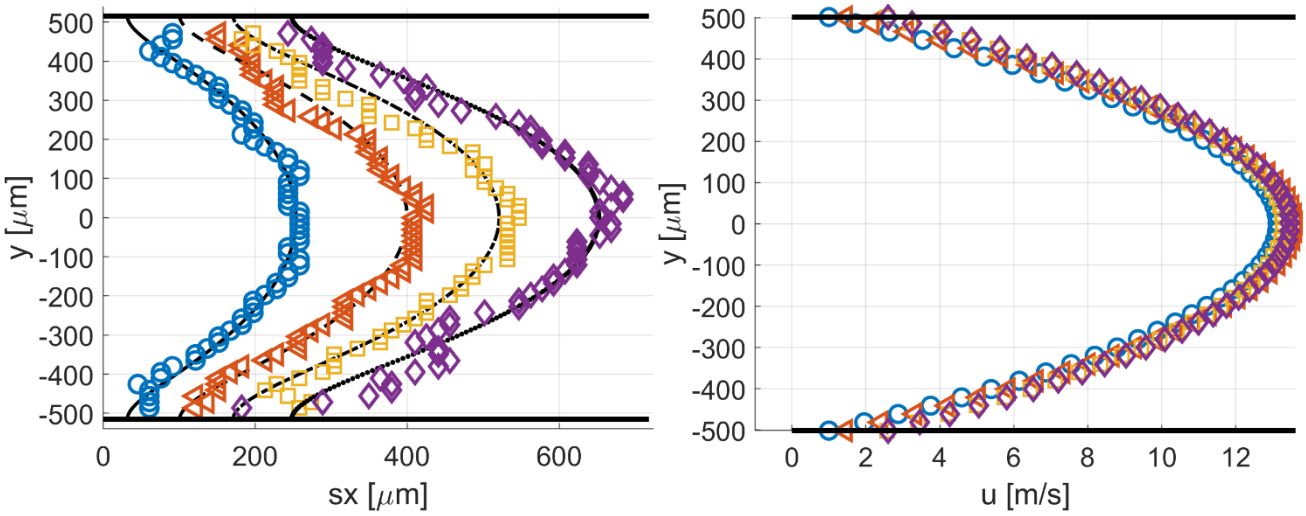

(a) (b)

Figure 6.34. (a) Displacement data computed by applying the Gaussian fitting per line to the images of Figure 6.33; velocity reconstruction from the displacement data in (b): t = 20 μs (○), 30 μs (◁), 40 μs (□) and 50 μs (◇).

Despite the inaccuracy on the slip velocity, the average velocity $\bar{u}_{MTV}$ of the reconstructed profile is very close to the values $\bar{u}_{CV}$ estimated from the mass flow rate measurements. As a matter of fact, the mean molecular displacement $\bar{s}_x$ is only weakly affected by the uncertainty on the value of the molecular slip at the wall. Table 6.5 reports the average velocities along with the uncertainty on $\bar{u}_{MTV}$ due to the CCD resolution and the uncertainty on $\bar{u}_{CV}$ due to variations of ±200 μm of the channel width b. The accuracy on the measurements of the displacement data is affected by the molecular diffusion more than for the gas flow at 30 kPa. Therefore, the range of possible values for $\bar{u}_{MTV}$ calculated from the relative uncertainty of the mean molecular displacement $\bar{s}_x$ with respect to the pixel size might be an underestimation of the real uncertainty on $\bar{u}_{MTV}$. Moreover, the inaccuracy in the velocity reconstruction due to the imprecision in capturing the molecular displacement at the wall contributes to increase the uncertainty on the average velocity. While the molecular displacement at the channel centerline is measured with accuracy, the mean molecular displacement $\bar{s}_x$ and, consequently, the average velocity $\bar{u}_{MTV}$ would result in a lower or higher value than the correct one if the molecular displacement at the wall is, respectively, underestimated or overestimated. This idea might explain why the measured $\bar{u}_{MTV}$ increases from t = 20 μs to t = 50 μs instead of decreasing as it was expected.

Because the 4 sets of displacement data do not correspond exactly to the same flow conditions, the TC reconstruction method described in Section 6.1.10 cannot be applied.

t [μs]	20	30	40	50
$\bar{u}_{CV}$ [m/s]	9.41 ± 0.34	9.32 ± 0.33	9.22 ± 0.33	9.12 ± 0.32
$\bar{u}_{MTV}$ [m/s]	9.14 ± 0.75	9.61 ± 0.49	9.74 ± 0.37	9.89 ± 0.3

Table 6.5. Average velocities $\bar{u}_{CV}$ and $\bar{u}_{MTV}$ calculated, respectively, from CV technique and MTV technique for the image data of Figure 6.33. The reported uncertainty on $\bar{u}_{CV}$ has been calculated by considering variations of the channel width of ±200 μm with respect to the estimated value 5800 μm. The uncertainty on $\bar{u}_{MTV}$ is calculated from the relative uncertainty of the measured mean molecular displacement due to the CCD resolution.

6.3.3 MTV application to helium-acetone flows in the slip regime

In this section, MTV is applied to helium-acetone mixture flow with χ = 20% in the slip regime. The experimental conditions of the gas flow here investigated correspond to those analyzed in detail in Section 6.2. Many MTV acquisitions have been carried out on this experimental flow, but only the acquisitions related to the flow conditions at an average pressure of about 1500 Pa are here presented. The results related to these thermodynamic conditions are representative of the evolution of the displacement profile in the slip regime. Moreover, the slip velocity characterizing the investigated velocity profile is approximatively the same for all the duration of the experimental run, as demonstrated by Figure 6.17. Figure 6.35 illustrates the tracer displacement for 4 different delay times after the laser excitation, at t = 20, 30, 40, and 50 μs.

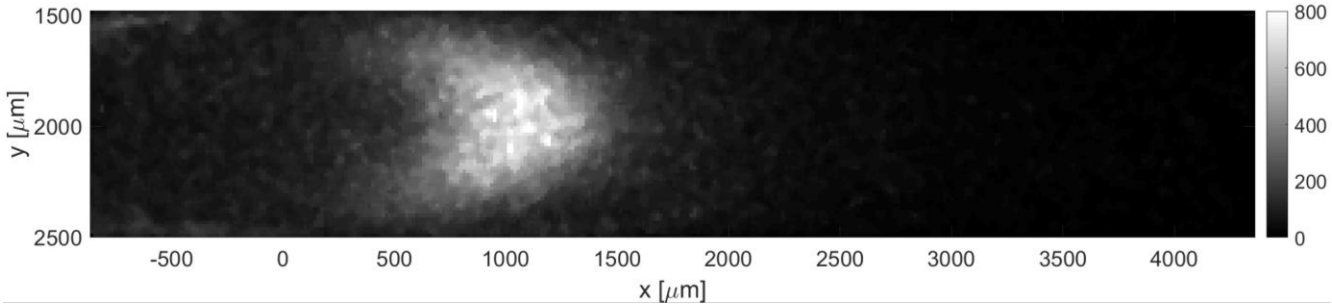

(a)

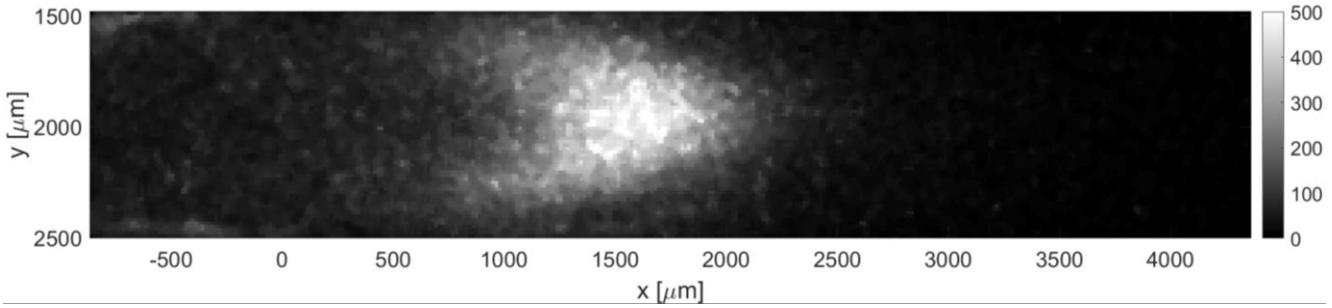

(b)

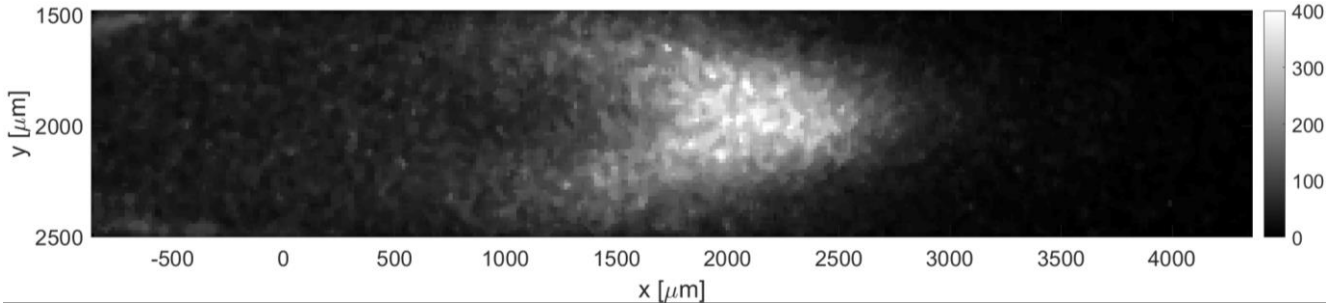

(c)

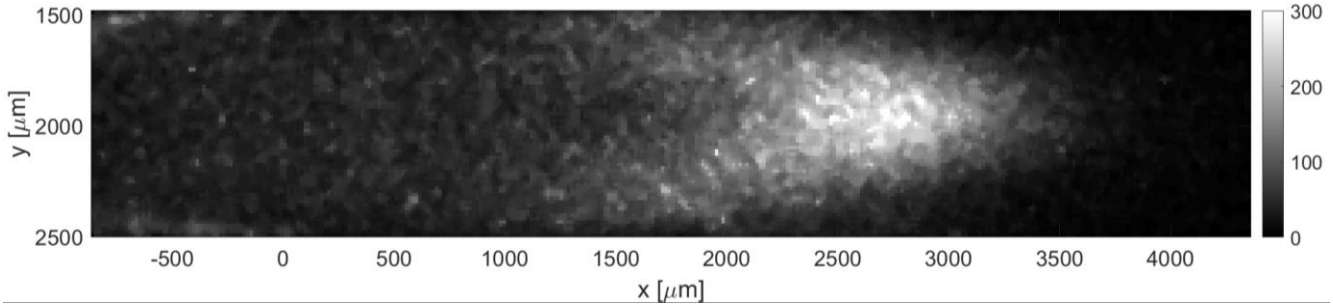

(d)

Figure 6.35. MTV acquisitions of helium-acetone flow with χ = 20%: (a) t = 20 µs, p_c = 1578.3 Pa, and Δp = 1800 Pa; (b) t = 30 µs, p_c = 1582.3 Pa, and Δp = 1801.6 Pa; (c) t = 40 µs, p_c = 1579.1 Pa, and Δp = 1799.6 Pa; (d) t = 50 µs, p_c = 1581.2 Pa, and Δp = 1800.4 Pa. The recording parameters are: N_l = 100, $N_i = 20$, $G = 100\%$, and $\Delta t_{gate} = 500$ ns. The acquisitions are made with a 4 × 4 binning. The laser pulse energy was varying between 80 and 120 µJ.

These images are the first flow visualizations ever obtained in confined and slightly rarefied gas flows. Indeed, they represent the experimental demonstration of the molecular displacement in a channel theoretically predicted by the diffusion-advection equation (6.16).

Because of the high repeatability of the experimental flow that the gas circuit can guarantee at low pressures, the experimental run of Figure 6.9 has been repeated 4 times. Differently from the image acquisitions related to argon-acetone flows presented in the previous section, MTV acquisitions have been carried out at one specific delay time for all the duration of each experiment. This procedure provided MTV data related to the same flow conditions and at different delay times. The 4 images of Figure 6.35 correspond, therefore, to the same thermodynamic conditions. All the properties of the visualized gas flow are reported in Table 6.6, along with their range of values that characterizes the images used for averaging.

	t [µs]	p_c [Pa]	Δp [Pa]	Ma [-]	Kn [-]	$\dot{m}$ [kg/s]	$\bar{u}_{CV}$[m/s]	$u_{slip,CV}$[m/s]
Figure 6.35a	20	1578.3 ± 3.6%	1800 ± 3.2%	0.066 ± 2.7%	3.96×10^{-3} ± 3.6%	1.7×10^{-6} ± 6.4%	38.14 ± 2.7%	1.66 ± 0.7%
Figure 6.35b	30	1582.3 ± 3.6%	1801.6 ± 3.2%	0.066 ± 2.7%	3.95×10^{-3} ± 3.6%	1.7×10^{-6} ± 6.4%	38.22 ± 2.7%	1.66 ± 0.7%
Figure 6.35c	40	1579.1 ± 3.6%	1799.6 ± 3.2%	0.066 ± 2.7%	3.96×10^{-3} ± 3.6%	1.71×10^{-6} ± 6.4%	38.08 ± 2.7%	1.66 ± 0.7%
Figure 6.35d	50	1581.2 ± 3.8%	1800.4 ± 3.3%	0.067 ± 4.8%	3.96×10^{-3} ± 3.7%	1.76×10^{-6} ± 8.6%	39.16 ± 4.8%	1.7 ± 1.2%

Table 6.6. Flow properties associated to the images of Figure 6.35. The reported percentage change indicates how much the properties vary inside the group of averaged images. The slip velocity is estimated from the mass flow rate measurements as explained in Section 6.2.5.

The Mach number and the Knudsen number are in average, respectively, Ma = 0.07 and Kn = 4×10^{-3}. The investigated gas flow can be then considered as incompressible and at the beginning of the slip flow regime. The slip velocity $u_{slip,CV}$ estimated from the mass flow rate measurement is also reported in Table 6.6. As for the case of argon-acetone flow, each image of Figure 6.35 represents the average of N_i = 20 images. For this experimental flow, the pumping power is set to maximum in order to maximize the thickness of the displacement profile, for reasons already discussed in Section 6.1.11. The resulting pressure difference and mass flow rate are, respectively, 1800 Pa and 1.7×10^{-6} kg/s. For this reason, the relative variations of the thermodynamic properties associated to a group of averaged images is higher than for the data of Table 6.2 and Table 6.4. However, even though the mass flow rate varies up to 8.6%, the variation on the estimated average velocity of the velocity profiles is limited to less than 3%. By comparing the images of Figure 6.35 with those of Figure 6.31 and Figure 6.33, it can be observed that the light emission is stronger for the data related to acetone-helium flow, even though the gas pressure is lower. This is because the IRO gate has been increased to Δt_{gate} = 500 ns and the average energy of the laser

excitation has been raised to values between 80 and 120 μJ. A peculiar noise is observed behind the wake of the moving emitting molecules, which origin is, at the moment, unclear. It is possible that this emission is provided by tagged molecules that diffused from the center towards the later walls of the channel, in which the gas velocity slows down.

Figure 6.36a and Figure 6.36b report, respectively, the displacement data and the reconstructed velocities. Because the displacement profiles correspond to the same thermodynamic conditions, the diffusion coefficient D used in the reconstruction method is the same for the 4 sets of displacement data and has been set to 1.4×10^{-3} m^2/s. Once again, the reconstruction method fails in extracting from the displacement data the correct velocity profile. The same issue encountered in the reconstruction of the velocity profile from the displacement data of argon-acetone flow at 6 kPa reappears here in an even more dramatic way. The reconstructed slip velocity ranges between about –16 and 20 m/s, while the expected value calculated is about $u_{slip,CV}$ = 1.66 m/s.

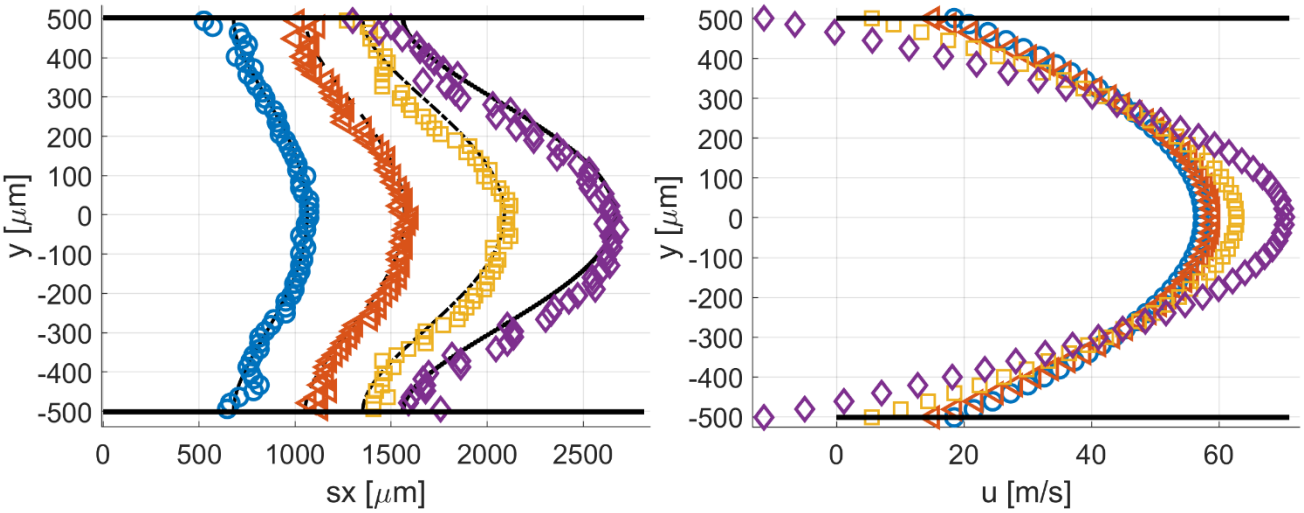

(a) (b)

Figure 6.36. (a) Displacement data computed by applying the Gaussian fitting per line to the images of Figure 6.35; (b) velocity reconstruction from the displacement data in (b): t = 20 μs (○), 30 μs (◁), 40 μs (□) and 50 μs (◇).

The sets of displacement data reported in Figure 6.36a, however, appears to be qualitatively very good, in the sense that the data dispersion around the numerical displacement profile is very limited. In comparison to the displacement profiles related to argon-acetone flows of Figure 6.32a and Figure 6.34a, the displacement profiles have a larger thickness. Table 6.7 reports the values of the thickness Δs_x related to the data of helium-acetone flow and the data of argon-acetone flow at 6 kPa in order to facilitate this comparison. Even though the higher molecular diffusion tends to make the displacement profile flatter, the helium flow is characterized by a flow speed that is about 4 times higher than that in argon flow.

t [μs]	20	30	40	50
Helium-acetone at 1.5 kPa	384.7 μm	528.5 μm	748.3 μm	1124.98 μm
Argon-acetone at 6kPa	206 μm	298.3 μm	334.96 μm	398.35 μm

Table 6.7. Thickness Δs_x of the displacement profile related to the data of helium-acetone flow (Figure 6.35) and of argon-acetone flow at 6 kPa (Figure 6.33).

As for the case of argon-acetone flow, even though the reconstructed velocity is inaccurate, the average velocity of profile is well extracted from the displacement data and is always approximatively the same independently of the delay time considered. Table 6.8 reports the measured values of $\bar{u}_{MTV}$ compared to those of $\bar{u}_{CV}$ with the relative uncertainty based, respectively, on the relative uncertainty of the mean molecular displacement with respect to the pixel size and the uncertainty on the channel width b.

t [μs]	20	30	40	50
$\bar{u}_{CV}$ [m/s]	38.14 ± 1.37	38.22± 1.38	38.08 ± 1.37	39.16 ± 1.4
$\bar{u}_{MTV}$ [m/s]	44.59 ± 0.76	44.47 ± 0.51	43.78 ± 0.38	43.19 ± 0.3

Table 6.8. Average velocities $\bar{u}_{CV}$ and $\bar{u}_{MTV}$ calculated, respectively, from CV technique and MTV technique for the image data of Figure 6.35. The reported uncertainty on $\bar{u}_{CV}$ has been calculated by considering variations of the channel width of ±200 μm with respect to the estimated value 5800 μm. The uncertainty on $\bar{u}_{MTV}$ is calculated from the relative uncertainty of the measured mean molecular displacement due to the CCD resolution.

Because the 4 images of Figure 6.35 represent the same flow conditions and, thus, the same velocity profile, the mean displacement of the tagged lines evolves linearly with time, as demonstrated in Figure 6.37.

A linear interpolation of these data provides a second measurement of the average velocity $\bar{u}_{MTV}$ = 42.07 m/s, which differs from the average of the reconstructed velocity profiles of about 5%. Because MTV technique provide a direct flow visualization of the displacement of gas through the channel, the average $\bar{u}_{MTV}$ is considered to be more reliable than $\bar{u}_{CV}$, which depends not only on the accuracy of the mass flow rate measurements provided by CV technique but also on the accuracy of the theoretical representation of the pressure distribution along the channel. With respect to the data of argon flow, the inlet-outlet pressure difference is here much stronger, so that the pressure distribution along the channel is far from being linear. If the compressibility effects on the pressure distribution are not correctly represented, the average pressure used for calculating $\bar{u}_{CV}$ is not accurate. In the case of argon flow the linearity of the pressure distribution eliminates this issue. As it can be ascertained from Table 6.8, the MTV velocity is always higher than the value estimated by CV technique. Therefore, it might be that the estimated average pressure at the middle position $x = L/2$ is overestimated and, consequently, the average velocity underestimated. However, because the pressure gradient and, consequently, the velocity gradient characterizing the helium-acetone gas flows are relatively high, it also might be that the discrepancies between

MTV and CV results are caused by a bias between acetone velocity and helium velocity. As a matter of fact, high velocity gradients may produce a separation of the species composing the gas mixture. It is possible that this mechanism makes acetone vapor travel faster than helium. In future works, this hypothesis might be verified by numerical analysis.

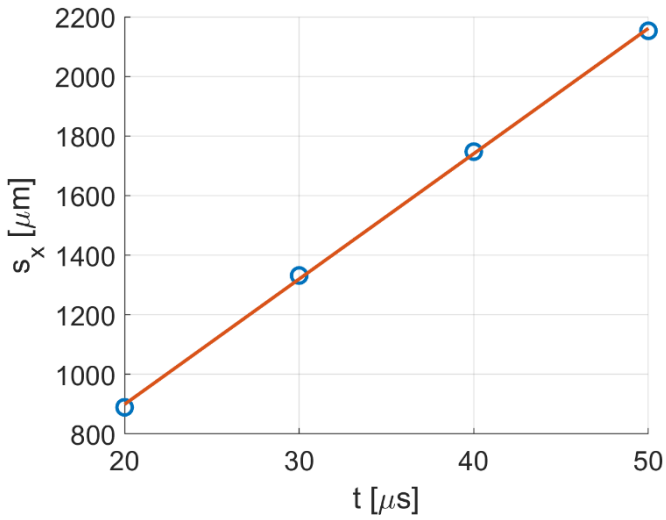

Figure 6.37. Mean molecular displacement $\bar{s}_x$ = 889.36, 1331.77, 1747.47, 2153.04 µm in helium flow, respectively, at times t = 20, 30, 40, and 50 µs. The red solid line represents the linear interpolation of the MTV data, which provides an average velocity $\bar{u}_{MTV}$ = 42.07 m/s.

Since the 4 sets of displacement data correspond to the same flow conditions, the TC reconstruction method can be applied. As discussed in Section 6.1.10, the TC method has been developed with the idea of eliminating the problem related to the uncertainty on the diffusion coefficient by extracting the velocity profile from displacement data related to more than one delay time. In particular, the application of the TC reconstruction algorithm to numerical experiments demonstrated its ability to extract both the correct velocity profile and the correct diffusion coefficient characterizing the numerical flow.

The TC reconstruction method has been applied to the displacement data of Figure 6.36a but the reconstructed velocity profile and the optimized diffusion coefficient are very far from the expected solution and, therefore, these results are not reported in this work. However, if the TC method is applied by fixing the diffusion coefficient to the estimated value 1.4×10^{-3} m^2/s, the reconstruction algorithm is able to extract a velocity profile with very good accuracy, as demonstrated in Figure 6.38b. Figure 6.38a report the comparison of the displacement data with the numerical displacement profile generated by the reconstructed velocity profile. The improvement provided by the TC method with respect to the original reconstruction method is outstanding, since the reconstructed velocity profile is characterized by a slip velocity $u_{slip,MTV}$ = 3.66 m/s that is much closer to the expected value 1.66 m/s. The average velocity $\bar{u}_{MTV}$ is equal to 43.37 m/s, unsurprisingly close to the values calculated from the

reconstructions of Figure 6.36b and from the linear fitting of the mean molecular displacement $\bar{s}_x$. In Figure 6.38b, the dashed line represents an example of initial guess for the velocity profile for highlighting the fact that, no matter how far the initial solution provided to the optimization algorithm is, the TC reconstruction method always converge to the same solution. This is an indication of the fact that the reconstructed velocity profile corresponds to a point of global minimum for the error between the numerical displacement profiles and the displacement data. The comparison between Figure 6.38a and Figure 6.36a reveals that very different velocity profile can generate, with the same diffusion coefficient, very similar displacement profiles. It is because of this reason that, as long as the displacement data available do not precisely represent the shape of the deformed tagged line, the traditional reconstruction method cannot extract the correct velocity profile. The measurement of the tagged line position close to the wall is made inaccurate by the relatively low SNR of the phosphorescence emission of the tracer, and the consequent uncertainty on the measured molecular slip prevents to detect which is the right shape of the displacement profile. Instead, by correlating the displacement data corresponding to different times, it appears that the problem related to uncertainty on the molecular slip at the wall is overcome.

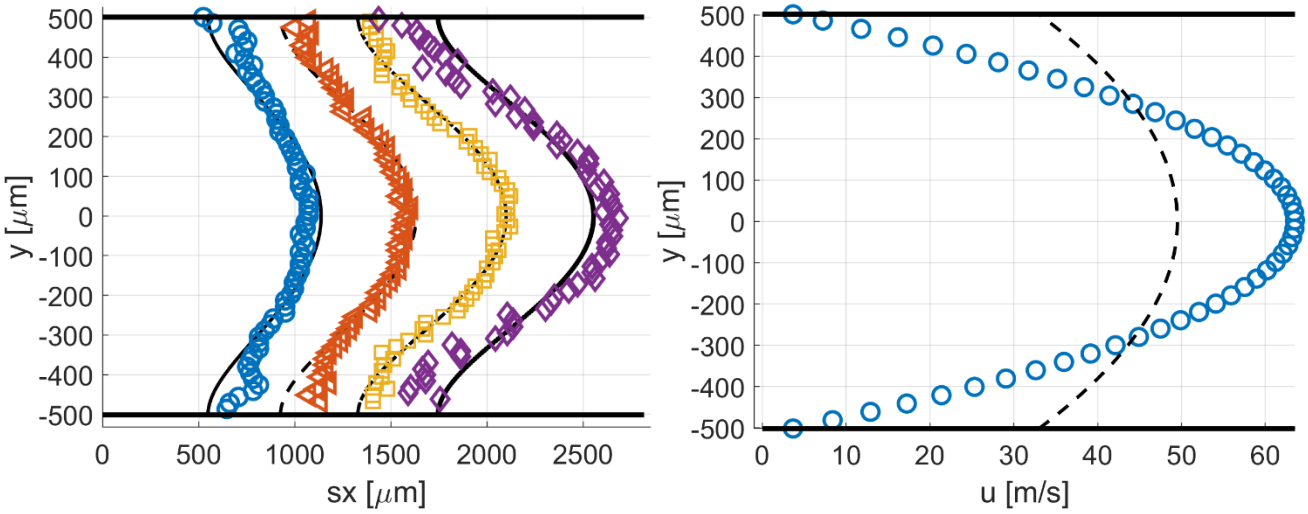

Figure 6.38. (a) Displacement data and corresponding numerical displacement profiles at t = 20 μs (○), 30 μs (◁), 40 μs (□) and 50 μs (◇); (b) reconstructed velocity by means of the TC reconstruction method. The dashed line represents an example of initial guess for the velocity profile.

6.4 Conclusions

Numerical experiments of helium-acetone flow with $Kn \in [0.15, 0.25]$ in a parallel plates channel have been generated by DSMC in order to analyze how the displacement profiles is flattened by Taylor dispersion. The thickness of the displacement profiles has been compared to the CCD resolution in order to verify the capability of the acquisition system to detect the actual shape of deformed tagged line. The reconstruction algorithm is successful in extracting from the numerical displacement data the velocity profile of the investigated gas flow.

However, a sensitivity analysis of the reconstructed velocity to the diffusion coefficient employed in the reconstruction algorithm demonstrated that variations of 20% on the value of the diffusion coefficient produce reconstruction errors on the slip velocity up to 100%. While the diffusion coefficient characterizing the numerical experiments can be known with the highest accuracy, the estimation of the diffusion coefficient in real experimental tracer-gas mixture flows is affected by numerous uncertainties, e.g., the uncertainty on the actual tracer concentration and on the kinetic diameter of acetone or diacetyl. In this context, the time-correlation (TC) reconstruction method has been developed, which is an improved version of the reconstruction method originally developed by Frezzotti *et al*. (2015). The TC method is able to extract both the correct velocity profile and the correct diffusion coefficient by correlating multiple sets of displacement data that belong to different delay times after the laser excitation. The application of the TC method to numerical experiments demonstrated high accuracy in measuring the diffusion coefficient and the slip velocity at the wall, for which the error is limited to a maximum of 4%.

The experimental flow generated by means of the experimental setup described in Chapter 4 has been thoroughly analyzed. CV technique has been applied to measure the mass flow rate at each instant during the experimental run. The experimental mass flow rate has been compared with the numerical mass flow rate and the discrepancies have been discussed. The theoretical solution for the pressure distribution along the channel allowed a complete characterization of the thermodynamic conditions inside the channel. In these calculations, the head losses between the measured pressure and the actual pressure at the inlet and the outlet of the channel have been estimated and taken into account. Moreover, the flow rate measurements from CV technique have been combined with the analytical solution of the pressure distribution and with the analytical velocity distribution of Ebert & Sparrow (1965) for providing an estimation of the average value of the velocity profile investigated by means of MTV.

The post-processing procedure applied to the set of images recorded by MTV has been described in detail. Because of the inherent unsteadiness of the experimental flow conditions, two strategies for averaging the images have been discussed but only the “horizontal” averaging has been applied in this work. The procedures for detecting the channel walls on the image, for identifying the initial position of the tagged line on the image, and for adjusting the set of displacement data inside the mathematical domain of the reconstruction method have been explained. The identification of the deformed tagged line position is based on a Gaussian fitting per line procedure. However, a new 2D fitting algorithm for extracting the displacement data from the whole light distribution has been developed. Even though this new approach for extracting the displacement profile has not been used to the experimental data presented in Section 6.3.2 and 6.3.3, the 2D fitting algorithm is the first step towards a future, more advanced reconstruction method, which can extract the velocity profile by exploiting the information related to the whole cloud of tagged molecules and not only to the peak of intensity of the tagged line.

Afterwards, MTV technique based on acetone vapor excited at 310 nm has been applied to experimental flows at low pressures. Firstly, argon-acetone flows at about 30 kPa and 6 kPa have been investigated by MTV in order to validate the new experimental setup for velocity measurements in non-rarefied conditions. The results shown in Section 6.3.2 represent, to the best of our knowledge, the first ever flow visualizations of the molecular displacement and local velocity measurements in confined gas flows at a pressure lower than 42 kPa. The improvement in the light signal quality with respect to the image acquisitions presented in previous works have also been pointed. The application of the reconstruction algorithm to the displacement data of argon-acetone at 30 kPa provides accurate velocity profiles, with a non-zero slip velocity at the wall. The comparison of average velocity $\bar{u}_{MTV}$ measured by MTV with average velocity $\bar{u}_{CV}$ estimated from by CV techniques combined with analytical solutions demonstrated that the two techniques provide very similar values and inside the estimated uncertainties. However, even though the average velocity measured by MTV is accurate, the velocity profiles reconstructed from the displacement data of argon-acetone flow at 6 kPa are characterized by a slip velocity at the wall that is quite higher than the expected one. This result has been explained to be caused by the uncertainty in measuring the molecular slip at the wall, which is a region on the image where the recorded light has a relatively low SNR. Because the sets of displacement data available at different delay times do not correspond to the same exact flow conditions, the TC reconstruction method could not be applied to these MTV data.

Finally, the application of MTV to helium-acetone flows at 1.5 kPa has been demonstrated. The thermodynamic conditions associated to the gas flows investigated in Section 6.3.3 correspond to Knudsen numbers of the order of 0.004, which are considered to be at the entrance of the slip flow regime. In this case, the measured average velocity $\bar{u}_{MTV}$ are higher than the average velocity $\bar{u}_{CV}$ estimated by CV technique. These discrepancies have been associated to an overestimation of the compressibility effects on the theoretical average pressure at the middle cross-section along the channel, which makes the estimated $\bar{u}_{CV}$ smaller than the real value. Moreover, because the average velocity provided by MTV is, indeed, a direct measurement based on visualizations of the mean molecular displacement of the tracer, $\bar{u}_{MTV}$ is believed to be more accurate. However, a possible alternative explanation of the discrepancies between $\bar{u}_{MTV}$ and $\bar{u}_{CV}$ is correlated to the possible existence of a bias between acetone velocity and helium velocity. This hypothesis needs further analysis to be verified. The application of the reconstruction method to the displacement data of helium-acetone flows provide velocity profiles with a problematic similar to that encountered in the case of argon-acetone flows at 6 kPa. The measured velocity slip is very far from the expected value, even though the displacement data are well fitted by the numerical solution.

For the MTV data presented in Section 6.3.3, The sets of displacement data related to different delay times correspond to the same exact flow conditions. For this reason, the TC reconstruction method could be applied in this case. When the diffusion coefficient is used as an optimization parameter, the velocity profile reconstructed is still far from the expected one and the optimized diffusion coefficient is very different from the estimated value.

However, when the diffusion coefficient is fixed to the value estimated by means of the Blanc's law (6.27), the TC method provides, surprisingly, a very good velocity profile. The resulting slip velocity is of the same orders of magnitude as the expected one. To the best of our knowledge, these are the first ever direct slip velocity measurements carried out by MTV. These results are very promising but only qualitatively good. The improvement of the slip velocity measurements from a quantitative point of view requires further analyses and, especially, the elimination of the uncertainties on the parameters of the reconstruction, that is the channel height and the diffusion coefficient.

MTV acquisitions in helium-acetone flows have been carried out even for pressures lower than 1500 Pa, down to 500 Pa. These results have not been presented in this work because qualitatively similar to the ones presented in Section 6.3.3. The phosphorescence emission provided by acetone vapor excited at 310 nm in helium flows at 500 Pa is still very intense and durable enough for measuring the tracer displacement. However, the molecular diffusion at 500 Pa is higher than that at 1500 Pa, and the stronger Taylor dispersion flattens even more the displacement profiles. At these pressures, the CCD resolution seems to be enough for resolving the thickness of the displacement profiles, but further analyses are required to quantitatively evaluate the accuracy of the measurement.

In the next and last chapter, the achievements of this work are briefly summarized, and the necessary future developments of the project are identified.

References

Almy, G. M., & Anderson, S. (1940). Lifetime of fluorescence in diacetyl and acetone. *The Journal of Chemical Physics*, 8(10), 805-814.

Bird, G. A. (1994). Molecular gas dynamics and the direct simulation monte carlo of gas flows. Clarendon, Oxford, 508, 128.

Blanc, A. (1908). Recherches sur les mobilités des ions dans les gaz. *J. Phys. Theor. Appl.*, *7*(1), 825-839.

Ebert, W. A., & Sparrow, E. M. (1965). Slip flow in rectangular and annular ducts. *Journal of Basic Engineering*, *87*(4), 1018-1024.

Frezzotti, A., Mohand, H. S. H., Barrot, C., & Colin, S. (2015). Role of diffusion on molecular tagging velocimetry technique for rarefied gas flow analysis. *Microfluidics and Nanofluidic*s, 19(6), 1335-1348.

Lempert, W. R., Boehm, M. Jiang, N., Gimelshein, S., & Levin, D. (2003). Comparison of molecular tagging velocimetry data and direct simulation Monte Carlo simulations in supersonic micro jet flows. *Experiments in Fluids*, 34(3), 403-411.

Marrero, T. R., & Mason, E. A. (1972). Gaseous diffusion coefficients. *Journal of Physical and Chemical Reference Data*, 1(1), 3-118.

Mohand, H. S. H., Frezzotti, A., Brandner, J. J., Barrot, C., & Colin, S. (2017). Molecular tagging velocimetry by direct phosphorescence in gas microflows: correction of Taylor dispersion. *Experimental Thermal and Fluid Science*, 83, 177-190.

Parmenter, C. S., & Poland, H. M. (1969). Fluorescence, Phosphorescence, and Triplet Formation in Biacetyl at Low Pressures. *The Journal of Chemical Physics*, *51*(4), 1551-1558.

Résibois, P., & De Leener, M. (1977). Classical kinetic theory of fluids.

Samouda, F., Colin, S., Barrot, C., Baldas, L., & Brandner, J. J. (2015). Micro molecular tagging velocimetry for analysis of gas flows in mini and micro systems. *Microsystem Technologies*, 21(3), 527-537.

Silva, E., Deschamps, C. J., Rojas-Cárdenas, M., Barrot-Lattes, C., Baldas, L., & Colin, S. (2018). A time-dependent method for the measurement of mass flow rate of gases in microchannels. International Journal of Heat and Mass Transfer, 120, 422-434.

Szalmas, L., Pitakarnnop, J., Geoffroy, S., Colin, S., & Valougeorgis, D. (2010). Comparative study between computational and experimental results for binary rarefied gas flows through long microchannels. *Microfluidics and nanofluidics*, 9(6), 1103-1114.

Chapter 7

Conclusions and perspectives

In this work, MTV technique has been applied to gas flows in a channel with rectangular cross-section in non-rarefied and slightly rarefied conditions.

Previous works (Samouda *et al*., 2015; Si-Hadj Mohand *et al*., 2017) already applied MTV to non-rarefied conditions, but the tracer employed, which was acetone vapor excited at 266 nm, did not allow to investigate gas flows in a channel at pressures lower than 42 kPa. The main obstacle preventing the application of MTV to gas flows in the slip regime was the lack of a suitable tracer able to provide a strong enough phosphorescence emission at low pressure.

The results of the experimental campaign presented in Chapter 5 removed this scientific barrier. The qualitative and the quantitative analysis of the phosphorescence data of acetone and diacetyl vapor provided results with very important consequences for the future of MTV, MTT, MTM applications in rarefied gas flows. The main achievements and the contributions provided in this chapter are here summarized:

1. experimental data on acetone and diacetyl phosphorescence at low pressure are provided;
2. phosphorescence intensity of acetone and diacetyl vapor has been optimized as a function of the excitation wavelength. The parametric study demonstrated that acetone phosphorescence can be amplified of 12 times if the excitation wavelength is moved from 266 nm up to 310 nm. For the excitation wavelength investigated, diacetyl phosphorescence is maximized at 410 nm;
3. phosphorescence lifetime has been qualitatively analyzed in helium-acetone mixtures and helium-diacetyl mixtures at pressures between 1000 and 500 Pa and with tracer concentration between 2% and 20%;
4. a mathematical model capable of describing the observed experimental data on acetone and diacetyl phosphorescence has been proposed in light of the data found in the literature;
5. a novel parameter identification algorithm has been developed for extracting simultaneously the triplet-triplet annihilation (TTA) rate and the self-diffusion coefficient of the vapor.

The experimental data on phosphorescence emission carried out in the static visualization chamber demonstrated that both acetone vapor excited at 310 nm and diacetyl vapor excited at 410 nm provide an intense and durable signal exploitable for MTV applications to gas flows at $Kn \in [0.015, 0.025]$.

Moreover, a comparison of the data found in the literature and the data gathered in this work revealed that the observed non-exponential decay of the phosphorescence emission and the observed dependency of the

phosphorescence lifetime from the vapor pressure is determined by the triplet-triplet annihilation process, that takes place when the triplet concentration is high enough. When the TTA mechanism is activated, the lifetime and the intensity of the phosphorescence emission is inevitably dependent on the vapor pressure and on the laser energy density. This observation has fundamental consequences for MTT and MTM applications in gas flows, which are based on inferring the temperature or pressure measurements from the lifetime or the intensity of the emission.

The parameter identification algorithm developed in this work for extracting the TTA constant rate and the self-diffusion coefficient at a function of the vapor pressure provided interesting results. The measured TTA constant rate is very close to the few values proposed in the literature. The measured diffusion coefficient is not inversely proportional with respect to the vapor pressure, which was unexpected. Surprisingly, the kinetic diameter calculated by means of the Chapman-Enskog formula (5.44) from the measured diffusion coefficients decreases linearly with the pressure. A possible explanation of this fact is that the temperature of the vapor increases quadratically with vapor pressure. As a matter of fact, the mathematical model (5.53) used for describing the triplet population lifetime does not represent in any way how the energy lost by means of internal and external non-radiative de-excitations increase the vapor temperature. In this context, numerical simulations might shed light on these experimental results.

Afterwards, the results of MTV technique applied to argon-acetone flows in non-rarefied conditions and to helium-acetone flows in the slip flow regime have been reported. The main achievements presented in Chapter 6 are here summarized:

1. numerical experiments of helium-acetone flow in parallel plates have been carried out by means of DSMC simulations for Knudsen numbers between 0.015 and 0.025.

2. the reconstruction method has been applied to the numerical displacement data in order to demonstrate the velocity profile can be accurately reconstructed despite the high molecular diffusion.

3. a sensitivity analysis of the reconstructed velocity with respect to variations of the diffusion coefficient has been carried out. This analysis demonstrated that if the diffusion coefficient used for the reconstruction differs from the real value of 20%, the error on the measured velocity slip goes up to 100%;

4. an improved version of the reconstruction method originally developed by Frezzotti *et al*. (2015) has been developed, that is the time-correlation (TC) reconstruction method. The new optimization algorithm is able to extract simultaneously the correct velocity profile and the correct diffusion coefficient from numerical experiments.

5. the novel experimental setup combining MTV and CV techniques have applied to argon-acetone and helium-acetone flows at low pressure. The theoretical solutions on the pressure distribution along a

rectangular channel and the analytical velocity distribution proposed by Ebert & Sparrow (1965) have employed for a complete characterization of the thermodynamic conditions of the experimental flow. Moreover, the mass flow rate measurement provided by CV technique combined with the analytical solutions in the rectangular channels provided an estimation of the average value of the velocity profile investigated by MTV;

6. MTV has been successfully applied to argon-acetone flows with χ = 20% at 30 kPa. As expected, the reconstructed velocity has a zero-velocity slip at the wall and an average velocity that corresponds to the estimated values provided by CV technique;

7. MTV has been applied to argon-acetone flows with χ = 20% at 6 kPa. At these thermodynamic conditions, the gas flow is still in the non-rarefied regime. Nevertheless, the effects of Taylor dispersion on the displacement profiles are already evident. The reconstruction method fails in extracting the correct velocity profile: the reconstructed slip velocity at the wall is, indeed, higher than the expected value. However, the reconstructed velocity has an average velocity that is closed to the value estimated by CV techniques. The TC reconstruction method could be applied to these experimental data;

8. MTV has been applied to helium-acetone flows with χ = 20% at 1.5 kPa. The reconstruction method does not extract accurate velocity profiles from the displacement data. The velocity slip is very far from the expected value. However, the application of the TC reconstruction method with a fixed diffusion coefficient is able to extract the correct velocity profile with a slip velocity close to the expected value.

To best of our knowledge, some of the experimental results presented in this work have never been obtained before and correspond to:

1. the flow visualizations of the tracer displacement and the accurate velocity reconstruction in argon-acetone flows in a channel at pressures of the order of 30 kPa;

2. the flow visualizations of the tracer displacement in argon-acetone flows in a channel at pressures as low as 6 kPa;

3. the flow visualizations of the tracer displacement in helium-acetone flows in a channel at pressures as low as 1.5 kPa, which are considered to be at the entrance of the slip flow regime;

4. the first qualitative measurements of the slip velocity at the wall by means of MTV.

During the development of this work, perspectives to develop in future works have been identified and are here summarized:

1. during this work, the inner dimensions of the tested channel could not be directly measured, but only estimated from alternative strategies, as explained in Chapter 3;

2. further analyses are required to understand the discrepancies between the experimental mass flow rate and the theoretical mass flow rate. Because of the relatively strong inlet-outlet pressure difference applied at the channel ends, it is possible that the generated gas flow is not in steady state conditions at each time. The verification of this hypothesis needs first to eliminate the uncertainties on the inner dimensions of the tested channel;

3. the strong velocity and pressure gradients characterizing the helium-acetone flows investigated by MTV in Section 6.3.3 might cause a bias between acetone velocity and helium velocity. This hypothesis needs to be verified by means of numerical experiments. In the DSMC simulations carried out in this work, the numerical gas flow is driven by a uniform external force and not by a real pressure gradient. In this context, velocity gradients in the flow direction cannot be represented. A development of the current DSMC program available is necessary to take into account of this aspect;

4. the current experimental channel still suffers of relevant leakage problems at the level of the Suprasil® windows. The main issue is given by the fact that the positioning of the Suprasil® windows inside the cavities of the channel needs to guarantee simultaneously good sealing properties and a perfect leveling with respect to the channel walls to minimize the perturbations in the investigated flow. Future designs of the tested channel may find a solution this problem by separating these two functionalities;

5. the current experimental channel is equipped with an access window for the laser excitation only at the middle position along the channel length. The analysis of the thermodynamic conditions characterizing the experimental flow presented in Chapter 6 showed that more favorable flow conditions for MTV applications can be found towards the outlet of the channel. Because of the expansion and acceleration due to the compressibility, the gas flow at the outlet region is characterized by higher Knudsen numbers and Mach numbers (but lower than 0.3), which is the best experimental conditions for carrying out MTV measurements of the slip velocity. Future designs of the tested channel may incorporate access windows close to the channel outlet;

In the experimental results presented in Chapter 6, only acetone vapor excited at 310 nm has been employed. However, preliminary MTV acquisitions have also been carried out by employing diacetyl vapor excited at 410 nm in helium flows. These first experimental tests, which are not reported in this work, revealed that diacetyl is not a suitable tracer for being used in MTV applications to confined gas flows. As it was already noticed during

the experiments on phosphorescence emission carried out in the static visualization chamber (Chapter 5), diacetyl vapor is affected by a very strong wall adsorption that produces a thin film of diacetyl molecules on the channel walls. At the moment of the laser excitation, the laser energy is inevitably partially diffused in the interior of the channel by the irregularities inside and at the surface of the Suprasil® windows. The scattered laser energy excites also the diacetyl molecules adsorbed by the channel walls, which produce a phosphorescence emission that generates a very strong background noise that makes the detection of the tagged line absolutely impossible.

Nevertheless, it is from the failure in the use of diacetyl vapor for MTV applications that the reasons of the success of acetone vapor excited at 310 nm become clear. In Chapter 4, the mechanisms at the molecular level that are associated to the light emission of acetone vapor excited at 310 nm have been discussed. The literature corroborates the fact that this light emission does not correspond to a simple excitation and de-excitation of acetone molecules, but it derives from a chemical decomposition and successive recombination in diacetyl molecules. The newly formed diacetyl molecules are, afterwards, excited to the triplet state by means of collisions with acetone triplets. The intramolecular mechanism of energy transfer between diacetyl molecules and acetone triplets is known as photosensitization, and the resulting strong light emission generated by excited diacetyl molecules is called sensitized phosphorescence (Yip *et al*., 1994). In this context, it is clear that the actual tagged molecules are not already present in the flow field, but they are generated only at the moment of the laser excitation and only in the region of the space covered by the laser beam. When diacetyl vapor excited at 410 nm is used, the tracer molecules that can be excited and can provide the light emission are everywhere inside the channel, and possible scattered laser energy produces the strong background noise observed. Differently, when acetone vapor excited at 310 nm is used, the excited molecules are present only in the region crossed by the laser beam, and for this reason the background noise is very low.

In Chapter 3, different implementations of MTV technique have been presented. The implementation used in this work has been said to be MTV by direct phosphorescence. In this version of MTV, the velocity measurement is based on the long-lived phosphorescence generated by a tracer that is pre-seeded in the flow. In this case, only one laser source is necessary. MTV technique based on acetone vapor excited at 266 nm or diacetyl vapor excited at 410 nm can be classified as MTV by direct phosphorescence. However, acetone vapor excited at 310 nm is based on intramolecular mechanisms that are different form the usual ones that characterize MTV by direct phosphorescence. MTV based on acetone excited at 310 nm is somehow similar to PHANTOMM techniques (described in Chapter 3), such as HTV, NTV, or OTV, in which the molecular tracer is generated by photochemical decomposition of a specific substance pre-seeded in the investigated flow. Nevertheless, MTV based on acetone excited at 310 nm does not require two laser sources as in the case of PHANTOMM techniques because the same laser source that generates the molecular tracer also provides the necessary excitation for enabling the phosphorescence emission. Because the version of MTV employed in this work seems to not fall in any of the

categories already existing, it might be legit to call the version of MTV technique used in this work as, for instance, MTV by sensitized phosphorescence.

References

Frezzotti, A., Mohand, H. S. H., Barrot, C., & Colin, S. (2015). Role of diffusion on molecular tagging velocimetry technique for rarefied gas flow analysis. *Microfluidics and Nanofluidic*s, 19(6), 1335-1348.

Mohand, H. S. H., Frezzotti, A., Brandner, J. J., Barrot, C., & Colin, S. (2017). Molecular tagging velocimetry by direct phosphorescence in gas microflows: correction of Taylor dispersion. *Experimental Thermal and Fluid Science*, 83, 177-190.

Samouda, F., Colin, S., Barrot, C., Baldas, L., & Brandner, J. J. (2015). Micro molecular tagging velocimetry for analysis of gas flows in mini and micro systems. *Microsystem Technologies*, 21(3), 527-537.

Yip, B., Lozano, A., & Hanson, R. K. (1994). Sensitized phosphorescence: a gas phase molecular mixing diagnostic. *Experiments in fluids*, *17*(1-2), 16-23.

Appendix A

Analytical solutions for the velocity distribution

Jang & Wereley (2004) developed a simplified analytical expression for the coefficients a_1 and a_2, by starting from the velocity distribution proposed by Erbert & Sparrow (1965):

$$a_1 = \frac{4}{3}\left(1 - \frac{192}{\pi^5}a\sum_{n=1,3,5,\ldots}^{\infty}\frac{1}{n^5}\tanh\left(\frac{n\pi}{2a}\right)\right), \tag{A.1}$$

$$\begin{aligned} a_2 = \frac{2-\sigma}{\sigma}\Bigg[\frac{32}{3}\left(1 - \frac{192}{\pi^5}a\sum_{n=1,3,5,\ldots}^{\infty}\frac{1}{n^5}\tanh\left(\frac{n\pi}{2a}\right)\right) \\ -\frac{256}{\pi^4}(1-a)\sum_{n=1,3,5,\ldots}^{\infty}\frac{1}{n^4}\tanh^2\left(\frac{n\pi}{2a}\right)\Bigg]. \end{aligned} \tag{A.2}$$

Morini & Spiga (1998) proposed a solution based on the integral transform method. The velocity distribution results in a double series of harmonic functions in the two directions *y* and *z*:

$$\begin{aligned} u^*(y^*,z^*) = \sum_{n=1}^{\infty}\sum_{m=1}^{\infty}\frac{N_{n,m}A_{n,m}}{\bar{\beta}_m^2+\bar{\delta}_n^2}\left[\bar{\beta}_m\cos\left(\bar{\beta}_m z^*/a\right)+\frac{\sin\left(\bar{\beta}_m z^*/a\right)}{\overline{Kn}_H}\right] \\ \times\left[\bar{\delta}_n\cos\left(\bar{\delta}_n y^*\right)+\frac{\sin\left(\bar{\delta}_n y^*\right)}{\overline{Kn}_H}\right], \end{aligned} \tag{A.3}$$

where $\overline{Kn}_H = \beta_{u1}(2-\sigma)/\sigma Kn_H$, the coefficients $N_{n,m}$ and $A_{n,m}$ have the expressions

$$N_{n,m} = \frac{16}{(1+a)^2}\left(\frac{\overline{Kn}_H^2\bar{\beta}_m^2+1}{\overline{Kn}_H^2}\right)\left(\frac{1}{a}+2\overline{Kn}_H\right)\left(\frac{\overline{Kn}_H^2\bar{\delta}_n^2+1}{\overline{Kn}_H^2}\right)(1+2\overline{Kn}_H), \tag{A.4}$$

$$A_{n,m} = \left(\sin\frac{\bar{\beta}_m}{a}+\frac{1-\cos\left(\bar{\beta}_m/a\right)}{\overline{Kn}_H\bar{\beta}_m}\right)\left(\sin\bar{\delta}_n+\frac{1-\cos\bar{\delta}_n}{\overline{Kn}_H\bar{\delta}_n}\right), \tag{A.5}$$

and where $\bar{\beta}_m$ and $\bar{\delta}_n$ are two sets of eigenvalues whose admissible values are those that make Eq. (A.3) satisfy the slip boundary conditions Eq. (2.55) and Eq. (2.56). The transcendental equations for $\bar{\beta}_m$ and $\bar{\delta}_n$ are

$$\tan\frac{\bar{\beta}_m}{a} = \frac{2\bar{\beta}_m\overline{Kn}_H}{\overline{Kn}_H^2\bar{\beta}_m^2-1}, \qquad \tan\bar{\delta}_n = \frac{2\bar{\delta}_n\overline{Kn}_H}{\overline{Kn}_H^2\bar{\delta}_n^2-1}. \tag{A.6}$$

In the same manner as for the solution developed by Ebert & Sparrow (1965), the mean velocity can be fitted through a linear polynomial function $a_1 + a_2 Kn_H$, and the mass flow rate calculated from Eq. (2.69).

The solution in terms of mass flow rate and velocity distribution can be accurate for $Kn > 0.1$ if a higher-order slip boundary condition is employed. As discussed in Section 2.5, various second-order boundary conditions have been proposed in literature. Here, the solution developed by Aubert & Colin (2001) is discussed, for which they considered the second-order slip boundary conditions of Deissler (1964):

$$u|_{y=\frac{H}{2}} = -\frac{2-\sigma}{\sigma}\lambda\left.\frac{\partial u}{\partial y}\right|_{y=\frac{H}{2}} - \frac{9}{16}\lambda^2\left(2\left.\frac{\partial^2 u}{\partial y^2}\right|_{y=\frac{H}{2}} + \left.\frac{\partial^2 u}{\partial z^2}\right|_{y=\frac{H}{2}} + \left.\frac{\partial^2 u}{\partial x^2}\right|_{y=\frac{H}{2}}\right), \tag{A.7}$$

$$u|_{z=\frac{b}{2}} = -\frac{2-\sigma}{\sigma}\lambda\left.\frac{\partial u}{\partial z}\right|_{z=\frac{b}{2}} - \frac{9}{16}\lambda^2\left(2\left.\frac{\partial^2 u}{\partial z^2}\right|_{z=\frac{b}{2}} + \left.\frac{\partial^2 u}{\partial y^2}\right|_{z=\frac{b}{2}} + \left.\frac{\partial^2 u}{\partial x^2}\right|_{z=\frac{b}{2}}\right), \tag{A.8}$$

The velocity expansion proposed by Ebert & Sparrow (1965) does not converge when higher-order slip boundary conditions are employed. For this reason, Aubert & Colin (2001) proposed to develop the velocity function as

$$u^*(y^*, z^*) = \sum_{n=1}^{\infty}\sum_{m=1}^{\infty} N_{n,m}A_{n,m}\cos\left(\bar{\beta}_m\,\frac{z^*}{a}\right)\cos(\bar{\delta}_n y^*) + \frac{9}{4}Kn_H^2, \tag{A.9}$$

with

$$\begin{aligned} N_{n,m}A_{n,m} = \frac{1}{\bar{\beta}_m^2 + \bar{\delta}_n^2}\Bigg\{&\frac{4\sin(\bar{\beta}_m/a)\sin\bar{\delta}_n}{\bar{\beta}_m\bar{\delta}_n} \\ &+ \frac{9}{2}\frac{\sigma}{2-\sigma}Kn_H\left(\frac{\sin(\bar{\beta}_m/a)\cos\bar{\delta}_n}{\bar{\beta}_m} + \frac{\cos(\bar{\beta}_m/a)\sin\bar{\delta}_n}{\bar{\delta}_n}\right)\Bigg\} \\ \times\Bigg\{&\left(\frac{1}{a} + \frac{\cos\left(\frac{\bar{\beta}_m}{a}\right)\sin\left(\frac{\bar{\beta}_m}{a}\right)}{\bar{\beta}_m}\right)\left(1 + \frac{\sin\bar{\delta}_n\cos\bar{\delta}_n}{\bar{\delta}_n}\right) + \frac{9}{4}\frac{\sigma}{2-\sigma}Kn_H \\ \times&\left(\cos^2\bar{\delta}_n\left[\frac{1}{a} + \frac{\cos\left(\frac{\bar{\beta}_m}{a}\right)\sin\left(\frac{\bar{\beta}_m}{a}\right)}{\bar{\beta}_m}\right] + \cos^2\bar{\beta}_m\left[1 + \frac{\sin\bar{\delta}_n\cos\bar{\delta}_n}{\bar{\delta}_n}\right]\right)\Bigg\}^{-1} \end{aligned} \tag{A.10}$$

and the set of eigenvalues are the solutions of the following transcendental equations:

$$1 - 2Kn_H\frac{2-\sigma}{\sigma}\bar{\delta}_n\tan\bar{\delta}_n - \frac{9}{4}Kn_H^2\bar{\delta}_n^2 = 0, \tag{A.11}$$

$$1 - 2Kn_H\frac{2-\sigma}{\sigma}\bar{\beta}_m\tan\bar{\beta}_m/a - \frac{9}{4}Kn_H^2\bar{\beta}_m^2 = 0. \tag{A.12}$$

By employing the velocity solution (A.9) for calculating the mean velocity on the cross-section, the mass flow rate reads

$$\dot{m}_{rect,S2} = -\frac{H^4}{4\mu a}\frac{dp}{dx}\frac{p}{R_S T}\left[\sum_{n=1}^{\infty}\sum_{m=1}^{\infty} N_{n,m}A_{n,m}\frac{a\sin\left(\frac{\bar{\beta}_m}{a}\right)\sin\bar{\delta}_n}{\bar{\beta}_m\bar{\delta}_n} + \frac{9}{4}Kn_H^2\right]. \tag{A.13}$$

The subscript 'rect, S2' indicates that the analytical expression of the mass flow rate is valid for second-order slip boundary conditions in a channel with rectangular section. Once again, the term in the brackets of Eq. (A.13) is fitted with a polynomial function of Kn_H in order to be able to easily integrate the mass flow rate along the channel length. Because of the square term $\frac{9}{4}Kn_H^2$, a quadratic polynomial $a_1 + a_2 Kn_H + a_3 Kn_H^2$ is necessary for perfectly fitting the term in the brackets, thus the mass flow rate takes the form

$$\dot{m}_{rect,S2} = -\frac{H^4}{4\mu a}\frac{dp}{dx}\frac{p}{R_S T}[a_1 + a_2 Kn_H + a_3 Kn_H^2]. \tag{A.14}$$

By considering that $p\,Kn_H$ is constant in an isothermal flow, the integration of Eq. (A.14) yields to the following expression for the mass flow rate:

$$\dot{m}_{rect,S2} = \frac{H^4}{4\mu a}\frac{p_{out}^2}{R_S T}\left[a_1\frac{\Pi^2-1}{2} + a_2(\Pi-1)Kn_{H,out} + a_3 Kn_{H,out}^2\ln\Pi\right], \tag{A.15}$$

which differs from Eq. (2.69) for the quadratic term in Kn_H. The three fitting coefficients depend on the aspect ratio a, whereas the coefficients a_2 and a_3 depend also on the momentum accommodation coefficient σ. The mass flow rate in the case of no-slip at the wall is deduced from Eq. (A.15) by setting Kn_H = 0:

$$\dot{m}_{rect,ns} = \frac{H^4}{4\mu a}\frac{p_{out}^2}{R_S T}a_1\frac{\Pi^2-1}{2}. \tag{A.16}$$

The non-dimensional mass flow rate takes the form

$$\dot{m}_{rect,S2} = \frac{\dot{m}_{rect,S2}}{\dot{m}_{rect,ns}} = \left[1 + 2\frac{a_2}{a_1}Kn_{H,out}\frac{1}{\Pi+1} + 2\frac{a_3}{a_1}Kn_{H,out}^2\frac{\ln\Pi}{\Pi^2-1}\right]. \tag{A.17}$$

Figure A.1 shows the effect of the aspect ratio and of the slip model on the non-dimensional mass flow rate for Kn_{out} = 0.1 and σ = 1. Large aspect ratios amplify the increase of mass flow rate due to the rarefaction, whereas high pressure ratios tend to reduce it. At Kn_{out} = 0.1 and low pressure ratios, the first-order slip model underestimates the mass flow rate of about 10% with respect to the value calculated with a second-order model. It is worthy to underline that some second-order boundary conditions proposed in the literature predict a mass flow

rate lower than the no-slip case, such as that proposed by Chapman & Cowling (1990). However, all the experimental data demonstrate that at higher Knudsen numbers the mass flow rate tends to increase.

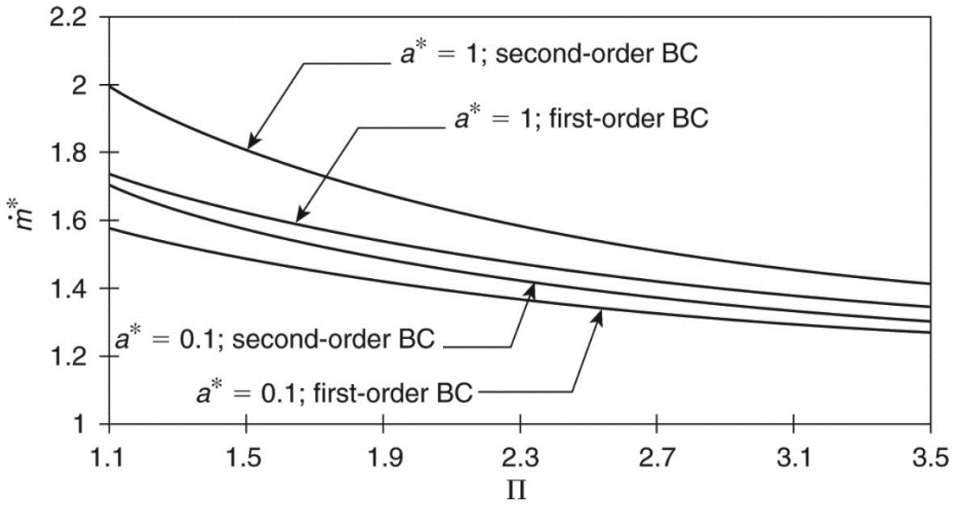

Figure A.1. Non-dimensional mass flow rate as a function of the inlet-outlet pressure ratio Π. The effect of the aspect ratio and of the slip model is illustrated. Figure from Kandlikar *et al*. (2014).

References

Aubert, C., & Colin, S. (2001). High-order boundary conditions for gaseous flows in rectangular microducts. *Microscale Thermophysical Engineering*, *5*(1), 41-54.

Chapman, S., Cowling, T. G., & Burnett, D. (1990). *The mathematical theory of non-uniform gases: an account of the kinetic theory of viscosity, thermal conduction and diffusion in gases*. Cambridge university press.

Deissler, R. G. (1964). An analysis of second-order slip flow and temperature-jump boundary conditions for rarefied gases. *International Journal of Heat and Mass Transfer*, *7*(6), 681-694.

Ebert, W. A., & Sparrow, E. M. (1965). Slip flow in rectangular and annular ducts. *Journal of Basic Engineering*, *87*(4), 1018-1024.

Jang, J., & Wereley, S. T. (2004). Pressure distributions of gaseous slip flow in straight and uniform rectangular microchannels. *Microfluidics and Nanofluidics*, *1*(1), 41-51.

Kandlikar, S., Garimella, S., Li, D., Colin, S., & King, M. R. (2014). *Heat transfer and fluid flow in minichannels and microchannels*. elsevier.

Morini, G. L., & Spiga, M. (1998). Slip flow in rectangular microtubes. *Microscale Thermophysical Engineering*, *2*(4), 273-282.

Appendix B

Initial triplet distribution

The spatial and time evolution of the de-excitation of the tracer molecules is very dependent on the actual shape of the initial distribution, as a consequence of the non-linearity given by the TTA process. For extracting the diffusion coefficient, self-quenching rate, and the phosphorescence rate from the experimental data, the proper initial excited molecules distribution must be applied. It is not possible to have a direct measurement of the spatial distribution of the excited molecules. Nevertheless, the concentration of excited molecules is proportional to the laser density energy following the Beer-Lambert law. The only direct measure available for each experimental data set is the total average energy of the laser pulse, but its spatial energy distribution could not be measured. An alternative strategy for estimating the real energy density distribution is through the light distribution recorded 5 ns after the laser pulse excitation. The early part of the de-excitation process is composed by both fluorescence and phosphorescence emission. The resulting very intense light that follows the laser excitation is representative of the axisymmetric laser energy density distribution $I_{in}(x,z)$.

The mathematical description of the diffusion and self-quenching of the excited molecules has been done in polar coordinates because of the axisymmetric feature of the excitation pattern. Nevertheless, the actual laser energy density distribution is not perfectly axisymmetric, nor the initial excited molecule distribution. However, the image acquisition of the emission shows a high symmetric profile with respect to the peak of emission. This observation demonstrates that the hypothesis of axisymmetry of the laser energy density distribution is absolutely reasonable.

The initial condition $n_{T_1}(r, t=0)$ for the differential equation in polar coordinates is a function of the radial position r from the centre of the axisymmetric distribution. However, the intensity profile obtained by the acquired image is the result of the projection of the 2D axisymmetric emission distribution into the CCD plane. Mathematically speaking, the integration along one direction of an axisymmetric function $f(x,z) = f(r)$ is the Abel transform, previously introduced in Eq. (5.64). Therefore, the initial condition $n_{T_1}(r, t=0)$ is found by applying an inverse Abel transform to the 1D intensity profile of the emission 5 ns after the laser pulse. The analytical inverse Abel transform is available only for some special functions, such as the Gaussian or the Lorentzian distribution. In most of the cases of our experimental data, the Gaussian fitting or the Lorentzian fitting provides a good analytical representation of the initial intensity profile. A Gaussian distribution in two dimensions is mathematically expressed as:

$$f(x,z) = a_0 \frac{1}{\sqrt{2\pi}\sigma_x} e^{-\frac{(x-x_0)^2}{2\sigma_x^2}} \frac{1}{\sqrt{2\pi}\sigma_z} e^{-\frac{(z-z_0)^2}{2\sigma_z^2}}, \tag{B.1}$$

where σ_x^2 is the variance of the distribution in the *x*-direction, σ_z^2 is the variance of the distribution in the *z*-direction, a_0 is the intensity of the distribution, and (x_0, z_0) is the centre of the distribution. If the Gaussian distribution is axisymmetric, the variance in the directions are equal, thus $\sigma_x^2 = \sigma_z^2 = \sigma_r^2$ and the distribution function becomes:

$$f(x,y) = f(r) = \frac{a_0}{2\pi\sigma_r^2} e^{-\frac{r^2}{2\sigma_r^2}}, \tag{B.2}$$

where $r^2 = (x - x_0)^2 + (z - z_0)^2$ is the radial coordinate from the centre of the distribution. A very important and useful property of the axisymmetric Gaussian distribution is that its integration along one direction, for instance the *z*-direction, provides again a Gaussian distribution characterised by the same variance σ_r^2 of Eq. (B.2):

$$\int_{-\infty}^{+\infty} \frac{a_0}{2\pi\sigma_r^2} e^{-\frac{(x-x_0)^2+(z-z_0)^2}{2\sigma_r^2}} dz = \frac{a_0}{\sqrt{2\pi}\sigma_r} e^{-\frac{(x-x_0)^2}{2\sigma_r^2}}. \tag{B.3}$$

Most of the time, the Gaussian fitting describes well the initial intensity profile of our experimental data, as in the example shown in Figure B.1.

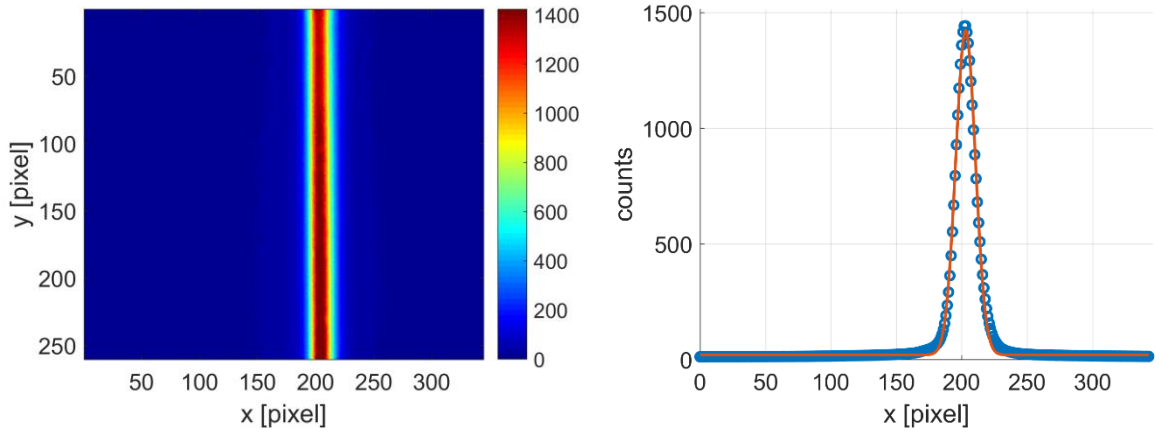

(a) (b)

Figure B.1. Example of raw image and Gaussian intensity profile; (a) phosphorescence emission of pure diacetyl 5 ns after the laser excitation at 1.74 kPa for $N_l = 100$, $N_i = 10$, $\Delta t_{gate} = 100$ ns, and $G = 56\%$; (b) Gaussian fitting (red solid line) of the emission profile $\tilde{S}(x,t)$ (O) that results from the averaging along the *y*-direction the image data shown in (a).

Other authors (Mirzaei *et al.*, 2012) found in the Lorentzian fitting a good description of the intensity profile. The Lorentzian function has the following expression:

$$f(x) = \frac{a_0}{\pi\hat{\sigma}^2} \frac{1}{\left(1 + \frac{(x - x_0)^2}{\hat{\sigma}^2}\right)}. \tag{B.4}$$

In Eq. (B.4), the parameter $\hat{\sigma}^2$ is not the variance of the distribution, which is in this case mathematically undefined, but it is the full width at half maximum (FWHM). The analytical expression of the inverse Abel transform of the Lorentzian function is known:

$$f(r) = \frac{a_0}{2\pi\hat{\sigma}^2} \frac{1}{\left(1 + \frac{r^2}{\hat{\sigma}^2}\right)^{3/2}}. \tag{B.5}$$

Thus, using Eq. (B.3) or (B.4) as a fitting function, the shape of the radial distribution of the laser energy density is given by Eq. (B.2) or (B.5), respectively. For our experimental data, the Lorentzian fitting does not represent well the initial intensity emission, while, most of the time, the Gaussian fitting is a quite good approximation of it.

However, there are some cases where neither the Gaussian function nor the Lorentzian function can well represent the initial intensity profile, because, for some reasons, the laser energy density distribution is more complex. For example, Figure B.2 shows a non-Gaussian emission profile provided by diacetyl vapor. The image has been recorded 5 ns after the laser pulses with an excitation wavelength of 410 nm.

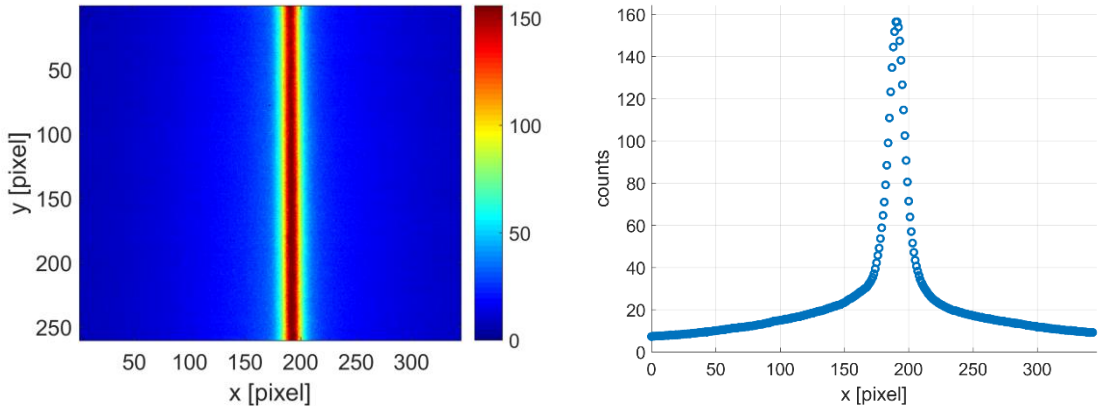

(a) (b)

Figure B.2. Example of raw image and non-Gaussian intensity profile; (a) phosphorescence emission of pure diacetyl 5 ns after the laser excitation at 1 kPa for $N_l = 100$, $N_i = 10$, $\Delta t_{gate} = 100$ ns, and $G = 56\%$; (b) emission profile $\tilde{S}(x,t)$ (O) that results from the averaging along the *y*-direction of the raw image shown in (a).

The laser energy distribution is wider when compared to Figure B.1. The use of a correct spatial energy distribution is of fundamental importance for the success of the mathematical model. For the same total average laser energy, a wider spatial energy distribution determines a longer life of the total emission, since the TTA efficiency is proportional to the excited molecules concentration. The reason behind the more spread energy distribution is due to modifications in the uniformity of the opacity of the access window for the laser beam. It happens that high energy laser pulses can deteriorate in time the uniformity of the transparency of the optical access, so that the laser

energy is diffused and, consequently, the excited molecules distribution, as shown in Figure B.2.

Even though an analytical function that fits well the emission profile of Figure B.2b might exist, the inverse Abel transform of it is usually not known in analytical form, and, thus, a numerical inversion must be considered. However, in this work a novel approach to this eventuality is presented. Every intensity profile can be well fitted by a linear combination of N_g Gaussian functions, namely:

$$f(x) = \sum_{i=1}^{N_g} \frac{a_i}{\sqrt{2\pi}\sigma_i^2} e^{-\frac{(x-x_{0,i})^2}{2\sigma_i^2}}, \tag{5.6}$$

each base function i characterized by its own amplitude a_i, variance σ_i^2, and centre line $x_{0,i}$. Since the fitting function needs to be symmetric as the emission intensity profile, the centre line parameters $x_{0,i}$ must be the same for each Gaussian function of the series. Figure B.3 shows the fitting of the data of Figure B.2b with a linear combination of 3 Gaussian functions. In the same figure, the Gaussian fitting and the Lorentzian fitting is shown for comparison.

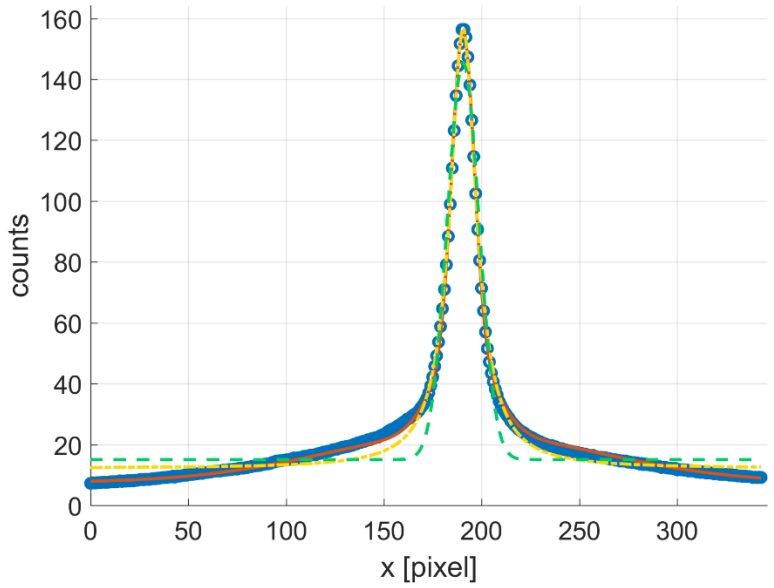

Figure B.3. Fitting of the data of Figure 2b: Gaussian fitting function (- -), Lorentzian fitting function (-.), and fitting function made of a linear combination of 3 Gaussian functions (—) of the initial emission profile (O).

Even though the fitting parameters a_i, σ_i^2, and x_0 of each base function may not have a particular physical meaning, the advantage of such artificial fitting function derives from the property of the axisymmetric Gaussian function described in Eq. (B.3). Indeed, the two-dimensional axisymmetric laser energy density distribution corresponds to the linear combination of the inverse Abel transform of each base function of Eq. (5.6):

$$f(r) = \sum_{i=1}^{N_g} \frac{a_i}{2\pi\sigma_i^2} e^{-\frac{(x-x_0)^2+(y-y_0)^2}{2\sigma_i^2}} = \sum_{i=1}^{N_g} \frac{a_i}{2\pi\sigma_i^2} e^{-\frac{r^2}{2\sigma_i^2}} \tag{B.7}$$

Finally, the laser energy density distribution $I(r)$ used for the experimental condition under consideration is a function of the fitting parameters σ_i^2 and a_i and the total average energy E_l of the laser pulse, which is measured by the power-meter. The relation between the amplitudes a_i and the laser energy E_l is found by integrating $I(r)$ on a cross section of the laser beam:

$$E_l = \int_{-\infty}^{+\infty} \int_{-\infty}^{+\infty} I(x,y)\, dxdy = \int_0^{2\pi} \int_0^{\infty} I(r) r dr d\theta = 2\pi \int_0^{\infty} I_{in}(r) r dr \tag{B.8}$$

In the case of a simple Gaussian fitting, the amplitude parameter a_0 that comes from the fitting of the intensity profile is of none interest. The fitting function is required only to find the shape of the distribution, and the final amplitude parameter is expressed as a function of the total average energy E_l. Thus, assuming as laser energy density distribution:

$$I_{in}(r) = \frac{a_0}{2\pi\sigma_r^2} e^{-\frac{r^2}{2\sigma_r^2}}, \tag{B.9}$$

the amplitude a_0 corresponds exactly to E_l, since:

$$E_l = 2\pi \int_0^{\infty} I_{in}(r) r dr = a_0. \tag{B.10}$$

When the fitting function of Eq. (5.6) is employed, the absolute values of the fitting parameters a_i is not relevant, while their ratios is important to maintain the correct distribution since they measure the weight of each Gaussian function in the series. The laser energy density function can be written in this case as

$$I_{in}(r) = \hat{E} \sum_{i=1}^{N_g} \frac{a_i^*}{2\pi\sigma_i^2} e^{-\frac{r^2}{2\sigma_i^2}}, \tag{B.11}$$

where the coefficients $a_i^* = \frac{a_i}{\bar{a}}$ are the normalization of the amplitudes a_i with $\bar{a} = \sqrt{\sum_{i=1}^{N_g} a_i^2}$. This normalization is arbitrary. The integration of the laser energy density provides the value of $\hat{E}$:

$$E_l = 2\pi \int_0^{\infty} I(r) r dr = 2\pi \int_0^{\infty} \hat{E} \sum_{i=1}^{N_g} \frac{a_i^*}{2\pi\sigma_i^2} e^{-\frac{r^2}{2\sigma_i^2}} r dr = \hat{E} \sum_{i=1}^{N_g} a_i^*. \tag{B.12}$$

Hence, $\hat{E} = E_l / \sum_{i=1}^{N_g} a_i^*$ and the laser energy density can be finally written as function of the laser energy E_l and the fitting parameters σ_i^2 and a_i^*:

$$I_{in}(r) = \frac{E_l}{\sum_{i=1}^{N_g} a_i^*} \sum_{i=1}^{N_g} \frac{a_i^*}{2\pi\sigma_i^2} e^{-\frac{r^2}{2\sigma_i^2}}. \tag{B.13}$$

If only one Gaussian function is used for the fitting, Eq. (B.9) is recovered. Hence, by considering Eq. (B.14), the initial condition for the excited molecule concentration $n_{T_{1,0}}(x, y, z)$ is generally expressed as:

$$n_{T_{1,0}}(x, y, z) = \frac{\sigma_{abs}(\lambda_{ex}, T) n E_l}{E_{ph}} \frac{1}{\sum_{i=1}^{N_g} a_i^*} \sum_{i=1}^{N_g} \frac{a_i^*}{2\pi\sigma_i^2} e^{-\frac{r^2}{2\sigma_i^2}}. \tag{B.14}$$

References

Mirzaei, M., Dam, N. J., & van de Water, W. (2012). Molecular tagging velocimetry in turbulence using biacetyl. *Physical Review E*, *86*(4), 046318.

Appendix C

2D fitting algorithm

As for the TC reconstruction method described in Section 6.1.10, the optimization problem is solved by applying a Gauss-Newton algorithm. By defining as $\boldsymbol{p}_i$ the optimization parameters at the *i*-th iteration, the update $\Delta\boldsymbol{p}_i$ is calculated by solving

$$\boldsymbol{J}(\boldsymbol{p}_i)^{\boldsymbol{T}}\boldsymbol{J}(\boldsymbol{p}_i)\,\Delta\boldsymbol{p}_i = \boldsymbol{J}(\boldsymbol{p}_i)^{\boldsymbol{T}}(\boldsymbol{F} - \boldsymbol{f_{2D}}(\boldsymbol{p_i})), \tag{C.1}$$

where the fitting data vector $\boldsymbol{f_{2D}}(\boldsymbol{p_i}) = \left(f_{2D}(x_1, y_1, \boldsymbol{p}_i), f_{2D}(x_2, y_2, \boldsymbol{p}_i), \dots, f_{2D}\left(x_{Nx}, y_{Ny}, \boldsymbol{p}_i\right)\right)^T$ and the data vector $\boldsymbol{F} = (F_{11}, F_{21}, \dots, F_{NxN_y})$ contain, respectively, the evaluation of the fitting function $f_{2D}(x, y, \boldsymbol{p})$ at the position of each pixel and the image data F_{ij} on each pixel of the image. The Jacobian matrix contains the derivatives of the fitting vector $f_{2D}(x, y, \boldsymbol{p})$ with respect to the fitting parameters $\boldsymbol{p}$, which can be calculated by applying the chain rule:

$$\boldsymbol{J}(\boldsymbol{p}_i) = \frac{\partial \boldsymbol{f_{2D}}}{\partial \boldsymbol{p}}\bigg|_{\boldsymbol{p}_i} = \frac{\partial \boldsymbol{f_{2D}}}{\partial \boldsymbol{a}}\bigg|_{\boldsymbol{a}_i} \frac{\partial \boldsymbol{a}}{\partial \boldsymbol{p}}\bigg|_{\boldsymbol{p}_i}. \tag{C.2}$$

The calculation of the Jacobian matrix $\frac{\partial \boldsymbol{f_{2D}}}{\partial \boldsymbol{a}}\Big|_{\boldsymbol{a}_i}$ can be easily carried out from the analytical expressions of the derivatives of the fitting vector $f_{2D}(x, y, \boldsymbol{a})$ with respect to coefficients $\boldsymbol{a} = (a_1, a_2, a_3, a_4)$, which are:

$$\frac{\partial f_{2D}}{\partial a_1} = 1, \tag{C.3}$$

$$\frac{\partial f_{2D}}{\partial a_2}(x, y) = \frac{1}{\sqrt{2\pi a_3(y)}} e^{-\frac{1}{2}\frac{(x - a_4(y))^2}{a_3(y)}}, \tag{C.4}$$

$$\frac{\partial f_{2D}}{\partial a_3}(x, y) = e^{-\frac{1}{2}\frac{(x - a_4(y))^2}{a_3(y)}} \frac{a_2}{2\sqrt{2\pi a_3}}\left[\frac{(x - a_4)^2}{a_3^2} - \frac{1}{a_3}\right], \tag{C.5}$$

$$\frac{\partial f_{2D}}{\partial a_4}(x, y) = \frac{a_2}{\sqrt{2\pi a_3}} \frac{1}{a_3}(x - a_4) e^{-\frac{1}{2}\frac{(x - a_4)^2}{a_3}}. \tag{C.6}$$

Similarly, the Jacobian matrix $\frac{\partial \boldsymbol{a}}{\partial \boldsymbol{p}}\Big|_{\boldsymbol{p}_i}$ is calculated from the analytical derivatives of coefficients $\boldsymbol{a}$ with respect to the fitting parameters $\boldsymbol{p} = \left(p_{1,1}, p_{2,1}, p_{2,2}, p_{3,1}, p_{3,2}, p_{4,1}, p_{4,2}, p_{4,3}, y_0\right)^T$, that is:

$$\frac{\partial a_1}{\partial \boldsymbol{p}} = [1 \quad 0 \quad 0 \quad 0 \quad 0 \quad 0 \quad 0 \quad 0 \quad 0], \tag{C.7}$$

$$\frac{\partial a_2}{\partial \boldsymbol{p}} = \begin{bmatrix} 0 & 1 & (y-y_0)^2 & 0 & 0 & 0 & 0 & 0 & -2p_{2,2}(y-y_0) \end{bmatrix}, \tag{C.8}$$

$$\frac{\partial a_3}{\partial \boldsymbol{p}} = \begin{bmatrix} 0 & 0 & 0 & 1 & (y-y_0)^2 & 0 & 0 & 0 & -2p_{3,2}(y-y_0) \end{bmatrix}, \tag{C.9}$$

$$\frac{\partial a_4}{\partial \boldsymbol{p}} = \begin{bmatrix} 0 & 0 & 0 & 0 & 0 & 1 & (y-y_0)^2 & (y-y_0)^4 & -2p_{4,2}(y-y_0) - 4p_{4,3}(y-y_0)^3 \end{bmatrix}. \tag{C.10}$$

Since y_0 is among the fitting parameters, the Jacobian matrix $\frac{\partial \boldsymbol{a}}{\partial \boldsymbol{p}}\Big|$ needs to be recalculated at each iteration of the optimization algorithm. Differently, weather y_0 is used as a fitting parameter or not, the Jacobian matrix $\frac{\partial \boldsymbol{f_{2D}}}{\partial \boldsymbol{a}}$ needs to be recalculated as the fitting parameters $\boldsymbol{p}$ varies at each iteration. Because of the local convergence properties of the algorithm, the initial guess $\boldsymbol{p}_0$ needs to be sufficiently close to the solution $\boldsymbol{p}$ that minimizes the objective function defined in Eq. (6.68). The Gaussian fittings per line carried out in the previous post-processing step is used for generating a good initial guess. The data related to the offset, the amplitude, the variance, and the peak position provided by each Gaussian function at each horizontal line of pixels are fitted, respectively, with the functions defined in Eq. (6.64), (6.65), (6.66), and (6.67) for determining a good starting set of parameters $\boldsymbol{p}$.

Appendix D

Displacement data

if the channel height is known a priori by direct measurements, a novel and rigorous post-processing procedure could be adopted for positioning the displacement data in the mathematical domain. The centerline axis $y = 0$, that is the middle point between the two walls, is an axis of symmetry for the displacement profile. The SNR of the tagged molecules emission at the channel centerline is always the highest with respect to other positions along the channel height, because the velocity gradient is null, the wall-triplet deactivation is absent, and the molecular oxygen quenching is the weakest. Therefore, the detection of the position y_{max} of maximum displacement $s_x(y = y_{max}) = s_{x,max}$ (or, equivalently, of the position of the axis of symmetry) is much easier and more accurate than that of the wall positions, where the SNR is the lowest. Once the location y_{max} of the displacement data has been determined, the y coordinate of all the displacement data $s_{x,j}$ is translated of the quantity y_{max}, so that the origin $y = 0$ of the mathematical domain and the axis of symmetry of the displacement data coincide. Because of the inherent statistical fluctuations characterizing the displacement data that result from the Gaussian fitting per line procedure, the identification of y_{max} passes through a 4-th polynomial fitting of the data. Figure D.1a visually illustrates this idea of repositioning the displacement data.

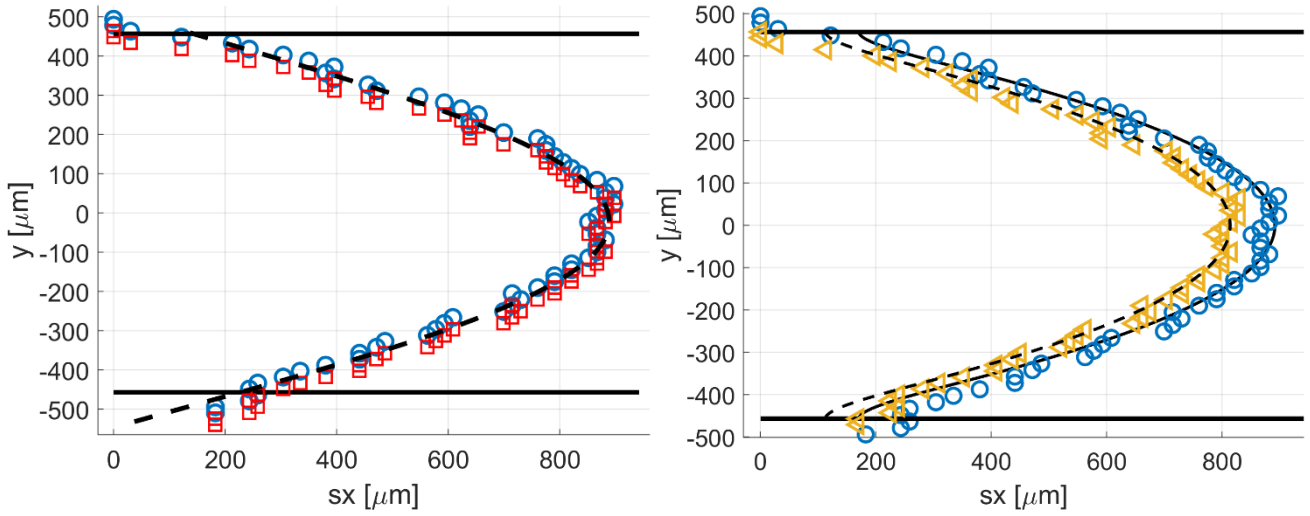

Figure D.1. Illustration of the post-processing procedure for (a) repositioning and (b) rescaling of the displacement data in the mathematical domain: original displacement data (□), centered displacement data (○), and rescaled displacement data (◁). The solid black lines represent the channel walls employed for the numerical reconstruction.

The proposed strategy for positioning the displacement data in the mathematical domain eliminates the problem related to the difficulty of detecting the channel walls. Sometimes the displacement data close to the walls extracted

from the images are very noisy. This is due to the low SNR and the inability to understand if that portion of light is related to tagged molecules, wall re-emission, or wall light reflections. Sometimes these data at the boundaries are, evidently, outliers with respect to the whole data set and are preferably eliminated from the group. As long as the point of maximum displacement is clearly detectable in the set of data, the displacement data can be positioned in the reconstruction domain. Even though the final set of displacement data does not cover all the mathematical domain, the reconstruction method is able in many occasions to provide an accurate velocity measurement.

As previously discussed, the detection of the channel walls on the image is also affected by optical deformations caused by a not perfect orientation of the channel and positioning of the laser beam with respect to the ICCD. These calibration imprecisions make the wall distance appear to be slightly smaller or bigger. The displacement data is affected by the same optical deformation. Even though the strategy above described does not require knowing where the wall lines are exactly on the image, the precise detection of the channel walls is, instead, necessary for determining if the magnification provide by the optics is different from that expected and, thus, for rescaling the displacement data accordingly. This problematic can be solved by a better calibration of the setup, but, unfortunately, it is very difficult to be done with precision. Indeed, there are always imperfections in the setup calibration. If the wall distance H was known, this problematic could be solved in post-processing, by rescaling the displacement data to the real dimension of the height, as illustrated in Figure D.1b. Once the scaling factor has been defined, if all the element of the experimental setup, that is the laser system, the channel, and the ICCD, do not move, the eventual optic deformations remain the same and the same scaling factor needs to be used.

Résumé de la thèse

Au cours des dernières années, les systèmes micro-électro-mécaniques (MEMS) ont connu un intérêt croissant pour leurs propriétés spécifiques liées à leur faible encombrement et pour leurs nombreuses applications dans une grande variété de domaines scientifiques. Notamment pour les systèmes micro-fluidique gazeux, beaucoup d'applications intéressantes ont été récemment développées, telles que les micro-buses (Gomez *et al*., 2016) pour des applications spatiales, les micro-actionneurs (Cattafesta *et al*., 2011) pour des applications aéronautiques et des micropompes Knudsen (An *et al*., 2014). L'intérêt porté à ces microsystèmes a poussé la communauté scientifique à analyser en détail les transferts de chaleur et de masse aux micro-échelles.

La réduction de la taille d'un système caractérisé par des écoulements gazeux amplifie les déséquilibres thermodynamiques, du fait d'un niveau de raréfaction plus élevé. Lorsque le libre parcours moyen λ, à savoir la distance moyenne parcourue par une molécule entre deux collisions successives, est non négligeable devant la longueur caractéristique du système L_c, la dynamique à l'échelle macroscopique est influencée par celle-là à l'échelle moléculaire, suite à une réduction du nombre de collisions intermoléculaires à l'intérieur du volume de contrôle. Le nombre de Knudsen, $Kn = \lambda/L_c$, quantifie alors le niveau de raréfaction du gaz. La majorité des microsystèmes gazeux évolue dans des écoulements en régime de glissement, caractérisé par une valeur de Kn dans la plage $[0.001 - 0.1]$. Le nombre de Knudsen peut se trouver dans cette plage lorsque L_c est suffisamment petit (microcanal) et/ou lorsque λ est suffisamment grand (basse pression). En réalité, à ce niveau de raréfaction, le gaz peut encore être modélisé comme un milieu continu et les équations de Navier-Stokes sont toujours utilisables. Par contre, lorsque des interactions entre le gaz et des surfaces solides sont présentes à l'intérieur du microsystème fluidique, la raréfaction produit localement à la paroi un état de déséquilibre thermodynamique. Malgré que l'effet de raréfaction soit limité à l'intérieur de la couche limite de Knudsen, qui a une épaisseur de l'ordre de λ [4], le déséquilibre thermodynamique local produit une modification de l'écoulement à l'échelle macroscopique sous la forme d'une vitesse de glissement et d'un saut de température à paroi. Par conséquent, même si la représentation continue du fluide est encore valable, les conditions aux limites à la paroi doivent être modifiées pour tenir compte de ces sauts causés par la raréfaction. Dans la littérature, différentes formes de conditions aux limites ont été proposées et toutes introduisent des coefficients d'accommodation qui dépendent du matériau qui constitue la surface solide, de sa rugosité et de la nature du fluide. Leur détermination est difficile et doit être obtenue de manière expérimentale. En outre, les données expérimentales actuellement disponibles dans la littérature sont toutes basées sur des mesures globales de l'écoulement gazeux, à savoir le débit massique, les pressions et les températures à l'amont et à l'aval du canal. La mesure du saut des quantités cinématiques et thermiques à la paroi est ainsi obtenue de manière indirecte. À notre connaissance, il n'y a pas à ce jour dans la littérature de mesures directes de la vitesse de glissement à la paroi.

Dans ce contexte, on a développé une technique de vélocimétrie par marquage moléculaire (MTV) avec pour objectif de mesurer le profil de vitesse à l'intérieur d'un canal de section rectangulaire dans des conditions de gaz raréfié. Le but est de mesurer de manière directe la vitesse de glissement aux parois du canal, pour un écoulement généré par différence de pression.

Pour atteindre la raréfaction souhaitée dans notre canal, on peut soit réduire sa profondeur, soit baisser la pression de l'écoulement gazeux. Comme pour des raisons technologiques la taille minimale du diamètre du faisceau laser est limitée à peu près 30 μm, on ne peut pas trop réduire la taille du canal pour conserver une résolution spatiale raisonnable et on est alors obligé de baisser la pression moyenne de l'écoulement pour atteindre le régime de glissement. En utilisant un canal d'1 mm de profondeur, on a besoin de baisser la pression du mélange gazeux à un niveau de l'ordre de 1000 Pa si l'on désire avoir des vitesses de glissement à paroi assez élevés pour être mesurables. Malheureusement, cette diminution de pression conduit à une réduction de la densité moléculaire du traceur et à une augmentation de la diffusion ayant pour effet une diminution considérable de l'intensité et de la durée exploitable du signal de phosphorescence. C'est pour cela qu'une analyse plus approfondie de la dépendance de la durée de vie et de l'intensité de la phosphorescence en fonction de la pression est nécessaire afin de trouver les conditions optimales pour appliquer la MTV aux cas d'écoulements gazeux raréfiés dans un canal.

Une première campagne expérimentale a été dédiée à l'investigation des phénomènes photo-physiques à basses pressions des traceurs d'intérêt, c'est-à-dire l'acétone et le diacètyle vapeurs. Dans le Chapitre 5 de ce manuscrit, une analyse très détaillée des phénomènes intramoléculaires qui ont lieu suite à l'excitation laser est présentée. Les résultats sur l'émission phosphorescente générée par l'acétone lors d'une excitation laser à 266 nm démontrent que cette longueur d'onde ne donne pas un signal lumineux assez durable pour l'application de la MTV à les conditions de pression d'intérêt. Pour cette raison, une étude sur les effets de la longueur d'onde d'excitation sur le temps de vie de la phosphorescence de l'acétone et du diacétyle a été mené. Cette analyse expérimentale a démontré que l'émission lumineuse peut être maximisée si une excitation laser à 310 nm et 410 nm sont utilisées, respectivement, pour l'acétone et le diacétyle. Dans ces conditions, soit l'acétone soit le diacètyle peuvent produire un signal lumineux assez intense et durable dans des mélanges avec des pressions moyennes de l'ordre de 1 kPa, ce qui rendre possible l'application de la MTV à des écoulements gazeux en régime de glissement.

Les résultats expérimentaux sur l'émission phosphorescente donnés par cette première campagne expérimentale ont été aussi exploités pour faire des mesures quantitatives des propriétés kinétiques et photo-physiques de l'acétone et du diacètyle. En fait, la comparaison des observations expérimentales de ce travail avec la littérature a dévoilé l'existence d'un processus intramoléculaire d'auto-quenching dénommé triplet-triplet annihilation (TTA) qui déterminent une décroissance non-exponentielle de l'émission phosphorescente au cours du temps. En particulier, un modèle mathématique qui tienne en compte des processus de de-excitation radiative et non-radiative plus importantes a été développé et a été utilisé pour extraire quantitativement le coefficient de rapidité d'auto-

quenching TTA et le coefficient d'autodiffusion moléculaire. Les mesures expérimentales du coefficient de diffusion à différentes pressions ont aussi permis d'estimer le diamètre kinétique du traceur à travers la théorie kinétique des gaz. En fait, les valeurs du diamètre moléculaire pour la molécule d'acétone et de diacètyle trouvées en littérature sont vraiment peu et il n'y a évidemment pas un accord entre les différents auteurs. Dans le contexte de la MTV, la possibilité d'avoir des estimations précises du coefficient de diffusion ou du diamètre kinétique du traceur moléculaire est essentiel soit pour avoir des études numériques qui bien simulent la diffusion du tracer dans un canal soit pour pouvoir extraire correctement le profil de vitesse de mesures expérimentales de déplacement obtenues par MTV.

Après avoir déterminer la longueur d'onde d'excitation et les conditions thermodynamiques optimales pour l'application de la MTV au cas d'écoulement gazeux raréfiés, une étude numérique a été mené pour vérifier que la résolution de la caméra CCD utilisée dans ce travail était suffisante pour correctement mesurer les profils de déplacement du traceur attendus dans cette conditions expérimentales. Des simulations directes de Monte Carlo (DSMC) ont été menées pour analyser les effets de la diffusion moléculaire des molécules traceuse marquées dans l'écoulement porteur. La diffusion moléculaire du traceur en combinaison avec les forts gradients de vitesse à paroi produit une distorsion de la ligne des molécules traceuse marquées qui empêche d'extraire le profil de vitesse à travers une simple transformation homothétique du profile de déplacements. Autrement dit, la vitesse du gaz ne peut pas être calculée simplement en divisant le déplacement du traceur marqué par le temps qui passe entre la position initiale et la position finale du traceur. Ce mécanisme combiné d'advection et de diffusion qui déforme le profil de déplacement est connu en littérature comme dispersion de Taylor. Dans ce cadre, Frezzotti *et al*. (2015) ont développé un algorithme numérique qui permet de reconstruire le profil de vitesse en prenant en compte soit l'advection soit la diffusion moléculaire du traceur. L'application de la méthode de reconstruction aux résultats numériques donnés par la DSMC a démontré que c'est possible d'extraire le profil de vitesse avec précision. Par contre, la réussite de la méthode de reconstruction développée par Frezzotti *et al*. (2015) dépende de la précision de l'estimation du coefficient de diffusion. Toutefois, le coefficient de diffusion est connu avec haute précision dans le cas des simulations DSMC, mais dans les cas des mesures expérimentales données par la MTV le coefficient de diffusion peut être seulement estimé en manière indirecte par des mesures de pressions et température et des valeurs de viscosité dynamique et du diamètre kinétique de molécules. Par conséquence, les incertitudes sur le coefficient de diffusion sont assez élevées, ce qui produisent des erreurs extrêmement élevées sur la vitesse reconstruite à paroi. Pour cette raison, dans ce travail de thèse, la méthode de reconstruction originalement développée par Frezzotti *et al.* (2015) a été modifiée dans la méthode de reconstruction avec corrélations en temps. Cette nouvelle version de la méthode de reconstruction, décrit au Chapitre 6 de ce manuscrit, permet d'extraire simultanément le profil de vitesse et le coefficient de diffusion à partir de plusieurs profils de déplacement correspondants à différent temps par rapport au moment de l'excitation laser. La méthode de reconstruction avec corrélations en temps a été appliquées à des expérimentes numériques générées par DSMC en

démontrant que le profil de vitesse et le coefficient de diffusion peuvent être simultanément extraits avec hautes précision.

Ensuite, un nouveau circuit de gaz capable de générer des écoulements de mélange gazeux et qui implémente la MTV aux cas des écoulements à basses pressions a été conçu et construit lors de cette travail de thèse. La difficulté de pouvoir avoir un système de gaz sans fuite en boucle fermé pour générer les conditions expérimentales d'intérêt a mené à la conception d'un système en cycle ouvert. Ce système, décrit au Chapitre 4 de ce manuscrit, permet de créer une mixture de gaz et vapeur, acétone ou diacètyle, en manière contrôlée dans un grand volume en amont du canal de test. En aval du canal, un système de pompage force la mixture gazeux dans les réservoirs à passer à travers le canal. La dimension du réservoir en amont a été choisie la plus grande possible afin de rendre les conditions thermodynamiques de l'écoulement dans le canal les plus stables possibles pendant les acquisitions MTV. Une comparaison entre les temps nécessaires pour mener des acquisitions MTV avec les temps caractéristiques de variation de la pression à l'amont et en aval du canal a démontré que le banc expérimental conçu est capable de maintenir les conditions thermodynamiques de l'écoulement pour un temps assez long. Malgré la non-stationnarité de l'écoulement introduit certaines complications expérimentales, cette condition se représente comme un avantage pour l'implémentation d'une deuxième technique expérimentale, dit à volumes constantes, pour mener des mesures de débit massique dans le canal. Cette technique associe la variation au cours de temps de la pression dans les réservoirs à l'amont et/ou en aval à la quantité de masse de gaz qui passe à travers le canal.

En fin, la MTV et la technique à volumes constantes ont été appliquées à des écoulements d'argon-acétone et hélium-acétone à basses pressions. Ces résultats expérimentaux sont présentés dans le Chapitre 6 de ce manuscrit et représentent les premières images jamais produites dans écoulement gazeux dans un canal millimétrique à des pressions entre 40 kPa et 1 kPa. Les images montrent clairement les effets de la dispersion de Taylor sur la distribution des molécules d'acétone marquées par l'excitation laser. Les nombres de Knudsen les plus élevées investiguées dans ce travail avec la MTV sont de l'ordre de 10^{-3}, des valeurs qui représentent un régime faiblement raréfié mais quand même dans le régime de glissement.

En appliquant la méthode de reconstruction de Frezzotti *et* al. (2015) aux données expérimentales de la MTV relatives au cas d'écoulement d'argon-acétone à des pressions de l'ordre de 40 kPa, des profils de vitesse corrects sont obtenus, avec des vitesses de glissement nulles comme attendu. Par contre, l'application de la méthode de reconstruction à des écoulement à plus basses pressions, qui sont caractérisées par une forte dispersion de Taylor, produit des profils de vitesse qui ne sont pas corrects. Plus précisément, la vitesse moyenne du profil reconstruit est comparable à la vitesse moyenne estimée par la technique à volumes constantes, mais la vitesse de glissement à paroi obtenue n'est pas tout à fais avec le bon ordre de grandeur attendu. Toutefois, la nouvelle méthode de reconstruction basée sur une corrélation temporelle de plusieurs images MTV est capable d'extraire un profil de

vitesse qui est caractérisée par une vitesse de glissement à paroi qui est de le bon ordre de grandeur. Ces résultats préliminaires sont les premières mesures directes de la vitesse de glissement à paroi jamais menées jusqu'à maintenant.

Références

An, S., Gupta, N. K., Gianchandani, Y. B. (2014). A Si-micromachined 162-stage two part Knudsen pump for on-chip vacuum. *Journal of Microelectromechanical Systems*, 23(2), 406-416.

Cattafesta, L. N., & Sheplak, M. (2011). Actuators for active flow control. *Annual Review of Fluid Mechanics*, 43, 247-272.

Frezzotti, A., Mohand, H. S. H., Barrot, C., & Colin, S. (2015). Role of diffusion on molecular tagging velocimetry technique for rarefied gas flow analysis. *Microfluidics and Nanofluidics*, 19(6), 1335-1348.

Gomez, J., & Groll, R. (2016). Pressure drop and thrust predictions for transonic micronozzle flows. *Physics of Fluids*, 28(2), 022008.